ISSN: 1411-9420 (print) 2460-1578 (online)

Indonesian Journal of Chemistry

Vol. 21, No. 6, December 2021

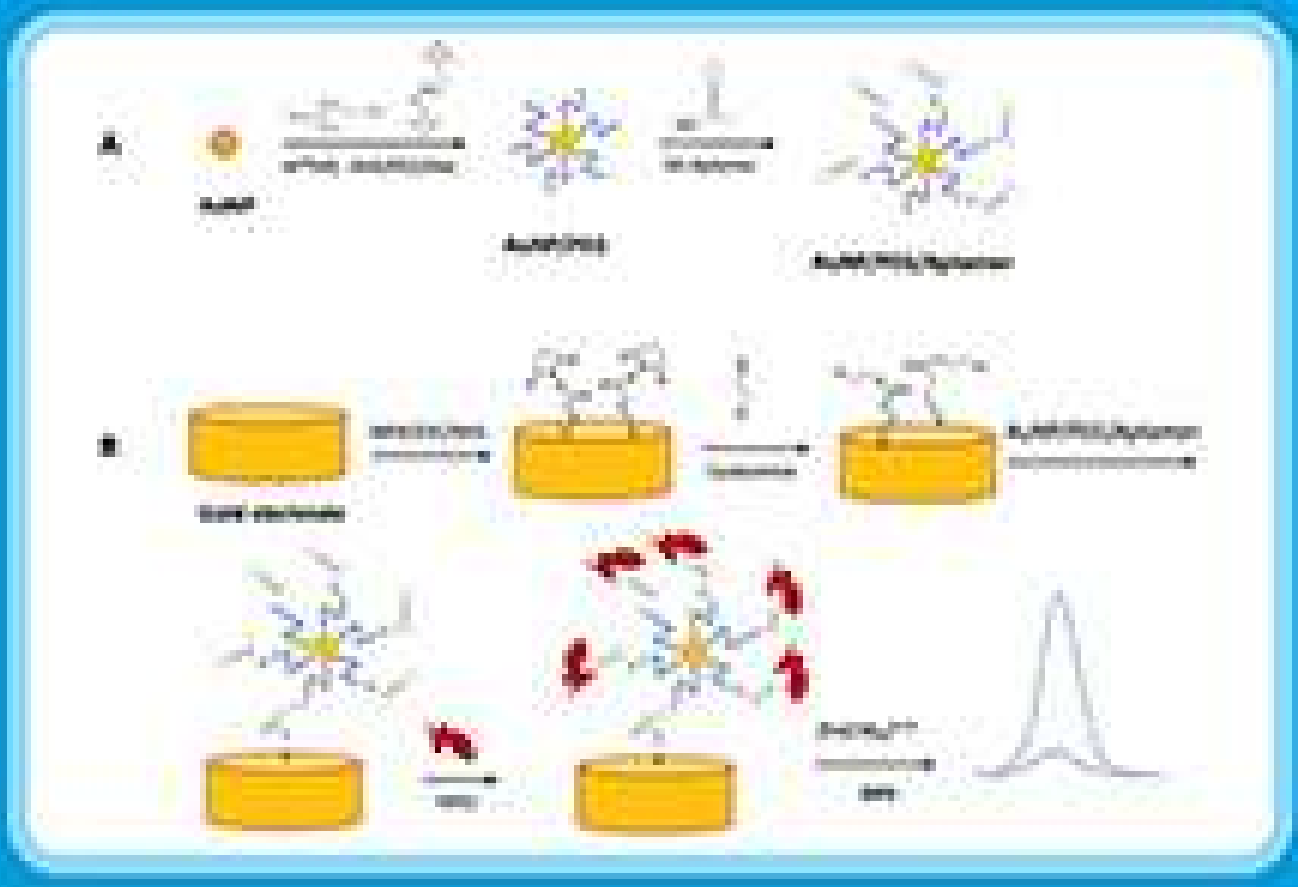

Accredited by RISTEKDIKTI
No. 30/E/KPT/2019

Synthesis of Symmetrical Acetophenone Azine Derivatives as Colorimetric and Fluorescent Cyanide Chemosensors

Nur Masyittah Irmi, Bambang Purwono*, and Chairil Anwar

Department of Chemistry, Faculty Mathematics and Natural Science, Universitas Gadjah Mada, Sekip Utara, PO BOX BLS 21, Yogyakarta 55281, Indonesia

* ***Corresponding author:***

email: purwono.bambang@ugm.ac.id

Received: March 1, 2021
Accepted: October 17, 2021

DOI: 10.22146/ijc.64428

Abstract: *Cyanide is a highly toxic anion and poison to the environment. Therefore, fast, effective, and efficient analysis methods to detect cyanide are needed. Herein, symmetrical chemosensor of 2'-hydroxy acetophenone azine (**1**) and 2',4'-dihydroxy acetophenone azine (**2**) has been synthesized tested as colorimetric and fluorescent cyanide chemosensor. The azines were produced from the condensation of acetophenone derivatives with hydrazine hydrate in ethanol under reflux or ultrasonic irradiation methods. Colorimetric and fluorescent chemosensor tests showed selectivity to acetate and cyanide anions in DMSO. The limit of detection (LOD) for colorimetric measurement of cyanide anion was 9.68×10^{-4} M for compound (**1**) and 9.63×10^{-5} M for compound (**2**), while the fluorescent method showed 15.90×10^{-4} M for compound (**1**) and 8.95×10^{-5} M for compound (**2**), respectively. In addition, test paper-strips containing sensor **2** indicated noticeable results for 'naked eye' detection of cyanide in an aqueous medium.*

Keywords: *acetophenone; azine; colorimetry; fluorescents; cyanide*

■ INTRODUCTION

Cyanide is a toxic anion that can affect the function of organ systems such as the vascular system, the sense of sight, central nervous system, heart, endocrine, and metabolic systems [1]. When cyanide ion enters the bloodstream, it disrupts the electron transport chain leading to cytotoxic hypoxia and death [2]. A small dose of cyanide ion around 0.5–3.5 mg of each kg body weight can cause death [3]. According to WHO, the cyanide detection limit in drinking waters is 0.07 mg per liter or about 2.69×10^{-6} M [4].

Cyanide is widely used in industries such as gold mining, electroplating, metallurgy, and polymer productions. These industries produced 140,000 tons of waste per year [5]. Cyanide also occurs naturally as cyanogen glycosides in at least 2,000 types of plants, including apple, mango seeds, and several essential crops such as almonds, cassava, cherries, corn, cotton, and potatoes. Cyanide is also found in cigarette smoke, incomplete combustion of nitrogen-containing compounds from a vehicle, reaction of coke, coal, and limestone [6]. Therefore, detection of cyanide is essential. Some techniques such as chromatography [7], atomic absorption spectrometry [8], and electrochemical [9] have been used to detect cyanide anion. Nowadays, colorimetric and fluorescence chemosensors are attracting much attention because of low cost, high selectivity, simplicity, sensitivity, and fast recognition in real-time circumstances [10].

Some organic molecules containing amide, pyrrole, thiourea, and phenol groups can be used as cyanide chemosensors. Detections involve the formation of hydrogen bonding or deprotonation between cyanide and chemosensors. For example, Azine derivatives bearing hydroxyl group have been used as colorimetric and fluorescent chemosensors [1,5,11-13]. Most azine chemosensors were produced from aryl benzaldehydes and hydrazine hydrates as starting materials under reflux condition [14-16]. This paper reports the synthesis of symmetrical azine **1** and **2** from acetophenone derivatives and hydrazine hydrate (Scheme 1). The azines were then applied as colorimetric and fluorescent chemosensors for cyanide anion.

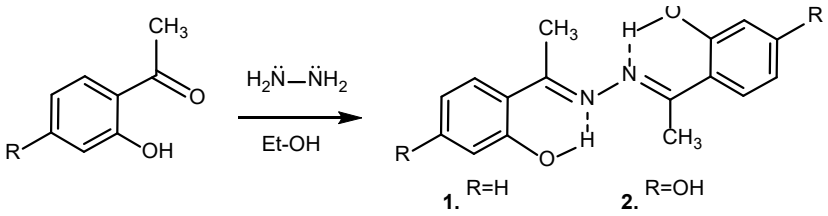

Scheme 1. Synthesis targeted compounds **1** and **2**

■ EXPERIMENTAL SECTION

Materials

The materials used in this study were hydrazine hydrate 80%, 2'-hydroxy acetophenone, 2',4'-dihydroxy acetophenone, sodium fluoride, sodium chloride, sodium bromide, sodium iodide, sodium cyanide, sodium acetate, sodium hydroxide and hydrochloric acid 37%, acetone, acetonitrile, dimethyl sulfoxide, ethanol, and distilled water. All chemicals used in this study were purchased from E. Merck with p.a. quality, while distilled water is obtained from the Organic Chemistry Laboratory of FMIPA-UGM.

Instrumentation

The equipment used in the experiment were laboratory glassware, hot plate, magnetic stirrer, thermometer 100 °C, Buchner filter, analytical scales (Libror EB-330 Shimadzu), and ultrasonic irradiation (Ultrasonic Branson 43 KHz, 43 Watts). The structure elucidation used FT-IR (Shimadzu Prestige-21), GC-MS (Shimadzu QP2010S), and ^{1}H-NMR and ^{13}C-NMR (JEOL JNM ECA-500, 500 MHz). The colorimetric study used UV-Vis Spectrophotometer (Shimadzu UV-1800), and the fluorescents study used Spectrofluorometer (Shimadzu RF-6000). The melting point was measured using uncorrected Electrothermal-9100.

Procedure

Synthesis of acetophenone azine

Acetophenone azines were synthesized based on the previous report with some modifications [16]. First, acetophenone derivative (10 mmol) was dissolved in 10 mL of absolute ethanol, then 0.25 mL (5 mmol) of hydrazine hydrate (80%) was added dropwise under stirring conditions. The solution was then heated under reflux for 2 h until a yellow precipitate formed. The stirring was continued at room temperature overnight. The residue was filtered and washed with cold ethanol and then dried. The solid was then determined its melting point, and the structures were elucidated by FTIR, GC-MS, and ^{1}H- and ^{13}C-NMR. A similar procedure was also carried out through ultrasonic irradiation methods at room temperature for 1 h.

Compound of 2'-hydroxy acetophenone azine (**1**) was obtained as a yellow solid in 73.13% yield for reflux method and 88.80% yield for ultrasonic irradiation methods (m.p. 197–198 °C, literature 197–198 °C [17]). IR (KBr cm^{-1}): 3448 (O–H), 1604 (C=N), 1496 and 1442 (C=C aromatic), 1356 (–CH_3), and 840 (Ar–**C**–CH_3); ^{1}H-NMR ($CDCl_3$): δ 2.56 (s, 6H), 6.93 (t.d, J = 8.4, 1.3 Hz, 2H), 7.02 (d.d, J = 8.3, 1.2 Hz, 2H), 7.36 (t.d, J = 8.6, 1.6 Hz, 2H), 7.63 (d.d, J = 8.1, 1.6 Hz), and 13.26 (s, 2H); ^{13}C-NMR ($CDCl_3$): δ 14.96, 118.01, 119.09, 119.14, 129.06, 133.00, 160.69, and 168.19. Mass spectra (m/z): 268 (M^+).

Compound of 2',4'-dihydroxy acetophenone azine (**2**) was obtained as a pale-yellow solid in 68% yields from reflux method, and 82.67% yields from ultrasonic irradiation methods (m.p. 271–272 °C, literature 269–270 [18]). IR (KBr cm^{-1}): 3417 (O–H), 1604 (C=N), 1504 and 1442 (C=C aromatic), 1357 (–CH_3), and 833 (Ar–**C**–CH_3); ^{1}H-NMR (DMSO): δ 2.41 (s, 6H), 6.27 (d, J = 2.5 Hz, 2H), 6.35 (d.d, J = 8.8, 2.5 Hz, 2H), 7.56 (d, J = 8.9, 2H), 10.12 (s, 2H), and 13.55 (s, 2H); ^{13}C-NMR (DMSO): δ 14.48, 103.42, 108.15, 111.84, 131.69, 162.16, 162.63, and 167.54. Mass spectra (m/z): 300 (M^+).

Solvatochromic effect on sensor compounds

Compounds **1** and **2** were dissolved in acetone, acetonitrile, DMSO, and ethanol, respectively, in a concentration of 10^{-3} M. Color of the solutions was observed and then measured with a UV-Vis spectrophotometer at a concentration of 5×10^{-5} M for **1** and 2×10^{-5} M for **2**.

Acid-base effect on sensor compounds

Color changes of solution (**1** and **2**) were observed after dropping 1 mL of HCl or NaOH 10% (w/v) into each sensor solution (5×10^{-5} M for **1** and 2×10^{-5} M for **2**) in DMSO for a total volume of 10 mL. The color of the solution was observed and then measured with a UV-Vis spectrophotometer. Distilled water (1 mL) was used as a reference solution.

Ionic effect on sensor compounds

Sodium salt solutions of NaF, NaCl, NaBr, NaI, NaCN, and CH_3COONa were prepared with a concentration of 1 M in distilled water. The 1 mL of sodium salt solution was added into solution **1** (5×10^{-5} M) and solution **2** (2×10^{-5} M) to a total volume of 10 mL. The color of the solution was observed and then measured with a UV-Vis spectrophotometer and spectrofluorometer.

Limit of detection for cyanide anion

The limit of detection was carried out by adding 1 mL of various concentrations of NaCN (10^{-4}–10^{-1} M) into solution **1** (5×10^{-5} M) and **2** (2×10^{-5} M) to a total volume of 10 mL. The spectra were measured using a UV-Vis spectrophotometer and spectrofluorometer. Then, a calibration curve was plotted cyanide concentration vs. absorbance correlation. The limit of detection (LOD) values were determined by the 3σ/m equation, where σ is the standard deviation and m is the slope of the calibration curve [19].

Interaction study between sensor compounds and cyanide

The interaction between sensor compounds and cyanide anion was determined by measuring Job's plot curve [20]. The concentration of sensor solution was 5×10^{-5} M for compound **1** and 2×10^{-5} M for compound **2** in DMSO, and a standard solution of NaCN 1 M was used to make a fraction of 0.1–0.9 into sensor solutions. Then the absorbance was measured using a UV-Vis spectrophotometer. The curve was plotted as the mole fraction of cyanide vs. the absorbance. Finally, the ^{1}H-NMR titration was conducted from a mixture of **2** and cyanide solutions in DMSO-d6.

Paper-strip sensor

Paper-strip sensor was carried out by immobilizing compounds **1** and **2** (1×10^{-3} M in DMSO) to filter paper (Whatman no. 42 - 1×3 cm) for 2 h and then dried using an oven. The test was conducted by dropping 2–3 drops of cyanide anion solution to the paper-strip sensor. The color change of paper-strip was observed directly and under a 365 nm UV lamp. As a negative control, distilled water was dropped on a paper-strip sensor.

■ RESULTS AND DISCUSSION

Solvatochromic Effect on Compounds 1 and 2

The solvatochromic test was carried out by dissolving compounds **1** and **2** in several solvents of acetone, acetonitrile, ethanol, and DMSO. The optical color change and UV-Vis spectra are shown in Fig. 1.

The different colors of sensor solution in various solvents were observed. Compound **1** showed colorlessness, while compound **2** showed a brighter yellow color in ethanol and DMSO (Fig. 1(a, b)). From UV-Vis spectra (Fig. 1(c)), compound **1** gave two absorption peaks at λ_{max} of 294, 290, 296, and 292 nm and the second peak at λ_{max} of 362, 354, 360, and 360 nm for acetone, acetonitrile, DMSO, and ethanol solvent respectively. Thus, the absorption peak of compound **1** solutions was at adjacent λ_{max}. These data indicated that the effect of solvent polarity is small for the color changes. From Fig. 1(d), compound **2** exhibits one λ_{max} at 378 nm in DMSO. Two absorption peaks were observed from acetone, acetonitrile, and ethanol solvents, respectively. One low peak was around λ_{max} at 300 nm and a peak at λ_{max} at 370, 368, 374 nm for acetone, acetonitrile, and ethanol solvent, respectively. These data also indicated that the effect of solvent polarity is small for the color changes. However, compound **2** in DMSO and ethanol still provided shoulder absorption at λ_{max} of the visible area.

Effect of Acid-Base Addition on Sensor Compounds

Strong acid and base addition were applied into sensor solutions by adding HCl 10% or NaOH 10%. As shown in Fig. 2, the color of solutions **1** and **2** was unchanged after adding HCl 10%. However, the addition of NaOH 10% caused the color change from colorless to a very light yellow for compound **1** and yellow for compound **2**.

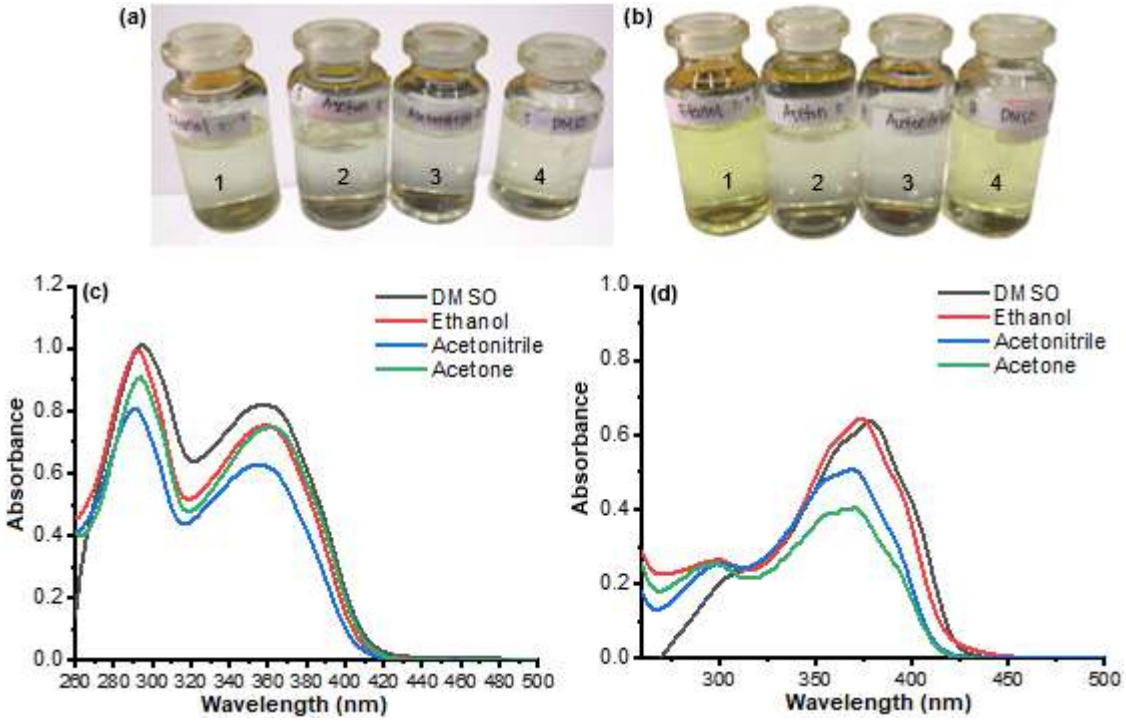

Fig 1. Optical color of (a) compound **1** and (b) **2** with a concentration of 10^{-3} M changes in (1) ethanol, (2) acetone, (3) acetonitrile, and (4) DMSO and UV-Vis absorption spectra of (c) compound **1** (5×10^{-5} M) and (d) **2** (2×10^{-5} M) in various solvents

The yellow color was obtained because the addition of bases can deprotonate the pH-sensitive groups [21]. Deprotonation of the H atom on hydroxyl group of compound **2** produced phenoxide ion and followed delocalization of electrons. Compound **2** has a more probable resonance structure than compound **1**. More resonance structures will create a distinct color change in the solution [22]. Therefore, compound **2** has stronger yellow color than compound **1**. The light-yellow color of compound **1** is produced from compound **1** with cyanide anion via hydrogen bonding formation, not deprotonation.

The color change of compounds **1** and **2** on the acid-base addition supported UV-vis spectra shown in Fig. 3. The addition of HCl to compound **1** causes a shift of two absorption peaks at λ_{max} of 296 and 360 nm into a peak at λ_{max} of 324 nm. The addition of NaOH produced a shift of λ_{max} from 296 and 360 nm to 266 and 354 nm. Both additions of acid and base did not create a bathochromic shift, so no color change was observed.

For compound **2**, the addition of HCl causes a shift

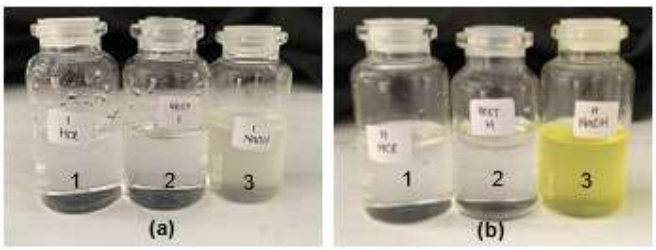

Fig 2. The color of solutions (a) compound **1** (5×10^{-5} M) and (b) compound **2** (2×10^{-5} M) in DMSO changes after addition (1) HCl 10%, (2) H_2O, and (3) NaOH 10%

of λ_{max} of 378 nm to two absorption peaks at λ_{max} of 280 and 316 nm. The addition of NaOH produced a change of λ_{max} on 378 nm to 272 nm and appearance shoulder peak at λ_{max} > 400 nm. The shoulder peak at λ_{max} > 400 nm supported a yellow color formation after the addition of NaOH.

Ionic Effect on Sensor Compounds

The ionic effect was carried out by anion addition into sensor solutions. The color change after addition 1 mL of 1 M sodium salt from NaF, NaCl, NaBr, NaI,

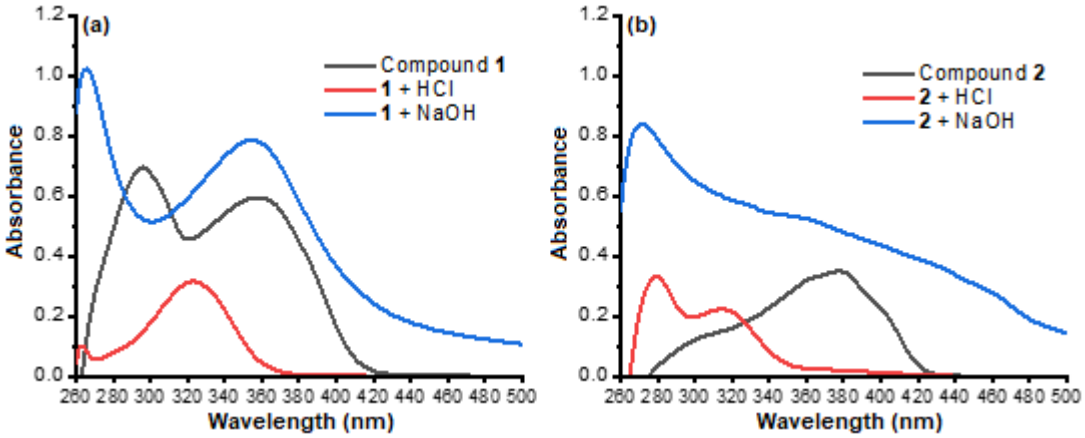

Fig 3. UV-Vis absorption spectra of (a) compound **1** (5×10^{-5} M) and (b) compound **2** (2×10^{-5} M) in DMSO after addition of HCl 10% and NaOH 10%

NaCN, NaOAc, and a mixture of all salts is shown in Fig. 4. Adding Cl^-, Br^- and I^- anion into compounds **1** and **2** did not produce a color change. The color change to yellow and cloudy was observed after addition F^- into compound **2**, while compound **1** was only cloudy with no color change. A significant color change was observed when CN^- anion was added to a solution of compounds **1** and **2**. The addition of AcO^- gave a significant intense yellow color change for compound **2**. The addition of a mixture of all anions into compounds **1** and **2** caused the color change to a slightly yellowish color for compound **1** and a significant yellow color change for compound **2**. These color changes indicated that there is no anion interference from those anions.

The color changes after the addition of anions were supported by the UV-Vis spectra shown in Fig. 5. The addition of Cl^-, Br^-, I^-, AcO^- to **1** did not give new absorption peaks in the visible light region. CN^- and the mixture of all anions increased absorbance at λ 420–440 nm. The addition of Cl^-, Br^- and I^- into the solution of **2** did not produce a change in λ_{max}. The λ_{max} shift toward visible light (about 430 nm) occurred when AcO^-, CN^- and the mixture of all anions was added into a solution of **2**.

The addition of F^- into compounds **1** and **2** caused the color of solutions to become cloudy, making good UV-VIS spectra impossible. The formation of cloudiness is due to a strong hydrogen bond formed

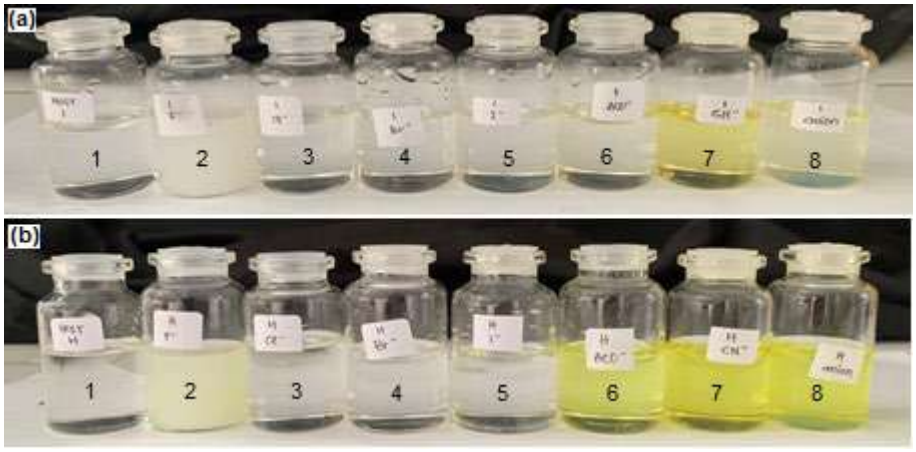

Fig 4. Color of solutions (a) compound **1** (5×10^{-5} M) and (b) compound **2** (2×10^{-5} M) in DMSO changes after addition (1) H_2O, 2) F^-, (3) Cl^-, (4) Br^-, (5) I^-, (6) AcO^-, (7) CN^-, and (8) mixture of all anions

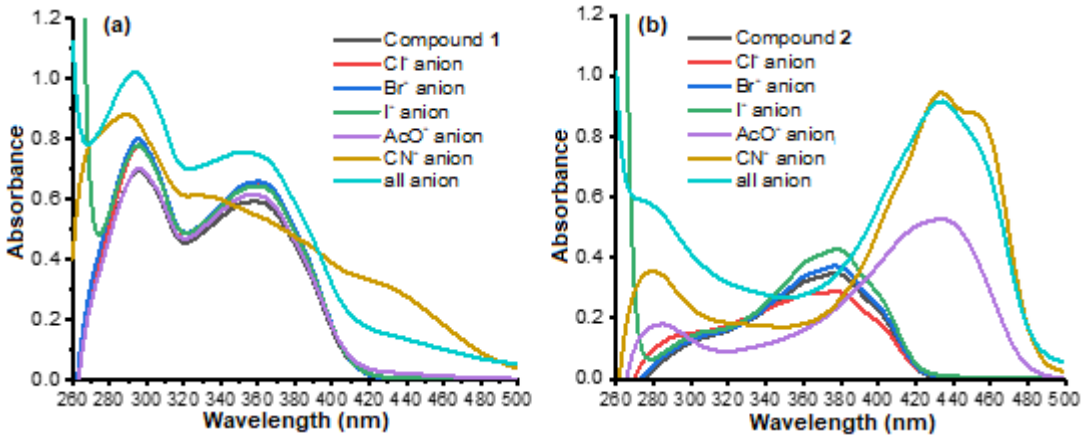

Fig 5. UV-Vis absorption spectra of (a) compound **1** (5×10^{-5} M) and (b) compound **2** (2×10^{-5} M) in DMSO after addition of anions

between F^- and water and may decrease anion solubility in DMSO.

Fluorescence properties were observed with a 365 nm UV light (Fig. 6). Both compounds **1** and **2** did not exhibit fluorescence. The addition of all tested anions showed the fluorescence intensities of compound **1**, while compound **2** did not give fluorescence with the addition of iodide ion only (Fig.6(a, b)).

The fluorescents changes were supported by emission spectra shown in Fig. 6(c) and d. In addition, CN^- anion gives a high-intensity emission for both compounds **1** and **2**. Excitation of compound **1** occurs at λ 335 nm with the highest emissions at λ_{max} around 400–450 nm, while compound **2** excites at λ_{max} 415 nm with the highest emission at 500–530 nm. The increasing fluorescents intensity of sensor solutions after addition

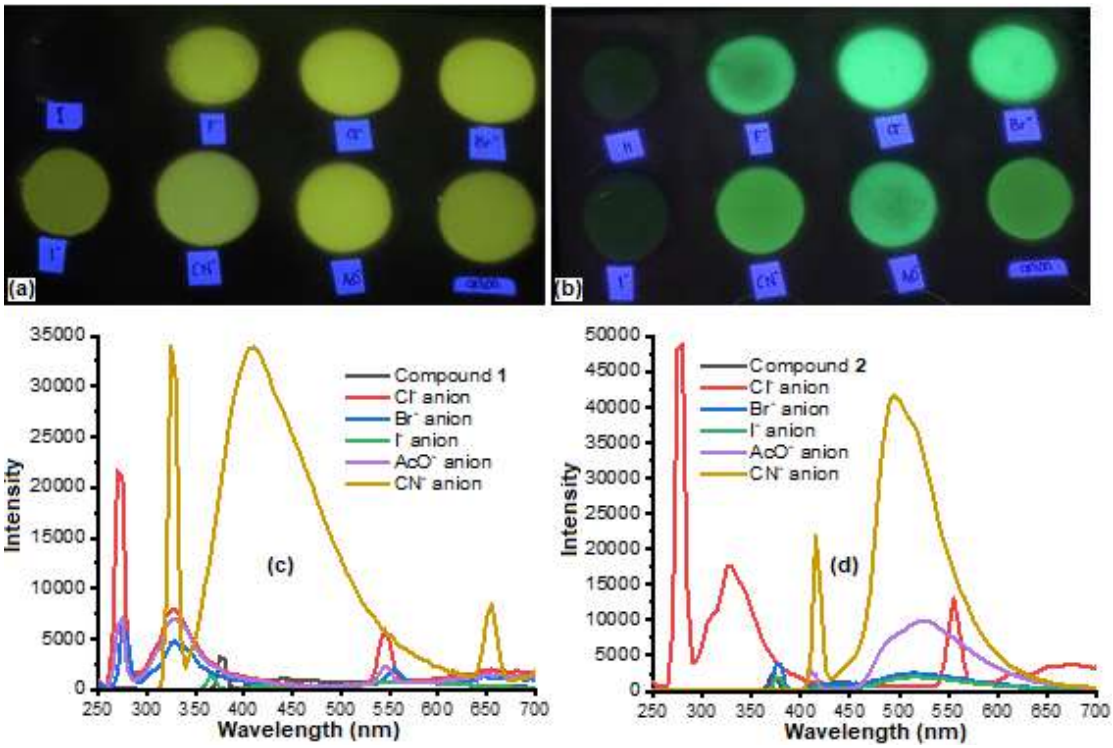

Fig 6. Fluorescents of solution (a) compound **1** (5×10^{-5} M) and (b) compound **2** (2×10^{-5} M) under a UV lamp 365 nm; and emission spectra of (c) compound **1** and (d) compound **2** in DMSO after addition of Cl^-, Br^-, I^-, AcO^-, and CN^-

of CN^- indicates an OFF-ON system due to interaction between sensor compound and anion [23].

Limit of Detection Value for Cyanide on Sensor Compounds

The color changes of sensor solutions after addition various CN^- concentrations are shown in Fig. 7. The solution color change into yellow was observed when the CN^- concentrations were 4×10^{-2} M for **1** and 1×10^{-3} M for **2**.

The UV-Vis spectra after the addition of various cyanide anion concentrations are shown in Fig. 8. For example, the addition of cyanide from a range concentration of 10^{-4}–10^{-2} M into compound **1** caused a decrease in absorbance at λ ~ 290 and 360 nm and increased a new peak at λ ~ 450 nm region (Fig. 8(a)). For compound **2**, increasing CN^- concentration from 10^{-5}–10^{-3} M caused a decrease in absorbance at λ_{max} 380 nm and a new peak at λ ~440 nm (Fig. 8(b)).

A ratiometric calibration curve was plotted from UV-Vis spectra to determine the limit of detection (LOD) cyanide anion of compounds **1** and **2**. The ratiometric calibration curve against various CN^- concentrations had a regression value (R^2) of 0.9916 with a LOD value of 9.6×10^{-4} M for compound **1** and 0.9917 with a LOD value of 9.63×10^{-5} M for compound **2**.

Fig 7. Optical color of (a) compound **1** and (b) compound **2** changes after addition of various concentrations of cyanide anion (10^{-4}–10^{-2} M for compound **1** and 10^{-5}–10^{-2} M for compound **2**)

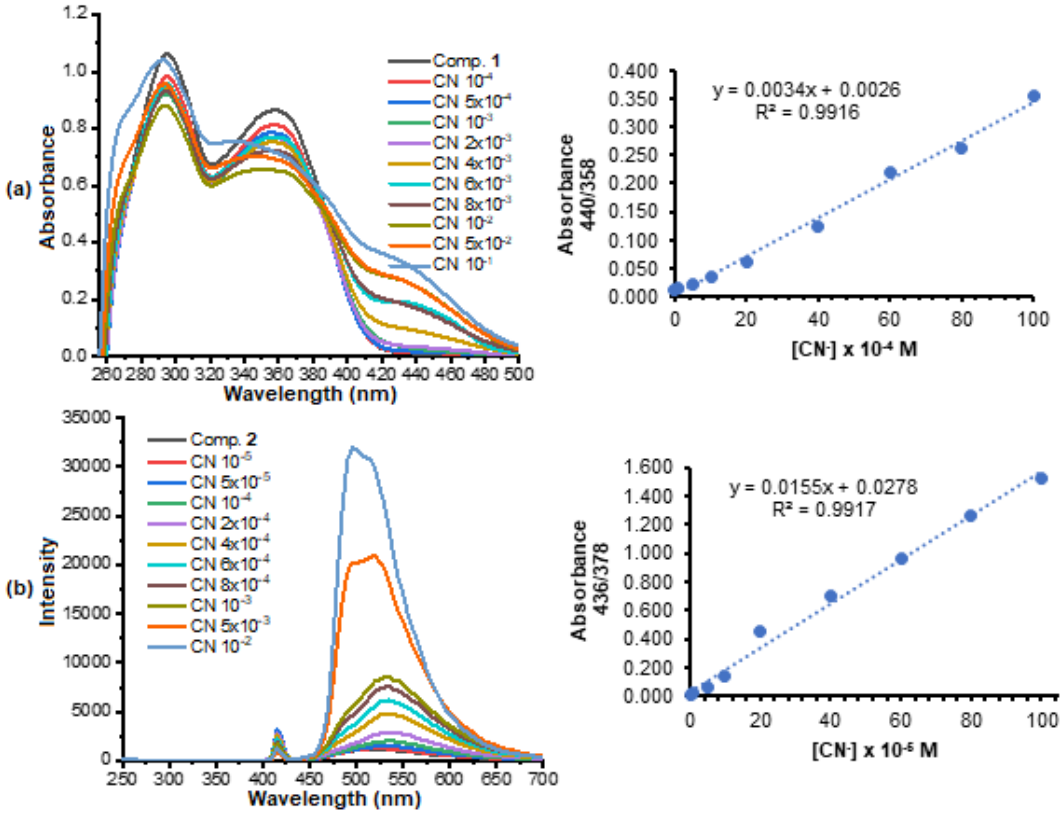

Fig 8. UV-Vis absorption spectra with the ratiometric curve of (a) compound **1** and (b) compound **2** after addition various concentrations of CN^-

The LOD value for CN^- anion was also performed using a spectrofluorometer. The fluorescence emission spectra and calibration curve are shown in Fig. 9. The emission spectra of compounds **1** and **2** increased with an increase of CN^- concentration. As a result, the calibration curve of the emission spectra of compounds **1** and **2** had an R^2 value of 0.9776 and 0.9928, and the LOD value was 15.90×10^{-4} M and 8.95×10^{-5} M.

Interaction Study between Sensor Compounds and Cyanide

The interaction study between sensor compounds and cyanide anions was performed through Job's plot [20]. The curves of absorbances against the cyanide fraction are shown in Fig. 10. The maximum absorbance was obtained at addition a cyanide fraction of 0.5. This value indicates that interaction between compounds **1** and **2** with the cyanide anion has a mole ratio of 1:1. The 1:1 ratio means that only one hydroxyl from the symmetrical azine interacts with one mole of cyanide anion.

The ^{1}H-NMR titration supported 1:1 ratio interaction for compound 2 (Fig. 11). The addition of 1

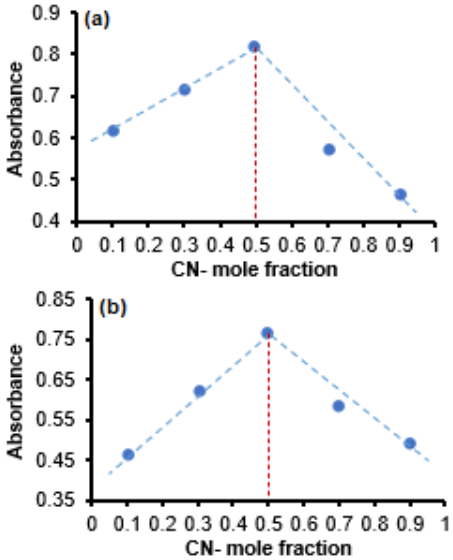

Fig 10. Job's Plot curve interaction between (a) compound **1** and (b) compound **2** with a fraction of cyanide addition

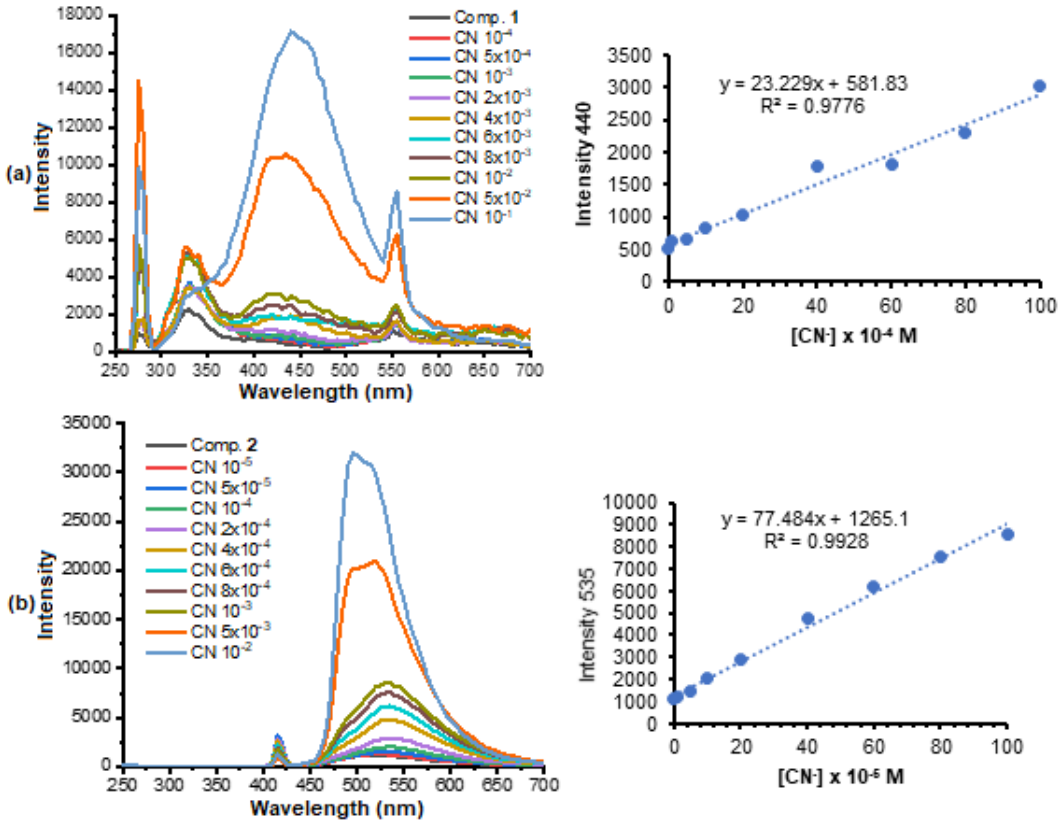

Fig 9. Emission spectra with the calibration curve of (a) compound **1** and (b) compound **2** at the excitation of 415 nm after addition various concentrations of CN^-

equivalent mole ratio of cyanide anion caused a signal at 13.55 ppm to disappear and followed a new signal at 8.51 ppm. The addition of 5 and 10 moles equivalents of cyanide anion, a signal at δ 8.51 ppm shifted towards upfield at 8.48 and 8.44 ppm accompanied by an increase in the absorption intensity. The proton of benzene peaks gradually showed a shift to the upfield area. This data indicated that deprotonation of the hydroxyl group has occurred in one hydroxyl group. These results are proposed to the mechanism of interactions in Scheme 2.

The proposed mechanism supported color change after the addition of cyanide. Interaction of compound **1** with cyanide indicated the formation of H-bond with cyanide anion in one hydroxyl group. This interaction did not produce delocalization of the benzene ring, so the color change was not intense. Interaction of compound **2** with cyanide indicated the deprotonation of one hydroxyl group followed with delocalization of the phenol anion producing color change.

Paper-Strip Sensor

A paper-strip sensor was done by dropping various concentrations of cyanide anion solution (0–1 M) to a Whatman filter immobilized with compounds **1** and **2**.

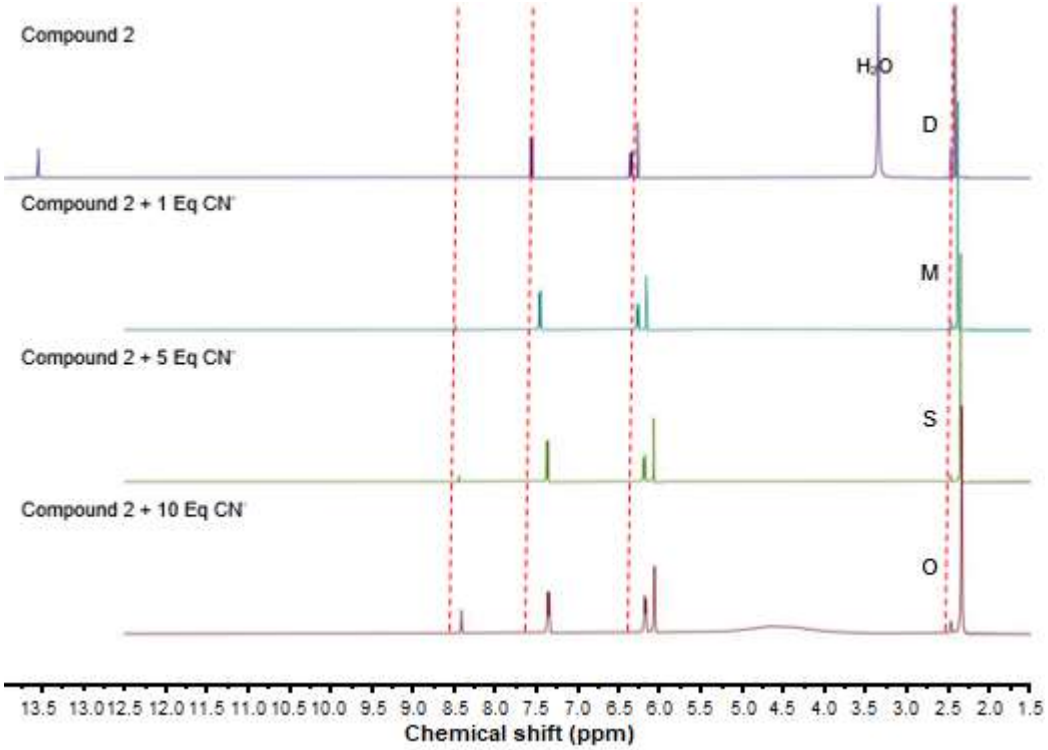

Fig 11. [1]H-NMR titration on compound **2** with the addition of cyanide ion

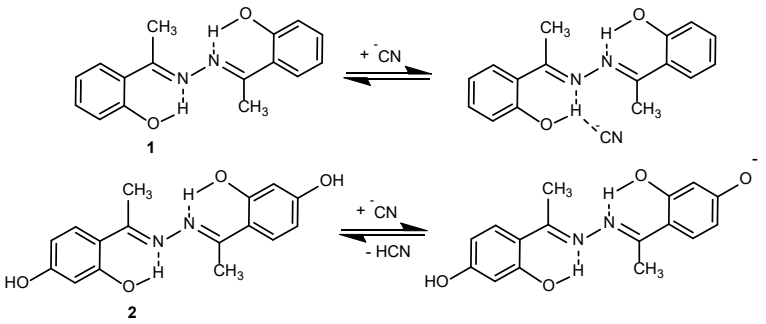

Scheme 2. Proposed mechanism of interaction **1** and **2** with cyanide anion

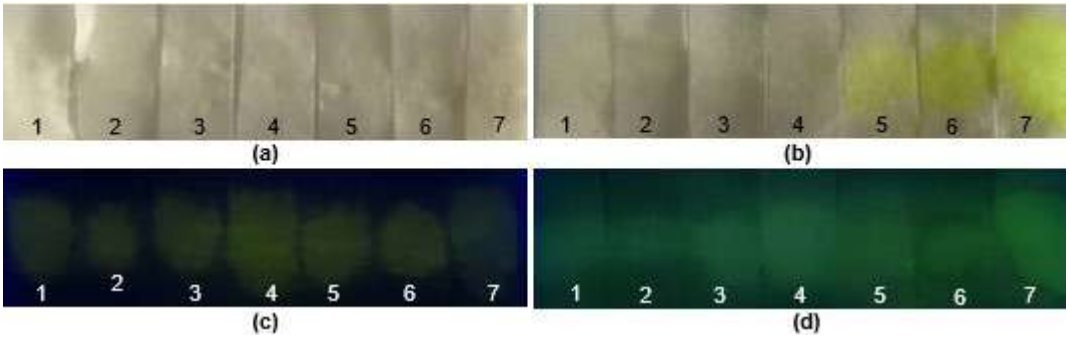

Fig 12. The paper-strip color of (a) sensor **1** and (b) sensor **2** changes after addition of various CN^- concentration (1) 0 M; (2) 10^{-5} M; (3) 10^{-4} M; (4) 10^{-3} M; (5) 10^{-2} M; (6) 10^{-1} M; and (7) 1 M, (c) sensor **1** and (d) sensor **2** under a 365 nm UV lamp

The results are shown in Fig. 12. The paper-strip sensor **1** produced no 'naked-eye' color change in addition to various cyanide anion concentrations. In contrast, paper-strip sensor 2 could detect the presence of cyanide anions at a concentration of 10–2 M with a concentration of a pale-yellow color. Observing the paper-strips under a 365 nm UV lamp, paper-strip sensors **1** and **2** glow when the cyanide is dripped with distilled water. Paper-strip **1** brought out a yellow glow, while paper-strip **2** gave a greenish-yellow glow. However, based on these results, it can be said that compound **1** and **2** is not sensitive to detect cyanide anions under UV light irradiation at a 365 nm UV lamp.

■ CONCLUSION

Acetophenone azine derivatives **1** and **2** have been synthesized in one-step condensation of acetophenone derivatives with hydrazine hydrate. Compounds **1** and **2** can act as dual-mode chemosensors (colorimetry and fluorometry) to detect cyanide anion. Compound **2** has more sensitivity than compound **1**. The LOD values for cyanide anion by colorimetry was 9.68×10^{-4} M for compound **1** and 9.63×10^{-5} M for compound **2**, while LOD values by fluorescent were 15.90×10^{-4} M for compound **1** and 8.95×10^{-5} M for compound **2**.

■ ACKNOWLEDGMENTS

We gratefully acknowledge to Indonesian Government through the LPDP scholarship to Nur Masyittah Irmi.

■ REFERENCES

[1] Pei, P.X., Hu, J.H., Chen, Y., Sun, Y., and Qi, J., 2017, A novel dual-channel chemosensor for CN^- using asymmetric double-azine derivatives in aqueous media and its application in bitter almond, *Spectrochim. Acta, Part A*, 181, 131–136.

[2] Jia, X., Yang, Y., He, Y., Ma, Q., and Liu, Y., 2019, Theoretical study on the sensing mechanism of a fluorescence chemosensor for the cyanide anion, *Spectrochim. Acta, Part A*, 216, 258–264.

[3] Erdemir, S., and Malkondu, S., 2020, On-site and low-cost detection of cyanide by simple colorimetric and fluorogenic sensors: Smartphone and test strip applications, *Talanta*, 207, 120278.

[4] Ferreira, N.L., de Cordova, L.M., Schramm, A.D.S., Nicoleti, C.R., and Machado, V.G., 2019, Chromogenic and fluorogenic chemodosimeter derived from Meldrum's acid detects cyanide and sulfide in aqueous medium, *J. Mol. Liq.*, 282, 142–153.

[5] Yu, B., Li, C.Y., Sun, Y.X., Jia, H.R., Guo, J.Q., and Li, J., 2017, A new azine derivative colorimetric and fluorescent dual-channel probe for cyanide detection, *Spectrochim. Acta, Part A*, 184, 249–254.

[6] Udhayakumari, D., 2018, Chromogenic and fluorogenic chemosensors for lethal cyanide ion. A comprehensive review of the year 2016, *Sens. Actuators, B*, 259, 1022–1057.

[7] Tracqui, A., Raul, J.S., Géraut, A., Berthelon, L., and

Ludes, B., 2002, Determination of blood cyanide by HPLC-MS, *J. Anal. Toxicol.*, 26 (3), 144–148.

[8] Dadfarnia, S., Haji Shabani, A.M., Tamadon, F., and Rezaei, M., 2007, Indirect determination of free cyanide in water and industrial waste water by flow injection-atomic absorption spectrometry, *Microchim. Acta*, 158 (1), 159–163.

[9] Taheri, A., Noroozifar, M., and Khorasani, M.M., 2009, Investigation of a new electrochemical cyanide sensor based on Ag nanoparticles embedded in a three dimensional solegel, *J. Electroanal. Chem.*, 628 (1-2), 48–54.

[10] Mergu, N., Singh, A.K., and Gupta, V.K., 2015, Highly sensitive and selective colorimetric and off-on fluorescent reversible chemosensors for Al^{3+} based on the rhodamine fluorophore, *Sensors*, 15 (4), 9097–9111.

[11] Sun, Y., Hu, J.H., Qi, J., and Li, J.B., 2016, A highly selective colorimetric and "turn-on" fluorimetric chemosensor for detecting CN^- based on unsymmetrical azine derivatives in aqueous media, *Spectrochim. Acta, Part A*, 167, 101–105.

[12] Pei, P.X., Hu, J.H., Long, C., and Ni. P.W., 2018, A novel colorimetric and "turn-on" fluorimetric chemosensor for selective recognition of CN^- ions based on asymmetric azine derivatives in aqueous media, *Spectrochim. Acta, Part A*, 198, 182–187.

[13] Hu, J.H., Sun, Y., Qi, J., Li, Q., and Wei, T.B., 2017, A new unsymmetrical azine derivative based on coumarin group as dual-modal sensor for CN^- and fluorescent "OFF-ON" for Zn^{2+}, *Spectrochim. Acta, Part A*, 175, 125–133.

[14] Hidayah, N., Purwono, B., and Pranowo, H.D., 2020, One step synthesis of symmetrical amino azine derivatives using hydrazine hydrate as a reagent, *Key Eng. Mater.*, 840, 257–264.

[15] Kagatikar, S., Sunil, D., Kekuda, D., Kulkarni, S.D., and Abdul Salam, A.A., 2020, New salicylaldehyde azine esters: Structural, aggregation induced fluorescence, electrochemical and theoretical studies, *J. Mol. Liq.*, 318, 114029.

[16] Lee, B., Lee, K.H., Cho, J., Nam, W., and Hur, N.H., 2011, Synthesis of azines in solid state: Reactivity of solid hydrazine with aldehydes and ketones, *Org. Lett.*, 13 (24), 6386–6389.

[17] Safari, J., and Gandomi-Ravandi, S., 2011, Highly efficient practical procedure for the synthesis of azine derivatives under solvent-free conditions, *Synth. Commun.*, 41 (5), 645–651.

[18] Li, W.J., and Han, H.F., 2016, Crystal structure of (*E,E*)-2',4'-dihydroxyacetophenone azine dimethylformamide disolvate, *Acta Crystallogr., Sect. E: Crystallogr. Commun.*, E72, 467–469.

[19] Mohammadi, A., and Yaghoubi, S., 2017, A new dual colorimetric chemosensor based on quinazolinone for CN^-, AcO^- and Cu^{2+} ions, *Sens. Actuators, B*, 241, 1069–1075.

[20] Nie, H.M., Gong, C.B., Tang, Q., Ma, X.B., and Chow, C.F., 2014, Visual and reversible detection of cyanide ions in protic solvents by a novel colorimetric receptor, *Dyes Pigm.*, 106, 74–80.

[21] Lin, S.L., Kuo, P.Y., and Yang, D.Y., 2007, Design and synthesis of a coumarin-based acidichromic colorant, *Molecules*, 12 (7), 1316–1324.

[22] Purwono, B., Anwar, C., and Hanapi, A., 2013, Syntheses of azo-imine derivatives from vanillin as an acid base indicator, *Indones. J. Chem.*, 13 (1), 1–6.

[23] Murugesan, K., Jeyasingh, V., Lakshminarayan, S., Selvapalam, N., Dass, G., and Piramuthu, L., 2021, Anion-binding-induced and reduced fluorescence emission (ABIFE & ABRFE): A fluorescent chemo sensor for selective turn-on/off detection of cyanide and fluoride, *Spectrochim. Acta, Part A*, 245, 118943.

Isolation of Ethyl *p*-Methoxycinnamate from *Azadirachta indica* Root Bark as Hong Kong Caterpillar (*Tenebrio molitor*) Antifeedant

Rosnani Nasution[1*], Cut Nyak Candein[1], Nurdin Saidi[1], Muhammad Bahi[1], and Marianne Marianne[2]

[1]*Department of Chemistry, Faculty of Mathematics and Natural Sciences, Universitas Syiah Kuala, Banda Aceh 23111, Indonesia*

[2]*Department of Pharmacology, Faculty of Pharmacy, Universitas Sumatera Utara, Medan 20155, Indonesia*

* ***Corresponding author:***

email: rosnani@unsyiah.ac.id

Received: March 4, 2021
Accepted: July 7, 2021

DOI: 10.22146/ijc.64487

Abstract: *This study aims to identify the antifeedant activity of* Azadirachta indica *A. Juss root bark against Hong Kong caterpillar (*Tenebrio molitor*).* A. indica *A. root was macerated in* n*-hexane, ethyl acetate, and methanol. The investigation of antifeedant activity was conducted by using the no choice leaf disk method. The antifeedant activity (%AI) tests showed that the extracts of* n*-hexane, ethyl acetate, and methanol with each concentration of 0.5% were 6.71, 71.78, and 40.14%, respectively. The ethyl acetate extract demonstrated the most active antifeedant activity. Ethyl acetate extract was fractionated to obtain five subfractions (A-E). Each subfraction with each concentration of 0.5% showed the %AI of 70.55, 85.29; 67.40, 82.70 and 82.22%, respectively. Furthermore, GC-MS results demonstrated that ethyl acetate extract contained 19 compounds. The main compounds are methyl hexadecanoate and methyl 8-octadecenoate. Further purification of fraction A, which has the highest amount, was then carried out. The obtained isolate, i.e., A3$_2$, was determined as ethyl* p*-methoxycinnamate confirmed by ^{13}C- and ^{1}H-NMR, FTIR, and MS spectra. The presence of ethyl* p*-methoxycinnamate makes* A. indica *A. root is potential as* T. molitor *antifeedant. The implication of these findings is to reference herbal antifeedants and reduce the use of synthetic pesticides.*

Keywords: Azadirachta indica *A. Juss root bark; antifeedant; ethyl* p*-methoxycinnamate;* Tenebrio molitor

■ INTRODUCTION

Aceh is a tropical region in Indonesia overgrown by various medicinal plants, like *Artocarpus camansi* [1-3], *Ficus racemosa*, *Morus alba* [4-5], and *Azadirachta indica* A. Juss. *A. indica* A. Juss or Meliaceae, known as Neem trees, originally came from India, Bangladesh, Thailand, Nepal, and Pakistan. However, this plant is commonly found in Aceh [6]. *A. indica* A. Juss is a tree with 10–15 m of height. It has roots, stems, leaves, flowers, fruit, and seeds. The stems structures are straight and woody [7]. This plant is one of the essential medicinal plants, which the UN declared as a 21st Century Tree. In India, the neem is called the divine tree, which means the tree of life, the natural pharmacy, and the elixir for all diseases [8-11]. Various chemical constituents are found in neem leaves, such as nimbin, nimbanene, 6-desacetylnimbinene, nimbandiol, nimbolide, ascorbic acid, *n*-hexacosanol, amino acids, 7-desacethyl-7-benzoylazadiradione,7-deacethyl-7-benzoylgedunin and nimbiol [11-13]. The secondary metabolites of *A. indica* A. Juss plants belong to the terpenoid, steroid, and flavonoid compounds [14]. These have been isolated from various parts of the *A. indica* A. Juss plant, and some of them showed antifungal, antitumor, and antimalarial activity [15]. The steroid saponin compounds, such as 2α,4α-dihydroxy-pregn-5-en-16-one-3α-*O*-*D*-glucopyranose, 6-deacetylnimbin, 6-deacetylnimbinal, nimbandiol, nimbolide, 2',3'-dehydrosalannol, 3β,4β,20α-trihydroxy-5-pregnen, 2α,3β-dihydroxy-5-pregnen-16-one, (+)-dehydro-vomifoliol, 3β-hydroxy-5α,6α-epoxy-7-megastigmen-9-one, and quercetin-3-gluco-pyranoside have been isolated from methanol extracts of

A. indica leaves, which known to have antibacterial activity [16].

Generally, antifeedant compounds are defined as compounds that temporarily or permanently stop the insect's appetite. The antifeedant identification of *A. indica* A. Juss seed water extract within a concentration of 80 g/L using the "No Choice Leaf Disk Method" resulted in 98.19% of antifeedant activity and potential repellent to the *Plutellaxylostella larvae* [17]. However, further study of the antifeedant activity from other parts of the *A. indica* A. Juss plant, including the root bark, is still in progress.

The Hong Kong caterpillar *Tenebrio molitor* is one of the pest organisms found in agricultural products [18]. The synthetic pesticides applied to the plant are unable to decompose, but plant roots can absorb them. Meanwhile, it will be accumulated in roots and leaves, and fruits, which animals eat. Moreover, the accumulated compounds will enter the human body via certain animals, which eat those leaves or fruits. Thus, the compound can affect the body's systems within the human body, such as nervous systems and others. This infected nervous system can cause mental retardation [19]. Therefore, the research about antifeedant activity from the compounds derived from neem root skin against the bioindicator of Hong Kong caterpillar (*T. molitor*) is necessary to be carried out.

■ EXPERIMENTAL SECTION

Materials

The root bark of *A. indica* A. Juss was collected from the Darussalam area, a part of Syiah Kuala sub-district Banda Aceh, in 2017. Dr. Saida Rasnovi identified the sample, number: 393/11.1.28.1/DT/UN 2017 and subjected it as the herbarium to the Biology Department, Faculty of Mathematics and Natural Sciences, Universitas Syiah Kuala.

Instrumentation

Mass spectra were measured using a Shimadzu GC-MS QP 2010 Ultra. In addition, the 1D spectra of ^{1}H- and ^{13}C-NMR were measured in $CDCl_3$ solvent using an ECA JEOL 400 MHz spectrophotometer. Furthermore, column chromatography was conducted on silica gel 60 (70-230 mesh, Merck), and the TLC analysis was carried out using precoated silica gel plates (Merck).

The methodology used for phytochemicals testing could be found in the Phytochemical Methods, Simplified Determination Method to Analyze Plants [20].

Procedure

Extraction of A. indica *A. Juss root bark*

About 2.2 kg root bark of *A. indica* A. Juss was dried as preparation for the maceration process. First, the root bark was macerated with *n*-hexane for 72 h; then, it was filtered to collect the residue. The obtained residue was soaked into the semi-polar solvent, ethyl acetate, for 72 h, then it was filtered for obtaining further residue. The residue obtained was macerated with methanol solvent for getting the next residue. Then, each obtained residue was evaporated by using the rotary evaporator. There were about 25.314 g (1.13%) collected residue concentrated from the *n*-hexane extract, 28.315 g (1.24%) from ethyl acetate extract, and 214 g (9.41%) from the methanol extract. All residues were subjected to identification of antifeedant activity. Then, the residue derived from ethyl acetate was determined as the most active antifeedant against *T. molitor* instar III. Therefore, the fractionation was conducted with the ethyl acetate extract, and its chemical composition was characterized by Gas Chromatography-Mass Spectrometry (GC-MS).

Fractionation of ethyl acetate extract

About 16 g of the ethyl acetate extract was fractionated using gravity column chromatography. The eluent system was using *n*-hexane: ethyl acetate with the ratio of *n*-hexane 100%, *n*-hexane:ethyl acetate (98:2); (95:5); (92:8); (90:10); (85:15); (80:20); (70:30); (60:40); (55:45); (50:50); *n*-hexane:ethyl acetate (40:60); 100% of ethyl acetate and 100% of methanol. The separation result showed 267 fractions (each 60 mL) obtained after being monitored by thin-layer chromatography (TLC). The same stain pattern was combined to form five fraction groups: A, B, C, D, and E. Fractions A and B contain terpenoids with the weight of 0.73 and 0.80 g, respectively. Fraction C, as brownish-black residue

contains alkaloids and terpenoids, resulted in 0.80 g. Fraction D, weighing 3.27 g as brownish-black, contains terpenoids and saponins, while fraction E, as brownish-black residue in 7.27 g weight, contains terpenoids. Then, those five fraction groups were subjected to the identification of antifeedant activity. The result determined that fractions A and B had the highest antifeedant activity. Furthermore, the separation of fraction A was relatively clean, and this group belongs to the active antifeedant fraction group (%AI = 62.03% at 0.1% concentration).

The fixed amount of 0.80 g of fraction A was addressed for gravity column chromatography with the eluent system of *n*-hexane:ethyl acetate (90:10). The 81 fractions were obtained with fractions 48 and 49 (A3) contained 0.04 g in each. Next, fraction A3 was subjected to further separation using *n*-hexane:ethyl acetate (90:10) eluent system. Another 19 fractions were obtained, whereas fractions 11-13 ($A3_2$) were determined relatively pure after TLC analysis performed with three different eluent systems. Furthermore, the $A3_2$ compound was characterized by ^{1}H-NMR, ^{13}C-NMR, infrared spectrometers and MS.

Preparation of bioindicators

The *T. molitor* instar III was used as bioindicators in this research. It was bought from mealworm breeders in Keutapang, Aceh Besar, and it fasted for 24 h before the antifeedant activity test.

Preparation of test solution

The test solution was generated in 10% wt/v concentration. Ten grams of methanol extract were dissolving into 100 mL of methanol. The solution was diluted into the 5, 1, and 0.5% of final concentrations. Moreover, the same treatment was repeated for the ethyl acetate and *n*-hexane extracts.

Test media preparation

A plastic with a 15 × 10 cm^2 size was prepared and covered with sterile gauze moistened by distilled water.

Antifeedant activity assay

Fresh spinach leaves were prepared and put into the crude extract of methanol (0.5%) for a minute. After that, it was left to dry for about 15 min, and the weight gain (x_1) was measured. The spinach leaves were placed into the test medium within a plastic container, which had been prepared previously. Furthermore, the 10 larvae of *T. molitor* instar III were placed into the container, covered with a cloth, and tied with a rubber band for 24 h. Then, the weight of spinach leaves was measured to calculate the weight lost (x_2), while the weight of leaves was found different between x_1 and x_2. The test was repeated 3 times. The negative control was fresh spinach leaves which were dipped into the extracting solvent used. The same treatment was carried out for concentrations of 1, 5, and 10% of ethyl acetate and *n*-hexane extracts, with 3 replications for each. All of the tests were repeated three times. The antifeedant percentage was calculated using the formula [21]. The standard deviation was obtained from the repetition of antifeedant activity assays, which have been carried out three times.

$$\text{Antifeedant Index (AI)} = \frac{C(x_1 - x_2) - T(x_1 - x_2)}{C(x_1 - x_2) + T(x_1 - x_2)} \times 100\%$$

whereas AI = Antifeedant Index; C = Control; x_1 = weight of leaf which was put into the crude extract as a control; x_2 = weight of leaf which was consumed by larvae as a control; and T = Treatment.

Statistical analysis

Statistical analysis was conducted using the SPSS program and Origin Pro software to create the different curves for the antifeedant activity.

■ RESULTS AND DISCUSSION

The antifeedant activity was identified among *n*-hexane, ethyl acetate, and methanol extract derived from *A. indica* A. Juss root bark. The ethyl acetate extract demonstrates the highest antifeedant activity (%AI = 71.78%) against *T. molitor* instar III compared to *n*-hexane (6.71%) and methanol extract (40.14%). Therefore, the isolation and activity test focused on the ethyl acetate extract. First, the ethyl acetate extract was separated by gravity column chromatography to obtain five subfractions, i.e., fraction A (0.8 g), B (0.73 g), C (0.8 g), D (3.27 g), and E (7.27 g). Then, the measurement of antifeedant activity for those five groups of fractions was applied to *T. molitor* instar III. The results of the antifeedant activity test of ethyl acetate

extract and the fraction groups (A, B, C, D, and E) are listed in Table 1.

Based on Table 1, the antifeedant activity test results showed that the %AI for various fraction groups is more than 50% at 0.1 and 0.5% of concentration. This antifeedant observation showed that fraction B is the most active antifeedant from ethyl acetate extracts and the various fraction groups, followed by fraction D, fraction E, fraction A, and fraction C. The relationship curve between %AI and the concentration of each extract is presented in Fig. 1. The obtained %AI is directly affected by the concentration of each fraction contained in the ethyl acetate extract.

The ethyl acetate extract of *A. indica* A. Juss root bark was characterized by a gas chromatography-mass spectrometry (GC-MS) to identify the composition of the compounds. The chromatogram is shown in Fig. 2. Several compounds are contained in the ethyl acetate extract derived from the root bark of *A. indica* A. Juss, and the result from GC-MS analysis are listed in Table 2. Nineteen compounds have above 70% of similarities. The two major compounds, methyl 8-octadecenoate (26.33%) and methyl hexadecanoate (14.18%) have 96% similarities. Therefore, we can conclude that ethyl acetate extract contains antifeedant compounds, like nimbin, patchouli alcohol, *p*-methoxycinnamate, terpenoid, and monoterpene. These compounds work simultaneously to give the highest antifeedant activity of ethyl acetate extract. Nimbin has been reported as an anti-microorganism, which is very useful in controlling plant disease [22]. In this experiment, the nimbin was found as a Nimbiol, also classified as a terpenoid. Terpenoid compounds could affect the feeding selection of insects. This finding is in good agreement with Wei et al. [15],

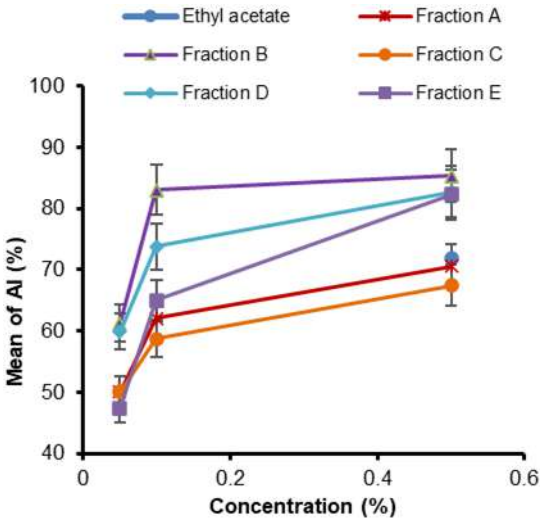

Fig 1. The differences antifeedant activity of ethyl acetate extracts and their fraction groups

Table 1. The antifeedant activity of ethyl acetate extract and fraction group A-E against *T. Molitor*

Conc.	Mean of %AI ± Standard Deviation					
(%)	Ethyl Acetate Extract	Fraction A	Fraction B	Fraction C	Fraction D	Fraction E
0.05		50.03 ± 2.97	61.25 ± 2.97	50.05 ± 18.44	59.9 ± 16.59	47.36 ± 13.56
0.1		62.03 ± 1.30	83.02 ± 6.05	58.72 ± 9.22	73.75 ± 15.43	65.01 ± 16.95
0.5	71.78 ± 19.99	70.55 ± 1.98	85.29 ± 5.36	67.4 ± 1.85	82.71 ± 4.53	82.22 ± 9.45

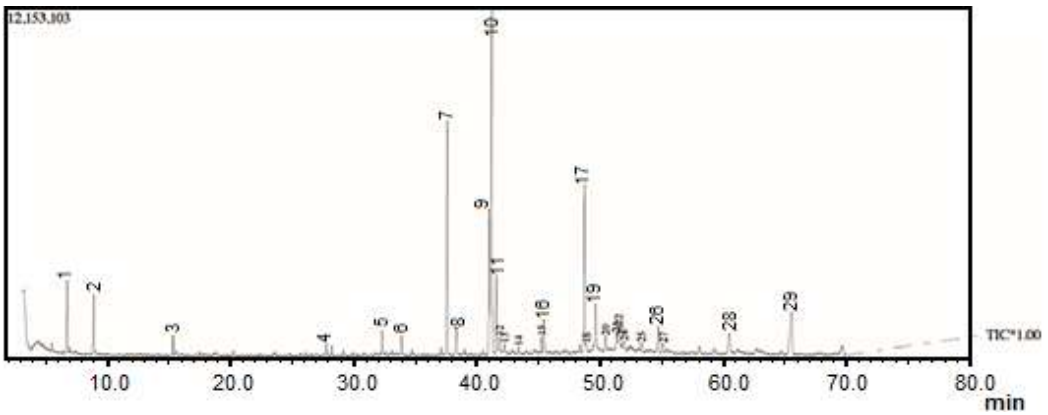

Fig 2. The chromatogram of the ethyl acetate extract derived from the root bark of *A. Indica* A. Juss

Table 2. Characterization results of the compounds contained in the ethyl acetate extract derived from *A. indica* A. Juss root bark by GC-MS (all of the structure should be rewritten and give the correct IUPAC name of the compounds)

No	Retention Time (min)	Area (%)	Compound	SI (%)
1	6.806	3.49	4-hydroxy-4-methyl-2-Pentanone	95
2	8.963	3.03	2-butoxy ethanol	98
3	15.366	0.75	2-Butoxyethyl acetate	94
4	27.832	0.47	2,4-bis(1,1-dimethylethyl) phenol	91
5	32.308	1.25	1,6-Methanonaphtalen-1(2H)-ol, octahydro-4,8a,9,9-tetramethyl-, [1R-(1.alpha,4.beta,4a.alpha,6.beta, 8a.alpha)]	95
6	33.928	0.98	Ethyl *p*-methoxycinnamate	71
7	37.630	14.18	Methyl hexadecanoate	96
8	38.400	1.48	Hexadecanoic acid	95
9	40.995	9.01	Methyl cis-9 cis-12-Octadecadienoate	94
10	41.212	26.33	Methyl Octadec 8-Enoate	96
11	41.602	3.70	Methyl n-octadecanoate	96
12	41.866	1.22	9Z,12Z-Octadecadienoic acid	88
13	45.243	0.69	Arachidic acid methyl ester	96
14	45.439	2.40	Podocarpa-6,8,11,13-tetraen-12-ol, 13-isopropil-, acetate	83
15	48.785	9.94	Bis(2-ethylhexyl) 1,2-Benzenedicarboxylate	97
16	48.900	0.53	Nimbiol	70
17	49.639	3.63	Podocarpa-8,11,13-triene-7beta, 13-diol,14-Isopropyl	74
18	50.469	0.87	7-isopropyl-1,1,4a,6-tetramethyl-2,3,4,4a,10,10a-hexahydrophenanthren-9(1H)-one	84
19	54.755	1.84	Piperidine, 1-[5-(1,3-benzodioxol-5-yl)-1-oxo-2,4-pentadienyl]-,(E,E)	90

who reported that terpenoids are potent for control insects.

Fraction A was addressed to further purification using chromatography to produce $A3_2$ isolate. It is due to the amounts of other fractions was too small. Even though the antifeedant activity of fraction A is lower than other fractions, it still has a reasonable antifeedant activity to be applied (~70%).

Based on Fig. 3, there are 12 carbon atoms present in the $A3_2$ isolate. The carbon at C-11 as a carbonyl ester appeared at δ_C 167.5 ppm and C-8 for OCH_3 at δ_C 55.5 ppm. The C-14 and C-15 at δ_C 60.4 and 14.5 ppm belong to CH_2 and CH_3. In addition, and alkene carbons of C-9 and C-10 were detected at δ_C 144.4 and 115.8 ppm. Atom C of C-1 to C-6 were aromatic carbons with δ_C of 127.3; 129.8; 114.4; 161.4; 114.4 and 129.8 ppm, respectively. According to previous research, the ^{13}C-NMR spectrum of the $A3_2$ isolate is very similar to ethyl *p*-methoxy cinnamate that has been reported [23].

The comparison of ^{1}H-NMR and ^{13}C-NMR spectra data of $A3_2$ isolate with ethyl *p*-methoxycinnamate compounds are listed in Table 3. Ethyl *p*-methoxycinnamate has various pharmacological activities, including anti-inflammatory [24] anti-hyperglycemic [25], and antibacterial [26]. The ethyl *p*-methoxycinnamate compound has been found in the chloroform extract of the leaves of *A. indica* A. Juss as an anti-inflammatory [27].

The ^{1}H-NMR spectrum of the $A3_2$ isolate showed in Fig. 4. The ^{1}H-NMR spectrum showed three aliphatic protons bound to H-15, which appeared as triplets at δ_H 1.33 ppm, and two aliphatic protons bound to H-14 showed as quartets at δ_H 4.25 ppm. This pattern happens because the protons attached to the H-14 atom are

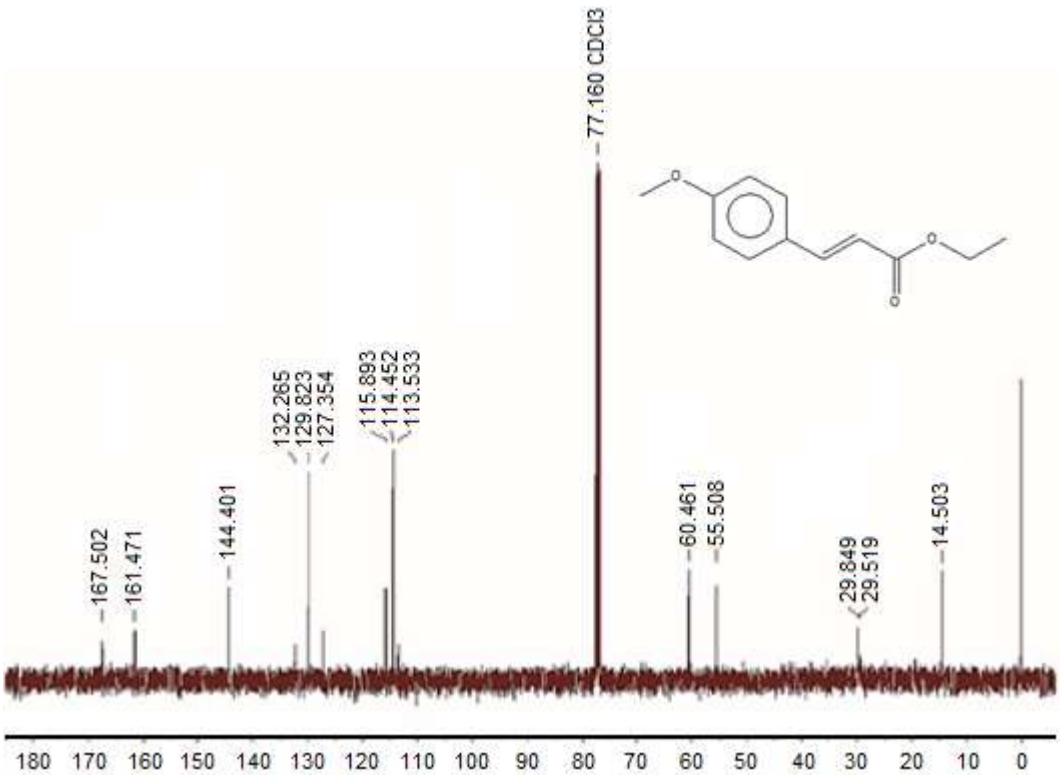

Fig 3. The ^{13}C-NMR spectra of the $A3_2$ isolate

Table 3. The comparison of ^{1}H-NMR and ^{13}C-NMR spectra data of $A3_2$ isolate with ethyl *p*-methoxycinnamate compounds

Position	Isolate $A3_2$	Ethyl*p*-methoxycinnamate	Isolate $A3_2$	Ethyl*p*-methoxycinnamate
	δ_H,ppm	δ_H, ppm	δ_C, ppm	δ_C, ppm
1	-	-	127.3	127.3
2	7.47 (*d*,2H)	7.42 (*d*,2H)	129.8	129.7
3	6.90 (*d*,2H)	6.90 (*d*,2H)	114.4	114.3
4	-	-	161.4	161.3
5	6.90 (*d*,2H)	6.90 (*d*,2H)	114.4	114.3
6	7.47 (*d*,2H)	7.42 (*d*,2H)	129.8	129.7
7	-	-	-	-
8	3.83 (*s*,3H)	3.82 (*s*,3H)	55.5	55.3
9	7.64 (*d*,1H)	7.65 (*d*,1H)	144.4	144.2
10	6.30 (*d*,1H)	6.31 (*d*,1H)	115.8	115.7
11	-	-	167.5	167.3
12	-	-	-	-
13	-	-	-	-
14	4.25 (*q*,2H)	4.25 (*q*,2H)	60.4	60.3
15	1.33 (*t*,3H)	1.32 (*t*,3H)	14.5	14.5

affected by the O atom's electronegativity, which causes a significant chemical shift value. Atom H on H-8 is a singlet signal defined as a methoxy proton with δ_H 3.3 ppm. The singlet signal indicates that the methoxy proton has no neighbor. The chemical shift values of H-9 and H-10 as alkene were signaled at δ_H 7.64 ppm (1H, d)

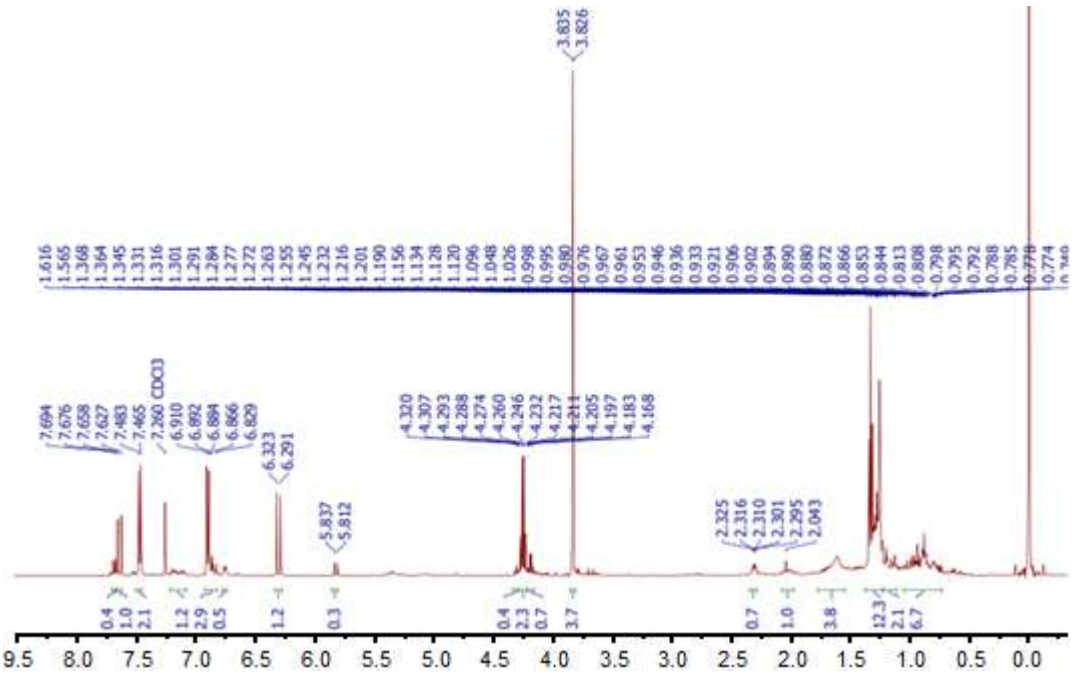

Fig 4. The ^{1}H-NMR spectrum of $A3_2$ isolate

and 6.30 ppm (1H, d), respectively. In addition, the presence of aromatic protons of H-2 and H-3 atoms were appeared at δ_H 7.47 ppm (2H, d) and 6.90 ppm (2H, d), respectively.

The FT-IR spectrum supported the $A3_2$ isolate as ethyl *p*-methoxycinnamate, which shows a carbonyl group (C=O) ester at the wavenumber 1738 cm^{-1}. The aliphatic C–H vibration at the wavenumbers of 2925 and 2854 cm^{-1} showed that the compound contains methyl (CH_3), methylene (CH_2), and methine (–CH) groups. Moreover, the absorption in the area 1634–1512 cm^{-1} indicated the presence of aromatic carbon-carbon double bonds (–C=C–), then an absorption at 829 cm^{-1} indicated the para-substitution. While the absorption at 1372 cm^{-1} showed the existence of stretch vibration (–C–H). Absorption at 1170 cm^{-1} indicated the presence of ether (–C–O) groups. These groups are relatively reactive and react with other compounds to form antifeedant substances, causing the AI to increase. In addition, the presence of conjugated double bonds in some compounds is responsible for their properties, which is easily evaporate, i.e., essential oil properties.

The identification of $A3_2$ isolate as ethyl *p*-methoxycinnamate is supported by MS data, as shown in Fig. 5. The fragmentation of the ethyl *p*-methoxycinnamate molecule occurs at m/z 206, 178, 161, 147, 134, and 118. The characteristic of the ethyl *p*-methoxycinnamate compound is found in the fragment of m/z 161 as a base peak [28]. Furthermore, it also reported the fragmentation pattern of ethyl *p*-methoxycinnamate, which is similar to the $A3_2$ isolate [28]. Based on the data above, the $A3_2$ isolate has a high similarity with the ethyl *p*-methoxycinnamate compound, so that the structure of the $A3_2$ isolate is determined to be an ethyl *p*-methoxycinnamate compound.

The *n*-hexane extract from *A. indica* A. Juss root bark contains alkaloids, steroids, terpenoids, and saponins, while the ethyl acetate extract contains alkaloids, steroids, terpenoids saponins, and phenolics. In comparison, the methanol extract contains steroids,

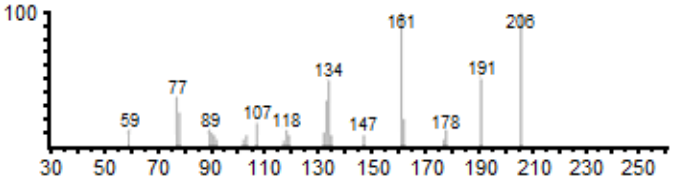

Fig 5. The MS spectrum of $A3_2$ isolate (from GC-MS)

terpenoids, saponins, flavonoids, and phenolics. The presence of terpenoids and steroids is commonly found in plants since terpenoids are known as the basic of steroid biosynthesis [29]. In addition, several secondary metabolites were found in *A. indica* A. Juss, such as terpenoids, steroids, and flavonoids [14]. Thus, it corresponds with the previous research, which exhibited that the ethyl acetate extract of *A. indica* A. Juss leaves contain an alkaloid, terpenoids, steroid, and phenolic metabolites [30].

While the identification result of secondary metabolite content showed no alkaloids detected in the methanol extract, it is appropriate with the study results [31], which reported that the methanol extract of *A. indica* A. Juss leaves contained terpenoids, flavonoids, and saponins. Thus, the differences between the chemical compounds derived from the extracts are due to the sample used (root, bark, or leaves) and the solvents used (nonpolar, semi-polar, and polar).

The antifeedant nature is suspected in *A. indica* A. Juss since the chemical compounds contained in the fraction group of ethyl acetate extract of are consist of alkaloids, such as piperidine, 1-[5-(1,3-benzodioxol-5-yl)-1-oxo-2,4-pentadienyl]-,(E,E), terpenoids, such aspodocarpa-6,8,11,13-tetraen-12-ol-13-isopropyl acetate, Nimbiol, podocarpa-8,11,13-triene-7beta, 13-diol,14-isopropyl and, 7-isopropyl-1,1,4a,6-tetramethyl-2,3,4,4a, 10,10a-hexa hydrophenanthren-9(1H)-one, according to GC-MS result. The content of these chemical compounds significantly affects the behavioral eating of insects; for instance, the alkaloid compounds exhibited a bitter taste to inhibit the antifeedant activity [20]. Moreover, the terpenoid compounds may affect insect feeding. This finding corresponds to the previous research, which reported that terpenoids could control insects by acting as antifeedants [15]. Furthermore, the saponins also could reduce the absorption of food within the gut of insects and inhibit the absorption of food in the intestine [32]. These saponins may also have an antifeedant activity to the other insects, such as *Spodopteralitura* [33].

According to the result of GS-MS analysis, two major compounds were detected, methyl hexadecanoate and methyl 8-octadecenoate determined to have an antioxidant, antibacterial, and anticancer activity, which can inhibit microbial growth [34]. In addition, nimbiol was detected, and it exhibited antibacterial and antifungal activity [22]. Moreover, this compound is commonly found in the *A. indica* A. Juss. Further research is required to observe the matrix in this field.

■ CONCLUSION

The results of the phytochemical test showed that the root bark extract of the plant *A. indica* A. Juss contained secondary metabolites of alkaloids, terpenoids, steroids, flavonoids, saponins, and phenolic compounds. *A. indica* A. Juss root bark has better antifeedant activity in ethyl acetate extract, and its subfraction, i.e., $A3_2$ was confirmed as ethyl *p*-methoxycinnamate from ^{13}C- and ^{1}H-NMR, FTIR, and MS spectra. This compound is responsible for the antifeedant activity of *A. indica* A. root extract. Therefore, *A. indica* root is the potential to be used as *T. molitor* instar III antifeedants.

■ ACKNOWLEDGMENTS

The authors acknowledge Universitas Syiah Kuala for providing financial support for this research.

■ AUTHOR CONTRIBUTIONS

RN and CNC conducted the experiment; NS conducted the calculations; MB and M wrote and revised the manuscript. All authors agreed to the final version of this manuscript.

■ REFERENCES

[1] Nasution, R., Barus, T., Nasution, P., and Saidi, N., 2014, Isolation and structure elucidation of steroid from leaves of *Artocarpus camansi* (Kulu) as antidiabetic, *Int. J. PharmTech Res.*, 6 (4), 1279–1285.

[2] Nasution, R., Fitrah, C.N., Helwati, H., Murniana, Arifin, B., Cutchamzurni, C., Rizal, Y., and Marianne, 2018, Antidiabetes activities extract hexane from the peels of *Artocarpus camansi* Blanco fruit, *Asian J. Pharm. Clin. Res.*, 11 (1), 12–17.

[3] Nasution, R., Mariane, Mustanir, and Roswita, M., 2015, Anti-obesity compounds from the leaves of plants *Morus alba* (moraceae), *Int. J. ChemTech. Res.*, 8 (10), 228–234.

[4] Nasution, R., Marianne, and Nur, H., 2015, β-Amyrin acetate of ethyl acetate extract of the bark plant *Artocarpus camansi* and its antidiabetic activity, *Pharma Chem.*, 7 (6), 71–78.

[5] Nasution, R., Mustanir, Marianne, and Marzuki, I., 2016, Isolation compound anti-obesity from the bark ara (*Ficus racemosa*) of Aceh, *Orient. J. Chem.*, 32 (5), 2693–2699.

[6] Arifin, B., Nasution, R., Saidi, N., Marianne, and Aprilia, S., 2014, *Vitex trifolia* plant control of mice environmentally friendly, *Int. J. Chemtech. Res.*, 6 (11), 4595–4600.

[7] Kardinan, A., 2011, Penggunaan pestisida nabati sebagai kearifan local dalam pengendalian hama tanaman menuju system pertanian organik, *Pengembangan Inovasi Pertanian*, 4 (4), 262–278.

[8] Kumar, V.S., and Navaratnam, V., 2013, Neem (*Azadirachta indica*): Prehistory to contemporary medicinal uses to humankind, *Asian Pac. J. Trop. Biomed.*, 3 (7), 505–514.

[9] Adam, R.P., 2001, *Identification of Essential Oil Components by Gas Chromatography/Mass Spectrometry*, Allured Publishing Corporation, Carol Stream, USA.

[10] Mondal, E., and Chakraborty, K., 2016, *Azadirachta indica*- A tree with multifaceted applications: An overview, *J. Pharm. Sci. Res.*, 8 (5), 299–306.

[11] Hossain, M.A., and Nagooru, M.R., 2011, Biochemical profiling and total flavonoids contents of leaves crude extract of endemic medicinal plant *Corydyline terminalis* L. Kunth, *Pharmacogn. J.*, 3 (24), 25–30.

[12] Shah, B., and Seth, A., 2012, *Textbook of Pharmacognosy and Phytochemistry*, Elsevier Health Sciences, New York, USA.

[13] Gokhale, S.B., Kokate, C., and Purohit, A.P., 2019, *Pharmacognosy-IV*, Nikali Prakashan, India.

[14] Patel, S.M., Venkata, K.C.N., Bhattacharyya, P., Sethi, G., and Bishayee, A., 2016, Potential of neem (*Azadirachta indica* L.) for prevention and treatment of oncologic diseases, *Semin. Cancer Biol.*, 40-41, 100–115.

[15] Wang, H.W., Liu, J.Q., Chen, J.X., Yang, Y.F., Yan, Y.X., Li, Z.R., and Qiu, M.H., 2013, New triterpenoids from the kernels of *Azadirachta indica*, *Nat. Prod. Bioprospect.*, 3 (1), 33–37.

[16] Liu, L., Zhao, Y.L., Chen, G.G., Chen, Y.Y., Qin, X.J., Song, C.W., Yang, X.W., Liu, Y.P., and Luo, X.D., 2014, Limonoid and steroidal saponin from *Azadirachta indica*, *Nat. Prod. Bioprospect.*, 4 (6), 335–340.

[17] Diabaté, D., Gnago, J.A., and Tano, Y., 2014, Toxicity, antifeedant and repellent, effect of *Azadirachta indica* A. Juss and *Jatropacarcus* L. aqueous extracts against *Plutellaxylostella* (Lepidoptera: Plutellidae), *J. Basic Appl. Sci. Res.*, 4 (11), 51–60.

[18] Kurniati, R., Saidi, N., and Nasution, R., 2018, Antifeedant activity from neem leaf extract (*Azadirachta indica* A Juss), *J. Nat.*, 18 (1), 7–10.

[19] Khan, N., Kennedy, A., Cotton, J., and Brumby, S., 2019, A pest to mental health? Exploring the link between exposure to agrichemicals in farmers and mental health, *Int. J. Environ. Res. Public Health*, 16 (8), 1327.

[20] Harborne, J.B., 2012, *Phytochemical Methods: A Guide to Modern Techniques of Plant Analysis*, Springer Science & Business Media, Netherlands.

[21] Jeyasankar, A., and Gokilamani, D., 2016, Biology and eco-friendly control of Amaranths pests, *Hymenia recurvalis* Fabricius and *Psara* basalis Walker (Lepidoptera: Crambidae), *Int. J. Acad. Stud.*, 2 (4), 218–230.

[22] Alzohairy, M.A., 2016, Therapeutics role of *Azadirachta indica* (neem) and their active constituents in diseases prevention and treatment, *Evidence-Based Complementary Altern. Med.*, 2016, 7382506.

[23] Hong, T.K., Kim, S.I., Heo, J.W., Lee, J.K., Choi, D.R., and Ahn, Y.J., 2011, Toxicity of *Kaempferia galanga* rhizome constituents to *Meloidogyne incognita* juveniles and eggs, *Nematology*, 13 (2), 235–244.

[24] Umar, M.I., Asmawi, M.Z., Sadikun, A., Abdul Majid, A.M.S., Al-Suede, F.S.R., Hassan, L.E., Altaf, R., and Ahamed, M.B.K., 2014, Ethyl-*p*-

methoxycinnamate isolated from *Kaempferia galanga* inhibits inflammation by suppressing interleukin-1, tumor necrosis factor-a, and angiogenesis by blocking endothelial functions, *Clinics*, 69 (2), 134–144.

[25] Chowdhury, M.Z., Al Mahmud, Z., Ali, M.S., and Bachar, S.C., 2014, Phytochemical and pharmacological investigations of rhizome extracts of *Kaempferia galanga*, *Int. J. Pharmacogn.*, 1 (3), 185–192.

[26] Elya, B., Kusuma I.K., Jufri, M., and Handayani, R., 2016, Antibacterial test against acne in vitro, the physical stability and patch test using cream containing ethyl *p*-methoxycinnamate extracted from *Kaempferia galanga* L., *Rhizoma*, *Res. J. Med. Plants*, 10 (8), 426–434.

[27] Umar, M.I., Asmawi, M.Z., Sadikun, A., Abdul Majid, A.M.S., Atangwho, I.J., Ahamed, M.B.K., Altaf, R., and Ahmad, A., 2014, Multi-constituent synergism is responsible for anti-inflammatory effect of *Azadirachta indica* leaf extract, *Pharm. Biol.*, 52 (11), 1411–1422.

[28] Hakim, A., Andayani, Y., and Rahayuan, B.D., 2018, Isolation of ethyl *p*-methoxy cinnamate from *Kaemferia galanga* L, *J. Phys.: Conf. Ser.*, 1095, 012039.

[29] Manitto, P., and Sammes, P.G., 1981, *Biosynthesis of Natural Products*, Ellis Horwood, Chichester, New York.

[30] Raphael, E., 2012, Phytochemical constituents of some leaves extract of *Aloe vera* and *Azadirachta indica* plant species, *Glob. Adv. Res. J. Environ. Sci. Toxicol.*, 1 (2), 14–17.

[31] Kiranmai, M., Usha Sri, B., Ibrahim, M., and Mahendra Kumar, C.B., 2012, Antioxidant activity and total flavonoids content of different extracts of *Azadirachta indica* A. Juss, *J. Med. Plants Res.*, 6 (46), 5737–5742.

[32] Hussain, M., Debnath, B., Qasim, M., Bamisile, B.S., Islam, W., Hameed, M.S., Wang, L., and Qiu, D., 2019, Role of saponins in plant defense against specialist herbivores, *Molecules*, 24 (11), 2067

[33] Rahman, M.M., Ahmad, S.H., Mohamed, M.T.M., and Ab Rahman, M.Z., 2014, Antimicrobial compounds from leaf extracts of *Jatropha curcas*, *Psidium guajava*, and *Andrographis paniculata*, *Sci. World J.*, 2014, 635240.

[34] Abdel-Hady, H., El-Wakil, E.A., and Abdel-Gawad, M., 2018, GC-MS analysis, antioxidant and cytotoxic activities of *Mentha spicata*, *Eur. J. Med. Plants*, 26 (1), 1–12.

Microwave-Assisted Hydrodistillation of Clove (*Syzgium aromaticum*) Stem Oil: Optimization and Chemical Constituents Analysis

Haqqyana Haqqyana, Ali Altway, and Mahfud Mahfud*

Department of Chemical Engineering, Faculty of Industrial Technology and Systems Engineering, Institut Teknologi Sepuluh Nopember, Surabaya 60111, Indonesia

* ***Corresponding author:***

email: mahfud@chem-eng.its.ac.id

Received: March 6, 2021
Accepted: July 7, 2021

DOI: 10.22146/ijc.64521

Abstract: *One of the extensively prosperous potential aromatic plants is the clove (*Syzgium aromaticum*). This is owing to all parts of this plant (bud, stem, and leaves) contain a decent amount of essential oils. The current study focuses on the use of microwave-assisted hydrodistillation (MHD) in extracting clove stem essential oils. This study aims to obtain the best possible combination of operating parameters for a high yield of clove stem oil using response surface methodology. The current study adopted a face-centered central composite design to optimize the MHD operational parameters, including the feed-to-solvent ratio, microwave power, and extraction time. The observed data from the experiments were fitted to a reduced quadratic polynomial equation. The three operational parameters were shown to significantly affect the extraction yield of the clove stem oil ($p < 0.05$), yet the statistical significance for the interaction between each parameter was considerably weak. Furthermore, the adjusted R^2 value measured comparably to the corresponding R^2 value with the difference below 0.2, implying a high correlation between experimental and model-predicted data. Thus, this result demonstrates the suitability of the model used in the experiment.*

Keywords: *face-centered central composite design; microwave-assisted hydrodistillation; reduced quadratic model; clove oil;* Syzgium aromaticum

■ INTRODUCTION

Syzygium aromaticum (*S. aromaticum*), commonly known as clove, is a kind of aromatic spice that has long been used in various applications such as kretek cigarettes manufacturers, food flavoring, fragrances, and pharmaceuticals. The use of clove plants further developed into the cosmetics industry, and lately, several findings show the potential of using cloves for other purposes, including fish anesthetic [1], natural insecticides [2], and fuel bio-additives [3]. This aromatic plant is commercially harvested in Indonesia, Sri Lanka, India, and some African countries, primarily in Tanzania and Madagascar [4].

Cloves have a pleasant aroma derived from essential oils, which are contained in large enough quantities, whether in its flowers (10–20%), stems (5–10%), and leaves (1–4%) [5]. The essential oil derived from cloves contains a mixture of different compounds, with eugenol, eugenyl acetate, and β-caryophyllene being the three main active chemicals. The eugenol constituent in cloves and other polyphenolic compounds are known to have antioxidant, antifungal, and antimicrobial activities [6-7].

Applying an effective extraction method to produce a high-quantity and high-quality yield of essential oil is necessary since the properties and compositions of oils could vary depending on extraction methods. Various approaches have been used for obtaining aromatic oil, such as solvent extraction, hydrodistillation, and steam distillation [8-9]. Aside from the conventional methods, microwave-assisted extraction has attracted extensive response in recent years as it offers many advantages include rapid energy transfer, effective heating, shorter extraction time while preserving a high yield extraction [10]. The microwave-assisted hydrodistillation (MHD) is an advanced

hydrodistillation method that utilizes water solvent for target component extraction, aided with microwave heating. Reports on the application of the MHD on extracting essential oils from numerous plant materials have also provided promising results [11-12].

The efficiency of the MHD process is influenced by microwave irradiation power and time, properties of the matrix, including its moisture content, and the solvent-to-feed ratio [13]. When properly and optimally selected, these parameters present maximum process efficiency while retaining the desired components' value. One of the most favorable tools for optimizing experiments' design process is response surface methodology (RSM). The RSM-based analysis allows investigating the possible interaction of the independent factors and their effects on the dependent variable(s). Compared to another classical approach, such as one-factor-at-a-time experimentation, the RSM provides convenience due to its reduced time and lower number of trials. This study was carried out to evaluate the effects of the MHD parameters (microwave power, feed-to-solvent ratio, and extraction time) on the extraction of the essential oil derived from *S. aromaticum* stem. Furthermore, to investigate the best response surface design for optimizing the *S. aromaticum* stem oil yield, a central composite with a face-centered design was considered.

■ EXPERIMENTAL SECTION

Materials

Sun-dried clove stems were collected from local farmland in Malang, East Java. The stems were cut into 2 cm segments. Distilled water was used as a solvent to extract clove stem oil. While *n*-hexane used was ACS grade (FULLTIME, CAS No. 110-54-3).

Instrumentation

The microwave hydrodistillation method was handled in a reworked domestic microwave oven (Electrolux EMM2308X). The modification and basic experimental set-up of the microwave extraction apparatus were conducted according to several related studies [14-15]. The microwave reactor operates at 2.45 GHz frequency with 800 W maximum power capability. A Clevenger-type apparatus coupled with a reflux condenser were mounted on top of the microwave oven. The distiller used was a one-neck 1000 mL round flask. Chemical compounds of the obtained oil were characterized using AGILENT 5973 Inert MS with AGILENT 6980N GC.

Procedure

Determination of proximate, tannin, and fixed oil

The proximate analysis of the clove stem was conducted following the Association of Official Agricultural Chemists (AOAC) standard procedures. Moisture content was measured by drying 10 g of the sample in an oven at 105 °C to a constant weight. Ash content was determined by burning 2 g of clove stem on a furnace at 600 °C for 2 h [16]. A semi micro-Kjeldahl method was applied to obtain the total crude protein content [17]. Then, tannin and fixed oil were determined using spectrophotometer and Soxhlet method, respectively.

Microwave hydrodistillation (MHD) of clove stem oil

For each extraction, the clove stem samples were then weighed, following pre-specified plant to water ratios. Distilled water with a fixed volume at 200 mL was used as a solvent. The starting time of essential oils accumulation was calculated when the distillation of the first oil droplets was observed. Two phases of condensate were obtained, namely the oil phase and the aqueous phase. Due to its difference in density, a significant amount of oil compounds heavier than water would accumulate at the bottom end of the Clevenger trap, while a small fraction of lower compounds would float at the top of the aqueous phase. The oil phase was collected and decanted using a separatory funnel. Both fractions (the lighter and the heavier-than-water oils) were added to obtain the total clove stem oil. The collected clove stem oils were weighed and stored at a cool and dry place. The obtained oil yield of the clove stem was calculated according to Eq. (1) [18].

$$y = \frac{V}{Z(1-x)} \times 100\% \quad (1)$$

where y is the clove stem oil yield (%, w/w), V is the weight of the clove stem oil (g), Z is the weight of clove stem (g), while x is the water content (%).

FCCD experimental design and analysis of statistic

An experimental design using response surface methodology (RSM) was performed to explore the influence of process variables and characterize the optimal conditions to extract the essential oil. Central composite design (CCD) was applied to study the effect of independent variables as well as the interactive behavior on the response. The total number of test runs required in CCD is $n = 2^k + 2k + n_C$ experiments. Whereas k, 2^k, 2k, and n_C represent the number of factors, factorial point, axial point, and center point runs, respectively.

In this study, the considered independent variables were microwave irradiation power (A: 300–600 W), feed/solvent ratio (B: 0.3–0.7 g mL^{-1}), and microwave extraction time (C: 40–120 min). The dependent variable chosen as the response was the yield of the clove stem oil (Y, % w/w). Each parameter used in the study was coded at three levels of factor points (– 1 for lower bound, 0 for center point, + 1 for upper bound). The coded and actual levels of factors for each experiment were summarized in Table 1. Furthermore, the results of the experimental design are presented in Table 2.

The experimental design for three-factors requires eight (2^3) factorial points, six (2 × 3) axial points, and center point replication (Table 2). In this study, the center points were measured for five replications, thus concluding the total number of experimental runs at n = 8 + 6 + 5 = 19. A total of 19 observations were conducted to fit the second-order polynomial equation as expressed in Eq. (2).

$$Y = \beta_0 + \sum_{j=1}^{k}\beta_j X_j + \sum_{j=1}^{k}\beta_{jj} X_j^2 + \sum_{i}\sum_{<j=2}^{k}\beta_{ij} X_i X_j + e_i \quad (2)$$

whereas Y, β_0, β_i, β_{ii}, β_{ij}, x_i, x_j, and e represent the response variable, regression coefficient depicting intercept value, linear coefficient, quadratic coefficient, interactive coefficient, coded independent parameters, and experimental error, respectively.

Table 1. Code and levels of desired factors

Factors	Factor level		
	-1(-α)	0	1(+α)
Microwave power (W) (A)	300	450	600
Feed-to-solvent ratio (g mL^{-1}) (B)	0.3	0.5	0.7
Extraction time (min) (C)	40	80	120

Table 2. Results of FCCD experiments for clove stem essential oil extraction

Run	Actual variables			Yield of clove stem oil (% w/w)		
	A (W)	B (g mL^{-1})	C (min)	Experimental	Predicted	Residue
1	450	0.5	80	4.6975	4.3509	0.3465
2	450	0.5	80	4.3259	4.3509	-0.0251
3	450	0.5	80	4.4587	4.3509	0.1078
4	450	0.7	80	3.2385	3.4422	-0.2037
5	450	0.3	80	5.4683	5.4184	0.0500
6	600	0.7	40	1.9860	2.1811	-0.1951
7	300	0.3	40	3.1804	3.5213	-0.3409
8	600	0.3	120	6.1023	6.1551	-0.0528
9	300	0.3	120	5.4959	5.2623	0.2336
10	300	0.7	40	1.8267	1.7354	0.0913
11	450	0.5	40	3.2348	2.9003	0.3345
12	450	0.5	80	4.1948	4.3509	-0.1561
13	300	0.5	80	4.1632	4.0753	0.0879
14	600	0.7	120	4.3185	3.9887	0.3298
15	300	0.7	120	3.7738	3.8456	-0.0718
16	450	0.5	120	4.1863	4.6746	-0.4883
17	450	0.5	80	4.3852	4.3509	0.0343
18	600	0.5	80	4.5029	4.7445	-0.2417
19	600	0.3	40	4.8270	4.7168	0.1102

All clove stem oil yields collected from the FCCD were analyzed using the Design Expert 12 (State-Ease, Inc., Minneapolis MN, USA; trial version). A statistical method, analysis of variance (ANOVA), was then carried out to calculate and model the optimum conditions for the MHD of clove stem essential oil. The model adequacy was determined by evaluating the coefficient of determination or R-squared value (R^2), the lack of fit, adjusted determination coefficient (R^2_{Adj}), and adequate precision. This study preferred a statistical significance at p-value < 0.05.

Gas chromatography-mass spectrometry (GC-MS) analysis of chemical component

In determining the quality of the clove stem essential oil obtained using the MHD method, it is necessary to identify the chemical properties of the essential oil. The analysis was performed by identifying the composition of clove stem essential oils using GC-MS (AGILENT 6980N chromatography gas coupled with AGILENT 5973 inert mass spectrometry). The sample was injected at 250 °C inlet temperature with a split ratio of 1:50. The flow rate inside the GC column was held constant at 1 mL min^{-1}. Wiley's mass spectral data library (version 7.0) is used to identify the chromatographic peaks. The peak percentage was calculated using the total ion chromatogram (TIC) peak area [19].

■ RESULTS AND DISCUSSION

Proximate, Tannin, and Fixed Oil Determination of the Clove Stem

It was found that the moisture content of the clove stem was 15.35%. The analysis results show that the clove stem contained a low amount of crude protein (4.95%). It is slightly lower than the crude protein amount from the clove stem measured by Tharpe [20]. It was reported that a relatively small amount of 5.8–6.0% protein was found on the clove stem. Meanwhile, the ash content of 8.94% found in this study is comparable to the previous study (6.9–9.0%). The fixed oil from the clove stem was extracted with n-hexane using the Soxhlet apparatus. We obtained a considerable amount of fixed oil and resin (7.25%), higher than Tharpe's (3.5–4.0%) [20]. Furthermore, a lower tannin content of 6.75% compared to the study reported by Tharpe (with approximately 10% of tannin) [20] was measured.

Model Fitting for Clove Stem Oil MHD

In the current study, the MHD parameters, including microwave irradiation power, feed-to-solvent ratio, and microwave extraction time, were optimized using FCCD to obtain the maximum value of clove stem essential oil yield. The experimental values for extraction yield (% w/w) as a response variable under different combinations were presented in Table 2. The clove stem oil yield varied broadly as a function of process parameters, ranging from 1.826–6.102% w/w.

The least-squares regression was applied to study the relationship of the response with the three regression variables. Tables 3 and 4 present the model fitting procedure generated from the Design Expert statistical software. The obtained experimental data were fitted to a series of regression models, including linear, first-order interaction (2FI), fully quadratic, and cubic models. The polynomial model that is used to approximate the response surface and optimization must not be an aliased model. Furthermore, the selected model must also be the highest-order polynomial with significant additional terms [21]. Due to the central composite design's inability to thoroughly estimate the cubic model parameters, labeled as aliased, thus the model is excluded from further consideration. Table 3 indicates that the fully quadratic model is appropriate because its lack of fit p-value displayed a favorable insignificant statistical trend with 0.0784 (> 0.05), compared to a linear model. An insignificant lack of fit is recommended. The difference between the predicted R-squared of the linear model and its adjusted R-squared is less than 0.2, which depicted a considerable agreement. However, further summarized in Table 3 and the ANOVA results (Table 5, as discussed in the following sub-chapter), the quadratic terms have an almost but not quite significant effect on the response; thus, omitting these factors could negatively affect the data analysis. Furthermore, higher-order polynomial models could explain variations in error terms for the corresponding low-order models [22]. Therefore, we indicated this model for provisional preference.

Table 3. Summary of the sequential model sum of squares (type I) and lack of fit tests from respective models

Source	SS[a]	DF[b]	MS[c]	*F*-value	*p*-Value[d]
Summary of the sequential model sum of squares (type I)					
Mean vs Total	323.23	1	323.23		
Linear vs Mean	18.73	3	6.24	36.80	< 0.0001
2FI vs Linear	0.4129	3	0.1376	0.7748	0.5302
Quadratic vs 2FI	1.17	3	0.3898	3.64	0.0573
Cubic vs Quadratic	0.7680	4	0.1920	4.94	0.0549
Residual	0.1944	5	0.0389		
Total	344.50	19	18.13		
Lack of fit tests					
Linear	2.41	11	0.2187	6.30	0.0452
2FI	1.99	8	0.2491	7.17	0.0372
Quadratic	0.8235	5	0.1647	4.74	0.0784
Cubic (*aliased*)	0.0554	1	0.0554	1.60	0.2751
Pure Error	0.1390	4	0.0347		

[a] Sum of squares
[b] Degree of freedom
[c] Mean sum of squares
[d] *p* values <0.05; significant

Table 4. Summary of respective model statistics

Source	Std. Dev.	R^2	Adjusted R^2	Predicted R^2	PRESS
Linear	0.4119	0.8804	0.8565	0.7918	4.43
2FI	0.4215	0.8998	0.8497	0.5082	10.46
Quadratic	0.3270	0.9548	0.9095	0.5107	10.41
Cubic	0.1972	0.9909	0.9671	-2.3965	72.26

Development of Regression Model and ANOVA Evaluation

A final quadratic polynomial equation regarding the actual factors was obtained by applying the multiple regression analysis, as shown in Eq. (3).

$$y = 1.2969 + 0.0042 * A - 4.8478 * B + 0.0794 * C - 0.0065 * AB - 1.3644e^{-05} * AC + 0.0108 * BC + 2.5194e^{-06} * A^2 + 1.9261 * B^2 - 0.0004 * C^2 \quad (3)$$

where y is the extraction yield of clove stem essential oil (% w/w), A is microwave power (W), B is the feed-to-solvent ratio (g mL^{-1}), and C is the time of extraction (min).

Following the developed equation, interpretation of each factor's effects' on the response regarding the sign and magnitude of the coefficients can be concluded [23]. Coefficients with a plus sign favor optimization thus could promote an increase in the response. Meanwhile, the minus sign indicates a contrary notion on the response, so that an increase in values of the coefficients will decrease the response values. The quadratic model implied that the linear coefficients for microwave power (A) and extraction time (C), the quadratic terms A^2 and B^2, and the interaction variables BC, established positive effects. In contrast, the linear term B, the interactive term AB, and the quadratic term C^2 displayed negative significances on the extraction yield.

The observed data were analyzed using ANOVA, and the results were summarized in Table 5. Evaluation of significance and suitability of the predictive quadratic model was considered by their *p*-value ($p < 0.05$) and Fisher *F*-value. As shown in Table 5, linear terms of feed-to-solvent ratio (B) and extraction time (C) had the most considerable effects ($p < 0.0001$) on the clove stem oil yield. The linear term of microwave power (A) and the quadratic term of the extraction time (C^2) were also significant but less substantial. Otherwise, all the

interaction effects of the model (AB, AC, BC) and the quadratic terms of microwave power (A^2) and the ratio of feed-to-solvent (B^2) were insignificant ($p > 0.05$). Hence, the result suggests that the yield of essential oil from the clove stem is highly dependent on the change of feed-to-solvent ratio and the extraction time. It was also noted that the quality of the quadratic model exhibits a good fit with an *F*-value of 21.11 and a *p*-value < 0.0001. However, the estimated *p*-value for lack of fit was approaching though not reaching the preset significance level (p 0.0784 > 0.05). The lack of fit F value 4.74 describes a 7.84% chance that the large value could occur due to noise. The relatively low probability (< 10%) is concerning. Insignificant model terms could be excluded in order to simplify and improve model sufficiency. The model equation for the MHD of the clove stem oil obtained after eliminating the non-significant effects is expressed in Eq. (4).

$$y = 2.15692 + 0.002198 * A - 4.96527 * B + 0.070905 * C - 0.000305C^2 \quad (4)$$

According to the ANOVA results for the reduced quadratic model summarized in Table 5, the estimated *p*-value for lack of fit is not significant (p 0.1109 > 0.05). This finding indicates that the model equation was adequate for predicting the relevant response. Thus, the variation in the responses could be explained by the model [23]. The values of R-squared (R^2), adjusted R-squared (R^2_{adj}), coefficient of variation (CV%), and adequate precision were also calculated to determine the goodness of the model fit to the experimental data. In this study, the R^2 and R^2_{adj} values were 0.9335 and 0.9145, respectively, indicating a relatively high correlation of the model developed through experimental data [24]. Moreover, the predicted R^2 of 0.8530 is statistically acceptable with the adjusted R^2 of 0.9145. The high value of predicted R^2 signified the model's capability to provide

Table 5. Summary of ANOVA test for the developed fully-quadratic and reduced quadratic model

DoE Model	Source	DF	SS	MS	*F*-value	*p*-Value	
FCCD - fully quadratic	Model	9	20.31	2.26	21.11	< 0.0001	
	A-Microwave power	1	1.09	1.09	10.16	0.0110	
	B-Feed/solvent ratio	1	9.86	9.86	92.22	< 0.0001	
	C-Extraction time	1	7.78	7.78	72.78	< 0.0001	
	AB	1	0.3000	0.3000	2.81	0.1283	[e] ns
	AC	1	0.0536	0.0536	0.5013	0.4968	[e] ns
	BC	1	0.0593	0.0593	0.5548	0.4754	[e] ns
	A^2	1	0.0088	0.0088	0.0821	0.7809	[e] ns
	B^2	1	0.0162	0.0162	0.1517	0.7060	[e] ns
	C^2	1	0.8746	0.8746	8.18	0.0188	
	Residual	9	0.9624	0.1069			
	Lack of fit	5	0.8235	0.1647	4.74	0.0784	[e] ns
	Pure error	4	0.1390	0.0347			
	Total	18	21.28				
FCCD - reduced quadratic	Model	4	19.86	4.97	49.15	< 0.0001	
	A-Microwave power	1	1.09	1.09	10.76	0.0055	
	B-Feed/solvent ratio	1	9.86	9.86	97.62	< 0.0001	
	C-Extraction time	1	7.78	7.78	77.04	< 0.0001	
	C^2	1	1.13	1.13	11.19	0.0048	
	Residual	14	1.41	0.1010			
	Lack of fit	10	1.28	0.1275	3.67	0.1109	[e] ns
	Pure error	4	0.1390	0.0347			
	Total	18	21.28				

[e] ns: not significant

valid predictions on new experimentations. The coefficient of variation (CV%) value of 7.71% indicated good precision and reliability of the experimental results. A value of the coefficient of variation below 10 is desired, implying that the model is reproducible [25]. In addition, an adequate precision level that is greater than 4 is preferred. The adequate precision resulted in this study was 27.0460, which defines as an adequate signal and signifies good fitness of the developed model. Thus, the reduced quadratic model could be applied to optimize the MHD extraction process.

Diagnostic of Reduced Second-Order Model Adequacy

Evidence on the relationship and model sufficiency is acquirable by plotting essential oil yield predicted and experimental values on a fitted-line plot. Fig. 1(a) displayed the normal probability plot of residuals derived from the reduced quadratic model for the yield of clove stem oil. The plot indicates that the residuals follow the straight line, thus reflected normal distribution. A small residual value is desirable since it implied that the model prediction is accurate [23]. Moreover, from Fig. 1(b), it was observed that the experimental values were adjacent to the straight line of the predicted yields. Appropriate prediction on the yield of the clove stem oil was apparent in the developed model, as revealed by the plot. This result thus corroborated the high calculated R^2 value (0.9335).

Fig. 2 demonstrated the relationship between externally studentized residuals and run number of (a) reduced quadratic and (b) fully quadratic models. The graph was plotted to evaluate the experimental data and identify the sufficient fit of the developed models [24]. The residuals between the observed data values and the model-predicted responses fall within the acceptable range of −4 to +4 shown in Fig. 2(a). Therefore, by applying the reduced quadratic model equation, it can be concluded that no outliers were identified among the actual data set obtained from the experiment. In contrast, there was one observation detected that was likely to be an outlier in Fig. 2(b).

Analysis of Response Surfaces and Contour Plots

To better understand the behavior of the developed reduced quadratic model, analysis of response surface and contour plots for each model were presented and discussed. Three-dimensional (3D) response surface and two-dimensional (2D) contour plots of the regression models were applied to represent the interrelation between independent and response variables (Fig. 3-4). The results demonstrated the effects of each independent variable (extraction time, irradiation power, the feed-to-solvent ratio) and their interactions on the oil yield of clove stem. In general, the extraction yield obtained in this study increases as the microwave power and extraction time increase.

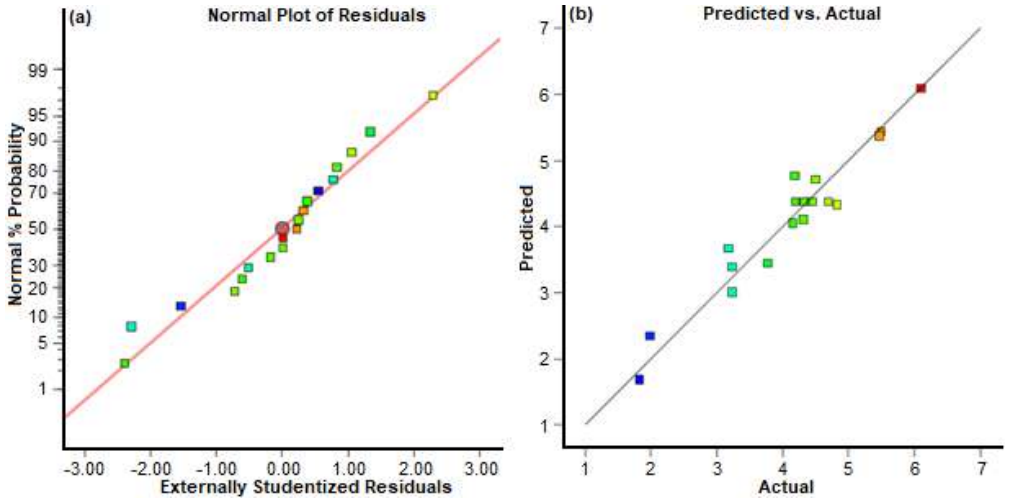

Fig 1. Plots of reduced quadratic model: (a) Normal % Probability, and (b) Predicted vs. Actual

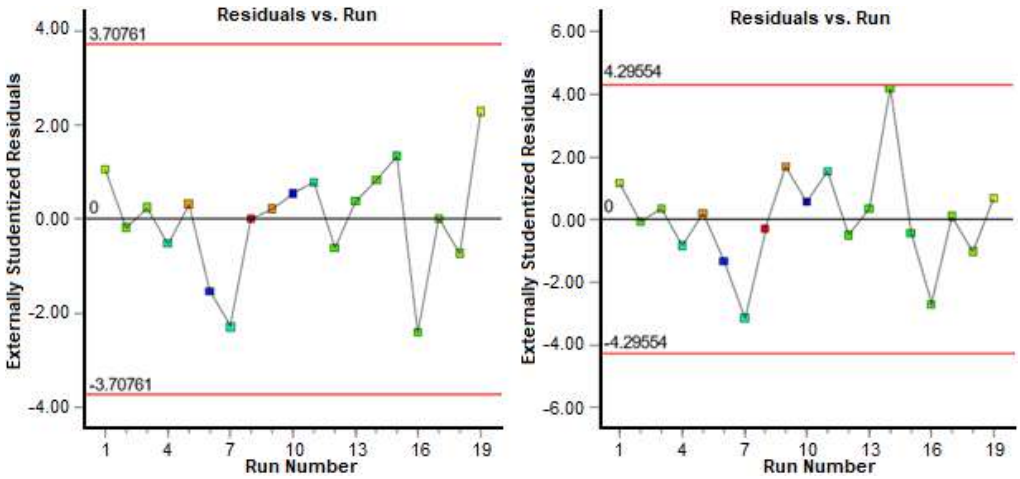

Fig 2. Externally studentized residuals vs. run number plots of (a) Reduced quadratic, and (b) Fully quadratic models

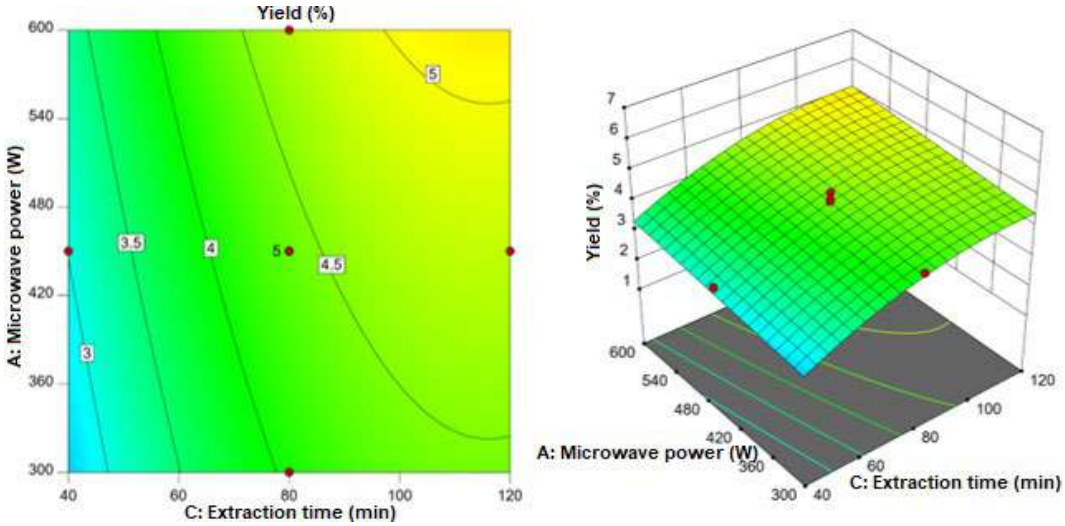

Fig 3. The 2D contour plot (left) and 3D response surface (right) of the reduced quadratic model displaying the effect of parameters (A) the microwave power and (C) the extraction time on the clove stem oil yield

Fig. 3 displays the mutual effects of microwave irradiation power and extraction time at a fixed 0.5 g mL^{-1} feed-to-solvent ratio. The increase of both microwave power (300–600 W) and extraction time (40–120 min) significantly improved the yield of clove stem oil, as portrayed in Fig. 3. Higher microwave power level promotes greater energy received by the solvent and plant matrix, which in turn causes the yield of clove stem essential oil to rise. The higher yield obtained follows the rapid increase in temperature due to the increasing amount of irradiation power emitted. An increase in solvent power is encouraged due to reduced solvent viscosity and surface tension between sample matrix and solvent. This behavior facilitates enhanced wetting of sample and solvent penetration, resulting in improved solubility and diffusion rates of solutes [26]. The result is similar to Singh et al. [27], who studied lemongrass oil extraction by microwave heating and showed that a high microwave power level could provide a higher yield and accelerate the extraction time. However, other studies have also suggested that further increasing microwave power up to a certain level causes degradation of thermolabile substances and volatiles, thus negatively affected the oil yields [28-29].

Nevertheless, the effect of irradiation power on the extracted clove oil yield at a low feed/solvent ratio was greater than the effect at a high feed/solvent ratio (Fig. 4). Fig. 4 describes the interactive effect of microwave

power and feed matrices to water ratio for a constant extraction time of 80 min. It can be implied that the microwave power and feed/solvent ratio have antagonistic effects on the yield of clove stem oil. The yield of oil from clove stem increased with decreasing feed/solvent ratio from 0.7 to 0.3 g mL^{-1}. Increasing the mass of raw materials reduces the surface area of the material that can be penetrated by the solvent, thereby reducing the solvent's ability to extract and isolate the essential oil out of the plant matrices [30-31].

Moreover, increased microwave power encourages the extraction rate of the essential oil, which improves the oil yield obtained. As depicted in Fig. 4, the highest oil yield was obtained at a higher irradiation power range from 470 up to 600 W and a lower range of feed/solvent ratios (0.3–0.4 g mL^{-1}). However, it was also observed that a higher feed/solvent ratio (0.6–0.7 g mL^{-1}) could only provide a slight amount of oil yield at any level of irradiation power. At high solid loading (lower ratio of solvent), the changes in microwave power showed no significant effect on the extract yield. This result might be due to the decrease of the incident microwaves per particle with the increase of solid loading in the vessel at a particular power level, thus reduced the dielectric heating effect [32]. This finding is comparable with phenolic compounds extraction from *V. cinerea leaves* under microwave radiation [33].

Optimization of Extraction Conditions of Essential Oil from Clove Stem

According to the reduced second-order model expressed in Eq. (4), the optimal experimental conditions to improve the clove stem essential oil yield were the level of microwave power 599.883 W, feed/solvent ratio 0.3 g mL^{-1}, and microwave extraction time 116.656 min. Under these conditions, the maximum yield of clove stem oil (6.102%, w/w) was obtained. Experiments were conducted to validate the optimum parameter conditions. Adjustment on some parameters, such as microwave power and extraction time, was made to facilitate the observation. The microwave power value used in this experiment was 600 W. Comparison of the optimized parameter derived from the reduced quadratic model and fully quadratic model was presented in Table 6. The results showed that the experimental yield obtained was approaching the predicted value of the reduced quadratic model. Thus, it can be implied that the reduced second-order model was provisionally adequate to describe the effects of corresponding variables on the yield of clove stem oil obtained from MHD.

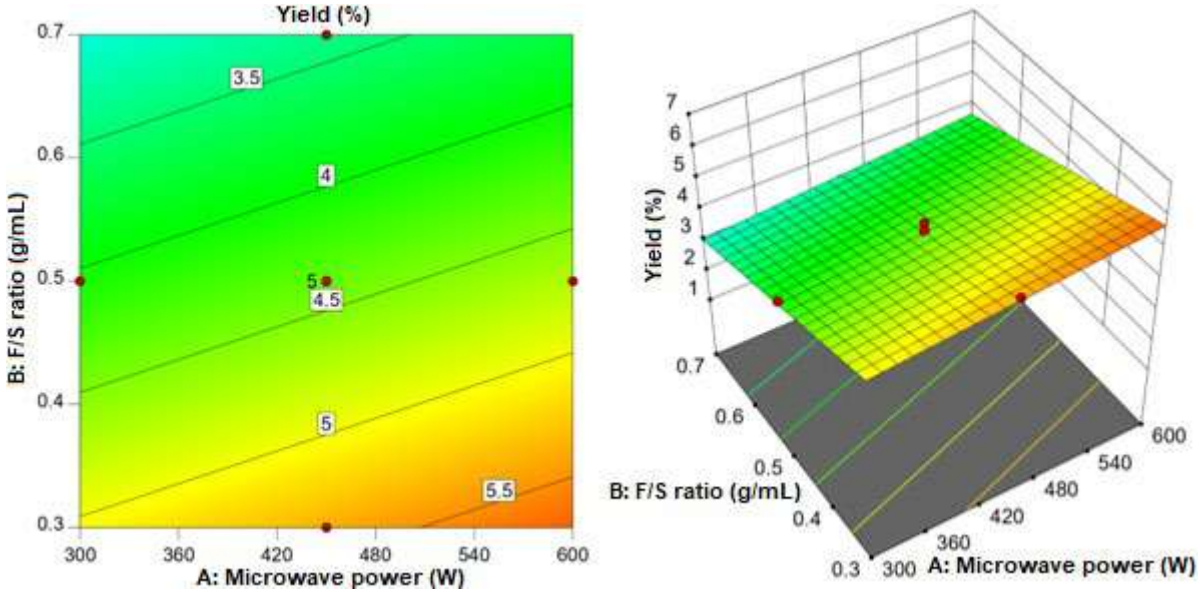

Fig 4. The 2D contour plot (left) and 3D response surface (right) of the reduced quadratic model displaying of the microwave power (A) and feed/solvent ratio (B) on the clove stem oil extraction yield

Table 6. Comparison of validation experiments

Model	Optimized parameter (predicted value)	Optimized parameter (experimental value)	Predicted yield (%, w/w)	Experimental yield (%, w/w)	Residuals (%, w/w)
Fully quadratic	597.62 W; 0.304 g mL^{-1}; 104.958 min	600 W; 0.304 g mL^{-1}; 105 min	6.194	4.997	1.197
Reduced quadratic	599.883 W; 0.3 g mL^{-1}; 116.656 min	600 W; 0.3 g mL^{-1}; 116 min 39 sec	6.102	5.585	0.517

The Chemical Constituents of The Clove Stem Essential Oil

The chemical composition of the clove stem oil obtained by MHD under the operating conditions; 600 W, feed/solvent ratio 0.5 g mL^{-1}, extraction time 120 min, was identified using GC-MS (Table 7). A total of 9 constituents of the clove stem oil yield obtained from this study were identified by GC-MS analysis, i.e. methyl salicylate, chavicol, eugenol, eugenyl acetate, methyl eugenol, caryophyllene oxide, and three unknown compounds. The major chemical substance was eugenol, which accounted for 95.91% of the total essential oil yield derived from clove stem. Compared with those several studies reported on the extraction of clove stem using conventional methods such as distillation [34] and steam distillation [35], eugenol was also present as the main chemical constituent.

Contrary to other reports that applied conventional-based methods [7,20,35-36], no β-caryophyllene (BCP) was observed in this study. In a previous study evaluating the effect of microwave extraction on the chemical composition of clove bud oil, a significant decrease in BCP content was described by Kennouche et al. [37]. It was reported that reduction in BCP was observed on the clove oil extracted using MHD (17.2%), but higher BCP content was attained using conventional hydrodistillation. No significant changes to caryophyllene oxide – a secondary oxidation product of BCP – were reported, despite a slight increase of other caryophyllene derivatives and isomers was identified upon irradiation. It could be implied that the evaporation of some of the more volatile terpenes (e.g., BCP) was slightly accelerated by microwave irradiation. The formation of other BCP derivatives could also suggest the effect of irradiation in BCP degradation.

Interestingly, another study conducted by Golmakani et al. [38] on clove bud oil extraction using conventional and microwave-assisted hydrodistillation reported different results. A significant increase in caryophyllene and humulene – a caryophyllene isomer – and a slight decrease in caryophyllene oxide were observed upon irradiation. Golmakani et al. [38] also disclosed in their study that reduction in eugenol, caryophyllene, and caryophyllene oxide was observed on the steam distillation product, compared to conventional and MHD methods. It was reported that a lower extraction rate was observed due to a longer duration required for conventional methods could affect the extracted oil.

Table 7. The clove stem oil composition obtained from this study

RT (min)	Constituents	% Normalized area
8.36	Methyl salicylate	0.34
10.70	Chavicol	0.13
11.68; 11.91; 11.96	Eugenol	95.91
12.34	Methyl Eugenol	0.61
13.47	Eugenyl acetate	0.93
13.94	Caryophyllene oxide	1.40
14.19	Unknown	0.14
18.21	Unknown	0.18
28.25	Unknown	0.37

While the current study indicated the presence of caryophyllene oxide (1.40%) and no presence of BCP and/or other BCP derivatives was identified, it is difficult to justify whether irradiation solely affected the oil compositions. Nevertheless, irradiation would probably affect the loss of BCP observed in the current study, owing to the volatileness and heat-sensitive characteristic of the terpene [39-40]. Other factors such as irrigation [41], crushing [42], drying process and storage [43], as well as the characteristics of plant matrix that is highly influenced by geographical and ecological situation [44], has also been reported to significantly influence the chemical constituents of essential oils.

■ CONCLUSION

An experimental design based on the FCCD was successfully implemented to optimize the MHD of essential oil yield derived from the clove stem. The reduced quadratic model was developed to optimize the operating conditions of the MHD extraction of clove stem oil. The coefficient determination (R^2) and adjusted R^2 (R^2_{adj}) of the developed reduced quadratic model were 0.9335 and 0.9145, respectively, showing a relatively high degree of precision between the model-predicted and experimental values. It was also found that the operating parameters, particularly microwave irradiation power and extraction time, had the most significant impact on the extraction yield. Furthermore, the MHD method is allusive as a conscientious technique for extracting essential oils derived from clove stem for numerous applications in industry, owing to its significant extraction efficiency.

■ ACKNOWLEDGMENTS

This work was supported by the Directorate General of the Science and Technology Resource and Higher Education through the *Pendidikan Magister Menuju Doktor untuk Sarjana Unggul* (*PMDSU*) Scholarship Batch IV scheme. We would like to thank Verycha F.W. Tania, Ayu M. Suyadi, and Heri S. Kusuma for their technical support on this project. We also appreciate the assistance given by the technical staffs of ULP Faculty of Pharmacy and Nutrition Lab Faculty of Public Health Universitas Airlangga.

■ REFERENCES

[1] Aydın, B., and Barbas, L.A.L., 2020, Sedative and anesthetic properties of essential oils and their active compounds in fish: A review, *Aquaculture*, 520, 734999.

[2] Tian, B.L., Liu, Q.Z., Liu, Z.L., Li, P., and Wang, J.W., 2015, Insecticidal potential of clove essential oil and its constituents on *Cacopsylla chinensis* (Hemiptera: Psyllidae) in laboratory and field, *J. Econ. Entomol.*, 108 (3), 957–961.

[3] Jeyakumar, N., and Narayanasamy, B., 2019, Clove as antioxidant additive in diesel–biodiesel fuel blends in diesel engines, *Int. J. Green Energy*, 16 (4), 284–292.

[4] Kuete, V., 2017, *Medicinal Spices and Vegetables from Africa Therapeutic Potential Against Metabolic, Inflammatory, Infectious and Systemic Diseases*, Academic Press, Amsterdam.

[5] Nurdjannah, N., 2016, Diversifikasi penggunaan cengkeh, *Perspektif*, 3 (2), 61–70.

[6] Hu, Q., Zhou, M., and Wei, S., 2018, Progress on the antimicrobial activity research of clove oil and eugenol in the food antisepsis field, *J. Food Sci.*, 83 (6), 1476–1483.

[7] Kaur, K., Kaushal, S., and Rani, R., 2019, Chemical composition, antioxidant and antifungal potential of clove (*Syzygium aromaticum*) essential oil, its major compound and its derivatives, *J. Essent. Oil-Bear. Plants*, 22 (5), 1195–1217.

[8] Guan, W., Li, S., Yan, R., Tang, S., and Quan, C., 2007, Comparison of essential oils of clove buds extracted with supercritical carbon dioxide and other three traditional extraction methods, *Food Chem.*, 101 (4), 1558–1564.

[9] Rastuti, U., Diastuti, H., Chasani, M., Purwati, and Hidayatullah, R., 2020, Chemical composition and antioxidant activities of citronella essential oil *Cymbopogon nardus* (L.) Rendle fractions, *AIP Conf. Proc.*, 2237, 020035.

[10] Golmakani, M.T., and Moayyedi, M., 2016, Comparison of microwave-assisted hydrodistillation and solvent-less microwave extraction of essential oil from dry and fresh Citruslimon (Eureka variety) peel, *J. Essent. Oil Res.*, 28 (4), 272–282.

[11] Kusuma, H.S., Putri, D.K., Triesty, I., and Mahfud, M., 2019, Comparison of microwave hydro-distillation and solvent-free microwave extraction for extraction of agarwood oil, *Chiang Mai J. Sci.*, 46 (4), 741–755.

[12] Marković, M.S., Milojević, S., Bošković-Vragolović, N.M., Pavićević, V.P., Babincev, L., and Veljković, V.B., 2019, A new kinetic model for the common juniper essential oil extraction by microwave hydro-distillation, *Chin. J. Chem. Eng.*, 27 (3), 605–612.

[13] Veggi, P.C., Martinez, J., and Meireles, M.A.A., 2013, "Fundamentals of Microwave Extraction" in

Microwave-assisted Extraction for Bioactive Compounds, Eds. Chemat, F., and Cravotto, G., Springer, US, 15–52.

[14] Abedi, A.S., Rismanchi, M., Shahdoostkhany, M., Mohammadi, A., and Mortazavian, A.M., 2017, Microwave-assisted extraction of *Nigella sativa* L. essential oil and evaluation of its antioxidant activity, *J. Food Sci. Technol.*, 54 (12), 3779–3790.

[15] Ma'sum, Z., Kusuma, H.S., Altway, A., and Mahfud, M., 2019, On the effect of the ratio of the distiler volume and that of the microwave cavity on the extraction of C*ymbopogon nardus* dried leaves by microwave hydro-distillation, *J. Chem. Technol. Metall.*, 54 (4), 778–786.

[16] AOAC, 2005, *Official Methods of Analysis of AOAC International*, 18th Ed., AOAC International, Gaithersburg, MD, USA, Official Method 942.05.

[17] AOAC, 2005, *Official Methods of Analysis of AOAC International*, 18th Ed., AOAC International, Gaithersburg, MD, USA, Official Method 978.04.

[18] Kusuma, H.S., Syahputra, M.E., Parasandi, D., Altway, A., and Mahfud, M., 2017, Optimization of microwave hydro-distillation of dried patchouli leaves by response surface methodology, *Rasayan J. Chem.*, 10 (3), 861–865.

[19] Kiliç, M., Pütün, A.E., Uzun, B.B., and Pütün, E., 2014, Converting of oil shale and biomass into liquid hydrocarbons via pyrolysis, *Energy Convers. Manage.*, 78, 461–467.

[20] Ketaren, S., 1985, *Pengantar Teknologi Minyak Atsiri*, Balai Pustaka, Jakarta.

[21] Myers, R.H., Montgomery, D.C., and Anderson-Cook, C.M., 2016, *Response Surface Methodology: Process and Product Optimization Using Designed Experiments*, 4th Ed., Wiley, Hoboken, New Jersey.

[22] Anderson, M.J., and Whitcomb, P.J., 2016, *RSM Simplified: Optimizing Processes Using Response Surface Methods for Design of Experiments*, 2nd Ed., CRC Press, Boca Raton, Florida.

[23] Belhachat, D., Mekimene, L., Belhachat, M., Ferradji, A., and Aid, F., 2018, Application of response surface methodology to optimize the extraction of essential oil from ripe berries of *Pistacia lentiscus* using ultrasonic pretreatment, *J. Appl. Res. Med. Aromat. Plants*, 9, 132–140.

[24] Maran, J.P., Manikandan, S., Vigna Nivetha, C., and Dinesh, R., 2017, Ultrasound assisted extraction of bioactive compounds from *Nephelium lappaceum* L. fruit peel using central composite face centered response surface design, *Arabian J. Chem.*, 10, S1145–S1157.

[25] Mason, R.L., Gunst, R.F., and Hess, J.L., 2003, *Statistical Design and Analysis of Experiments, with Applications to Engineering and Science,* 2nd Ed., Wiley-Interscience, New Jersey.

[26] Ameer, K., Shahbaz, H.M., and Kwon, J.H., 2017, Green extraction methods for polyphenols from plant matrices and their byproducts: A review, *Compr. Rev. Food Sci. Food Saf.*, 16 (2), 295–315.

[27] Singh, N., Shrivastava, P., and Shah, M., 2014, Microwave-assisted extraction of lemongrass essential oil: Study of the influence of extraction method and process parameters on extraction process, *J. Chem. Pharm. Res.*, 6 (11), 385–389.

[28] Liu, B., Fu, J., Zhu, Y., and Chen, P., 2018, Optimization of microwave-assisted extraction of essential oil from lavender using response surface methodology, *J. Oleo Sci.*, 67 (10), 1327–1337.

[29] Tran, T., Nguyen, H., Nguyen, D., Nguyen, T., Tan, H., Nhan, L., Nguyen, D., Tran, L., Do, S., and Nguyen, T., 2018, Optimization of microwave-assisted extraction of essential oil from Vietnamese basil (*Ocimum basilicum* L.) using response surface methodology, *Processes*, 6 (11), 206.

[30] Ballard, T.S., Mallikarjunan, P., Zhou, K., and O'Keefe, S., 2010, Microwave-assisted extraction of phenolic antioxidant compounds from peanut skins, *Food Chem.*, 120 (4), 1185–1192.

[31] Rostagno, M.A., and Prado, J.M., 2013, *Natural Product Extraction: Principles and Applications*, Royal Society of Chemistry, Cambridge.

[32] Desai, M.A., and Parikh, J., 2012, Microwave assisted extraction of essential oil from *Cymbopogon flexuosus* (steud.) Wats.: A parametric and comparative study, *Sep. Sci. Technol.*, 47 (13), 1963–1970.

[33] Alara, O.R., Abdurahman, N.H., Ukaegbu, C.I., and Azhari, N.H., 2018, *Vernonia cinerea* leaves as the source of phenolic compounds, antioxidants, and anti-diabetic activity using microwave-assisted extraction technique, *Ind. Crops Prod.*, 122, 533–544.

[34] Guenther, E., 1950, *The Essential Oils: Vol. 4: Individual Essential Oils of the Plant Families Gramineae, Lauraceae, Burseraceae, Myrtaceae, Umbelliferae and Geraniaceae*, D. Van Nostrand Company, Inc., New York.

[35] Gaylor, R., Michel, J., Thierry, D., Panja, R., Fanja, F., and Pascal, D., 2014, Bud, leaf and stem essential oil composition of *Syzygium aromaticum* from Madagascar, Indonesia and Zanzibar, *Int. J. Basic Appl. Sci.*, 3 (3), 224–233.

[36] Boughendjioua, H., 2018, Essential oil composition of *Syzygium aromaticum* (L.), *Int. Res. J. Pharm. Med. Sci.*, 1 (3), 26–28.

[37] Kennouche, A., Benkaci-Ali, F., Scholl, G., and Eppe, G., 2015, Chemical composition and antimicrobial activity of the essential oil of *Eugenia caryophyllata* cloves extracted by conventional and microwave techniques, *J. Biol. Act. Prod. Nat.*, 5 (1), 1–11.

[38] Golmakani, M.T., Zare, M., and Razzaghi, S., 2017, Eugenol enrichment of clove bud essential oil using different microwave-assisted distillation methods, *Food Sci. Technol. Res.*, 23 (3), 385–394.

[39] Wang, F., Teng, Z., Liu, D., Wang, Y., Lou, J., and Dong, Z., 2020, β-Caryophyllene liposomes attenuate neurovascular unit damage after subarachnoid hemorrhage in rats, *Neurochem. Res.*, 45 (8), 1758–1768.

[40] Sköld, M., Karlberg, A.T., Matura, M., and Börje, A., 2006, The fragrance chemical β-caryophyllene - Air oxidation and skin sensitization, *Food Chem. Toxicol.*, 44 (4), 538–545.

[41] Sałata, A., Buczkowska, H., and Nurzyńska-Wierdak, R., 2020, Yield, essential oil content, and quality performance of *Lavandula angustifolia* leaves, as affected by supplementary irrigation and drying methods, *Agriculture*, 10 (12), 590.

[42] Safrudin, I., Maimulyanti, A., and Prihadi, A.R., 2015, Effect of crushing of clove bud (*Syzygium aromaticum*) and distillation rate on main constituents of the essential oil, *Am. J. Essent. Oils Nat. Prod.*, 2 (3), 12–15.

[43] Hastuti, L.T., Saepudin, E., Cahyana, A.H., Rahayu, D.U.C., Murni, V.W., and Haib, J., 2017, The influence of sun drying process and prolonged storage on composition of essential oil from clove buds (*Syzygium aromaticum*), *AIP Conf. Proc.*, 1862, 030092.

[44] Tran, T.H., Nguyen, D.C., Phu, T.N.N., Ho, V.T.T., Vo, D.V.N., Bach, L.G., and Nguyen, T.D., 2019, Research on lemongrass oil extraction technology (hydro-distillation, microwave-assisted hydro-distillation), *Indones. J. Chem.*, 19 (4), 1000-1007.

Adsorption of Pb(II) from Aqueous Solutions onto Humic Acid Modified by Urea-Formaldehyde: Effect of pH, Ionic Strength, Contact Time, and Initial Concentration

Meidita Kemala Sari[1], Rahmat Basuki[2,3], and Bambang Rusdiarso[4*]

[1]*Master Programs, Department of Chemistry, Faculty Mathematics and Natural Science, Universitas Gadjah Mada, Sekip Utara, PO BOX BLS 21, Yogyakarta 55281, Indonesia*

[2]*Doctoral Programs, Department of Chemistry, Faculty Mathematics and Natural Science, Universitas Gadjah Mada, Sekip Utara, PO BOX BLS 21, Yogyakarta 55281, Indonesia*

[3]*Department of Chemistry, Faculty of Military Mathematics and Natural Sciences, Universitas Pertahanan RI, Bogor 16810, Indonesia*

[4]*Department of Chemistry, Faculty Mathematics, and Natural Science, Universitas Gadjah Mada, Sekip Utara, PO BOX BLS 21, Yogyakarta 55281, Indonesia*

** **Corresponding author:***

tel: +62-8156860897
email: brusdi_mipa@ugm.ac.id

Received: March 9, 2021
Accepted: July 22, 2021

DOI: 10.22146/ijc.64600

Abstract: *Humic acid (HA) and urea-formaldehyde (UF) have been frequently reported as heavy metal adsorbents. However, the literature has never written HA modification by UF to improve the adsorbent's performance. In this study, a new adsorbent of humic acid-urea formaldehyde (HA-UF) was synthesized. The reaction of the conducted the formation of HA-UF –COOH group of HA with the –NH_2 group of UF was evidenced by decreasing total acidity from 549.26 cmol/kg (in HA) to 349.30 cmol/kg (in HA-UF). The success of HA-UF formation was characterized by attenuated total reflection-infrared (ATR-IR), energy dispersive X-Ray (EDX), and X-ray diffraction (XRD). The high stability of HA-UF was shown by 96.8% remaining in solid form at pH 12.4. Adsorption behavior of Pb(II) onto HA-UF was influenced by the ionic strength and pH, which were mainly driven by the ion exchange mechanism (E_{DR} = 9.75 kJ/mol). The higher ionic strength will affect decreasing adsorbed Pb(II) at the optimum pH of 5.5. The effect of initial Pb(II) concentration (isotherm) shows that the data fitted well with the Langmuir-b isotherm model indicated the monolayer adsorption of Pb(II) onto homogenous surfaces of the HA-UF with the adsorption capacity of 2.26 × 10^{-4} mol/g (which is higher than its original HA of 1.12 × 10^{-4} mol/g). The Ho (pseudo-second-order) kinetics model represented the effect of contact time (kinetics) was represented by the Ho kinetics model. The synthesized adsorbent is also reusable, with 88.59% of adsorption capacity remaining in the fifth recycle run. Therefore, the adsorbent of HA-UF is suggested to be a promising candidate for adsorption applications.*

Keywords: *humic acid-urea formaldehyde (HA-UF); Pb(II) adsorption; pH and ionic strength; isotherm; kinetics studies*

■ INTRODUCTION

According to the World Health Organization (WHO), the heavy metals requiring immediate attention to remove from the environment are Cr, Cd, Zn, Fe, Hg, Co, and Pb [1]. Therefore, removing heavy metals from water or wastewater is a major concern in water treatment. Various methods are reported to reduce heavy metals, such as ionic exchange, electrolysis, membrane separation, chemical precipitation, and adsorption. Of all the methods above, adsorption is considered one of the simplest and most effective techniques [2]. To date, various effective adsorbents such as activated carbon [3], humic acid (HA) [4], MWCNTs [5], γ-alumina [5], chitosan-coated Fe_3O_4 [6], granular ferric hydroxide [7],

and urea-formaldehyde (UF) [8] have been reported in the literature.

Recently, HA has been widely utilized to reduce heavy metals, pigments, radioactive and organic pollutants in water. HA contains various functional groups involved in the binding and entrapment of metal ions. In addition, HA is economically affordable, eco-friendly, abundant sources, and does not cause secondary pollution. Although it possesses many promising properties, natural HA is easy to dissolve in an alkaline medium, reducing its performance as an adsorbent. Previous works have successfully modified HA with chitin or chitosan [9], magnetite [10], titanium dioxide [11], Ca-montmorillonite [12], attapulgite [13], starch [14], and carboxymethylcellulose (CMC) [15], to achieve HA-based high-performance adsorbent. As reported in the literature, the requirements of HA modifiers are relatively stable at high pH, low cost, high availability, and abundant functional groups materials. One of the materials that possess these properties, but no publication reported it as HA modifier, is urea-formaldehyde (UF).

UF is a low-cost polymeric condensation product of urea and formaldehyde, consisting of [–CH_2–NH–CO–NH–CH_2–] repeating units. UF is rich in amine, amide, hydroxyl, and carbonyl groups which can interact with many metal ions in an aqueous solution through a complexation mechanism. Other researchers have previously reported the study of UF as an adsorbent for heavy metal ions [8,16-19]. The study results showed that UF adsorbent could efficiently remove highly concentrated heavy metal ions from aqueous solutions. However, no publications were found investigating HA-UF as a heavy metal adsorbent. In contrast, the modification of HA by UF can enhance an HA-based adsorbent with high stability, low cost, and high performance.

This study aims to investigate the formation of HA-UF and the adsorption performances of HA-UF in three aspects, i.e., the effect of pH and ionic strength, initial concentration (isotherm study), and contact time (kinetics study). Pb(II) was selected as the adsorbate model for evaluating HA-UF performance because of its toxic properties and wide application in food cane solders, ceramic glaze, batteries, cosmetics, and mining industries [20]. Further, the reusability of the HA-UF as Pb(II) adsorbent was also investigated in this work.

■ EXPERIMENTAL SECTION

Materials

HA was extracted from 100 mesh dry peat soil powder of Indragiri Hilir, Riau, Indonesia. The extraction and the purification of HA were performed by the IHSS (International Humic Substance Society) method. The urea used in this study was commercial urea which is available in Yogyakarta. All reagents were pro analyst grade, i.e., formaldehyde solution 37%, NaOH pellet, HCl fuming 37%, HF solution 48%, HNO_3 solution 65%, CH_3COOH glacial 100%, $Ba(OH)_2$ powder, $Pb(CH_3COO)_2{\cdot}2H_2O$ powder, and NaCl powder produced by Merck® and they are used without further purifications.

Procedure

Preparation of the adsorbent

Five grams of urea were dissolved in 14 mL of 37% formaldehyde (mole ratio = 1:2). After 3 min of stirring, dissolved HA (5 g) was added in 200 mL of NaOH 0.1 M. The mixture was stirred and refluxed for 4 h at 75 °C. The mixture was then cooled to room temperature and neutralized by adding HCl 2.5 M dropwise. The mixture was separated by 3950 rpm centrifugation for 10 min to obtain sediment (the sediment was a dark brown solid, and the filtrate was a yellow liquid). The solid was washed with distilled water and dried at 60 °C as HA-UF dry adsorbent. HA-UF was characterized with Attenuated Total Refection-IR (ATR-IR Thermo Scientific Nicolet iS50 at 400–4000 cm^{-1} wavenumber), XRD (PANalytical X'pert PRO MRD with Ni-filtered Cu Kα radiation as the X-Ray source between 2θ = 3°–90°), and SEM-EDX (Analysis Phenom-World JSM 6510LA-Phenom world Analysis).

Properties of synthesized adsorbent

The difference of total acidity also carried out HA-UF properties, pH point of zero charges (pH_{PZC}), and stability at varied pH with the original HA as a comparison. The Baryta indirect potentiometric titration method was determined by the total acidity of HA-UF

and HA. The pH_{PZC} was conducted by dissolving 50 mg of sample (HA-UF and HA) in 25 mL of distilled water with a pH range of 2.0–11.0. The mixture was shaken at 250 rpm for 1 h and aged for 48 h. The pH_{PZC} was identified by plotting the initial pH vs. the final and initial pH difference (ΔpH). The stability of the adsorbent was carried out by dissolving 0.1 g of each sample in distilled water with a pH range of 1.0–14.0 in different test tubes. After 24 h stirring, the remaining solids were weighed, and the percentage was calculated as the stability of the adsorbent.

Effect of medium acidity and ionic strength

A series of 20 mL of Pb(II) 20 mg/L at adjusted pH by adding HCl and NaOH solution ranging from 2.2–8.8 was prepared. Into each of the prepared solutions, 50 mg of HA-UF was added. After 3 h of shaking by 250 rpm, the mixture was filtered, and the filtrate was analyzed with Flame-AAS (Perkin Elmer 3110) to obtain adsorbed Pb(II). The highest adsorbed Pb(II) was clearing as the optimum pH.

The effect of ionic strength was carried out in two aspects: pH_{PZC} of adsorbent and Pb(II) adsorption. The effect of ionic strength on the pH_{PZC} adsorbent was conducted by a similar procedure to determine pH_{PZC}. However, NaCl was added to each sample so that the final concentration of NaCl was 0.1 M. The effect of ionic strength on Pb(II) adsorption was studied by preparing a 5 series of 20 mL of Pb(II) 20 mg/L at optimum pH. NaCl was added to the solution so that the final concentrations of NaCl were 0.1, 0.2, 0.3, 0.4, and 0.5 M. After 3 h shaking at 250 rpm, the mixture was filtered, and the filtrate was analyzed with Flame-AAS to measure the adsorbed Pb(II).

Every sample was accompanied by a blank solution containing no HA-UF adsorbent, and both of them were treated under identical conditions. The amount of Pb(II) adsorbed into the HA-UF was considered to be the difference between the initial (blank solution) and the remaining amount of Pb(II) in the sample.

Isotherm and kinetic adsorption experiments

The isotherm experiments were carried out by contacting the adsorbent with Pb(II) at various concentrations. Fifty milligrams of adsorbent were interacted with 20 mL of Pb(II) solutions with various concentrations (5, 10, 20, 30, 40, 60, 80, 100, 150, and 200 mg/L) at optimum pH. After 180 min of 250 rpm shaking, the mixture was filtered, and the filtrate was analyzed with Flame-AAS.

The kinetics experiments were carried out by contacting 50 mg adsorbent with 20 mL of Pb(II) 20 mg/L at different contact times (10, 20, 30, 50, 60, 90, and 180 min). A similar procedure was also performed with different initial concentrations of Pb(II) (50 and 100 mg/L). After being shaken at 250 rpm at a determined contact time, the mixture was filtered, and the Pb(II) concentration in the filtrate was analyzed with Flame-AAS.

Every sample was accompanied by a control solution containing no HA-UF adsorbent indicating Pb's actual initial concentration (II). Under the same condition as a sample solution, a control solution was also analyzed. The amount of Pb(II) adsorbed into the HA-UF was considered to be the difference between the initial (control solution) and the remaining amount of Pb(II) in the sample.

Error analysis

Six error functions of average relative error (ARE), sum squares errors (SSE), hybrid fractional error function (HYBRID), sum of absolute error (EABS), nonlinear chi-square test (χ^2), and standard deviation of relative errors (S_{RE}) were applied to evaluate the match of the linear and nonlinear adsorption isotherm (and kinetics) parameters [21]. These error functions estimate the deviation between the experimental data and parameters values predicted by the isotherm models. Six error functions are expressed, as follows:

$$ARE = \frac{100}{x}\sum_{i=1}^{x}\left|\frac{q_{e,means} - q_{e,calc}}{q_{e,means}}\right| \quad (1)$$

$$SSE = \sum_{i=1}^{x}(q_{e,calc} - q_{e,means})_i^2 \quad (2)$$

$$HYBRID = \frac{100}{x-p}\sum_{i=1}^{x}\left[\frac{q_{e,means} - q_{e,calc}}{q_{e,means}}\right] \quad (3)$$

$$EABS = \sum_{i=1}^{x}\left|q_{e,means} - q_{e,calc}\right| \quad (4)$$

$$\chi^2 = \sum_{i=1}^{x}\frac{(q_{e,calc} - q_{e,means})^2}{q_{e,means}} \quad (5)$$

$$S_{RE} = \sqrt{\frac{\sum_{i=1}^{x}\left[\left(qe,means - qe,calc\right)_i - ARE\right]^2}{x-1}} \quad (6)$$

where $q_{e,means}$ and $q_{e,calc}$ are measured adsorbed Pb(II) from isotherm model (mg/g) and calculated adsorbed Pb(II) at equilibrium (mg/g), respectively.

The performance of the error function for the approximation of adsorption isotherm parameters can be evaluated using the procedure of normalizing and combining the error results to determine the Sum of Normalized Errors (SNE). After the SNE values for each parameter set are compared, the model provided the lowest SNE value is considered the most relevant result.

Reusability

A reusability study of HA-UF was carried out by performing the five consecutive cycles of the adsorption-desorption runs. Adsorption of Pb(II) onto HA-UF was conducted by contacting 50 mg of HA-UF with 25 mL of Pb(II) 20 mg/L at optimum pH. After 60 min of 250 rpm shaking, HA-UF loaded Pb(II) was filtered, and the filtrate solution's pH was measured. A control solution containing no HA-UF adsorbent was also prepared, indicating the actual initial concentration of Pb(II). The desorption of adsorbed-Pb(II) on HA-UF was performed by conducting HA-UF loaded Pb(II) with 25 mL of three different eluents: HCl 0.01 M, HNO_3 0.01 M, and CH_3COOH 0.01 M. After 60 min shaking at 250 rpm, the HA-UF released Pb(II) was filtered and washed with deionized water until pH neutral. The process was repeated for five consecutive cycle runs. The adsorption and desorption process filtrate was analyzed with Flame-AAS to quantify absorbed and desorbed Pb(II), respectively. The amount of Pb(II) adsorbed into the HA-UF was considered to be the difference between the initial (control solution) and the remaining amount of Pb(II) in the filtrate. The amount of Pb(II) desorbed from the HA-UF was considered to be the difference between the adsorbed Pb(II) and desorbed Pb(II) in the filtrate.

■ RESULTS AND DISCUSSION

Characterization of HA-UF

The characteristic band of urea using ATR-IR at wavenumber 1690 cm^{-1} was attributed to the C=O amide stretching, 3310 cm^{-1} could be assigned to secondary amine N–H stretching, and between 1250–1020 cm^{-1} was designated for amide C–N stretching (Fig. 1(a)) [22]. In addition, the sharp bands at 1585 and 1453 cm^{-1} were associated with the N–H bonds and fewer characteristics of C–O–H due to the aliphatic side groups of the amino acid residues in commercial urea [23], respectively.

The peaks between 2830–2695 cm^{-1} referred to the C–H aliphatic stretching, and at 1655 cm^{-1} referred to the aldehyde C=O stretching, which was characteristic spectra of formaldehyde (Fig. 1(a)) [18]. Five characteristic bands of HA were displayed at 3300–3400 cm^{-1} (attributed to O–H and N–H stretching), 2918 cm^{-1} (designated for C–H aliphatic stretching), 1715 cm^{-1} (referred to C=O from carboxylic acid stretching), 1620 cm^{-1} (assigned to aromatic C=C stretching), and 1236 cm^{-1} (attributed to C–O from ester stretching) (Fig. 1(b)).

ATR-IR spectrum of the UF prepared by the reflux method is shown in Fig. 1(a). Important broadband around 3650–3000 cm^{-1} can be attributed to the hydrogen-bonded O–H and N–H, and its broadness might be due to water and formaldehyde monomers. This O–H group of water and formaldehyde of UF may form hydrogen bonds with reactive functional groups such as CH_2OH, NH_2, and NH [22]. The small band in the region of 2920 cm^{-1} is the C-H stretching vibrations of UF. The overlapped peak at 1720 cm^{-1} is related to C=O stretching. The two peaks area at the 1500–1600 cm^{-1} are attributed to –N–H bending vibrations of secondary amide. A relatively intense and broad peak at 1236–1249 cm^{-1} is assigned to C–N stretching vibrations of secondary amide. Finally, the quietly strong peak at 1017 cm^{-1} is due to the C–C–O stretching mode of CH_2OH [24].

The success of HA-UF synthesis characterized with ATR-IR can be seen from the combination peak of original urea, formaldehyde, and HA as a constituent of HA-UF in HA-UF spectra, i.e., emerging peak between 1250–1020 cm^{-1} was ascribed to the C–N stretching of amide III (Fig. 1(a)) [22]. This emerging peak leads to the notion that the formation of HA-UF occurred through

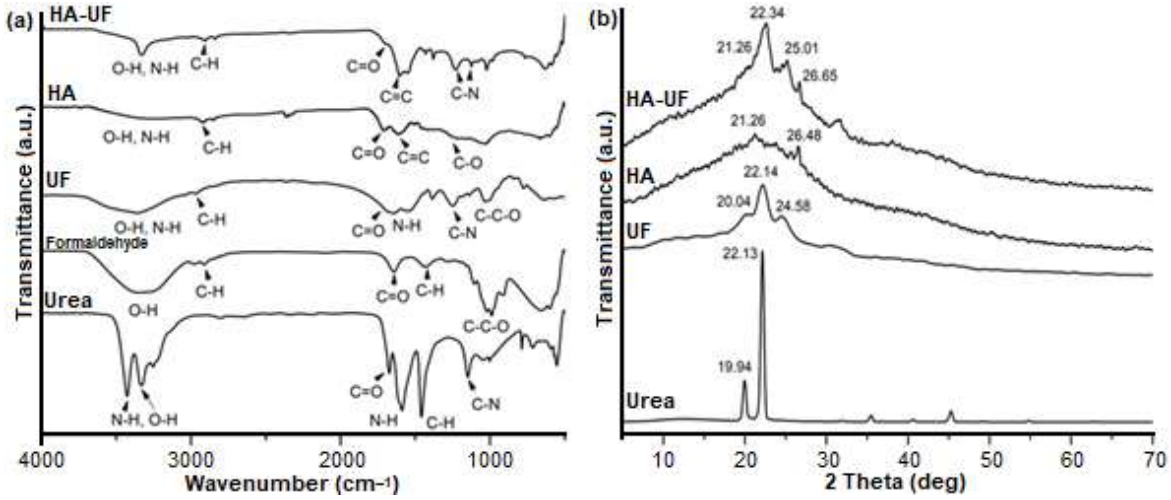

Fig 1. (a) ATR-IR spectra of HA-UF, HA, UF, formaldehyde, and urea; (b) XRD Diffractogram of urea, HA, UF, and HA-UF

C–N bonding. This fact is due to an increase in the intensity of C–N stretching at 1236 cm^{-1} in HA-UF spectra (Fig. 1(a)).

Fig. 1(b) presents the X-ray diffractograms of urea, HA, UF, and HA-UF. As shown, urea exhibited a high crystalline order with double sharp peaks at 2θ = 19.94° and 22.23°. The peak at 2θ around 22° was ascribed to (002) interlayer reflection of urea [25-26]. The UF diffractogram showed three sharp, strong 2θ peaks at 20.04°, 22.14°, and 24.58°. The first two peaks indicate the urea crystal, and the apparent additional peak (24.58°) is the typical peak on the XRD diffractogram of pure UF composites [17]. It was also observed that the position of the peak at 2θ = 19.94° (urea) shifted right to 20.04° (UF), probably due to the small urea that could intercalate into the UF composite interlayer [27]. The increasing crystallinity measurement from 54.09% (urea) to 76.59% (UF) strengthened the successful formation of UF. In contrast to urea, HA exhibited no specific sharp peak with high intensity due to the amorphous material [25-26], as demonstrated by XRD analysis [28]. Compared to UF, HA-UF occurred decreasing in crystallinity to 51.75% due to fairly semi-crystalline as it appears at 2θ around 22° and 25°. Hence, the measured reduction in the crystallinity of HA-UF is related to the amorphous structure of HA.

The results of the cross-sectional SEM analysis are displayed in Fig. 2 that represents the morphology of HA, UF, and HA-UF by magnifying 5000 times from the original image size. Arshad et al. [22] reported that different phases of UF presented in the SEM micrograph were identified using their differences in colors and contrasts. Related to that, the SEM micrograph in Fig. 2(b) broadly depicts two different phases in HA-UF due to their color contrast. However, the distribution of these phases is fairly homogeneous and similar. Supporting these findings, elemental composition analysis with EDX showed an increase in the N atoms in HA-UF (23.46%, Table 1) from HA. Further, the elemental composition of HA-UF seems the average combination of the elemental composition of HA and UF. These results ascertain that there are two phases of HA and UF that occur, and the UF contains N atoms that truly bind to HA.

The stability of HA-UF compared to HA is presented in Fig. 3. As shown, the synthesized HA-UF started to dissolve at pH 12.0, whereas HA was dissolved at a pH greater than 5.0. The increased stability of HA-UF indicates that the formation of HA and UF involves covalent bonds. The decrease in the total acidity of HA (549.26 cmol/kg) compared with HA-UF (349.30 cmol/kg), the bonds of HA and UF are strongly presumed by the carboxylic group of HA with the nitrogen atom in the UF molecules. This hypothesis follows the increased intensity of C–N stretching at 1236 cm^{-1} in the HA-UF spectra (Fig. 1(a)). This carboxylic group bonding contributes to an increase in pH_{PZC} of HA

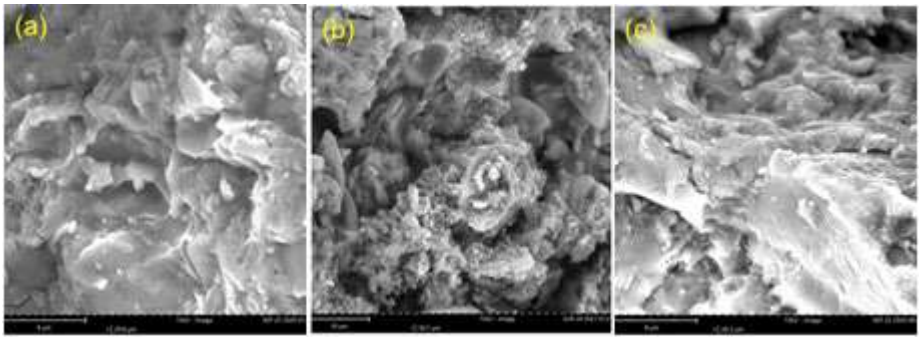

Fig 2. Morphology analyses by SEM-EDX of (a) HA, (b) UF, and HA-UF

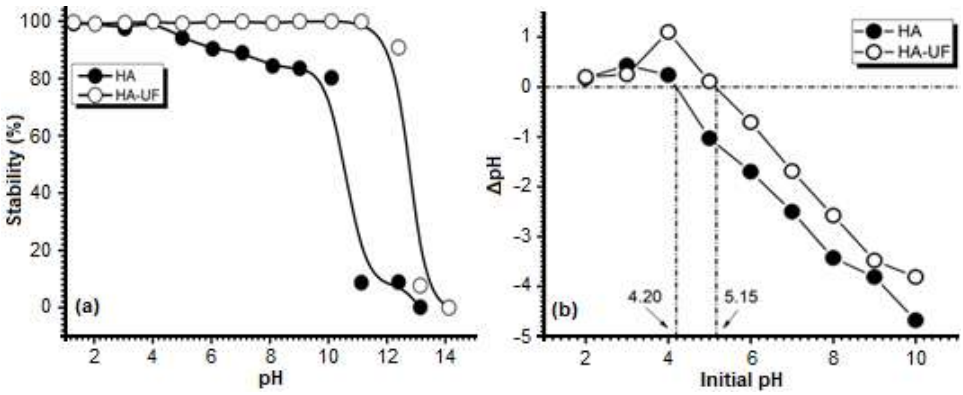

Fig 3. Comparative analysis of the stability (a) and the pH_{PZC} (b) of HA and HA-UF

Table 1. Elemental weight (%) of HA, UF, and HA-UF by EDX

Element	Weight (%)		
	HA	UF	HA-UF
Carbon	57.60	28.56	46.13
Oxygen	35.55	24.38	30.23
Nitrogen	6.860	47.06	23.46

(Fig. 3(b)). The higher the $pH_{PZC,}$ the lower the negatively surface charges [16,25].

From these results, the proposed mechanism for HA-UF formation is presented in Fig. 4. The reflux process accelerates the reaction by heating without reducing the volume of the reacting substance at a temperature of 70–80 °C to prevent swelling of HA and hydrolysis of ammonia carboxylates. The reaction occurs under alkaline conditions to activate the carboxylic ion in the HA. The electrostatic interaction between carboxylic ions and ammonia leads to the

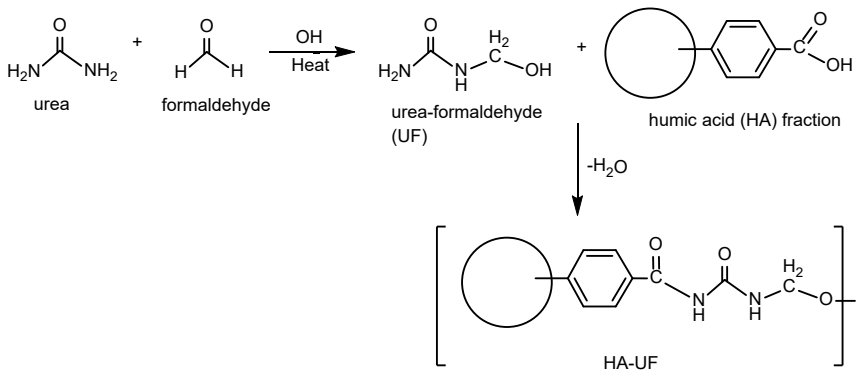

Fig 4. Proposed mechanism of HA-UF formation

formation of ammonium salts due to the low reactivity of carboxylate ions toward addition-elimination of the nucleophile. The further reaction will evaporate water as a dehydration reaction to produce amides. Ammonia salt will efficiently hydrolyze both acidic and alkaline conditions. The precipitation of HA-UF was obtained by acidifying the mixture with the addition of HCl.

Effect of Medium pH and Ionic Strength

The effect of medium pH on Pb(II) adsorption on HA-UF is shown in Fig. 5(a). The adsorbed Pb(II) increases with the increasing pH from 2.0 to 5.0. In this condition, the surface of HA-UF begins to deprotonate, with the result that the HA-UF surface is negatively charged. Hence, Pb^{2+} species will easily be attracted to the HA-UF surface. At high acidity (pH < 3.0), the protonation occurs and competes with Pb^{2+} species to be attracted onto the HA-UF surface. Protonation causes the HA-UF surface to be zero/positively charged, leading to inactivity/repulsion between Pb^{2+} species and active sites of HA-UF. Therefore, Pb(II) adsorption is low on HA-UF is low under low pH conditions. The highest Pb(II) adsorption on HA-UF was obtained at a pH above 5.0 (Fig. 5(a)). However, at pH approximately above 6.0, the formation of solid $Pb(OH)_2$ initially began. Thus, high Pb(II) adsorption at pH > 6.0 is not due to Pb(II) being adsorbed onto HA-UF, but it is Pb(II) precipitated as solid $Pb(OH)_2$. Considering the existence of Pb^{2+} species and the formation of solid $Pb(OH)_2$, the optimum pH of Pb(II) adsorption onto HA-UF was achieved between pH 5.0 and 6.0. As illustrated in Fig. 5(a), it can also be seen that the maximum adsorption value of Pb(II) on HA-UF was obtained at initial pH > pH_{PZC}. Therefore, electrostatic attractions between negatively charged surfaces of the HA-UF and Pb^{2+} species can occur and contribute to adsorption. Previous findings in the adsorption of Pb(II)

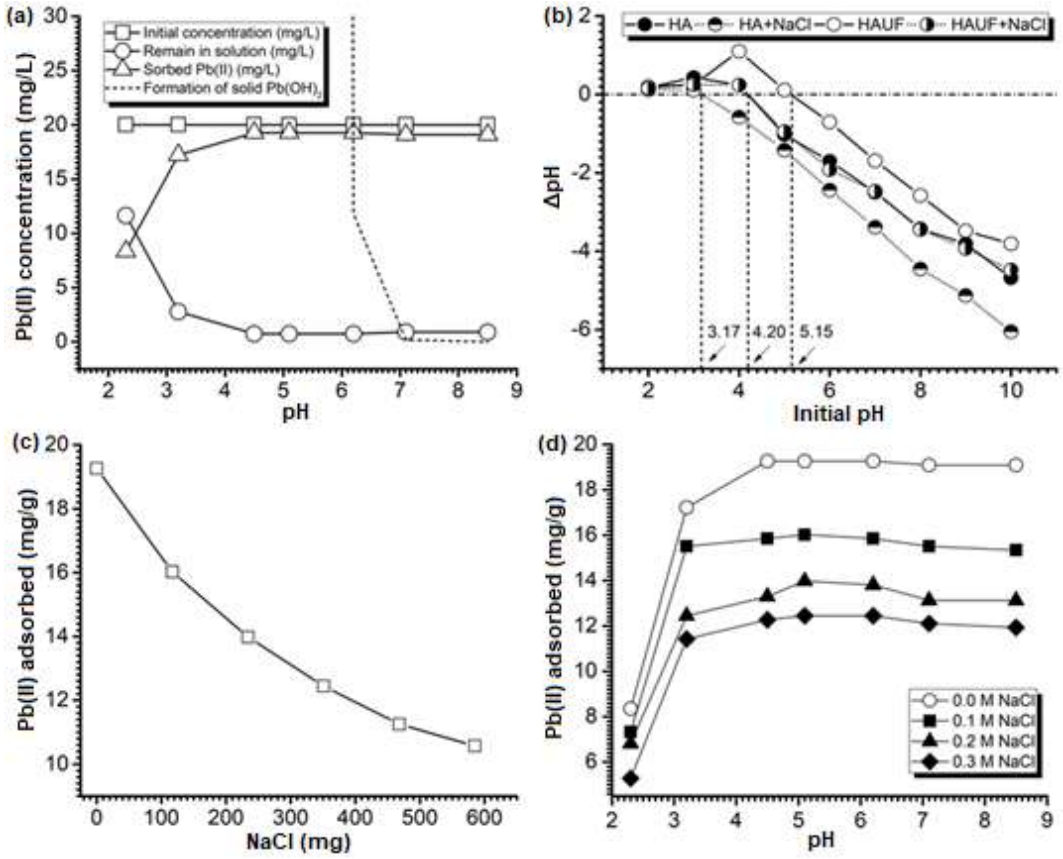

Fig 5. (a) Profile of Pb(II) adsorption onto HA-UF as a function of pH, (b) Effect of the 0.1 M NaCl presence to the pH_{PZC} of HA and HA-UF, (c) Effect of the NaCl salt addition to the adsorbed Pb(II) onto HA-UF at pH 5.50, (d) Profile of Pb(II) adsorption onto HA-UF as a function of pH in the NaCl presence (20 mL of Pb(II) 20 mg/L, 50 mg HA-UF)

onto HA-based adsorbents showed similar results to this work: an optimum pH of 5.0 in peat-HA [28], and an optimum pH of 5.5 in a magnetite/HA/chitosan adsorbent [10].

The effect of the ionic strength with the addition of NaCl to pH_{PZC} is presented in Fig. 5(b). The pH_{PZC} of HA and HA-UF decreased 4.2–3.17 and 5.15–4.2, in the presence of 0.1 M NaCl, respectively (Fig. 5(b)). A decrease in pH_{PZC} indicates that the HA and HA-UF surfaces' zero-point charge occurs at stronger acidic conditions (more H^+ ions). It means that additional H^+ is needed to enhance Cl^- from the addition of NaCl in the solution. The result is that there are more H^+ ions in the solution than on the adsorbent surface, so that the adsorbent surface is negatively charged in a more acidic solution.

The effect of the ionic strength with the addition of NaCl on the Pb(II) adsorption is presented in Fig. 5(c). As shown, the higher the concentration of NaCl reduces the adsorption of Pb(II) onto HA-UF. The low adsorption of Pb(II) in this work (or other divalent metal cations) has been attributed to different factors: (1) adsorbent active site blocking by salt, (2) repulsion between free positive charge adsorbate and positively charged of adsorbent surfaces, (3) competition between positively charged species (H^+ and Pb^{2+}) and free adsorbate to the sorbent active sites, (4) lower formation of complexes/chelate with metal ions due to protonation of surface functional groups, and (5) combination of several of these factors [29]. The presence of NaCl has been observed to cause a decrease in adsorbed Pb(II) onto HA-UF (Fig. 5(d)). The sorption of Pb(II) on HA-UF is influenced by ionic strength at pH < 4.50, whereas no drastic difference of Pb(II) adsorption was found at pH > 4.50 in three different NaCl concentrations. The results presented in Fig. 5(c) and 5(d) showed that the adsorption of Pb(II) onto HA-UF seems to be affected by the first and third factors because even at the optimum pH (5.50) and the optimum pH > pH_{PZC}, the Pb(II) adsorption continues to decrease with the increase of ionic strength (NaCl concentration).

Isotherm Adsorption Study

The equilibrium adsorption isotherm is essential in describing the interactive behavior between the adsorbate, Pb(II), and adsorbent, HA-UF. For example, Fig. 6(a) presents Pb (II) adsorbed onto HA and HA-UF with different Pb(II) initial concentrations at an optimum pH of 5.5. The adsorbed Pb(II) increases with an increase of equilibrium concentration of Pb(II), and reaches the saturation plateau. As exhibited, the saturation plateau of HA-UF was higher than that of HA. It is indicated that the adsorption capacity of HA-UF is higher than HA due to modification with UF.

The equilibrium adsorption parameters were obtained from a linear and nonlinear form of four styles Langmuir, Freundlich, Dubinin-Radushkevich (D-R) [30], and Temkin [31] isotherm models (Table 2). The nomenclatures of the symbols are b (mg/g or mol/g), which represent is the monolayer adsorption capacity, q_e (mol/g) denote Pb(II) adsorption on the adsorbent at equilibrium, K_L (L/mol) is Langmuir equilibrium constant, E_L (kJ/mol) is the monolayer adsorption energy [E_L=-RT ln K_L], C_0 and C_e are Pb(II) initial concentration (mol/L) and remains Pb(II) concentration at equilibrium (mol/L), respectively. The B (mg/g or mol/g) is the multilayer adsorption capacity, n is the heterogeneity parameter of the adsorbent surface, β is Dubinin-Radushkevich (D-R) isotherm constant (mol^2/kJ^2), ε is Polanyi potential [RT In(1+1/C_e)] (J^2/mol^2), q_{D-R} (mol/g) is the theoretical isotherm saturation capacity, b_T (J/mol) and A_T (L/g) are Tempkin isotherm parameters, R (8.314 J/mol K) is the gas constant, and T is the absolute temperature. The closest correlation coefficient (R^2) to the unity among the Langmuir styles and the three other models were then evaluated by a six error function (Eq. (1–6)) to compare the linear and nonlinear adsorption fitness isotherm parameters.

The plot of experimental data to the four styles of Langmuir, Freundlich, D-R, and Temkin models is presented in Fig. 6(b–h). From the plot among Langmuir linear model (Fig. 6(b–e)), the Langmuir-b shows the highest value of R^2 (Fig. 6(c)). The adsorption isotherm parameters value and the calculated error value were listed in Table 3. For the linear regression method, the Langmuir isotherm emerged to be the most appropriate model for the adsorption of both HA and HA-UF due to the higher R^2 value. In the nonlinear

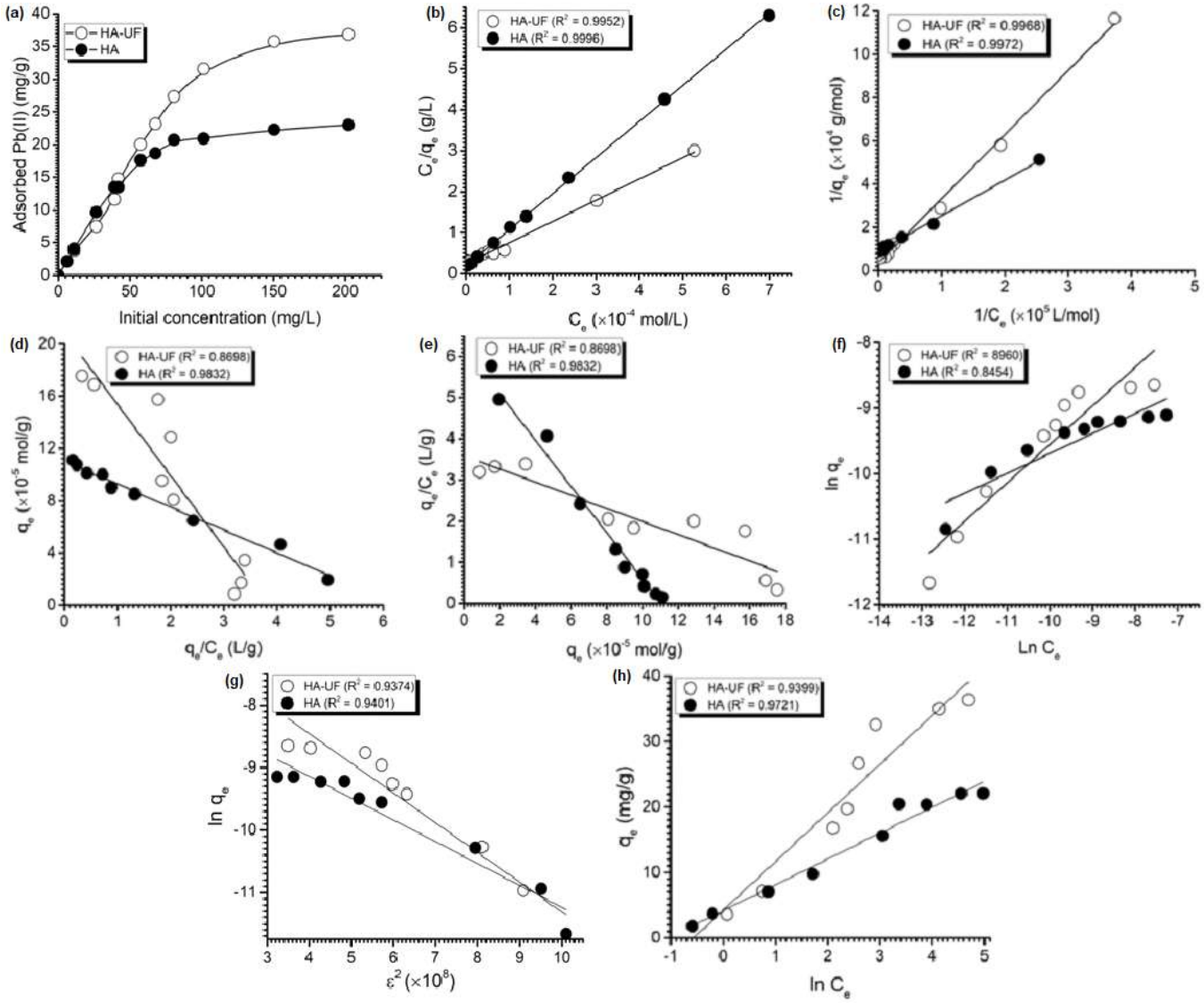

Fig 6. (a) Effect of Pb(II) initial concentration to the adsorbed Pb(II) onto HA and HA-UF; the plot of isotherm experimental data to the (b) Langmuir-a; (c) Langmuir-b; (d) Langmuir-c; (e) Langmuir-d; (f) Freundlich; (g) D-R; and (h)Temkin linear form model

method, the Freundlich isotherm presented lower error values than other nonlinear isotherm models for both HA and HA-UF adsorbents. However, the Freundlich isotherm parameter sets obtained from the nonlinear model differed from the linear regression value.

Conversely, several Langmuir-a isotherm parameter sets generated from the nonlinear regression were similar to the linear regression values. Among the isotherm parameter sets are determined using nonlinear regression. It was noticed that the isotherm parameter sets derived by ARE and S_{RE} were similar. In order to choose the appropriate isotherm parameter set, the sum of normalized errors (SNE) was considered. The SNE was calculated by dividing the error values by the maximum error of that error function. The parameter set yielded the smallest SNE value was proclaimed as the appropriate parameter set. As seen in Table 3, the lowest SNE was obtained from the Langmuir-a parameter set for both HA and HA-UF adsorbents. It means that the Langmuir-a isotherm model assigned the match close to the experimental data.

Table 2. Linear and nonlinear form of the isotherm models

Isotherm models	Nonlinear form	Linear form	Plot (x vs. y)	Slope	Intercept	Ref.
Langmuir-a	$q_e = \frac{K_L b C_e}{1 + b C_e}$	$\frac{C_e}{q_e} = \frac{1}{K_L b} + \frac{1}{b} C_e$	C_e vs. $\frac{C_e}{q_e}$	$\frac{1}{b}$	$\frac{1}{K_L b}$	[32]
Langmuir-b		$\frac{1}{q_e} = \frac{1}{b} + \frac{1}{b K_L C_e}$	$\frac{1}{C_e}$ vs. $\frac{1}{q_e}$	$\frac{1}{K_L b}$	$\frac{1}{b}$	[32]
Langmuir-c		$q_e = b - \frac{q_e}{K_L C_e}$	$\frac{q_e}{C_e}$ vs. q_e	$\frac{1}{K_L}$	b	[32]
Langmuir-d		$\frac{q_e}{C_e} = K_L b - q_e K_L$	q_e vs. $\frac{q_e}{C_e}$	K_L	$K_L b$	[32]
Freundlich	$q_e = B C_e^{1/n}$	$\ln q_e = \ln B + \frac{1}{n} \ln C_e$	$\ln C_e$ vs. $\ln q_e$	$\frac{1}{n}$	$\ln B$	[33]
D–R	$q_e = (q_{D-R}) \exp(-\beta \varepsilon^2)$	$\ln q_e = \ln q_{D-R} - \beta \varepsilon^2$	ε^2 vs. $\ln q_e$	β	$\ln q_{D-R}$	[30]
Temkin	$q_e = \frac{RT}{b_T} \ln A_T C_e$	$q_e = \frac{RT}{b_T} \ln A_T + \frac{RT}{b_T} \ln C_e$	$\ln C_e$ vs. q_e	$\frac{RT}{b_T}$	$\frac{RT}{b_T} \ln A_T$	[31]

Table 3. Linear regression of adsorption isotherm parameters and error analysis calculation

Models	Adsorbent	Parameter	Linear regression	Nonlinear regression					
				ARE	SSE	HYBRID	EABS	$\chi 2$	S_{RE}
Langmuir-b	HA-UF	b (mg/g)	46.80	46.40	46.40	46.40	46.40	46.40	46.40
		K_L (L/mol)	12143	21884	21884	21884	21884	21884	21884
		E_L (kJ/mol)	23.30	23.30	23.30	23.30	23.30	23.30	23.30
		R^2	0.9968						
		Error value		0.279	2.35×10^{-9}	0.439	6.90×10^{-6}	1.05×10^{-5}	0.279
		SNE	0.378	0.636	5.35×10^{-9}	1.00	1.57×10^{-5}	2.39×10^{-5}	0.635
	HA	b (mg/g)	23.12	37.60	37.60	37.60	37.60	37.60	37.60
		K_L (L/mol)	53507	43961	43961	43961	43961	43961	43961
		E_L (kJ/mol)	23.22	23.33	23.33	23.33	23.33	23.33	23.33
		R^2	0.9996						
		Error value		0.103	3.38×10^{-7}	0.162	2.06×10^{-5}	1.86×10^{-4}	0.102
		SNE	0.378	0.636	2.09×10^{-7}	1.00	1.27×10^{-5}	1.15×10^{-3}	0.633
Freundlich	HA-UF	B (mg/g)	5179	64740	64740	64740	64740	64740	64740
		n	1.71	2.90	2.90	2.90	2.90	2.90	2.90
		R^2	0.8960						
		Error value		0.091	0.010	0.143	0.003	0.034	0.087
		SNE	0.430	0.636	0.075	1.00	0.021	0.240	0.610
	HA	B (mg/g)	414	2736	2737	2737	2737	2737	2737
		n	3.29	5.39	5.39	5.39	5.39	5.39	5.39
		R^2	0.8454						
		Error value		0.092	1.90×10^{-5}	0.145	1.35×10^{-4}	1.44×10^{-3}	0.091
		SNE	0.379	0.636	1.31×10^{-4}	1.00	9.25×10^{-4}	9.89×10^{-3}	0.631

Table 3. Linear regression of adsorption isotherm parameters and error analysis calculation (*Continued*)

Models	Adsorbent	Parameter	Linear regression	Nonlinear regression					
				ARE	SSE	HYBRID	EABS	$\chi 2$	S_{RE}
D-R	HA-UF	qD (mg/g)	438.06	438.06	438.06	438.06	438.06	438.06	438.06
		E_{DR} (kJ/mol)	9.75	9.75	9.75	9.75	9.75	9.75	9.75
		R^2	0.9374						
		Error value		0.110	4.51×10^{-7}	0.174	2.58×10^{-5}	2.13×10^{-4}	0.110
		SNE	0.378	0.636	2.59×10^{-6}	1.00	1.480×10^{-4}	1.22×10^{-3}	0.633
	HA	qD (mg/g)	84.22	84.21	84.21	84.21	84.21	84.21	84.21
		E_{DR} (kJ/mol)	12.55	12.55	12.55	12.55	12.55	12.55	12.55
		R^2	0.9401						
		Error value		0.145	1.29×10^{-8}	0.229	6.52×10^{-6}	3.17×10^{-5}	0.145
		SNE	0.378	0.636	5.62×10^{-8}	1.00	2.84×10^{-5}	1.38×10^{-4}	0.634
Temkin	HA-UF	b_T (J/mol)	319.07	117.99	117.99	117.99	117.99	117.99	117.99
		A_T (L/g)	1.51	1.24	1.24	1.24	1.24	1.24	1.24
		q_e (mg/g)	26.96	68.79	68.79	68.79	68.79	68.79	68.79
		R^2	0.9399						
		Error value		0.218	6.83×10^{-9}	0.343	7.98×10^{-6}	2.06×10^{-5}	0.218
		SNE	0.379	0.636	1.99×10^{-8}	1.00	2.32×10^{-5}	5.99×10^{-5}	0.635
	HA	b_T (J/mol)	640.99	172.41	172.41	172.41	172.41	172.41	172.41
		A_T (L/g)	4.36	1.12	1.12	1.12	1.12	1.12	1.12
		q_e (mg/g)	19.27	52.12	52.12	52.12	52.12	52.12	52.12
		R^2	0.9721						
		Error value		0.179	3.93×10^{-9}	0.281	4.97×10^{-6}	1.56×10^{-5}	0.179
		SNE	0.379	0.636	1.40×10^{-8}	1.00	1.76×10^{-5}	5.54×10^{-5}	0.635

The R_L value of Pb(II) adsorption onto HA and HA-UF in this study shows that the R_L values of HA (0.427–0.022) and HA-UF (0.395–0.019) are between 0 and 1, which indicates the adsorption is a favorable process. It suggests the homogeneity of the HA-UF surface. The adsorption capacity of Pb(II) adsorption onto HA-UF (2.26×10^{-4} mol/g or equal to 46.80 mg/g) is two times higher than that of HA (1.12×10^{-4} mol/g or equal to 23.12 mg/g). Comparison of the adsorption capacity (b) of HA-UF as Pb(II) adsorbent with the HA- or UF-based adsorbents were listed in Table 4. Since the total acidity has decreased from 549.26 cmol/kg (HA) to 349.30 cmol/kg (HA-UF), it can be concluded that Pb(II) adsorption involves the interaction between Pb(II) and the lone pair electron of the N atom in UF. The higher adsorption capacity of HA-UF can be increased in two ways: using HA with higher total acidity and optimizing the polymerization reaction of HA-UF. With the UF polymer, the loss of one site of the HA–COOH group due to the bonding reaction with the UF polymers will be replaced by more than one N containing the lone pair electron in UF that possibly bind to Pb(II).

Table 4. Comparison of adsorption capacity (b) of the HA-UF as Pb(II) adsorbent

HA-/UF-based Adsorbent	b (mg/g)	References
HA-peat (Polland)	82.31	[34]
Magnetite-HDHA	57.64	[10]
HA-UF	46.80	This work
HA-peat (Riau)	23.12	This work
UF-foam	21.50	[35]
HA-soil (India)	19.60	[36]
HA-peat	15.00	[28]
UF-thiourea-bentonite	13.40	[37]
UF-melamine	4.900	[38]

It is frequently studied that D-R adsorption energy (E_{DR}) is useful for investigating the interaction between the adsorbate and the adsorbent. The interaction could be classified as physical interaction (E_{DR} < 8 kJ/mol), ion

exchange mechanism ($8 < E_{DR} < 16$ kJ/mol), and chemisorption that is stronger than ion exchange ($E_{DR} > 16$ kJ/mol) [39]. The values of E_{D-R} calculated in this study were 9.75 kJ/mol (HA-UF) and 12.55 (HA), which indicated that ion exchange is the major interaction involved in the adsorption process. Furthermore, the Temkin isotherm describes the indirect relation of multilayer interaction between the adsorbate and the adsorbent with the adsorption energy of the layer [40]. As seen in Table 3, the b_T of HA-UF (319.07 J/mol) is smaller than HA (640.99 J/mol) that indicates Pb(II) at the outer layer interact stronger with HA's surface than HA-UF surfaces [40].

Kinetics Adsorption Study

The adsorbed Pb(II) calculated by $(C_0-C_t)/(W/V)$ onto HA-UF as a function of time is presented in Fig. 7(a). It is obvious from Fig. 7(a) that the adsorption amount increases rapidly in the first 20 min, and after 20 min slower adsorption occurs and reaches equilibrium at 100 min. Rapid adsorption within the first 20 min indicates a strong electrostatic interaction between the negative sites of HA-UF and the Pb(II) cations. Four kinetics models (Lagergren [41], Ho [42], Santosa [43], and RBS [10,44-46]) (Table 5) were used to explore kinetics parameters of Pb(II) adsorption onto HA-UF. The nomenclatures of the symbols are q_t (mol/g), which represent the amount Pb(II) that was adsorbed at time t (min); x (mol/L) and x_e (mol/L) are the amount of Pb(II) adsorbed on the adsorbent at time t and equilibrium, respectively; X (g/L) in Santosa's kinetics model is w/vmr, where w (g) is the mass of the adsorbent, v (L) is the volume of sorption medium, and m_r: the molar weight of adsorbate; C_b (mol/L) is the concentration of Langmuir capacity (C_b=bw/v); k_{Lag} (min^{-1}), k_{Ho} (g/mol.min), k_s (L/mol.min), k_a (L/mol.min) are the Lagergren, Ho, Santosa, and RBS rate constants, respectively. The application of empirical data to the plot of these four kinetics models is presented in Fig. 7(b-f).

The corresponding linear regression coefficient (R^2) value of the Ho (Pseudo-Second Order) kinetics model is higher than the other three kinetics models (Table 6). Moreover, the calculated q_e (Calc. q_e) value (5.27×10^{-5} mol/g) from the Ho kinetics model agrees well with the experimental q_e (5.05×10^{-5} mol/g) better than that of Lagergren and RBS kinetics models. Thus,

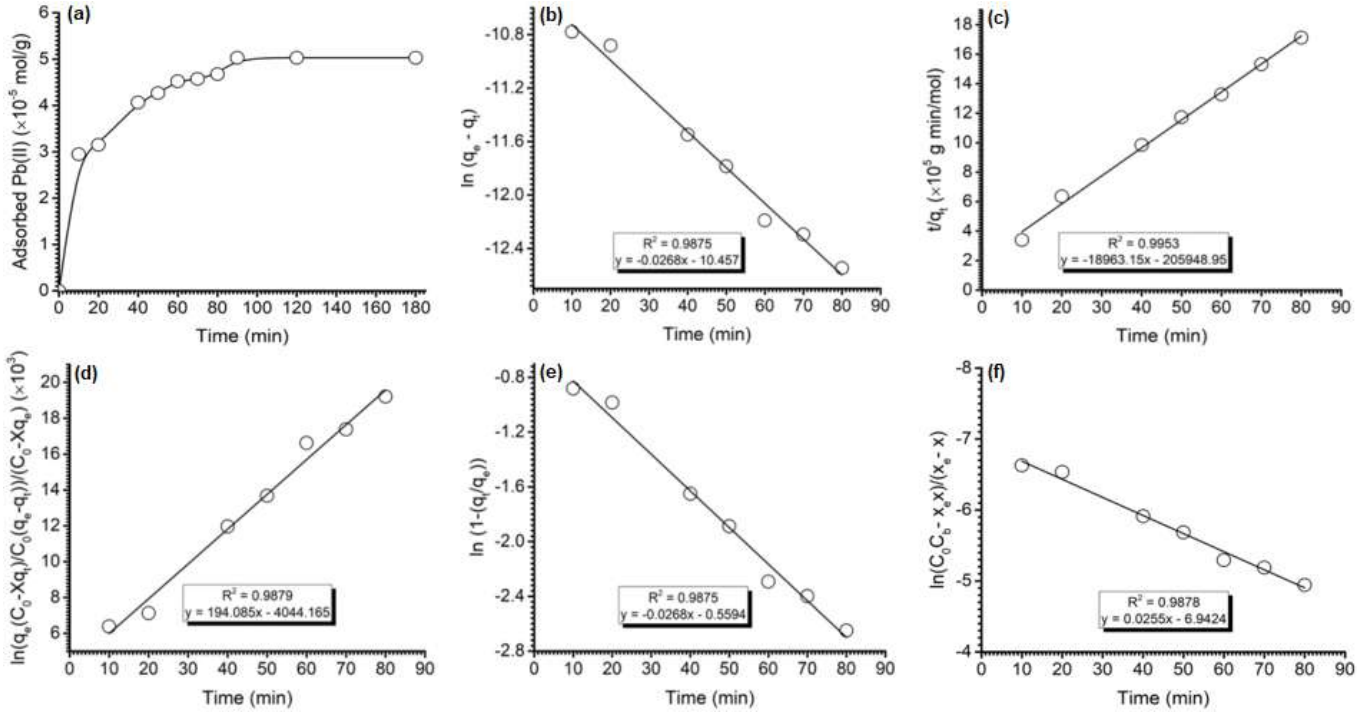

Fig 7. (a) Profile of adsorbed Pb(II) as a function of time; applying of experimental kinetics data to the (b) Lagergren, (c) Ho, (d) Santosa-a), (e) Santosa-b to determine the k_d, and (f) RBS models

Table 5. Kinetics models to determine the kinetics adsorption parameter of HA-UF

Kinetics Model	Linear Form	Plot (*x vs. y*)	Slope	Intercept	Ref.
Lagergren	$\ln(q_e - q_t) = \ln q_e - k_{Lag} t$	t vs. $\ln(q_e - q_t)$	k_{Lag}	$\ln q_e$	[41]
Ho	$\frac{t}{q_t} = \frac{1}{k_{Ho}(q_e^2)} + \frac{1}{q_e} t$	t vs. $\frac{t}{q_t}$	$\frac{1}{q_e}$	$\frac{1}{k_{Ho}(q_e^2)}$	[42]
Santosa	$\frac{1}{C_0 - Xq_e}$ $\ln\left(\frac{q_e(C_0 - Xq_t)}{C_0(q_e - q_t)}\right) = k_s t$	t vs. $\frac{1}{C_0 - Xq_e}$ $\ln\left(\frac{q_e(C_0 - Xq_t)}{C_0(q_e - q_t)}\right)$	k_s	-	[43]
Rusdiarso-Basuki-Santosa (RBS)	$\ln\left(\frac{C_0C_b - x_e x}{x_e - x}\right) =$ $k_a\left(\frac{C_0C_b - x_e^2}{x_e}\right) t - \ln\left(\frac{x_e}{C_0C_b}\right)$	t vs. $\ln\left(\frac{C_0C_b - x_e x}{x_e - x}\right)$	$k_a\left(\frac{C_0C_b - x_e^2}{x_e}\right)$	$\ln\left(\frac{x_e}{C_0C_b}\right)$	[10,44-46]

Table 6. Kinetics parameters of Pb(II) adsorption onto HA-UF

Kinetics Model	Kinetics adsorption parameters				
Lagergren	Calc. q_e (mol/g)	k_{Lag} (min^{-1})	k_d	K	R^2
	2.88×10^{-5}	0.027	-	-	0.9875
Ho	Calc. q_e (mol/g)	k_{Ho} (g mol^{-1} min^{-1})	k_d	K	R^2
	5.27×10^{-5}	1746.04	-	-	0.9953
Santosa	Calc. q_e	k_s ($(mol/L)^{-1}$ min^{-1})	k_{ds} (min^{-1})	K_S $(mol/L)^{-1}$	R^2
	-	194.08	4.46×10^{-5}	4.36×10^{6}	0.9875
RBS	Calc. q_e (mol/g)	k_{RBS} ($(mol/L)^{-1}$ min^{-1})	k_d (min^{-1})	K_{RBS} $(mol/L)^{-1}$	R^2
	1.31×10^{-5}	51.47	2.26×10^{-3}	22780	0.9878

the Ho kinetics model is evidence to demonstrate the adsorption of Pb(II) onto HA-UF. The prediction of adsorption energy through the calculation of E = - RT ln (k_a/k_d) shows that the RBS model (E_{RBS} = 24.86 kJ/mol) presents a closer value than the Santosa model (E_S = 37.87 kJ/mol) to E_L of Langmuir-b (23.30) kJ/mol).

Six different error functions were examined for the nonlinear model of kinetics data (Table 7). The error value of all kinetics models seems to have a different value from the kinetics parameter value calculated from linear regression. However, after being divided by the maximum error (SNE), the lowest value of SNE and the best coherent fitting of the models is for the Ho kinetics model. The SNE value increases in order Ho > RBS > Lagergren. The Santosa kinetics model cannot estimate the error value because the model cannot obtain the $q_{e,calc}$. According to this result, Ho (known as pseudo-second-order) is the best model to represent the kinetics data.

Reusability

Reusability study of HA-UF adsorbent was performed by the five consecutive cycles of the adsorption-desorption process with three different desorption eluents: HCl 0.01 M, CH_3COOH 0.01 M, and HNO_3 0.01 M. The % metal recovery for HA-UF by HCl, CH_3COOH, and HNO_3 after reuse for five consecutive cycles was 90.47%, 67.93%, and 94.32%, respectively. It was observed that the best performance of desorption eluent in this work was HNO_3. A similar result was reported by Basuki et al. [10] in the desorption study of Pb(II) from MHDHA. It might be due to the NO_3^- affinity to make a more stable complex with Pb(II) rather than Cl^- and CH_3COO^- [47].

The pH solution in each adsorption cycle indicates that the pH decreased from the optimum pH (5.50) to 2.91, 3.03, and 2.03 by desorption eluent HCl, CH_3COOH, and HNO_3, respectively, after five consecutive

Table 7. Linear regression of adsorption kinetics parameters and error analysis calculation

Kinetics model	Parameter	Linear regression	Nonlinear regression					
			ARE	SSE	HYBRID	EABS	$\chi 2$	MPSD
Lagergren	Calc q_e ($\times 10^{-5}$ mol/g)	2.88	6.27	6.27	6.27	6.27	6.27	6.27
	k_{Lag} (min^{-1})	0.027	0.064	0.064	0.064	0.064	0.064	0.064
	k_d	-	-	-	-	-	-	-
	R^2	0.9875						
	Error value		0.310	4.29×10^{-11}	0.516	1.95×10^{-6}	6.84×10^{-7}	0.172
	SNE	0.322	0.600	8.31×10^{-11}	1.00	3.77×10^{-6}	1.32×10^{-6}	0.334
Ho	Calc q_e (mol/g)	5.27×10^{-5}	3.33×10^{12}	3.33×10^{12}	3.33×10^{12}	3.33×10^{12}	3.33×10^{12}	3.33×10^{12}
	k_{Ho} (g mol^{-1} min^{-1})	1746.04	2.70×10^{35}	2.70×10^{35}	2.70×10^{35}	2.70×10^{35}	2.70×10^{35}	2.70×10^{35}
	k_d	-	-	-	-	-	-	-
	R^2	0.9953						
	Error value		1.30×10^{8}	1.92×10^{-10}	2.164×10^{8}	4.33×10^{-6}	577.298	3.029×10^{16}
	SNE	0.166	4.29×10^{-9}	6.35×10^{-27}	7.144×10^{-9}	1.43×10^{-22}	1.91×10^{-14}	1.00
Santosa	Calc q_e	-	-	-	-	-	-	-
	k_s ($(mol/L)^{-1}$ min^{-1})	194.08	-	-	-	-	-	-
	k_{ds} ($\times 10^{-5}$ min^{-1})	4.46	-	-	-	-	-	-
	K_s ($\times 10^{-6}$ $mol/L)^{-1}$	4.36	-	-	-	-	-	-
	R^2	0.9875	-	-	-	-	-	-
	Error value		-	-	-	-	-	-
	SNE	-	-	-	-	-	-	-
RBS	Calc q_e (mol/g)	1.31×10^{-5}	9.76×10^{-8}	9.76×10^{-8}	9.76×10^{-8}	9.76×10^{-8}	9.76×10^{-8}	9.76×10^{-8}
	k_{RBS} ($(mol/L)^{-1}$ min^{-1})	51.47	2.01×10^{-2}	2.01×10^{-2}	2.01×10^{-2}	2.01×10^{-2}	2.01×10^{-2}	2.01×10^{-2}
	k_d (min^{-1})	2.26×10^{-3}	8.86×10^{-7}	8.86×10^{-7}	8.86×10^{-7}	8.86×10^{-7}	8.86×10^{-7}	8.86×10^{-7}
	K_{RBS} $(mol/L)^{-1}$	22780	22780	22780	22780	22780	22780	22780
	R^2	0.9878						
	Error value		442.322	1.92×10^{-10}	737.20	4.32×10^{-6}	1.96×10^{-3}	3.260×10^{-5}
	SNE	0.167	1.36×10^{-3}	5.88×10^{-16}	2.26×10^{-3}	1.32×10^{-11}	6.02×10^{-9}	1.00

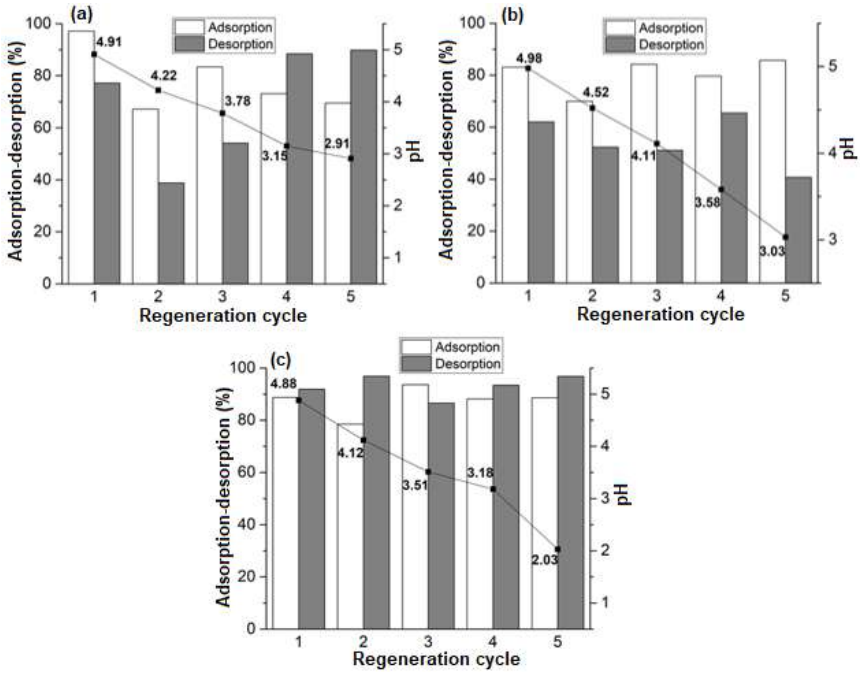

Fig 8. Adsorption-desorption study of HA-UF and pH change in five consecutive cycles with the different eluents: (a) HCl, (b) CH_3COOH, and (c) HNO_3

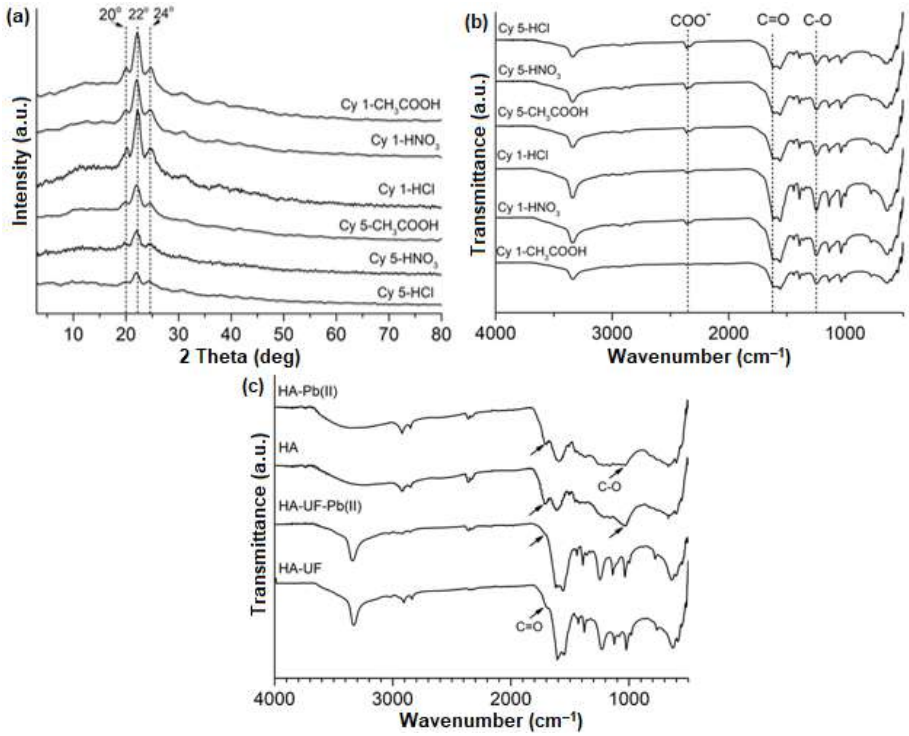

Fig 9. (a) Diffractogram and (b) ATR-IR spectra of HA-UF after the first (Cy1), and fifth cycle (Cy5) adsorption-desorption process with the three different eluents: HCl, CH_3COOH, HNO_3; (c) ATR-IR spectra of HA and HA-UF loaded Pb(II)

adsorption-desorption cycles (Fig. 8). This fact strengthened the calculated E_{D-R} in this work (9.75 kJ/mol) that ion exchange is the main interaction between H^+ of HA-UF surface and Pb(II) ions. Fig. 9(c) showed the interaction Pb(II) with the C=O functional group. At the adsorption process, the H^+ ions were replaced by the Pb(II) ions, and the desorbed H^+ moved into the solution resulting in decreased pH. The H^+ from desorption eluent replaced the adsorbed Pb(II), and the desorbed Pb(II) formed a stable complex with the anion from desorption eluent at the desorption phase.

The five consecutive adsorption-desorption cycles of HA-UF represent the virtuous regeneration ability of HA-UF as an adsorbent. The claim was proved by the XRD and ATR-IR analysis of HA-UF after the fifth adsorption-desorption cycle (Fig. 9). It was observed that there was no significant damage in the crystal system and functional group of the HA-UF. Therefore, the HA-UF offers an efficient, un-expensive, and effective adsorbent for Pb(II) removal from contaminated wastewater.

■ CONCLUSION

The formation of HA-UF and the adsorption performances of the synthesized HA-UF for Pb(II) adsorption were studied. The HA-UF formation was identified as the reaction between the –COOH groups of HA and $–NH_2$ of UF (C–N bonding). The reaction was based on a decrease in the total acidity from 549.26 cmol/kg (HA) to 349.30 cmol/kg (HA-UF), the peak appeared between 1250–1020 cm^{-1} (by ATR-IR), an increase of 23.46% (w/w) N atoms in HA-UF (elemental analysis by EDX), the peaks appeared at 2θ around 22° correspond to (002) interlayer reflection of urea in HA-UF (by XRD) and increased the HA-UF stability in solids form until pH 12.0. The adsorption of Pb(II) onto HA-UF was strongly affected by ionic strength and pH. The higher the ionic strength by adding NaCl salt, the lower the Pb(II) adsorbed at the optimum pH of 5.50. The adsorption isotherm data as the effect of initial Pb(II) concentration variation and its error analysis was fitted well to the Langmuir-b model,

illustrating monolayer ion-exchange adsorption (EDR = 9.75 kJ/mol) on the homogenous surfaces with an average capacity of 2.26×10^{-4} mol/g (equal to 46.80 mg/g). The results of time variation analysis showed that the adsorption followed the Ho (Pseudo-Second order) kinetics model with the rate constant 1746.04 g mol^{-1} min^{-1} and the comparable value of $q_{e,calc}$ (5.27×10^{-5} mol/g) with the experimental $q_{e,exp}$ (5.05×10^{-5} mol/g). The reusability study of HA-UF shows the remarkable performance of up to 95% metal recovered after five consecutive adsorption-desorption cycles by the HNO_3 desorption agent. Therefore, the HA-UF is a promising adsorbent for Pb(II) adsorption in wastewater treatment.

■ ACKNOWLEDGMENTS

The authors thank the Universitas Gadjah Mada for financing this wok through the RTA 2020 Programs (Grant Number: 607/UN1/DITLIT/DIT-LIT/PT/2020).

■ AUTHOR CONTRIBUTIONS

Author 1 conducted the experiments; authors 2 and 3 conceived the theory, formulated the methodology, sourced and presented the data. Authors 1, 2, and 3 prepared and edited the manuscript. The results were reviewed and commented on by all of the authors. All authors agreed with the final version of this manuscript.

■ REFERENCES

[1] Dehghani, M.H., Heibati, B., Asadi, A., Tyagi, I., Agarwal, S., and Gupta, V.K., 2015, Reduction of noxious Cr (VI) ion to Cr (III) ion in aqueous solutions using H_2O_2 and UV/ H_2O_2 systems, *J. Ind. Eng. Chem.*, 33, 10–13.

[2] Siyal, A.A., Shamsuddin, M.R., Rabat, N.E., Zulfiqar, M., Man, Z., and Low, A., 2019, Fly ash based geopolymer for the adsorption of anionic surfactant from aqueous solution, *J. Cleaner Prod.*, 229, 232–243.

[3] Heidarinejad, Z., Dehghani, M.H., Heidari, M., Javedan, G., Ali, I., and Sillanpää, M., 2020, Methods for preparation and activation of activated carbon: A review, *Environ. Chem. Lett.*, 18 (2), 393–415.

[4] Santosa, S.J., Kunarti, E.S., Aprilita, N.H., Wulandari, B., and Bawani, D.N., 2019, Sorption mechanism and performance of peat soil humin for methylene blue and *p*-nitrophenol, *Indones. J. Chem.*, 19 (1), 198–210.

[5] Dehghani, M.H., Yetilmezsoy, K., Salari, M., Heidarinejad, Z., Yousefi, M., and Sillanpää, M., 2020, Adsorptive removal of cobalt(II) from aqueous solutions using multi-walled carbon nanotubes and γ-alumina as novel adsorbents: Modelling and optimization based on response surface methodology and artificial neural network, *J. Mol. Liq.*, 299, 112154.

[6] Rasoulzadeh, H., Dehghani, M.H., Mohammadi, A.S., Karri, R.R., Nabizadeh, R., Nazmara, S., Kim, K.H., and Sahu, J.N., 2020, Parametric modelling of Pb(II) adsorption onto chitosan-coated Fe_3O_4 particles through RSM and DE hybrid evolutionary optimization framework, *J. Mol. Liq.*, 297, 111893.

[7] Shams, M., Nodehi, R.N., Dehghani, M.H., Younesian, M., and Mahvi, A.H., 2010, Efficiency of granular ferric hydroxide (GFH) for removal of fluoride from water, *Fluoride*, 43 (1), 61–66.

[8] Dehghani, M.H., Tajik, S., Panahi, A., Khezri, M., Zarei, A., Heidarinejad, Z., and Yousefi, M., 2018, Adsorptive removal of noxious cadmium from aqueous solutions using poly urea-formaldehyde: A novel polymer adsorbent, *MethodsX*, 5, 1148–1155.

[9] Rusdiarso, B., and Basuki, R., 2020, Stability improvement of humic acid as sorbent through magnetite and chitin modification, *J. Kim. Sains Apl.*, 23 (5), 152–159.

[10] Basuki, R., Rusdiarso, B., Santosa, S.J., and Siswanta, D., 2021, Magnetite-functionalized horse dung humic acid (HDHA) for the uptake of toxic lead(II) from artificial wastewater, *Adsorpt. Sci. Technol.*, 2021, 5523513.

[11] Chen, Q., Yin, D., Zhu, S., and Hu, X., 2012, Adsorption of cadmium(II) on humic acid coated titanium dioxide, *J. Colloid Interface Sci.*, 367 (1), 241–248.

[12] Wu, P., Zhang, Q., Dai, Y., Zhu, N., Dang, Z., Li, P., Wu, J., and Wang, X., 2011, Adsorption of Cu(II), Cd(II) and Cr(III) ions from aqueous solutions on humic acid modified Ca-montmorillonite, *Geoderma*, 164 (3), 215–219.

[13] Zhang, X., Lei, Q., Wang, X., Liang, J., Chen, C., Luo, H., Mou, H., Deng, Q., Zhang, T., and Jiang, J., 2019, Removal of Cr(III) using humic acid-modified attapulgite, *J. Environ. Eng.*, 145 (6), 04019028.

[14] Chen, R., Zhang, Y., Shen, L., Wang, X., Chen, J., Ma, A., and Jiang, W., 2015, Lead(II) and methylene blue removal using a fully biodegradable hydrogel based on starch immobilized humic acid, *Chem. Eng. J.*, 268, 348–355.

[15] Lu, S., Liu, W., Wang, Y., Zhang, Y., Li, P., Jiang, D., Fang, C., and Li, Y., 2019, An adsorbent based on humic acid and carboxymethyl cellulose for efficient dye removal from aqueous solution, *Int. J. Biol. Macromol.*, 135, 790–797.

[16] Tiwari, D., Bhunia, H., and Bajpai, P.K., 2016, Urea-formaldehyde derived porous carbons for adsorption of CO_2, *RSC Adv.*, 6 (113), 111842–111855.

[17] Chen, S., Lu, X., Pan, F., Wang, T., and Zhang, Z., 2017, Preparation and characterization of urea-formaldehyde resin/reactive montmorillonite composites, *J. Wuhan Univ. Technol., Mater. Sci. Ed.*, 32 (4), 783–790.

[18] Liu, M., Wang, Y., Wu, Y., and Wan, H., 2018, Hydrolysis and recycling of urea formaldehyde resin residues, *J. Hazard. Mater.*, 355, 96–103.

[19] Wibowo, E.S., and Park, B.D., 2020, Determination of crystallinity of thermosetting urea-formaldehyde resins using deconvolution method, *Macromol. Res.*, 28 (6), 615–624.

[20] Nadeem, R., Manzoor, Q., Iqbal, M., and Nisar, J., 2016, Biosorption of Pb(II) onto immobilized and native *Mangifera indica* waste biomass, *J. Ind. Eng. Chem.*, 35, 185–194.

[21] Foo, K.Y., and Hameed, B.H., 2010, Insights into the modeling of adsorption isotherm systems, *Chem. Eng. J.*, 156 (1), 2–10.

[22] Arshad, M.A., Maaroufi, A., Pinto, G., El-Barkany, S., and Elidrissi, A., 2016, Morphology, thermal stability and thermal degradation kinetics of cellulose-modified urea-formaldehyde resin, *Bull. Mater. Sci.*, 39 (6), 1609–1618.

[23] Nandiyanto, A.B.D., Oktiani, R., and Ragadhita, R., 2019, How to read and interpret FTIR spectroscope of organic material, *Indones. J. Sci. Technol.*, 4 (1), 97–118.

[24] Tiwari, D., Bhunia, H., and Bajpai, P.K., 2016, Urea-formaldehyde derived porous carbons for adsorption of CO_2, *RSC Adv.*, 6 (113), 111842–111855.

[25] Shen, Y., Lin, H., Gao, W., and Li, M., 2020, The effects of humic acid urea and polyaspartic acid urea on reducing nitrogen loss compared with urea, *J. Sci. Food Agric.*, 100 (12), 4425–4432.

[26] Wang, J., and Guo, X., 2020, Adsorption kinetic models: Physical meanings, applications, and solving methods, *J. Hazard. Mater.*, 390, 122156.

[27] Li, J., and Zhang, Y., 2021, Morphology and crystallinity of urea-formaldehyde resin adhesives with different molar ratios, *Polymers*, 13 (5), 673.

[28] Zehra, T., Lim, L.B.L., and Priyantha, N., 2015, Removal behavior of peat collected from Brunei Darussalam for Pb(II) ions from aqueous solution: Equilibrium isotherm, thermodynamics, kinetics and regeneration studies, *Environ. Earth Sci.*, 74 (3), 2541–2551.

[29] Yang, X., Yang, S., Yang, S., Hu, J., Tan, X., and Wang, X., 2011, Effect of pH, ionic strength and temperature on sorption of Pb(II) on NKF-6 zeolite studied by batch technique, *Chem. Eng. J.*, 168 (1), 86–93.

[30] Dubinin, M.M., and Radushkevich, L.V., 1947, The equation of the characteristic curve of the activated charcoal, *Proc. Acad. Sci. USSR Phys. Chem. Sect.*, 55, 331–337.

[31] Tempkin, M.I., and Pyzhev, V., 1940, Kinetics of ammonia synthesis on promoted iron catalyst, *Acta Phys. Chim. USSR*, 12 (1), 327–356.

[32] Basuki, R., Yusnaidar, Y., and Rusdiarso, B., 2018, Different style of Langmuir isotherm model of non-competitive sorption Zn(II) and Cd(II) onto horse dung humic acid (HD-HA), *AIP Conf. Proc.*, 2026, 020009.

[33] Freundlich, H., 1907, Über die Adsorption in Lösungen, *Z. Phys. Chem.*, 57U (1), 385–470.

[34] Bartczak, P., Norman, M., Klapiszewski, Ł., Karwańska, N., Kawalec, M., Baczyńska, M., Wysokowski, M., Zdarta, J., Ciesielczyk, F., and

Jesionowski, T., 2018, Removal of nickel(II) and lead(II) ions from aqueous solution using peat as a low-cost adsorbent: A kinetic and equilibrium study, *Arabian J. Chem.*, 11 (8), 1209–1222.

[35] Qu, P., Li, Y., Huang, H., Wu, G., Chen, J., He, F., Wang, H., and Gao, B., 2020, Foamed urea-formaldehyde microspheres for removal of heavy metals from aqueous solutions, *Chemosphere*, 241, 125004.

[36] Kushwaha, A., Rani, R., and Patra, J.K., 2020, Adsorption kinetics and molecular interactions of lead [Pb(II)] with natural clay and humic acid, *Int. J. Environ. Sci. Technol.*, 17 (3), 1325–1336.

[37] El-Korashy, S.A., Elwakeel, K.Z., and El-Hafeiz, A.A., 2016, Fabrication of bentonite/thiourea-formaldehyde composite material for Pb(II), Mn(VII) and Cr(VI) sorption: A combined basic study and industrial application, *J. Cleaner Prod.*, 137, 40–50.

[38] Ming, G., Duan, H., Meng, X., Sun, G., Sun, W., Liu, Y., and Lucia, L., 2016, A novel fabrication of monodisperse melamine-formaldehyde resin microspheres to adsorb lead(II), *Chem. Eng. J.*, 288, 745–757.

[39] Saha, P., Chowdhury, S., Gupta, S., and Kumar, I., 2010, Insight into adsorption equilibrium, kinetics and thermodynamics of Malachite Green onto clayey soil of Indian origin, *Chem. Eng. J.*, 165 (3), 874–882.

[40] Duran, C., Ozdes, D., Gundogdu, A., and Senturk, H.B., 2011, Kinetics and isotherm analysis of basic dyes adsorption onto almond shell (*Prunus dulcis*) as a low cost adsorbent, *J. Chem. Eng. Data*, 56 (5), 2136–2147.

[41] Lagergren, S., 1898, About the theory of so called adsorption of soluble substances, *K. Sven. Vetenskapsakad. Handl.*, 24 (4), 1–39.

[42] Ho, Y.S., McKay, G., Wase, D.A.J., and Forster, C.F., 2000, Study of the sorption of divalent metal ions on to peat, *Adsorpt. Sci. Technol.*, 18 (7), 639–650.

[43] Santosa, S.J., 2014, Sorption kinetics of Cd(II) species on humic acid-based sorbent, *CLEAN - Soil Air Water*, 42 (6), 760–766.

[44] Rusdiarso, B., Basuki, R., and Santosa, S.J., 2016, Evaluation of Lagergren kinetics equation by using novel kinetics expression of sorption of Zn^{2+} onto horse dung humic acid (HD-HA), *Indones. J. Chem.*, 16 (3), 338–346.

[45] Basuki, R., Ngatijo, Santosa, S.J., and Rusdiarso, B., 2018, Comparison the new kinetics equation of noncompetitive sorption Cd(II) and Zn(II) onto green sorbent horse dung humic acid (HD-HA), *Bull. Chem. React. Eng. Catal.*, 13 (3), 475–488.

[46] Ngatijo, N., Basuki, R., Rusdiarso, B., and Nuryono, N., 2020, Sorption-desorption profile of Au(III) onto silica modified quaternary amines (SMQA) in gold mining effluent, *J. Environ. Chem. Eng.*, 8 (3), 103747.

[47] Baker, H.M., Khalili, F.I., and Aldulaimy, B.I.A., 2020, Removal of lead ions from aqueous solutions by insolubilized Iraqi humic acid, *Desalin. Water Treat.*, 206, 286–296.

Simple Method of 9,10-Anthraquinone Assay in *Eleutherine americana* (Aubl.) Merr. ex K. Heyne using High-Performance Liquid Chromatography

Sophi Damayanti[1*], Samuel Gunadi Tanusondjaja[1], Benny Permana[1], Rika Hartati[2], Dian Ayu Eka Pitaloka[3,4], and Indra Wibowo[5]

[1]*Department of Pharmacochemistry, School of Pharmacy, Bandung Institute of Technology, Jl. Ganesa 10, Bandung 40132, Indonesia*

[2]*Department of Pharmaceutical Biology, School of Pharmacy, Bandung Institute of Technology, Jl. Ganesa 10, Bandung 40132, Indonesia*

[3]*Department of Pharmacology and Clinical Pharmacy, Faculty of Pharmacy, Universitas Padjadjaran, Jl. Raya Bandung-Sumedang KM.21, Sumedang, 45363, Indonesia*

[4]*Center for Translational Biomarker Research, Universitas Padjadjaran, Jl. Raya Bandung-Sumedang KM.21, Sumedang, 45363, Indonesia*

[5]*Department of Physiology, Animal Development and Biomedical Science, School of Life Science and Technology, Bandung Institute of Technology, Jl. Ganesa 10, Bandung 40132, Indonesia*

* ***Corresponding author:***

tel: +62-81394075730
email: sophi.damayanti@fa.itb.ac.id

Received: March 15, 2021
Accepted: May 3, 2021

DOI: 10.22146/ijc.64701

Abstract: Eleutherine americana *(*E. americana*) is a medicinal plant commonly found on the island of Borneo, Indonesia. This plant is known to have several biological activities. However, anthraquinone residues are generally present as contaminants. This study was aimed to develop a method of determining the levels of 9,10-anthraquinone in plant extracts and fractions using High Performance Liquid Chromatography (HPLC). The research aims to optimize the mobile phase, the system suitability test, and the system validation. The optimal mobile phase was acetonitrile:distilled water 1:1 v/v with a flow rate of 1.25 mL/min. The validation result shows that the linearity was obtained with a correlation coefficient (r) of 0.9995 and an r^2 coefficient of 0.9991. The estimated limits for detection and quantification values were 0.178 and 0.594 μg/mL, respectively. In the intraday and inter-day accuracy test, the coefficient of variance for reference was 0.627 and 0.774, while the results for the sample were 2.966 and 2.658. The percentage recovery rate for reference was between 98.976–101.452%, and for the sample, the result was 89.191–94.667%. The average 9,10-anthraquinone content in the acetate fraction of* E. americana *plant was 9.799 μg/g ± 5.243.*

Keywords: Eleutherine americana*; 9,10-anthraquinone; mobile phase; validation; HPLC*

■ INTRODUCTION

Eleutherine americana (E. americana) is a plant in the Iridaceae family group. This plant contains natural compounds that are classified based on the structure into anthraquinones, naphthalene, and naphthoquinones. Several compounds from this group that were found in plants include stigmasterol-3-O-β-D-glucopyranoside, kadsuric acid, and stigmasterol [1]. Until now, anthraquinone derivatives have been widely studied in various research topics.

Anthraquinone is reported to have antifungal [2] and antimicrobial activity [3]. These compounds belong to the quinone, electrophilic, and other metabolic groups of benzene, phenol, and aromatics, including polycyclics. Anthraquinones have been shown to have a negative property, namely carcinogenicity [4]. However, the risks to airborne organisms, birds, and arthropods

are considerably low [5]. 9,10-Anthraquinone is a compound that can occur due to the use of pesticides [6]. Therefore, an analysis of this compound is of high importance.

To date, the analysis of compounds in *E. americana* has been carried out using the thin layer chromatography method. The method was used to observe the antihypertensive activity and lipid profile in hypoestrogenic mice [7]. In addition, anthraquinone analysis is also carried out using Gas Chromatography-Mass Spectrometry (GC-MS) and High Performance Liquid Chromatography (HPLC) to determine the analyte as an active compound or contaminant [8-10].

However, hyphenated GC-MS is unfortunately still limited in some laboratories, particularly in Indonesia. Therefore, the HPLC method was developed in this study using various specific eluent compositions (acetonitrile-bidistilled water and methanol) to obtain optimal elution of 9,10-anthraquinone. This study aims to develop a validation method for 9,10-anthraquinone in *E. americana* using HPLC. Thus, this study is expected to provide an alternative solvent selection using HPLC to analyze 9,10-anthraquinone.

■ EXPERIMENTAL SECTION

Materials

Samples (ethanol extract, hexane fraction, water fraction, and ethyl acetate fraction of the bulbs of *E. americana*) were provided by the Biology Pharmaceutical Lab of the Bandung Institute of Technology (Indonesia). 9,10-anthraquinone with a purity of 97% was purchased from Sigma-Aldrich (St. Louis, MO. USA). HPLC-grade acetonitrile, HPLC-grade Methanol, bidistilled water, and micropore membrane 0.45 μm were purchased from Sigma-Aldrich (St. Louis, MO. USA).

Instrumentation

The instruments used in this research include Waters e2695 High Performance Liquid Chromatography (HPLC), Waters 2489 UV Detector, 4.6 × 150 mm ODS-3 Inertsil Column, autosampler tube, Hewlett Packard 8453 Diode Array Spectrophotometer, Empower software, sonicator, syringe and filter holder.

Procedures

Mobile phase development

Several compositions of the mobile phase were made to obtain the optimum mobile phase for the 9,10-anthraquinone analysis. The mobile phase components were previously mixed, filtered with a 0.45 μm micropore membrane, and sonicated. The composition of the mobile phases is listed in Table 1.

Preparation of the 9,10-anthraquinone stock solution

Stock solution with a concentration of 300 μg/mL was prepared from 15 mg of 9,10-anthraquinone and diluted with 40 mL of the mobile phase. The solution was then stirred, and the volume of the solution was added to 50 mL with the mobile phase.

Determination of the maximum wavelength absorption of 9,10-anthraquinone

A solution of 9,10-anthraquinone with a concentration of 6 μg/mL was prepared from stock solutions. Determination of the wavelength with maximum absorption was carried out in the 200–390 nm range using the Hewlett Packard 8453 Diode Array Spectrophotometer.

HPLC system optimization

HPLC optimization was conducted by determining the flow rate, injection volume, and mobile phase. Afterwards, it was proceeded by calculating several chromatographic parameters, such as relative standard deviation and tailings factor. The system that gave the best results was then selected to be used in this study.

HPLC system

The HPLC system in this study used an Inertsil ODS-3 4.6 × 150 mm stationary phase, a mobile phase of acetonitrile-bidistilled water (50:50), a UV-Visible detector with a wavelength of 250 nm, a flow rate of 1.25 mL/min and injection volume of 10 μL.

Table 1. Mobile phase composition variance

Mobile Phase	Composition
Bidistilled Water-Methanol	35:65
Acetonitrile–Methanol	45:55
Acetonitrile–Bidistilled Water	50:50

System suitability test

9,10-Anthraquinone standard solution containing 6 µg/mL was injected into the HPLC by the system mentioned above for 6 replications. The relative standard deviation, tailings factor, column efficiency, capacity factor, and resolution were calculated.

Validation method

Linearity, limit of detection (LOD), limit of quantification (LOQ). A series of 9,10-anthraquinone standard solutions were prepared from the stock solution using a dilution method in the 1.2–6.0 µg/mL range. The stock solution was diluted to give the concentrations listed in Table 3, with 10 mL for each solution. Each solution was placed into a different flask and sonicated for 10 min. From each solution, 1 mL was taken and filtered with a 0.45 µm micropore membrane. The solution was then placed into an autosampler, and after that, it was injected into the HPLC. The HPLC response to the injection was then recorded for each concentration (3 replications). Based on the results, a calibration curve was drawn and the regression equation was determined. Furthermore, the correlation coefficients, the LOD and the LOQ values were calculated.

Precision. There were 2 precision tests carried out namely, for the standard solution and for the sample solution. The spiked sample solution was tested using 1.25 g of the sample added with 1800 µL of 9,10-anthraquinone 6 µg/mL working solution. The mobile phase was added to 5 mL for the standard solution test. The same concentration of the standard solution was added for the spiked sample. For both tests, 6 replications were carried out. Sonication was then performed for both solution groups. For the spike sample solution, 1 mL of each solution was filtered with a 0.45 µm micropore membrane. The solution was then placed in the autosampler for injection. The precision tests that were carried out included the intraday tests and inter-day tests.

Accuracy. The accuracy test was carried out on the standard solution and the spiked sample solution. The spiked sample solution was tested using 1.25 g of sample added with 1440, 1800, and 2160 µL of 9,10-anthraquinone 6 µg/mL working solution. Each of the 3 samples were then added with the mobile phase to reach a volume of 5 mL. Solutions of the same concentration were also used for the test solution of spiked samples. For both tests, 3 replications were carried out. Sonication was then performed for both solutions. For the spike sample solution, the solution was filtered with a 0.45 µm micropore membrane. The solution was then placed in the autosampler for injection.

Sample solution preparation. Ethanol, water, hexane, and ethyl acetate fractions of E. americana were weighed 1.25 g each, and was then added with the mobile phase to reach a volume of 5 mL. Then 1 mL was taken from each sample solution and filtered with a 0.45 µm micropore membrane, and later placed into an autosampler for injection into the HPLC.

■ RESULTS AND DISCUSSION

The limitations of the laboratory for providing hyphenated chromatography and mass spectrometry are driving research for alternative methods. HPLC has been used to determine 9,10-anthraquinone. In this study, a variety of solvents have been explored. Several combinations of eluent variant compositions have been developed. The details of the new findings are elaborated as follows:

Determination of the Maximum Wavelength Absorption of 9,10-Anthraquinone

The UV-Visible detector was used in this study to determine the maximum wavelength of 9,10-anthraquinone absorption. Based on the research results, the maximum wavelength of 9,10-anthraquinone absorption is 250 nm. This result is in line with the study conducted by Dixon [11].

HPLC System Optimization

The HPLC system optimization aimed to obtain the best chromatogram and find the best elution for 9,10-anthraquinone in the HPLC. Several parameters were used in the research: Inertsil ODS-3 4.6 × 150 mm for the stationary phase, UV-Visible detector, and isocratic elution method. The optimization included the choice of mobile phase and the flow rate. There were 3 combinations of the mobile phase (Table 1). In the

optimization process, 9,10-anthraquinone standard solution with a concentration of 30 μg/mL was injected.

The first part of the experiment was done with the flow rate of 1 mL/min, and elution was carried out with the 3 mobile phases. It was found that the retention time was too long using the bidistilled water-methanol (35:65) mobile phase. However, the retention time was too short using the acetonitrile-methanol (45:55) mobile phase. The difference between the retention time of 9,10-anthraquinone and the column dead time was only 0.4 sec for acetonitrile-methanol (45:55). The retention time was shorter for the acetonitrile-bidistilled water (50:50) mobile phase compared to the bidistilled water-methanol (35:65). This may be caused by the difference in the polarity strength of the elution of acetonitrile and methanol. Elution by acetonitrile was found to be stronger than methanol [11], and this resulted in the shorter retention time of 9,10-anthraquinone with the acetonitrile-bidistilled water (50:50) mobile phase when compared to the bidistilled water-methanol (35:65) mobile phase.

Based on the results, acetonitrile-bidistilled water (50:50) showed the best analysis performance, and therefore it was selected for further research. This result revealed a new composition of solvent to be used in HPLC for the determination of 9,10-anthraquinone. The optimization of flow rate gave 1.25 mL/min as the best result. It can be concluded that the HPLC system used in this study were as follows: Inertsil ODS-3 4.6 × 150 mm column, acetonitrile-bidistilled water (50:50) as the mobile phase, the flow rate of 1.25 mL/min, isocratic elution method, UV Waters 2489 detector with a wavelength of 250 nm and an injection volume of 10 μL.

System Suitability Test

The system suitability test was carried out by injecting a standard solution of 9,10-anthraquinone with a concentration of 6 μg/mL into the HPLC 6 times. The parameters analyzed included relative standard deviation, tailings factor, resolution, column efficiency, and capacity factor resulting from the system suitability test (Table 2). Based on these results, all tested parameters have met the requirements. Therefore, the optimized HPLC system can be used for method validation.

Method Validation

The parameters for the analysis of the method validation consist of selectivity, linearity, intraday precision test, inter-day precision test, and accuracy test [12-14]. The selectivity test included comparing the chromatogram of the standard solution and the chromatogram of various samples. Two compounds were retained in the range of 9,10-anthraquinone's retention time in the ethanol extract of *E. americana* (Fig. 1).

The results showed that this method was not selective for 9,10-anthraquinone in the ethanol extract of *E. americana* due to the presence of other compounds in the retention time range. The ethyl acetate fraction of *E. americana* showed no other peaks disturbing the 9,10-anthraquinone peak. This implies that the method is already selective [12-14]. Based on these results, it can be concluded that the HPLC system is selective against 9,10-anthraquinone in the ethyl acetate fraction of *E. americana*.

The linearity test was carried out by determining the response of the instrument three times to 5 different standard solutions of 9,10 anthraquinones with different concentrations. Based on the calibration curve (Table 2, Fig. 2), the equation y = 18456x + 109415 was obtained. The minimum acceptable correlation coefficient value

Table 2. System suitability result

System Suitability Test Parameters	Result	Requirement [12-14]
Relative Standard Deviation for AUC	0.4%	≤ 2%
Relative Standard Deviation for Retention Time	0.3%	≤ 2%
Tailing Factor	1.39	≤ 2
Resolution	5.823	≥ 1.5
Column Efficiency	8113	> 2000
Capacity Factor	4.999	1< k' < 10

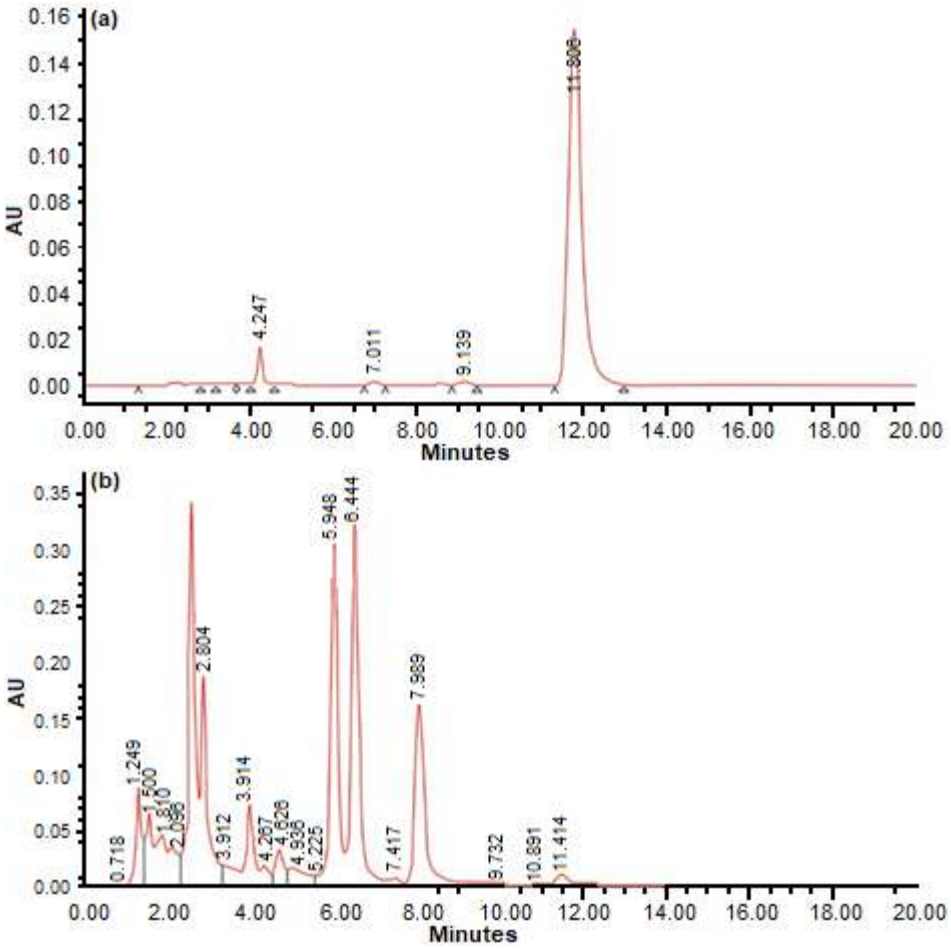

Fig 1. Comparison of the standard 9,10-anthraquinone solution (a) and ethyl acetate fraction of *E. americana* bulbs (b)

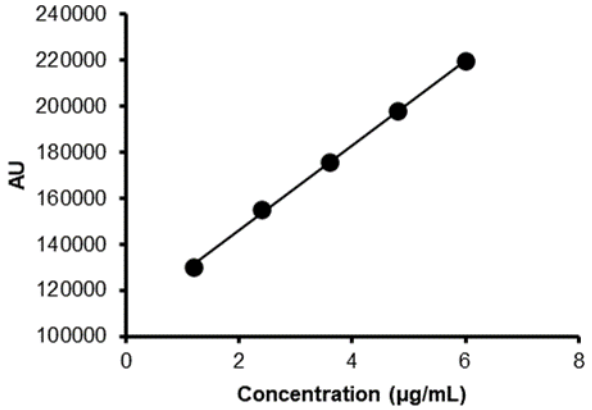

Fig 2. Calibration curve of Standard 9,10-anthraquinone solution (y=18456x +109415, r = 0.9995, r^2 = 0.9991)

was 0.9914. The value of the correlation coefficient (r) based on the calibration curve was 0.9995, and the coefficient of determination (r^2) was 0.9991. The Vxo value can also be used to determine linearity. Curves can have a very good Vxo value if they are below 5% [12-14]. In the experiment, the Vxo value was 1.779%. Based on the 2 parameters above, it can be concluded that the calibration curve has met the requirements. Estimated LOD and LOQ were calculated by a calibration curve, using standard deviation, which is the square root of each concentration variant [12-14]. Based on the calibration curve, the estimated LOD value is 0.178 µg/mL, and the LOQ is 0.594 µg/mL.

The precision test was carried out for the standard solution and the spiked sample solution. The precision of the analytical procedure reveals the closeness of agreement (degree of scattering) between a series of measurements obtained from multiple sampling of the same homogeneous sample under defined conditions [141]. In the accuracy test, 6 response instruments were recorded twice a day (intraday) and on 2 different days (inter-day).

Table 3. Result of spiked sample solution precision test

Precision test	Period	Spiked sample solution[a]	% CV[b]
Intraday	Time 1	3.473 ± 1.998	2.966
	Time 2	3.783 ± 3.934	
Inter-day	Day 1	3.473 ± 1.998	2.658
	Day 2	2.837 ± 3.317	

Notes: (a) Average of the concentration (μg/mL) ± RSD (%); n = 6 (b) Average of the RSD (%)

Precision can be determined by assessing the relative standard deviation (RSD). The RSD value for the 9,10-anthraquinone concentration in the sample should be equal to or less than 4% [12-14].

Based on the experiment, RSD values of the intraday test for the spiked sample solution were 1.998% and 3.934%, and for the inter-day test, the values were 1.998% and 3.317% (Table 4). In the standard solution, the intraday test's RSD values were 0.56% and 0.693%, as for the inter-day test, the values were 0.56% and 0.988%. The result for the 2 precision tests already fulfilled the requirement stated by AOAC.

The accuracy of an analytical procedure expresses the closeness of agreement between the value received, as either an actual conventional value or the reference value, and the value found [12-14]. The accuracy test was carried out for the standard solution and spiked sample solution. The accuracy test began with standard addition to the sample at concentrations of 80%, 100% and 120% based on the sample content [12-14]. The accuracy test was also carried out on the standard solution with the same concentration added to the spiked sample solution. For each concentration, the test was carried out 3 times. The results of the accuracy test are shown as percent recovery. The results of the accuracy test are shown in Table 5.

The % recovery rate should be between 85–110% [14]. Based on the results, the recovery value of the spiked sample solution was 89.191–94.667%, and for the standard solution the recovery value was 98.976–101.452%. This result meets the requirement stated by AOAC.

The validation results show that the method can be applied to the sample. This study can be used as an alternative to the 9,10-anthraquinone analysis that has been developed by other researchers [15-17].

Analytical Method Assay for the Samples

After the validation parameters are met, the next research stage was to test the sample using HPLC. Ethanol, water, hexane, and ethyl acetate fractions of *E. americana* bulbs were weighed, placed into several containers, and added to the mobile phase. Sonication was carried out to increase the solubility of 9,10-anthraquinone in the solvent. After sonication, two filtrations were carried out. Filtration aimed to prevent particles that could damage the HPLC column. In this study, the anthraquinone peaks were between 11.4 and 11.6 min after the HPLC response was obtained. The

Table 4. Result of standard solution precision test

Precision test	Period	Standard Solution[a]	% CV[b]
Intraday	Time 1	1.354 ± 0.56	2.966
	Time 2	1.745 ± 0.693	
Inter-day	Day 1	3.473 ± 1.998	2.658
	Day 2	2.837 ± 3.317	

Notes: (a) Average of the concentration (μg/mL) ± RSD (%); n = 6 (b) Average of the RSD (%)

Table 5. Result of accuracy test

Concentration (%)	Spiked sample solution[a]	% Recovery for spiked sample solution[b]	Standard solution[a]	% Recovery for standard solution[b]
80	3.635 ± 1.109	89.191 ± 3.401	1.346 ± 1.067	101.167 ± 1.067
100	3.964 ± 2.433	94.667 ± 6.368	1.584 ± 1.498	98.976 ± 1.498
120	4.208 ± 1.454	91.629 ± 3.479	1.948 ± 0.683	101.452 ± 0.683

Notes: (a) Average of the concentration (μg/mL) ± RSD (%); n =3 (b) Average of the % Recovery (%) ± RSD (%)

Table 6. The amount of 9,10-anthraquinone in the ethyl acetate fraction of the bulbs of *E. americana*

Assay	Content (μg/g)
1	9.207
2	10.068
3	10.123
Average of Assay (μg/g)	9.799
RSD (%)	5.243

results were then entered into a calibration curve.

Testing of hexane and water fractions of *E. americana* bulbs showed no trace of 9,10-anthraquinone. 9,10-Anthraquinone may not be detected in this fraction because hexane is a non-polar solvent, whereas water is a polar solvent. Thus, 9,10-anthraquinone as a semi-polar compound was not detected. In the ethanol extract of *E. americana*, there were overlapping peaks in the range of anthraquinone retention times. Therefore, 9,10-anthraquinones could not be determined, because the separation of the detected compounds was not yet complete. However, the ethyl acetate fraction of *E. americana* bulbs was found to contain 9,10 anthraquinone (Table 6).

9,10-Anthraquinone obtained from the sample did not meet the requirement set by EFSA in 2012 in which the amount of 9,10-anthraquinone in the sample must be less than 0.01 mg/kg. This requirement may be intended for all residue of pesticides, not specifically for 9,10-anthraquinone. The specific requirement for 9,10-anthraquinone has not been stated until today. However, the anthraquinon analysis should be determined and the toxicity of anthraquinon should be avoided [18-20].

■ CONCLUSION

The analytical method development for 9,10-anthraquinone from the bulbs of *E. americana* was done by using HPLC with the system of Inertsil ODS-3 4.6 × 150 mm column, acetonitrile-bidistilled water (50:50), flow rate of 1.25 mL/min, isocratic elution method, UV-Visible detector with the wavelength of 250 nm, and injection volume of 10 μL. This method resulted in 9,10-anthraquinone peaks at 11.4–11.6 min.

The developed method already fulfilled all requirements for the system suitability test and method validation. In the sample, there was no 9,10-anthraquinone in the hexane and water fraction of the bulbs of *E. americana* but it was detected in the ethanol extract of the bulbs of *E. americana*, even though it was not separated. The 9,10-anthraquinone content in the ethyl acetate fraction of the bulbs of *E. americana* was 9.799 μg/g ± 5.243.

■ ACKNOWLEDGMENTS

The research was funded by the Ministry of Research, Technology and Higher Education PDUPT 2017-2018.

■ REFERENCES

[1] Insanu, M., Kusmardiyani, S., and Hartati, R., 2014, Recent studies on phytochemicals and pharmacological effects of *Eleutherine americana* Merr., *Procedia Chem.*, 13, 221–228.

[2] Kuntorini, E.M., and Misrina, M.D., 2016, Anatomical structure and antioxidant activity of red bulb plant (*Eleutherine americana*) on different plant age, *Biodiversitas*, 17 (1), 229–233.

[3] Malmir, M., Serrano, R., and Silva, O., 2017, "Anthraquinones as potential antimicrobial agents-A review" in *Antimicrobial Research: Novel Bioknowledge and Educational Programs*, Eds. Mendez-Vilas, A., Formatex Research Center, Badajoz, Spain, 55–61.

[4] Yusiasih, R., Pitoi, M.M., Ariyani, M., Koesmawati, T.A., and Maulana, H., 2019, Anthraquinone in Indonesia infusion tea: analysis by HPLC-UV and risk assessment, *Chem. Biol. Technol. Agric.*, 6, 19.

[5] European Food Safety Authority, 2012, Reasoned opinion on the review of existing maximum residue levels (MRLs) for anthraquinone according to article 12 of regulation (EC) No 396/2005, *EFSA J.*, 10 (6), 2761.

[6] DeLiberto, S.T., and Werner, S.J., 2016, Review on anthraquinone for pest management and agricultural crop protection, *Pest. Manage. Sci.*, 72 (10), 1813–1825.

[7] Bahtiar, A., and Chumala, D.Y., 2018, Dayak onions (*Eleutherine bulbosa* (Mill.) Urb.) bulbs extracts

reduces blood pressure of hypoestrogen model rats by controlling lipids profile, *Int. J. Morphol.*, 36 (3), 1016–1021.

[8] Rani, V.S., and Nair, B.R., 2015, Pharmacognostic and physiochemical evaluation of bulbs of *Eleutherine bulbosa* (Miller) urban, a medicinal plant, *J. Pharmacogn. Phytochem.*, 4 (3), 273–277.

[9] Paramapojn, S., Ganzera, M., Gritsanapan, W., and Stuppner, H., 2008, Analysis of naphthoquinone derivatives in the Asian medicinal plant *Eleutherine americana* by RP-HPLC and LC-MS, *J. Pharm. Biomed. Anal.*, 47 (4), 990–993.

[10] Kumar, R.B., 2017, Application of HPLC and ESI-MS techniques in the analysis of phenolic acids and flavonoids from green leafy vegetables (GLVs), *J. Pharm. Anal.*, 7 (6), 349–364.

[11] Dixon, J.M., Taniguchi, M., and Lindsey, J.S., 2005, PhotochemCAD 2: A refined program with accompanying spectral databases for photochemical calculations, *Photochem. Photobiol.*, 81, 212–213.

[12] Suresh, R., Anarthanan, S.V.J., Manavalan, R., and Valliappan, K., 2010, Aspects of validation in HPLC method development for pharmaceutical analysis-comparison of validation requirements by FDA, USP, and ICH, *Int. J. Pharm. Sci. Res.*, 1 (12), 123–132.

[13] AOAC International, 2002, AOAC *Guidelines for Single Laboratory Validation of Chemical Methods for Dietary Supplements and Botanicals*, AOAC International, Arlington, Virginia, US.

[14] Analytical Laboratory Accreditation Criteria (ALACC), 2017, *AOAC International Guidelines for Laboratories Performing Microbiological and Chemical Analyses of Food, Dietary Supplements and Pharmaceuticals: An Aid to Interpretation of ISO/IEC 17025*, AOAC International, Rockville, Maryland, US.

[15] Hemmateenejad, B., Shamsipur, M., Safavi, A., Sharghi, H., and Amiri, A.A., 2008, Reversed-phase high performance liquid chromatography (RP-HPLC) characteristics of some 9,10-anthraquinone derivatives using binary acetonitrile-water mixtures as mobile phase, *Talanta*, 77 (1), 351–359.

[16] Xu, L., Chan, C.O., Lau, C.C., Yu, Z., Mok, D.K.W., and Chen, S., 2012, Simultaneous determination of eight anthraquinones in Semen Cassiae by HPLC-DAD, *Phytochem. Anal.*, 23 (2), 110–116.

[17] Wei, S.Y., Yao, W.X., Ji, W.Y., Wei, J.Q., and Peng, S.Q., 2013, Qualitative and quantitative analysis of anthraquinones in rhubarbs by high performance liquid chromatography with diode array detector and mass spectrometry, *Food Chem.*, 141 (3), 1710–1715.

[18] IARC, 2013, *IARC Monographs on the evaluation of carcinogenic risks to humans, Volume 101, Some Chemicals Present in Industrial and Consumer Products, Food and Drinking-water*, International Agency for Research on Cancer, Lyon, France.

[19] Duval, J., Pecher, V., Poujol, M., and Lesellier, E., 2016, Research advances for the extraction, analysis and uses of anthraquinones: A review, *Ind. Crops Prod.*, 94, 812–833.

[20] Shukla, V., Asthana, S., Gupta, P.K., Dwivedi, P.D., Tripathi, A., and Das, M., 2017, Toxicity of naturally occurring anthraquinones, *Adv. Mol. Toxicol.*, 11, 1–50.

Ferrate(VI) Synthesis Using $Fe(OH)_3$ from Waste Iron Electrolysis and Its Application for the Removal of Metal Ions and Anions in Water

Gunawan Gunawan*, Abdul Haris, Nor Basid Adiwibawa Prasetya, Eka Pratista, and Azis Amrullah

Department of Chemistry, Faculty of Sciences and Mathematics, Diponegoro University, Jl. Prof. H. Soedarto, SH, Tembalang, Semarang 50275, Indonesia

* ***Corresponding author:***

email: gunawan@live.undip.ac.id

Received: March 20, 2021
Accepted: October 20, 2021

DOI: 10.22146/ijc.64824

Abstract: *Ferrate(VI) salt is an effective oxidant and coagulant for water treatment and removal of metal ions. This study demonstrates a new approach to processing metal ions and anions in water by Fe(VI) through Fe(III) obtained from the electrolysis of waste iron transformer. The electrolysis was successfully carried out in the Na_2SO_4 electrolyte using waste iron and zinc plates as anode and cathode, respectively. Fe(III) electrolysis results through the characterization of FTIR and XRD indicate compliance with $Fe(OH)_3$ standards. Synthesis of ferrate was carried out by adding Fe(III) from electrolysis with NaOCl in alkaline conditions. The formed ferrate solution shows a purple color with a typical maximum wavelength of 505 nm. Furthermore, the ferrate obtained is used to remove metal ions (Fe(III), Cu(II), Zn(II), Mg(II), Pb(II)) and anions (sulfate, nitrate, and carbonate) in water with pH variations. Ferrate treatment filtrate was analyzed using AAS for metal ions, while sulfate, nitrate, and carbonate anions used UV-Vis spectrophotometry, turbidimetry, and titration methods. The results showed that ferrate effectively eliminates metal ions and anions in water with optimum pH 6. The heavy metal removal by ferrate(VI) occurred through ionic bonding and adsorption mechanisms.*

Keywords: *ferrate; electrolysis; water treatment; metal ion; anion*

■ INTRODUCTION

Wastewater is one of the most severe challenges facing our world today, as various pollutants such as metal ions (lead, zinc, magnesium, iron, copper, and cadmium) and anions (sulfate, nitrate, and carbonate) continue to enter the aquatic environment from various industrial and household sectors [1]. Therefore, it is essential to study the treatment of polluted water into clean water free of contaminants. One of the methods used for the treatment of polluted water is to use oxidizers. Ferrate (FeO_4^{2-}) is a powerful and environmentally friendly oxidation agent in the aqueous media [2]. Ferrate(VI) has various functions, such as oxidation, disinfectant, coagulation, sterilization, adsorption, and deodorization [3-6]. Fe(VI) as a coagulant is very effective in removing metals and non-metals in water, dyes [7-9], and greywater [10]. The main iron species that act as coagulants is nanocrystal Fe(III) oxide/hydroxide, produced through Fe(VI) reduction. The use of ferrate as a coagulant in water treatment and polluted water containing inorganic chemicals, such as thorium, cyanide, and thiocyanate [11-14].

Iron is one of the metals widely used in almost all areas of life, but after it is unused, iron will become a waste because it is difficult to degrade. Meanwhile, according to Barisci et al. [15], iron is an oxidizing agent with a positive standard reduction potential. Iron metal is electrolyzed to form gelatin $Fe(OH)_3$ to be used as a source of Fe(III) ions for ferrate synthesis. Reusing waste transformer iron as an anode is also able to reduce environmental pollution. Wet ferrate synthesis is mainly carried out by reacting iron(III) ions with sodium hypochlorite under very alkaline conditions [7]. In general, the iron(III) used comes from commercial iron(III) such as $FeCl_3$, $Fe(NO_3)_3$, and $FeSO_4$. Meanwhile, research on the use of transformer waste as

an iron(III) ion source by electrolysis based on our view has never been carried out.

This paper studied the ferrate synthesis through electrolysis process from iron(III) waste by reacting iron(III) and NaOCl in an alkaline solution. The ferrate was used as a coagulant for the removal of Pb(II), Zn(II), Mg(II), Fe(III), Cu(II), Cd(II), sulfate, nitrate, and carbonate ions at various pH ranges.

■ EXPERIMENTAL SECTION

Materials

The solutions containing Pb(II), Zn(II), Mg(II), Fe(III), Cu(II), Cd(II), sulfate, nitrate, and carbonate ions were prepared from their salts, $Pb(NO_3)_2$, $ZnCl_2$, $MgCl_2$, $FeCl_3$, $CuSO_4$, $CdSO_4$, Na_2SO_4, $NaNO_3$, and Na_2CO_3, respectively. All these salts were obtained from Merck with analytical grade. NaOH, $KMnO_4$, H_2SO_4, and KCNS were also supplied from Merck while NaOCl was supplied from Sigma Aldrich (analytical grade). Iron plate (i-shaped) was got from the transformer waste as the anode and zinc plate was used as cathode electrode.

Instrumentation

The instruments used were magnetic stirrer with a magnetic bar, multimeter (DT-830B), the analytical balance of Ohaus (Pioneer), power supply with regulator (Aditeg APS 3005), FTIR (Fourier Transform Infrared Spectrophotometer, Spotlight 200), SEM (Scanning Electron Microscopy), EDX (Energy Dispersive X-Ray, JEOL JSM-6510LA), and XRD (X-Ray Diffraction Shimadzu XRD-7000), XRF (X-ray Fluorescence Spectrometer, Rigaku Supermini 200). UV-Vis Spectrophotometer (UH 5300 Spectrophotometer), and AAS (Atomic Absorption Spectroscopy, Analyse-400 Perkin Elmer).

Procedure

Synthesis of Fe(III) hydroxide by electrolysis of waste iron plate as anode

Iron and zinc plates were assembled in an electrolysis chamber. Before use, iron and zinc plates were cleaned with soap, distilled water, and alcohol to remove impurities that stick to the surface of the plate. Next, iron and zinc plates were positioned as anode and cathode electrodes, respectively. Then, the electrodes were connected to a DC power supply, and they were immersed in 100 mL Na_2SO_4 1 M solution and electrolyzed with a potential of 3 V for 60 min. The iron area immersed was 3.0 cm × 1.2 cm. The electrolysis solution was filtered, and a blackish-brown precipitate of $Fe(OH)_3$ was obtained. The precipitate formed was dried at 110 °C, then characterized using FTIR, XRD, SEM, and EDX. In addition, the waste iron plate after and before use was characterized using SEM, and to know the contents of the initial iron plate was investigated using XRF.

Effect of electrolysis time. The effect of time on the concentration of iron(III) hydroxide produced was determined by varying the electrolysis times with the interval time of 15 min (15, 30, 45, and 60 min). After the electrolysis process, the solution was added using concentrated H_2SO_4 to dissolve the $Fe(OH)_3$ formed until the solution turned clear. After that, all solutions resulting from the variation of electrolysis time were added with 1 M KSCN as a complexing agent to prove the formation of Fe(III) ions in the electrolysis results. KSCN only reacts with Fe(III) ions to form a brick-red $Fe(SCN)^{2+}$ complex. After stirring, a red brick solution was obtained. The solution was measured using a UV-Vis spectrophotometer at 200–800 nm. Absorbance data were converted to Fe(III) concentration using calculations based on Fe(III) standard calibration.

Synthesis of Ferrate using $Fe(OH)_3$ and NaOCl in alkaline condition

The synthesis of ferrate(VI) was carried out by the wet oxidation method. A precipitate of $Fe(OH)_3$ (5 g) obtained from transformer iron waste electrolysis was added with NaOH 14 M and 50 mL NaOCl in beakers accompanied by stirring for 1 h. The solution was stored for one night in a dark bottle. The color of the solution was changed to purple, and the remaining $Fe(OH)_3$ deposits were removed by filtering using glass wool. Ferrate was the result of the filtrate from filtering the precipitate. The wavelength and concentration of Fe(VI) were determined using the spectrophotometer UV-Vis. (Ferrate concentration = 535.7 mg/L).

Characterization of electrolysis product, iron plate, and analysis of metal ions and anions

The surface morphology of the electrolysis product was characterized using SEM. The chemical element composition was determined by EDX analysis. Characterization using FTIR was used to determine the presence of functional groups and bonds in the sample. The crystal phase of the sample was checked by X-ray diffraction (XRD) with Cu Kα radiation (1.5406 A) at an angle of 10–80°. The composition of the initial iron plate was investigated using XRF. UV-Vis spectrophotometer was used to measure the electrolysis solution's absorption spectra and determine synthesized ferrate. Absorption measurements were performed at 200–800 nm. The filtrates of ferrate-treated solutions were analyzed using AAS to determine the decreased values of metal ions. In contrast, for anions of nitrate (NO_3^-), sulfate (SO_4^{2-}), and carbonate (CO_3^{2-}) ions were tested using UV-Vis spectrophotometry (APHA Method 4500-NO_3), turbidimetry (SNI 06-6989.20-2004), and titration methods (SNI 06-6989 12-2004), respectively.

Application of ferrate for removal of metal ions and anions in water

Treatment of metal ions (cations) with ferrate. Metal ion solutions of Cu(II), Pb(II), Zn(II), Mg(II), Cd(II), and Fe(III) were prepared from the stock solution. As much as 25 mL of 20 mg/L metal ion solution was prepared from a stock solution of 1000 mg/L. The metal ion solution then adjusted pH from 6–12 to determine the effect of pH on the degradation of metal ions by ferrate. As much as 25 mL of 20 mg/L ferrate solution was prepared from a ferrate solution from electrolysis with a concentration of 535.7 mg/L. The pH of the ferrate solution was also adjusted from 6–12. The final concentration of metal ion and ferrate was set at 10 mg/L in 50 mL. The mixture solution was stirred for 10 min and then filtered. After stirring, a brownish floating precipitate was obtained. The filtrate was analyzed by the AAS method to determine the concentration of metal ions (reduced metal ion concentrations after being treated by ferrate).

Treatment of anion with ferrate. The procedure was similar to the metal ion treatments, using sulfate, carbonate, nitrate ions with concentrations of 100 mg/L. The results were filtered, and the solution was analyzed using a UV-Vis spectrophotometer, turbidimeter, and titration, respectively.

■ RESULTS AND DISCUSSION

Initial Characterization of Transformer Waste Iron Plate

Using XRF spectrometer, measurement of used iron transformers as an iron source provides results in the form of a spectrum of elements contained in used iron transformers. The component of these elements is shown in Table 1. From the table, it was found that the dominant element contained in the iron transformer is iron. However, the XRF results showed that the transformer scrap iron used as an anode is not 100% pure, but other elements are contained in it.

Synthesis of Fe(III) Hydroxide by Electrolysis of Waste Iron Plate as Anode

Fe(III) formation was done by electrolysis with iron as anode and zinc as the cathode. Electrolysis was carried out on Na_2SO_4 electrolyte because it was in a neutral pH. In the electrolysis system, an oxidation-reduction reaction occurs. At the anode, an oxidation process occurs, namely the iron plate is oxidized to produce iron cations (Fe^{2+}), while at the cathode, there is a water reduction reaction to produce hydrogen gas and hydroxide anions (OH^-). The electrolysis process obtained decomposition voltage or potential c.a. 2.03 V as shown in Fig. 1, so for the following process, the potential used was 3 V to produce iron(III) ions.

Table 1. XRF analysis of iron from transformer waste

Component	Result (%)
Fe	96.40
Mg	1.35
Si	0.83
Cr	0.79
Mn	0.37
P	0.08
S	0.07
Ca	0.05
K	0.04
Cl	0.02

The iron plate, after oxidation in the electrolysis system, will produce $Fe(OH)_3$. The following mechanisms occur when the formation of $Fe(OH)_3$ [16]:

Anode:

$3\ Fe(s) \rightarrow 3\ Fe^{2+}(aq) + 6e^-$ (1)

Cathode:

$6\ H_2O(l) + 6e^- \rightarrow 3\ H_2(g) + 6\ OH^-(aq)$ (2)

$3\ Fe^{2+}(aq) + 6\ OH^-(aq) \rightarrow 3\ Fe(OH)_2(s)$ (3)

Overall:

$3\ Fe(s) + 6\ H_2O(l) \rightarrow 3\ Fe(OH)_2(s) + 3\ H_2(g)$

The presence of dissolved oxygen and oxygen from electrolysis causes ferrous hydroxide to be oxidized to ferric hydroxide.

Anode:

$4\ Fe(s) \rightarrow 4\ Fe^{2+}(aq) + 8e^-$

$4\ Fe^{2+}(aq) + 10\ H_2O(l) + O_2(g) \rightarrow 4\ Fe(OH)_3(s) + 8\ H^+(aq)$

$4\ Fe(s) + 10\ H_2O(l) + O_2(g) \rightarrow 4\ Fe(OH)_3(s) + 8\ H^+(aq) + 8e^-$ (4)

Cathode:

$8\ H^+(aq) + 8e^- \rightarrow 4\ H_2(g)$ (5)

Overall:

$4\ Fe(s) + 10\ H_2O(l) + O_2(g) \rightarrow 4\ Fe(OH)_3(s) + 4\ H_2(g)$

Electrolysis products are blackish-brown deposits and then characterized using UV-Vis spectrophotometers, FTIR, SEM, and EDX to prove the formation of $Fe(OH)_3$.

Variation of electrolysis time

The electrolysis product is iron(III) ions which could be proved by reacting the electrolyzed solution with KSCN. However, KSCN only reacts with Fe(III) ions to form a brick-red complex. The complex ions formed may vary, such as $[Fe(SCN)_2]^{2+}$, $[Fe(SCN)_2]^+$, $[Fe(SCN)_4]^-$, $[Fe(SCN)_5]^{2-}$, and $[Fe(SCN)_6]^{3-}$. The complex depends on the relative amounts of iron and thiocyanate present in the solution.

Fig. 2(a) shows the spectra of Fe(III) complexed with thiocyanate with different iron(III) standard concentrations, and Fig. 2(b) is the standard curve for iron(III)-thiocyanate measured using UV-Vis spectrophotometer at a maximum wavelength of 465 nm. The solution resulting from the variation of electrolysis time after being added using KSCN produced a reddish-orange color, indicating that the electrolysis solution contains Fe^{3+} ions. Furthermore, the wavelength scanning showed that the longer the electrolysis time, the greater the absorbance of the electrolysis, the longer the electrolysis process, the greater the concentration of Fe^{3+}, as shown in Fig. 2(c). From these results, the concentration of Fe^{3+} from the variation of electrolysis time at 15, 30, 45, and 60 min was 0.000509, 0.000925, 0.001394, and 0.001904 mol/L. Table 2 showed that the average efficiency of the formation of $Fe(OH)_3$ through electrolysis using iron waste as an anode is 29.6%, with the reaction rate following reaction order 1 [17-18].

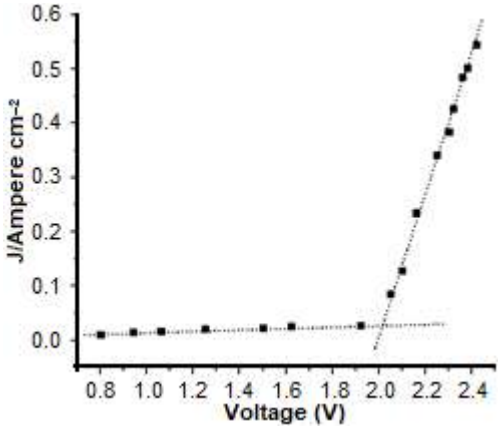

Fig 1. The current-voltage curve for electrolysis using iron waste anode

Table 2. Results of variation in electrolysis time

T (second)	Mass of $Fe(OH)_3$ (mg)	$[Fe(OH)_3]$ (mol/L)	% Efficiency
900	5.44	0.000509	31.5
1800	9.90	0.000925	28.6
2700	14.91	0.001394	28.8
3600	20.37	0.001904	29.5

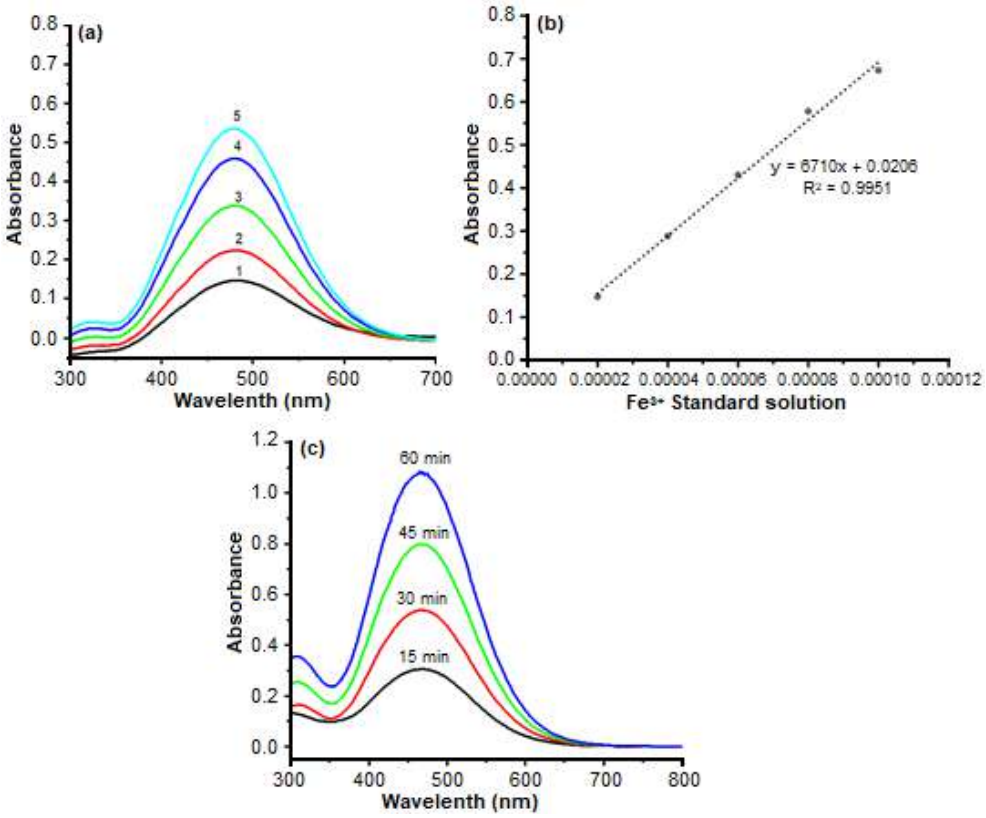

Fig 2. (a) Relation of absorbance and wavelength with variations in the concentration of iron(III) standard complexed with thiocyanate, (b) standard curve of iron(III)-thiocyanate and (c) curve of the effect of electrolysis time on iron(III) ions formed in solution (measured by the thiocyanate method)

Characterization

FTIR and XRD spectra of $Fe(OH)_3$ are shown in Fig. 3. The absorption at 620 and 874 cm^{-1} was associated with the Fe-O stretching vibration indicating the formation of $Fe(OH)_3$. Absorption at 1640 cm^{-1} showed the OH bending vibration of H_2O [19-20]. The peaks that appear at 2θ = 35.00, 43.01, 52.61, 57.69, and 62.57° indicate a good agreement with $Fe(OH)_3$ (JCPDS no 22-0346) [21]. In addition, the peaks at 2θ = 36.87, 47.13, 59.44, and 71.67° indicated a congruence with α-FeO(OH) (goethite) (JCPDS no 29-0713). The peaks at 2θ = 23.53, 33.88, and 48.80° indicate a correspondence with β-FeO(OH) (akaganeite) (JCPDS no 34-1266). XRD and FTIR results show that the resulting electrolysis product is Iron hydroxide $Fe(OH)_3$. The crystal size (D) was calculated using the following Scherrer formula [22]:

$$D = k\lambda/(\beta\cos\theta) \quad (6)$$

Using the Scherrer formula, the average crystal size of $Fe(OH)_3$ was 81.23 nm.

Surface analysis of the sample using SEM is shown in Fig. 4. It can be seen that the iron plate that has been used for electrolysis has been changed. Before being used for electrolysis, the waste iron plate shows a uniform and homogeneous surface. Meanwhile, after being used, the iron plate dissolves into iron ions, thus, the surface becoming porous and heterogeneous. In the iron(III) precipitate, it can be seen that the surface forms aggregates.

The elemental composition of $Fe(OH)_3$ is shown in Table 3. The presence of the Fe and O components in EDX confirms the formation of the desired material, namely iron hydroxide. The carbon peaks in the EDX spectrum are due to the carbon bands used during SEM and EDX measurements. Some of the other elements present in the sample may come from waste iron which is not pure iron.

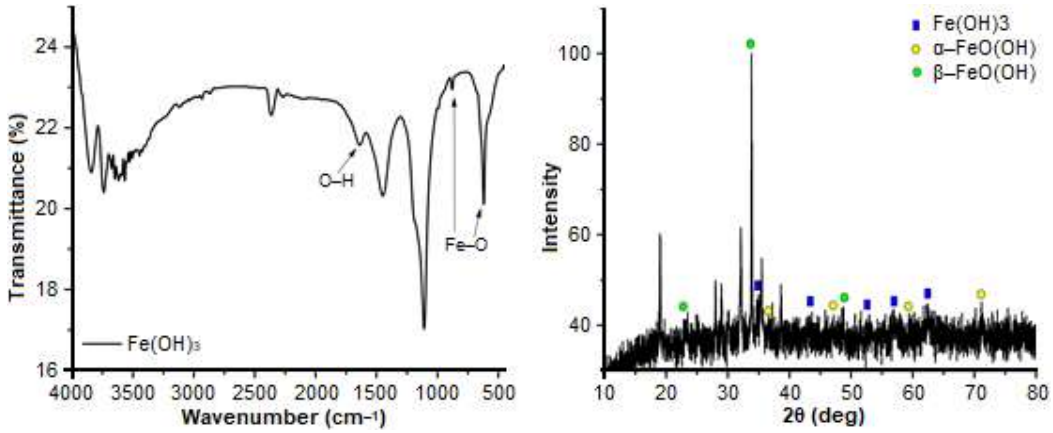

Fig 3. FTIR spectra (left) and XRD diffractogram (right) of $Fe(OH)_3$

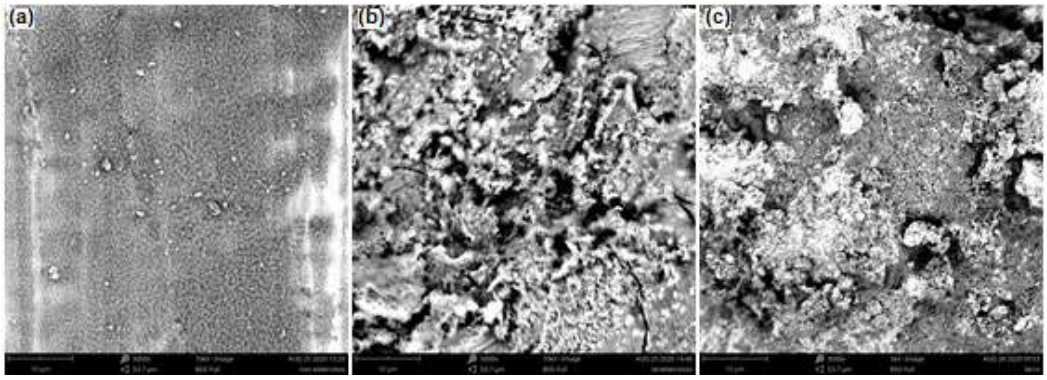

Fig 4. SEM images on (a) iron plate before electrolysis, (b) after 4× electrolysis, (c) $Fe(OH)_3$ precipitate at 5000× magnification

Table 3. EDX of $Fe(OH)_3$

Element	Percentage (%)
O	51.57
Fe	17.98
N	11.41
C	9.96
Na	7.90
S	0.69
Si	0.49

Synthesis of Ferrate

The synthesis of ferrate solution in this study was done by wet chemical method, using $Fe(OH)_3$ as a source of Fe(III) added with NaOCl as the oxidation agent in a strong alkaline condition (NaOH) and produced a purple ferrate solution. The ferrate formation reaction is presented below:

$$\underset{\text{brown}}{2Fe^{3+}} + 3ClO^- + 10OH^- \rightarrow \underset{\text{purple}}{2FeO_4^{2-}} + 3Cl^- + 5H_2O \quad (7)$$

The formed ferrate solution (sodium ferrate) was then determined its wavelength and concentration using a UV-Vis spectrophotometer. The measurement result showed the maximum wavelength at 505 nm with an absorbance of 0.944 (Fig. 5). The absorption spectrum of ferrate at 505 nm had been confirmed by other studies [23-24]. Furthermore, from the literature, it can be seen that the molar extinction coefficient of ferrate at this wavelength is 1170 M^{-1} cm^{-1} so that in the synthesis, ferrate can be seen that the resulting ferrate concentration is 535.74 mg/L (with a dilution factor of 4x) [25].

Furthermore, ferrate stability was performed by measuring wavelengths using UV-Vis from day to day. The results showed a decrease in absorbance from the first day of 0.563 to 0.327; 0,281; 0.254, and 0.196, respectively, on days 2, 3, 4, and 8. The decrease in the ferrate absorbance value indicates that the ferrate

solution has undergone reduction and decreased concentration, as shown in Fig. 6(a). Ferrate has low stability, so if left too long in unsuitable conditions will be reduced from Fe(VI) purple to Fe(III) brown. The decrease of ferrate for a longer time follows reaction order 2 (Fig. 6(b)) with a k value of 1.8×10^{-10} s^{-1}. Reduction of ferrate from Fe(VI) to Fe(III) according to Bartzatt and Carr [26] shown in the following reaction:

$$2FeO_4^{2-} + 5H_2O \rightarrow 2Fe(OH)_3 + 3/2O_2 + 4OH^- \quad (8)$$

Application of Ferrate for Removal of Cations and Anions in Water

Treatment of metal ions (cation) with ferrate

Ferrate is a coagulant substance that effectively removes metals and non-metals in water [26-27]. Fig. 7 and 8 show that ferrate is proven effective for eliminating metal ions and anions. At pH 6, Cd ion concentration after treatment experienced a significant decrease than before treatment from 8.62 to 0.54 mg/L. Thus, even Mg metal could be entirely eliminated. Ferrate is also effective for eliminating nitrate anions at pH 6 by 65% [28].

The mechanism of heavy metal removal by ferrate(VI) can be explained by ionic bonding and adsorption [29]. Ferrate(VI) is present in the form of species $H_3FeO_4^+$, H_2FeO_4, $HFeO_4^-$, dan FeO_4^{2-} depending on the pH of the solution. In neutral solution (approximately pH 6–7), ferrate(VI) exists as the $HFeO_4^-$ species. Under these experimental conditions, heavy metals present as divalent cations (Cu^{2+}, Mg^{2+}, Pb^{2+}, Cd^{2+}, Fe^{2+}, and Zn^{2+}) can precipitate through ionic bonds with $HFeO_4^-$, ferrate(VI) anion species. At pH 7 or less, Fe(VI) species readily self-decompose and thus result in rapid oxidation of metal ions. With increasing pH (> 7), the main species Fe(VI) becomes FeO_4^{2-}, which is more stable but has a weak oxidation capacity [30], thus explaining the decrease in metal ion degradation. In this study, the highest removal efficiency by ferrate is observed in neutral conditions (pH = 6). Similar effects have also been reported for the ferrate reaction with 2,4,6-trichlorophenol (TCP), which shows the highest degradation at pH 5.8 [31]. Filip et al. [32] found that various metal ions (e.g., Cu^{2+} and Zn^{2+}) can combine into the crystalline structure of iron(III) oxide or hydroxide nanoparticles, which are formed from the decomposition of Fe(VI), and with thus yielding a metallic ferrite spinel

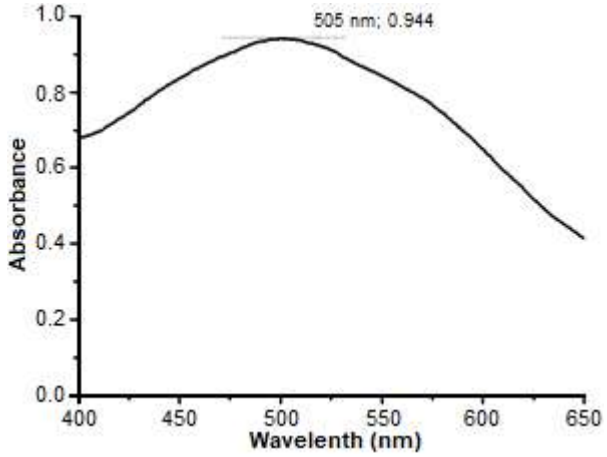

Fig 5. Ferrate solution spectrum measured using UV-Vis spectrophotometer

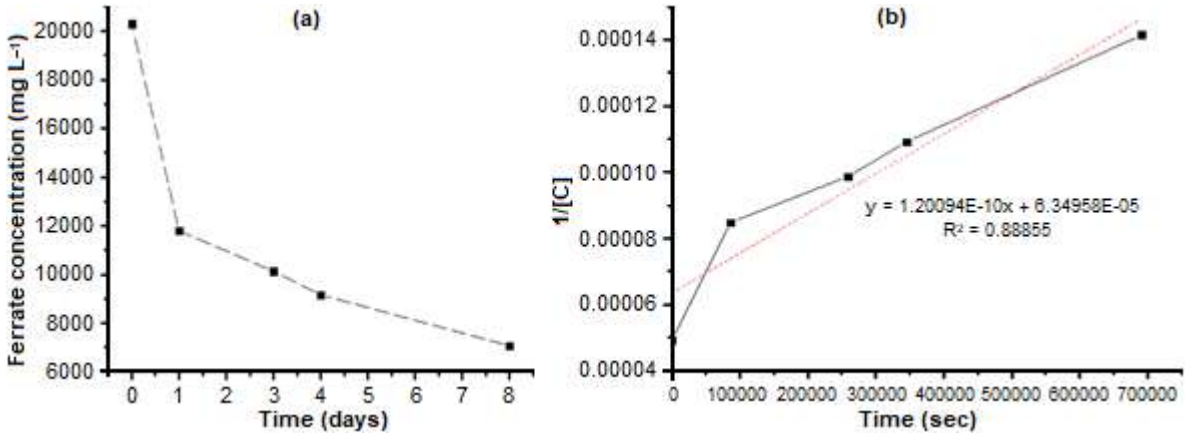

Fig 6. Ferrate concentration as a function of time (a) and the decrease of ferrate as a function of time follows reaction order 2 (b)

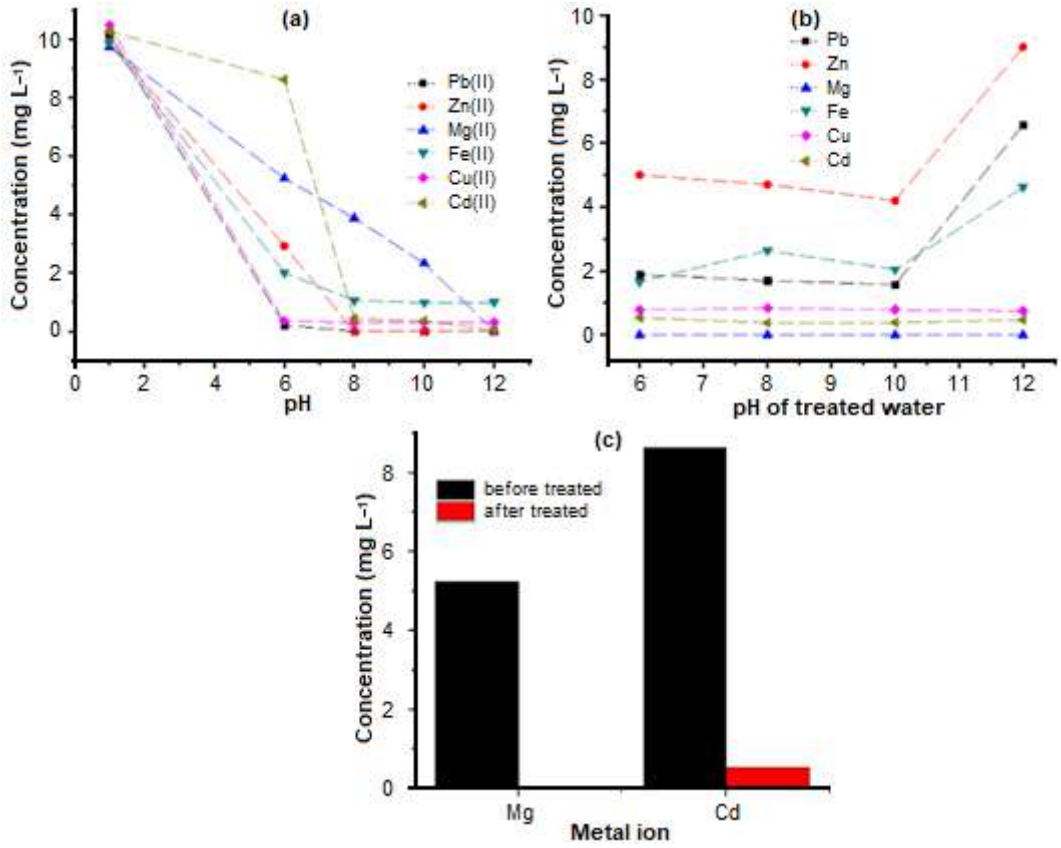

Fig 7. (a) The effect of pH on the initial metal ion concentrations, (b) Metal ion concentrations after treatment with ferrate, and (c) Results of Mg and Cd metal treatments with ferrate at pH 6

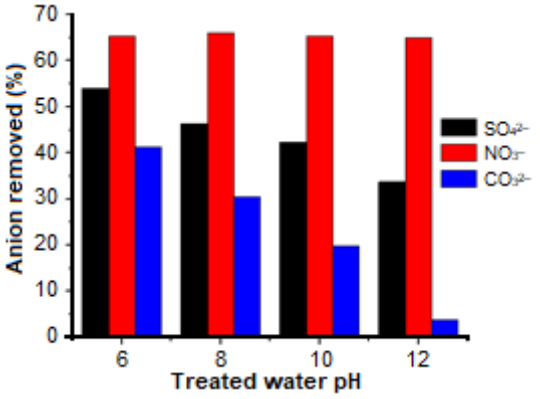

Fig 8. Anion treatment results with ferrate at pH 6, 8, 10 and 12

phase (e.g., $CuFe_2O_4$ and $ZnFe_2O_4$). In contrast, the Cd(II) ion does not form a ferrite spinel structure or is not incorporated into the iron(III) oxide phase lattice but through absorption on the y-Fe_2O_3/y-FeOOH core/shell nanoparticles [14]. The iron(VI) removal mechanism for various metals may depend on each metal ion's ionic radius, valence, and electronic structure. The overall reaction of metal ions with Ferrate [33]:

$$Fe(VI) + M(II) \rightarrow Fe(III) + \text{Product} \quad (9)$$

The interaction between CO_3^{2-} (or HCO_3^-) and Fe hydroxide will occur and form an inner spherical monodentate complex through a ligand exchange reaction (Eq. (9)) [30].

$$Fe-OH + CO_3^{2-} \rightarrow Fe-O-CO_2^- + OH^- \quad (10)$$

Hydrolysis of CO_3^{2-} ions can increase the pH of the solution, thereby reducing the oxidation potential of Fe(VI) and reducing the efficiency of anion reduction [34].

■ CONCLUSION

Synthesis of ferrate using iron ions from the electrolysis of the used transformer iron has been successfully obtained. Electrolysis occurs with E_d = 2.03 V. The iron ion was then reacted with sodium hypochlorite in alkaline conditions to produce ferrate

with a purple solution color. The resulted ferrate synthesis was applied as metal ion and anion treatments with pH variations of 6, 8, 10, and 12. The characterization of the electrolyzed iron plate showed that there was the dissolution of iron into iron(III) ions with a different surface from the previous plate. The results showed that ferrate is effective for eliminating metal ions and anions in water with the optimum condition at pH 6

■ ACKNOWLEDGMENTS

This research was funded by the Directorate of Research and Community Service, Deputy for Strengthening Research and Development of the Ministry of Research and Technology/National Research and Innovation Agency for the 2020 Fiscal Year (PDUPT research grant with contract number 225-91/UN7.6.1/PP/2020).

■ REFERENCES

[1] Chávez-Guajardo, A.E., Medina-Llamas, J.C., Maqueira, L., Andrade, C.A.S., Alves, K.G.B., and de Melo, C.P., 2015, Efficient removal of Cr(VI) and Cu(II) ions from aqueous media by use of polypyrrole/maghemite and polyaniline/ maghemite magnetic nanocomposites, *Chem. Eng. J.*, 281, 826–836.

[2] Sharma, V.K., Chen, L., and Zboril, R., 2015, Review on high valent Fe(VI) (Ferrate): A sustainable green oxidant in organic chemistry and transformation of pharmaceuticals, *ACS Sustainable Chem. Eng.*, 4 (1), 18–34.

[3] Munyengabe, A., and Zvinowanda, C., 2019, Production, characterization and application of ferrate(VI) in water and wastewater treatments, *Braz. J. Anal. Chem.*, 6 (25), 40–57.

[4] Barışçı, S., 2017, The disinfection and natural organic matter removal performance of electro-synthesized ferrate(VI), *J. Water Process Eng.*, 20, 84–89.

[5] McBeath, S.T., Wilkinson, D.P., and Graham, N.J.D., 2020, Exploiting water contaminants: *In-situ* electrochemical generation of ferrates using ambient raw water iron (Fe^{2+}), *J. Environ. Chem. Eng.*, 8 (4), 103834.

[6] Majid, D., and Kim, I.K., 2018, Degradation of toluene by liquid ferrate(VI) and solid ferrate(VI) in aqueous phase, *J. Environ. Eng.*, 144 (9), 04018093.

[7] Karelius, K., and Asi, N.B., 2016, Sintesis ferrat (FeO_4^{2-}) dari $Fe(NO_3)_3$ dan NaOCl sebagai pendagradasi methylene blue, *Sains dan Terapan Kimia*, 10 (1), 1–7.

[8] Malik, S.N., Ghosh, P.C., Vaidya, A.N., Waindeskar, V., Das, S., and Mudliar, S.N., 2017, Comparison of coagulation, ozone and ferrate treatment processes for color, COD and toxicity removal from complex textile wastewater, *Water Sci. Technol.*, 76 (5), 1001–1010.

[9] Soni, B.D., Patel, U.D., Agrawal, A., and Ruparelia, J.P., 2017, Application of BDD and DSA electrodes for the removal of RB 5 in batch and continuous operation, *J. Water Process Eng.*, 17, 11–21.

[10] Song, Y., Men, B., Wang, D., and Ma, J., 2017, Online batch production of ferrate with a chemical method and its potential application for greywater recycling with Al(III) salt, *J. Environ. Sci.*, 52, 1–7.

[11] Liu, C., Zhou, Z., Yuan, B., Liu, S., Li, F., and Sharma, V.K., 2018, Synthesis of ferrate(VI) in two cathodes and one anode cell: Enhanced efficiency and treatment of thiocyanate in wastewater, *J. Environ. Eng.*, 144 (10), 04018105.

[12] Zeng, F., Chen, C., and Huang, X., 2020, Enhanced electro-generated ferrate using Fe(0)-plated carbon sheet as an anode and its online utilization for removal of cyanide, *Chemosphere*, 241, 125124.

[13] Micic, R., Jokic, A., Simonovic, R., Arsic, B., Mitic, M., Galonja-Coghill, T., Cekerevac, M., and Nikolic-Bujanovic, L., 2019, Application of electrochemically synthesized ferrates(VI) for the removal of Th(IV) from natural water samples, *J. Water Chem. Technol.*, 41 (2), 101–104.

[14] Prucek, R., Tuček, J., Kolařík, J., Hušková, I., Filip, J., Varma, R.S., Sharma, V.K., and Zbořil, R., 2015, Ferrate(VI)-prompted removal of metals in aqueous media: Mechanistic delineation of enhanced efficiency via metal entrenchment in magnetic

oxides, *Environ. Sci. Technol.*, 49 (4), 2319–2327.

[15] Barişçi, S., Ulu, F., Särkkä, H., Dimoglo, A., and Sillanpää, M., 2014, Electrosynthesis of ferrate(VI) ion using high purity iron electrodes: Optimization of influencing parameters on the process and investigating its stability, *Int. J. Electrochem. Sci.*, 9, 3099–3117.

[16] Vidal, J., Espinoza, C., Contreras, N., and Salazar, R., 2017, Elimination of industrial textile dye by electrocoagulation using iron electrodes, *J. Chil. Chem. Soc.*, 62 (2), 3519–3524.

[17] van der Grift, B., Behrends, T., Osté, L.A., Schot, P.P., Wassen, M.J., and Griffioen, J., 2016, Fe hydroxyphosphate precipitation and Fe(II) oxidation kinetics upon aeration of Fe(II) and phosphate-containing synthetic and natural solutions, *Geochim. Cosmochim. Acta*, 186, 71–90.

[18] Singh, K., and Kumar, A., 2019, Kinetics of complex formation of Fe(III) with caffeic acid: Experimental and theoretical study Kinetics of complex formation of Fe(III) with caffeic acid: Experimental and theoretical study, *Spectrochim. Acta, Part A*, 211, 148–153.

[19] Macera, L., Taglieri, G., Daniele, V., Passacantando, M., and D'Orazio, F., 2020, Nano-sized Fe(III) oxide particles starting from an innovative and eco-friendly synthesis method, *Nanomaterials*, 10 (2), 323.

[20] Zhu, B.S., Jia, Y., Jin, Z., Sun, B., Luo, T., Kong, L.T., and Liu, J.H., 2015, A facile precipitation synthesis of mesoporous 2-line ferrihydrite with good fluoride removal properties, *RSC Adv.*, 5 (103), 84389–84397.

[21] Yan, F., Zhang, S., Zhang, X., Li, C., Zhu, C., Zhang, X., and Chen, Y., 2018, Growth of $CoFe_2O_4$ hollow nanoparticles on graphene sheets for high-performance electromagnetic wave absorbers, *J. Mater. Chem. C*, 6 (47), 12781–12787.

[22] Gunawan, G., Haris, A., Widodo, D.S., Suyati, L., and Septina, W., 2020, Degradation of methylene blue using cadmium sulfide photoanode in photofuel cell system with variation of electrolytes, *Indones. J. Chem.*, 21 (1), 97–107.

[23] Cheung, P.C.W., Williams, D.R., Barrett, J., Barker, J., Kirk, D.W., Barrett, D.R., Barker, J., Kirk, J., Paeng, K.J., and Pettignano, A., 2021, On the origins of some spectroscopic properties of "purple iron" (the tetraoxoferrate(VI) ion) and its Pourbaix safe-space, *Molecules*, 26 (17), 5266.

[24] Luo, Z., Strouse, M., Jiang, J.Q., and Sharma, V.K., 2011, Methodologies for the analytical determination of ferrate(VI): A Review, *J. Environ. Sci. Health, Part A: Toxic/Hazard. Subst. Environ. Eng.*, 46 (5), 453–460.

[25] Bartzatt, R., 2016, Reduction of metal ion species in contaminated water by utilizing potassium ferrate (K_2FeO_4) treatment, *Br. J. Environ. Clim. Change*, 6 (4), 227–235.

[26] Talaiekhozani, A., Talaei, M.R., and Rezania, S., 2017, An overview on production and application of ferrate(VI) for chemical oxidation, coagulation and disinfection of water and wastewater, *J. Environ. Chem. Eng.*, 5 (2), 1828–1842.

[27] Nguema, P.F., and Jun, M., 2016, Application of ferrate(VI) as disinfectant in drinking water treatment processes: A review, *Int. J. Microbiol. Res.*, 7 (2), 53–62.

[28] Dong, S., Mu, Y., and Sun, X., 2019, Removal of toxic metals using ferrate(VI): A review, *Water Sci. Technol.*, 80 (7), 1213–1225.

[29] Zhang, B.L., Qiu, W., Wang, P.P., Liu, Y.L., Zou, J., Wang, L., and Ma, J., 2020, Mechanism study about the adsorption of Pb(II) and Cd(II) with iron-trimesic metal-organic frameworks, *Chem. Eng. J.*, 385, 123507.

[30] Zhao, J., Wang, Q., Fu, Y., Peng, B., and Zhou, G., 2018, Kinetics and mechanism of diclofenac removal using ferrate(VI): Roles of Fe^{3+}, Fe^{2+}, and Mn^{2+}, *Environ. Sci. Pollut. Res.*, 25 (23), 22998–23008.

[31] Laksono, F.B., and Kim, I.K., 2015, Application of in situ liquid ferrate(VI) for 2-bromophenol removal, *J. Korean Soc. Water Wastewater*, 29 (6), 685–692.

[32] Filip, J., Yngard, R.A., Siskova, K., Marusak, Z., Ettler, V., Sajdl, P., Sharma, V.K., and Zboril, R., 2011, Mechanisms and efficiency of the simultaneous removal of metals and cyanides by using ferrate(VI): Crucial roles of nanocrystalline iron(III) oxyhydroxides and metal carbonates, *Chem. Eur. J.*, 17 (36), 10097–10105.

[33] Sharma, V.K., and Virender, K., 2011, Oxidation of inorganic contaminants by ferrates (VI, V, and IV)-kinetics and mechanisms: A review, *J. Environ. Manage.*, 92 (4), 1051–1073.

[34] Wang, H., Liu, Y., and Jiang, J.Q., 2016, Reaction kinetics and oxidation product formation in the degradation of acetaminophen by ferrate(VI), *Chemosphere*, 155, 583–590.

Utilization of Corn Oil through Water Degumming Process for Lecithin Emulsifier Production

Fahmi Arifan*, Muhammad Kelvin Nandita, Enrico Fendy Sapatra, and Salsabila Salsabila

Department of Industrial Chemical Engineering Technology, Vocational School, Diponegoro University, Jl. Prof. H. Soedarto, SH, Tembalang, Semarang 50275, Central Java, Indonesia

* ***Corresponding author:***

tel: +62-8156520216
email: fahmiarifan@live.undip.ac.id

Received: April 8, 2021
Accepted: August 30, 2021

DOI: 10.22146/ijc.65195

Abstract: *Lecithin is an emulsifier that plays an active role in reducing surface tension in making emulsions. The production of lecithin from other vegetable oils allows the use of other types of vegetable oil as a source of lecithin production to replace soy-based oil, which has begun to be used as a bioenergy raw material. This study aims to find an alternative source of new lecithin derived from corn oil by knowing the characteristics of lecithin and applied to mayonnaise. The resulting lecithin was used in mayonnaise with a 2 factorial randomized block design method consisting of 3 levels. Based on the results obtained, the characteristic of corn oil lecithin is that the largest content is hexadecanoic acid which is 44.79%, and the strongest vibration band is CH_2 vibration with stretching modes of symmetry and asymmetry at 2922 and 2853 cm^{-1} and the terminal CH_3 group in the 1374 cm^{-1}. L3C3 treatment was the best result with 60% fat content, 4% emulsion stability, 2.12 cP viscosity, and 1.42 × 10^{-3} N/m surface tension. Organoleptic showed a preference value, namely color 4.4 (like), taste 3.2 (sufficient like), smell 4 (like), and texture 3.80 (like it).*

Keywords: *corn lecithin; water degumming; mayonnaise*

■ INTRODUCTION

Food is anything that comes from biological sources and water, whether it is processed or not, which is intended as food or drinks for human consumers, including food additives and other materials used in preparing, processing, and making food or drinks [1]. Phosphatidylcholine (PC), phosphatidylethanolamine (PE), and phosphatidylinositol (PI) are acetone-insoluble phosphatides. They are mixed with other substances such as triglycerides, fatty acids, and other minor compounds to form lecithin [2]. Lecithin or phosphatidylcholine is an important natural emulsifier found widely in many food fields [3]. However, commercial lecithin comes from the isolation of animal organs such as pigs which are haram. Lecithin derived from commercial vegetable oils comes only from soybean oil. Therefore, the production of lecithin from other vegetable oils can be a solution for the availability of halal vegetable lecithin such as corn oil and allows the use of other types of vegetable oil as a source of lecithin production to replace soybean-based oil, which has begun to be used as raw material for bioenergy or in the field of food diversification [4]. Based on previous research studies, corn oil can be used as raw material for making lecithin. Corn oil contains 0.7–2.0% gum phosphatide, which is commonly used to produce crude lecithin. This amount is greater than coconut oil and palm oil [5]. The degumming step in the refining of crude oils extracted from soybean, rapeseed, sunflower, and corn germ, among others, yields lecithin [6].

Lecithin can be used as an emulsifier in a broad range of emulsions. However, its multicomponent nature limits its versatility [7]. Therefore, the lecithin obtained is expected to be applied as an emulsifier, one of which is mayonnaise (an oil-in-water emulsion) [8]. Mayonnaise is a food product in the form of an emulsion which is currently well known as a sauce used in salads, sandwiches, and other foods. Although the emulsifier that has been used by mayonnaise is egg yolk, one of the efforts to reduce the fat content in mayonnaise is to reduce the use of egg yolk by using other emulsifiers.

Using an emulsifier other than egg yolk can reduce overall fat content and increase stability [9]. This study aims to determine the production of vegetable lecithin from corn oil through a water degumming process and find alternative sources of new lecithin derived from corn oil by knowing the characteristics of lecithin and applying it to mayonnaise to determine the effect on physical, chemical, and organoleptic properties.

■ EXPERIMENTAL SECTION

Materials

The materials used were corn oil (100% purity, conducted from CV. KIE Food Industry), distilled water, cooking oil, CMC, H_2SO_4 (98% purity Merck, Germany), salt, and sugar.

Instrumentation

Magnetic stirrer and centrifuge used to extract gum (crude corn lecithin) by following previously reported procedure [4]. In addition, gas Chromatography-Mass Spectrometry (GC-MS) and Fourier Transform Infra-Red (FT-IR) were applied for analysis and corn lecithin characterization.

Procedure

Steps to make gum (crude corn lecithin)

Extracting gum from corn oil was carried out by mixing 250 mL of corn oil with distilled water (15 mL), then heated at a temperature of 80 °C, were kept constant, and stirred for 2 h. In this process, a clear colored layer will be obtained, which will be taken and dried. The result of this drying is called gum. The clear layer obtained from heating was separated using a centrifuge at 500 rpm for 20 min. The thin layer obtained after the centrifuge process was then dried using an oven with a temperature of 90.5 °C for 5 days [10].

Step to make mayonnaise

Mayonnaise was made using a 2 factorial randomized block design method consisting of 3 levels. Factorial 1 was the addition of lecithin emulsifier with a weight of 0, 20, and 30 g, while factorial 2 was the addition of CMC with 0, 20, and 30 g that 9 treatment combinations were obtained with 3 replications.

Corn lecithin characteristics test phase

The 10 mL of corn lecithin obtained from corn oil were tested using GC-MS to determine the acyl lecithin chain structure. In addition, an FTIR was used to determine the functional groups of corn lecithin emulsifiers.

Mayonnaise test phase with the addition of corn lecithin and CMC

Mayonnaise with the addition of corn lecithin and CMC was tested for its physical, chemical properties in the form of fat content, emulsion stability, viscosity, and immersion stress, and an organoleptic test as well. Data analysis was performed using ANOVA with a 5% confidence interval. If there is an interaction between factors, it is continued into the DMRT (Duncan Multiple Range Test) tests. The selection of the best treatment used Multiple Attributes.

■ RESULTS AND DISCUSSION

Analysis of the Characteristics of Corn Lecithin Emulsifier

Corn lecithin emulsifier was tested in advance using GC-MS to determine the content of the corn lecithin emulsifier. Testing by GC-MS to determine the content of corn lecithin is considered effective because it does not require a longer retention time, and the results can be proven accurate. Analysis by GC-MS was carried out to determine the acyl chain structure of lecithin [11]. The GC-MS test result data is presented in tabular form and shown in Table 1.

From Table 1, it can be seen that the content of corn lecithin emulsifier through the results of mass spectroscopic analysis of each of these peaks shows a fragmentation pattern of 0.09% lauric acid (dodecanoic acid), 0.94% myristic acid (tetradecanoic acid), 44.79% palmitic acid (hexadecanoic acid), 40.08% oleic acid (9-octadecenoic acid (Z)-), 5.99% stearic acid (octadecanoic acid), 1.83% oxiraneoctanoic acid and 1.66% oxiraneoctanoic acid. From these results, it can be seen that the fatty acid residues of the phospholipids, GC-MS results correspond to the fatty acid components present in corn oil. Corn oil contains palmitic acid, linoleic acid, stearic acid, linolenic acid, and oleic acid [12]. From the

Table 1. The emulsifying component of corn lecithin is the GC-MS test result

No	R. Time	Content (%)	Component name	Structural formulas
1	28.23	0.09	Dodecanoic acid	$C_{13}H_{26}O_2$
2	34.06	0.94	Tetradecanoic acid	$C_{15}H_{30}O_2$
3	39.406	44.79	Hexadecanoic acid	$C_{17}H_{34}O_2$
4	43.44	40.08	9-Octadecenoic acid (Z)-	$C_{19}H_{36}O_2$
5	44.08	5.99	Octadecanoic acid	$C_{19}H_{38}O_2$
6	47.22	1.83	Oxiraneoctanoic acid, 3-octyl-, methyl ester, cis- (CAS)	$C_{19}H_{36}O_3$
7	47.44	1.66	2-Oxiraneoctanoic acid, 3-octyl-, methyl ester (CAS)	$C_{19}H_{36}O_3$

table, we can also see that the largest content of corn lecithin emulsifier is palmitic acid (hexadecanoic acid) which is 44.79%. Thus, the isolated phospholipids from corn oil gum have a polar and a non-polar part. In the research conducted by the compilers, only the non-polar parts were analyzed using GC-MS analysis, which results had components that matched the components of corn oil so that this part could dissolve in the oil. The things above cause the phospholipids to easily be on the interface of corn oil and water so that the emulsion that is formed is relatively stable [13].

Furthermore, corn lecithin was tested using FTIR to determine its functional groups from the corn lecithin emulsifier. Fourier transforms infrared (FTIR) spectroscopy is widely used to authenticate certain food products [14]. FTIR instruments have many advantages over conventional dispersive instruments, with more energy yield, excellent wavenumber reproducibility and accuracy, broad and precise spectral manipulation capabilities, and advanced chemometric software to handle calibration development [15]. The FTIR spectrum of corn lecithin emulsifier is shown in Fig. 1.

The FTIR results in Fig. 1 show that the strongest band is CH_2 vibrations with the symmetrical strain mode and asymmetry at 2922 and 2853 cm^{-1}. This wavenumber is usually "sensitive to conformation" it is affected by changes in the trans/gauche conformation ratio in the acyl chain. There is also an absorption band for the terminal CH_3 groups in the area 1374 cm^{-1}. Vibration for the ester groups, especially for the C=O stretch, appears in the region of 1742.49 cm^{-1}. The vibration for the anhydride, especially for the C–O stretch, appears in the 1159.07 cm^{-1} regions. The result shows that the corn lecithin emulsifier has almost the same absorbance pattern in the specific absorption regions for lecithin. The IR spectra for lecithin can be divided into spectral regions arising from the vibrations of the lipophilic tail molecule, the interface region, and the head group [14].

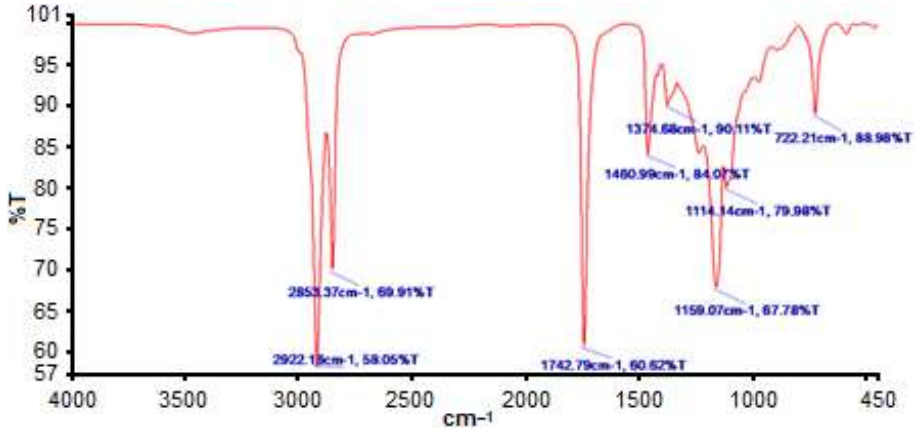

Fig 1. FTIR spectra of corn lecithin emulsifier

Analysis of mayonnaise with the addition of Corn Lecithin Emulsifier

Analysis of fat content in mayonnaise

Mayonnaise sauce is one of the oldest and most used in the food world, accompanying popular salads, seafood, and filling sandwiches. Nevertheless, one main problem with egg yolk is its high cholesterol content [16]. Therefore, the product expected from using Corn Lecithin is to reduce the fat content contained and produce the desired product, namely using vegetable lecithin. Although the emulsifier that has been used is egg yolk, one of the efforts to reduce the fat content in mayonnaise is to reduce the use of egg yolk by using other emulsifiers. Using an emulsifier other than egg yolk can reduce overall fat content and increase stability [17]. The value of the fat content (%) in mayonnaise is shown in Table 2.

Table 2 shows that the highest fat content was found in adding emulsifier corn lecithin and CMC to L3C3 treatment of 60%, which in L3C3 treatment used 30 g Corn Lecithin independent variables and 30 g CMC. The theory suggests that the higher the lecithin and CMC emulsifier added, the higher the fat content. The increase in fat content is due to the increasing concentration of lecithin emulsifier, increasing the hydrophobic group, which affects mayonnaise fat content. Lecithin is an emulsifier that tends to be non-polar, which has a hydrophobic group as a fat-binding group and a hydrophilic one as a water-binding group [18]. The fat content of standard mayonnaise on the market is 80.73% [19], whereas, in the research conducted by the author, the L3C3 treatment found 60% results, which means that it is still far below the standard to be marketed. However, when compared with the quality requirements of mayonnaise (SNI 01-4473-1998), which is at least 65%, the results of this research are almost approaching SNI.

Based on the analysis of the fat content in mayonnaise, the variable has an average value of 41.66 and a standard deviation of 13.95. The results showed that the standard deviation value was smaller than the value average.

Emulsion stability analysis on mayonnaise

Emulsification processes also improve the texture, stability, and shelf-life of food products [20]. The product that is expected from the use of Corn Lecithin is good emulsion stability. Lecithin as an emulsifier can stabilize oil and water, which is clear from its structure. Emulsion stability is also influenced by particle size, type, and quantity of emulsifier, the density difference between the two phases, particle movement, and viscosity of the external phase. Using an emulsifier other than egg yolk can reduce overall fat content and increase stability [9]. The emulsion stability value (%) in mayonnaise is shown in Table 3.

Table 2. Fat content (%) in mayonnaise with the addition of corn lecithin emulsifier

Run (Code)	Lecithin (g)	CMC (g)	Readable volume (mL)	Sample volume (mL)	Fat level (%)
L1C1	0	0	1	5	20
L1C2	0	20	1.2	5	24
L1C3	0	30	1.3	5	26
L2C1	20	0	2	5	40
L2C2	20	20	1	2	50
L2C3	20	30	1	2	50
L3C1	30	0	1	2	50
L3C2	30	20	1.1	2	55
L3C3	30	30	1.2	2	60*
Average					41.66
SD					13.95

Note: (*) = The best result

Table 3. Emulsion stability (%) in mayonnaise with the addition of an emulsifier corn lecithin

Run (Code)	Lecithin (g)	CMC (g)	Separate volume (mL)	Sample volume (mL)	Emulsion stability (%)
L1C1	0	0	9.9	10	1
L1C2	0	20	9.8	10	2
L1C3	0	30	9.75	10	2.5
L2C1	20	0	9.78	10	2.2
L2C2	20	20	9.77	10	2.3
L2C3	20	30	9.76	10	2.4
L3C1	30	0	9.68	10	3.2
L3C2	30	20	9.65	10	3.5
L3C3	30	30	9.6	10	4*
Average					2.56
SD					0.83

Note: (*) = The best result

Table 3 shows that there are differences in the stability of using emulsifiers. In the table above, it shows that the L3C3 treatment has a high level of stability of 4% because the addition of 30 g lecithin causes the emulsion to be more stable compared to the addition of other lecithin's, which is indicated by the less oil that separated at the time of centrifuge. The higher the concentration of the emulsifier lecithin and CMC added, it will be more stable because the emulsifier can reduce the surface tension so that the emulsion will coalesce. Adding an emulsifier will make the bond between the fat and water stronger. The emulsifier will be dispersed in water so that the hydrophilic part will absorb water. Water previously moving freely outside the grains will become bound. The theory shows that it causes the emulsifier to be more stable [18].

Based on the stability analysis of the mayonnaise emulsion, this variable has an average value of 2.56 and a standard deviation of 0.83. The results showed that the standard deviation value was smaller than the value average.

Viscosity analysis of mayonnaise

The difference in the viscosity of mayonnaise corresponds to the increasing concentration of vegetable oil and the emulsifier added. The difference in viscosity/viscosity can also be caused by the type of vegetable oil used, with the characteristics of each vegetable oil being different. This theory is in line with the opinion of Setyawardhani et al. that each type of vegetable oil has different characteristics depending on the fatty acid content contained in it besides vegetable oil which acts as an internal phase that greatly affects the viscosity of mayonnaise so that at different concentrations it will make a difference to the viscosity of mayonnaise [21]. The viscosity (cP) value of mayonnaise is shown in Table 4.

Table 4 shows a difference in the level of viscosity or viscosity of the mayonnaise with the addition of corn lecithin emulsifier. The table above shows that the L3C3 treatment has a greater viscosity level than the 2.1 cP. Commercial lecithin is used as an emulsifier, and lecithin effectively lowers the interfacial tension between fat and water but can maintain the stability of the emulsion in the dough. In addition, the lecithin emulsifier can reduce friction on the sugar fat, thus preventing the formation of solid lumps. Therefore, the greater the concentration of lecithin added, the greater the viscosity of mayonnaise. The standard mayonnaise viscosity in the market is 3346.7 cP [22].

Meanwhile, in the research conducted by the author, the best viscosity was 2.12 cP, which indicates that it is still far from the viscosity of mayonnaise on the market and still unable to be used commercially. According to SNI (Indonesian National Standard), 01-4473-1998, the mayonnaise viscosity standard is 2540 cP (Indonesian National Standardization Agency, 1998).

Table 4. Viscosity (CP) of mayonnaise with the addition of corn lecithin

Run (Code)	Empty pycnometer weight (g)	Fill in the weight of the pycnometer (g)	Pycnometer volume (mL)	Sample density (g/mL)	Time (second)	Viscosity (cP)
L1C1	26.91	50.91	25	0.96	1.7	1.63
L1C2	26.91	51.93	25	1.0008	1.7	1.701
L1C3	26.91	51.85	25	0.99	1.74	1.73
L2C1	26.91	51.05	25	0.96	1.8	1.73
L2C2	26.91	52.01	25	1.004	1.78	1.78
L2C3	26.91	53.54	25	1.06	1.71	1.82
L3C1	26.91	51.03	25	0.96	1.89	1.82
L3C2	26.91	53.59	25	1.06	1.9	2.02
L3C3	26.91	52.22	25	1.01	2.1	2.12*
Average						1.82
SD						0.14

Note: (*) = The best result

Based on research conducted, the author is still far from the established SNI. Based on the viscosity analysis of mayonnaise, the variable has an average value of 1.82 and a standard deviation of 0.14. The results showed that the standard deviation value was smaller than the value average.

Surface Tension Analysis on Mayonnaise

The expected product from the use of corn lecithin is to reduce surface tension. The surface-active agent, in this case, lecithin as an emulsifier, is oriented at the interface that will gradually decrease the surface tension over time and the addition of the surface-active agent until a constant value is reached [23]. The value of surface tension (N/m) on mayonnaise is shown in Table 5.

Table 5 shows that the L3C3 treatment has a smaller surface tension value than the others, equal to 0.001 N/m. Crude lecithin is usually obtained from soybeans and egg yolks. This lecithin is a mixture of lipids (phospholipids) with phosphatidylcholine, ethanolamine, and inositol as the main components. Commercially, phospholipids are mainly obtained as a by-product in the production of vegetable oils. Therefore, the more lecithin is added, the decrease in surface tension will occur [16]. If one of the liquid interfacial tension decreases, it will facilitate the fluid phase to separate [24]. Emulsion stability with surface tension has a negative or opposite correlation, in that a high stabilizer concentration can cause the surface tension to decrease until it reaches a constant interface tension and the emulsion stability is maintained. Based on the surface tension analysis on mayonnaise, the variable has an average value of $2.09 \pm 0.71 \times 10^{-3}$ N/m. The results showed that the standard deviation value was smaller than the value average.

Table 5. Surface tension (N/m) on mayonnaise with the addition of corn lecithin

Run (Code)	Sample density (g/mL)	Sample height (cm)	Surface tension ($\times 10^3$ N/m)
L1C1	0.96	0.02	3.36
L1C2	1.0008	0.02	2.80
L1C3	0.99	0.02	2.79
L2C1	0.96	0.01	2.03
L2C2	1.004	0.01	1.69
L2C3	1.06	0.01	1.64
L3C1	0.96	0.01	1.62
L3C2	1.06	0.01	1.49
L3C3	1.01	0.01	1.42
Average			2.09
SD			0.71

Note: (*) = The best result

Organoleptic Analysis

Organoleptic test on food panelists, namely mayonnaise with the addition of corn lecithin. The tests carried out included the color, taste, smell, and texture of the mayonnaise.

Color

Organoleptic test results on color for mayonnaise

with corn lecithin and CMC are shown in Table 6.

Color is a very important physical parameter of food. The consumer's preference for food products is also determined by color because the product's color is the first attribute seen by consumers. Table 6 shows the color aspect; run 9 got the highest average score among the others, namely 4.4, followed by the notation "a" and also the second-highest score was obtained by run 6 with an average score of 4.3 and also followed by the notation "a" which means both panelists prefer treatment with run 9 and 6. The theory shows that the higher the concentration of lecithin emulsifier added, the lower the brightness level. Meanwhile, the addition of a CMC emulsifier shows that a CMC emulsifier also affects the increase in color brightness [18]. The addition of the lecithin emulsifier has a yellow color, which affects the color of the final mayonnaise product.

Taste

Organoleptic test results on the taste for mayonnaise with the addition of corn lecithin and CMC are shown in Table 7.

Table 7 shows that in terms of taste, run 9 gets the highest score among the others, namely 3.2, with the following notation "a", which means that the panelists prefer the treatment on running 9. The theory suggests that mayonnaise with the addition of lecithin emulsifier has an unpleasant taste. It was derived from corn oil extract, thus reducing the taste preferences of the panelists, while the addition of a CMC emulsifier has an increasing tendency. CMC is a cellulose derivative with a sweetness level of 69% so that with the addition of the CMC emulsifier, the panelists' preference for taste increases [18]. However, in terms of taste, the highest score obtained does not get the maximum value. The result shows that the resulting taste is not as strong as the typical taste of mayonnaise in the market, so that the level of preference for neutral consumers leads to somewhat like it.

Smell

The results of the organoleptic test on smell for mayonnaise with the addition of corn lecithin and CMC are shown in Table 8.

Table 8 shows that in terms of smell or aroma, run 9 gets the highest score among the others, namely 4 with the following notation "a", which means that the panelists prefer the treatment on running 9. The theory

Table 6. Panelists average preferred level of mayonnaise color with the addition of corn lecithin and CMC

Treatment	Average color value	Notation
Run 1	1.4	d
Run 2	2.3	c
Run 3	2.9	bc
Run 4	3.1	b
Run 5	3.4	b
Run 6	4.3	a
Run 7	2.9	bc
Run 8	3	b
Run 9	4.4*	a

Table 7. Average levels of panelists preference to mayonnaise flavor with the addition of corn lecithin and CMC

Treatment	Average taste score	Notation
Run 1	1.5	b
Run 2	1.6	b
Run 3	1.7	b
Run 4	1.7	b
Run 5	3	a
Run 6	3	a
Run 7	2.9	a
Run 8	2.9	a
Run 9	3.2*	a

Table 8. The panelists average preferred level of mayonnaise odor with the addition of corn lecithin and CMC

Treatment	Average smell value	Notation
Run 1	1.6	d
Run 2	1.9	d
Run 3	1.9	d
Run 4	2.1	d
Run 5	2.2	cd
Run 6	3.1	b
Run 7	2.9	bc
Run 8	2.9	bc
Run 9	4*	a

suggests that the CMC is in powder form, white, odorless, and tasteless so that it does not affect the product's aroma, while the lecithin emulsifier has a slightly unpleasant aroma that can affect the aroma of mayonnaise [18]. This study's results follow the research which states that the consumer has given a normal or neutral rating to the unscented mayonnaise. The result shows that the aroma of mayonnaise is not as strong as the aroma of mayonnaise. The aroma shows sensory properties that require sensitivity to taste and smell food, and also, the aroma of food can form delicacy and is more related to the sense of smell.

Texture

Organoleptic test results on texture for mayonnaise with corn lecithin and CMC are shown in Table 9.

Table 9 shows that in terms of smell or aroma, run 9 gets the highest score among the others, which is 3.8 with the following notation "a", which means that the panelists prefer the treatment on running 9. Also, CMC has a higher value. It is higher compared to the addition of lecithin emulsifier, although it is not too significant. The texture that panelists prefer is the one that is easier to smear [18]. Consumers who like the texture may feel that the resulting texture is closer to the typical mayonnaise texture, which is semi-solid. The texture of mayonnaise is very thick and soft, which consumers prefer compared to the watery texture [25]. The authors' research supports this, where run 9 has a thicker texture due to the addition of corn lecithin and CMC.

Table 9. Panelists average preferred level of mayonnaise texture with the addition of corn lecithin and CMC

Treatment	Texture value average	Notation
Run 1	1.4	e
Run 2	1.8	de
Run 3	2.1	cde
Run 4	2.2	cde
Run 5	2.4	bcd
Run 6	2.8	bc
Run 7	3.1	ab
Run 8	2.9	bc
Run 9	3.8*	a

■ CONCLUSION

Based on the results obtained, in the analysis of corn lecithin emulsifier for GC-MS analysis, the largest content of corn lecithin emulsifier was palmitic acid (hexadecanoic acid), with its content of44.79%. In contrast, FTIR analysis had almost the same absorbance pattern in specific absorption areas for lecithin. The L3C3 treatment was obtained in the mayonnaise analysis, namely 60% fat content, 4% emulsion stability, 2.12 cP viscosity, and 0.00141736 N/m surface tension, which were the best results. The results of the organoleptic research showed that the panelists' preferred values of mayonnaise with L3C3 treatment were color 4.4 (like), taste 3.2 (sufficient like), smell 4 (like), and texture 3.8 (like it).

■ ACKNOWLEDGMENTS

The author would like to thank all parties in the Nutrition Laboratory and Food Technology Laboratory of Diponegoro University.

■ REFERENCES

[1] Nissa, C., Arifan, F., Febrianto, R., Aditya, W., Dwimawanti, I.H., and Widyasmara, R.P., 2019, Effect of sugar on nutrient composition and shelf life of red guava jams, *IOP Conf. Ser.: Earth Environ. Sci.*, 406, 012027.

[2] Reckziegel, Y., 2015, Characterization and Comparison of The Functionality of Fractionated Lecithin from Different Sources, *Thesis*, Universiteit Gent, Ghent, Belgium.

[3] Robert, C., Couëdelo, L., Vaysse, C., and Michalski, M.C., 2020, Vegetable lecithins: A review of their compositional diversity, impact on lipid metabolism and potential in cardiometabolic disease prevention, *Biochimie*, 169, 121–132.

[4] Hamad, A., Septhea, G.A., and Ma'ruf, A., 2005, Kemampuan daya emulsifier corn lecithin yang dihasilkan dari water degumming process minyak jagung, *J. Inov. Tek. Kim.*, 1 (2), 88–92.

[5] Thakur, S., and Gogate, P.R., 2020, Synthesis of Pd/C catalyst using formaldehyde reduction method

and application for ultrasound assisted transfer hydrogenation of corn oil, *Chem. Eng. Process.*, 152, 107939.

[6] Sun, X., Zhang, L., Tian, S., Yang, K., and Xie, J., 2020, Phospholipid composition and emulsifying properties of rice bran lecithin from enzymatic degumming, *LWT*, 117, 108588.

[7] Okuro, P.K., Gomes, A., Costa, A.L.R., Adame, M.A., and Cunha, R.L., 2019, Formation and stability of W/O-high internal phase emulsions (HIPEs) and derived O/W emulsions stabilized by PGPR and lecithin, *Food Res. Int.*, 122, 252–262.

[8] Tavernier, I., Wijaya, W., Van der Meeren, P., Dewettinck, K., and Patel, A.R., 2016, Food-grade particles for emulsion stabilization, *Trends Food Sci. Technol.*, 50, 159–174.

[9] Evanuarini, H., Nurliyani, N., Indratiningsih, I., and Hastuti, P., 2019, Kestabilan emulsi dan oksidasi low fat mayonnaise menggunakan kefir sebagai alternatif emulsifier, *JIIP*, 29 (1), 83–94.

[10] Paisan, S., Chetpattananondh, P., and Chongkhong, S., 2017, Assessment of water degumming and acid degumming of mixed algal oil, *J. Environ. Chem. Eng.*, 5 (5), 5115–5123.

[11] Balcaen, M., Steyls, J., Schoeppe, A., Nelis, V., and Van der Meeren, P., 2021, Phosphatidylcholine-depleted lecithin: A clean-label low-HLB emulsifier to replace PGPR in w/o and w/o/w emulsions, *J. Colloid Interface Sci.*, 581, 836–846.

[12] Gunstone, F.D., 2011, "Production and Trade of Vegetable Oils" in *Vegetable Oils in Food Technology: Composition*, Properties and Uses, 2nd Ed., John Wiley & Sons, Ltd, Hoboken, 1–24.

[13] Barrera-Arellano, D., Badan-Ribeiro, A.P., and Serna-Saldivar, S.O., 2018, "Corn Oil: Composition, Processing, and Utilization" in *Corn*, 3rd Ed., AACC International Press, Oxford, 593–613.

[14] Sadhukhan, S., Bhattacharjee, A., Sarkar, U., Baidya, P.K., and Baksi, S., 2018, Simultaneous degumming and production of a natural gum from *Crotalaria juncea* seeds: Physicochemical and rheological characterization, *Int. J. Biol. Macromol.*, 111, 967–975.

[15] Nzai, J.M., and Proctor, A., 1999, Soy lecithin phospholipid determination by Fourier transform infrared spectroscopy and the acid digest/arseno-molybdate method: A comparative study, *J. Am. Oil Chem. Soc.*, 76 (1), 61–66.

[16] Zaouadi, N., Cheknane, B., Hadj-Sadok, A., Canselier, J.P., and Hadj Ziane, A., 2015, Formulation and optimization by experimental design of low-fat mayonnaise based on soy lecithin and whey, *J. Dispersion Sci. Technol.*, 36 (1), 94–102.

[17] Kim, J.S., Kim, M.J., and Lee, J.H., 2018, The critical micelle concentration of lecithin in bulk oils and medium chain triacylglycerol is influenced by moisture content and total polar materials, *Food Chem.*, 261, 194–200.

[18] Fitriyaningtyas, S.I., and Widyaningsih, T.D., 2015, Pengaruh penggunaan lesitin dan CMC terhadap sifat fisik, kimia, dan organoleptik margarin sari apel manalagi (*Malus sylfertris* Mill) tersuplementasi minyak kacang tanah, *Jurnal Pangan dan Agroindustri*, 3 (1), 226–236.

[19] Gaonkar, G., Koka, R., Chen, K., and Campbell, B., 2010, Emulsifying functionality of enzyme-modified milk proteins in O/W and mayonnaise-like emulsions, *Afr. J. Food Sci.*, 4 (1), 16–25.

[20] Delacharlerie, S., Petrut, R., Deckers, S., Flöter, E., Blecker, C., and Danthine, S., 2016, Structuring effects of lecithins on model fat systems: A comparison between native and hydrolyzed forms, *LWT Food Sci. Technol.*, 72, 552–558.

[21] Setyawardhani, D.A., Sulistyo, H., Sediawan, W.B., and Fahrurrozi, M., 2016, Peranan waktu pengadukan terhadap karakteristik kompleksasi urea sebagai sarana pemisahan asam lemak omega dari minyak nabati, *Reaktor*, 16 (2), 81–86.

[22] Al-Bachir M.Z.R., 2006, Effect of gamma irradiation on some characteristics of shell eggs and mayonnaise prepared from irradiated from irradiated eggs, *J. Food Saf.*, 26 (4), 348–360.

[23] Lachman, L., Lieberman, H.A., and Kanig, J.L., 1991, *The Theory and Practice of Industrial Pharmacy*, 3rd Ed., Varghese Publishing House, India.

[24] Erfando, T., Khalid, I., and Bahari, R., 2021, Experimental of alternative demulsifier formulation from corn oil in overcoming water-oil emulsion, *Mater. Today: Proc.*, 39, 1061–1064.

[25] Thakur, S., and Gogate, P.R., 2020, Synthesis of Pd/C catalyst using formaldehyde reduction method and application for ultrasound assisted transfer hydrogenation of corn oil, *Chem. Eng. Process.*, 152, 107939.

The Biotransformation and Biodecolorization of Methylene Blue by Xenobiotic Bacterium *Ralstonia pickettii*

Adi Setyo Purnomo*, Asranudin, Didik Prasetyoko, and Yulinar Dwi Nur Azizah

Department of Chemistry, Faculty of Science and Data Analytics, Institut Teknologi Sepuluh Nopember (ITS), Kampus ITS Sukolilo, Surabaya 60111, Indonesia

** Corresponding author:*

email: adi_setyo@chem.its.ac.id

Received: May 10, 2021
Accepted: August 26, 2021

DOI: 10.22146/ijc.65806

Abstract: *The biotransformation and biodecolorization of methylene blue (MB) dye using the bacterium* Ralstonia pickettii *was investigated. This experiment was conducted in a nutrient broth (NB) medium after adding MB at 100 mg L^{-1} concentration. Approximately 98.11% of MB was decolorized after 18 h of incubation. In addition, the metabolic products detected by LC-TOF/MS were Azure A (AA), thionine, leuco-MB, and glucose-MB, which indicated the MB degradation through a reductase that attacked the heterocyclic central chromophore group present in the structure. Moreover, azure A and thionine fragments resulted from the* N*-demethylase enzyme that attacked the auxochrome group. Thus, this research was assumed to be the first scientific report suggesting the potential to use* R. pickettii *in the biodecolorization and biotransformation of dye waste, particularly MB.*

Keywords: *decolorization; biotransformation; xenobiotic bacteria;* Ralstonia pickettii*; methylene blue*

■ INTRODUCTION

Water pollution has become a major problem that can negatively impact humans and the environment [1]. Synthetic dyes are typical water pollutants widely used in the cosmetic, pharmaceuticals, textile, printing, and food industries [2]. In addition, approximately 280,000 tons of dye wastes are discharged into the environment, especially water bodies, without any treatment [3-4]. These direct exposures negatively affect the ecosystem following the interference with sunlight penetration, lowered dissolved oxygen concentration, and disrupted photosynthetic processes for some aquatic organisms [5]. Moreover, other hazardous effects are observed with biomagnification, carcinogenicity, and mutagenicity towards the environment and human health [6-7]. Methylene blue (MB) is one of the dyes used in leather, cotton, cosmetic, plastic, and silk industries [8], especially in the coloring process, where only 5% is absorbed, while 95% is released as waste to the aquatic environment [9]. The disposal of the MB directly contaminates humans and causes diseases, including diarrhea, eye damage, vomiting, gastric disorders, methemoglobinemia, headaches, and dizziness, especially in pregnant women and babies [10-11]. Furthermore, the death of some aquatic organisms around the disposal area has also been reported [12-13]. This high contamination incidence indicates the need to manage waste before discharge to minimize the negative impacts properly.

Moreover, microbiological treatment approaches using bacteria or fungi are less costly and more effective in handling color substance waste than physical, chemical, photocatalytic, and electrochemical methods [10]. The biodecolorization or biodegradation of dyes ensues through the reductive and oxidative activities produced by various extracellular enzymes, observed at the chromophore and auxochrome sites of the molecules [11]. Specifically, decolorization is initiated by reducing MB at the molecular level with NADPH-dependent dehydrogenase quinone into a form of leuco-MB [14-15]. The attacks on chromophore groups instigate the opening of aromatic rings within the heterocyclic center, which first produces intermediate compounds estimated to cleave the structures further [16]. Meanwhile, other degradation mechanisms include oxidative

demethylation by demethylase enzymes, comprising aminopyrine *N*-demethylase, assumed to interact with the auxochrome group to produce fragmented metabolic products of azure B (AB), azure A (AA), azure C (AC), and thionine [17]. The microbiological approach towards degradation requires various processes influenced by numerous factors, including the reaction substrate type and the wealth of microbial genetic strains [13]. Therefore, different microbes act through various mechanisms produce diverse results after waste treatment [18]. However, some species demonstrate the degradation ability, including *Daedalea dickinsii* [16], *Bacillus subtilis* strain MTCC 441 [19], *Ralstonia eutropha* [20], *Alcaligenes* species [5], *Alcaligenes faecalis* [21], *Aspergillus niger* LAG [22], and *Rhodococcus* strain UCC 0003 [23]. These microbes potentially remove more than 85% MB and are confirmed to affect degradation cases with other xenobiotic wastes.

Ralstonia pickettii is a xenobiotic bacterial with the capacity to biodegrade some organic pollutants. This phenomenon is confirmed by numerous reports obtained with various related wastes, resulting from the metabolic complexity alongside the encoding genes for biodegradation enzymes [24]. Furthermore, the toluene-3-monooxygenase, phenol/cresol hydroxylase [25], and meta-cleavage pathway enzymes are secreted to convert catechol and methyl catechol tricarboxylic acid cycle intermediates [26]. These intrinsic constituents promotes the ability to decompose a variety of wastes, including DDT [18], crude oil [27], phenol [28], chlorobenzene [29], toluene and meta-cresol [30], BTEX (benzene, ethylbenzene, toluene, xylenes) [31] and 2,4,6-trichlorophenol [30]. The application of *R. pickettii* as a bioremediation agent was more advantageous than other bacteria because of the non-detection as a phytopathogen or pathogen of animals. In addition, reports have shown significant resilience in low-nutrient environments [30], and it is also considered a good choice for the biodecolorization and biodegradation of MB as well as for broader purposes such as degradation of xenobiotic pollutants (toluene and trichloroethylene) [30], crude oil [27] and pesticide [32]. Therefore, the biotransformation and biodecolorization of MB dye using the bacterium *R. pickettii* were investigated in this study.

■ EXPERIMENTAL SECTION

Materials

The bacterium *R. pickettii* NBRC 102503 (NITE Biological Resources Center, Chiba, Japan) was collected from the Microbial Chemistry laboratory. This specimen was maintained as a culture on nutrient agar (NA; Merck, Darmstadt, Germany), while methanol (Merck, 99%), MB (Merck, C.I. 52015), and D-glucose (Merck-Germany) were purchased from Sumber Ilmiah Persada (SAP, Indonesia).

Procedure

Biodecolorization of methylene blue by R. pickettii

A single *R. pickettii* culture was used to biodecolorize MB, which involved inoculating 10% pre-incubated bacteria into an Erlenmeyer flask containing 50 mL nutrient broth and then incubation at 30 °C for 30 h [33]. Non-inoculated flasks were prepared as controls. Subsequently, the MB was added to attain a final concentration of 100 mg L^{-1} before the cultures were placed in a shaker incubator (VELP scientifica) for 18 h at 30 °C with a shaking speed of 120 rpm. The entire process was monitored for 0, 3, 6, 9, 12, 15, and 18 h, with biomass separation, was performed at each time frame to obtain the supernatants, using 2000 G centrifugation for 10 min [16]. Furthermore, absorbance measurements were carried out with a UV-VIS spectrophotometer at a 400–800 nm wavelength. In addition, the control group contained a 100 mg L^{-1} concentration mixture of NB and MB, while the percentage of sample decolorized was evaluated using the following Eq. (1).

$$\% \text{ Decolorization} = \frac{Ao - At}{Ao} \times 100\% \quad (1)$$

whereas Ao was the absorbance of the control solution while At was the absorbance of the treated sample.

Analysis of metabolic products

The metabolic products were analyzed by evaluating the filtrates through LC-TOF/MS (AB SCIEX). TM RSLC Acclaim 120 C18 column was also used with a 2.1 × 100 mm dimension and set to 33 °C temperature

[16]. In addition, ionizing electrospray (ESI) served as a source of ionization within a mass range of 50–500, where the sample elution flow rate was determined and graded at 0.3 mL min^{-1} for 4 min and 0.4 mL min^{-1} for 6 min. The methanol:water mixture (99:1 v/v) served as the mobile phase within the first 3 min and followed by 61:39 v/v on the remaining 7 min.

■ RESULTS AND DISCUSSION

Biodecolorization Study

This study expresses the *R. pickettii* ability to degrade MB in a NB medium. In addition, each culture was inoculated with 1 mL of pre-incubated bacterium (1 mL bacterium was equivalent to 1.44×10^{13} CFU), and incubated at 30 °C for 18 h, with a biodecolorization monitor time of 0, 3, 6, 9, 12, 15, and 18. Fig. 1 showed the absorbance profile versus wavelength in which 670 nm was determined to be the optimum wavelength. The absorbance pattern profiles at H0 to H9 showed a small decrease in intensity, although there was a significant difference with the absorbance control MB. These conditions indicated the inability *R. pickettii* during incubation time at 0–9 h to show structural degradation activities or transformation performance. However, H12-H18 (incubation 12 and 18 h, respectively) demonstrated a significant change in the absorbance pattern. In addition, *R. pickettii* was capable of thoroughly countering the MB at H18. The elevated cell biomass also contributes to further dye adsorption and reduced absorbance [16].

The optimum decolorization of MB (100 mg L^{-1}) by *R. pickettii* was observed at 18 h (up to 98.11%). This process ensued from the inception of incubation, where 23.33% was reported. In addition, the t-test indicated significant differences in decolorization between 0 to 12 h, which was stationary from 12 to 18 h (Table 1). Thus, the effects of *R. pickettii* were related to the extracellular enzyme content during the incubation period [23]. Moreover, every microorganism demonstrates varying decolorization strength, possibly attributed to the discrepancies in microbe strains or species, incubation time, dye concentration, and other performance-related supporting factors [21,34].

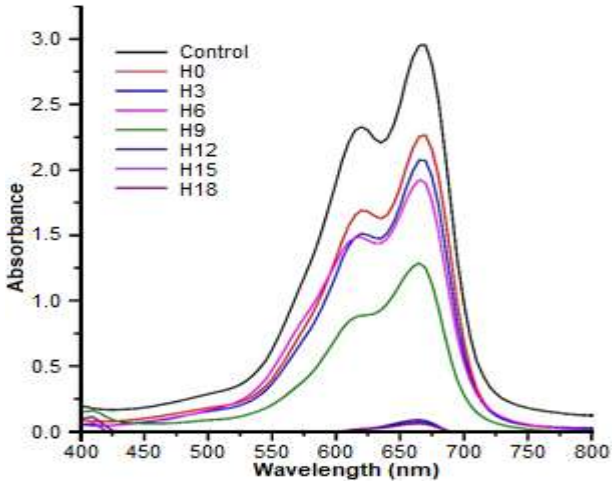

Fig 1. Methylene blue (MB) decolorization absorbance profiles of *R. pickettii*. Data are means (n = 3), where H0 = 0 h, H3 = 3 h, H18 = 18 h incubation

Table 1. Biodecolorization of MB by *R. pickettii* in nutrient broth during 18-day incubation period

Incubation time (h)	Absorbance	% Decolorization
Control	2.95 ± 0.01	-
0	2.27 ± 0.07 [a]	23.33 ± 0.68 [a]
3	2.07 ± 0.11 [b]	29.94 ± 0.42 [b]
6	1.90 ± 0.02 [c]	35.64 ± 0.22 [c]
9	1.25 ± 0.21 [d]	57.71 ± 0.27 [d]
12	0.08 ± 0.04 [e]	97.21 ± 0.43 [e]
15	0.07 ± 0.02 [e]	97.70 ± 0.01 [e]
18	0.06 ± 0.03 [e]	98.11 ± 0.22 [e]

The decolorizing ability of *R. pickettii* was seamless in contrast with other bacteria species, although some bacteria showed satisfactory results, such as *Alcaligenes* species, with maximum decolorization of 88.06% (100 mg L^{-1}, 40 d) [5]; *Camamonas aquatica* at 67% (50 mg L^{-1}, 96 h) [35]; *B. subtilis* strain MTCC 441 at 91.68% (20 mg L^{-1}, 6 h) [19]; *Bacillus thuringiensis* 016 with 95% (25 mg L^{-1}, 2 h) [36]; and *Bacillus* sp. strain MZS10 at 93.55% (0.04 g L^{-1}, 14 h) [14]; as well as *Bacillus licheniformis* strain IFO 12200, *Bacillus circulans* strain IFO 13626, and *Bacillus pomilus* strain IFO 12092, with a maximum of 97.5%; 88.0%; 65.0%, respectively (1.1×10^{-5} mol L^{-1}, 24 h) [37]. In addition, some fungi also confer these effects on MB, although longer incubation is time required. These fungi were *Phanerochaete chrysosporium*, with maximum decolorization of 84.8%

(0.4 g L^{-1}, 22 d) [36]; *D. dickinsii* at 54% (50 mg L^{-1}, 14 d) [16], while *Phaseolus coccineus*, *Coriolus versicolor*, *Fomes fomentarius*, *Trametes suaveolens*, and *Stereum ostrea* decolorized approximately 40% (100 mg L^{-1}, 20 d) [38].

The early interaction with MB ensues on the cell wall surface, which is achieved through adsorption and ionic interactions between the negative charge of the carboxylate (–COOH) or hydroxyl (–OH) group and the positive MB charge [19]. The reactions possibly occur via the reduction of MB to leuco-MB. In addition, extracellular enzymes, including NADH/NADPH-dependent reductase, are widely reported to be responsible for the procedure, as shown in Fig. 2, where colorless Leuco-MB was generated [39]. This reaction also requires oxidative dehydrogenation to yield products characterized by the potential to produce hydrogen peroxide with functionalities through other media or to be decomposed into O_2 and H_2O molecules [40]. This reaction demonstrates redox properties with MB, hence the tendency to use staining and cell density detection. In addition, color loss indicates a substantial cell population implicated in surface adsorption and reduction of MB [41].

The dye decolorization process ensued through a different mechanism for various microorganisms[23,32], where the carbon and nitrogen sources influence the cell's ability to act effectively [14]. The procedure possibly occurs through enzyme and non-enzyme (Fenton) mechanisms, and the latter is adopted with brown-rot fungi [16,42-43]. In addition, some other enzyme groups exploited for dye decolorization include azoreductase [44], lignin peroxidases [38], laccase [45], manganese peroxidase [17], peroxidase and polyphenol oxidase [39], and microperoxidase-11 [46]. The MB in this current investigation was exposed to biotransformation and biodegradation. In addition, the resulting metabolic products were generated through reduction and demethylation reactions on the structure. These mechanisms ensure the support provided by the extracellular enzymatic activities of *R. pickettii* in a liquid NB medium [38].

Identification of Metabolic Products

The MB metabolic products generated after biodegradation treatment with *R. pickettii* were identified using LC-TOF/MS, as shown in Fig. 3. Furthermore, the LC-TOF/MS chromatogram demonstrates 4 metabolic product peaks, where one with a retention time of 5.57 min indicated MB molecule at m/z = 284 [14,16]. Remarkably, the intensity was lower than the control, further confirming the sample transformation within the incubation period, following the incidence of extracellular metabolic products activities. Fig. 3 showed the 4 peaks, characterized by retention times of 2.67, 5.01, 6.49, and 7.79 min, with each possessing an m/z value of 256 (azure A) [14,17], 224 (thionine) [47], 285 (leuco-MB) [15], and 447 (glucose-MB) [14], respectively.

The yields from each microorganism comprised different fragments of compounds, which applied bacteria or fungi outputs [5,16]. In addition, photocatalytic decomposition processes yield a variety of smaller and large molecular fragments [47]. The mechanisms mostly adopted currently involve the working principle of microbes, photocatalytic, and a combination of both mechanisms. Fig. 3 showed the LC-TOF/MS chromatogram and further demonstrated *R. pickettii* transforming MB into some metabolic products, including azure A, thionine, Leuco-MB, and Glu-MB. Moreover, certain bacteria or fungi were identified to yield similar output, although some of them were also different. The *Alcaligenes* species yielded 4-amino-1-benzylpiperidinium dichloride ($C_{12}H_{18}ClN_2$) and

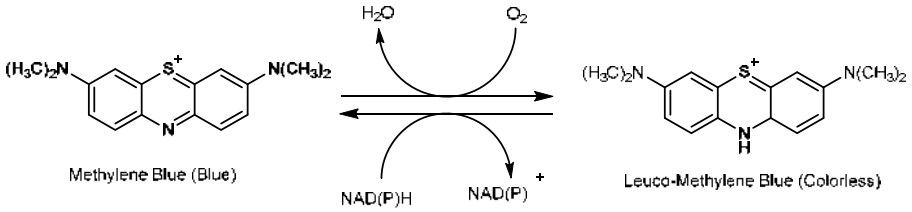

Fig 2. Redox cycling of Methylene blue (MB)

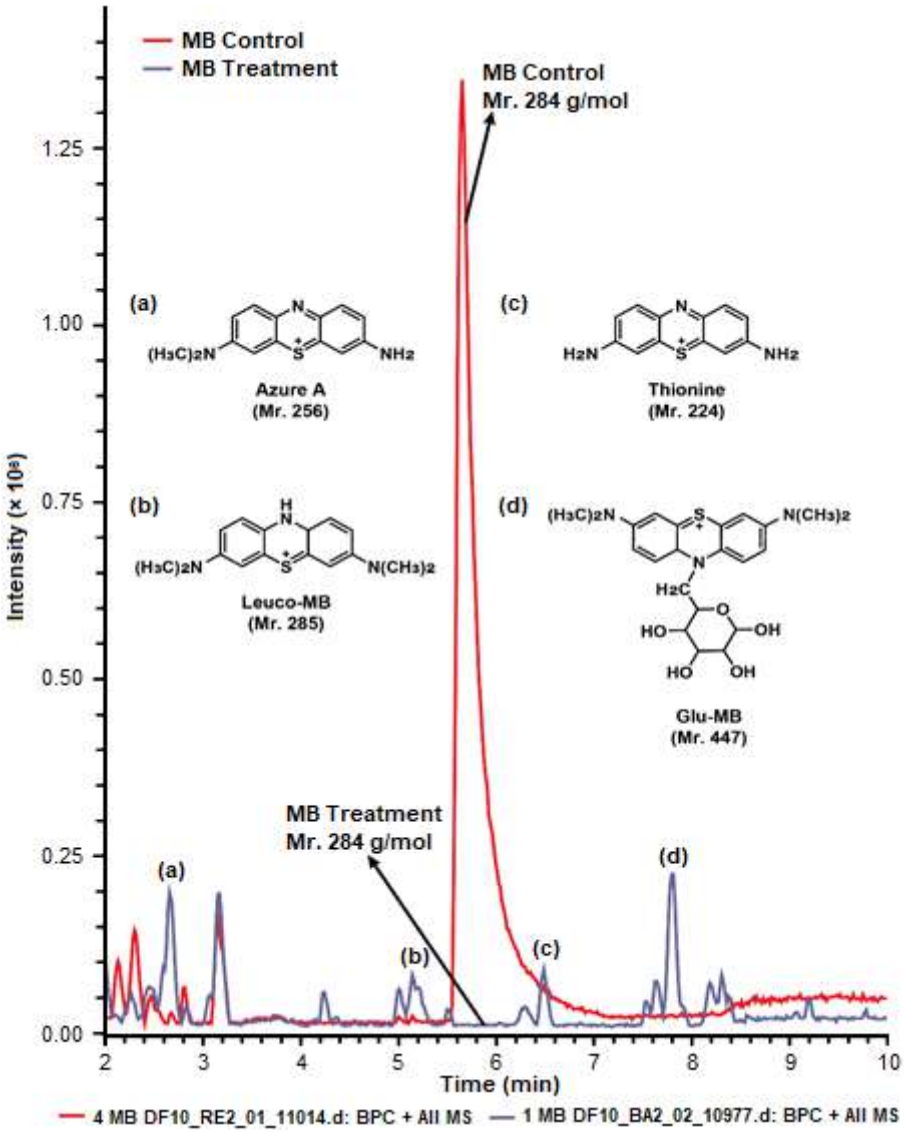

Fig 3. LC-MS chromatogram profile of MB transformation by *R. pickettii*

4,4'-diaminodiphenyl sulfide ($C_{12}H_{12}N_2S$) [5], while azure B (m/z = 270); 3,7-bis (dimethylamino)-4aH-phenothiazin-5-one (m/z = 300), and 4-(dimethylamino)-2-[*m*-(dimethylamino) phenyl sulfinyl] benzenamine were observed with *D. dickinsii* (m/z = 303) [16]. Fig. 4 showed the summary for the proposed MB transformation pathway using 3 microbes.

The molecular fragments identified as products after treatment with photocatalytic and natural oxidizing agents were more diverse, despite the similarity between some metabolic products of bacteria or fungi, including azure A, azure B, and thionine [47]. The MB degradation process using natural MnOx yielded 7 metabolic products, comprising azure B (m/z = 270), azure A (m/z = 256), 2-methyl-2,3,4,5-tetrahydro-1,4-thiazin-1-ium (m/z = 115), 7-amino-2,3-dimethylbenzo[b][1,4]thiazin-1-ium (m/z = 186), benzene-1,4-diamine (m/z = 105), benzo[b][1,4]thiazin-1-ium (m/z = 156), and aniline (m/z = 98.5) [17]. Meanwhile, photocatalysis with materials from sugarcane bagasse cellulose (SBC)-TiO_2 generated fragments of $C_{16}H_{21}N_3SO$, $C_{16}H_{19}N_3S$ (azure B), $C_8H_{12}N_2SO_3$, C_6H_7NO, and C_6H_7N [11]. The use of ZnO:Eu nanoparticles under the sun rays produced a similar outcome as observed with *R. picketii,* while leuco-MB and azure B were identified with *D. dickinsii* [48]. In addition, the microbes and material sources

considerably influenced the variations between specific metabolic products produced. The degradation mechanisms adopted by each bacteria or fungi are associated with the intrinsic enzyme complexity enzymes [4,16,33], while photocatalysis is influenced by the energy source and the material composition [47].

The microbial approach is entirely controlled by extracellular enzyme activities [49]. Furthermore, the effects on synthetic dyes are generally achieved through varied mechanisms to attain a structural transformation. These bacteria and fungi secrete extracellular enzymes after induction in the media. Moreover, *R. pickettii* was presumed to affect modifications to MB by involving the reductase enzymes, including quinone dehydrogenase (QD) dependent NADPH and demethylase. Mainly, QD is an enzyme involved in xenobiotic metabolism processes and confers protection from quinone free radical derivatives [50]. The reductase enzyme, including azo reductase, influences azo dye degradation, with a specific effect on the bond –N=N– [39]. These enzymatic involvements are based on the metabolic products identified in the LC-MS analysis (see Fig. 3).

Proposed Methylene Blue (MB) Transformation Pathway

The identification for metabolic produced during MB degradation, using LC-TOP/MS, and determined based on the approximate pathway after transformation by *R. pickettii* showed in Fig. 4. The proposed procedure recognized the essential roles played by QD in the decolorization process by the hydrogenation of MB to form colorless Leuco-MB. The proposed procedure recognized the essential roles played by QD in the decolorization process by the hydrogenation of MB to form colorless Leuco-MB. This output is more stable, resulting from the Glucose-MB molecules formed by dehydration between the hydroxyl group (–OH) from glucose and the -NH present in MB [14]. Furthermore, QD was produced and identified in some bacteria, including the *Bacillus* sp. strain MZS10 and *Bacillus* sp. strain LD003, following the degradation of dye azure B [50].

The biodecolorization process is generally attributed to enzymatic oxidation or reduction activities. These are some of the various extracellular types involved: H_2O_2

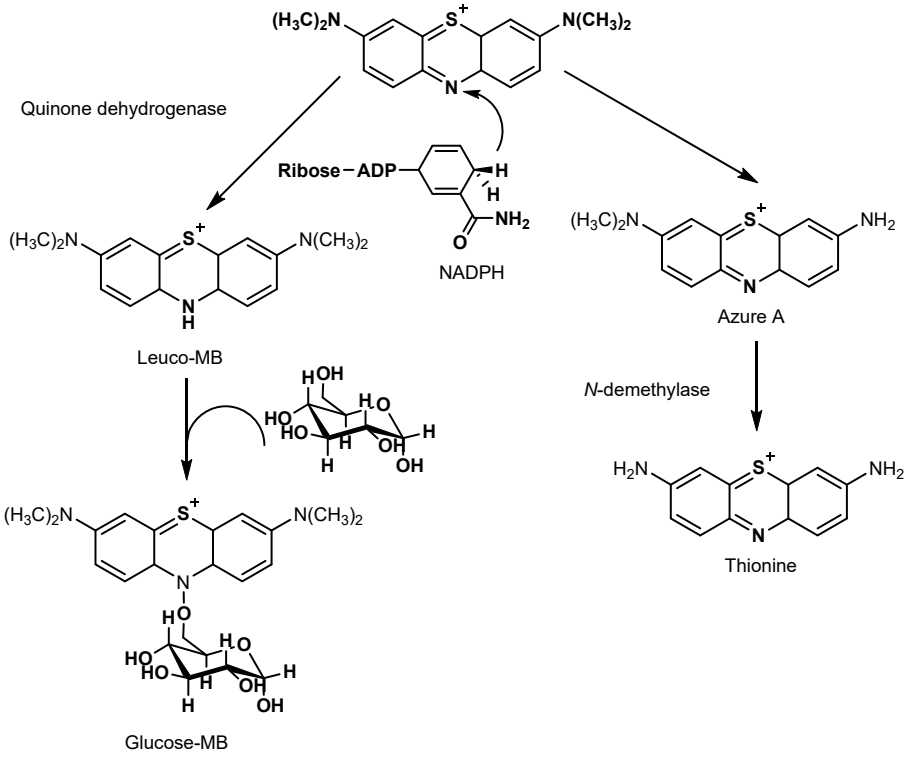

Fig 4. Proposed methylene blue (MB) transformation pathway by *R. pickettii*

independent oxidase, laccase, and azoreductase to degrade the reactive yellow of 84A by *Exiguobacterium* sp. RD3 [51]. Also, *Pseudomonas aeruginosa* BCH is known to secrete tyrosinase, NADH-DCIP reductase, veratryl alcohol oxidase, and laccase are implicated in amaranth azo dye decomposition [52].

Fig. 4 showed oxidative demethylation of MB as another mechanism exploited to form azure A (AA) and thionine molecules. Particularly, demethylation commonly facilitates the conversion into azure B (AB), azure A (AA) or sym-dimethylthionine, Azure C (AC), and thionine [50]. Fig. 5 showed the degradation in potato dextrose broth (PDB), using *D. dickinsii* to produce azure B molecules. Conversely, oxidation with sulfur and reduction at the C=N bond instigated the production of 3,7-bis(dimethylamino)-4aH-phenothiazine-5-one and 4-(dimethylamino)-2-[*m*-(dimethylamino)-phenylsulfinyl] benzenamine [16]. Furthermore, the MB degradation process involving *Alcaligenes* generated a derivative with smaller BM. This effect was attributed to enzymes secreted to perform total demethylation and C=N bond reduction resulting in the 4,4-diaminodiphenyl sulfide fragment [5]. In addition, other metabolic products emanated from demethylation, deamination, and oxidation procedures, with characteristic fragments of 4-amino-1-benzylpiperidinium dichloride [5]. The Lignin peroxidase (LiP) and horseradish peroxidase (HRP) from *P. chrysosporium* instigated the demethylation of MB and azure B. Based on HPLC analysis, the HRP produced more derivatives (AB, AA, AC) than the LiP, while individual activity depended on H_2O_2 concentration [53].

Moreover, there are limited detailed reports on demethylation reaction mechanisms involving microbes, as most were based only on the modification approach towards the groups present on the metabolic product. Therefore, the biodegradation of dyes with *R. pickettii* has not been substantially evaluated, and the predominant enzymes involved are not currently identified. Today, the enzymes identified in *R. pickettii* involved in the degradation of xenobiotic pollutants are oxygenase groups such as catechol-1,2-dioxygenase and hydroxyquinol-1,2-dioxygenase [24,30].

Furthermore, there have been extensive studies on demethylation, including the oxidative aminopyrine approach, involving various enzyme types, e.g., microsomal cytochrome P-450, HRP, metmyoglobin, and protohemin [54]. The catalytic demethylation on dye

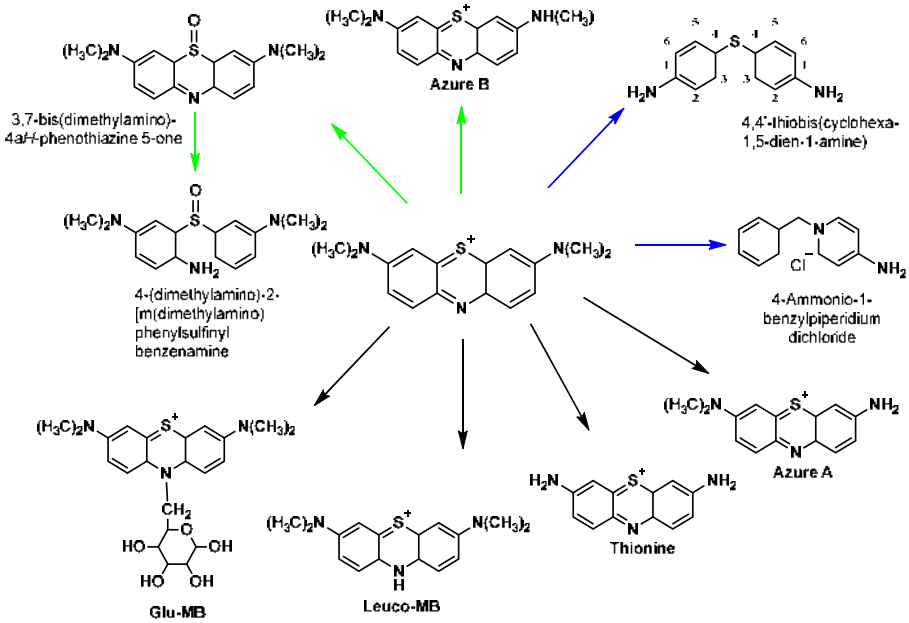

Fig 5. Summary of the proposed methylene blue (MB) transformation pathway by *R. pickettii* (black line; this study), *Alcaligenes* (blue line) [21], *D. dickinsii* (green line) [16]

structure was reported to have occurred during biodegradation through a similar mechanism, although with aminopyrine *N*-demethylase (AND). This pathway was confirmed during the bio-decomposition of Direct Blue-6 by *Pseudomonas desmolyticum* strain NCIM 2112 [55] and methyl red by *Brevibacillus laterosporus* strain MTCC 2298.

In addition, several enzyme types were also involved in the structural biotransformation of methyl red, including lignin peroxidase, laccase, NADH-DCIP reductase, and malachite green reductase [10]. The AND catalytic activity was also detected after the decolorization of Red BLI by *Pseudomonas* sp. SUK1 [56]. Moreover, the demethylation mechanisms exhibited with some dyes involve the activity of various enzymes, encompassing laccase at Brown 3REL [57], lignin peroxidation to convert N,N,N',N',N",N"-hexamethylpararosaniline (crystal violet) into N,N,N',N',N"-penta-, N,N,N',N"-tetramethyl pararosaniline, and N,N',N"-trimethylpararosaniline [58]. The demethylation at crystal violet ensued in the intermediate compounds Michler's Ketone by *Shewanella* sp. strain NTOU1 [59].

Furthermore, MB degradation through microbial mechanisms is similar to the photocatalytic method, based on generated metabolic products. The latter showed decomposition or structural transformation by attacks on the chromophores and auxochrome units. Particularly, *R. pickettii* predominantly decomposed the dye at the auxochrome to yield fragments of demethylation, including azure A and thionine. In addition, similar pathway and metabolic products were reported with *D. dickinsii* [16], and *Bacillus* sp. strain MZS10 [14]. The decomposition through a group of auxochrome with photocatalytic techniques using P2ABSA-modified TiO_2 nanocomposite yielded more organized demethylation products, comprising azure B, A, C, and thionine. However, chemical agents, including manganese oxides, also generate compounds between azure B and A [17]. The chromophore pathway (a conjugation system of N-S on the core aromatic ring) involving attacks by hydroxyl radical, which instigate the opening of a center aromatic ring, is implicated in the production of intermediate compounds. These include 3-((3-(dimethylamino)-cyclo hexa-2,4-dien-1-yl)sulfinyl)-N,N'-dimethyl benzene-1,4-diamine ($C_{16}H_{23}N_3OS$; m/z = 303) [47]. Meanwhile, compounds related to $C_{16}H_{23}N_3OS$ were also recognized during biodegradation using *D. dickinsii* and combined with photocatalytic-biodegradation [11,16].

These biological, chemical, photocatalytic approaches and the combination, initiated with the group of chromophores, facilitate cleavage development at the center aromatic ring of MB and generate monocyclic fragments. Simultaneously, degradation observed on the auxochrome group yields intermediate demethylation products, including azure B, A, and C, and thionine, before advanced decomposition into simpler compounds. Table 2 shows the summary of MB metabolic products after degradation through various means. The intermediate compounds generated, including 3-((3-(dimethylamino)cyclohexa-2,4-dien-1-yl)sulfinyl)-N,N'-dimethyl benzene-1,4-diamine ($C_{16}H_{23}N_3OS$; m/z = 303) were first identified after the sulfhydryl group (–C-S^+=C) was oxidized. An electron rearrangement process characterizes this into C–S(=O)–C, which leads to the opening of a center aromatic ring required before the intermediate compounds are formed. The reaction mechanism involves photocatalysis [47-48], Fenton [60], oxidizing agents [17], and microbes [16], instigated by hydroxyl radical attacks.

Furthermore, advanced degradation is experienced after cleavage at the heterocyclic center to yield a variety of simple fragments, including 4-amino-1-benzylpiperidinium dichloride ($C_{12}H_{18}ClN_2$, m/z = 225.74) and 4,4'-diaminodiphenyl sulfide ($C_{12}H_{12}N_2S$, m/z = 216) [5]. The structure auxochrome of MB are decomposed through oxidative demethylation to produce azure B, A, C, and thionine molecules as intermediates. These specimens are estimated to encounter advanced metabolism for subsequent conversion into simpler compounds. The ability for *R. pickettii* to transform MB on a group of chromophores and auxochrome indicates the potency for microbes to prevent dye wastes. In addition, there are numerous records on the capacity to degrade a variety of xenobiotic wastes due to the genetic complexity used to encode various degradation-related enzymes [24,27-28,30,42].

Table 2. A comparison of different metabolic products for the treatment of MB

Microbial/Material		Metabolic products	m/z	Analytical method	Ref.
D. dickinsii	1	Azure B	270	LC-MS	[16]
	2	3,7-bis(dimethylamino)-4aH-phenothiazin-5-one ($C_{16}H_{19}N_3S$)	300		
	3	4-(dimethylamino)2-[*m*(dimethylamino) phenylsulfinyl] benzenamine ($C_{16}H_21N_3SO$)	303		
Alcaligenes	1	4-amino-1-benzylpiperidinium dichloride ($C_{12}H_{18}ClN_2$)	225.74	GC-MS	[5]
	2	4,4'-diaminodiphenyl sulfide ($C_{12}H_{12}N_2S$)	216.3		
Bacillus sp. *MZS10*	1	Azure B ($C_{15}H_{16}N_3S$)	270	UPLC-MS	[14]
	2	Azure A ($C_{14}H_{14}N_3S$)	256		
R. pickettii	1	Azure A ($C_{14}H_{14}N_3S$)	256	LC-MS	This study
	2	Thionine ($C_{12}H_{10}N_3S$)	228		
	3	Leuco-MB	285		
	4	Glucose-MB ($C_{22}H_{31}N_3SO_5$)	447		
MnOx	1	Azure B	270.1	HPLC-MS	[17]
	2	Azure A	256.1		
	3	7-amino-2,3-dimethylbenzo[b] [1,4]thiazin-1-ium	191.06		
	4	Benzo[b] [1,4] thiazin-1-ium	148.02		
	5	2-methyl-2,3,4,5-tetrahydro-1,4-thiazin-1-ium	116.05		
	6	Benzene-1,4-diamine	108.7		
	7	Aniline	93		
Photocatalysis-Biodegradation	1	3-((3-(dimethylamino) cyclohexa-2,4-dien-1-yl) sulfinyl)-*N*,*N*'-dimethylbenzene-1,4-diamine	303.30	HPLC-MS	[11]
	2	3,7-bis (dimethylamino)-10,10a-dihydro-4aH-phenothiazine 5-oxide	301.14		
	3	2-amino-5-(dimethylamino) benzenesulfonic acid	216.17		
	4	2-aminophenol	109.10		
	5	Aniline	93		
P2ABSA-modified TiO_2 nanocomposite	1	Azure B	270	UHR-TOF-MS	[47]
	2	Azure A	256		
	3	Azure C	242		
	4	Thionine	228		
	5	Phenol	94		
	6	3-((3-(dimethylamino) cyclohexa-2,4-dien-1-yl) sulfinyl)-*N*,*N*'-dimethylbenzene-1,4-diamine	303.30		
	7	2-amino-5-(*N*-methylformamido) benzenesulfonic acid	230		
	8	2-amino-4-hydroxy-5-(methylamino) benzenesulfonic acid	218		
	9	benzenesulfonic acid	158		

■ CONCLUSION

R. pickettii was able to decolorize and degrade the molecular structure of MB. Approximately 98.11% of MB was decolorized after 18 h of incubation. Based on the analysis of metabolic products, *R. pickettii* was revealed to have the ability of MB transformation into Azure A (AA), thionine, leuco-MB, and glucose-MB, which indicated the MB degradation through a reductase that

attacks the heterocyclic central chromophore group present in the structure. Moreover, azure A and thionine fragments resulted from the attacks on the auxochrome group by *N*-demethylase enzyme. This research provides evidence for the potential to use *R. pickettii* in the biodecolorization and biotransformation of dye waste, particularly MB.

■ REFERENCES

[1] Tkaczyk, A., Mitrowska, K., and Posyniak, A., 2020. Synthetic organic dyes as contaminants of the aquatic environment and their implications for ecosystems: A review, *Sci. Total Environ.*, 717, 137222.

[2] Bommavaram, K., Bhattacharjee, A., Yadav, D., Andra, N., Pandey, P., and Ibrahim, H., 2020, Tea residue as a bio-sorbent for the treatment of textile industry effluents, *Int. J. Environ. Sci. Technol.*, 17 (7), 3351–3364.

[3] Abu-Talha, M., Goswami, M., Giri, B.S., Sharma, A., Rai, B.N., and Singh, R.S., 2018, Bioremediation of Congo red dye in immobilized batch and continuous packed bed bioreactor by *Brevibacillus parabrevis* using coconut shell biochar, *Bioresour. Technol.*, 252, 37–43.

[4] Purnomo, A.S., and Mawaddah, M.O., 2020, Biodecolorization of methyl orange by mixed cultures of brown-rot fungus *Daedalea dickinsii* and bacterium *Pseudomonas aeruginosa*, *Biodiversitas*, 21 (5), 2297–2302.

[5] Geed, S.R., Samal, K., and Tagade, A., 2019, Development of adsorption-biodegradation hybrid process for removal of methylene blue from wastewater, *J. Environ. Chem. Eng.*, 7 (6), 103439.

[6] Zhou, Y., Lu, J., Zhou, Y., and Liu, Y., 2019, Recent advances for dyes removal using novel adsorbents: A review, *Environ. Pollut.*, 252, 352–365.

[7] Shah, M.P., 2019, Chapter 6 - Bioremediation of azo dye" in *Microbial Wastewater Treatment*, Eds. Shah, M.P., and Rodriguez-Couto, S., Elsevier, Netherlands, 103–126.

[8] Zaini, M.A.A., Ngiik, T.C., Kamaruddin, M.J., Mohd. Setapar, S.M., and Che Yunus, M.A., 2014, Zinc chloride-activated waste carbon powder for decolourization of Methylene blue, *Jurnal Teknologi*, 67 (2), 37–44.

[9] Ehrampoush, M.H., Moussavi, G.R., Ghaneian, M.T., Rahimi, S., and Ahmadian, M., 2011, Removal of methylene blue dye from textile simulated sample using tubular reactor and TiO_2/UV-C photocatalytic process, *Iran. J. Environ. Health Sci. Eng.*, 8 (1), 35–40.

[10] Kurade, M.B., Waghmode, T.R., Xiong, J.Q., Govindwar, S.P., and Jeon, B.H., 2019, Decolorization of textile industry effluent using immobilized consortium cells in upflow fixed bed reactor, *J. Cleaner Prod.*, 213, 884–891.

[11] Xiong, J., Guo, S., Zhao, T., Liang, Y., Liang, J., Wang, S., Zhu, H., Zhao, J.R., and Chen, G., 2020, Degradation of methylene blue by intimate coupling photocatalysis and biodegradation with bagasse cellulose composite carrier, *Cellulose*, 27 (6), 3391–3404.

[12] Boelan, E.G., and Purnomo, A.S., 2018, Abilities of Co-cultures of white-rot fungus *Ganoderma lingzhi* and bacteria *Bacillus subtilis* on biodegradation DDT, *J. Phys.: Conf. Ser.*, 1095, 012015.

[13] Sariwati, A., Purnomo, A.S., and Kamei I., 2017, Abilities of co-cultures of brown-rot fungus *Fomitopsis pinicola* and *Bacillus subtilis* on biodegradation of DDT, *Curr. Microbiol.*, 74 (9), 1068–1075.

[14] Li, H, Zhang, R, Tang, L., Zhang, J., and Mao, Z., 2014, Evaluation of *Bacillus* sp. MZS10 for decolorizing Azure B dye and its decolorization mechanism, *J. Environ. Sci.*, 26 (5), 1125–1134.

[15] Schirmer, R.H., Adler, H., Pickhardt, M., and Mandelkow, E., 2011, Lest we forget you - methylene blue, *Neurobiol. Aging*, 32 (12), 2325.e7–2325.e16.

[16] Rizqi, H.D., and Purnomo, A.S., 2017, The ability of brown-rot fungus *Daedalea dickinsii* to decolorize and transform methylene blue dye, *World J. Microbiol. Biotechnol.*, 33 (5), 92.

[17] Zhou, S., Du, Z., Li, X., Zhang, Y., He, Y., and Zhang, Y., 2019, Degradation of methylene blue by

natural manganese oxides: Kinetics and transformation products, *R. Soc. Open Sci.*, 6 (7), 190351.

[18] Purnomo, A.S., Rizqi, H.D., Fatmawati, S., Putro, H.S., and Kamei, I., 2018, Effects of bacterium *Ralstonia pickettii* addition on DDT biodegradation by *Daedalea dickinsii*, *Res. J. Chem. Environ.*, 22, 151–156.

[19] Upendar, G., Dutta, S., Bhattacharya, P., and Dutta, A., 2017, Bioremediation of methylene blue dye using *Bacillus subtilis* MTCC 441, *Water Sci. Technol.*, 75 (7), 1572–1583.

[20] Habibi, A., and Mehrabi, Z., 2017, Aerobic degradation of methylene blue from colored effluents by *Ralstonia eutropha*, *Pollution*, 3 (3), 395–406.

[21] Bharti, V., Vikrant, K., Tiwari, H., Sonwani, R.K., Lee, J., Tsang, D.C.W., Kim, K.H., Saeed, M., Kumar, S., Rai, B.N., Giri, B.S., and Singh, R.S., 2019, Biodegradation of methylene blue dye in a batch and continuous mode using biochar as packing media, *Environ. Res.*, 171, 356–364.

[22] Bankole, P.O., Adekunle, A.A., and Govindwar, S.P., 2019, Demethylation and desulfonation of textile industry dye, thiazole yellow G by *Aspergillus niger* LAG, *Biotechnol. Rep.*, 23, e00327.

[23] Maniyam, M.N., Hari, M., and Yaacob, N.S., 2020, Enhanced methylene blue decolourization by *Rhodococcus* strain UCC 0003 grown in banana peel agricultural waste through response surface methodology, *Biocatal. Agric. Biotechnol.*, 23, 101486.

[24] Ryan, M.P., Pembroke, J.T., and Adley, C.C., 2011, Genotypic and phenotypic diversity of *Ralstonia pickettii* and *Ralstonia insidiosa* isolates from clinical and environmental sources including high-purity water, diversity in *Ralstonia pickettii*, *BMC Microbiol.*, 11 (1), 194.

[25] Byrne, A.M., and Olsen, R.H., 1996, Cascade regulation of the toluene-3-monooxygenase operon (tbuA1UBVA2C) of *Burkholderia pickettii* PKO1: Role of the tbuA1 promoter (PtbuA1) in the expression of its cognate activator, TbuT, *J. Bacteriol.*, 178 (21), 6327–6337.

[26] Purnomo, A.S., Rizqi, H.D., Harmelia, L., Anggraeni, S.D., Melati, R.E., Damayanti, Z.H., Shafwah, O.M., and Kusuma, F.C., 2019, Biodegradation of crude oil by *Ralstonia pickettii* under high salinity medium, *MJFAS*, 15 (3), 377–380.

[27] Al-Zuhair, S., and El-Naas, M.H., 2012, Phenol biodegradation by *Ralstonia pickettii* extracted from petroleum refinery oil sludge, *Chem. Eng. Commun.*, 199 (9), 1194–1204.

[28] Zhang, L.L., Leng, S.Q., Zhu, R.Y., and Chen, J.M., 2011, Degradation of chlorobenzene by strain *Ralstonia pickettii* L2 isolated from a biotrickling filter treating a chlorobenzene-contaminated gas stream, *Appl. Microbiol. Biotechnol.*, 91 (2), 407–415.

[29] Ryan, M.P., Pembroke, J.T., and Adley, C.C., 2007, *Ralstonia pickettii* in environmental biotechnology: Potential and applications, *J. Appl. Microbiol.*, 103 (4), 754–764.

[30] Purnomo, A.S., Sariwati, A., and Kamei, I., 2020, Synergistic interaction of a consortium of the brown-rot fungus *Fomitopsis pinicola* and the bacterium *Ralstonia pickettii* for DDT biodegradation, *Heliyon.*, 6 (6), e04027.

[31] Wahyuni, S., Suhartono, M.T., Khaeruni, A., Purnomo, A.S., Asranudin, Holilah, and Riupassa, P.A., 2016, Purification and characterization of thermostable chitinase from *Bacillus* SW41 for chitin oligomer production, *Asian J. Chem.*, 28 (12), 2731–2736.

[32] Khan, R., Patel, V., and Khan, Z., 2020, "Chapter 5 – Bioremediation of Dyes from Textile and Dye Manufacturing Industry Effluent" in *Abatement of Environmental Pollutants Trends and Strategies*, Eds. Singh, P., Kumar, A., and Borthakur, A., Elsevier, Netherlands, 107–125.

[33] Maniyam, M.N., Yaacob, N.S., Azman, H.H., Ab Ghaffar, N.A., and Abdullah, H., 2018, Immobilized cells of *Rhodococcus* strain UCC 0004 as source of green biocatalyst for decolourization and biodegradation of methyl orange, *Biocatal. Agric. Biotechnol.*, 16, 569–578.

[34] Zeng, G., Cheng, M., and Huang, D., 2015, Study of the degradation of methylene blue by semi-solid-state fermentation of agricultural residues with *Phanerochaete chrysosporium* and reutilization of fermented residues, *Waste Manage.*, 38, 424–430.

[35] Michelle, Siregar, R.A.N., Sanjaya, A., Lucy, J., and Pinontoan, R., 2020, Methylene blue decolorizing bacteria isolated from water sewage in Yogyakarta, Indonesia, *Biodiversitas*, 21 (3), 1136–1141.

[36] Jayasinghe, C., Imtiaj, A., Lee, G.W., Im, K.H., Hur, H., Lee, M.W., Yang, H.S., and Lee, T.S., 2008, Degradation of three aromatic dyes by white rot fungi and the production of ligninolytic enzymes, *Mycobiology*, 36 (2), 114–120.

[37] Singh, S.N., 2015, *Microbial Degradation of Synthetic Dyes in Wastewaters*, Springer Nature, Switzerland.

[38] Liu, Y.N., Zhou, X., Wang, X., Liang, K., Yang, Z.K., Shen, C.C., Imran, M., Sahar, S., and Xu, A.W., 2017, Hydrogenation/oxidation induced efficient reversible color switching between methylene blue and leuco-methylene blue, *RSC Adv.*, 7, 30080–30085.

[39] Singh, R.L., Singh, P.K., and Singh, R.P., 2015, Enzymatic decolorization and degradation of azo dyes - A review, *Int. Biodeterior. Biodegrad.*, 104, 21–31.

[40] Purnomo, A.S., Rizqi, H.D., Harmelia, L., Anggraeni, S.D., Melati, R.E., Damayanti, Z.H., Shafwah, O.M., and Kusuma, F.C., 2019, Biodegradation of crude oil by *Ralstonia pickettii* under high salinity medium, *MJFAS*, 15 (3), 377–380.

[41] Purnomo, A.S., Maulianawati, D., and Kamei, I., 2019, *Ralstonia pickettii* enhance the DDT biodegradation by *Pleurotus eryngii*, *J. Microbiol. Biotechnol.*, 29, 1424–1433.

[42] Deska, M., and Kończak, B., 2019, Immobilized fungal laccase as "green catalyst" for the decolourization process – State of the art, *Process Biochem.*, 84, 112–123.

[43] Misal, S.A., and Gawai, K.R., 2018, Azoreductase: A key player of xenobiotic metabolism, *Bioresour. Bioprocess.*, 5 (1), 17.

[44] Xu, L., Sun, J., Qaria, M.A., Gao, L., and Daochen, Z., 2021, Dye decoloring peroxidase structure, catalytic properties and applications: Current advancement and futurity, *Catalysts*, 11 (8), 955.

[45] Yang, C., Dong, W., Cui, G., Zhao, Y., Shi, X., Xia, X., Tang, B., and Wang, W., 2017, Highly efficient photocatalytic degradation of synergetic effect of TiO_2 and P2ABSA, *RS Adv.*, 7 (38), 23699–23708.

[46] Trandafilović, L.V., Jovanović, D.J., Zhang, X., Ptasińska, S., and Dramićanin, M.D., 2017, Enhanced photocatalytic degradation of methylene blue and methyl orange by ZnO:Eu nanoparticles, *Appl. Catal., B*, 203, 740–752.

[47] Kurade, M.B., Waghmode, T.R., Kagalkar, A.N., and Govindwar, S.P., 2012, Decolorization of textile industry effluent containing disperse dye Scarlet RR by a newly developed bacterial-yeast consortium BL-GG, *Chem. Eng. J.*, 184, 33–41.

[48] Bandounas, L., Pinkse, M., de Winde, J.H., and Ruijssenaars, H.J., 2013, Identification of a quinone dehydrogenase from a *Bacillus* sp. involved in the decolourization of the lignin-model dye, Azure B, *New Biotechnol.*, 30 (2), 196–204.

[49] Dhanve, R.S., Kalyani, D.C., Phugare, S.S., and Jadhav, J.P., 2009, Coordinate action of exiguobacterial oxidoreductive enzymes in biodegradation of reactive yellow 84A dye, *Biodegradation.*, 20 (2), 245–255.

[50] Jadhav, S.B., Patil, N.S., Watharkar, A.D., Apine, O.A., and Jadhav, J.P., 2013, Batch and continuous biodegradation of Amaranth in plain distilled water by *P. aeruginosa* BCH and toxicological scrutiny using oxidative stress studies, *Environ. Sci. Pollut. Res.*, 20 (5), 2854–2866.

[51] Ferreira, V.S., Magalhães, D.B., and Kling, S.H., 2000, *N*-demethylation of methylene blue by lignin peroxidase from *Phanerochaete chrysosporium*. Stoichiometric relation for H_2O_2 consumption, *Appl. Biochem. Biotechnol.*, 84-86, 255–265.

[52] Griffin, B.W., and Ting, P.L., 1978, Mechanism of N-demethylation of aminopyrine by hydrogen peroxide catalyzed by horseradish peroxidase,

metmyoglobin, and protohemin, *Biochemistry*, 17 (11), 2206–2211.

[53] Kalme, S.D., Parshetti, G.K., Jadhav, S.U., and Govindwar, S.P., 2007, Biodegradation of benzidine based dye Direct Blue-6 by *Pseudomonas desmolyticum* NCIM 2112, *Bioresour. Technol.*, 98 (7), 1405–1410.

[54] Kalyani, D.C., Patil, P.S., Jadhav, J.P., and Govindwar, S.P., 2008, Biodegradation of reactive textile dye Red BLI by an isolated bacterium *Pseudomonas* sp. SUK1, *Bioresour. Technol.*, 99 (11), 4635–4641.

[55] Dawkar, V.V., Jadhav, U.U., Jadhav, S.U., and Govindwar, S.P., 2008, Biodegradation of disperse textile dye Brown 3REL by newly isolated *Bacillus* sp. VUS, *J. Appl. Microbiol.*, 105 (1), 14–24.

[56] Bumpus, A., and Brock, B.J., 1988, Biodegradation of crystal violet by the white rot fungus *Phanerochaete chrysosporium, Appl. Environ. Microbiol.*, 54 (5), 1143–1150.

[57] Chen, C.H., Chang, C.F., Ho, C.H., Tsai, T.L., and Liu, S.M., 2008, Biodegradation of crystal violet by a *Shewanella* sp. NTOU1, *Chemosphere*, 72 (11), 1712–1720.

[58] Wang, Q., Tian, S., and Ning, P., 2013, Degradation mechanism of methylene blue in a heterogeneous Fenton-like reaction catalyzed by ferrocene, *Ind. Eng. Chem. Res.*, 53 (2), 643–649.

Synthesis and Molecular Docking Studies of New Dispiropyrrolidines on West Nile Virus NS2B-NS3 Protease

Nadia Mohamed Yusoff[1], Hasnah Osman[1], Mohd. Zaheen Hassan[1,2], Mohamed Ashraf Ali[1,3], Yeong Keng Yoon[4,5], Ezatul Ezleen Kamarulzaman[6], Muhammad Solehin Abd Ghani[1], Unang Supratman[7], and Mohamad Nurul Azmi Mohamad Taib[1*]

[1]*School of Chemical Sciences, Universiti Sains Malaysia, Minden 11800 Penang, Malaysia*

[2]*College of Pharmacy, King Khalid University, Abha, Saudi Arabia*

[3]*Department of Medicinal Chemistry, Sunrise University Alwar, Rajasthan-301030, India*

[4]*Institute for Research in Molecular Medicine, Universiti Sains Malaysia, Minden 11800 Penang, Malaysia*

[5]*School of Science, Monash University Malaysia Campus, Bandar Sunway, 47500, Subang Jaya, Selangor, Malaysia*

[6]*School of Pharmaceutical Sciences, Universiti Sains Malaysia, Minden 11800 Penang, Malaysia*

[7]*Department of Chemistry, Faculty of Mathematics and Natural Sciences, Universitas Padjadjaran, Jl. Raya Bandung-Sumedang Km. 21, Jatinangor, Sumedang 45363, Indonesia*

Corresponding author:

email: mnazmi@usm.my

Received: May 21, 2021
Accepted: August 13, 2021

DOI: 10.22146/ijc.66017

Abstract: *West Nile virus (WNV) is among the other four flavivirus genus, rapidly spreading worldwide. The number of cases increases globally as there are no clinically available approved drugs and vaccines against this disease. Based on our previous finding related to a flavivirus, a series of spiropyrrolidine derivatives were regioselectively synthesized via [3+2]-cycloaddition reaction of three components between isatins, sarcosine, and (E)-3,5-bis (arylidene)-4-piperidones. The yield of synthesized compounds was in a range between 81–95%. The structures of all the synthesized compounds were characterized using FT-IR, 1D- and 2D-NMR, and HRMS. Molecular docking studies of spiropyrrolidines on NS2B-NS3 protease were done to understand and explore the ligand-receptor interactions and hypothesize the drug's refinements. The inhibition of NS2B-NS3 protease has been considered a promising strategy because this enzyme is responsible for the viral replication process. Among them, compound 5c shows an excellent binding affinity with −7.71 kcal/mol free binding energy and an inhibition constant of 1.73 μM. It also showed the binding orientation into the active site of WNV NS2B-NS3 protease on Asn84, Tyr1161, Gly1151, and Gly1153.*

Keywords: *spiropyrrolidine; [3+2]-cycloaddition; molecular docking; West Nile virus; WNV NS2B-NS3 protease*

■ INTRODUCTION

The flaviviral disease is an infectious disease transmitted by mosquitoes. The members of the Flavivirus genus include dengue virus (DENV), West Nile virus (WNV), yellow fever virus (YFV), and Japanese encephalitis (JEV) [1-3]. The number of cases increases day by day worldwide [1-3]. Thus, there is a pressing need to develop newer agents against these viruses. Discovered in 1937 in the West Nile district of Uganda, WNV was first isolated from the blood of a woman with mild febrile infection [4-5]. Since then, primary and sporadic outbreaks have been commonly recorded in Africa, Middle East, and Europe in the 1960s [4-5]. Infections in humans are typically asymptomatic or cause a moderate flu-like disease called West Nile fever for a few days. Recent WNV infections have been associated with much

higher fatality rates, especially among the elderly [6-8].

WNV is transmitted to humans by the bites of infected mosquitoes of several species, including *Culex* sp., *Aedes* sp., and *Anopheles* sp. [9]. Symptomatic cases cause headaches, fever, drowsiness, lethargy, dizziness, nausea, and confusion, escalating to encephalitis, convulsions, seizures, and eventually death. Among all arthropod-borne Flaviviruses, WNV has the broadest geographic distribution and the most diverse vector and host variety, increasing its potential as a global health threat [9]. In 2020, there were 315 human cases of WNV infection in Mediterranean countries reported by the European Centre for Disease Prevention and Control (ECDC). Greece and Spain reported the highest cases with 143 and 77, respectively [10]. In WNV, an NS3 protease is associated with NS2B, forming a complex enzymatic NS2B-NS3, which is important for synthesizing the polyprotein precursor in viral replication [11-12]. Hence, NS2B-NS3 protease has been considered a favorable target to prevent virus infection and lead to flaviviral death [11,13-15]. Most of the research for flaviviral infections focuses on the inhibition of the NS2B-NS3 protease. In addition, the complexity of this enzyme is very challenging due to its shallow and open pocket active site [16].

Previous studies reported considerable biological activities of the dispiropyrrolidines on antimycobacterial [17-20], antifungal [21], antimicrobial [22-25], antitumor [26-28], anti-neoplastic [29], and antidiabetic activities [30-31]. No reported data explained the activity and interaction between dispiropyrrolidines and their roles as WNV NS2B-NS3 protease inhibitors. Previously, we reported the synthesis of new dibenzylidene-1-phenylethylpiperidine-4-ones and new dispiropyrrolidines to evaluate their application as antimycobacterial against *Mycobacterium tuberculosis* [17-19,32]. Based on our previous achievement and our continuation on this research domain, this manuscript focuses on synthesizing new dispiropyrrolidines as a WNV NS2B-NS3 protease inhibitor, which is the recent finding dibenzylidene-1-phenylethylpiperidine-4-ones are employed as dipolarophiles in [3+2]-cycloaddition reactions of azomethine ylide for the synthesis of new dispiropyrrolidines. The dispiropyrrolidines were investigated as potential WNV NS2B-NS3 protease inhibitors using a molecular docking approach. This information is very useful for predicting the binding behavior in the rational design of drugs and elucidating the fundamentals of biochemical processes.

■ EXPERIMENTAL SECTION

Materials

Unless otherwise noted, materials were purchased from Sigma-Aldrich Co., Acros Organics, QReC, and Merck Chemical Co., i.e., 1-phenylethyl-4-piperidone 98%, Benzaldehyde 99%, 4-Methoxybenzaldehyde 98%, 4-Methylbenzaldehyde 97%, 4-Methoxybenzaldehyde 97%, Isatin 98%, 5-Chloroisatin 95%, Sarcosine 98%, Acetone, AR Grade, Ethanol, AR Grade, Methanol, AR Grade, Hexane AR Grade and Methyl sulfoxide-d_6-deuteration degree for NMR. All chemicals and solvents were of reagent grade and were used without further purification. Column chromatography was performed using Merck silica gel (40–63 μm).

Instrumentation

Thin-layer chromatography (TLC) was performed on alumina plates pre-coated with silica gel (Merck silica gel, 60 F254), which were visualized by the quenching of UV fluorescence when applicable (λ_{max} = 254 nm and/or 366 nm) and/or by spraying with vanillin or anisaldehyde in acidic ethanol followed by heating with a heat gun. It was performed using a solvent system of benzene-methanol (8:2) and toluene-ethyl formate-formic acid (5:4:1) to check the reactions' completion. All reactions were carried out in heat-dried glassware under a dry nitrogen atmosphere unless otherwise stated. All liquids transfer was conducted using standard syringe or cannula techniques. All spectral data were obtained on the following instruments: Infrared spectra were recorded on a Perkin Elmer 2000 FTIR spectrometer at wavenumber from 4000-600 cm^{-1}. ^1H (500 MHz) and ^{13}C (125 MHz) Nuclear magnetic resonance spectra were obtained on Bruker AVN 500 MHz spectrometers (Bruker Bioscience, Billerica, MA, USA) which were reported in units of ppm on the δ scale. NMR analyses were done using solvent DMSO-d_6 and TMS as the

internal standard. Data were analyzed via the TopSpin software package. The chemical shift was internally referenced to the solvent signals in DMSO-d_6 (^{1}H δ 2.50; ^{13}C δ 39.5). The coupling constants are given in Hz. The mass spectra were measured using the Waters Xevo QTOF MS system.

Procedure

Synthesis of (3E,5E)-3,5-bis(substitutedarylidene)-1-phenethyl piperidin-4-one (1a-c)

The procedure of preparation of dibenzylidene-1-phenylethylpiperidine-4-ones **1a-c** was reported previously by our group [32]. 1-phenylethyl-4-piperidone (1.0 equiv.) and appropriate aldehyde (2.0 equiv.) were dissolved together in ethanol (10 mL) and 30% sodium hydroxide (5 mL; prepared in ethanol). The reaction mixture was stirred for 2–6 h at room temperature until completion (TLC). The mixture was then poured into crushed ice. The precipitated solid was filtered, washed with water, and purified by recrystallization. The spectroscopic data were compared with the literature [32].

(3E,5E)-3,5-dibenzylidene-1-phenylethyl-4-piperidinone (1a). 1-Phenylethyl-4-piperidone (1.22 g, 6.0 mmol) and benzaldehyde (1.27 g, 12.0 mmol) were dissolved together in ethanol (10 mL) and 30% sodium hydroxide (5 mL; prepared in ethanol) according to the general procedure above. The precipitated solid was filtered, washed with water and purified by recrystallization to give a bright yellow solid (2.12 g, 94.6%), M.p. 167–170 °C. FTIR (ATR, cm^{-1}): 3026 (w, C–H), 1669 (s, C=O), 1608 (s, C=C), 1181 (m, C–N). ^{1}H-NMR (500 MHz, DMSO-d_6): δ_H, ppm 2.70 (2H, t, *J* = 7.5 Hz, 8-CH_2), 2.81 (2H, t, *J* = 7.5 Hz, 7-CH_2), 3.88 (4H, s, 2-CH_2, 6-CH_2), 7.14-7.23 (5H, m, H-10, H-11, H-12, H-13, H-14), 7.42-7.51 (10H, m, H-17, H-18, H-19, H-20, H-21), 7.58 (2H, s, H-15). ^{13}C-NMR (125 MHz, DMSO-d_6): δ_C, ppm 33.3, 54.5, 58.3, 126.3, 128.6, 129.0, 129.2, 129.7, 131.0, 134.3, 135.1, 135.3, 140.5, 187.4. HRMS (TOF-ES$^+$): m/z 380.2139 (MH^+ $C_{27}H_{26}NO^+$ requires 380.2009).

(3E,5E)-3,5-bis(4-methylbenzylidene)-1-phenylethyl-4-piperidinone (1b). 1-Phenylethyl-4-piperidone (1.22 g, 6.0 mmol) and 4-methylbenzaldehyde (1.44 g, 12.0 mmol) were dissolved together in ethanol (10 mL) and 30% sodium hydroxide (5 mL; prepared in ethanol) according to the general procedure above. The precipitated solid was filtered, washed with water and purified by recrystallization to give a yellow solid (2.19 g, 90.1%), M.p. 118–121 °C. FTIR (ATR, cm^{-1}): 3024 (w, C–H), 1668 (s, C=O), 1606 (m, C=C), 1174 (m, C–N). ^{1}H-NMR (500 MHz, DMSO-d_6): δ_H, ppm 2.36 (6H, s, 22-CH_3), 2.71 (2H, t, *J* = 7.5 Hz, 8-CH_2), 2.81 (2H, t, *J* = 7.5 Hz, 7-CH_2), 3.86 (4H, s, 2-CH_2, 6-CH_2), 7.14-7.24 (5H, m, H-10, H-11, H-12, H-13, H-14), 7.29 (4H, d, *J* = 8.5 Hz, H-18, H-20), 7.40 (4H, d, *J* = 8.50 Hz, H-17, H-21,), 7.58 (2H, s, H-15). ^{13}C-NMR (125 MHz, DMSO-d_6): δ_C, ppm 21.5, 33.3, 54.6, 58.4, 126.3, 128.7, 129.0, 129.9, 131.0, 132.4, 133.5, 135.2, 139.6, 140.5, 187.3. HRMS (TOF-ES$^+$): m/z 408.2324 (MH^+ $C_{29}H_{30}NO^+$ requires 408.2322).

(3E,5E)-3,5-bis(4-methoxybenzylidene)-1-phenylethyl-4-piperidinone (1c). 1-Phenylethyl-4-piperidone (0.61 g, 3.0 mmol) and 4-methoxybenzaldehyde (0.82 g, 6.0 mmol) were dissolved together in ethanol (5 mL) and 30% sodium hydroxide (3 mL; prepared in ethanol) according to the general procedure above. The precipitated solid was filtered, washed with water and purified by recrystallization to give a yellow solid (1.13 g, 85.4%), M.p. 143–146 °C, Lit. M.p. 147 °C. FTIR (ATR, cm^{-1}): 3023 (w, C–H), 1667 (s, C=O), 1596 (m, C=C), 1166 (m, C–N); ^{1}H-NMR (500 MHz, DMSO-d_6): δ_H, ppm 2.73 (2H, t, *J* = 7.5 Hz 8-CH_2,), 2.82 (2H, t, *J* = 7.5 Hz, 7-CH_2), 3.82 (6H, s, 22-OCH_3), 3.84 (4H, s, 2-CH_2, 6-CH_2), 7.04 (4H, d, *J* = 8.5 Hz, 18-CH, 20-CH,), 7.15-7.25 (5H, m, 10-CH, 11-CH, 12-CH, 13-CH, 14-CH), 7.45 (4H, d, *J* = 8.5 Hz, 17-CH, 21-CH), 7.56 (2H, s, H-15). ^{13}C-NMR (125 MHz, DMSO-d_6): δ_C, ppm 33.3, 54.7, 55.8, 58.5, 113.7, 114.8, 126.3, 127.7, 128.7, 129.0, 132.2, 132.9, 134.9, 140.6, 160.5, 187.1. HRMS (TOF-ES$^+$): m/z 440.2399 (MH^+ $C_{29}H_{30}NO_3^+$ requires 440.2226).

Synthesis of spiropyrrolidines 5 and 6

3,5-Bis(substitutedarylidene)-1-phenethylpiperidin-4-one (**1**) (1.0 equiv.) was refluxed together with appropriate isatins **3** or **4** (1.0 equiv.) and sarcosine (**2**) (2.0 equiv.) in methanol (20 mL) for 4–7 h. After completing the reaction, the excess solvent in the mixture was removed under reduced pressure and cooled before being poured onto crushed ice. The

products were filtered, washed with water, and purified by recrystallization.

1-Methyl-4(phenyl)pyrrolo-(spiro[2.3'']oxindole)-spiro[3.3']-5'-(phenylmethylidene)-1'-phenylethyl-4'-piperidinone (5a). 3,5-Bis(substitutedarylidene)-1-phenethylpiperidin-4-one **1a** (0.10 g, 0.26 mmol) was refluxed together with appropriate isatin **3** (0.04 g, 0.26 mmol) and sarcosine (**2**) (0.05 g, 0.52 mmol) in methanol (20 mL) according to the general procedure above. Products obtained were filtered, washed with water and purified by recrystallization to give pale yellow solid (Yield = 0.13 g (89.6%), M.p. 117–120 °C. FTIR (ATR, cm^{-1}): *ν* 3346 (w, N–H), 3027 (w, C–H), 1697 (s, C=O), 1599 (m, C=C), 1182 (m, C–N). ^{1}H-NMR (500 MHz, DMSO-d_6): δ_H, ppm: 1.76 (1H, d, *J* = 12.5 Hz, 7'-CH_{2a}), 2.00 (s, 3H, *N*-CH_3), 2.34-2.45 (m, 4H, 2′-CH_2, 6′-CH_2), 3.06 (dd, 1H, *J* = 2.4, 2.5 Hz, 5-CH_{2a}), 3.20-3.25 (m, 2H, 7′-CH_{2b}, 8′-CH_{2a}), 3.36 (*overlap signal, 1H, 5-CH_{2b}), 3.82-3.86 (m, 1H, 8′-CH_{2a}), 4.64–4.68 (m, 1H, H-4), 6.65–7.33 (19H, m, ArH), 10.46 (s, 1H, NH). ^{13}C-NMR (125 MHz, DMSO-d_6) δ_C, ppm: 32.0, 34.1, 45.2, 53.9, 56.2, 56.3, 59.1, 64.6, 75.2, 108.7, 120.7, 125.8, 126.75, 126.85, 126.91, 128.18, 128.20, 128.46, 128.47, 128.6, 128.9, 129.1, 129.1, 130.0, 132.9, 134.5, 136.6, 138.4, 140.0, 143.4, 176.6, 198.2. HRMS (TOF-ES$^+$): m/z 554.2899 (MH^+ $C_{37}H_{36}N_3O_2^+$ requires 554.2803).

1-Methyl-4(-4-methylphenyl)pyrrolo-(spiro[2.3'']oxindole)-spiro[3.3']-5'-(4–methylphenylmethylidene)-1'-phenylethyl-4'-piperidinone (5b). 3,5-Bis(substitutedarylidene)-1-phenethylpiperidin-4-one **1b** (0.10 g, 0.26 mmol) was refluxed together with appropriate isatin **3** (0.04 g, 0.26 mmol) and sarcosine (**2**) (0.05 g, 0.52 mmol) in methanol (20 mL) according to the general procedure above. Products obtained were filtered, washed with water and purified by recrystallization to give pale yellow solid (Yield = 0.13 g (88.7%), M.p. 192–195 °C. FTIR (ATR, cm^{-1}): ν 3397 (w, N–H), 3023 (w, C–H), 1694 (s, C=O, 1605 (m, C=C), 1177 (m, C–N). ^{1}H-NMR (500 MHz, DMSO-d_6) δ_H, ppm: 1.78 (d, 1H, *J* = 12.5 Hz, 7′-CH_{2a}), 1.98 (s, 3H, N-CH_3), 2.27 (d, 6H, *J* = 5.8 Hz, 2×CH_3), 2.33–2.46 (m, 4H, 2′-CH_2, 6′-CH_2), 3.05 (dd, 1H, *J* = 2.4, 2.5 Hz, 5-CH_{2a}), 3.17–3.22 (m, 2H, 7′-CH_{2b}, 8′-CH_{2a}), 3.26 (*overlap signal, 1H, 5-CH_{2b}), 3.78-3.82 (m, 1H, 8′-CH_{2b}), 4.58 (dd, 1H, *J* = 7.4, 7.5 Hz, H-4), 6.63–7.26 (18H, m, ArH), 10.36 (s, 1H, NH). ^{13}C-NMR (125 MHz, DMSO-d_6) δ_C, ppm: 20.6, 20.9, 32.1, 34.1, 44.8, 54.0, 56.3, 56.4, 59.1, 64.5, 75.2, 108.6, 120.6, 125.8, 126.88, 126.93, 128.2, 128.5, 128.4, 128.8, 129.0, 129.1, 130.2, 131.7, 132.1, 135.3, 135.7, 136.6, 138.8, 140.1, 143.4, 176.6, 198.2. HRMS (TOF-ES$^+$): m/z 582.3081 (MH^+ $C_{39}H_{40}N_3O_2^+$ requires 582.3115, 604.2894 (MNa^+ $C_{39}H_{39}N_3NaO_2^+$ requires 604.2935).

1-Methyl-4(-4-methoxyphenyl)pyrrolo-(spiro[2.3'']oxindole)-spiro[3.3']-5'-(4-methoxyphenylmethylidene)-1'-phenylethyl-4'-piperidinone (5c). 3,5-Bis(substitutedarylidene)-1-phenethylpiperidin-4-one **1c** (0.10 g, 0.26 mmol) was refluxed together with appropriate isatin **3** (0.04 g, 0.26 mmol) and sarcosine (**2**) (0.05 g, 0.52 mmol) in methanol (20 mL) according to the general procedure above. Products obtained were filtered, washed with water and purified by recrystallization to give pale yellow solid (Yield = 0.13 g (88.9%), M.p. 130–133 °C. FTIR (ATR, cm^{-1}): 3289 (w, N–H), 2934 (w, C–H), 1706 (s, C=O), 1580 (m, C=C), 1247 (m, C–O), 1173 (m, C–N). ^{1}H-NMR (500 MHz, DMSO-d_6): δ_H, ppm 1.76 (1H, d, *J* = 12.5 Hz, 7′-CH_{2a}), 1.97 (3H, s, N-CH_3), 2.31–2.46 (4H, m, 2′-CH_2, 6′-CH_2), 3.04 (1H, dd, *J* = 2.3, 2.4 Hz, 5-CH_{2a}), 3.16–3.19 (2H, m, 7'-CH_{2b}, 8'-CH_{2a}), 3.40 (1H, *overlap signal, 5-CH_{2b}), 3.72 (3H, s, OCH_3), 3.76 (1H, *overlap signal, 8′-CH_{2b}), 3.82 (3H, s, OCH_3), 4.57 (1H, dd, *J* = 7.5, 7.5 Hz, H-4), 6.64–7.26 (20H, m, ArH), 10.38 (1H, s, NH). ^{13}C-NMR (125.8 MHz, DMSO-d_6): δ_C, ppm 32.6, 34.5, 45.0, 54.7, 55.4, 55.7, 55.8, 56.7, 57.1, 59.8, 64.8, 75.9, 109.1, 121.1, 126.3, 127.4, 127.5, 127.6, 127.7, 128.7, 128.9, 129.0, 130.6, 130.8, 131.2, 132.2, 132.9, 132.9, 137.0, 140.6, 143.9, 177.2, 198.6. HRMS (TOF-ES$^+$): m/z 614.3027 (MH^+ $C_{39}H_{40}N_3O_4^+$ requires 614.3019).

1-Methyl-4(phenyl)pyrrolo-(spiro[2.3'']-5''-chlorooxindole)-spiro[3.3']-5'-(phenylmethylidene)-1'-phenylethyl-4'-piperidinone (6a). 3,5-Bis(substitutedarylidene)-1-phenethylpiperidin-4-one **1a** (0.10 g, 0.26 mmol) was refluxed together with appropriate 5-chloroisatin **4** (0.04 g, 0.26 mmol) and sarcosine (**2**) (0.05 g, 0.52 mmol) in

methanol (20 mL) according to the general procedure above. Products obtained were filtered, washed with water and purified by recrystallization to give pale yellow solid (Yield = 0.15 g (95.4%), M.p. 131–134 °C. FTIR (ATR, cm^{-1}): ν 3244 (w, N–H), 3027 (w, C–H), 1698 (s, C=O), 1615 (m, C=C), 1182 (m, C–N). ^{1}H-NMR (500 MHz, DMSO-d_6) δ_H, ppm: 1.74–1.77 (d, 1H, *J* = 12.6 Hz, 7′-CH_{2a}), 2.02 (s, 3H, N-CH_3), 2.37–2.44 (m, 4H, 2′-CH_2, 6′-CH_2), 3.09–3.12 (dd, 1H, *J* = 2.4, 2.5, Hz, 5-CH_{2a}), 3.22–3.25 (m, 2H, 7′-CH_{2b}, 8′-CH_{2a}), 3.37 (*overlap signal, 1H, 5-CH_{2b}), 3.80–3.84 (1H, m, 8′-CH_{2b}), 4.63–4.67 (m, 1H, H-4), 6.66–6.83 (1H, m, ArH), 7.11–7.37 (19H, m, ArH), 10.57 (s, 1H, NH). ^{13}C-NMR (125 MHz, DMSO-d_6) δ_C, ppm: 32.0, 34.2, 45.1, 54.0, 56.3, 56.4, 59.1, 65.1, 75.2, 110.3, 125.0, 125.9, 126.8, 126.9, 128.27, 128.34, 128.5, 128.6, 128.7, 129.17, 129.23, 129.1, 130.1, 133.1, 134.3, 137.2, 138.1, 140.0, 142.4, 176.3, 198.2. HRMS (TOF-ES$^+$): m/z 588.2390 (MH^+ $C_{37}H_{35}{}^{35}ClN_3O_2^+$ requires 588.2413).

1-Methyl-4(-4-methylphenyl)pyrrolo-(spiro[2.3'']-5''-chlorooxindole)-spiro[3.3']-5'-(4-methylphenylmethylidene)-1'-phenylethyl-4'-piperidinone (6b). 3,5-Bis(substitutedarylidene)-1-phenethyl piperidin-4-one **1b** (0.10 g, 0.26 mmol) was refluxed together with appropriate 5-chloroisatin **4** (0.04 g, 0.26 mmol) and sarcosine (**2**) (0.05 g, 0.52 mmol) in methanol (20 mL) according to the general procedure above. Products obtained were filtered, washed with water and purified by recrystallization to give pale yellow solid (Yield = 0.13 g (84.4%), M.p. 186–189 °C. FTIR (ATR, cm^{-1}): ν 3180 (w, N–H), 3025 (w, C–H), 1691 (s, C=O), 1607 (m, C=C), 1182 (m, C–N). ^{1}H-NMR (500 MHz, DMSO-d_6) δ_H, ppm: 1.75 (d, 1H, *J* = 12.5 Hz, 7′-CH_{2a}), 2.01 (s, 3H, N-CH_3), 2.30 (d, 6H, *J* = 11.6 Hz, 2×CH_3), 2.36 (s, 2H, 6′-CH_2), 2.42–2.46 (m, 2H, 2′-CH_2), 3.08 (dd, 1H, *J* = 1.8, 1.9 Hz, 5-CH_{2a}), 3.17–3.22 (m, 2H, 7′-CH_{2b}, 8′-CH_{2b}), 3.39 (*overlap signal, 1H, 5-CH_{2b}), 3.76–3.80 (m, 1H, 8′-CH_{2b}), 4.60 (dd, 1H, *J* = 7.4, 7.4 Hz, H-4), 6.64–7.40 (19H, m, ArH), 10.54 (s, 1H, NH). ^{13}C-NMR (125 MHz, DMSO-d_6) δ_C, ppm: 20.6, 20.9, 32.0, 34.1, 44.6, 54.0, 56.3, 56.4, 59.0, 64.9, 75.2, 110.1, 124.8, 125.8, 126.8, 128.2, 128.3, 128.4, 128.8, 128.9, 129.1, 129.2, 130.1, 131.5, 132.2, 135.0, 135.8, 137.1, 139.1, 139.9, 142.3, 176.2, 198.1. HRMS (TOF-ES$^+$): m/z 616.2735 (MH^+ $C_{39}H_{39}{}^{35}ClN_3O_2^+$ requires 616.2726), 638.2595 (MNa^+ $C_{39}H_{38}{}^{35}ClN_3O_2Na^+$ requires 638.2545).

1-Methyl-4(-4-methoxyphenyl)pyrrolo-(spiro[2.3'']-5''-chlorooxindole)-spiro[3.3']-5'-(-4-methoxyphenylmethylidene)-1'-phenylethyl-4'-piperidinone (6c). 3,5-Bis(substitutedarylidene)-1-phenethylpiperidin-4-one **1c** (0.10 g, 0.26 mmol) was refluxed together with appropriate 5-chloroisatin **4** (0.04 g, 0.26 mmol) and sarcosine (**2**) (0.05 g, 0.52 mmol) in methanol (20 mL) according to the general procedure above. Products obtained were filtered, washed with water and purified by recrystallization to give pale yellow solid (Yield = 0.11 g (81.3%), M.p. 187–190 °C. IR (ATR, cm^{-1}): 3297 (w, N–H), 2943 (w, C–H), 1709 (s, C=O), 1578 (m, C=C), 1250 (C–O), 1172 (C–N). ^{1}H-NMR (500 MHz, DMSO-d_6): δ_H, ppm 1.76 (d, 1H, d, *J* = 12.5 Hz, 7′-CH_{2a}), 2.00 (s, 3H, N-CH_3), 2.37–2.43 (m, 4H, 2′-CH_2, 6′-CH_2), 3.10 (dd, 1H, *J* = 2.4, 2.5 Hz, 5-CH_{2a}), 3.16–3.21 (m, 2H, 7′-CH_{2b}, 8′-CH_{2a}), 3.38 (*overlap signal, 1H, 5-CH_{2b}), 3.73 (s, 3H, OCH_3), 3.75 (*overlap, 1H, 8′-CH_{2b}), 3.78 (s, 3H, OCH_3), 4.60 (dd, 1H, *J* = 7.65, 7.55 Hz, H-4), 6.65–7.27 (17H, m, ArH), 10.55 (s, 1H, NH). ^{13}C-NMR (125.8 MHz, DMSO-d_6): δ_C, ppm 32.5, 34.6, 44.8, 54.7, 55.4, 55.7, 56.8, 57.2, 59.7, 65.2, 75.8, 110.5, 124.8, 125.3, 126.3, 128.3, 128.4, 128.7, 128.8, 128.9, 129.7, 130.5, 130.6, 131.3, 132.7, 135.1, 135.9, 137.5, 139.0, 140.5, 142.8, 176.8, 198.5. HRMS (TOF-ES$^+$): m/z 670.2453 (MNa^+ $C_{39}H_{38}ClN_3O_4Na^+$ requires 670.2449).

Molecular docking studies

Autodock 4.2 software was used to dock the ligands to the catalytic triad of NS3-NS2B protease. The target protein of West Nile virus (PDB: 2YOL) structure with a resolution of 3.20 Å was retrieved from the RCSB Protein Data Bank. Water and chlorine atoms molecules were removed from the crystal structure. The native ligand, EBN in the 2YOL, was extracted and re-docked with a grid box in a dimension of 40 Å × 40 Å × 40 Å along the x, y, z coordinates to investigate the root mean square deviation (rmsd) between crystal geometry and the docked pose. The low rmsd value of 1.50–1.82 Å indicated that the docking was able to reproduce the native conformation.

■ RESULTS AND DISCUSSION

Chemistry

In the first step, we prepared the starting material of a dipolarophile known as dibenzylidene-1-phenylethyl piperidine-4-ones (**1**) via Claisen-Schmidt condensation between 1-phenylethyl-4-piperidone with an appropriate aromatic aldehyde in dilute ethanolic sodium hydroxide at room temperature. The completion of the reaction was checked using thin-layer chromatography (TLC) [32]. Next, we examined the three-component reaction of **1** and sarcosine (**2**) and isatin analogs (**3** or **4**) in methanol under reflux conditions to give the spiropyrrolidines (**5** and **6**), according to the method developed in our laboratory [19]. The reaction of spiropyrrolidine was conducted using two different isatin types: isatin (**3**) and 5-chloroisatin (**4**). The compounds **5** and **6** described in this study are shown in Scheme 1. The yield of synthesized compounds was in a range between 81–95%.

The structures and regiochemistry of products **5**-**6** were characterized by IR, 1D- and 2D-NMR spectroscopy data, and HRMS analysis. Compound **6b** is taken as an example to describe the result of analyses done. The FT-IR spectrum of compound **6b** manifests an absorption band at 3180 cm^{-1} attributed to the N–H bending vibration, the aromatic band of C–H stretch at 3025 cm^{-1}, and C–N stretching occur at 1182 cm^{-1}. In addition, the aromatic C=C stretching band can be observed at 1606 cm^{-1}. The strong corresponding out of the plane C–H bending vibration band appears at 820 cm^{-1}, indicating a *para*-disubstituted ring in compound **6b**. The structure of dispiropyrrolidine **6b** is agreed with the 1D- and 2D-NMR spectroscopic data. The ^{1}H-NMR spectrum of **6b** displayed two singlets at δ_H 2.01, and 10.54 was corresponding to the *N*–CH_3 and N–H, while the doublet at δ_H 2.30 (J= 11.6 Hz) was corresponding to 29′-CH_3 and 28′-CH_3, respectively. The doublet at δ_H 1.75 (J = 12.5 Hz) and multiplet at δ_H 2.42–2.46 were assigned to 7′-CH_{2a} and 2′-CH_2, respectively. The proton signal of 5-CH_{2a} and H-4 appeared as doublets of a doublet at δ_H 3.08 (J = 1.8, 1.9 Hz) and 4.60 (J = 7.4, 7.4 Hz).

The ^{1}H-^{1}H-COSY spectrum of **6b** revealed a cross peak between two neighboring protons of H-7′ and H-8′, while H-4 showed a cross peak with its neighboring proton of 5-H_{2a}. Two multiplets at δ_H 3.17–3.22 and 3.76–3.80 were assigned to 7′-CH_{2b}/8′-CH_{2b} and 8′-CH_{2b}, respectively. The presence of pyrrolidine ring attached at C-3′ causes H-2′ to become more shielded than H-6′. Hence, the proton signal of H_a-2′ is located at more upfield than H_b-6′ in **6b**. The multiplet proton signals that appeared in the aromatic region at δ_H 6.64–7.40 were

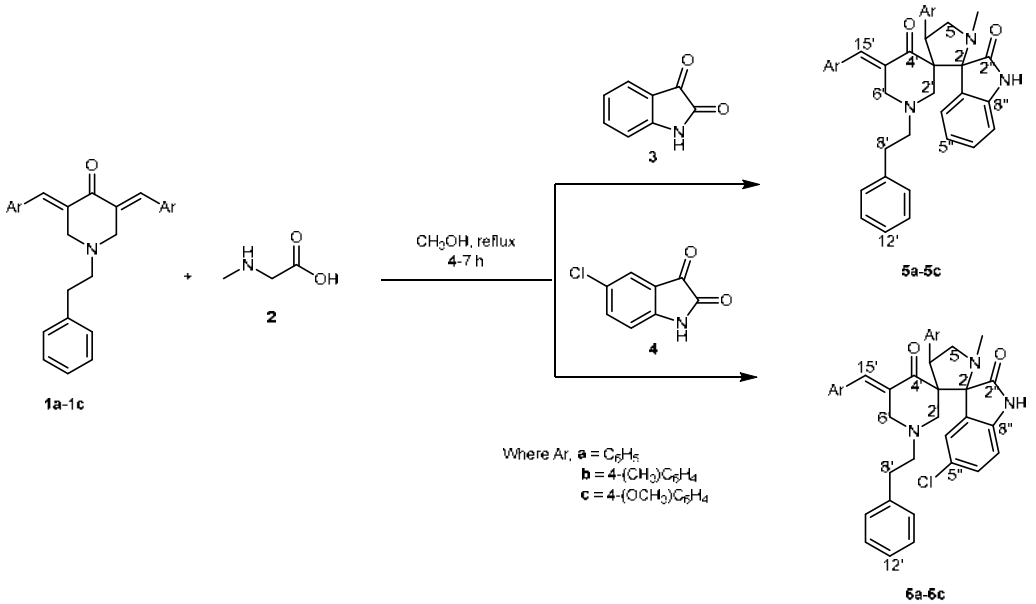

Scheme 1. Reaction scheme of synthesis of spiropyrrolidines **5** and **6**

assigned to aromatic protons. The HSQC spectrum data of **6b** showed all direct correlations between protons with their respective carbons in molecule **6b**. The carbon signals of *N*–CH_3, C-2″, C-4′ and two methyl (–CH_3) substituent of C-28′ and C-29′ were assigned in ^{13}C-NMR at δ_C 34.6, 176.7 and 198.6, respectively. Two methyl (–CH_3) substituent of CH_3-28′ and CH_3-29′ showed a correlation with carbon signals at δ_C 21.38 (C-28′) and 21.12 (C-29′). The signal of H-29′ showed correlation with δ_C 20.6 (C-29′), H-28′ with δ_C 20.9 (C-28′), H-8′ with δ_C 32.0 (C-8′), H-4 with δ_C 44.6 (C-4), H_a-2′ and H_b-2′/H_a-6′ with δ_C 56.3 (C-2′), H_b-6′ and H_b-2′/H_a-6 with δ_C 56.4 (C-6′), and H-7′ with δ_C 59.0 (C-7′). The peak of C-4″ in **6b** shifted slightly to downfield due to chlorine atom (-Cl) attach at C-3″. The carbon signal at δ_C 54.0 was assigned to C-5 due to its correlation with two signals of proton H_a-5 and water signal. It was suggested H_b-5 overlapped with the water signal at δ_C 3.39. Based on the DEPT135 spectrum of **6b**, two quaternary carbons at δ_C 75.2 and 64.9 were assigned due to the spiro carbons C-2 and C-3, respectively. The carbon for the carbonyl group can be observed at a downfield of ^{13}C-NMR. The signals at δ_C 176.7 and 198.6 were due to the carbonyl group and the carbonyl group of oxindole, respectively.

The HMBC spectrum data (Fig. 1) showed correlations of H-4 with C-3, C-2', C-4', and C-aromatic. The proton of *N*–CH_3 with C-3, C-5, and C-4'. These cross-correlations of proton and carbon further confirming the position of C-4, C-5, and *N*–CH_3 and two spiro carbon, C-2, and C-3, in the same pyrrolidine ring of compound **6b**. In addition, H-15′ and H-28' correlation with C-17′/ C-21′ and C-18′/C-20′, while CH_2-6 with C-15′. Similar correlations were observed between H-4′ and H-29' with C-23′/C-27′ and C-24′/C-26′. These correlations confirmed the presence of the aromatic rings. The H-15′ was correlated with C-5′ and C-4', thus confirming the location of the aromatic ring with piperidinone. The H-2′/H-6′ show correlation with C-2, C4', C-3/C-5′, C-7′, and C-15′. The H-7′ show correlation with C-2′/C-6′, and C-9′. The H-8′ show correlation with C-7′, C-9′, and C-aromatic (C-10′ and C11'). The H-aromatic show correlation with C-9′ and C-aromatic. These correlations confirmed the aromatic ring with piperidinone ring of

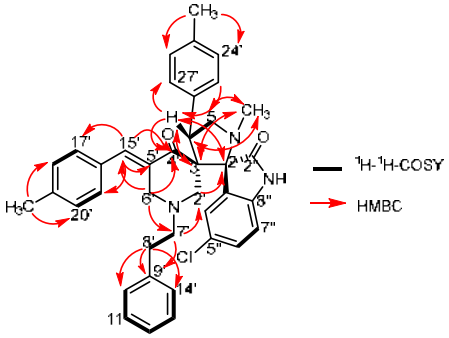

Fig 1. Selected ^{1}H-^{1}H COSY and HMBC correlations of **6b**

compound **6b**. The elucidated structure of the compound was further confirmed with mass spectroscopy analysis. The spectral of compounds obtained agreed with the proposed structure.

A proposed reaction mechanism for the formation of the spiro-pyrrolidine is shown in Scheme 2. The mechanism involves the formation of azomethine ylides, formed via decarboxylative condensation of isatin analogs (**3** or **4**) and sarcosine (**2**), which then undergo [2+3] cycloaddition to give the spiro-pyrrolidines **5** and **6**, respectively. Previous studies showed that spiropyrrolidine reactions are chemoselective and regioselective [26,33]. A dipole addition has occurred only to the available C=C bond and not at the C=O functional group of **1**. The nucleophilic carbon of azomethine ylide tends to attack the end of enone fragment of the exocyclic dipolarophiles substrate **1** to produce cycloadducts **5** and **6**, respectively. This reaction was conducted in methanol solvent. A previous study reported that methanol solvent has a high stabilization of polar transition state. Thus, it produces a good yield of spiro-pyrrolidine in a shorter reaction time [34]. The stereochemistry of spiropyrrolidines was compared with literature and confirmed with x-ray structure reported by Girgis et al. [28-29].

Molecular Docking Studies

The compounds **5** and **6** were constructed using Chemdraw Professional 15.1 and were converted from sdf to pdb format before starting the docking process. The native ligand, EBN in the active site of WNV NS2B-NS3 protease, was removed and re-dock (-8.20 kcal/mol)

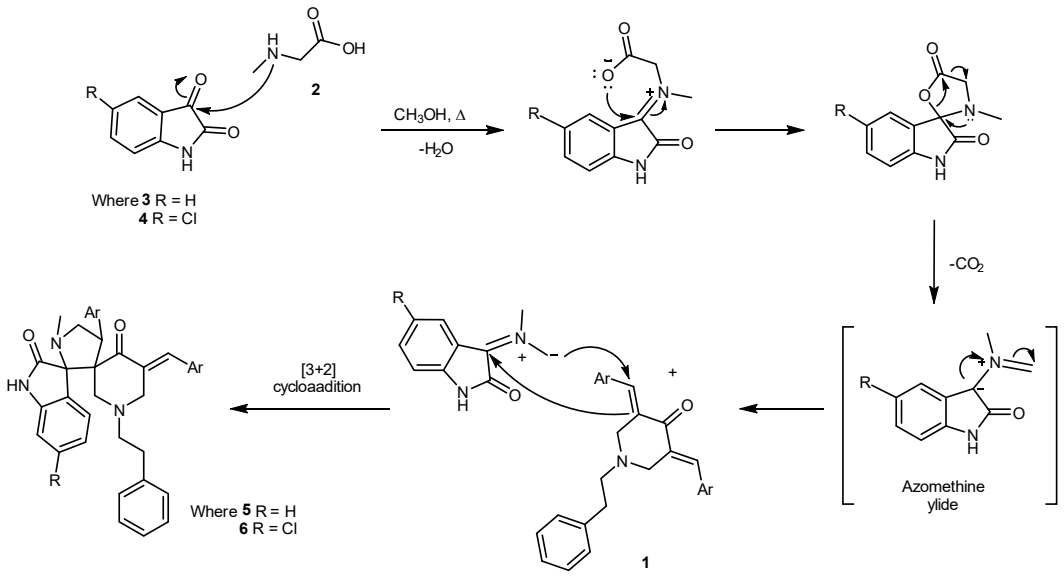

Scheme 2. Proposed mechanism for the formation of spiropyrrolidines

with the synthesized compounds using Autodock 4.2. From Table 1, it was found that all the synthesized compounds docked well into the enzyme's active site. The low binding energy indicates the formation of a favorable stable enzyme-ligand complex with a low inhibitory constant, K_i value [35]. Hydrogen bonds were the primary interaction between compounds **5** and **6** with catalytic triad residue of WNV NS2B-NS3 serine protease (His51, Asp75, and Ser135) [36]. Compound **5c** was postulated from the docking results to form four hydrogen bonds, while the other compounds may have two or fewer hydrogen bonds.

Based on this result, Compound **5c** was deemed to have a good binding affinity with the enzyme with the free binding energy of -7.71 kcal/mol and estimated inhibition constant, K_i of 1.73 μM. Fig. 2 showed the binding orientation of compound **5c** into the active site of WNV NS2B-NS3 protease (PDB: 2YOL) with two hydrogen interactions (yellow dotted lines) formed between **5c** and

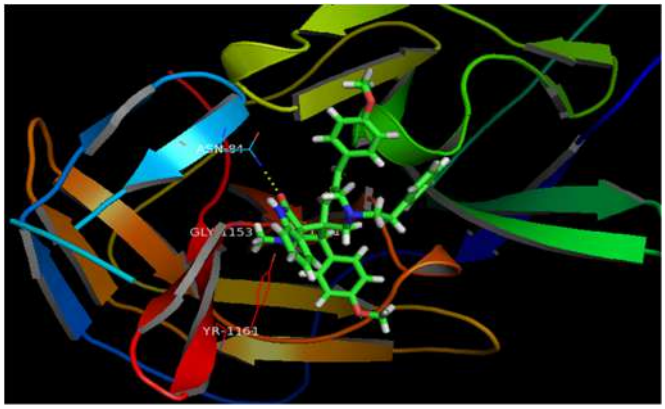

Fig 2. Docking pose of compound **5c** in the active site of WNV NS2B-NS3 protease (PDB code: 2YOL). Hydrogen bonds which are shown as yellow dotted lines were formed between **5c** and residues Asn84

Table 1. Binding energy and inhibitory constant of synthesized spiropyrrolidine compounds

Compd.	Ar	Binding energy (kcal/mol)	Estimated inhibition constant, K_i (μm)	RMSD (Å)
5a	Phenyl	-7.49	1.82	1.50
5b	4-Methylphenyl	-7.54	1.76	1.76
5c	4-Methoxyphenyl	-7.71	1.73	1.54
6a	Phenyl	-7.56	1.86	1.82
6b	4-Methylphenyl	-7.83	1.71	1.60
6c	4-Methoxyphenyl	-7.84	1.83	1.58
EBN	-	-8.20	0.98	-

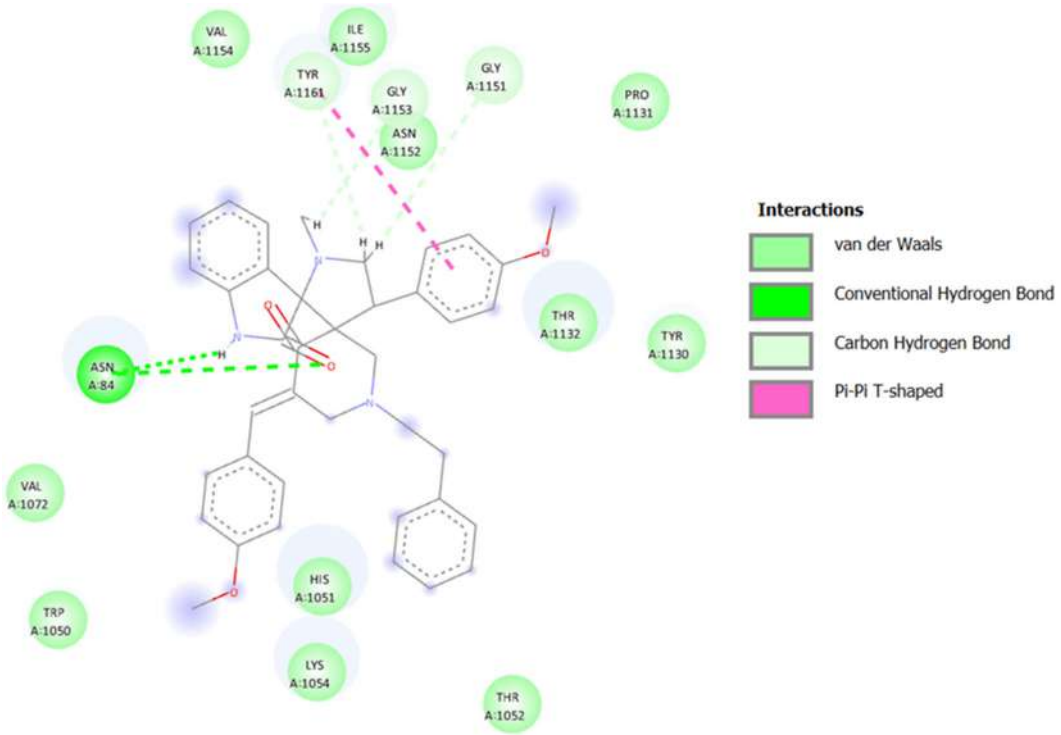

Fig 3. 2D interaction diagram of **5c** with the residues within 2 Å in the active pocket. Hydrogen bonding interactions were represented by green dashed lines

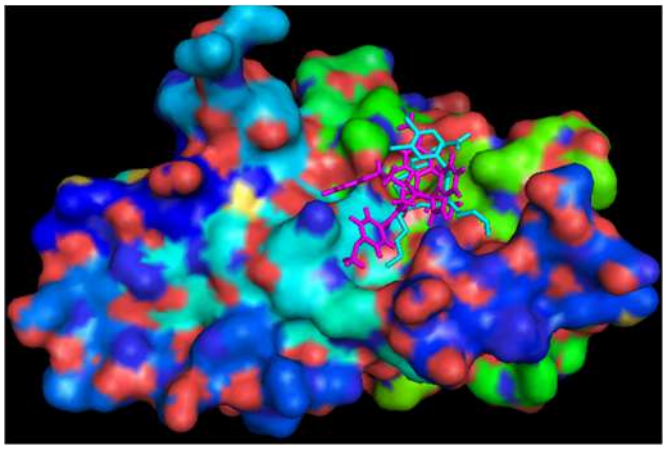

Fig 4. Comparison of docking pose of the native ligand (cyan) and **5c** (magenta) in the active site of WNV N2B-NS3 protease

residues Asn84 (2.139 Å). The distance of hydrogen bond interaction between hydrogen and heteroatom is within the range of 2.5–3.5 Å, with a bond angle at 109–110° [37]. π-π interactions between the Tyr1161 and terminal phenyl ring and two Van der Waals interactions with the Gly1151 and Gly1153 residues were also observed. The hydrogen bond formed between **5c** with the Asn84 through the C=O and -NH of the oxindole ring (Fig. 3). However, there was no interaction has been detected between compound **5c** with the catalytic triad of NS2B-NS3. It was observed that the complexes are exhibiting a similar type of interactions occupying the same active site pocket compared to the reference compound of the native ligand. Fig. 4 showed docking poses of native ligand and **5c**. The structure of synthesized compounds was more complex and bulkier, thus hindering them from embedding well into the enzyme's active site. As this is a preliminary prediction, further experimental studies are needed to validate the docking results.

■ CONCLUSION

The facile one-pot, three components [3+2]-cycloaddition protocol leading to the synthesis of new spiro-pyrrolidines has been described. In docking studies, compound **5c** shows a promising result as the inhibitor for WNV with four hydrogen bonding occur with active site residue, the free binding energy of -7.71 kcal/mol and estimated inhibition constant, Ki of 1.73 μm. Although the series can be useful for developing anti-

dengue agents, further study is required to understand the interaction, improvise, and validate the result.

■ ACKNOWLEDGMENTS

Mohamed Yusoff, N. thanks to the Malaysian government for the scholarship (MyBrain15) and Universiti Sains Malaysia (USM) under grant no. [RUI 1001/PKIMIA/8011072] to financially support this research.

■ AUTHOR CONTRIBUTIONS

Conceptualization, HO, MAA, YKY, and MNA; methodology, NMY, MAA, YKY, HO, MNA, and VM; software, MZH, and EEK; validation, HO, and MNA; formal analysis, NMY, MZH, MSAG, and EEK; investigation, NMY, MSAG, MZH, EEK, and the US; resources, HO, and MNA; data curation, NMY, and MSAG; writing-original draft preparation, NMY, MSAG, MZH, and MNA; writing-review and editing, MNA, US, EEK, and MZH; visualization, NMY, and MNA; supervision, HO, and MNA; project administration, HO, and MNA; funding acquisition, HO, and MNA; All authors have read and agreed to the published version of the manuscript.

■ REFERENCES

[1] Pierson, T.C., and Diamond, M.S., 2020, The continued treat of emerging flaviviruses, *Nat. Microbiol.*, 5 (6), 796–812.

[2] Mackenzie, J.S., Gubler, D.J., and Petersen, L.R., 2004, Emerging flaviviruses: The spread and resurgence of Japanese encephalitis, West Nile and dengue viruses, *Nat. Med.*, 10 (12), S98–S109.

[3] Lim, S.P., 2019, Dengue drug discovery: Progress, challenges and outlook, *Antiviral Res.*, 163, 156–178.

[4] World Health Organization, 2017, *West Nile virus*, https://www.who.int/news-room/fact-sheets/detail/west-nile-virus, accessed on 25 August 2021.

[5] Peterson, L.R., Brault, A.C., and Nasci, R.S., 2013, West Nile virus: Review of the literature, *JAMA*, 310 (3), 308–315.

[6] Richner, J.M., Gmyrek, G.B., Govero, J., Tu, Y., van der Windt, G.J.W., Metcalf, T.U., Haddad, E.K., Textor, J., Miller, M.J., and Diamond, M.S., 2015, Age-dependent cell trafficking defects in draining lymph nodes impair adaptive immunity and control of West Nile virus infection, *PLoS Pathog.*, 11 (7), e1005027.

[7] Yao, Y., and Montgomery, R.R., 2016, Role of immune aging in susceptibility to West Nile virus, *Methods Mol. Biol.*, 1435, 235–247.

[8] Montgomery, R.R., 2017, Age-related alterations in immune responses to West Nile virus infection, *Clin. Exp. Immunol.*, 187 (1), 26–34.

[9] da Silva-Júnior, E.F., and de Araújo-Júnior, J.X., 2019, Peptide derivatives as inhibitors of NS2B-NS3 protease from Dengue, West Nile, and Zika flaviviruses, *Bioorg. Med. Chem.*, 27 (18), 3963–3978.

[10] Bakonyi, T., and Haussig, J.M., 2020, West Nile virus keeps on moving up in Europe, *Eurosurveillance*, 25 (46), 2001938.

[11] Luo, D., Vasudevan, S.G., and Lescar, J., 2015, The flavivirus NS2B–NS3 protease-helicase as a target for anti-viral drug development, *Antiviral Res.*, 118, 148–158.

[12] Bastos Lima, A., Behnam, M.A.M., El Sherif, Y., Nitsche, C., Vechi, S.M., and Klein, C.D., 2015, Dual inhibitors of the dengue and West Nile virus NS2B–NS3 proteases: Synthesis, biological evaluation and docking studies of novel peptide-hybrids, *Bioorg. Med. Chem.*, 23 (17), 5748–5755.

[13] Chappell, K., Stoermer, M., Fairlie, D., and Young, P., 2008, West Nile virus NS2B/NS3 protease as anti-viral target, *Curr. Med. Chem.*, 15 (27), 2771–2784.

[14] Li, Z., Sakamuru, S., Huang, R., Brecher, M., Koetzner, C.A., Zhang, J., Chen, H., Qin, C.F., Zhang, Q.Y., Zhou, J., Kramer, L.D., Xia, M., and Li, H., 2018, Erythrosin B is a potent and broad-spectrum orthosteric inhibitor of the flavivirus NS2B-NS3 protease, *Antiviral Res.*, 150, 217–225.

[15] Skoreński, M., Milewska, A., Pyrć, K., Sieńczyk, M., and Oleksyszyn, J., 2019, Phosphonate inhibitors of West Nile virus NS2B/NS3 protease, *J. Enzyme Inhib. Med. Chem.*, 34 (1), 8–14.

[16] Kang, C., Gayen, S., Wang, W., Severin, R., Chen, A.S., Lim, H.A., Chia, C.S.B., Schüller, A., Doan,

D.N.P., Poulsen, A., Hill, J., Vasudevan, S.G., and Keller, T.H., 2013, Exploring the binding of peptidic West Nile virus NS2B–NS3 protease inhibitors by NMR, *Antiviral Res.*, 97 (2), 137–144.

[17] Wei, A.C., Ali, M.A., Yoon, K.Y., Ismail, R., Choon, T.S., Kumar, R.S., Arumugam, N., Almansour, A.I., and Osman, H., 2012, Antimycobacterial activity: A facile three-component [3+2]-cycloaddition for the regioselective synthesis of highly functionalised dispiropyrrolidines, *Bioorg. Med. Chem. Lett.*, 22 (15), 4930–4933.

[18] Wei, A.C., Ali, M.A., Yoon, K.Y., Ismail, R., Choon, T.S., and Kumar, R.S., 2013, A facile three-component [3+2]-cycloaddition for the regioselective synthesis of highly functionalised dispiropyrrolidines acting as antimycobacterial agents, *Bioorg. Med. Chem. Lett.*, 23 (5), 1383–1386.

[19] Wei, A.C., Ali, M.A., Yoon, K.Y., Ismail, R., Choon, T.S., Khaw, K.Y., Murugaiyah, V., and Lakshmipathi, V.S., 2014, Synthesis of highly functionalised dispiropyrrolidine derivatives as novel acetylcholinesterase inhibitors, *Lett. Drug Des. Discovery*, 11 (2), 156–161.

[20] Kumar, R.S., Rajesh, S.M., Perumal, S., Banerjee, D., Yogeeswari, P., and Sriram, D., 2010, Novel three-component domino reactions of ketones, isatin and amino acids: Synthesis and discovery of antimycobacterial activity of highly functionalised novel dispiropyrrolidines, *Eur. J. Med. Chem.*, 45 (1), 411–422.

[21] Lawson, S., Arumugam, N., Almansour, A.I., Kumar, R.S., and Thangamani, S., 2020, Dispiropyrrolidine tethered piperidone heterocyclic hybrids with broad-spectrum antifungal activity against *Candida albicans* and *Cryptococcus neoformans*, *Bioorg. Chem.*, 100, 103865.

[22] Karthikeyan, K., Sivakumar, P.M., Doble, M., and Perumal, P.T., 2010, Synthesis, antibacterial activity evaluation and QSAR studies of novel dispiropyrrolidines, *Eur. J. Med. Chem.*, 45 (8), 3446–3452.

[23] Hassaneen, H.M., Eid, E.M., Eid, H.A., Farghaly, T.A., and Mabkhot, Y.N., 2017, Facial regioselective synthesis of novel bioactive spiropyrrolidine/pyrrolizine-oxindole derivatives via a three components reaction as potential antimicrobial agents, *Molecules*, 22 (3), 357.

[24] Bhaskar, G., Arun, Y., Balachandran, C., Saikumar, C., and Perumal, P.T., 2012, Synthesis of novel spirooxindole derivatives by one pot multicomponent reaction and their antimicrobial activity, *Eur. J. Med. Chem.*, 51, 79–91.

[25] Almansour, A.I., Arumugam, N., Kumar, R.S., Althamili, D.M., Periyasami, G., Ponmurugan, K., Al-Dhabi, N.A., Perumal, K., and Premnath, D., 2019, Domino multicomponent approach for the synthesis of functionalized spiro-Indeno[1,2-*b*]quinoxaline heterocyclic hybrids and their antimicrobial activity, synergistic effect and molecular docking simulation, *Molecules*, 24 (10), 1962–1976.

[26] Almansour, A.I., Kumar, R.S., Beevi, F., Shirazi, A.N., Osman, H., Ismail, R., Choon, T.S., Sullivan, B., McCaffrey, K., Nahhas, A., and Parang, K., 2014, Facile, regio-and diastereoselective synthesis of spiro-pyrrolidine and pyrrolizine derivatives and evaluation of their antiproliferative activities, *Molecules*, 19 (7), 10033–10055.

[27] Girgis, A.S., Panda, S.S., Ahmed Farag, I.S., El-Shabiny, A.M., Moustafa, A.M., Ismail, N.S.M., Pillai, G.G., Panda, C.S., Hall, C.D., and Katritzky, A.R., 2015, Synthesis, and QSAR analysis of anti-oncological active spiro-alkaloids, *Org. Biomol. Chem.*, 13 (6), 1741–1754.

[28] Girgis, A.S., Panda, S.S., Aziz, M.N., Steel, P.J., Hall, C.D., and Katritzky, A.R., 2015, Rational design, synthesis, and 2D-QSAR study of anti-oncological alkaloids against hepatoma and cervical carcinoma, *RSC Adv.*, 5 (36), 28554–28569.

[29] Girgis, A.S., Panda, S.S., Shalaby, E.M., Mabied, A.F., Steel, P.J., Hall, C.D., and Katritzky, A.R., 2015, Regioselective synthesis and theoretical studies of an anti-neoplastic fluoro-substituted dispirooxindole, *RSC Adv.*, 5 (19), 14780–14787.

[30] Murugan, R., Anbazhagan, S., and Narayanan, S.S., 2009, Synthesis and in vivo antidiabetic activity of

novel dispiropyrrolidines through [3+2] cycloaddition reactions with thiazolidinedione and rhodanine derivatives, *Eur. J. Med. Chem.*, 44 (8), 3272–3279.

[31] Toumi, A., Boudriga, S., Hamden, K., Sobeh, M., Cheurfa, M., Askri, M., Knorr, M., Strohmann, C., and Brieger, L., 2021, Synthesis, antidiabetic activity and molecular docking study of rhodanine-substitued spirooxindole pyrrolidine derivatives as novel α-amylase inhibitors, *Bioorg. Chem.*, 106, 104507.

[32] Ali, M.A., Lakshmipathi, V.S., Beevi, F., Kumar, R.S., Ismail, R., Choon, T.S., Wei, A.C., Yoon, Y.K., and Basiri, A., 2013, Antimycobacterial activity: Synthesis and biological evaluation of novel substituted (3E,5E)-3,5-diarylidene-1-phenethylpiperidine-4-one derivatives, *Lett. Drug Des. Discovery*, 10 (5), 471–476.

[33] Shalaby, E.M., Girgis, A.S., Moustafa, A.M., ElShaabiny, A.M., El-Gendy, B.E.M., Mabied, A.F., and Farag, I.S.A., 2014, Regioselective synthesis, stereochemical structure, spectroscopic characterization and geometry optimization of dispiro [3*H*-indole-3,2′-pyrrolidine-3′,3″-piperidines], *J. Mol. Struct.*, 1075, 327–334.

[34] Kumar, R.S., and Perumal, S., 2007, Novel three-component tandem reactions of cyclic mono ketones, isatin and sarcosine: Formation of dispiropyrrolidines, *Tetrahedron Lett.*, 48 (40), 7164–7168.

[35] Osman, H., Idris, N.H., Kamarulzaman, E.E., Wahab, H.A., and Hassan, M.Z., 2017, 3,5-Bis(arylidene)-4-piperidones as potential dengue protease inhibitors, *Acta Pharm. Sin. B,* 7 (4), 479–484.

[36] Skoreński, M., Milewska, A., Pyrć, K., Sieńczyk, M., and Oleksyszyn, J., 2019, Phosphonate inhibitors of West Nile virus NS2B/NS3 protease, *J. Enzyme Inhib. Med. Chem.*, 34(1), 8–14.

[37] de Oliveira, A.S., Gazolla, P.A.R., Oliveira, A.F.C.S., Pereira, W.L., de S Viol, L.C., Maia, A.F.S., Santos, E.G., da Silva, Í.E.P., Mendes, T.A.O., da Silva, A.M., Dias, R.S., da Silva, C.C., Polêto, M.D., Teixeira, R.R., and de Paula, S.O., 2019, Discovery of novel West Nile Virus protease inhibitor based on isobenzonafuranone and triazolic derivatives of eugenol and indan-1,3-dione scaffolds, *PLoS One,* 14 (9), e0223017.

Synthesis, Characterization and Theoretical Studies of New Organotellurium Compounds Based on (4-(((1S,E)-1,7,7-trimethylbicyclo[2.2.1]heptan-2-ylidene)amino)phenyl)mercury(II) Chloride

Nuha Hussain Al-Saadawy

Department of Chemistry, College of Science, University of Thi-Qar, Thi-Qar, Iraq

* ***Corresponding author:***

email: nuh.hussain@sci.utq.ed.iq

Received: May 27, 2021
Accepted: July 7, 2021

DOI: 10.22146/ijc.66143

Abstract: *The current study aimed to prepare new organomercury and organotellurium compounds based on the condensation reaction of 1,7,7-trimethylbicyclo[2.2.1]heptan-2-one (camphor) and p-aminophenyl mercuric(II) chloride. All the prepared compounds were characterized using different methods such as infrared spectroscopy, nuclear magnetic resonance, and CHN analysis. The analysis results concurred with the suggested chemical structures of the prepared compounds. Density functional theory has been applied with the basis set of 3-21G to investigate the molecular structure of the prepared organotellurium compounds. Geometrical structure, HOMO surfaces, LUMO surfaces, and energy gap have been produced throughout the geometry optimization. The molecular geometry and contours for organotellurium compounds have been investigated throughout the geometrical optimization. Also, the donor and acceptor have been studied by comparing the HOMO energies of the prepared organotellurium compounds. Finally, the electronegativity, electrophilicity, ionization potential, electron affinity, and lower case of organotellurium compounds have been calculated and discussed.*

Keywords: *organotellurium; HOMO and LUMO energies; camphor and Density functional theory*

■ INTRODUCTION

Although the first organotellurium compound was prepared in 1840, this field of organic chemistry had not been systematically studied until the middle of the present century [1]. The first serious attempt to systematize organotellurium chemistry was undertaken by Rheinboldt, a German chemist who introduced chemistry in Brazil in 1934 [1]. In the last ten years, considerable development of organic tellurium chemistry has been observed, and several review articles and books on the subject have been published, focusing on the general reactions used to prepare the organotellurium compounds and the useful synthetic transformations promoted or suffered by them [2-5]. Recently, emphasis has been given to the recent contributions of the related laboratory where they explored old reactions trying to establish their generality or make transformations into the organotellurium compounds, which can lead to applicable synthetic methodologies [4,6-11]. The quantum mechanical wave function contains all the information about the studied system. Then, the allowed energy states of the system can be determined. Some approximations must involve a solved problem, albeit tricky [12-13]. Density functional theory (DFT) is referred by computational codes in the Gaussian 09 program and can be used in applications to investigate the structural, electronic, and some physical properties of the molecules and materials, such as the binding energies of the molecules in chemistry, physics, and other areas [14-17]. Density functional theory deals with Gaussian orbitals, in which Gaussian function changes exponentially with the square value of the position [18-19]. One of the most popular 12 basis sets in density functional theory is the hybrid functional B3LYP [20]. The purpose of the present study is to prepare organomercury and organotellurium compounds derived from 1,7,7-trimethylbicyclo[2.2.1]heptan-2-one (camphor) and *p*-aminophenyl mercuric(II) chloride and their derivatives by a condensation reaction.

■ EXPERIMENTAL SECTION

Materials

The chemicals used included Camphor, ethanol absolute, glacial acetic acid, mercuric acetate, bromine, chloroform, dioxin, sodium metal, potassium hydroxide, toluene, hydrazine hydrate, methanol, petroleum ether (60–80 °C) (Sigma-Aldrich), Aniline (Avantor), Lithium chloride (VWR), Tellurium powder (Strem chemicals Inc.), Hydrochloric acid (HGB), and Molecular sieves (ACS). All were used without further purification.

Instrumentation

^{1}H-NMR spectra were recorded on Bruker 500 MHz spectrometers with TMS as an inner reference utilizing soluble DMSO-d_6. Elemental analysis for carbon, hydrogen, and nitrogen was performed using a Euro vector EA 3000A Elemental Analysis (Italy). Infrared spectra were recorded with KBr circles utilizing an FT-IR spectrophotometer Shimadzu model 8400 S in 4000–250 cm^{-1}.

Procedure

(E)-(4-((1,7,7-trimethylbicyclo[2.2.1]heptan-2-ylidene) amino)phenyl)mercury(II) chloride (A)

1,7,7-Trimethylbicyclo[2.2.1]heptan-2-one (0.04 mol, 6.08 g)was dissolved in 25 mL of hot ethanol. Then, 3 drops of glacial acetic acid were added and the mixture was stirred for 15 min in a water bath (70 °C). The formed solution of 0.04 mol (13.13 g) (4-aminophenyl) mercury(II) chloride [21-22] was then added to 25 mL of ethanol and the mixture was stirred for 16 h in a water bath (70 °C), then filtrated and cooled at a room temperature. White crystals were formed with a yield of 85% and a melting point of 179–181 °C. CHN: theoretical %: C, 41.56; H, 4.36; N, 3.03; practical %: C, 41.40; H, 4.95; N, 3.45; FT-IR using KBr: υ (C–H) Aliphatic = 2337 cm^{-1}, υ (C–H) Aromatic = 3164 cm^{-1}, υ (C =N) Aliphatic = 1612 cm^{-1}, υ (C–N) Aromatic = 1249 cm^{-1}, υ (C=C) Aromatic = 1490 cm^{-1}; ^{1}H-NMR (500 MHz, DMSO-d_6) δ $_{10}$CH$_3$, $_{11}$CH$_3$ (6H, s, 1.90); $_1$CH$_3$ (3H, s, 2.33); $_7$CH$_2$, $_8$CH$_2$ (4H, m, 2.75–2.79); $_5$CH$_2$ (2H, t, 4.85); $_6$CH (1H, s, 5.77); Ar-H (4H, m, 8.23–9.20). As shown in Scheme 1, Table 1 and 2, Fig. 1.

(E)-1,7,7-trimethyl-N-(4-(tribromo-l4-tellaneyl) phenyl) bicyclo[2.2.1]heptan-2-imine (B)

A solution of (E)-(4-((1,7,7-trimethylbicyclo[2.2.1] heptan-2-ylidene)amino)phenyl) mercury(II) chloride (0.008 mol., 3.69 g) and tellurium tetrabromide (0.008 mol., 3.57 g) in dry dioxane 60 mL was refluxed for 14 h. The solution was filtered while hot. After cooling to room temperature [23], the formed brown precipitate was collected by filtration. Recrystallization by using glacial acetic acid to give reddish-brown crystals, yield 65%, m.p. 165–166 °C, CHN: theoretical %: C, 32.37; H, 3.40; N, 2.36; practical %: C, 31.99; H, 3.23; N, 2.76; FT-IR using KBr: υ (C–H) Aliphatic = 2300 cm^{-1}, υ (C–H) Aromatic = 3170 cm^{-1}, υ (C =N) Aliphatic = 1629 cm^{-1}, υ (C–N) Aromatic = 1224 cm^{-1}, υ (C =C) Aromatic = 1402 cm^{-1}; ^{1}H-NMR (500 MHz, DMSO-d_6) δ $_{10}$CH$_3$, $_{11}$CH$_3$ (6H, s, 1.91); $_1$CH$_3$ (3H, s, 1.35); $_7$CH$_2$, $_8$CH$_2$ (4H, s, 2.08); $_5$CH$_2$ (2H, s, 5.95); $_6$CH (1H, s, 2.35); Ar-H (4H, m, 7.83–9.12). As shown in Scheme 1, Table 1 and 2, Fig. 2.

(E)-4-(dibromo(4-((1,7,7-trimethylbicyclo[2.2.1] heptan -2-ylidene)amino)phenyl)-l4-tellaneyl)aniline (C)

A solution of (E)-1,7,7-trimethyl-N-(4-(tribromo-l4-tellaneyl)phenyl)bicyclo[2.2.1]heptan-2-imine (0.0035 mol., 2.07 g) and (4-aminophenyl)mercury(II) chloride (0.0035 mol., 1.14 g) in (25 mL) of dry dioxane was refluxed for 4 h. The hot mixture was then filtered, and the filtrate was cooled to room temperature, leading to the precipitation of white plates of 2:1 complexes of dioxane and mercuric bromochloride that were filtered off. The filtrate was poured into 100 mL of cold distilled water to form brown crystals [23], with a yield of 59%, and a melting point of 143–145 °C, CHN: theoretical %: C, 43.61; H, 4.33; N, 4.62; practical %: C, 43.34; H, 4.13; N, 4.43; FT-IR using KBr: υ (C–H) Aliphatic = 2925 cm^{-1}, υ (C–H) Aromatic = 3068 cm^{-1}, υ (C=N) Aliphatic = 1627 cm^{-1}, υ (C–N) Aromatic = 1280 cm^{-1}, υ (C=C) Aromatic = 1460 cm^{-1}; ^{1}H-NMR (500 MHz, DMSO-d_6) δ $_1$CH$_3$, $_{10}$CH$_3$, $_{11}$CH$_3$, $_5$CH, $_7$CH$_2$, $_8$CH$_2$ (13H, m, 1.80–2.31); $_6$CH (1H, s, 5.74); Ar-H (8H, m, 7.92–8.90); NH$_2$ (2H, s, 4.19) as shown in Scheme 2., Table 1 and 2, Fig. 3.

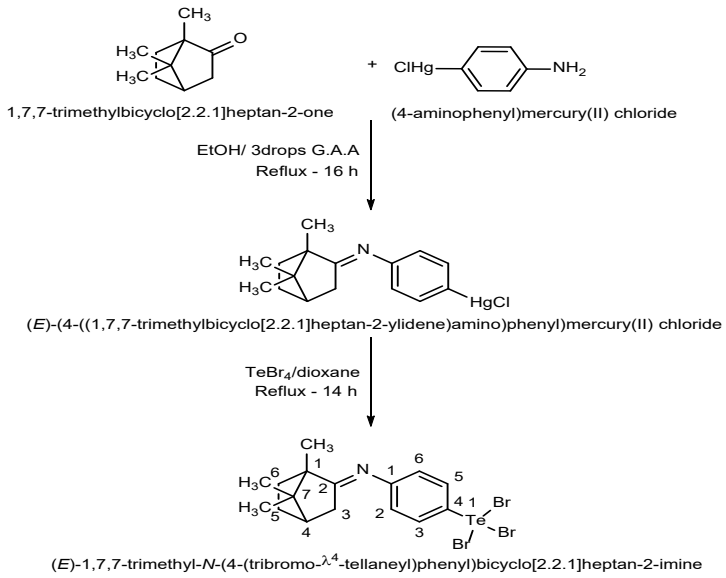

Scheme 1. Preparation of organomercury and organyl tellurium tribromide compounds

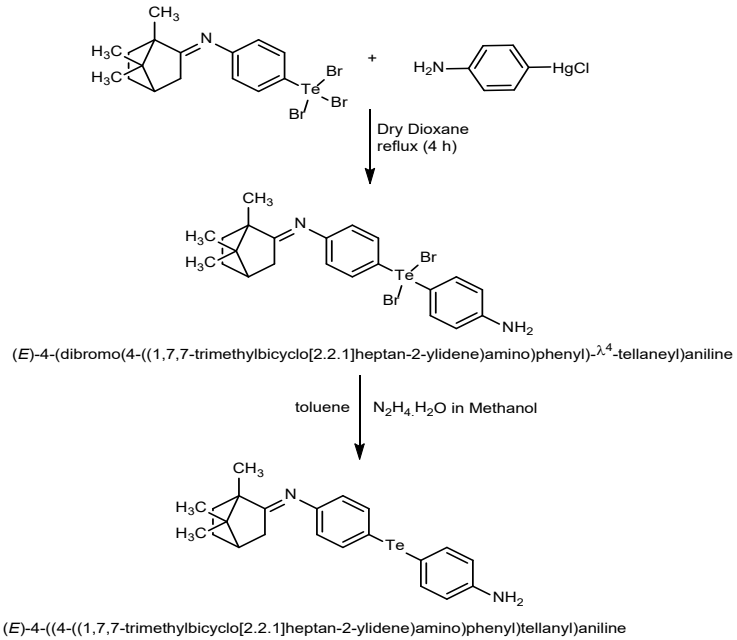

Scheme 2. Preparation of organyl tellurium dibromide and diorganyl telluride

(E)-4-((4-((1,7,7-trimethylbicyclo[2.2.1]heptan-2-ylidene)amino)phenyl)tellanyl)aniline (D)

(E)-4-(dibromo(4-((1,7,7-trimethylbicyclo[2.2.1]heptan-2-ylidene)amino)phenyl)-l4-tellaneyl)aniline (0.0032 mol., 1.94 g) was dissolved in toluene (30 mL). To the refluxing solution, hydrazine hydrate (0.0032 mol, 0.16 g) in methanol (30 mL) was added dropwise. The resulting solution was poured into cold water (100 mL) and the brown solid that had formed was recrystallized from petroleum ether (60–80 °C) to give brown crystals [23], with a yield of 53%, and a melting point of 81–82 °C; CHN: theoretical %: C, 59.24; H, 5.88; N, 6.28; practical %: C, 59.10; H, 5.31; N, 6.44; FT-IR using KBr: υ (C–H) Aliphatic = 2854 cm^{-1}, υ (C–H) Aromatic = 3205 cm^{-1}, υ (C=N) Aliphatic = 1635 cm^{-1}, υ (C–N) Aromatic = 1280 cm^{-1}, υ (C=C) Aromatic = 1415 cm^{-1}; ^{1}H-NMR (500 MHz, DMSO-d_6) δ $_{10}CH_3$, $_{11}CH_3$ (6H, s, 1.90); $_1CH_3$ (3H, s, 2.06); $_7CH_2$, $_8CH_2$ (4H, s, 2.20); $_5CH_2$ (2H, d, 2.33);

Table 1. ^{1}H-NMR spectral data of selected compounds

	Structure of the compound	^{1}H-NMR (DMSO-d_6); TMS = 0 ppm
A	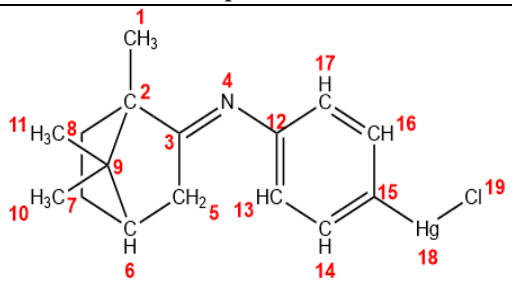	$_{10}CH_3$, $_{11}CH_3$ (6H, s, 1.90); $_{1}CH_3$ (3H, s, 2.33); $_{7}CH_2$, $_{8}CH_2$ (4H, m, 2.75–2.79); $_{5}CH_2$ (2H, t, 4.85); $_{6}$CH (1H, s, 5.77); Ar-H (4H, m, 8.23–9.20).
B	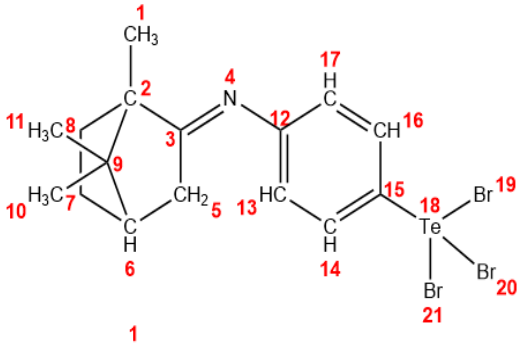	$_{10}CH_3$, $_{11}CH_3$ (6H, s, 1.91); $_{1}CH_3$ (3H, s, 1.35); $_{7}CH_2$, $_{8}CH_2$ (4H, s, 2.08); $_{5}CH_2$ (2H, s, 5.95); $_{6}$CH (1H, s, 2.35); Ar-H (4H, m, 7.83–9.12).
C	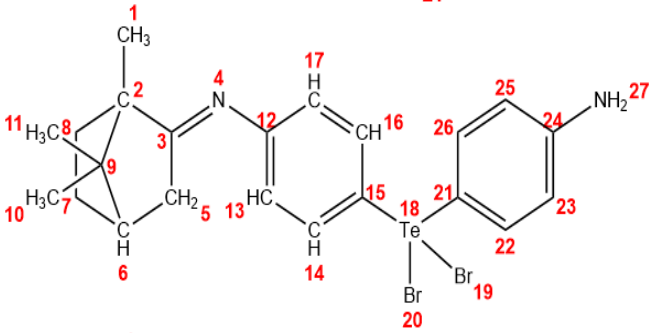	$_{1}CH_3$, $_{10}CH_3$, $_{11}CH_3$, $_{5}$CH, $_{7}CH_2$, $_{8}CH_2$ (13H, m, 1.80–2.31); $_{6}$CH (1H, s, 5.74); Ar-H (8H, m, 7.92–8.90); NH_2 (2H, s, 4.19)
D	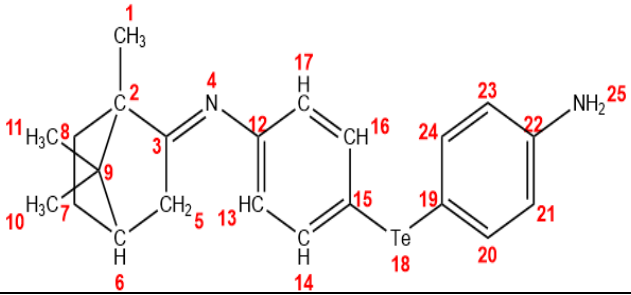	$_{10}CH_3$, $_{11}CH_3$ (6H, s, 1.90); $_{1}CH_3$ (3H, s, 2.06); $_{7}CH_2$, $_{8}CH_2$ (4H, s, 2.20); $_{5}CH_2$ (2H, d, 2.33); $_{6}$CH (1H, t, 5.77); Ar-H (8H, m, 8.02–9.02); NH_2 (2H, s, 4.09)

$_{6}$CH (1H, t, 5.77); Ar-H (8H, m, 8.02–9.02); NH_2 (2H, s, 4.09) as shown in Scheme 2, Table 1 and 2, Fig. 4.

■ RESULTS AND DISCUSSION

The present study involved the preparation of organomercury and organotellurium compounds derived from 1,7,7-trimethylbicyclo[2.2.1]heptan-2-one (camphor) by reacting 1,7,7-trimethylbicyclo[2.2.1]heptan-2-one and (4-aminophenyl)mercury(II) chloride in absolute ethanol and adding three drops of glacial acetic acid to obtain (E)-(4-((1,7,7-trimethyl bicyclo[2.2.1]heptan-2-ylidene) amino)phenyl)mercury(II) chloride. (E)-(4-((1,7,7-trimethyl bicyclo[2.2.1]heptan-2-ylidene)amino)phenyl) mercury(II) chloride then reacted with tellurium tetrabromide to give tellurium tribromide derivatives, starting materials for the remaining compounds prepared in this research.

^{1}H-NMR spectra [24, 25] of the compounds (A–D)

Table 2. FT-IR spectral data of selected compounds

Compound	Aliphatic C–H	Aromatic C–H	Aliphatic C=N	Aromatic C–N	Aromatic C=C
A	2337	3164	1612	1249	1490
B	2300	3170	1629	1224	1402
C	2925	3068	1627	1280	1460
D	2854	3205	1635	1280	1415

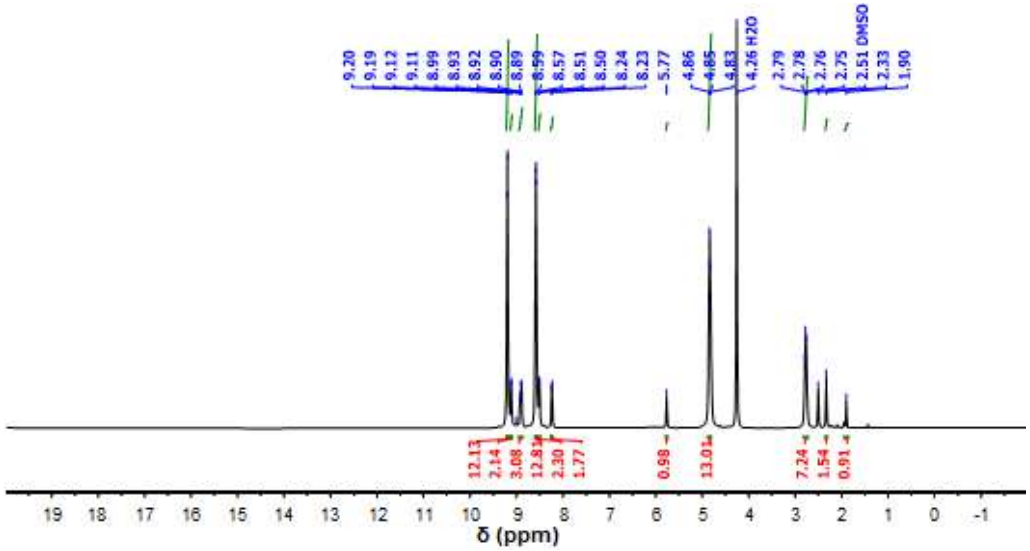

Fig 1. [1]H-NMR spectrum of compound A

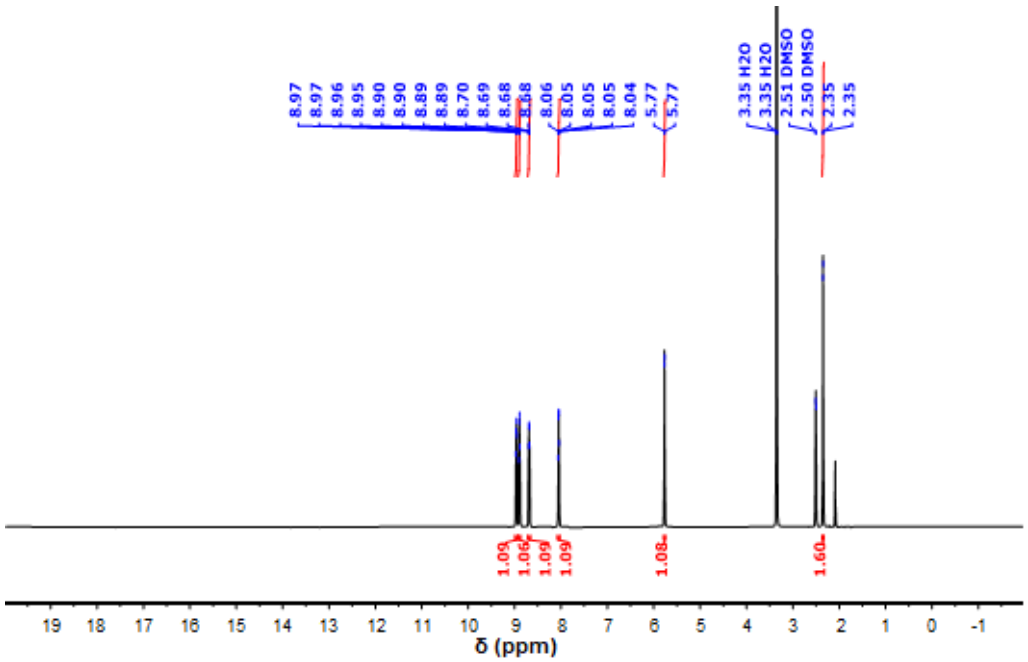

Fig 2. [1]H-NMR spectrum of compound B

showed all the expected peaks. All the spectra in deuterated DMSO are given in Table 1 and explained in Fig. (1–4).

All prepared compounds' IR spectra displayed common features in specific regions and characteristic bands in the fingerprint and other regions. The suggested

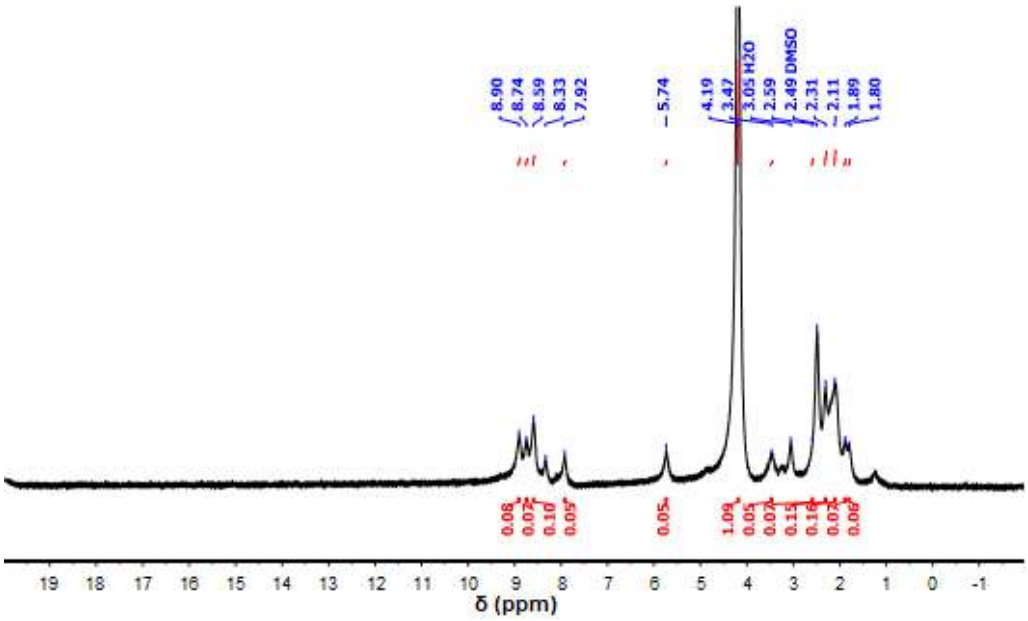

Fig 3. [1]H-NMR spectrum of compound C

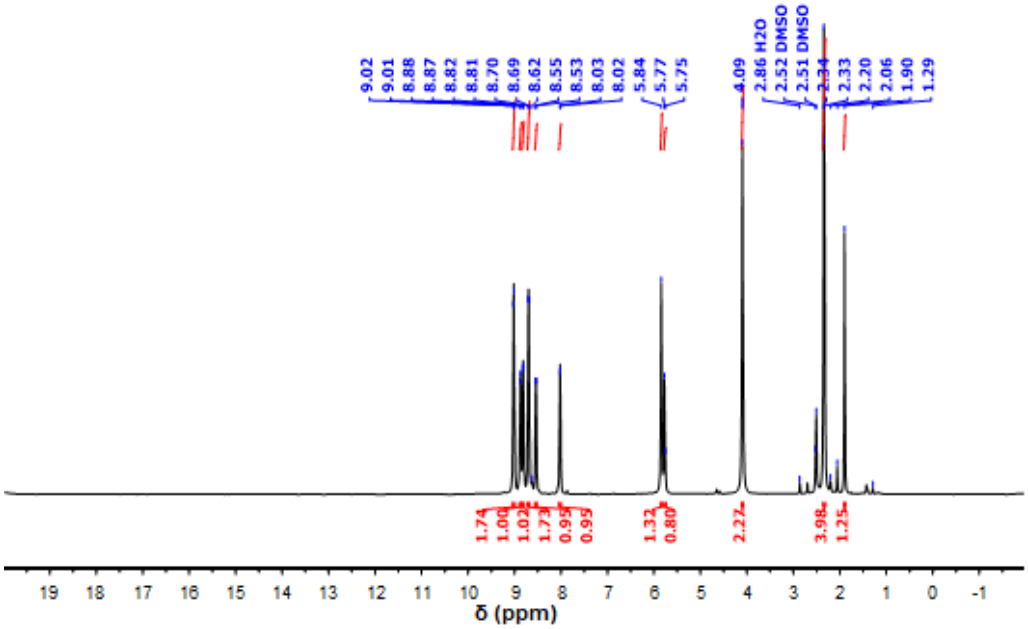

Fig 4. [1]H-NMR spectrum of compound D

structure for the prepared compounds was confirmed using the IR spectra [24-25], as shown in Table 2. The aromatic C–H [24-25] appeared at 3068–3205 cm^{-1} for organomercury and organotellurium derivatives, whereas the aliphatic C–H was obtained at 2925–2300 cm^{-1} for the prepared compounds. On the other hand, the aliphatic C=N group displayed an apparent band at 1612–1635 cm^{-1}, while the band at the range of 1224–1280 cm^{-1} [24-25] was attributed to the aromatic C–N for organomercury and organotellurium derivatives. The C=C aromatic bond appeared at the range of 1402–1490 cm^{-1} [24-25], as shown in Table 2.

Computational Study

All the organotellurium compounds under study were labeled as shown in Fig. 5–16. The accuracy of the

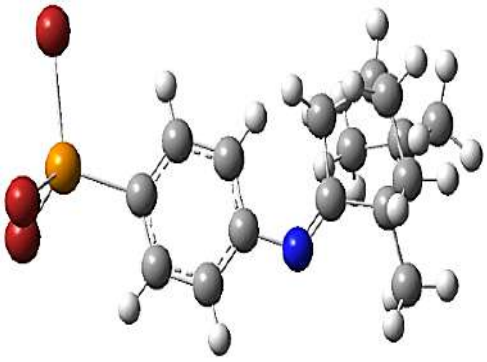

Fig 5. Molecular structure of compound B

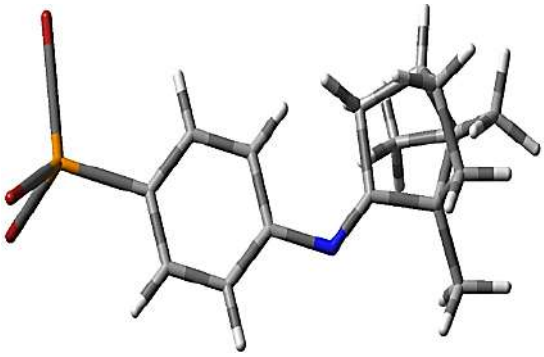

Fig 6. Sticks Molecular model of compound B

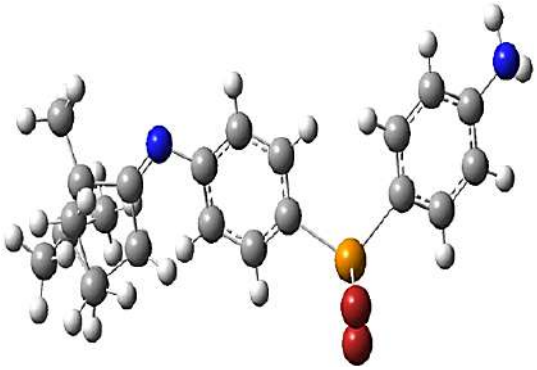

Fig 7. Molecular structure of compound C

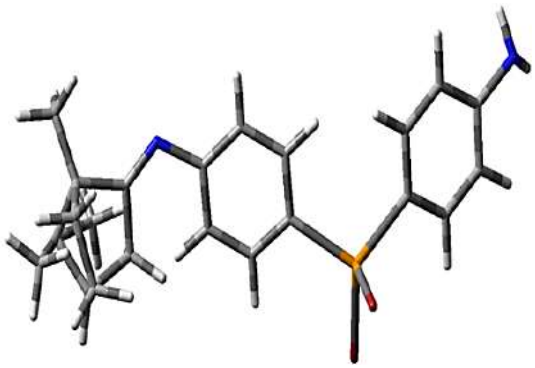

Fig 8. Sticks Molecular model of compound C

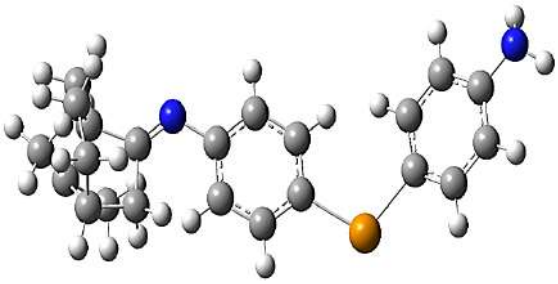

Fig 9. Molecular structure of compound D

Fig 10. Sticks Molecular model of compound D

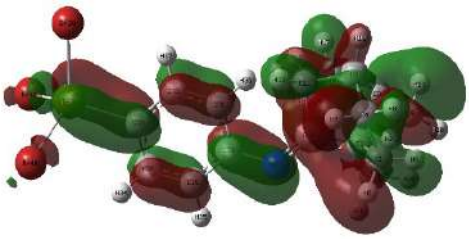

Fig 11. Molecular orbital (HOMO) of compound B

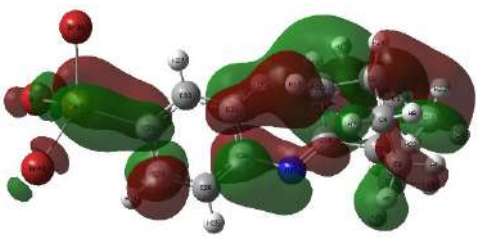

Fig 12. Molecular orbital (LUMO) of compound B

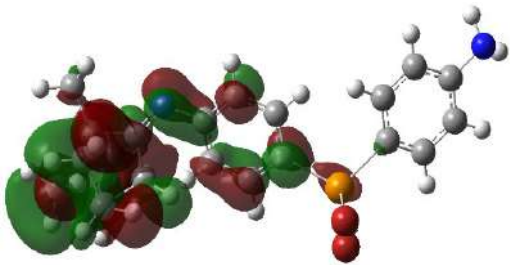

Fig 13. Molecular orbital (HOMO) of compound C

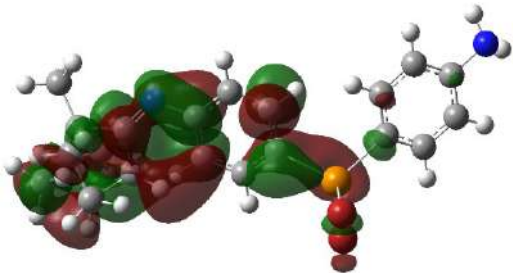

Fig 14. Molecular orbital (LUMO) of compound C

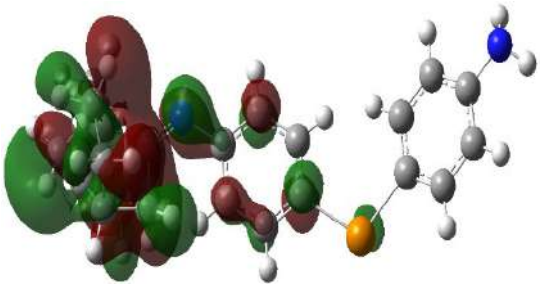

Fig 15. Molecular orbital (HOMO) of compound D

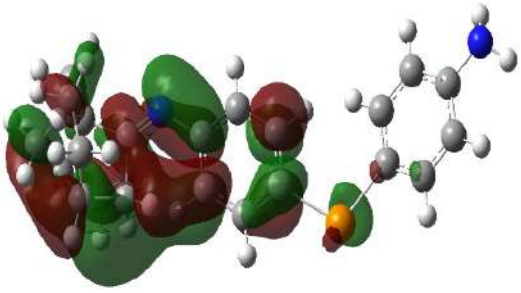

Fig 16. Molecular orbital (LUMO) of compound D

method was examined to describe the properties of the compound in the gas phase. The geometric structures and electronic properties were studied at all quantum calculations with the density functional theory (DFT) achieved at the hybrid functional B3LYP, which combines Becke's exchange and Lee, Yang, and Parr's correlation functional computational level [15,17]. This method described all atoms using the 3-21G basis set with Gaussian 09 program [19]. The reactivity and the stability of the compounds were evaluated using DFT-based descriptors that were calculated [26-27]:

$$\mu = \left(\frac{\partial E}{\partial N}\right)_{V(\vec{r}),T} \quad (1)$$

$$\eta = \frac{1}{2}\left(\frac{\partial^2 E}{\partial N^2}\right)_{V(\vec{r}),T} \quad (2)$$

$$S = \frac{1}{2\eta} \quad (3)$$

$$\omega = \frac{\mu^2}{2\eta} \quad (4)$$

Where μ, η, S, and ω are the chemical potential, chemical hardness, chemical softness, and electrophilicity, respectively, while E, N, and $V(\vec{r})$ are the total electron energy, number of electrons, and external potential, respectively. Two different methods were used to compute the above global quantities; the first is a finite difference approximation, based on the differences of total electronic energies when an electron is removed or added following the neutral molecule, and the second is Koopman's theorem, which is based on the differences between the HOMO and LUMO energies of the molecule [26-28]. By using a finite difference approximation, the global quantities can be given by [26-28]:

$$\chi = \frac{(IP + EA)}{2} \quad (5)$$

$$\eta = \frac{(IP - EA)}{2} \quad (6)$$

Then, using Koopman's theorem, the above equations are given by [28]:

$$\chi = \frac{(E_{HOMO} + E_{LUMO})}{2} \quad (7)$$

$$\eta = \frac{(E_{HOMO} - E_{LUMO})}{2} \quad (8)$$

Electronic Properties

The equilibrium geometries for all the study compounds were fully optimized at the DFT level of theory using a B3LYP functional along with the standard 3-21G basis set in the gaseous phase, see Fig. 5–16.

HOMO (High Occupied Molecular Orbital) and LUMO (Low Unoccupied Molecular Orbital) energies are the electronic states, referring to certain places of the existence of the electrons with quantized energies, where the molecular orbitals are in linear combination to the atomic orbitals. The difference between HOMO gives energy bandgap (E_g) as the relation [7]. The energy gap is a fundamental property in solids because it allows the prediction of the material, whether it is a conductor or insulator, or semiconductor. It stands for the energy difference between the lower virtual energy level and the higher full energy level [29], see Fig. (5–16) and Table 3.

$$Eg = E_{LUMO} - E_{HOMO} \quad (9)$$

Electronegativity and electrophilicity

We can define electronegativity as the measure of the tendency of an atom to attract a shared pair of electrons (or electron density) towards itself. In contrast, relative rate constants measure electrophilicity for reactions of different electrophilic reagents towards a common substrate (usually involving an attack at a carbon atom). Electronegativity and electrophilicity can be calculated from the relations 10 and 11 [15,20], see Table 4.

$$x = \frac{E_{HOMO} + E_{LUMO}}{2} \quad (10)$$

$$\omega = \frac{x^2}{2\eta} \quad (11)$$

Ionization potential and electron affinity

Ionization potential measures the binding force between the electron and the atom. It is equivalent to the required energy to remove one electron from a neutral atom in the gas state. Electron affinity can be defined as the energy released when an atom gains an electron. It is equivalent to the required energy that can remove an electron from a negative ion. According to Koopman's theory [15], as shown in Table 5.

$$I.P = -E_{HOMO} \quad (12)$$

$$E.A = -E_{LUMO} \quad (13)$$

Hardness softness acid base (HSAB principle)

This principle describes the behavior of molecules or atoms as the acids and bases in chemistry. First, it is necessary to show that the soft and hard bases represent donors, but soft and hard acids stand for acceptors. The following equations [28,30-32] can express hardness and softness:

$$\eta = \frac{I.P - E.A}{2} \quad (14)$$

$$\sigma = \frac{1}{2\eta} \quad (15)$$

η refers to chemical hardness, and σ refers to chemical softness. As explained in Table 6.

Table 3. Demonstrates electronic states of the organotellurium compounds

Compound	HOMO (eV)	LUMO (eV)	E_g (eV)
B	-6.0017	-5.6591	0.3426
C	-5.1209	-4.6333	0.4876
D	-5.1312	-4.8507	0.2805

Table 4. Electronegativity and electrophilicity of the organotellurium compounds

Compound	Electronegativity (eV) (X)	Electrophilicity (eV) (w)
B	-5.8304	-99.2223
C	-7.7923	-124.5281
D	-4.9909	-88.8341

Table 5. Ionization potential and electron affinity of the organotellurium compounds

Compound	Ionization potential (eV) (I.P)	Electron affinity (eV) (E.A)
B	6.0017	5.6591
C	5.1209	4.6333
D	5.1312	4.8507

■ CONCLUSION

The present work describes the efficient routes to synthesis some novel unsymmetrical organotellurium compounds by a simple and convenient method. Compounds A, B, C, and D were obtained with a yield of 53–85%. Findings from the present study on the CHN elemental analysis, FT-IR, and ^{1}H-NMR concur with previous research, confirming the correctness of the proposed structures for all the prepared compounds. As for the theoretical study, it can be concluded that the density functional theory used in this study is a powerful method, and B3LYP functional is a suitable and efficient

function for studying the electronic properties of these structures. The geometrical parameters of 6-31G (d,p) concurred with the experimental data. Therefore, the density functional theory method has been used in this work to study geometry optimization and the electronic properties of naphthalene and di-amino naphthalene by using B3LYP functional.

The geometric structures and total energies donor-acceptor system show that this structure is highly stable. Furthermore, the donor-acceptor system has large average polarizability compared with donor and acceptor and this system has higher reactivity than others. The results obtained in this work help us to select a type of bridge to interact with the donor and acceptor to calculate the physical properties of the donor-bridge-acceptor.

■ REFERENCES

[1] Irgolic, K.J., 1974, *The Organic Chemistry of Tellurium*, Gordon and Breach Science Publishers.

[2] Gedridge, R.W., Higa, K.T., and Nissan, R.A., 2011, New organotellurium precursors for the pyrolytic and photolytic deposition of $Hg_{1-x}Cd_xTe$, *MRS Online Proc. Libr.*, 131, 69–73.

[3] Torubaev, Y.V., Pavlova, A.V., and Pasynskii, A.A., 2012, Metal-metal bond cleavage in $[Cp(CO)_2Fe-Fe(CO)_2Cp]$ under the action of organotellurium(IV) tribromides, *Russ. J. Coord. Chem.*, 38 (3), 219–223.

[4] Al-Asadi, R.H., 2020, Synthesis and molecular structure study of new organotellurium and organomercury compounds based on 4-bromonaphthalen-1-amine, *Russ. J. Gen. Chem.*, 90 (9), 1744–1749.

[5] Wang, S., Yan, C., Zhao, W., Liu, X., Yuan, C.S., Zhang, H.L., and Shao, X., 2021, A *tellura*-Baeyer–Villiger oxidation: One-step transformation of tellurophene into chiral tellurinate lactone, *Chem. Sci.*, 12 (16), 5811–5817.

[6] Al-Fregi, A.A., and Adnan, M.A., 2016, Synthesis, characterization and analytical study of tellurated Schiff base of bis[2-(3-nitrobenzylideneamino)-5-nitrophenyl]telluride and its complexation reactions with Mn(II), Co(II) and Ni(II) ions, *Eur. J. Chem.*, 7 (2), 195–200.

[7] Al-Asadi, R.H., 2019, Synthesis, DFT calculation and biological activity of some organotellurium compounds containing azomethine group, *Orbital: Electron. J. Chem.*, 11 (7), 402–410.

[8] Al-Asadi, R.H., Mohammed, M.K., and Dhaef, H.K., 2020, Mercuration and telluration of 2-fluoro-5-nitroaniline: Synthesis, antibacterial, and computational study, *Russ. J. Gen. Chem.*, 90 (4), 703–709.

[9] Al-Saadawy, N.H., and Abowd, M.I., 2019, Synthesis and identification of new organoselenium compounds derived from 4-(chloromethyl)-2-hydroxybenzaldehyde, *J. Int. Pharm. Res.*, 46 (6), 133–138.

[10] Ahmed, W.M., Al-Saadawy, N.H., and Abowd, M.I., 2021, Synthesis and characterization of a new organoselenium and organotellurium compounds depending on 9-chloro-10-nitro-9,10-dihydroanthracene, *Ann. Romanian Soc. Cell Biol.*, 25 (4), 11035–11043.

[11] Kadhim, M.A., and Al-Saadawy, N.H., 2021, Synthesis and characterization for some new organoselenium compounds depending on 8-hydroxyquinoline, *Ann. Romanian Soc. Cell Biol.*, 25 (2), 2162–2172.

[12] El Adnani, Z., Mcharfi, M., Sfaira, M., Benzakour, M., Benjelloun, A., and Touhami, M.E., 2013, DFT theoretical study of 7-R-3methylquinoxalin-2(1H)-thiones (R=H; CH_3; Cl) as corrosion inhibitors in hydrochloric acid, *Corros. Sci.*, 68, 223–230.

[13] Lu, Y., and Yamago, S., 2019, One-step synthesis of dendritic highly branched polystyrenes by organotellurium-mediated copolymerization of styrene and a dienyl telluride monomer, *Angew. Chem. Int. Ed.*, 58 (12), 3992–3996.

[14] Bursch, M., Hansen, A., Pracht, P., Kohn, J.T., and Grimme, S., 2021, Theoretical study on conformational energies of transition metal complexes, *Phys. Chem. Chem. Phys.*, 23 (1), 287–299.

[15] Salih, N.G., and Obayes, H.R., 2021, Theoretical study of [N]-helicene structure (N= 6, 12, 18, 24, 30, 36, 42, 48, 54) using DFT, *Solid State Technol.*, 64 (2), 3909–3919.

[16] Gusakova, J., Wang, X., Shiau, L.L., Krivosheeva, A., Shaposhnikov, V., Borisenko, V., Gusakov, V., and Tay, B.K., 2017, Electronic properties of bulk and monolayer TMDs: Theoretical study within DFT framework (GVJ-2e method), *Phys. Status Solidi A*, 214 (12), 1700218.

[17] Asadi, N., Ramezanzadeh, M., Bahlakeh, G., and Ramezanzadeh, B., 2020, Theoretical MD/DFT computer explorations and surface-electrochemical investigations of the zinc/iron metal cations interactions with highly active molecules from *Lemon balm* extract toward the steel corrosion retardation in saline solution, *J. Mol. Liq.*, 310, 113220.

[18] Shaw, R.A., 2020, The completeness properties of Gaussian-type orbitals in quantum chemistry, *Int. J. Quantum Chem.*, 120 (17), e26264.

[19] McClain, J., Sun, Q., Chan, G.K.L., and Berkelbach, T.C., 2017, Gaussian-based coupled-cluster theory for the ground-state and band structure of solids, *J. Chem. Theory Comput.*, 13 (3), 1209–1218.

[20] Pereira, F., Xiao, K., Latino, D.A.R.S., Wu, C., Zhang, Q., and Aires-de-Sousa, J., 2017, Machine learning methods to predict density functional theory B3LYP energies of HOMO and LUMO orbitals, *J. Chem. Inf. Model.*, 57 (1), 11–21.

[21] Larock, R., 1985, *Organomercury Compounds in Organic Synthesis*, Springer-Verlag, New York.

[22] Al-Saadawy, N.H., Alyassin, F.F., and Faraj, H.R., 2016, Preparation and characterization of some new complexes of Schiff bases derived from benzoin and glycine, *Global J. Pure Appl. Chem. Res.*, 4 (1), 13–20.

[23] Al-Rubaie, A.Z., Al-Salim, N.I., and Al-Jadaan, S.A.N., 1993, Synthesis and characterization of new organotellurium compounds containing an *ortho*-amino group, *J. Organomet. Chem.*, 443 (1), 67–70.

[24] Silverstein, R.M., Webster, F.X., and Kiemle, D.J., 2005, *Spectrometric Identification of Organic Chemistry Compounds*, 7th Ed., John Wiley & Sons, New York, USA.

[25] Shriner, R.I., and Hermann, C.K., 2004, *Spectroscopic Techniques for Organic Chemistry*, John Wiley & Sons, New York, USA.

[26] Ajeel, F.N., Khudhair, A.M., and Mohammed, A.A., 2015, Density functional theory investigation of the physical properties of dicyano pyridazine molecules, *Int. J. Sci. Res.*, 4 (1), 2334–2339.

[27] Ajeel, F.N., 2017, Analytical insight into the effect of electric field on molecular properties of homonuclear diatomic molecules, *Curr. Smart Mater.*, 2 (2), 153–161.

[28] Alwan, A.S., Ajeel, S.K., and Jabbar, M.L., 2019, Theoretical study for Coronene and Coronene-Al, B, C, Ga, In and Coronene-O interactions by using Density Functional theory, *Univ. Thi-Qar J.*, 14 (4), 1–14.

[29] Oftadeh, M., Naseh, S., and Hamadanian, M., 2011, Electronic properties and dipole polarizability of thiophene and thiophenol derivatives via density functional theory, *Comput. Theor. Chem.*, 966 (1-3), 20–25.

[30] Hanoon, F.H., Jabbar, M.L., and Alwan, A.S., 2017, Effect of thickness on the fractal optical modulator for MgF_2, LiF, Al_2O_3 materials by testing modulation transfer function (MTF), *J. Coll. Educ. Pure Sci.*, 7 (4), 168–182.

[31] Hamd, E.K., Alwan, A.S., and Irthiea, I.K., 2018, Study the effect of welding heat input on the microstructure, hardness, and impact toughness of AISI 1015 steel, *Al-Khwarizmi Eng. J.*, 14, 118–127.

[32] Alwan, A.S., 2020, Density functional theory investigation of $(C_4H_2N_2)_3$ nanocluster and $(C_4H_2N_2)_3$–P, Al, As, B, C and In nanoclusters, *AIP Conf. Proc.*, 2292, 030013.

Characterization of Bottom Ash Waste Adsorbent from Palm Oil Plant Boiler Burning Process to Adsorb Carbon Dioxide in a Fixed Bed Column

Novi Sylvia[1,2], Fitriani Fitriani[2], Rozanna Dewi[2], Rizka Mulyawan[2], Abrar Muslim[3], Husni Husin[3], Yunardi Yunardi[3*], and Mutia Reza[4]

[1]*Doctoral Program, School of Engineering, Post Graduate Program, Universitas Syiah Kuala, Banda Aceh 23111, Indonesia*

[2]*Department of Chemical Engineering, Malikussaleh University, Lhokseumawe, 24351, Indonesia*

[3]*Department of Chemical Engineering, Universitas Syiah Kuala, Banda Aceh 23111, Indonesia*

[4]*Department of Chemical Engineering, Institut Teknologi Kalimantan, Indonesia*

Corresponding author:

email: yunardi@unsyiah.ac.id

Received: June 10, 2021
Accepted: September 18, 2021

DOI: 10.22146/ijc.66509

Abstract: *Palm oil bottom ash utilization from mill boilers as CO_2 adsorbent has been in use for few years. This study aims to examine adsorbent characteristics and capabilities of bottom ash produced from boiler combustion in palm oil industry for CO_2 adsorption before and after utilization, such as compound functional group using the Fourier Transform Infra-Red (FT-IR) spectrophotometer, adsorbent morphology through Scanning Electron Microscopy (SEM), and compound amount using Energy Dispersive X-Ray Spectroscopy (EDX). The CO_2 adsorption was carried out in fixed-bed column. Process variables consist of volumetric flow rate, contact time and bed height. Results showed that SiO_2 compounds in the heterogeneous form with average particle size of 1073 nm, as supported by FT-IR spectrum finding indicating SiO_2 signal at wavelength of 958–954 cm^{-1}. Additionally, EDX analysis showed Silica and Oxygen content of 11.88% and 36.90%, resulting 70% CO_2 adsorption capacity of 0.350 mg/g at discharge of 5 L/min, contact time of 40 min, and bed height of 12 cm. Langmuir isotherm model was obtained with R^2 of 0.998, q_m of 1.588, and k_L of 0.144. Meanwhile, the kinetic model followed a simple first-order prototypical with R^2 of 0.952, $C0_2$ of 0.260, and k_1 of 0.006.*

Keywords: *adsorption; adsorbent; bottom ash; CO_2 gas; fixed-bed column*

■ INTRODUCTION

Global warming from climate change has been considered a severe issue in the last decades. Several types of research related to climate change show an increase in the Earth's temperature due to human activities [1]. Various human activities such as deforestation, industrial waste smoke, vehicle smoke, and others have caused greenhouse gas emissions to the atmosphere; hence, solar radiation is trapped and increases the Earth's average temperature [2-3]. Numerous efforts have been developed to absorb carbon dioxide (CO_2) to decrease the greenhouse gas effect [4]. The Indonesian government is also aware of the issue and commits to reducing greenhouse gas emissions [5]. In the Conference of Parties (COP) 21 on United Nations Framework about Climate Change (UNFCCC) in Paris, France, 30 November 2015, President Joko Widodo stated Indonesia's commitment to reduce greenhouse gas emissions in the amount of 29% by nation effort and 41% through international support until 2030.

Indonesia also has a national action plan to reduce greenhouse gas emissions as in Presidential Decree No. 61 of 2011 on the National Action Plan on Greenhouse Gas Emission and Presidential Decree No. 71 of 2011 on implementing a National Greenhouse Gases Inventory. The inventory shows that industrial activity is one of the primary sources of greenhouse gas (GHG) emissions is CO_2 [6-7]. More than 75% of GHG composition in the atmosphere is CO_2. Currently, CO_2 concentration has risen from 280 ppm in the pre-industrial period to be

400 ppm. Meanwhile, the recommended limit is 350 ppm. Therefore if CO_2 contribution in diverse activities is significantly reduced, then the global warming effect to climate change can be suppressed [8].

Several methods to handle CO_2 gas emissions have been reported, including physical and chemical absorption, cryogenic, separation with membrane, microalga bio-fixation, and adsorption [9-10]. Among the mentioned methods, the most commonly applied method is the absorption method using an amine functional group compound, in which a gas component is separated from a gas mixture by passing it through liquid [11-13]. However, there are drawbacks in this separation process like amine mixture degradation due to impurities in the gas phase at low temperature (below 50 °C), apparatus corrosion, the extensive energy requirement for regeneration, solvent quality degradation due to impregnation with other products, and amine escape by vaporization [14].

The adsorption method is preferable to the absorption method due to adsorption is more economical, able to remove organic materials, and no poisonous side effects occur [15]. Furthermore, the adsorption method is a promising alternative to adsorb CO_2, considering its relatively inexpensive, more straightforward process and no liquid waste produced [4]. Many reports have discussed several types of research on different adsorbents for the adsorption CO_2 process, namely activated carbon, zeolite, silica mesopores, alumina, double-layered hydroxide, and metal oxide. A summary of the adsorption capacity reported for employing various types of adsorbents is presented in Table 1.

Biomass and waste-based adsorbent materials are usually preferable for commercial purposes, namely solid waste from palm oil plants, palm shells, and husk [16]. Many plants utilize shell and husk as fuel to boiler producing steam. Palm shell and husk burning liberate ash left at the furnace as solid granules or crust, usually called bottom ash. Bottom ash contains silica (SiO_2) and alumina (Al_2O_3), which is the primary content of zeolite. Zeolite has adsorption selectivity CO_2/N_2 5 to 10 times higher than carbon-based adsorbent in fixed-bed columns [3,12,17]. Bottom ash has the same content as zeolite; hence it can absorb CO_2.

Studies on bottom ash-based adsorbents have been done to adsorb heavy metals but are still limited for CO_2 adsorption. Currently, the utilization of bottom ash is not optimum and well managed yet. Bottom ash is an issue in the palm oil industry since the storage occupies a large area, increasing annually [18]. Laharto et al. [16] used the synthesis of mesoporous silica from bottom ash waste for CH_4 adsorption. The adsorption capacity at a pressure of 1 atm and a temperature of 30 °C is 0.923 mmol/g. Lira-Zúñiga et al. [17] used biomass combustion ashes on agricultural to CO_2 adsorption. The bottom ash sample from the combustion of wheat bran (agricultural biomass) and its pellets showed a higher adsorption capacity for most of the temperatures studied. The pelletized bottom ash reached the maximum adsorption capacity (0.07 mmol CO_2/g), followed by the non-pelletized bottom ash (0.06 mmol CO_2/g).

By considering the above concern, this research is aimed to study the characteristics and capability of bottom ash from the palm oil industry burning in the boiler as adsorbent to adsorb CO_2. Adsorption is conducted at the fixed-bed column. Previous studies using this absorbent to absorb CO_2 have been done [5,8,14]. However, variation of the flow rate and bed height has not been studied yet. Therefore, this research

Table 1. The adsorption capacity of diverse adsorbents

Adsorbent	Temperature (°C)	Pressure (atm)	Adsorption capacity (mmol/g)	References
Activated Carbon	25	1	1.202	[13]
Activated Carbon	50	1	0.450	[14]
Activated Carbon	25	1	2.828	[15]
Zeolite 13 X	25	1	4.245	[15]
Zeolite 4A	25	1	3.263	[15]

focuses on various volumetric flow rates, contact times, and bed heights. Adsorption equilibrium is generally studied through the adsorption isotherm approach [19]. In this study, the Langmuir and Freundlich adsorption equilibrium models were evaluated. The effectiveness of the adsorption in a fixed-bed column using bottom ash as adsorbent is then examined.

■ EXPERIMENTAL SECTION

Materials

The raw material that was used in this research was bottom ash from boiler burning of Palm Oil Plant PT. Syaukad Sejahtera, Kuta Blang, Gerugok, North Aceh, Indonesia and it was used as adsorbent. The supporting raw material was tapioca flour (SMS Genigel 48 Modified) and distilled water as a mixture for making tapioca glue.

Instrumentation

The adsorbent is applied at the acrylic pipe as an adsorption column with a 6.4 cm diameter and 30 cm length, as shown in Fig. 1, done at a single column. Additional used apparatuses were oven (Memmert UN 30), valve (VG 16 DD), hot plate (Heidolph C-MAG MS 4), sieve mesh 20 mesh (AMB No 20), adsorbent mold (tube mold stainless steel 1.5 × 1 cm), furnace (FNC-2 B-One Furnace), desiccator, spatula, beaker glass 500 mL, measuring cup 100 mL, porcelain cup, CO_2 tube detector from China (HT-2000 CO_2 meter), Scanning electron microscope/energy-dispersive X-ray spectroscopy (SEM/EDX, CARL ZEISS type EVO MA 10), X-Ray Diffraction (XRD, Shimadzu XRD-6100), and Fourier Transform Infra-Red spectrophotometer (FT-IR, IR Prestige 21).

Procedure

The raw palm kernel shell was washed with deionized water several times to remove all traces, such as oil and dirt. Next, the material was dried in an oven with a temperature of 100 °C. The preparation process was initiated by sieving 100 g of bottom ash using a 20 mesh sieve. Then 15 g of tapioca flour and 45 mL of distilled water are heated until they become glue. Furthermore, 100 g of bottom ash and the glue are mixed and stirred until evenly distributed. Next, the mixture was printed using a 1.5 cm diameter mold with a thickness of 1 cm then dry in the oven for 2 h using a temperature of 105 °C. After that, the mixture was calcinated with a furnace at 600 °C for 120 min. The adsorbent is then cooled using a desiccator to room temperature and ready for the CO_2 absorption process.

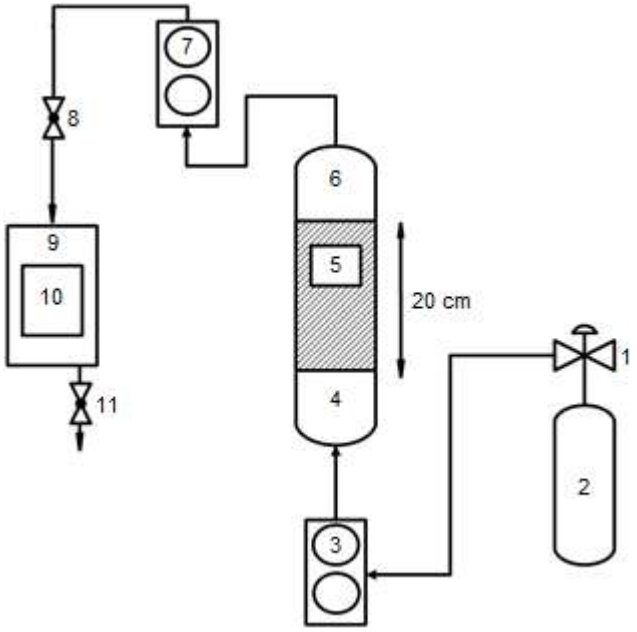

Fig 1. Single column adsorption column diagram of experimental apparatus for fixed-bed adsorption: (1) valve; (2) CO_2 gas cylinder; (3) flow meter CO_2 in; (4) bottom column adsorption (5) fixed-bed adsorber; (6) top column adsorption; (7) flowmeter CO_2 out; (8) valve; (9) box detector gas (10) CO_2 analyzer; (11) stop valves

The adsorption process was initiated by flowing CO_2 (C_0) 500 ppm into an adsorption column. First, the bottom ash adsorbent used was placed in a column of 30 cm and 6.4 cm in diameter, whereas the height of adsorbent (Z) in a column was varied of 4 cm (14 g), 8 cm (28), and 12 cm (42 g). Next, CO_2 was flown into a column with flow rates 10, 15, and 20 L/min and varied contact times of 10, 20, 30, and 40 min, as shown in Fig. 1. After that, the efficiency and adsorption capacity of CO_2 was calculated with the following Eq. (1) and (2) [5,14]:

$$\text{Efficiency} = \frac{CO_{2\ \text{Initial}} - CO_{2\ \text{Final}}}{CO_{2\ \text{Initial}}} \times 100\% \quad (1)$$

$$\text{Adsorption Capacity} = \frac{\text{Flowrate } (CO_{2\ \text{Initial}} - CO_{2\ \text{Final}})}{\text{Sample Mass}} \quad (2)$$

■ RESULTS AND DISCUSSION

This activation is purposed to switch cations to be H^+ and release Al, Fe, Mg, and other impurities (containing alkaline/alkaline Earth) from the structural grid. Impurities on the adsorbent surface covering active sites of adsorbent can be removed by burning during activation. As a result, the adsorbent structure has a broader area and improves the active site, exposing covered active sites and new active site occurrence. In addition, the surface area specified pores improvement and the active sites enable adsorption capability enhancement. The CO_2 adsorption mechanism is shown in Fig. 2.

Adsorbent Characterization

FT-IR analysis

FT-IR measurement results in the form of the spectrum before and after adsorption is shown in Fig. 3. Peaks appeared identifies several functional groups. The peak at wave number 3387–3010 cm^{-1}, stretching vibration from the OH group, showed water in the sample. The peak affirms this interpretation at 1629–1504 cm^{-1} from the –OH group's bending vibration. The peak at 958–954 cm^{-1} showed the Si–O–Si group that identified silica in the bottom ash. The other peaks are at 812 cm^{-1}, showing the Al–O–Al group of alumina and at 505 cm^{-1} for the Si–O–Al adsorption band. Finally, CO_2 gas adsorption is shown at 2337 cm^{-1}. This result is suitable to adsorbing peak reported by other researchers who showed adsorbing band of CO_2 in the range of 2500–2000 cm^{-1} [16-19].

SEM/EDX analysis

SEM/EDX Analysis was to comprehend the bottom ash adsorbent characteristic before and after adsorption. SEM testing was applied to observe the morphology or material surface description and EDX to analyze the adsorbent's material components or atomic composition. The SEM analysis result can be seen in Fig. 3 and 4.

Fig. 4 shows bottom ash SEM results before adsorption that had been physically activated with activation temperature 600 °C, causing reduction of water molecules and organic materials from pore channels, increasing the number of pore volume and adsorbent surface area. The average pore size is 767 nm.

Fig. 4 shows the adsorbent SEM after adsorption, it can be seen that the pore diameter became varied, and the pore hollows became tighter with an average diameter

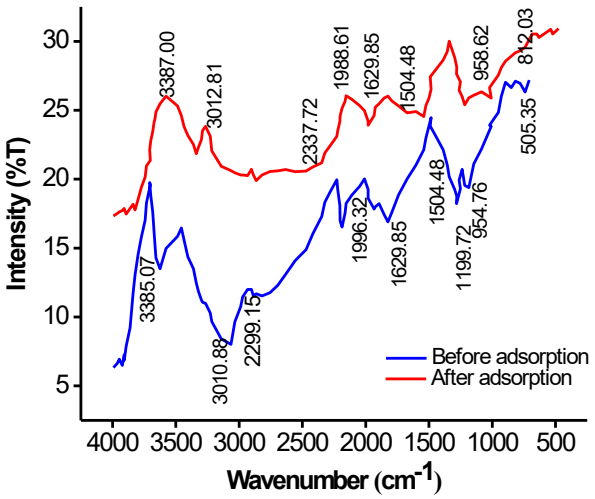

Fig 3. Bottom ash FT-IR result

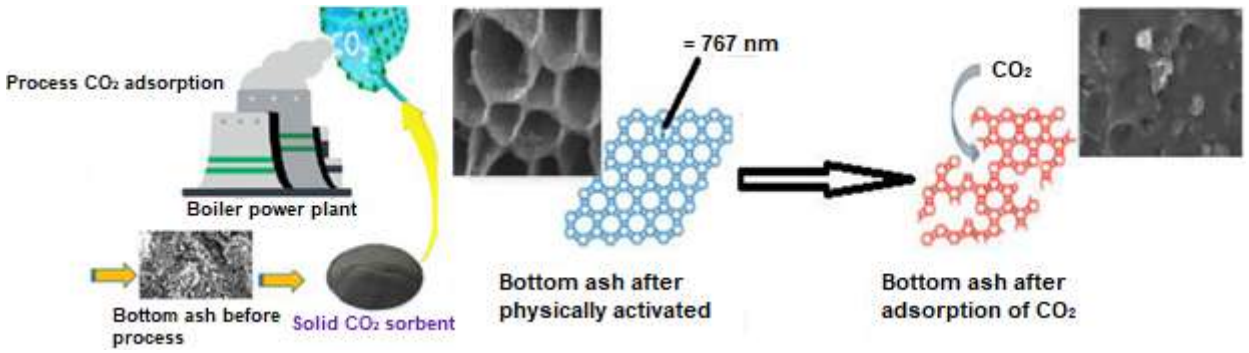

Fig 2. Carbon dioxide adsorption mechanism

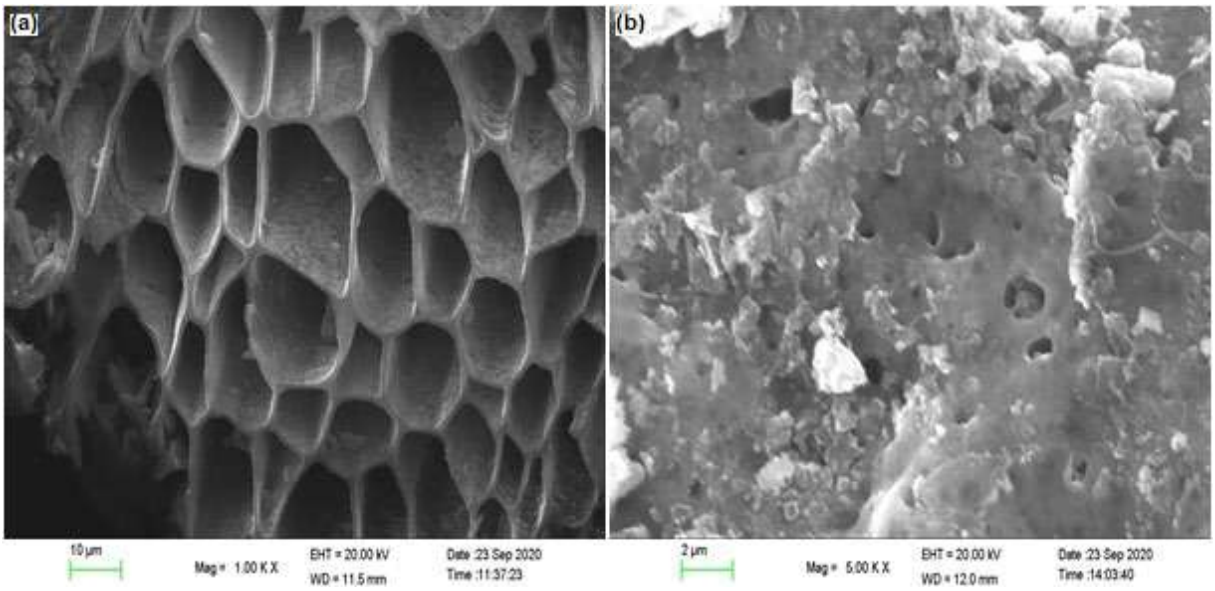

Fig 4. Adsorbent SEM result (a) before and (b) after adsorption

after adsorption 564 nm. The pore diameter became hollows because CO_2 gas was adsorbed so that adsorbent pores were covered and bound. SEM analysis shows that the adsorbent based on the bottom ash of the palm oil plant had a pore size of more than 50 nm. According to the size, the adsorbent is classified as macropores typed adsorbent and suitable as reported by other literature stating that POFA has three types; macropore (55 nm and > 55 nm), mesopore (7 nm and 8 nm), and micropore (< 1 nm) [2].

The bottom ash EDX analysis result is shown in Fig. 5 and Table 1. Table 1 shows that bottom ash components are C, O, Mg, Al, Si, P, S, K, Ca, and Fe elements. The highest composition components were carbon, oxygen, and silica, identifying that bottom ash has silica oxide (SiO_2) as an adsorbent composing component. The EDX analysis result fits with the XRD characteristics result and demonstrates the same composing elements. SiO_2 is proven to have good activity in the adsorption process.

Effect of flow rate on the breakthrough curve. The breakthrough curve for a column was determined by plotting the ratio of C_t/C_0 against time, as shown in Fig. 5. The column was found to perform effectively at the lowest rate of 5 L/min. Previously, breakthrough and exhaustion were reached at a flow rate of 5 to 20 L/min. The column

Table 1. Adsorbent EDX analysis results before adsorption and after adsorption

No	Element	Atom (%)		
		Bottom ash	Before Adsorption	After Adsorption
1	C	40.35	45.77	69.02
2	O	36.29	36.90	23.63
3	Mg	1.21	1.01	0.90
4	Al	0.42	0.36	0.10
5	Si	7.68	11.88	1.84
6	P	0.63	0.55	0.31
7	S	0.56	-	0.19
8	K	0.39	1.88	1.79
9	Ca	7.47	1.36	1.63
10	Fe	0.44	0.28	0.07
11	Cl	0.42	-	-

breakthrough time ($C_t/C_0 = 0.05$) was reduced from 150 min to 10 min by flow rate was increasing between 5 to 20 L/min. The decline of contact time has limited the contact of CO_2 against bottom ash CO_2 did not have sufficient time to diffuse into the pores of bottom ash at a higher flow rate, and CO_2 was out of the column before equilibrium. Similar results were found in the adsorption of CO_2 of the fixed-bed system in the column [20].

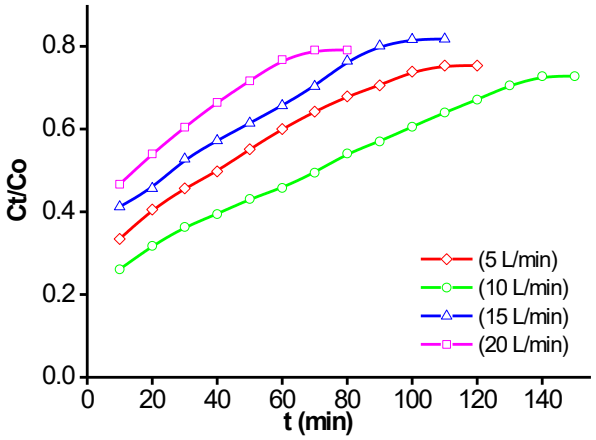

Fig 5. Breakthrough curves: the effect of flow rate on CO_2 adsorption (C_0 = 500 mg/L and Z = 12 cm)

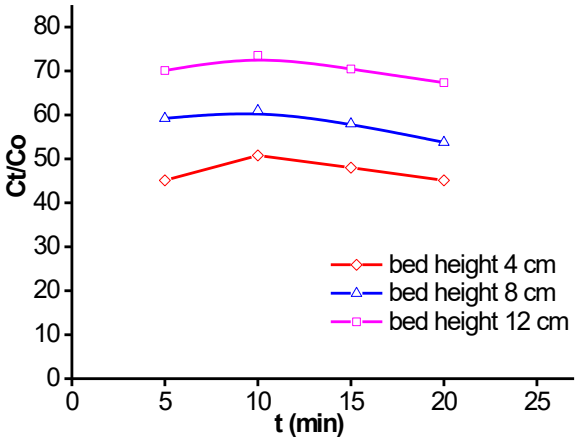

Fig 6. Correlation between flow rate and CO_2 adsorption efficiency graph at different bed height

Effects of flow rate, contact time, and bed height to CO_2 adsorption efficiency and adsorption capacity. CO_2 flow rate and bed height have significant effects on adsorption efficiency. Fig. 6 shows that a greater flow rate yielded a lower adsorption efficiency. The highest adsorption efficiency was at 10 L/min flow rate and bed height 12 cm. As the flow rate of CO_2 is getting higher, the contact time between CO_2 and adsorbent becomes shorter, thus the less CO_2 adsorption efficiency percentage [20]. These results are proportional to reported research from several works of literature that the flow rate significantly affects the adsorption process [21].

Contact time and collision are essential factors in adsorption. According to collision theory, the rate of reaction is the number of collisions in the time unit. The longer the contact time, the more collisions occur, hence the faster chemical reaction to reach equilibrium. The duration needed to achieve adsorption equilibrium are different. The type of interaction between adsorbent and adsorbate has influenced the result. The influence of contact time on the efficiency of adsorbent adsorbs CO_2 gas is shown in Fig. 7.

Fig. 7 shows the adsorption contact time started from 10 to 40 min. The best contact time took place at 40 min alongside the highest adsorption efficiency of 70% at 12 cm of bed height. The ability of the adsorbent declined after the twentieth minute implied that the adsorbent was saturated after that period because the adsorbent surface has a certain number of active adsorption sites. The

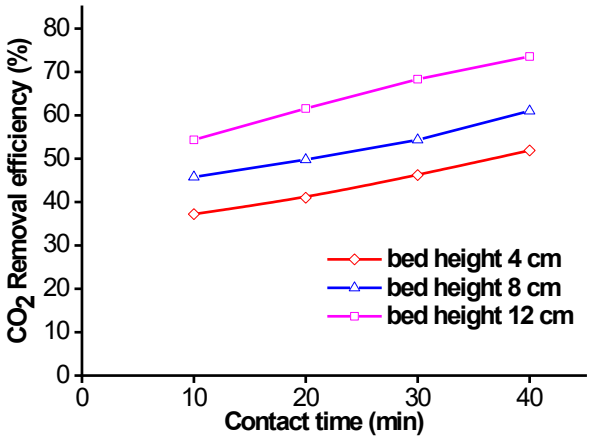

Fig 7. Correlation between contact time and CO_2 adsorption efficiency graph at different bed heights

number of active sites is proportional to the adsorbent surface area. The active site is the adsorbate attaching media on the adsorbent surface. After some time, the active site becomes saturated, and desorption occurs, the detachment of adsorbed molecules on the surface. Thus, after the twentieth-minute desorption happened in which the adsorbed molecules were detached, the CO_2 composition increased, or CO_2 adsorption efficiency declined.

Effects of contact time and bed height to adsorption capacity. Determination of adsorption capacity was done to understand the bottom ash capability in adsorbing CO_2. The effects of contact time and bed height on adsorption capacity are shown in Fig. 8.

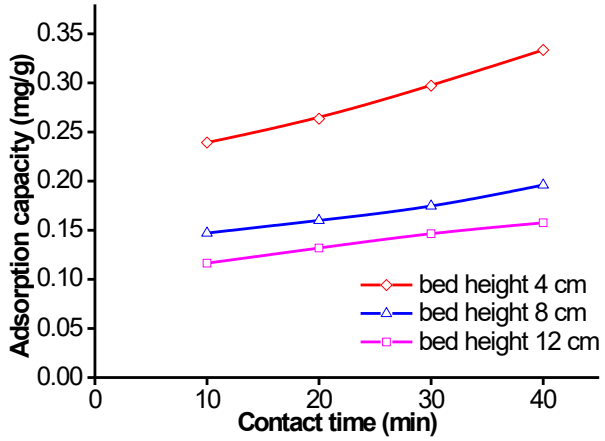

Fig 8. Contact time to adsorption capacity relation graphs at different bed height

Fig. 8 shows that the adsorption capacity increases as the bed height increases. The increment can be correlated with adsorbent surface area and its active sites. The higher bed height means the larger surface area of adsorbent to more CO_2 adsorption capacity [22]. The highest adsorption capacity was 0.350 mg/g was achieved at a contact time of 40 min and bed height 4 cm. At the beginning of contact time, the adsorption process took place at a fast rate since the active site of the adsorbent was still large so that the binding of adsorbate molecules frequency became sufficiently high. As the contact time increases, the amount of adsorbate adsorbed to the adsorbent surface becomes higher until the equilibrium point is reached. Excessive contact time between adsorbent and adsorbate causes adsorbent to be saturated and detached from adsorbate [23-25].

Isothermal Adsorption

Adsorption equilibrium, which is generally studied through the adsorption isotherm approach, is an essential foundation for understanding an adsorption process, especially for finding out how many adsorbate molecules can be adsorbed by a porous material. The adsorption equilibrium model for pure components was based on Langmuir's [14-15] theory about monolayer adsorption on an ideal surface. Langmuir and Freundlich's models are used to represent data adsorption balance. Langmuir's model assumes that the adsorbent surface is homogeneous where the constant energy adsorption on the entire surface of the adsorbent. This model also assumes that the adsorption is localized, and each location can only accommodate one molecule or atom. Adsorption isotherms Freundlich and Langmuir of CO_2 are shown in Table 2. A suitable isotherm model for the equilibrium curve must be determined to optimize the design of the sorption system for the absorption of CO_2 in bottom ash. In this study, the balance model that has been analyzed is Langmuir and Freundlich. The predicted value of the model and the experimental data was validated by comparing the experimental adsorption capacity with the adsorption capacity estimated by this model via a coefficient of determination (R^2, value close to or equal to 1) [19-20], shown in Fig. 9.

Table 2. Parameter isotherm Langmuir and Freundlich for adsorption CO_2 in bottom ash

Type	Parameters	Unit	Equation non-Linear
Langmuir			
q_m	1.588	mg/g	$q = \frac{q_m k_L C_e}{1 + k_L C_e}$
k_L	0.144	-	
R^2	0.998	-	
Freundlich			
k_F	6.519	-	$q = k_f C_e^{\frac{1}{n}}$
n	-1.812	-	
R^2	0.815	-	

where: q is the amount of adsorbed CO_2 per unit weight of bottom ash at equilibrium, and C_e is the unadsorbed CO_2 concentration in effluent at equilibrium (mg/L). k_L is the Langmuir equilibrium constant, q_m is the amount of CO_2 adsorbed with monolayer coverage, k_F is the Freundlich constant, and n is the Freundlich exponent

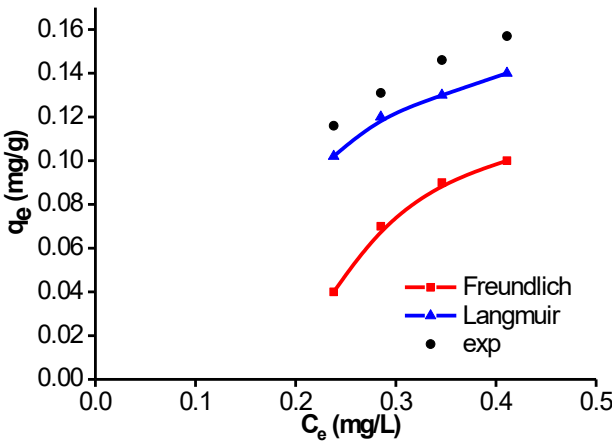

Fig. 9. Contact time to adsorption capacity relation graphs at different bed height

Table 3. Parameter kinetic models for adsorption CO_2 in bottom ash

Kinetic models	Parameters	Unit	Equation non-Linear
Simple first-order			
k_1	0.006	min^{-1}	$C_t = C_0 e^{k_1 t}$
C_0	0.260	mg/L	
R^2	0.952		
Pseudo-second-order k_2			
k_2	0.043	$mg^{-1}\ min^{-1}$	$\frac{dq_t}{dt} = k_2 (q_e - q_t)^2$
q_e	0.055	mg/g	
R^2	0.903		

Fig. 9 shows that the Langmuir model is very close to the experimental data as seen from the R^2 constant, which is 0.998. It can be explained that bottom ash is an adsorbent that absorbs CO_2 in the monolayer at a pressure of 1 atm and a temperature of 25 °C.

Kinetic Studies

An analysis of the kinetic adsorption process is a helpful tool to estimate the time of residence for the adsorption process to complete and determine adsorption dynamics and its performance in the industrial scale of a fixed bed or flow-through system. Thus, the simple first-order and pseudo-second-order models were performed in this study. The kinetic parameters of these models are shown in Table 3. Comparing the values of determination coefficients as stated in Table 3, the simple first-order model gives a better fit than the pseudo-second-order, with an R^2 value is 0.952 [20-23].

■ CONCLUSION

A similar result was supported with FT-IR spectrum at the wavelength 958–954 cm^{-1}, showing that the Si–O–Si group and EDX analysis show silica and oxygen atomic contents were 11.88% and 36.90%, respectively. The CO_2 adsorption efficiency was 70%, while adsorption capacity was 0.350 mg/g at 12 cm bed height operating condition. The isotherm model obtained in this study was Langmuir, while the kinetic model was simple first order. Therefore, bottom ash can be used to capture CO_2 emissions.

■ ACKNOWLEDGMENTS

The author thanks the ministry of Malikussaleh University for financial support through the research project PNBP, No. 530/UN45/KPT/2021.

■ REFERENCES

[1] Abunowara, M., Bustam, M.A., Sufian, S., and Eldemerdash, U., 2016, Description of carbon dioxide adsorption and desorption onto Malaysian coals under subcritical condition, *Procedia Eng.*, 148, 600–608.

[2] Silva, J.A.C., Schumann, K., and Rodrigues., A.E., 2012, Sorption and kinetics of CO_2 and CH_4 in binderless beads of 13X zeolite, *Microporous Mesoporous Mater.*, 158, 219–228.

[3] Kongnoo, A., Tontisirin, S., Worathanakul, P., and Phalakornkule, C., 2017, Surface characteristics and CO_2 adsorption capacities of acid-activated zeolite 13X prepared from palm oil mill fly ash, *Fuel*, 193, 385–394.

[4] Chen, S.J., Zhu, M., Fu, Y., Huang, Y.X., Tao, Z.C., and Li, W.L., 2017, Using 13X, LiX, and LiPdAgX zeolites for CO_2 capture from post-combustion flue gas, *Appl. Energy*, 191, 87–98.

[5] Hauchhum, L., and Mahanta, P., 2014, Carbon dioxide adsorption on zeolites and activated carbon by pressure swing adsorption in a fixed bed, *Int. J. Energy Environ. Eng.*, 5 (4), 349–356.

[6] Girimonte, R., Formisani, B., and Testa, F., 2017, Adsorption of CO_2 on a confined fluidized bed of pelletized 13X zeolite, *Powder Technol.*, 311, 9–17.

[7] Campo, M.C., Ribeiro, A.M., Ferreira, A.F.P., Santos, J.C., Lutz, C., Loureiro, J.M., and Rodrigues A.E., 2016, Carbon dioxide removal for methane

upgrade by a VSA process using an improved 13X zeolite, *Fuel Process. Technol.*, 143, 185–194.

[8] Ridha, F.N., Manovic, V., Macchi, A., and Anthony, E.J., 2015, CO_2 capture at ambient temperature in a fixed bed with CaO-based sorbents, *Appl. Energy*, 140, 297–303.

[9] Gouveia, L.G.T., Agustini, C.B., Perez-Lopez, O.W., and Gutterres, M., 2020, CO_2 adsorption using solids with different surface and acid-base properties, *J. Environ. Chem. Eng.*, 8 (4), 103823.

[10] Regufe, M.J., Ribeiro, A.M., Ferreira, A.F.P., and Rodrigues, A., 2019, "CO_2 storage on zeolites and other adsorbents" in *Nanoporous Materials for Gas Storage, Green Energy and Technology*, Eds. Kaneko, K., and Rodríguez-Reinoso, F., Springer, Singapore, 359–381.

[11] Gil, A., Arrieta, E., Vicente, M.A., and Korili, S.A., 2018, Synthesis and CO_2 adsorption properties of hydrotalcite-like compounds prepared from aluminum saline slag wastes, *Chem. Eng. J.*, 334, 1341–1350.

[12] Bezerra, D.P., da Silva, F.W.M., de Moura, P.A.S., Sousa, A.G.S., Vieira, R.S., Rodriguez-Castellon, E., and Azevedo, D.C.S., 2014, CO_2 adsorption in amine-grafted zeolite 13X, *Appl. Surf. Sci.*, 314, 314–321.

[13] Bezerra, D.P., Silva, F.W.M., de Moura, P.A.S., Sousa, A.G.S., Vieira, R.S., Rodriguez-Castellon, E., Azevedo, D.C.S., 2014, Adsorption of CO_2 on amine grafted activated carbon, *Adsorpt. Sci. Technol.*, 32, 141–151.

[14] Dantas, T.L.P., Luna, F.M.T., Silva, I.J., de Azevedo, D.C.S., Grande, C.A., Rodrigues, A.E., and Moreira, R.F.P.M., 2011, Carbon dioxide–nitrogen separation through adsorption on activated carbon in a fixed bed, *Chem. Eng. J.*, 169 (1-3), 11–19.

[15] Laharto, P.B.F., Anggraini, A.P.K., Fauzany, U.S., Kurniawan, R.Y., and Endang, P.S., 2019, Synthesis of mesoporous silica from bottom ash waste for CH_4 adsorption, *Mater. Sci. Forum*, 964, 130–135.

[16] Liu, Q., He, P., Q, Qian, X., Fei, Z., Zhang, Z., Chen, X., Tang, J., Cui, M., Qiao, X., and Shi, Y., 2017, Enhanced CO_2 adsorption performance on hierarchical porous ZSM-5 zeolite, *Energy Fuels*, 31 (12), 13933–13941.

[17] Lira-Zúñiga, S., Sáez-Navarrete, C., Rodríguez-Córdova, L., Herrera-Zeppelin, L., and Herrera-Urbina, R., 2016, CO_2 adsorption on agricultural biomass combustion ashes, *Maderas, Cienc. Tecnol.*, 18 (4), 607–616.

[18] Lee, S.Y., and Park, S.J., 2015, A review on solid adsorbents for carbon dioxide capture, *J. Ind. Eng. Chem.*, 23, 1–11.

[19] Sylvia, N., Mutia, R., Malasari, M., Dewi, R., Bindar, Y., and Yunardi, Y., 2019, A computational fluid dynamic comparative study on CO_2 adsorption performance using activated carbon and zeolite in a fixed bed reactor, *IOP Conf. Ser.: Mater. Sci. Eng.*, 536, 012042.

[20] Yoro, K.O., Singo, M., Mulopo, J.L., and Daramola, M.O., 2017, Modelling and experimental study of the CO_2 adsorption behaviour of polyaspartamide as an adsorbent during post-combustion CO_2 capture, *Energy Procedia*, 114.

[21] Lakapu, M.M., and Widiastuti, N., 2017, Synthesis of zeolite-X supported on kapok fiber for CO_2 capture material: Variation of immersion time during fiber activation, *Indones. J. Chem.*, 17 (3), 471–476.

[22] Haider, M.B., Jha, D., Sivagnanam, B.M., and Kumar, R., 2018, Thermodynamic and kinetic studies of CO_2 capture by glycol and amine-based deep eutectic solvents, *J. Chem. Eng. Data*, 63 (8), 2671–2680.

[23] Ghazali, Z., Yarmo, M.A., Hassan, N.H., Teh, L.P., and Othaman, R., 2020, New green adsorbent for capturing carbon dioxide by choline chloride: Urea-confined nanoporous silica, *Arabian J. Sci. Eng.*, 45 (6), 4621–4634.

[24] Wardani, A.R.K., and Widiastuti, N., 2016, Synthesis of zeolite-X supported on glasswool for CO_2 capture material: Variation of immersion time and NaOH concentration at glasswool activation, *Indones. J. Chem.*, 278, 16 (1), 1–7.

[25] Minzatu, V., Adina, N., Davidescu, C.M., Duda, C.S., Ciopec, M., Duteanu, N., Negrea, P., Seiman, D.D., and Pascu, I., 2018, Arsenic adsorption into the fixed bed column from drinking groundwater, *WIT Trans. Ecol. Environ.*, 228, 101–110.

Preparation of Biodegradable and Low-Cost Lignin-Based PVOH Carbon Fibers Prepared by Electrospinning

Amir Hamzah Siregar[1,2], Aditia Warman[3], Mahyuni Harahap[1,4], Grace Nainggolan[1,2], Dellyansyah Dellyansyah[1,2], and Saharman Gea[1,2*]

[1]*Cellulosic and Functional Materials Research Centre, Universitas Sumatera Utara, Jl. Bioteknologi No. 1, Medan 20155, Indonesia*

[2]*Department of Chemistry, Faculty of Mathematics and Natural Sciences, Universitas Sumatera Utara, Jl. Bioteknologi No. 1, Medan 20155, Indonesia*

[3]*Department of Physics, Faculty of Mathematics and Natural Sciences, Universitas Sumatera Utara, Jl. Bioteknologi No. 1, Medan 20155, Indonesia*

[4]*Department of Chemistry, Universitas Sari Mutiara Indonesia, Jl. Kapten Muslim, Medan 20124, Indonesia*

* ***Corresponding author:***

email: s.gea@usu.ac.id

Received: June 14, 2021
Accepted: September 2, 2021

DOI: 10.22146/ijc.66606

Abstract: *A polyvinyl alcohol (PVOH)/lignin nanofiber was prepared by the electrospinning method as a precursor for biodegradable and low-cost carbon fibers. PVOH 15% was dissolved in water, and various concentration of lignin (5, 10, 15, 20, and 25%) was added. The presence of lignin in PVOH solution increased the viscosity and conductivity. From SEM analysis, PVOH solution produced smooth fiber, whereas the addition of lignin produced fibers in bead forms. The presence of lignin above 20% in PVOH did not produce spun-fiber. FTIR analysis confirmed that lignin was able to form hydrogen bonds with PVOH. TGA analysis showed that PVOH/lignin nanofibers had the highest residual mass, i.e., 40% at 600 °C. The morphology of the carbon fibers showed flake forms with many pores and had 58.07% carbon content.*

Keywords: *lignin; carbon fiber; electrospinning; polyvinyl alcohol*

■ INTRODUCTION

In the last few years, the demand for carbon fibers (CF), such as vapor grown carbon nanofibers (VGCNF), multi-walled carbon nanotube (MWCNT), and single-walled carbon nanotube (SWCNT) [1-2], has increased significantly in various industrial applications. CF has superior properties compared to other carbonaceous materials, which are high mechanical properties and strength-to-weight ratio, fatigue resistance, and low cost [3]. The demand for CF was reported to have globally increased almost twice every year [4]. However, the growth rate of the CF industry has not been able to supply to the fast-growing demand, especially due to the main precursor for CF, i.e., polyacrylonitrile (PAN) is expensive and petroleum-based [5]. Hence, the search for inexpensive CF alternatives based on biobased resources, biodegradable, and low-cost precursors is the main topic of current investigation to cope with large-scale manufacturing constraints caused by PAN. These polymers, as biobased, biodegradable, and low-cost, include lignin [6], cellulose [7], and biomass resins [8].

Lignin, the most abundant non-cellulosic polymer on earth, is complex aromatic (phenolic) macromolecules present in the cell wall of plants. It comprises three main phenylpropanoid monomers or precursors: coniferyl, sinapyl, and *p*-coumaryl alcohol [9]. Lignin has been studied for its various applications, such as in the production of biomass from crude bio-oil as energy generation [10], composite carbon nanofibers [11], compatibilizer [12], and carbon fibers [13]. The carbon content and chemical structures of lignin showed potential for carbonized material production, especially carbonized lignin fibers [14]. Lignin was isolated from either

hardwood or softwood, whose chemical structures differed. It was also found as the major by-product in paper industries.

Lignin could be extracted by several methods, such as lignosulfonates, alkali lignin, kraft lignin, and organosolv lignin. Each method produced a different lignin character with different purity and lignin fraction sizes. These properties influenced the fiber spinning formation and the quality of CF products [3]. It was estimated that the cost of lignin precursor was lower than the PAN precursor. However, the manufacturing process of lignin-based CF could be more expensive than PAN's, as the currently preferred method was melt-spinning. The process involved complex and accurate control of the lignin, spinning conditions, and treatment temperature. Lignin required critical controlling at the melt-spinning step because it naturally oxidized partially [5].

Electrospinning is a fiber spinning technology to produce fibers from micro to nano-sized diameters. Fibers are produced as nonwoven fiber mats, or they can be in the shape of aligned fiber strings. In the electrospinning process, an electrical field is injected into the polymer solution. The solution jet is stretched and elongated by electrical forces, while the viscoelastic forces prevent it from breaking. Then, the thin solution jet dries before reaching the ground surface, where fibers are collected [15]. Pure lignin solution usually does not have enough viscoelasticity for spinning. Therefore, it is blended with another polymer known as binder solution, such as electrospun poly (ethylene oxide) (PEO), polyacrylonitrile (PAN), and poly (vinyl alcohol) (PVOH) [14]. PVOH is a semicrystalline polymer with high carbon amount (54.5%) and hydroxyl groups, making it easy to use as a precursor to producing carbon materials [16]. In this work, we presented a simple and straightforward experimental method to get carbon nanofibers precursor by the electrospinning of lignin solutions at room temperature with the addition of polymer in a single step and carbonization to produce carbon nanofibers.

■ EXPERIMENTAL SECTION

Materials

Lignin alkali, partially soluble 13.4 wt.% loss on heating 316 °C, pH: 6.5 (25 °C, 5% aqueous solution, d: 1.3 g/mL) was purchased from Sigma Aldrich, USA. PVOH, fully hydrolyzed (Mw approx. 60,000) with viscosity 20 °C (4%; water), degree of hydrolysis ≥ 98.0%, was purchased from the same supplier. No further purification was carried out to lignin and PVOH used for the aqueous solution for electrospinning.

Procedure

Polymer solution preparation

Preliminary experiment, PVOH 10% (w/v) was prepared by dissolving 10 g of PVOH in 100 mL distilled water for 4 h in aquatic reflux. This concentration was used to prepare lignin/PVOH blend solution throughout the experiment. PVOH powder was gradually added and constantly stirred during the dissolving stage to avoid agglomeration of particles at 110 °C and 600 rpm for 6 h to dissolve the polymer completely. This process resulted in a colorless and viscous PVOH solution. After that, lignin was added to PVOH solution with different concentration ratios PVOH to lignin of (10:0); (10:5); (10:15); (10:20); and (10:25) v/w% by using an ultrasonic for 6 h. The electrospun polymer solutions were characterized for the conductivity and viscosity.

Electrospinning process

The fresh polymer solution was directly electrospun by horizontal electrospinning (basic series electrospinning unit Brand NLI, Nanolab Instruments Sdn Bhd, Malaysia) at room temperature with the following conditions: (i) a voltage of 15 kV; (ii) feed rate of 0.1 mL/h; (iii) needle tip-to-collector distance of 15 cm; (iv) disposable 18-G syringe; and (v) speed of collector 300 rpm. The collector was coated with aluminum foil sheets to attach the fibers. Next, the electrospun mat was dried at room temperature and stored for further characterization.

Carbonization process

PVOH/lignin nanofiber was carbonized in a furnace under a nitrogen atmosphere. Pre-carbonization was carried out from 25 to 100 °C with a heating rate of 5 °C/min. At 100 °C, the process was isothermally held for 30 min. The second step was carried out at a temperature between 100 and 200 °C and a heating rate

of 5 °C/min, then isothermally held for 30 min. Next, the carbonization process was continued from 200 to 600 °C with a heating rate of 5 °C/min and held isothermally for 1 h. The morphology of carbon fiber was investigated by using SEM.

Characterization

Conductivity and viscosity. The conductivity and viscosity of the electrospun polymer solution were examined prior to the electrospinning process. A 10% PVOH was added to several different concentrations of lignin (0, 5, 10, 15, and 20%). The electrical conductivity was examined by using Multiparameter Bench Meter Mi 180, Milwaukee, by immersing the probe into the solution without having bubbles trapped inside the sleeves. The conductivity value was displayed on the primary LCD. Meanwhile, the viscosity was determined by using HAAKE Viscotester 550. The homogenized sample solution was put into the viscometer tank at room temperature in the Kohlrausch flask below the viscometer. Both conductivity and viscosity tests were repeated three times.

Scanning electron microscopy analysis. The surface morphology of samples was observed using scanning electron microscopy (SEM) Hitachi TM3030 (JEOL, Ltd., Tokyo, Japan) with accelerating voltage EHT of 20.00 kV, probe = 101 Pa, and signal A = SE1. Samples were placed on an adhesive-backed carbon tape and secured to the specimen. After that, they were sputter-coated with a thin layer of gold alloy (SC 500 Emscope) to reduce charging during analysis.

Thermogravimetric analysis. The mass-loss characteristics of the materials used in this project were characterized by using a thermogravimetric analyzer (model TASC 414/4 NETZSCH). The specimen was heated from 25 to 900 °C with a heating rate of 10 °C/min under an argon atmosphere.

Differential scanning calorimetry analysis. The thermal properties of the samples were studied by using differential scanning calorimetry (DSC) X-DSC7000 (Hitachi medical system, Tokyo, Japan) in a range temperature between 30 and 250 °C with a heating rate of 10 °C/min.

■ RESULTS AND DISCUSSION

Morphological Characterization of Electrospun PVOH/Lignin Nanofiber

The images from SEM for PVOH and PVOH/lignin electrospun nanofibers are shown in Fig. 1. Whereas the conductivity and viscosity are presented in Fig. 2. Lignin/PVOH-based fiber mats were produced by electrospinning technique, with the compositions of lignin corresponding to PVOH varied from 0, 5, 10, 15, 20, and 25%. As shown in Fig. 1(a), PVA solution at 10% concentration produced smooth, bead-free fibers with a diameter of 124.8 nm. However, the addition of lignin PVOH solution produced fibers in bead forms. This might be due to the increase in viscosity of polymer solution with the presence of lignin. The viscosity was 4.4 Nm/s^2 for PVOH 10%, and 7.8, 9.4, 10.5, 17.4, and 23.6 Nm/s^2 for PVOH/lignin solution ratio of 100:5, 100:10, 100:15, 100:20, and 100:25, respectively. The increase in the concentration of polymer solution has been reported to cause larger friction of fluid and hinder

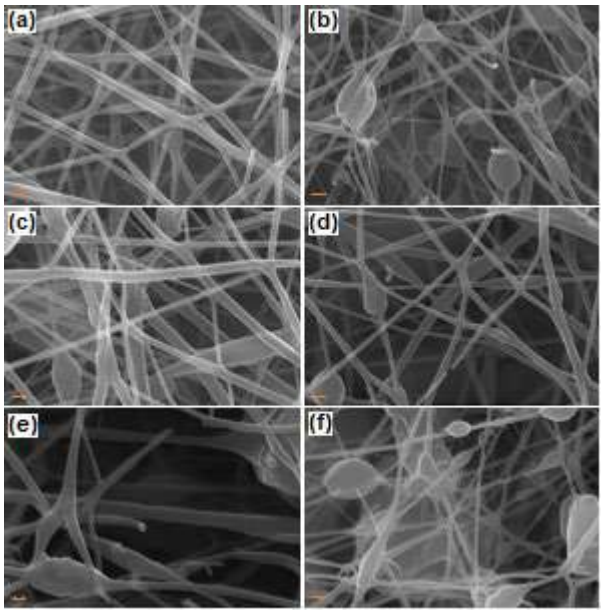

Fig 1. SEM images of electrospun PVOH/lignin nanofiber at different lignin concentrations: (a) 0%; (b) 5%; (c) 10%; (d) 15%; (e) 20%; and (f) 25% lignin, with magnification of 3000×. Scale bar = 200 nm

electrostatic forces in attracting droplets to Taylor cone and polymer jets [17].

Moreover, SEM images (Fig. 1) revealed that the average diameters of spun-fibers decreased with the increase in the concentration of the lignin, such as from 63.38 nm at 5 wt.% lignin to 55.83, 52.90, 48.38, and 42.43 nm at 10 wt.%, 15 wt.%, 20 wt.%, and 25 wt.% lignin, respectively. This happened as salts in lignin increased the conductivity, as shown in Fig. 2. High conductivity increases the electrostatic charge density of polymer solution to produce thicker fiber. The same result was reported by another author who reported that PVOH solution could be readily electrospun, while bead-fibers were created with the addition of lignin [18]. More fibers with ribbon-shaped morphology were produced by increasing the amount of lignin in spin dope. Spin dope with high lignin amount had the tendency to form thin and tube-like jet/filament during electrospinning, which could further collapse with the rapid vaporization of solvent [19]. In this study, the presence of lignin onto PVOH with the concentration of 20% and 25% could not undergo electrospinning because of the cohesiveness of the solution. The viscosity of the polymer solution at these concentrations limits the followability of the polymer solution.

FTIR Analysis

The FTIR spectra for PVOH, commercial lignin, PVOH nanofiber, and PVOH/lignin nanofiber are shown in Fig. 3. Regarding Fig. 3, several wavenumbers were selected to identify the lignin. Firstly, absorption bands between 3600 cm^{-1} and 3000 cm^{-1} attributed to hydroxyl groups in aromatic and aliphatic structures. C–H stretching of the aliphatic and aromatic structure was observed at 2480 cm^{-1}. C=O stretching of carboxyl groups was identified at 1705 cm^{-1}. The peaks at 1600 and 1611 cm^{-1} attributed to the C–C stretching of the aromatic skeleton and the vibrations of the aromatic rings. Vibrations of C–H bonds in aromatic rings and C–O(H) + C–O(Ar) stretching appeared at 1328 cm^{-1}. The vibrations of C–H bonds in aromatic rings were observed at 834 cm^{-1}. These absorption bands were also

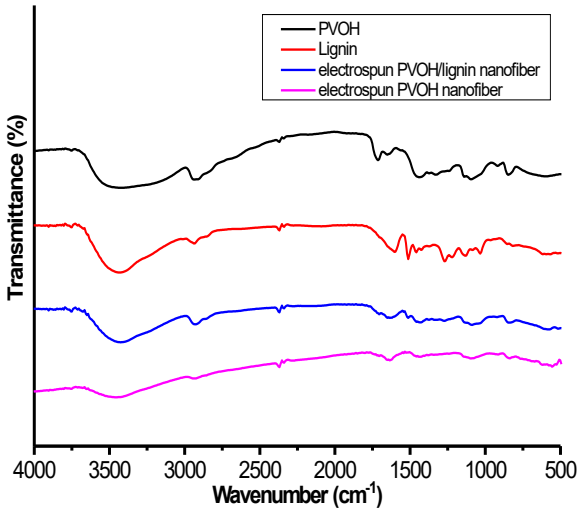

Fig 3. FTIR spectra of PVOH, lignin, PVOH nanofiber, and PVOH/lignin nanofiber

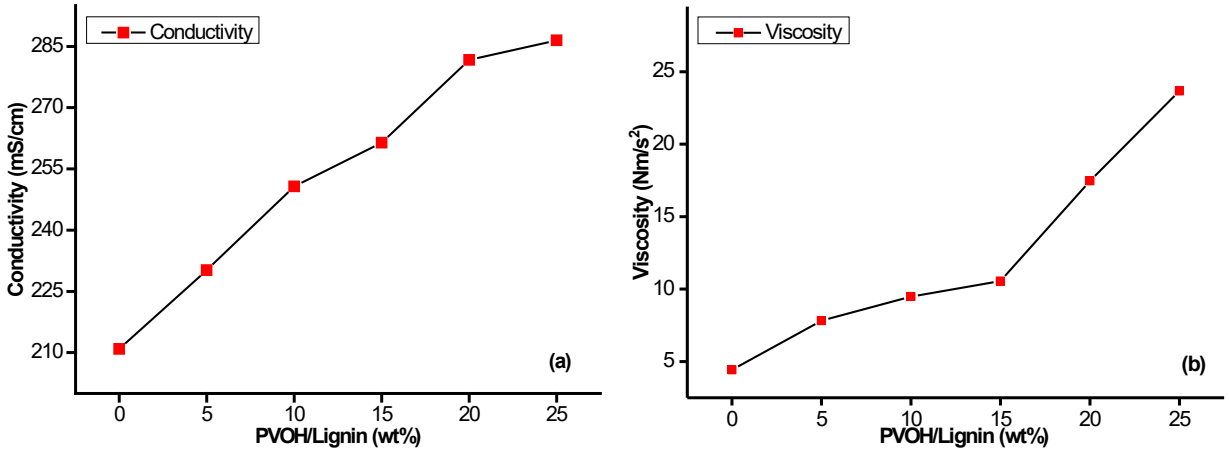

Fig 2. (a) The conductivity and (b) the viscosity of 10 wt.% PVOH solution in distilled water at different lignin concentrations 0%, 5%, 10%, 15%, 20% and 25%

reported by other authors [4]. FTIR also confirmed the chemical structures of PVOH nanofiber, showing dominant absorption peaks at 3650, 2941, 1733, 1428, 1090, and 844 cm^{-1}, which attributed to OH, CH_2, C=O, CH–C–H, C–O, and C–C, respectively. The acetate group in the PVOH was represented in the 1959 cm^{-1} band [15].

Meanwhile, FTIR spectroscopy was used to investigate the blending of PVOH and lignin. In the hydroxyl-stretching region (3000–3700 cm^{-1}), the OH in the PVOH was at 3650 cm^{-1}. This band shifted to lower wavenumber (3323 cm^{-1}) after the blending with lignin (OH) due to a new hydroxyl bond formed during the blending process, either within the PVOH or between lignin and PVOH. FTIR analysis confirmed that lignin was able to form hydrogen bonds with PVOH. The blending of PVOH/lignin film had formed a strong hydrogen bond between the hydroxyl groups in PVOH and lignin [20]. The interaction confirmed the excellent mechanical strength of the nanofiber precursor [21].

Thermal Properties of Electrospun PVOH/Lignin Nanofiber

The thermal properties of lignin, PVOH, PVOH nanofiber, and PVOH/lignin nanofiber were studied using TGA and DSC analysis with a heating rate of 10 °C/min under an argon gas atmosphere. Fig. 4 depicts TGA traces for pristine lignin, PVOH, PVOH nanofiber, and PVOH/lignin nanofiber. All TGA traces showed three distinct regions. The first step was the elimination of water and moisture from the samples. The second was to remove some organic volatiles, and the last was to form amorphous or semicrystalline carbon [22].

The TGA curve of lignin showed dehydration from room temperature to 100 °C. At this stage, there was 3% weight loss. Second, the thermal degradation of lignin between 225 and 350 °C. Last, lignin with a residual mass of approximately 35% at 600 °C provides lignin as a good carbon fiber precursor.

The TGA traces for PVOH nanofiber and PVOH/lignin nanofiber had the first weight loss observed from room temperature to 100 °C. There was 5–10 wt.% weight loss at this temperature. The same result was observed in PVOH. Then, second weight loss occurred at

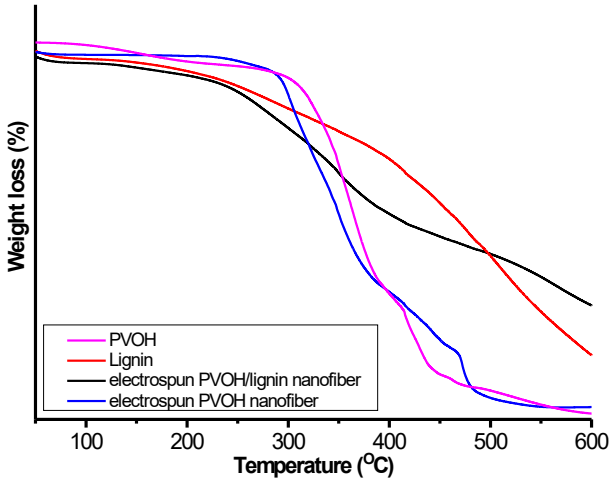

Fig 4. TGA curve of lignin, PVOH, PVOH nanofiber, and PVOH/lignin nanofiber with a heating rate of 10 °C/min

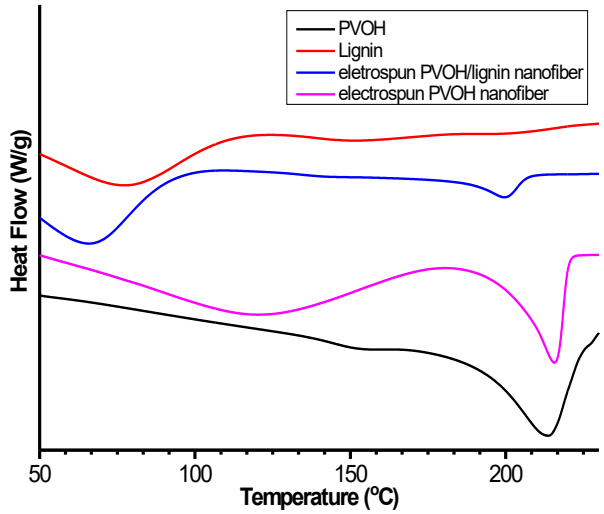

Fig 5. DSC thermogram for lignin, PVOH, PVOH nanofiber, and PVOH/lignin nanofiber with a heating rate of 10 °C/min

300 °C to 450 °C for PVOH and PVOH nanofiber. This region shifted to a lower temperature between 250 and 400 °C for PVOH/lignin nanofiber. At this stage, PVOH and PVOH nanofiber had lost more than 50% of their mass, while PVOH/lignin nanofiber lost only 30% of its weight. This was mainly associated with the decomposition of OH and acetate groups in PVOH and lignin [23]. Lastly, the decomposition of PVOH backbone structure for PVOH and PVOH nanofiber was observed at below 450 °C, while it has a percent residue of 3%.

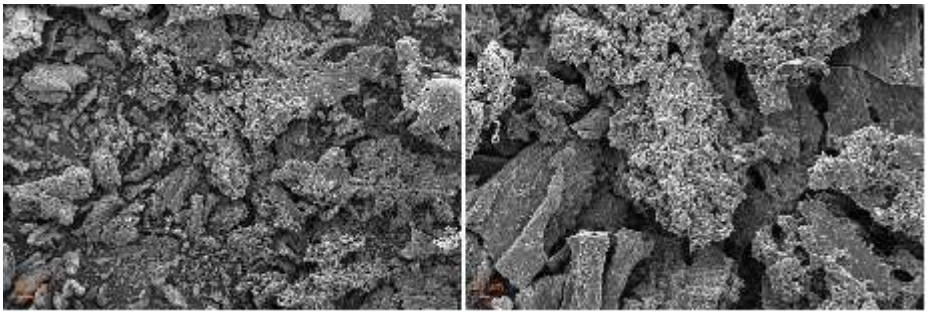

Fig 6. SEM-EDS analysis of lignin/PVOH based nanofiber with a magnification of 100× (left) and 300× (right)

However, PVOH/lignin nanofiber had the highest residual mass (40% at 600 °C).

Fig. 5 shows DSC curves of lignin, PVOH, PVOH nanofiber, and PVOH/lignin nanofiber. PVOH/lignin nanofiber had a peak at 70 °C, which was associated with the dehydration of the sample. The melting temperature (T_m) of PVOH and PVOH nanofiber was the same at 225 °C. In comparison, PVOH/lignin nanofiber has a T_m of 200 °C. This is due to a new hydroxyl bond being formed during the blending process, either within the PVOH or between lignin and PVOH, as shown in FTIR spectra.

The Morphology of PVOH/Lignin Carbon Fiber

The morphology of the as-spun fiber after carbonization is shown in Fig. 6. The sample was carbonized at 600 °C with a heating rate of 5 °C/min. The morphology of the carbon fiber was flake with many pores. In addition, SEM-EDS analysis showed that the carbon fiber had 58.07% carbon content, which was still low compared to commercial carbon fibers. In addition, fiber forms could not be observed after the pyrolysis, possibly due to the low compatibility between lignin and PVOH. Other authors reported that PVOH melted during the isothermal treatment (250 °C), producing higher curvature and fusing into the network structure [24]. This study concluded that PVOH/lignin could be an excellent precursor for carbon fibers. Another study reported that the carbonized lignin had mesopores and an amorphous graphitic structure [25].

■ CONCLUSION

In this paper, electrospun PVOH/lignin nanofibers as carbon fiber precursors have been successfully prepared. The spun fibers show smooth and good morphology, but it produces bead-fibers after the addition of lignin to PVOH due to low compatibility with PVOH. Meanwhile, lignin improves the viscosity and conductivity of the polymer solution. The presence of lignin at up to 20% in PVOH cannot produce spun-fiber. FTIR analysis confirms that lignin is able to form hydrogen bonds with PVOH. TGA analysis shows that PVOH/lignin nanofibers have the highest residual mass, i.e., 40% at 600 °C. The morphology of the carbon fibers is flake with many pores, and the carbon content is 58.07%.

■ ACKNOWLEDGMENTS

This research was funded by the TALENTA USU with contract number 4167/UN5.1.R/PPM/2019.

■ REFERENCES

[1] Zhang, J., Chevali, V.S., Wang, H., and Wang, C.H., 2020, Current status of carbon fibre and carbon fibre composites recycling, *Composites, Part B*, 193, 108053.

[2] Al-Saleh, M.H., and Sundararaj, U., 2009, A review of vapor grown carbon nanofiber/polymer conductive composites, *Carbon*, 47 (1), 2–22.

[3] Ding, R., Wu, H., Thunga, M., Bowler, N., and Kessler, M.R., 2016, Processing and characterization of low-cost electrospun carbon fibers from organosolv lignin/polyacrylonitrile blends, *Carbon*, 100, 126–136.

[4] Gea, S., Siregar, A.H., Zaidar, E., Harahap, M., Indrawan, D.P., and Perangin-Angin, Y.A., 2020, Isolation and characterisation of cellulose nanofibre and lignin from oil palm empty fruit bunches, *Materials*, 13 (10), 2290.

[5] Baker, D.A., and Rials, T.G., 2013, Recent advances in low-cost carbon fiber manufacture from lignin, *J. Appl. Polym. Sci.*, 130 (2), 713–728.

[6] Chio, C., Sain, M., and Qin, W., 2019, Lignin utilization: A review of lignin depolymerization from various aspects, *Renewable Sustainable Energy Rev.*, 107, 232–249.

[7] Harahap, M., Hararak, B., Khan, I., Pandita, S., and Gea, S., 2019, Wet-spinning of cellulose acetate reinforced with acetylated nano-crystalline cellulose as carbon fibre precursors, *IOP Conf. Ser.: Mater. Sci. Eng.*, 553, 012038.

[8] Cao, Q., Zhang, Y., Chen, J., Zhu, M., Yang, C., Guo, H., Song, Y., Li, Y., and Zhou, J., 2020, Electrospun biomass based carbon nanofibers as high-performance supercapacitors, *Ind. Crops Prod.*, 148, 112181.

[9] Salas, C., Ago, M., Lucia, L.A., and Rojas, O.J., 2014, Synthesis of soy protein-lignin nanofibers by solution electrospinning, *React. Funct. Polym.*, 85, 221–227.

[10] Chio, C., Sain, M., and Qin, W., 2019, Lignin utilization: A review of lignin depolymerization from various aspects, *Renewable Sustainable Energy Rev.*, 107, 232–249.

[11] Ko, F.K., Goudarzi, A., Lin, L.T., Li, Y., and Kadla, J.F., 2016, "Lignin-Based Composite Carbon Nanofibers" in *Lignin in Polymer Composites*, William Andrew Publishing, Oxford, UK, 167–194.

[12] Ilmiati, S., Hafiza, J., Fatriansyah, J.F., Kustiyah, E., and Chalid, M., 2018, Synthesis and characterization of lignin-based polyurethane as a potential compatibilizer, *Indones. J. Chem.*, 18 (3), 390–396.

[13] Trogen, M., Le, N.G., Sawada, S., Guizani, C., Lourençon, T.V., Pitkänen, L., Sixta, H., Shah, R., O'Neill, H., Balakshin, M., Byrne, N., and Hummel, M., 2020, Cellulose-lignin composite fibres as precursors for carbon fibres. Part 1- Manufacturing and properties of precursor fibres, *Carbohydr. Polym.*, 252, 117133.

[14] Poursorkhabi, V., Mohanty, A.K., and Misra, M., 2015, Electrospinning of aqueous lignin/poly(ethylene oxide) complexes, *J. Appl. Polym. Sci.*, 132 (2), 41260.

[15] Misran, E., Wirdjosentono, B., Noor, N.M., Gea, S., Situmorang, S.A., and Harahap, M., 2020, Preparation and characterisation of electrospun composite nanofibre polyvinyl alcohol/nanofibrillated cellulose isolated from oil palm empty fruit bunches, *BioResources*, 15 (4), 7906–7917.

[16] Fatema, U.K., Uddin, A.J., Uemura, K., and Gotoh, Y., 2011, Fabrication of carbon fibers from electrospun poly(vinyl alcohol) nanofibers, *Text. Res. J.*, 81 (7), 659–672.

[17] Fatimah, I., Sari, T.I., and Anggoro, D., 2020, Effect of concentration and nozzle-collector distance on the morphology of nanofibers, *Key Eng. Mater.*, 860, 315–319.

[18] Ago, M., Okajima, K., Jakes, J.E., Park, S., and Rojas, O.J., 2012, Lignin-based electrospun nanofibers reinforced with cellulose nanocrystals, *Biomacromolecules*, 13 (3), 918–926.

[19] Lai C., Zhou, Z., Zhang, L., Wang, X., Zhou, Q., Zhao, Y., Wang, Y., Wu, X.F., Zhu, Z., and Fong, H., 2014, Free-standing and mechanically flexible mats consisting of electrospun carbon nanofibers made from a natural product of alkali lignin as binder-free electrodes for high-performance supercapacitors, *J. Power Sources*, 247, 134–141.

[20] Korbag, I., and Mohamed Saleh, S., 2016, Studies on the formation of intermolecular interactions and structural characterization of polyvinyl alcohol/lignin film, *Int. J. Environ. Stud.*, 73 (2), 226–235.

[21] Roman, J., Neri, W., Derré, A., and Poulin, P., 2019, Electrospun lignin-based twisted carbon nanofibers for potential microelectrodes applications, *Carbon*, 145, 556–564.

[22] Rampe, M.J., Setiaji, B., Trisunaryanti, W., and Triyono, T., 2011, Fabrication and characterization of carbon composite from coconut shell carbon, *Indones. J. Chem.*, 11 (2), 124–130.

[23] Ko, H.U., Zhai, L., Park, J.H., Lee, J.Y., Kim, D., and Kim, J., 2018, Poly(vinyl alcohol)–lignin blended resin for cellulose-based composites, *J. Appl. Polym. Sci.*, 135 (34), 46655.

[24] Ago, M., Borghei, M., Haataja, J.S., and Rojas, O.J., 2016, Mesoporous carbon soft-templated from lignin nanofiber networks: Microphase separation boosts supercapacitance in conductive electrodes, *RSC Adv.*, 6 (89), 85802–85810.

[25] Widiyastuti, W., Rois, M.F., Setyawan, H., Machmudah, S., and Anggoro, D., 2020, Carbonization of lignin extracted from liquid waste of coconut coir delignification, *Indones. J. Chem.*, 20 (4), 842–849.

Modification of Fishbone-Based Hydroxyapatite with $MnFe_2O_4$ for Efficient Adsorption of Cd(II) and Ni(II) from Aqueous Solution

Poedji Loekitowati Hariani[1,2], Addy Rachmat[1,2*], Muhammad Said[1,2], and Salni Salni[3]

[1]*Department of Chemistry, Faculty of Mathematics and Natural Sciences, Universitas Sriwijaya, Jl. Palembang Prabumulih Km. 32, Ogan Ilir 30662, Indonesia*

[2]*Research Centre of Advanced Material and Nanocomposite, Faculty of Mathematics and Natural Sciences, Universitas Sriwijaya, Jl. Palembang Prabumulih Km. 32, Ogan Ilir 30662, Indonesia*

[3]*Department of Biology, Faculty of Mathematics and Natural Sciences, Jl. Palembang Prabumulih Km. 32, Ogan Ilir 30662, Indonesia*

* ***Corresponding author:***

email: addy_rachmat@unsri.ac.id

Received: June 22, 2021
Accepted: August 16, 2021

DOI: 10.22146/ijc.66888

Abstract: *Due to their toxicity, Cd(II) and Ni(II) ions in the environment are severe. The hydroxyapatite composite was improved with magnetic $MnFe_2O_4$ to remove Cd(II) and Ni(II) ions from an aqueous solution. Hydroxyapatite was extracted from Snakehead (*Channa striata*) fish bones via alkaline-heat treatment. The hydroxyapatite/$MnFe_2O_4$ composite performance was analyzed through XRD, FTIR, SEM-EDS, BET analysis, and VSM, and the results reveal that the hydroxyapatite/$MnFe_2O_4$ composite shows good magnetic properties of 21.95 emu/g. The kinetics evaluation confirmed that the pseudo-second-order kinetics model was more suitable to describe the adsorption of Cd(II) and Ni(II) ions by hydroxyapatite/$MnFe_2O_4$ composite from the solution. The Langmuir isotherm model was suitable to describe the adsorption process of the Cd(II) and Ni(II) ions, where the adsorption capacities for Cd(II) and Ni(II) are 54.3 and 47.4 mg/g, respectively. Desorption of Cd(II) and Ni(II) ions from hydroxyapatite/$MnFe_2O_4$ composite using NaCl as the eluent was more effective than EDTA. The findings of this study indicate that hydroxyapatite/$MnFe_2O_4$ can reduce Cd(II) and Ni(II) ions in wastewater so that it can recover natural resources.*

Keywords: *hydroxyapatite/$MnFe_2O_4$ composite; adsorption; Cd(II); Ni(II); desorption*

■ INTRODUCTION

Wastewater discharged from industrial activities is one of the environmental issues; hence its treatment is a paramount concern. Wastewater containing heavy metals is a notable concern due to its toxicity and ease of accumulating in the food chain. It is harmful to human life and the environment as well [1-2]. Some industries generate wastes containing heavy metals such as mining, ceramics, pesticides, smelting, and steel [2-3]. Cadmium poisoning causes a detrimental effect on kidneys, lungs, hypertension, liver, in addition to the teratogenic impacts [4]. Exposure to nickel can trigger kidney, lung, and cardiovascular disorders [5]. It also causes headaches, dermatitis, and respiratory disorders [6-7]. According to the World Health Organization, the maximum thresholds of Cd and Ni in drinking water are 0.003 mg/L and 0.07 mg/L, respectively.

Various methods have been developed to reduce the concentration of heavy metals in water, such as adsorption [3], membrane processes [8], bioremediation [9], reverse osmosis [10], and ion exchange [11]. Among these methods, adsorption is the most commonly used due to ease of operation, flexible design, and non-toxic properties [1-2]. In addition, using low-cost adsorbents makes the adsorption method even economical. These low-cost adsorbents can be obtained from various sources such as calcium alginate/spent coffee grounds composite beads [3], expanded perlite [12],

hydroxyapatite [13], green logan hull [14], and succinylated hay [15].

Hydroxyapatite ($Ca_{10}(PO_4)_6(OH)_2$) is widely used as catalyst, fertilizer, and adsorbent in wastewater treatment, chromatography, bone, and dental implants [16-17]. Hydroxyapatite had been used to adsorb various metal cations such as Cd(II), Pb(II), and Ni(II) [13]. Hydroxyapatite prepared from different precursors was also reported for Pb(II) [18-19]. Some natural materials containing calcium, such as fishbone, can be used for making hydroxyapatite. It is estimated that 30–40% of total fish production leaves solid waste [20]. Using fishbones as a source of hydroxyapatite provide advantages due to its cheapness, abundance in nature, and its capability of reducing solid waste. Several types of fish as a source of hydroxyapatite include Gray triggerfish skin and Black scabbardfish [21], *Scomberomorus commerson* and *Chirocentrus nudus* [22], and Snakehead fish [23]. Indonesia's people widely consume snakehead fish. Therefore, snakehead fish bones availability provides a potential source of hydroxyapatite. Hydroxyapatite from snakehead fish bones reported possess antibacterial activity against *Escherichia coli* and *Staphylococcus aureus* [24].

Several authors developed hydroxyapatite combined materials to increase the effectiveness of adsorption in the form of hydroxyapatite-rice husk [17], hydroxyapatite-magnetite [25], hydroxyapatite-Fe_3O_4-β-cyclodextrin [26], and hydroxyapatite-chitosan [27]. Adsorbents with magnetic properties recently have been developed. After the adsorption process, the adsorbent can be separated rapidly and effectively using an external magnet without the filtration process [28]. Activated carbon-$MnFe_2O_4$ showed a large adsorption capacity to the removal of As(II) and As(V) [29]. On the other hand, graphite modified with $MnFe_2O_4$ is effective in the removal of Pb(II) and Ni(II) [30].

In this study, hydroxyapatite was extracted from snakehead fish bones by alkaline-heat treatment. The resulting materials were incorporated with $MnFe_2O_4$ by using the co-precipitation method. $MnFe_2O_4$ is a ferrite compound with a large surface area, large magnetic properties, and excellent chemical stability [28]. The composite was used to remove Cd(II) and Ni(II) ions. The adsorption process is carried out in batch mode. Desorption and regeneration were also carried out to evaluate economic interest.

■ EXPERIMENTAL SECTION

Materials

The chemicals used were HCl, NaOH, $MnCl_2{\cdot}4H_2O$, $FeCl_3{\cdot}6H_2O$, $CdCl_2$, $NiCl_2{\cdot}6H_2O$, KNO_3, NaCl, EDTA ($C_{10}H_{14}N_2Na_2O_8{\cdot}2H_2O$), all purchased from Merck, Germany and used without further purification. Snakehead fishbone was obtained from the local market in the city of Palembang, South Sumatra, Indonesia.

Instrumentation

The diffractogram pattern was measured using X-ray diffraction (XRD Shimadzu XD-610) with Cu-Kα radiation of 1.54 Å, and the intensity was scanned at 2θ angle from 10° to 80° to observe the crystalline structure. The functional groups were determined using a Fourier transform infrared spectroscopy (FTIR Thermo Fisher Scientific) at 400–4000 cm^{-1}. Surface area calculated according to data recorded by ASAP 2020 analyzer. A vibrating sample magnetometer (VSM Lakeshore 74004) was used to measure saturation magnetization, while a scanning electron microscope/energy-dispersive X-ray spectroscopy (SEM-EDX Shimadzu AA-700) aimed to observe surface morphology and determine the elemental composition. Cd(II) and Ni(II) ions concentration using atomic absorption spectroscopy (AAS Shimadzu AA 7000).

Procedure

Extraction of hydroxyapatite

The extraction of hydroxyapatite was conducted using alkali-heat treatment. Snakehead fish bones prior extraction process were screened from impurities and washed using distilled water. A hundred grams of the bones were placed in the oven for 60 min at 105 °C. The bones were crushed by fast milling tool to obtain 200 mesh particle size. The powder was then washed using 0.1 N HCl to remove the protein, followed by distilled water several times. Next, 100 mL NaOH 50% was added to the powder, heated at 60 °C, and stirred with a magnetic stirrer for 5 h. The powder was washed using distilled

water several times until reaching its neutral condition. The product was finally calcined at 750 °C for 3 h.

Preparation of hydroxyapatite/$MnFe_2O_4$ composite

The synthesis of hydroxyapatite/$MnFe_2O_4$ composite was carried out by the co-precipitation method. The mass ratio of hydroxyapatite and $MnFe_2O_4$ was 1:1. Hydroxyapatite of 11.53 g was added to a 200 mL solution of 0.05 mol manganese(II) chloride and 0.1 mol iron(III) chloride at room temperature. The mixture was stirred and added by 3 M NaOH solution gradually until reaching a pH of 11. The product was washed with distilled water until reaching a neutral pH and then calcined at 600 °C for 1 h at 10 °C/min heating rate.

Determination of pH_{PZC}

The pH change at the point of zero charges (pH_{PZC}) was determined by adding 0.25 g of hydroxyapatite/$MnFe_2O_4$ composite into 50 mL of 0.1 M KNO_3 solution. Sequentially, a pH ranging from 2 to 10 was set up using 1 M HCl and 1 M NaOH solutions. Next, each of the solutions obtained was stirred at 120 rpm for 24 h at room temperature. The final pH values were measured using a pH meter.

Batch adsorption study

The adsorption of Cd(II) and Ni(II) ions was processed in a batch experiment under the effects of pH solution, initial concentration, and contact time. The pH solution effect was observed in 250 mL conical flasks containing 0.1 g of the composite and 100 mL of Cd(II) and Ni(II) ions solution with a concentration of 10 mg/L. Variations in pH of solutions made from 2 to 8 were adjusted by adding HCl 1 M and NaOH 1 M solutions. The solutions were stirred using a shaker at 200 rpm for 60 min. After the adsorption, the concentration of Cd(II) and Ni(II) ions in each solution was determined by AAS. The effect of the initial concentration was evaluated on the concentration variations of 10–80 mg/L. Meanwhile, the contact time was evaluated from 10 to 150 min. All experiments were carried out in triplicate, and the mean values were used for data analysis.

Desorption process

In the batch desorption method, the hydroxyapatite/$MnFe_2O_4$ composite was reused to adsorb Cd(II) and Ni(II) ions. Desorption of Cd(II) and Ni(II) ions from hydroxyapatite/$MnFe_2O_4$ composite was studied using 1 M NaCl solution and 0.1 M EDTA [1]. A total of 100 mL of the desorbing eluent was poured into a 250 mL Erlenmeyer containing 0.1 g of the composite, which had absorbed Cd(II) and Ni(II) ions with an initial concentration of 60 mg/L. The desorption process was carried out using a shaker for 3 h at room temperature. The Cd(II) and Ni(II) ions desorbed concentrations were determined using AAS.

■ RESULTS AND DISCUSSION

Characteristic of Hydroxyapatite/$MnFe_2O_4$ Composite

XRD pattern was used to identify the purity and crystallinity of the adsorbent. The XRD patterns of hydroxyapatite and hydroxyapatite/$MnFe_2O_4$ composite are shown in Fig. 1. The figure shows that the diffractogram of hydroxyapatite/$MnFe_2O_4$ is more amorphous than hydroxyapatite because $MnFe_2O_4$ is more amorphous than hydroxyapatite. The characteristics of the snakehead fish bone-based hydroxyapatite peaks are per JCPDS No. 09-0432. The peaks appear at 2θ = 25.78°, 31.72°, 32.06°, 32.40°, 46.02°, and 49.48°, in accordance with 2θ of JCPDS, namely at 25.879° (002), 31.773° (211), 32.196° (112), 32.902° (300), 46.711° (222), and 49.648° (213). Therefore, hydroxyapatite has a hexagonal crystal structure. The peaks of hydroxyapatite/$MnFe_2O_4$ composite were overlapping

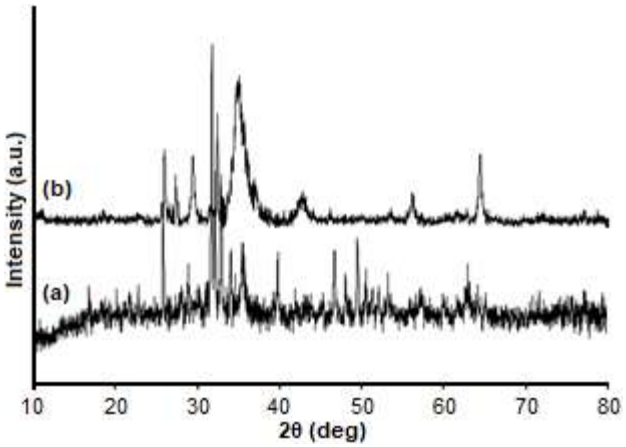

Fig 1. XRD patterns for the (a) hydroxyapatite and (b) hydroxyapatite/$MnFe_2O_4$ composite

hydroxyapatite and $MnFe_2O_4$, the latter of which appeared at 2θ = 18.72°, 29.54°, 35.0°, 43.12°, 53.74°, 56.22°, and 64.54°, indicating the *hkl* plane, namely (111), (220), (311), (400), (422), (511), and (440), following JCPDS 74-2403. Based on these peaks, it can be confirmed that $MnFe_2O_4$ has a face-centered cubic structure with a lattice constant of 8.470 Å.

Fig. 2 shows the FTIR spectra of hydroxyapatite and hydroxyapatite/$MnFe_2O_4$ composite. The wavenumbers at 3418 and 1626 cm^{-1} appear on hydroxyapatite are O–H stretching vibrations and indicating the adsorption of water molecules. Wavenumbers at 3416 and 1628 cm^{-1} also appear in hydroxyapatite/$MnFe_2O_4$ composite. Stretching vibrations of P–O bonds are shown at wavenumbers of 567, 602, 964, and 1036 cm^{-1} in hydroxyapatite, and at 565, 601.7, 962, and 1038 cm^{-1} in hydroxyapatite/$MnFe_2O_4$ composite. The wavenumber corresponds to the tetrahedral PO_4^{3-} vibration [31]. The CO_3^{2-} groups can be identified at wavenumbers of around 870 and 1402–1460 cm^{-1} [32]. In hydroxyapatite, the CO_3^{2-} group appears at 876 and 1414 cm^{-1}, whereas hydroxyapatite/$MnFe_2O_4$ composite is at 870 and 1404 cm^{-1}. These groups come from fish bones that remain in the extraction process. The presence of CO_2 in hydroxyapatite and hydroxyapatite/$MnFe_2O_4$ composite comes from the air can be identified at wavenumbers 2365 and 2369 cm^{-1}. The main peak in wavenumbers below 1000 cm^{-1} in the hydroxyapatite/$MnFe_2O_4$ composite indicates the presence of ferrites [29]. Stretching vibrations at 471 and 604 cm^{-1} show the formation of the spinel ferrite structure. The absorption band at wavenumber 565 cm^{-1} reflects manganese ferrite's intrinsic vibration, which peak overlaps with stretching P–O vibrations.

FTIR spectra of hydroxyapatite/$MnFe_2O_4$ composite after adsorbing Ni(II) and Cd(II) showed a shift in wavenumbers. The shifted wavenumbers are 3416, 1628, 1404, 1038, 962, and 565 cm^{-1}. After Ni(II) adsorption, they shifted to 3412, 1584, 1433, 990, 920, 561, and 525 cm^{-1}, while after Cd(II) adsorption, they were observed at 3385, 1603, 1435, 1013, 930, 570, and 534 cm^{-1}. The peak shifts to the lower frequencies indicate that the formation of composite bonds with Ni(II) and Cd(II) requires less energy for vibration [33].

Fig. 3 shows the surface morphology of hydroxyapatite and hydroxyapatite/$MnFe_2O_4$ composite. No significant change in the surface morphology of hydroxyapatite after the composite was formed occurred, but the composite surface appeared to be more

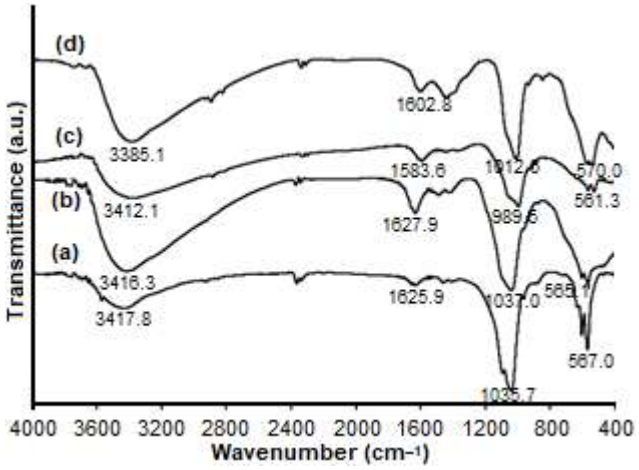

Fig 2. FTIR spectra of (a) hydroxyapatite and (b) hydroxyapatite/$MnFe_2O_4$ composite (c) hydroxyapatite/$MnFe_2O_4$ composite after Ni(II) adsorption and (d) hydroxyapatite/$MnFe_2O_4$ composite after Cd(II) adsorption

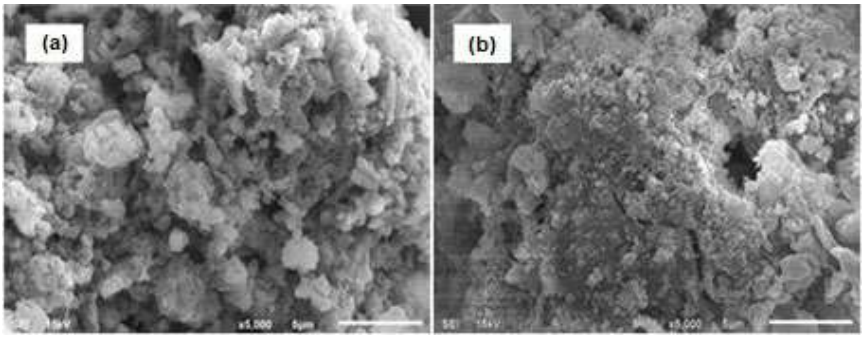

Fig 3. SEM image (5000×) of (a) hydroxyapatite and (b) hydroxyapatite/$MnFe_2O_4$ composite

compact than hydroxyapatite. $MnFe_2O_4$ is deposited randomly on the hydroxyapatite surface. Table 1 shows the composition of the hydroxyapatite and hydroxyapatite/$MnFe_2O_4$ composite due to EDX analysis. In this research, the Ca/P molar ratio of hydroxyapatite was 1.65, close to the theoretical value, i.e., 1.67. The presence of Mn in the composite shows that the process of forming the composite succeed.

The magnetic properties of hydroxyapatite/$MnFe_2O_4$ composite were determined by using VSM at room temperature. Hysteresis curves show the magnetic behavior of a material. Fig. 4 shows the saturation magnetization of hydroxyapatite/$MnFe_2O_4$ composite, which is super magnetic with a saturation magnetization of 21.95 emu/g. Another study reported that the synthesize of $MnFe_2O_4$-activated carbon composite had a saturation magnetization of 17.91 emu/g [34]. Thus, the saturation magnetization value of the $MnFe_2O_4$-activated carbon composite is smaller than the pure $MnFe_2O_4$.

Table 2 presents the BET surface area, mean pore diameter, and pore volume of the samples. It was found that the surface area of hydroxyapatite/$MnFe_2O_4$ composite is more diminutive than hydroxyapatite. The presence of $MnFe_2O_4$ partially fills the pores of hydroxyapatite; hence the surface area is reduced. The hydroxyapatite/$MnFe_2O_4$ composite has a mean pore diameter larger than hydroxyapatite. $MnFe_2O_4$ particles possibly underwent agglomeration and are positioned on the surface of the hydroxyapatite, which causes an increase in the mean pore diameter [35]. The same phenomenon was reported in $MnFe_2O_4$-activated carbon composites [29]. The presence of ferrite compounds causes the surface area to decrease, and the mean pore diameter increases.

The pH value at the zero charge (pH_{PZC}) is one of the adsorbent characteristics affecting adsorption capacity. The pH_{PZC} value provides information about the nature of the hydroxyapatite/$MnFe_2O_4$ composite surface charge. Under the condition of pH solution < pH_{PZC}, the composite surface is positively charged, and conversely, it is negatively charged if the pH of the solution > pH_{PZC} [36]. In this study, the pH_{PZC} of hydroxyapatite/$MnFe_2O_4$ composite was 5.8 (Fig. 5).

Batch Sorption

The batch adsorption method was used to study the adsorption properties of hydroxyapatite/$MnFe_2O_4$ composite against Cd(II) and Ni(II) ions. This research

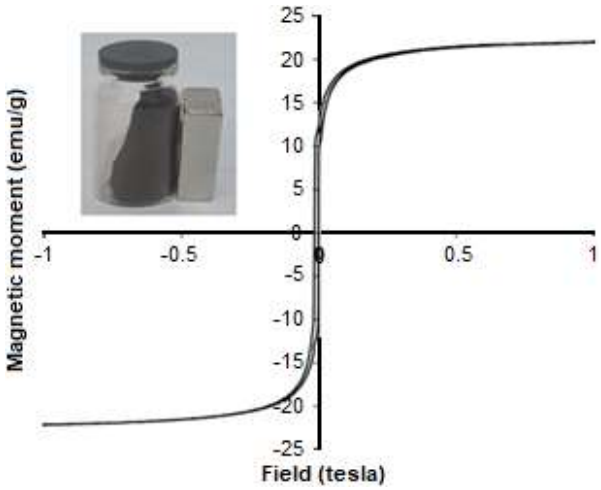

Fig 4. Magnetic saturation of hydroxyapatite/$MnFe_2O_4$ composite

Table 1. Element composition of hydroxyapatite and hydroxyapatite/$MnFe_2O_4$ composite

Element	Percentage (%)	
	Hydroxyapatite	Composite
P	18.72	9.12
O	41.35	36.42
Ca	39.93	19.20
Mn	-	11.06
Fe	-	24.20

Table 2. Characteristic of hydroxyapatite and hydroxyapatite/$MnFe_2O_4$ composite using the BET method

Characteristic	Hydroxyapatite	Hydroxyapatite/$MnFe_2O_4$ composite
BET surface area (m^2/g)	110.5	97.8
Average pore diameter (nm)	7.92	10.52
Pore volume (cm^3/g)	0.41	0.32

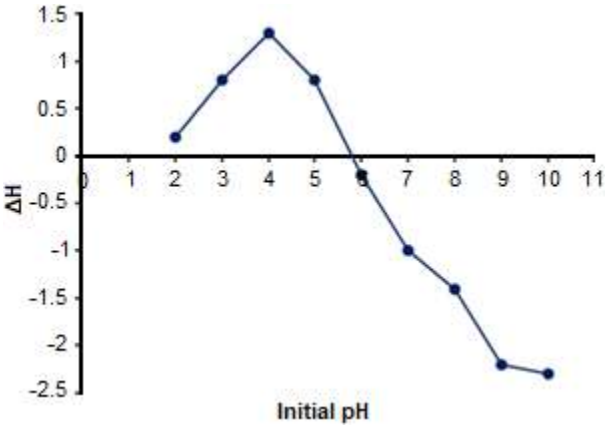

Fig 5. pH_{PZC} of hydroxyapatite/$MnFe_2O_4$ composite

studied the influence of pH, contact time, and initial concentration on the adsorption capacity of hydroxyapatite/$MnFe_2O_4$ composites. pH is one of the essential variables in the adsorption process. The adsorption mechanism depends on the pH of the solution, which affects the degree of ionization, the adsorbent surface charge, and the adsorbate speciation [1].

Adsorption of Cd(II) and Ni(II) ions by hydroxyapatite/$MnFe_2O_4$ composites was carried out in the pH range of 2–8 (Fig. 6). The concentration of Cd(II) and Ni(II) ions was 10 mg/L in 100 mL, the amount of hydroxyapatite/$MnFe_2O_4$ composites was 0.1 g. Therefore, the optimum pH was 6 for Cd(II) and Ni(II) ions. Under the condition of pH < pH_{PZC}, the hydroxyapatite/$MnFe_2O_4$ composite was negatively charged, so competition occurred between H^+ ions and metal ions. Consequently, the adsorption capacity decreased. Under the condition of pH > pH_{PZC}, the hydroxyapatite/$MnFe_2O_4$ composite has a negative charge resulting in electrostatic attraction with positively charged Cd(II) and Ni(II) ions, thus increasing the adsorption capacity. Another author reported the same results that the optimum pH of the adsorption of Cu(II) and Cd(II) ions using Fe_3O_4/hydroxyapatite/β-cyclodextrin composite is 6, where the pH_{PZC} adsorbent was 5 [26]. At pH above 7, Cd(II) and Ni(II) ions bind to hydroxide and form precipitate [14].

The effects of the initial concentration of Cd(II) and Ni(II) ions on the adsorption capacity of hydroxyapatite/$MnFe_2O_4$ composites are depicted in Fig. 7. The adsorption process was carried out with adsorbent weight 0.1 g, solution volume of 100 mL, pH 6, and contact time of 60 min. As the concentration of Cd(II) and Ni(II) ions increases, the more significant number of Cd(II) and Ni(II) ions is being adsorbed by hydroxyapatite/$MnFe_2O_4$ composite. Interactions between metal ions and hydroxyapatite/$MnFe_2O_4$ composite occurred due to electrostatic interactions and ion exchange. The Ca(II) ions in hydroxyapatite can be replaced by metal ions(M) according to the following reaction [20,25].

$$Ca_{10}(PO_4)_6(OH)_2 + xM^{2+} \rightarrow Ca_{10-x}M_x(PO_4)_6(OH)_2 + xCa^{2+} \quad (1)$$

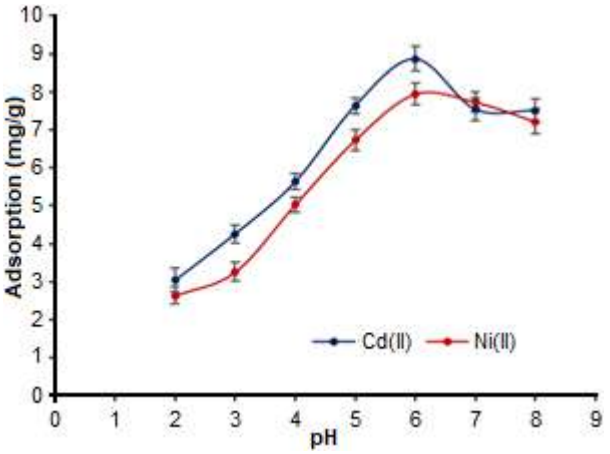

Fig 6. Effect of pH solution on the adsorption of Cd(II) and Ni(II) ions by hydroxyapatite/$MnFe_2O_4$ composite

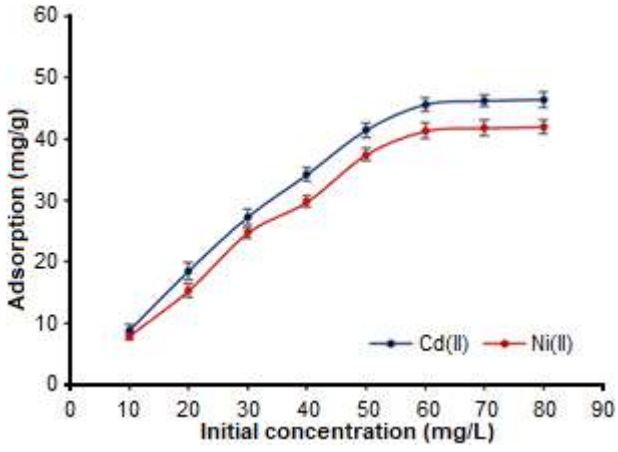

Fig 7. Effect of initial concentration on the adsorption of Cd(II) and Ni(II) ions by hydroxyapatite/$MnFe_2O_4$ composite

The contact time effect was evaluated under experiment conditions as follows: 0.1 g of hydroxyapatite/$MnFe_2O_4$ composite, 100 mL of Cd(II) and Ni(II) ions with a concentration of 60 mg/L, solution pH of 6, room temperature with a contact time of 10–150 min. Fig. 8 shows that the amount of Cd(II) and Ni(II) ions adsorbed is proportional to the contact time until equilibrium is achieved. Optimum contact times for Cd(II) and Ni(II) ions were obtained at 90 and 100 min, respectively.

Adsorption Kinetics

Adsorption kinetics study provides information about optimum conditions, mechanism of sorption, and possible rate-controlling step. In this study, the kinetics of Cd(II) and Ni(II) adsorption by hydroxyapatite/$MnFe_2O_4$ were evaluated based on two models, namely the pseudo-first-order and pseudo-second-order models. The model uses equations as follows [30]:

$$\log(q_e - q_t) = \log q_e - \frac{k_1}{2.303} \quad (2)$$

$$\frac{t}{q_t} = \frac{1}{k_2 q_e^{\,2}} + \frac{t}{q_e} \quad (3)$$

where q_e (mg/g) is the adsorption capacity at equilibrium, q_t (mg/g) is the adsorption capacity at time t (min), and k_1 (1/min) and k_2 (g/mg/min) are the pseudo-first-order and pseudo-second-order constants, respectively.

Fig. 9 shows the graphs of the pseudo-first-order and pseudo-second-order adsorption kinetics of Cd(II) and Ni(II) ions by hydroxyapatite/$MnFe_2O_4$ composite. The correlation coefficient (R^2) value of the pseudo-first-order is lower than the pseudo-second-order for both Cd(II) and Ni(II) ions. However, R^2 for the pseudo-second-order is closer to 1 ($R^2 > 0.995$), indicating that the adsorption kinetics that is suitable for describing the adsorption of Cd(II) and Ni(II) ions by hydroxyapatite/$MnFe_2O_4$ composite is the pseudo-second-order.

Table 3 shows the kinetics parameters of the adsorption of Cd(II) and Ni(II) ions by hydroxyapatite/$MnFe_2O_4$ composite. The values of k_1 and k_2 for Cd(II) ions were lower than those of Ni(II) ions, indicating that Cd(II) ions were adsorbed more

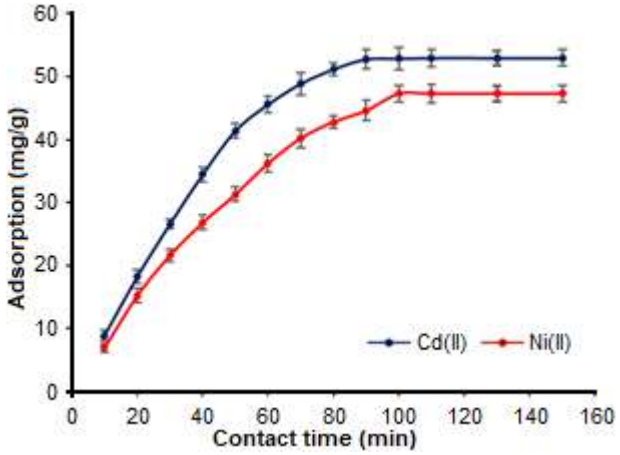

Fig 8. Effect of contact time on the adsorption of Cd(II) and Ni(II) ions by hydroxyapatite/$MnFe_2O_4$ composite

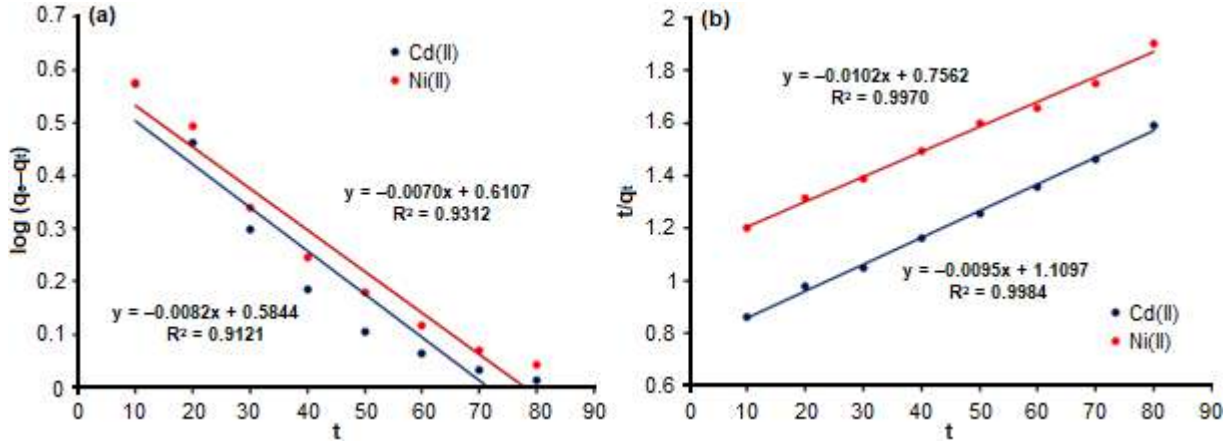

Fig 9. Pseudo- (a) first-order and (b) second-order kinetics of adsorption of Cd(II) and Ni(II) ions by hydroxyapatite/$MnFe_2O_4$ composite

Table 3. Parameters of kinetics for adsorption of Cd(II) and Ni(II) ions by hydroxyapatite/$MnFe_2O_4$ composite

Parameters	Metal ions	
	Cd(II)	Ni(II)
Pseudo-first order		
R^2	0.9121	0.9312
k_1 (1/min)	0.00351	0.00304
q_e (mg/g)	3.841	3.838
Pseudo-second order		
R^2	0.9984	0.9970
k_2 (g/mg min)	8.1×10^{-5}	13.7×10^{-5}
q_e (mg/g)	105.263	98.038

quickly by hydroxyapatite/$MnFe_2O_4$ composite than Ni(II) ions. Furthermore, the q_e value of Cd(II) ions is higher than that of Ni(II) ions in the pseudo-first-order and pseudo-second-order. However, other studies reported the adsorption of heavy metal ions followed pseudo-second-order, i.e., Cd(II) and Ni(II) ions studied using expanded perlite [12] and succinylated hay [15].

Isotherm of Adsorption

Two models of adsorption isotherm often used are Langmuir and Freundlich's isotherm models. The Langmuir isotherm model assumes monolayer adsorption, in which the adsorption occurs in a limited number and the active sites are localized and identical. Meanwhile, the Freundlich isotherm model describes a multilayer isotherm model with a heterogeneous surface and non-uniform heat distribution. Furthermore, the adsorption energy decreases exponentially after the adsorption process [3]. The equation that describes both the Langmuir and Freundlich isotherm models is as follows:

$$\frac{C_e}{q_e} = \frac{1}{K_L q_{max}} + \frac{C_e}{q_{max}} \quad (4)$$

$$\log q_e = \log K_f + \frac{1}{n}\log C_e \quad (5)$$

where C_e (mg/L) is the concentration of metal ions at equilibrium, q_e (mg/g) is the amount of metal ions adsorbed at equilibrium, q_{max} (mg/g) is the maximum number of metal ions absorbed per mass of adsorbent, and K_L (L/g) is the adsorption equilibrium constant. K_f (mg/g(mg/L)$^{1/n}$ is the constant fo Freundlich and $\frac{1}{n}$ is the adsorption intensity.

Fig. 10 shows the Langmuir and Freundlich isotherm adsorption models of Cd(II) and Ni(II) ions by hydroxyapatite/$MnFe_2O_4$ composite. The adsorption parameters are presented in Table 4. The adsorption of Cd(II) and Ni(II) ions follows the Langmuir isotherm model. The correlation coefficient (R^2) of the Langmuir isotherm model was more significant than the Freundlich isotherm model. The Langmuir isotherm also indicates that there is no interaction between adsorbates [26].

R_L is defined as a separation factor, and an essential parameter in the Langmuir isotherm used to determine the favorableness of the adsorption processes. If the value of $R_L > 1$, then the adsorption process is unfavorable,

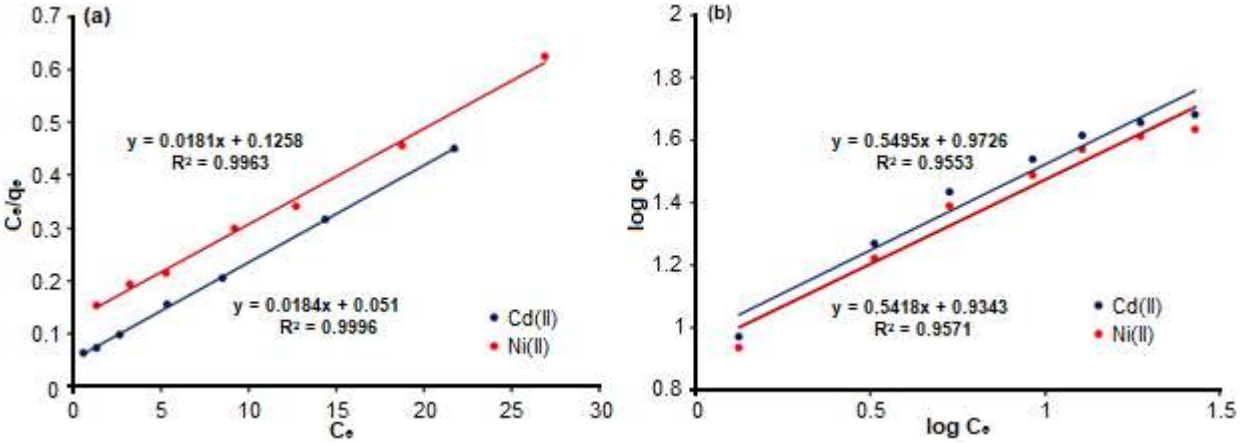

Fig 10. (a) Langmuir dan (b) Freundlich isotherm models adsorption of Cd(II) and Ni(II) ions by hydroxyapatite/$MnFe_2O_4$ composite

Table 4. Parameters of isotherm for adsorption of Cd(II) and Ni(II) ions by hydroxyapatite/$MnFe_2O_4$ composite

Parameters	Metal ions	
	Cd(II)	Ni(II)
Langmuir isotherm		
R^2	0.9996	0.9963
K_L (L/g)	0.3608	0.1677
q_{max} (mg/g)	54.348	47.393
Freundlich isotherm		
R^2	0.9553	0.9751
K_f (mg/g(mg/L)$^{1/n}$	9.36	8.02
n	1.819	1.678
q_{exp} (mg/g)	52.810	47.330

while if $R_L < 1$, then the process is favorable. The value R_L is determined based on the following equation:

$$R_L = \frac{1}{(1 + K_L C_0)} \quad (6)$$

C_0 (mg/L) is the initial concentration. The results show that the R_L values for various initial concentrations are between $0 < R_L < 1$. These findings indicate that the adsorption processes are favorable. These results were also confirmed by the values of n, which were n > 1, indicating that the adsorption process is favorable. The n values for the adsorption of Cd(II) and Ni(II) ions are 1.819 and 1.678, respectively.

The adsorption capacity data results showed that the calculated adsorption capacity (q_{max}) was greater than that of the experiment (q_{exp}) for both metal ions. The maximum adsorption capacity of hydroxyapatite/$MnFe_2O_4$ composite for Cd(II) ions is 54.3 mg/g greater than Ni(II) ions, 47.3 mg/g. The effectivity of adsorption depends on the size of the ions in solution, ionic radius, and atomic mass [37]. The ionic radius of Cd(II) (109 pm) is greater than Ni(II) (83 pm), so it is reasonable that the adsorption capacity of hydroxyapatite/$MnFe_2O_4$ composite for Cd(II) ions is greater [1]. The other research reported that the selectivity of metal ions against calcium alginate is Pb > Cu > Cd > Ni > Zn > Co, based on equilibrium constant (K). K_{Cd} value (172 kg L/mol^2) is greater than K_{Ni} (30.8 kg L/mol^2) [38]. Table 5 shows the adsorption capacities of several adsorbents against Cd(II) and Ni(II) ions. The adsorption capacity of hydroxyapatite/$MnFe_2O_4$ composites is greater than other adsorbents.

Desorption

In this study, hydroxyapatite/$MnFe_2O_4$ composite regeneration was carried out using two eluents, namely NaCl (inorganic eluent) and EDTA (organic eluent) solutions. Cd(II) and Ni(II) ions from hydroxyapatite/$MnFe_2O_4$ composite desorbed easier when using NaCl compared to EDTA (Fig. 11). The desorption mechanism using NaCl involved electrostatic attraction or ion exchange, whereas when desorption is using EDTA, it occurs due to the chemical bond formed by the chelating agent [1].

Table 5. The adsorption capacity of several adsorbents against Cd(II) and Ni(II) ions at room temperature

Sorbent	pH	Adsorption capacity (mg/g)		Reference
		Cd(II)	Ni(II)	
Expanded perlite	6	1.791	2.24	[13]
Chitosan-Methylmethacrylic acid	5	2.42	1.13	[1]
Bottlebrush seeds	6	39.525	-	[39]
Ag-$MnFe_2O_4$-bentonite	6	48.31	-	[2]
Green longan hull	5	4.19	3.96	[14]
Calcium alginate beads (CA)	6	38.049	14.668	[3]
Spent coffee ground (SCGs)	6	10.671	5.608	[3]
CA-SCGs	6	25.495	12.320	[3]
Graphite decorated manganese oxide	5		0.110	[30]
Callinectes sapidus biomass	6	29.23	29.15	[40]
Sludge	5	1.53	-	[41]
Hydroxyapatite/$MnFe_2O_4$ composite	6	54.348	47.393	In this study

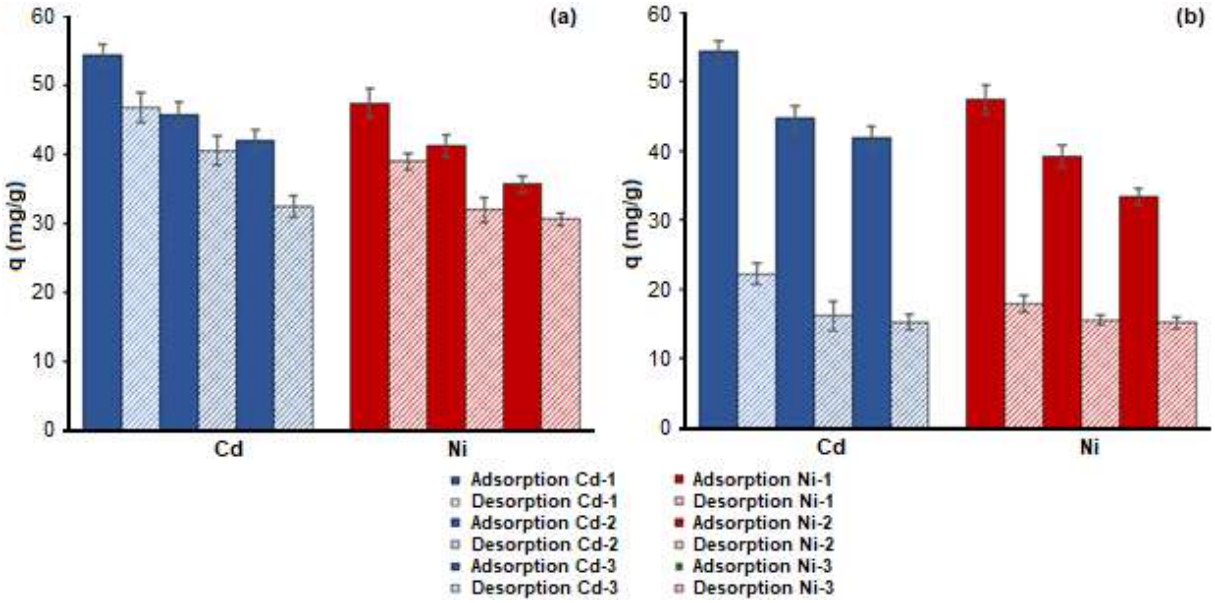

Fig 11. Adsorption-desorption of Cd(II) and Ni(II) ions using eluents (a) NaCl and (b) EDTA

Other studies on the desorption of Cd(II) and Pb(II) ions from $MnFe_2O_4$-graphene showed that desorption occurred electrostatically using HCl as an eluent [42]. The percentage of desorption depends on the type of metal ions and eluents used [25]. Desorption of Cu(II), Pb(II), and Cd(II) ions adsorbed by spent-coffee-grounds shows different results, i.e., citric acid is effective for desorption of Cu(II) ions, calcium chloride is effective for desorption of Pb(II) ions, and HNO_3 can properly desorb these three metal ions.

■ CONCLUSION

Hydroxyapatite/$MnFe_2O_4$ composite having magnetic properties was successfully synthesized to adsorb Cd(II) and Ni(II) ions from solutions. The optimum adsorption process for Cd(II) ions occurs at pH of 6, initial concentration of 60 mg/L, and contact time of 90 min, while Ni(II) ions adsorbed optimally at a pH of 6, initial concentration of 60 mg/L, and contact time of 100 min. The pseudo-second-order adsorption kinetics best suit for describing the adsorption kinetics of Cd(II) and Ni(II) ions by hydroxyapatite/$MnFe_2O_4$ composite. The adsorption capacity of hydroxyapatite/$MnFe_2O_4$ composite for Cd(II) ion (54.348 mg/g) is more significant than Ni(II) ion (47.393 mg/g). The Cd(II) and Ni(II) ions can be desorbed from hydroxyapatite/$MnFe_2O_4$ composite using NaCl and EDTA, provided that NaCl is a better eluent than EDTA. It can be suggested that hydroxyapatite/$MnFe_2O_4$ composite can reduce pollutants, primarily metal ions, in solutions. Hydroxyapatite/$MnFe_2O_4$ composite has magnetic properties; hence the adsorbent can be separated simply by using an external magnet.

■ ACKNOWLEDGMENTS

The author greatly thanks the Ministry of Research, Technology and Higher Education of Indonesia, who supports funding under the *Hibah Penelitian Dasar Unggulan Perguruan Tinggi* 2020 (No. 0125.02/UN9/SB3.LP2M.PT/2020).

■ AUTHOR CONTRIBUTIONS

Poedji Loekitowati Hariani, Muhammad Said, Addy Rachmat, and Salni carried out the experiment. Poedji Loekitowati Hariani and Muhammad Said contributed to the synthesis and characterization of materials, Addy Rachmat and Salni contributed to adsorption and desorption data interpretation. Finally, all the authors discuss and contribute to the final manuscript.

■ REFERENCES

[1] Heidari, A., Younesi, H., Mehraban, Z., and Heikkinen, H., 2013, Selective adsorption of Pb(II), Cd(II), and Ni(II) ions from aqueous solution using chitosan-MAA nanoparticles, *Int. J. Biol. Macromol.*, 61, 251–263.

[2] Li, Q., Zhao, Y., Qu, D., Wang, H., Chen, J., and Zhou, R., 2018, Preparation of Ag-$MnFe_2O_4$-bentonite magnetic composite for Pb(II)/Cd(II) adsorption removal and bacterial inactivation in wastewater, *Chem. Res. Chin. Univ.*, 34 (5), 808–816.

[3] Torres-Caban, R., Vega-Olivencia, C.A., and Mina-Camilde, N., 2019, Adsorption of Ni^{2+} and Cd^{2+} from water by calcium alginate/spent coffee grounds composite beads, *Appl. Sci.*, 9 (21), 4531.

[4] Liao, V.H.C., Chien, M.T., Tseng, Y.Y., and Qu, K.L., 2006, Assessment of heavy metal bioavailability in contaminated sediments and soils green fluorescent protein-based bacterial biosensors, *Environ. Pollut.*, 142 (1), 17–23.

[5] Soylak, M., Kars, A., and Narin, I., 2008, Coprecitation of Ni^{2+}, Cd^{2+} and Pb^{2+} for preconcentration in environmental samples prior to flame atomic absorption spectrometric determination, *J. Hazard. Mater.*, 159 (2-3), 435–439.

[6] Kasprzak, K.S., Sunderman Jr., F.W., and Salnikow, K., 2003, Nickel carcinogenesis, *Mutat. Res., Fundam. Mol. Mech. Mutagen.*, 533 (1-2), 67–97.

[7] Sobhanardakani, S., and Zandipak, R., 2015, Adsorption of Ni(II) and Cd(II) from aqueous solutions using modified rice husk, *Iran. J. Health Sci.*, 3 (1), 1–9.

[8] Qdais, H.A., and Moussa, H., 2004, Removal of heavy metals from wastewater by membrane processes: A comparative study, *Desalination*, 164 (2), 105–110.

[9] Igiri, B.E., Okoduwa, S.I.R., Idoko, G.O., Akabuogu, E.P., Adeyi, A.O., and Ejiogu, I.K., 2018, Toxicity and bioremediation of heavy metals contaminated ecosystem from tannery wastewater: A review, *J Toxicol.*, 2018, 2568038.

[10] Thaçi, B.S., and Gashi, S.T., 2019, Reverse osmosis removal of heavy metals from wastewater effluents using biowaste materials pretreatment, *Pol. J. Environ. Stud.*, 28 (1), 337–341.

[11] Zewail, T.M., and Yousef, N.S., 2015, Kinetic study of heavy metal ions removal by ion exchange in batch conical air spouted bed, *Alexandria Eng. J.*, 54 (1), 83–90.

[12] Torab-Mostaedi, M., Ghassabzadeh, H., Ghannadi-Maragheh, M., Ahmadi, S.J., and Taheri, H., 2010, Removal of cadmium and nickel from aqueous solution using expanded perlite, *Braz. J. Chem. Eng.*, 27 (2), 299–308.

[13] Wijesinghe, W.P.S.L., Mantilaka, M.M.M.G.P.G., Peiris, T.A.N., Rajapakse, R.M.G., Wijayantha, K.G.U., Pitawala, H.M.T.G.A., Premachandra, T.N., Herath, H.M.T.U., and Rajapakse, R.P.V.J., 2018, Preparation and characterization of mesoporous hydroxyapatite with non cytotoxicity and heavy metal adsorption capacity, *New J. Chem.*, 42 (12), 10271–10278.

[14] Guo, X., Tang, S., Song, Y., and Nan, J., 2018, Adsorptive removal of Ni^{2+} and Cd^{2+} from wastewater using a green longan hull adsorbent, *Adsorpt. Sci. Technol.*, 36 (1-2), 762–773.

[15] Lin, P., Wu, J., Ahn, J., and Lee, J., 2019, Adsorption characteristic of Cd(II) and Ni(II) from aqueous solution using succinylated hay, *Int. J. Miner. Metall. Mater.*, 26 (10), 1239–1246.

[16] Roy, S., and Das, P., 2016, Thermodynamic and kinetics study of de-fluoridation in wastewater using hydroxyapatite (Hap) as adsorbent: optimization using response surface methodology, *Front. Nanosci. Nanotechnol.*, 2 (3), 121–128.

[17] Hamzah, S., Yatim, N.I., Alias, M., Ali, A., Rasit, N., and Abuhabib, A., 2019. Extraction of hydroxyapatite from fish scales and its integration with rice husk for ammonia removal in aquaculture wastewater, *Indones. J. Chem.*,19 (4), 1019–1030.

[18] Iconaru, S.L., Heino, M.M., Guegan, R., Beuran, M., Costecu, A., and Predoi, D., 2018, Adsorption of Pb(II) ions onto hydroxyapatite nanopowders in aqueous solution, *Materials*, 11 (11), 2204.

[19] Le, D.T., Le, T.P.T., Do, H.T., Vo, H.T., Pham, N.T., Nguyen, T.T., Cao, H.T., Nguyen, P.T., Dinh, T.M.T., Le, H.V., and Tran, D.L., 2019, Fabrication

of porous hydroxyapatite granules as an effective adsorbent for the removal of aqueous Pb(II) ions, *J. Chem.*, 2019, 8620181.

[20] Dabiri, S.M.H., Rezaie, A.A., Moghimi, M., and Rezaie, H., 2018, Extraction of hydroxyapatite from fishbone and its application, *BioNanoScience*, 8 (3), 823–834.

[21] Idea, P., Degli Esposti, L., Miguel, C.C., Adamiano, A., Iafisco, M., and Castilho, P.C., 2021, Extraction and characterization of hydroxyapatite-based materials from grey triggerfish skin and black scabbardfish bones, *Int. J. Appl. Ceram. Technol.*, 18 (1), 235–243.

[22] Zairin, D.A., and Phang, S.W., 2018, Calcination time and temperature effect on natural hydroxyapatite obtained from fish bones for bone tissue engineering, *Int. J. Eng. Sci. Technol*., Special issue August, 39–51.

[23] Hariani, P.L., Muryati, M., and Said, M., 2019, Kinetic and thermodynamic adsorption of nickel(II) onto hydroxyapatite prepared from Snakehead (*Channa striata*) fish bone, *Mediterr. J. Chem.*, 9 (2), 85–94.

[24] Hariani, P.L., Muryati, M., Said, M., and Salni, S., 2020, Synthesis of nano-hydroxyapatite from Snakehead (*Channa striata*) fish bone and its antibacterial properties, *Key Eng. Mater.*, 840, 293–299.

[25] Dong, L., Zhu, Z., Qiu, Y., and Zhao, Z., 2010, Removal of lead from aqueous solution by hydroxyapatite/magnetite composite adsorbent, *Chem. Eng. J*., 165 (3), 827–834.

[26] Ansari, A., Vahedi. S., Tavakoli, O., Khoobi, M., and Faramarzi, M.A., 2018, Novel Fe_3O_4/hydroxyapatite/β-cyclodextrin nanocomposite adsorbent: synthesis and application in heavy metal removal from aqueous solution, *Appl. Organomet. Chem.*, 33 (1), e4634.

[27] Ragab, A., Ahmed, I., and Bader, D., 2019, The removal of brilliant green dye from aqueous solution using hydroxyapatite/chitosan composite as sorbent, *Molecules*, 24 (5), 847.

[28] Shao, L., Ren, Z., Zhang, G., and Chen, L., 2012, Facile synthesis, characterization of a $MnFe_2O_4$/activated carbon magnetic composite and its effectiveness in tetracycline removal, *Mater. Chem. Phys.*, 135 (1), 16–24.

[29] Podder, M.S., and Majumder, C.B., 2016, Studies on the removal of As(III) and As(V) through their adsorption onto granular activated carbon/$MnFe_2O_4$ composite: Isotherm studies and error analysis, *Compos. Interfaces*, 23 (4), 327–372.

[30] Do, Q.C., Choi, S., Kim, H., and Kang, S., 2019, Adsorption of lead and nickel on to expanded graphite decorated with manganese oxide nanoparticles, *Appl. Sci*., 9 (24), 5375.

[31] Soejoko, D.S., and Tjia, M.O., 2002, Infrared spectroscopy and X-ray diffraction study on the morphological variations of carbonate and phosphate compounds in giant prawn (*Macrobrachium rosenbergii*) skeletons during its moulting period, *J. Mater. Sci*., 38 (9), 2087–2093.

[32] Wang, P., Li, C., Gong, H., Jiang, X., Wang, H., and Li, K., 2013, Effects of synthesis conditions on the morphology of hydroxyapatite nanoparticles produced by wet chemical process, *Powder Technol.*, 203 (2), 315–321.

[33] Yari Moghaddam, N., Lorestani, B., Cheraghi, M., and Jamebozorgi, S, 2019, Adsorption of Cd and Ni from water by graphene oxide and graphene oxide-almond shell composite, *Water Environ. Res.*, 91 (6), 475–482.

[34] Riyanti, F., Hariani, P.L., Purwaningrum, W., Elfita, E., Damarril, S.S., and Amelia, I., 2018, The synthesis of $MnFe_2O_4$-activated carbon composite for removal of methyl red from aqueous solution, *Molekul*, 13 (2), 123–132.

[35] Danmaliki, G.I., and Saleh, T.A., 2016, Influence of conversion parameters of waste tires to activated carbon on adsorption of dibenzothiophene from models fuels, *J. Cleaner Prod.*, 117, 50–55.

[36] Kausar, A., Naeem, K., Hussain, T., Nazli, Z.I.H., Bhatti, H.N., Jubeen, F., Nazir, A., and Iqbal, M., 2019, Preparation and characterization of

chitosan/clay composite for direct rose FRN dye removal from aqueous media: Comparison of linear and non-linear regression methods, *J. Mater. Res. Technol.*, 8 (1), 1161–1174.

[37] Hossain, M.A., Ngo, H.H., Guo, W.S., Nghiem, L.D., Hai, F.I., Vigneswaran, S., and Nguyen, T.V., 2014, Competitive adsorption of metals on cabbage waste from multi-metal solutions, *Bioresour. Technol.*, 160, 79–88.

[38] Jodra, Y., and Mijangos, F., 2001, Ion exchange selectivities of calcium alginate gels for heavy metals, *Water Sci. Technol.*, 43 (2), 237–244.

[39] Rao, R.A.K., and Kashifuddin, M., 2014, Kinetics and isotherm studies of Cd(II) adsorption from aqueous solution utilizing seeds of bottlebrush plant (*Callistemon chisholmii*), *Appl. Water Sci.*, 4 (4), 371–383.

[40] Foroutan, R., Mohammadi, R., Farjadfard, S., Esmaeili, H., Saberi, M., Sahebi, S., Dobaradaran, S., and Ramavandi, B., 2019, Characteristic and performance of Cd, Ini, and Pb bio-adsorption using *Callinectes sapidus* biomass: Real wastewater treatment, *Environ. Sci. Pollut. Res. Int*., 26, 6336–6347.

[41] Du, X., Cui, S., Fang, X., Wang, Q., and Liu, G., 2020, Adsorption of Cd(II), Cu(II), and Zn(II) by granules prepared using sludge from a drinking water purification plant, *J. Environ. Chem. Eng*., 8 (6), 104530.

[42] Chella, S., Kollu, P., Komarala, E.V.P.R., Doshi, S., Saranya, M., Felix, S., Ramachandran, R., Saravanan, P., Koneru, V.L., Venugopal, V., Jeong, S.K., and Grace, A.N., 2015, Solvothermal synthesis of $MnFe_2O_4$-graphene composite—Investigation of its adsorption and antimicrobial properties, *Appl. Surf. Sci*., 327, 27–36.

Adsorption of Toxic Heavy Metal Methylmercury (MeHg) on Germanene in Aqueous Environment: A First-Principles Study

Muhammad Rifqi Al Fauzan[1], Trias Prima Satya[1], Galih Setyawan[1], Imam Fahrurrozi[1], Fitri Puspasari[1], Juliasih Partini[2], and Sholihun Sholihun[2*]

[1]*Department of Electrical Engineering and Informatics, Vocational College, Universitas Gadjah Mada, Sekip Unit III, Yogyakarta 55281, Indonesia*

[2]*Department of Physics, Faculty of Mathematics and Natural Sciences, Universitas Gadjah Mada, Sekip Utara BLS 21, Yogyakarta 55281, Indonesia*

* ***Corresponding author:***

email: sholihun@ugm.ac.id

Received: June 22, 2021
Accepted: August 27, 2021

DOI: 10.22146/ijc.66902

Abstract: *We perform first-principles calculations to investigate the adsorption process of methyl mercury (MeHg) on germanene with the presence of water molecules. We calculate the formation energy and density of states to determine the effect of the adsorption of MeHg on the structural and electronic properties of germanene. Our results show that MeHg is chemisorbed on germanene through a spontaneous reaction. The calculated formation energy of the system is -1.61 eV. We also carry out charge distribution and charge transfer calculations based on the Mulliken model to understand the adsorption mechanism of MeHg.*

Keywords: *methylmercury; germanene; adsorption; formation energy; the density of states*

■ INTRODUCTION

Mercury (Hg) poses a severe danger to humans and the environment, e.g., Hg exposure causes a wide range of health problems. This element can affect the lungs, brain, and skin and cause permanent damage to the nervous system [1-2]. Anthropogenic and natural sources contribute to the accumulation of Hg in soil. With intervention from microbial methylation reaction, inorganic Hg in the soil can be transformed into methylmercury (MeHg), one of the most toxic forms of organic Hg [3]. The MeHg molecule penetrates from soil to aquatic systems through runoff. It can bioaccumulate and biomagnify up the aquatic food chain. Therefore, MeHg is a major hazard to humans [4].

Remediation techniques are needed to control MeHg contamination in aquatic systems. Wang et al. reported several techniques that are needed to counter the MeHg pollution [5]. They explained the commonly used and emerging remediation techniques such as stabilization (solidification), nanotechnology, phytoextraction, etc. This study uses the adsorption mechanism by using germanene, as a host material. Germanene is a two-dimensional germanium-based material analog of graphene [6] and has been successfully grown on various substrates such as Au(111) [7], Pt(111) [8], and Al(111) [9]. Germanene exhibits strong sensitivity to chemical and environmental changes. Previous studies showed that germanene successfully adsorbs 3d transitional metal atoms (Sc, Ti, V, Cr, Mn, Fe, Co, Ni, Cu, and Zn) [10], alkali metal atoms (Li, Na, and K) [11-12] and various gas molecules [13]. From the calculated adsorption energy, germanene more easily adsorbs small gas molecules than silicene [14-15]. Therefore, the study of molecule adsorption on germanene, particularly that of a toxic molecule such as MeHg is necessary.

In the present work, we perform first-principles density-functional-theory (DFT) calculations to investigate the capability of germanene to adsorb the heavy metal MeHg in aqueous conditions. Supercell with 32 atomic sites is involved, and all atoms are relaxed to find the optimized geometry. We calculate the formation energy (E_{form}), the density of states (DOS), and charge transfer to study the adsorption mechanism of MeHg in germanene.

■ COMPUTATIONAL METHODS

The DFT calculations are performed using OpenMX (Open-source package for Material eXplorer) code [16-18] based on pseudo-atomic localized basis functions. In this code, the norm-conserving pseudopotential is used [19], and the wave functions are expanded by a linear combination of multiple pseudo-atomic orbitals [17-18]. The exchange-correlation functional is evaluated using the generalized gradient approximation with the Perdew-Burke-Ernzerhof method [20]. A 25-point grid is applied in the Brillouin zone integration. The energy convergence of the self-consistent calculations is adjusted at 10^{-4} Ha.

In this study, we use a supercell model in which the germanene surface lies on the x–y plane (Fig. 1). The supercell is generated by using a two-atoms unit cell with the optimized lattice constant. Lattice parameter optimization is carried out using the Murnaghan equation of states as follows [21-26]:

$$E(V) = E_0 + B_0 V_0 \left[\frac{1}{B_0'\left(B_0' - 1\right)} \left(\frac{V}{V_0} \right)^{1-B_0'} + \frac{1}{B_0'} \left(\frac{V}{V_0} \right) - \frac{1}{B_0' - 1} \right] \quad (1)$$

where E_0, V_0, B_0, and B_0' are the fitting parameters calculated at the constant volume. E_0 is total energy, and V_0 is lattice volume while B_0 and B_0' are bulk modulus and its first derivative, respectively.

A 20 Å vacuum parameter, which is large enough to prevent interactions between adjacent layers, is applied perpendicularly to the germanene surface (Fig. 1(b)). A 4×4×1 supercell containing 32 atoms is used as the host material. To model the aqueous environment, we introduce water molecules on the surface of germanene. We then calculate the formation energy E_{form} and charge transfer. The E_{form} is defined by using the following equation [27-31]:

$$E_{form} = E_{subs/host} - \left(E_{subs} + E_{host}\right) \quad (2)$$

where E_{subs}, E_{host}, and $E_{subs/host}$ are the total energies of the isolated substrate, clean host material, and adsorption system, respectively. The same size of the unit cell is used for the system of interest. Using this definition, a negative value of E_{form} indicates spontaneous adsorption, and a positive value refers to non-spontaneous adsorption where the adsorbed state has more positive energy than the isolated one. Thus, external energy is needed to carry out the adsorption process. Meanwhile, the charge density difference was obtained by subtracting the total charge of the adsorption system from the individual charges of the isolated substrate and the host material [14,31], as follows:

$$\Delta\rho = \rho_{MeHg/Ge} - \left(\rho_{MeHg} + \rho_{Ge}\right) \quad (3)$$

where ρ_{MeHg}, ρ_{Ge}, and $\rho_{MeHg/Ge}$ are the charge density of MeHg with water molecules, germanene, and the adsorption system, respectively.

■ RESULTS AND DISCUSSION

Germanene in an Aqueous Environment

We perform first-principles calculations of the germanene supercell with the presence of water molecules and MeHg molecule. We first optimize the

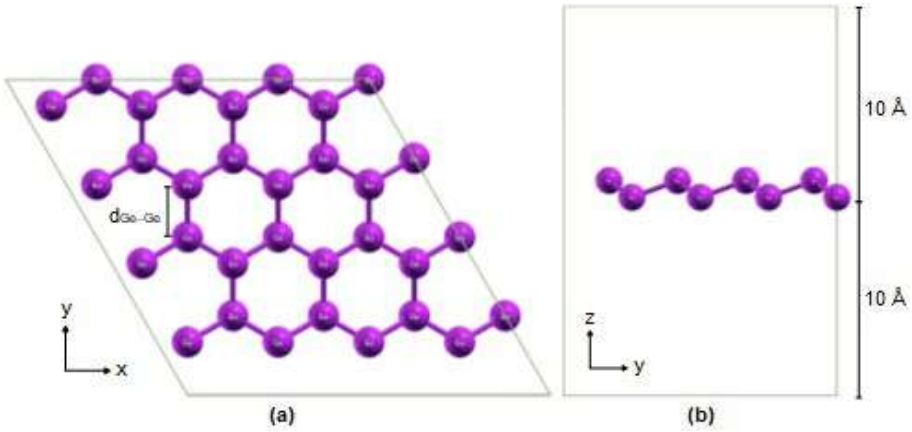

Fig 1. Pristine germanene supercell: (a) front-view overlaying the x–y plane and (b) side-view showing the vacuum parameter in the z-direction. The purple balls denote germanium atoms

germanene unit cell. The lattice constant of 4.06 Å is calculated using Eq. (1). This result agrees with the previous calculations [6,25]. The lattice constant of germanene is higher than that of silicene (3.86 Å) [32]. As for the bond lengths, the calculated Ge–Ge bond (d) is 2.46 Å, which is slightly higher than that of the Si–Si bond in silicene (2.24 Å) [33]. This result is in agreement with the results of previous theoretical [25,34] and experimental studies [7].

We next calculate the formation energy E_{form} using Eq. (2) and found that the system of germanene with water molecules (H_2Os/G) has E_{form} of +0.05 eV. The positive value of E_{form} implies the endothermicity of the adsorption process. Therefore, the adsorption only occurs in the presence of external energy.

We calculate the DOS to determine the electronic properties of the systems. Our results show that the presence of water molecules on the surface of germanene causes no change in the electronic state near the Fermi level, i.e., the shape of the DOS is the same, and there is no gap created. As shown in Fig. 2(a), the electronic state of pristine germanene is a semimetal with a zero bandgap at Dirac point. With the presence of water, the electronic state remains the same as in the pristine germanene (Fig. 2(b)). The difference in magnitude of the DOS at some energy ranges, e.g., at about -5 eV and +8 eV, is due to water molecules in the system.

Adsorption of MeHg on germanene

We introduce the MeHg molecule on germanene with water molecules, that is, MeHg/G. Fig. 3 shows the stable structure of this system. The calculated E_{form} of

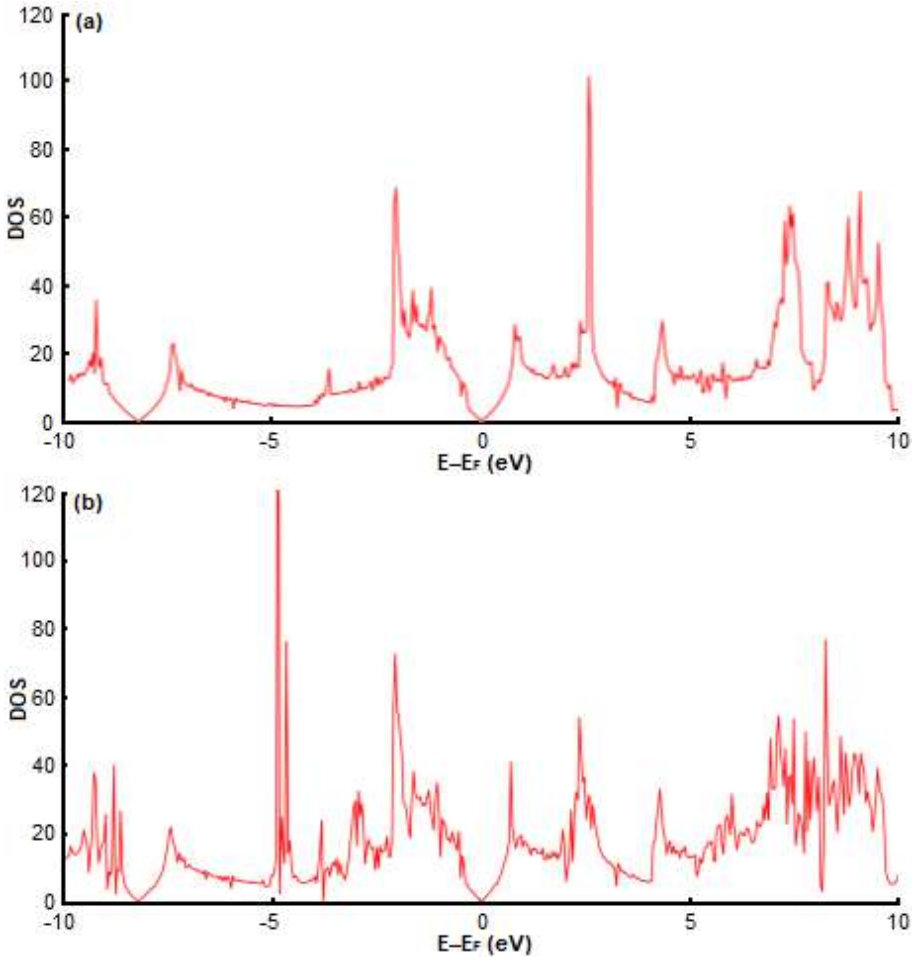

Fig 2. The density of states (DOS) of (a) pristine germanene and (b) germanene with water molecules. The Fermi level is set to zero

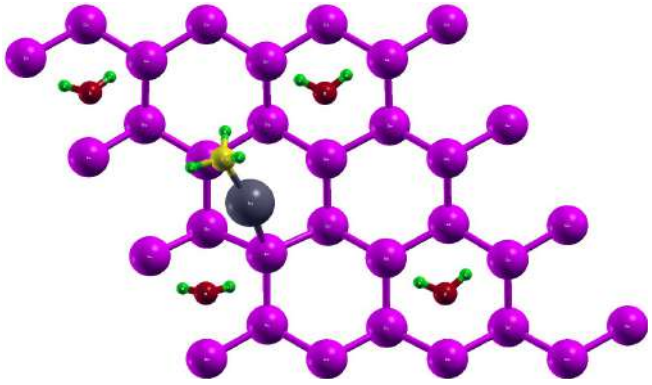

Fig 3. Stable structure of MeHg adsorption on germanene in aqueous condition. The black, yellow, green, red, and purple balls denote mercury, carbon, hydrogen, oxygen, and germanium atoms, respectively

MeHg/G is -1.61 eV. In contrast to the H_2Os/G system, the interaction between MeHg and germanene indicates a spontaneous reaction (negative E_{form}). Therefore, the adsorption of MeHg on germanene easily occurs without external energy.

Calculations for electronic properties showed that the DOS of germanene changes after adsorbing MeHg (Fig. 4). The MeHg adsorption opens a narrow bandgap, making germanene a semiconductor with a 0.20 eV bandgap. Ye et al. reported a similar result: germanene has a narrow bandgap ranging from 0.02 eV to 0.31 eV after adsorbing several alkali metal atoms [12].

The adsorption mechanism can be investigated by considering charge transfer between atoms in MeHg and germanium. We calculate the charge difference distribution $\Delta\rho$ as expressed in Eq. (3) to investigate the presence of charge transfer between two materials. Fig. 5 shows the isosurface of the charge and indicates the charge transfer between germanene and MeHg in an aqueous environment.

We then employ the Mulliken charge analysis to evaluate the net charge transfer between the materials. We observe that germanene loses its electron charge by about 0.25 e. On the other hand, heavy metal MeHg in an aqueous environment receives electron charge from germanene. This result agrees with the charge difference distribution as plotted in Fig. 5, where the depletion and accumulation of charges are observed between MeHg and Ge atoms of germanene.

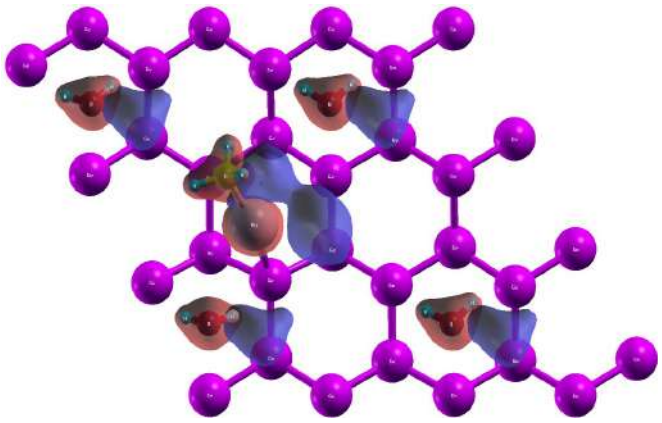

Fig 5. Charge difference distribution of the MeHg/G system. Red and blue areas illustrate the accumulation and loss of charge, respectively. Electron charges move from blue to red areas

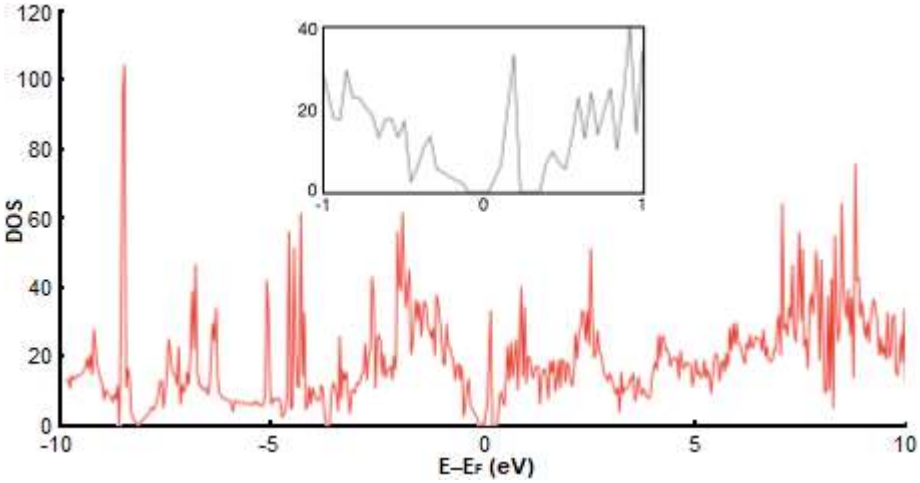

Fig 4. DOS of MeHg/G system with magnification around the Fermi level

Atomic Path

At the initial geometry, the Hg atom is placed on the center of the honeycomb structure of germanene with a vertical distance of 2.5 Å to the surface of germanene (Fig. 6). During relaxation, the Hg atom diffuses to the Ge1 atom and creates a covalent bond. The calculated bond length of Hg–Ge1 is 2.84 Å in the transition geometry, whereas the bond length shortens to 2.70 Å in the final geometry. The presence of MeHg affects the position of its adjacent atoms particularly Ge1–Ge13. As a result, the atoms undergo vertical distortions in various magnitudes, as listed in Table 1.

In the final geometry, the formation of MeHg remains as that of its molecular form with the Hg–C and C–H bond lengths of 2.19 and 1.11 Å, respectively. Given that MeHg is symmetric under C_3 (rotation by 2π) and symmetric under the vertical mirror σ_v, it shows a C_{3v} symmetry. Meanwhile, the water has a C_{2v} molecule with the O–H bond length of 0.99 Å.

■ CONCLUSION

We perform DFT calculations to investigate the adsorption mechanism of MeHg on germanene with the presence of water molecules. MeHg is chemisorbed on germanene with a E_{form} of -1.61 eV. To determine the mechanism of interaction, we carry out charge difference distribution and charge transfer calculations. Our results show that germanene distributes an electron charge of 0.25 e to MeHg under aqueous conditions.

■ ACKNOWLEDGMENTS

The authors would like to thank Universitas Gadjah Mada for the computer facilities during finishing this research. In addition, the authors (S. and J.P.) thank the Ministry of Research and Technology for the financial support through the *Penelitian Dasar* 2021 research grant.

Table 1. Magnitudes of vertical distortion of MeHg neighboring atoms. The values are obtained by subtracting the initial state coordinates from the final state coordinates. Positive and negative values indicate that the Ge atom is moving away and moving closer to MeHg in the z-direction, respectively

Atom	Magnitude (Å)	Atom	Magnitude (Å)
Ge1	0.23	Ge8	0.22
Ge2	0.40	Ge9	0.17
Ge3	0.52	Ge10	-0.03
Ge4	0.60	Ge11	0.11
Ge5	0.98	Ge12	0.15
Ge6	0.72	Ge13	0.59
Ge7	0.45		

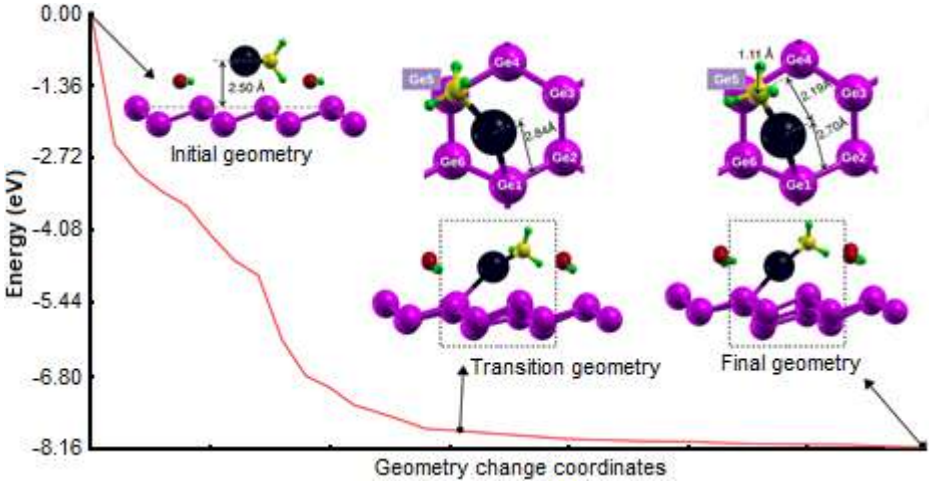

Fig 6. Atomic path of MeHg/G system, the initial, transition, and final geometries are shown. The areas inside the dashed rectangular are also illustrated in the top view for clarity. The zero level is referenced to that the energy of initial geometry

■ REFERENCES

[1] Liu, G., Cai, Y., O'Driscoll, N., Feng, X., and Jiang, G., 2011, "Overview of Mercury in the Environment" in *Environmental Chemistry and Toxicology of Mercury*, Eds. Liu, G., Cai, Y., and O'Driscoll, N., Wiley, New Jersey, 1–12.

[2] Fitzgerald, W.F., and Lamborg, C.H., 2007, Geochemistry of Mercury in the Environment, *Treatise Geochem.*, 9, 1–47.

[3] Gasong, B.T., Abrian, S., and Setyabudi, F.M.C.S., 2017, Methylmercury biosorption activity by methylmercury-resistant lactic acid bacteria isolated from West Sekotong, Indonesia, *HAYATI J. Biosci.*, 24 (4), 182–186.

[4] National Research Council, 2000, *Toxicological Effects of Methylmercury*, National Academy Press, Washington, DC.

[5] Wang, J., Feng, X., Anderson, C.W.N., Xing, Y., and Shang, L., 2012, Remediation of mercury contaminated sites - A review, *J. Hazard. Mater.*, 221-222, 1–18.

[6] Acun, A., Zhang, L., Bampoulis, P., Farmanbar, M., van Houselt, A., Rudenko, A.N., Lingenfelder, M., Brocks, G., Poelsema, B., Katsnelson, M.I., and Zandvliet, H.J.W., 2015, Germanene: The germanium analogue of graphene, *J. Phys.: Condens. Matter*, 27, 443002.

[7] Dávila, M.E., Xian, L., Cahangirov, S., Rubio, A., and Le Lay, G., 2014, Germanene: A novel two-dimensional germanium allotrope akin to graphene and silicene, *New J. Phys.*, 16, 095002.

[8] Li, L., Lu, S.Z., Pan, J., Qin, Z., Wang, Y.Q., Wang, Y., Cao, G.Y., Du, S., and Gao, H.J., 2014, Buckled germanene formation on Pt(111), *Adv. Mater.*, 26 (28), 4820–4824.

[9] Derivaz, M., Dentel, D., Stephan, R., Hanf, M.C., Mehdaoui, A., Sonnet, P., and Pirri, C., 2015, Continuous germanene layer on Al(111), *Nano Lett.*, 15 (4), 2510–2516.

[10] Kaloni, T.P., 2014, Tuning the structural, electronic, and magnetic properties of germanene by the adsorption of 3d transition metal atoms, *J. Phys. Chem. C*, 118 (43), 25200–25208.

[11] Pang, Q., Zhang, C.L., Li, L., Fu, Z.Q., Wei, X.M., and Song, Y.L., 2014, Adsorption of alkali metal atoms on germanene: A first-principles study, *Appl. Surf. Sci.*, 314, 15–20.

[12] Ye, M., Quhe, R., Zheng, J., Ni, Z., Wang, Y., Yuan, Y., Tse, G., Shi, J., Gao, Z., and Lu, J., 2014, Tunable band gap in germanene by surface adsorption, *Physica E*, 59, 60–65.

[13] Xia, W., Hu, W., Li, Z., and Yang, J., 2014, A first-principles study of gas adsorption on germanene, *Phys. Chem. Chem. Phys.*, 16 (41), 22495–22498.

[14] Al Fauzan, M.R., Astuti, W.D., Al Fauzan, G., and Sholihun, 2018, The interaction of air pollutant molecules with germanene and silicene: A density functional theory study, *Molekul*, 13 (1), 92–97.

[15] Liu, G., Liu, S.B., Xu, B., Ouyang, C.Y., and Song, H.Y., 2015, First-principles study of the stability of free-standing germanene in oxygen atmosphere, *J. Appl. Phys.*, 118, 124303.

[16] Ozaki, T., Kino, H., Yu, J., Han, M.J., Ohfuchi, M., Ishii, F., Sawada, K., Kubota, Y., Mizuta, Y.P., Ohwaki, T., Duy, T.V.T., Weng, H., Shiihara, Y., Toyoda, M., Okuno, Y., Perez, R., Bell, P.P., Ellner, M., Xiao, Y., Ito, A.M., Kawamura, M., Yoshimi, K., Lee, C.C., and Terakura, K., 2009, *User's manual of OPENMX v.3.8.*, http://www.openmxsquare.org.

[17] Ozaki, T., 2003, Variationally optimized atomic orbitals for large-scale electronic structures, *Phys. Rev. B*, 67, 155108.

[18] Ozaki, T., and Kino, H., 2004, Numerical atomic basis orbitals from H to Kr, *Phys. Rev. B*, 69, 195113.

[19] Troullier, N., and Martins, J.L., 1991, Efficient pseudopotentials for plane-wave calculations, *Phys. Rev. B*, 43, 1993.

[20] Perdew, J.P., Burke, K., and Ernzerhof, M., 1996, Generalized gradient approximation made simple, *Phys. Rev. Lett.*, 77, 3865.

[21] Zhuravlev, K.K., 2007, PbSe vs. CdSe: Thermodynamic properties and pressure dependence of the band gap, *Physica B*, 394 (1), 1–7.

[22] Murnaghan, F.D., 1944, The compressibility of media under extreme pressures, *Proc. Natl. Acad. Sci. U.S.A.*, 30 (9), 244–247.

[23] Birch, F., 1947, Finite elastic strain of cubic crystals, *Phys. Rev.*, 71 (11), 809–824.

[24] Amalia, W., Nurwantoro, P., and Sholihun, 2019, Density-functional-theory calculations of structural and electronic properties of vacancies in monolayer hexagonal boron nitride (h-BN), *Comput. Condens. Matter*, 18, e00354.

[25] Hastuti, D.P., Nurwantoro, P., and Sholihun, 2019, Stability study of germanene vacancies: The first-principles calculations, *Mater. Today Commun.*, 19, 459–463.

[26] Sholihun, Amalia, W., Hastuti, D.P., Nurwantoro, P., Nugraheni, A.D., and Budhi, R.H.S., 2019, Magic vacancy-numbers in h-BN multivacancies: The first-principles study, *Mater. Today Commun.*, 20, 100591.

[27] Śpiewak, J.P., Vanhellemont, J., and Kurzydlowski, K.J., 2011, Improved calculation of vacancy properties in Ge using the Heyd-Scuseria-Ernzerhof range-separated hybrid functional, *J. Appl. Phys.*, 110, 063534.

[28] Corsetti, F., and Mostofi, A.A., 2011, System-size convergence of point defect properties: The case of the silicon vacancy, *Phys. Rev. B*, 84, 035209.

[29] Probert, M.I.J., and Payne, M.C., 2003, Improving the convergence of defect calculations in supercells: An ab initio study of the neutral silicon vacancy, *Phys. Rev. B*, 67, 075204.

[30] Sholihun, Kadarisman, H.P., and Nurwantoro, P., 2018, Density-functional-theory calculations of formation energy of the nitrogen-doped diamond, *Indones. J. Chem.*, 18 (4), 749–754.

[31] Al Fauzan, M.R., Astuti, W.D., Al Fauzan, G., and Sholihun, 2018, A first-principles investigation of the adsorption of CO and NO molecules on germanene, *IOP Conf. Ser.: Mater. Sci. Eng.*, 367, 012051.

[32] Lee, K.W., and Lee, C.E., 2020, Strain and doping effects on the antiferromagnetism of AB-stacked bilayer silicene, *Physica B*, 577, 411816.

[33] Umam, K., Sholihun, Nurwantoro, P., Absor, M.A.U., Nugraheni, A.D., and Budhi, R.H.S., 2018, Biaxial strain effects on the electronic properties of silicene: The density-functional-theory-based calculations, *J. Phys.: Conf. Ser.*, 1011, 012074.

[34] Scalise, E., Houssa, M., Pourtois, G., van den Broek, B., Afanas'ev, V., and Stesmans, A., 2013, Vibrational properties of silicene and germanene, *Nano Res.*, 6 (1), 19–28.

Two Rival Newly Fabricated Potentiometric Sensors to Enhance Selectivity Toward Cu(II) Ions

Gamal Abdel-Hafiz Mostafa[1], Hazem Mohamed Abu Shawish[2*], Salman Mustafa Saadeh[3], and Essam Ezzeldin[1,4]

[1]*Department of Pharmaceutical Chemistry, College of Pharmacy, King Saud University, P.O. Box 2457, Riyadh 11451, Saudi Arabia*

[2]*Department of Chemistry, College of Sciences, Al-Aqsa University, Gaza, Palestine*

[3]*Department of Chemistry, Faculty of Science, The Islamic University, Gaza, Palestine*

[4]*Bioavailability Laboratory, Central laboratory, College of Pharmacy, King Saud, University, P.O. Box 2457, Riyadh 11451, Saudi Arabia*

* ***Corresponding author:***

email: hazemona1@yahoo.co.uk

Received: June 22, 2021
Accepted: August 26, 2021

DOI: 10.22146/ijc.66938

Abstract: *Utilizing the well-known ability of Schiff base ligands to bind metal ions, two newly fabricated ligands, namely: 2-((2-hydroxybenzylidene)amino)benzoic acid (L1) and 2-(furan-2-ylmethyleneamino)phenol (L2) were employed to coordinate copper(II) (Cu(II)) producing the characteristically stable complexes that performed as the ionophores in the presently fabricated electrodes A and B. Thus it was possible to build these electrodes that have attractive properties and expected behavior, namely, low detection limits: 2.32×10^{-7} and 1.14×10^{-6} M Cu(II), Nernstian slope of 29.13 and 30.85 mV/decade Cu(II), broad concentration ranges from 3.98×10^{-7}–1.00×10^{-2} and 1.52×10^{-6}–1.00×10^{-2} M for sensors A and B, respectively, as well as short response time (ca. 3–5 s) with distinct selectivity toward Cu(II) over the other cations and applicability over the pH range 1.5–5.5 for miscellaneous samples: aqueous solutions, urine, and blood serum. Thus, these sensors surpass many others towards fulfilling the intended function of Cu(II) determination in various applications.*

Keywords: *Cu(II); ligands; modified carbon paste electrode; potentiometry*

■ INTRODUCTION

Copper is one of the trace metals essential to all organisms. Plants and animals need it even in small amounts for the proper function of the body. For example, in an average 70 kg human, the mass of copper element is 72 mg and plays several crucially important biological roles: electron transfer systems in blue copper proteins; O_2 storage and transport in hemocyanin and Cu transport proteins ceruloplasmin [1]. Copper is mainly obtained from food such as liver and nuts and whole grain products [2]. The Institute of Medicine recommended 10 mg per day as an upper intake [3-5]. Copper deficiency results in health problems such as anemia, growth retardation, heart failure, and gastrointestinal disturbances [6]. Despite being a moderately toxic element, exposure to high levels of copper is associated with gastrointestinal disturbances, Wilson disease, symptoms of hypertension, and dermatitis [7]. Compounds of copper are utilized in various applications such as fungicides, insecticides, and wood preservatives [8], which make liability for exposure for many people.

Advanced analytical methods requiring expensive instrumentation are reported to determine copper(II) (Cu(II)) in various matrices at trace levels. These methods are neutron activation analysis [9], X-ray fluorescence [10], pulse polarography [11], inductively coupled plasma emission spectrophotometry (ICP-ES) [12], graphite furnace atomic absorption spectrophotometry (GF-AAS) [13], and flame atomic

absorption spectrometry (FAAS) [14-16]. These analytical techniques are highly sensitive and selective, but they are quite expensive for developing countries. Also, they require well-qualified laboratory personnel and superior laboratory equipment. In addition, many of the reported methods have some shortcomings, such as the availability of sophisticated instruments, time-consuming operation, tedious work, multi-step processes for pre-concentration of the analyte, and low selectivity with more serious interference problems [17].

The potentiometric analysis is the most often used analytical procedure for analysis for it is simple, many ligands have been used to determine Cu(II) [18-22]. However, these procedures have various limitations, such as a high limit of detection, a narrow range, or interferences from many ions. Modified carbon paste electrodes (MCPE) have attractive characteristic properties. Being chemically inert, robust, easy to prepare and use, having a renewable surface, low ohmic resistance, and no need for an internal solution give a stable response and are thus considered suitable for various applications [23-25]. Educated selection of constituents and their relative composition followed by relevant experiments to spot the combination that gives the best response will show up in the fabrication of new electrodes proven helpful for implementation in the intended chemical analysis. In this context, there are some reports on the determination of Cu(II) ions using carbon paste electrodes [18,26-28] that utilize different types of modifiers.

Schiff base ligands are readily prepared by condensation of aldehydes and primary amines. These ligands can coordinate many different metals and stabilize them in various oxidation states [29]. Multidentate Schiff bases have been widely used as ligands because they form highly stable coordination compounds with metal ions. These compounds have been found helpful as ionophores in metal sensors [30]. Tridentate ligands with N, N, and O donor atoms are considered hard Lewis bases. Cu(II) is considered a hard Lewis acid. Hard Lewis acids and bases have a preference in combination to form complexes. Metal complexes of tridentate ligands such as N-, N- and O-chelating ligands have received considerable attention for their attractive physicochemical properties. Cu(II) is notable for more flexible bonding to many ligands, especially non-symmetric polydentate ones.

In this contribution, two novel Cu(II)-selective carbon paste electrodes based on tridentate Schiff base ligands that strongly bind its ions were fabricated and characterized. These electrodes have attractive properties of low detection limits, wide linear concentration ranges, fast response, selectivity, accuracy, and reproducibility proven in applications for Cu(II) determination in water, blood, and biological samples.

■ EXPERIMENTAL SECTION

Materials

Chemicals of analytical grade were used and obtained from commercially available sources. 2-aminophenol, 2-aminobenzoic acid, and furfural-dehyde were from Merck; salicylaldehyde from Riedel de Haen. Reagent grade graphite powder and the plasticizers: bis(2-ethylhexyl) adipate (DOA), dioctyl phthalate (DOP), dibutyl phthalate (DBP), tris(2-ethylhexyl) phosphate (DOPh), dioctyl sebacate (DOS), paraffin oils (P.O.), and all-metal salts such as chlorides, nitrates, and sulfates were from Aldrich. All materials were used with no further purification.

Instrumentation

Electromotive force (EMF) measurements were made using the following assembly:
Hg, Hg_2Cl_2(s), KCl(sat.) || sample solution | carbon paste electrode.

A digital millivoltmeter (SR-MUL-3800) was utilized for potential measurements, a digital pH meter (HANNA pH 211) for pH measurements, and a saturated calomel electrode was used as a reference electrode to complete the electrochemical cell containing ion-selective electrodes. Elemental Analyzer EA 1110-CHNS CE Instrument was used in the analysis for carbon, hydrogen, and nitrogen. A PerkinElmer FTIR spectrophotometer using a KBr disk was used to record the infrared spectra of the materials in the range 4000–400 cm^{-1}.

Procedure

Synthesis of ligands

2-((2-Hydroxybenzylidene)amino)benzoic acid, as shown in Fig. 1, was prepared as described in the literature [31] by the reaction of equimolar amounts of 2-aminobenzoic acid and salicylaldehyde in hot alcoholic solutions. Similarly, 2-(furan-2-ylmethyleneamino)phenol (Fig. 2) was prepared from furfuraldehyde and 2-aminophenol [32]. The mixtures were allowed to stand and cool. The red-orange solids that separated were filtered off, washed with little amounts of the solvent, and dried. The product ligands were confirmed by the infrared and NMR spectra of both compounds. IR spectrum of 2-((2-hydroxybenzylidene)amino)benzoic acid: 3233 cm^{-1} (br, OH str), 1616 cm^{-1} (C=N str). NMR spectrum: 6.49–7.89 ppm (aromatic protons, 8.86 ppm (azomethine protons), 10.27 ppm (OH), 10.71 ppm (COOH). IR spectrum of 2-(furan-2-ylmethyleneamino)phenol: 3405 cm^{-1} (br, OH str), 1643 cm^{-1} for ν(C=N), 1018 cm^{-1} (s, C–O str). NMR spectrum: 5.0 ppm (s, OH), 6.1–7.7 ppm (m, aromatic) 8.45 ppm (s, CH imine).

Preparation of modified carbon paste electrode

A previously reported method [33] was followed to prepare the modified carbon paste electrode. First, weighed amounts of the ionophore, high purity graphite, and plasticizers, as shown in Table 1, were thoroughly mixed in plastic Petri dishes to make a uniformly wet paste used in constructing the sensors. Next, a 1 mL polypropylene syringe (3 mm i.d.) was used as the electrode body, and its tip was cut off. The paste was packed in, and a copper wire was used for electrical contact with the carbon paste. The paste was squeezed to expel some of it out. The expelled amount was scraped to expose a fresh mass at the tip of the electrode. The tip was polished on smooth paper to make a shiny surface. The plunger of the syringe was forced in to expel the paste at the tip. The expelled amount was scraped to expose a fresh mass there. Finally, the paste was polished on smooth paper to make a shiny surface. The electrode was then used directly for potentiometric measurements without pre-conditioning.

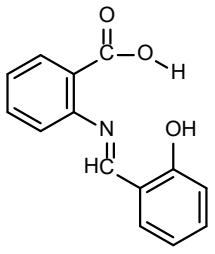

Fig 1. The chemical structure of ligand 1 [2-((2-hydroxybenzylidene)amino)benzoic acid]

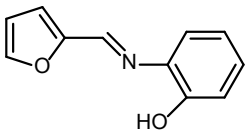

Fig 2. The chemical structure of ligand 2 [2-(furan-2-ylmethyleneamino)phenol]

Selectivity of the electrode

The separate solution method (SSM) [23] and the modified separate solution method (MSSM) [34] were applied to check the potentiometric selectivity factors of the electrode. The SSM involves measuring the potential of a cell comprising a working electrode and a reference electrode in two separate solutions, one of the Cu(II) ions and the other of the interfering ion (J), measured separately. The selectivity coefficient was calculated from the following equation:

$$\log K^{pot}_{Cu^{2+}J^{z+}} = \frac{E_{J-E_{Cu^{2+}}}}{S} + \left(1 - \frac{Z_{Cu^{2+}}}{Z_J}\right)\log a_{Cu^{2+}}$$

where E_J is the measured potential of the interfering ion, S is the slope of the calibration graph, $Z_{Cu^{2+}}$ is the charge on copper ion, and Z_J is the charge of the interfering species respectively.

The modified separate solution method (MSSM) involves measuring the potentiometric calibration curves of the primary (I) and interfering ions (J) and plotting the measured potential vs. the concentration of ionic species, the Cu(II) ion or the interfering ion. The potential corresponding to 1.0 M concentration is obtained by extrapolation to zero potential. The selectivity coefficients for the studied electrode are calculated from the equation below:

$$\log K^{pot}_{Cu^{2+}J^{z+}} = \frac{E^0_J - E^0_{Cu^{2+}}}{S_{Cu^{2+}}}$$

Table 1. The paste compositions and the electrode characteristics of electrode A and electrode B

No.	Composition (%)							
	L	g	p	S	D.R. (M)	L O D (M)	R.S.D	R(s)
Electrode A								
Ligand 1								
1	0.2	50.4	49.4 (P.O.)	30.89	7.45×10^{-7}–1.00×10^{-2}	5.64×10^{-7}	0.87	4
2	0.5	50.3	49.2 (P.O.)	29.13	3.98×10^{-7}–1.00×10^{-2}	2.32×10^{-7}	0.75	3
3	1.0	50.0	49.0 (P.O.)	29.27	1.00×10^{-6}–1.00×10^{-2}	7.21×10^{-7}	0.81	3
4	2.0	49.5	48.5 (P.O.)	28.79	1.18×10^{-6}–1.00×10^{-2}	1.10×10^{-6}	1.24	4
5	3.0	.490	48.0 (P.O.)	28.09	1.31×10^{-6}–1.00×10^{-2}	1.27×10^{-6}	1.38	5
6	4.0	48.5	47.5 (P.O.)	28.86	2.00×10^{-6}–1.00×10^{-2}	1.38×10^{-6}	1.54	5
7	5.0	.480	47.0 (P.O.)	30.34	3.25×10^{-6}–1.00×10^{-2}	2.00×10^{-6}	1.43	5
8	10.0	45.5	44.5 (P.O.)	32.81	4.00×10^{-6}–1.00×10^{-2}	2.00×10^{-6}	1.57	5
Effect of plasticizers								
9	0.5	50.3	49.2 (P.O.)	29.13	3.98×10^{-7}–1.00×10^{-2}	2.32×10^{-7}	0.75	3
10	0.5	50.3	49.2 (DOP)	28.54	3.81×10^{-6}–1.00×10^{-2}	1.25×10^{-6}	1.22	5
11	0.5	50.3	49.2 (DBP)	34.73	7.53×10^{-6}–1.00×10^{-2}	4.84×10^{-6}	1.35	5
12	0.5	50.3	49.2 (DOPh)	34.49	1.67×10^{-5}–1.00×10^{-2}	1.18×10^{-5}	1.77	4
13	0.5	50.3	49.2 (DOS)	35.18	4.13×10^{-6}–1.00×10^{-2}	2.13×10^{-6}	0.98	5
14	0.5	50.3	49.2 (DOA)	29.91	3.87×10^{-6}–1.00×10^{-2}	2.86×10^{-6}	1.62	5
Electrode B								
Ligand 2								
15	0.2	51.1	48.7 (P.O.)	28.27	1.65×10^{-6}–5.00×10^{-2}	1.16×10^{-6}	0.87	5
16	0.5	50.5	49.0 (P.O.)	30.85	1.52×10^{-6}–1.00×10^{-2}	1.14×10^{-6}	1.21	3
17	1.0	50.2	.488 (P.O.)	30.00	1.59×10^{-6}–1.00×10^{-2}	1.37×10^{-6}	1.33	3
18	2.0	49.7	48.3 (P.O.)	30.47	1.85×10^{-6}–1.00×10^{-2}	1.52×10^{-6}	1.17	4
19	3.0	.492	.478 (P.O.)	29.16	1.53×10^{-6}–1.00×10^{-2}	1.19×10^{-6}	0.98	4
20	4.0	.478	47.3 (P.O.)	28.63	4.00×10^{-6}–1.00×10^{-2}	3.21×10^{-6}	0.63	5
21	5.0	.482	.468 (P.O.)	30.06	2.74×10^{-6}–1.00×10^{-2}	1.55×10^{-6}	0.63	5
22	10.0	45.7	44.3 (P.O.)	31.75	1.28×10^{-6}–1.00×10^{-2}	1.19×10^{-6}	0.63	5
Effect of plasticizers								
23	0.5	50.5	48.5 (P.O.)	.3085	1.52×10^{-6}–1.00×10^{-2}	1.14×10^{-6}	1.21	3
24	0.5	50.5	49.0 (DOP)	31.14	2.37×10^{-6}–1.00×10^{-2}	1.25×10^{-6}	1.72	4
25	0.5	50.5	49.0 (DBP)	31.43	2.91×10^{-6}–1.00×10^{-2}	1.49×10^{-6}	1.67	5
26	0.5	50.5	49.0 (DOPh)	31.69	2.67×10^{-5}–1.00×10^{-2}	1.38×10^{-5}	1.13	4
27	0.5	50.5	49.0 (DOS)	30.63	3.32×10^{-6}–1.00×10^{-2}	1.59×10^{-6}	1.14	5
28	0.5	50.5	49.0 (DOA)	29.95	3.94×10^{-6}–1.00×10^{-2}	2.32×10^{-6}	1.93	5

L, Ligand; g, graphite; p, plasticizer S, slope (mV/decade); D.R., Dynamic range (M); LOD, low of detection (M); R, response time (s)

where log $K^{pot}_{Cu^{2+}J^{z+}}$ selectivity coefficient; E^0_J and $E^0_{Cu^{2+}}$ are values from the extrapolated to log(a) = 0 calibration curves for every interfering species and copper ion, and $S_{Cu^{2+}}$ is slope of the copper electrode.

Determination of Cu(II) ion in water and biological samples

Potentiometric titration method. Practically, a 25.0 mL sample of 1.0×10^{-3} M Cu(II) solutions was potentiometrically titrated with 1.0×10^{-2} M EDTA. Plots of the potential versus concentration were constructed to get the curves representing the titrations performed. The endpoints were taken at the sharpest change in the slope of each titration curve.

Each titration was represented graphically by a plot

of the measured potentials versus the corresponding concentrations to obtain the titration curve of that titration process. The endpoint is taken as the point that marks the sharpest change in the slope of that curve. This procedure is repeated for each titration.

Calibration graph method. This method involves the addition of known different amounts of copper ion ranging from 2.0×10^{-7}–1.0×10^{-2} M to 50.0 mL of distilled water and measuring the resulting potential using the present sensors. The measured potentials were plotted versus the logarithms of the Cu(II) activity at these points representing the titration process to make the calibration curve or the calibration line. This line was used to determine the concentration of a copper ion in various sample solutions by matching the measured potential resulting from a particular sample to the concentration corresponding to it on the line.

The measured potentials were plotted versus the logarithms of the Cu(II) activity to build the calibration curve. The determination is made by matching the measured potential resulting from a particular sample to the corresponding concentration on the line.

Analysis of Cu(II) ion in biological fluids. Solutions of 1.96×10^{-5}, 7.14×10^{-5}, and 1.66×10^{-4} M Cu(II) made by spiking urine and copper samples ranging from 1.0 mL down to 0.1 mL with proper amounts of Cu(II), stirring for 5 min, transferred to 50.0 mL volumetric flasks, diluted to volume and shaken to make homogeneous. The resulting solutions were analyzed for Cu(II) by the calibration curve method.

Analysis of water samples for Cu(II) ion. There is no need for pretreatment of drinking water samples before analyzing Cu(II) using the present sensors. Therefore, 50.0 mL samples of water were analyzed following spiking of the samples with Cu(II) ranging from 5.0×10^{-7}–5.0×10^{-3} M $CuCl_2$.

Potentiometric titration method. Titration of 20.0 mL samples of copper solutions versus 0.1 M solution of EDTA was performed by measuring the potential against the volume of the titrant being added in small amounts. Then, the potential was plotted against the volume of the titrant. Finally, the endpoint was taken at the steepest change of the slope of the plot of the measured potential vs. volume of volume added EDTA solution.

■ RESULTS AND DISCUSSION

Ion-selective electrodes (ISEs) are sensors commonly used to detect and determine certain ionic species. The ISEs behave as ion-exchangers where the analyte partitions into and out of the membrane or paste material, but the counter ion does not. The ion-exchanger site is confined to its phase in the paste and does not partition into the sample solution. Charge separation and a phase boundary develop, leading to a local equilibration at this interface. The electrical potential difference across the sample-membrane phase boundary depends on the analyte concentrations at these sites. Efforts toward the construction of selective and sensitive sensors mainly depend on using effective ionophores or ligands for binding the intended ion. Logically, a ligand should selectively and strongly bind the intended ion, which stems from its structure and consequent properties, toward which extended research was made over the years to design suitable electrodes for various analytical purposes. Fabrication of new efficient electrodes for some objectives follows these guidelines [23-25].

Characteristics of the Electrode

A sensor is characterized by determining its sensitivity as well as its linear working range and selectivity coefficients. Essential features of a carbon paste electrode depend on its constituents, namely the properties of each component and its relative amount. To be specific: graphite, ligands, the plasticizer significantly affect the sensitivity and selectivity of the sensor.

Response of the present electrodes to Cu(II) ions

Ionophore-based ISEs are lipophilic host molecules with adequate polar functional groups for ion recognition at sites covalently anchored onto the backbone. They allow one to achieve a selectivity pattern following the thermodynamically stable but kinetically labile complexes with the analyte ion that forms in the

membrane [35]. The selectivity depends on the structure of the ligands and their relative amount in the paste. Most ionophores are neutral and are highly lipophilic to be compatible with and strongly retained by the hydrophobic membrane phase resulting in operational sensor lifetimes ranging from weeks to years.

Lewis bases, also called ligands, are electron-pair donors that form coordinate bonds to metal ions. Two ligands were used in this work, namely: 2-((2-hydroxybenzylidene)amino)benzoic acid (L1) and 2-(furan-2-ylmethyleneamino)phenol (L2), which are shown in Fig. 1 and Fig. 2, respectively. They are tridentate ligands that form two stable chelate rings on complexation to a metal ion. However, the product complexes have slightly different stabilities due to differences in the size of the rings and the strength in electron donation of the donor pendant atoms in these ligands. For example, complexes of metal ions with L1 incorporate two 6-membered chelate rings, but those with L2 incorporate the slightly more stable 5-membered rings. However, the furan moiety in ligand 2 is a hard Lewis base which is a strong donor, but L1 has the COOH moiety, which is a weaker donor and both ligands have the phenol moiety.

The potentiometric response of the present electrodes A and B were tested for different cations such as Na(I), K(I), NH_4(I), Li(I), Ca(II), Zn(II), Ni(II), Mg(II), Ba(II), Mn(II), Cu(II), Co(II), Pb(II), and Al(III) ions. The results of these tests are presented in Fig. 3 and Fig. 4. These figures show that the responses of the sensors are non-Nernstian for most of the tested cations. The results are shown in Fig. 3 and Fig. 4 for electrode 1 electrode 2, respectively. It can be seen from these figures that the responses of the sensors are non-Nernstian for most of the tested cations.

Notably, Cu(II) has the closest Nernstian response over a wide concentration range with a low detection limit, indicating that these ligands may be used as ionophores of copper(II) sensors.

Cu(II) is has a d^9 electron configuration and adopts a tetragonally distorted structure in its octahedral complexes owing to the extra stability attained on this lowering the symmetry. This ion exemplifies such distortion. Moreover, this expected behavior can bond many ligands more strongly over other cations under the same conditions. This behavior amounts to selectivity to Cu(II) over other ions encountered in the solution. Cu(II) is considered a Lewis acid with intermediate strength that prefers to bind ligands of similar strength which means that copper(II) complex with L1 is more stable than L2. Thus, it is a case of two competing factors affecting the behavior of these ligands.

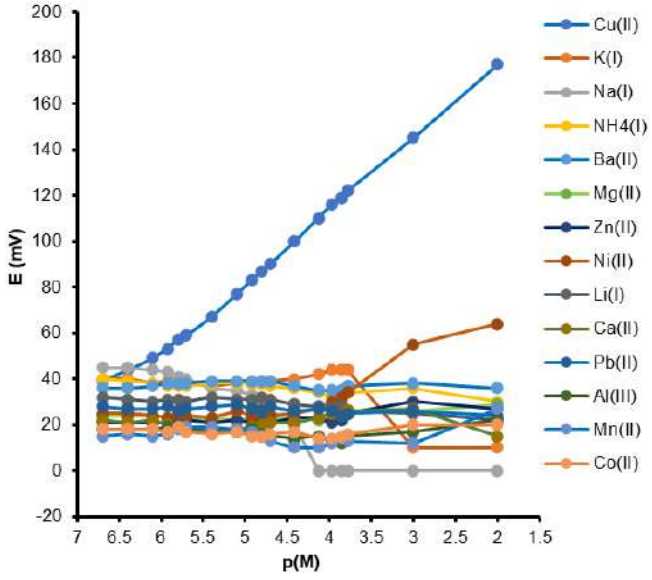

Fig 3. Potential response of various metal ions for sensor A

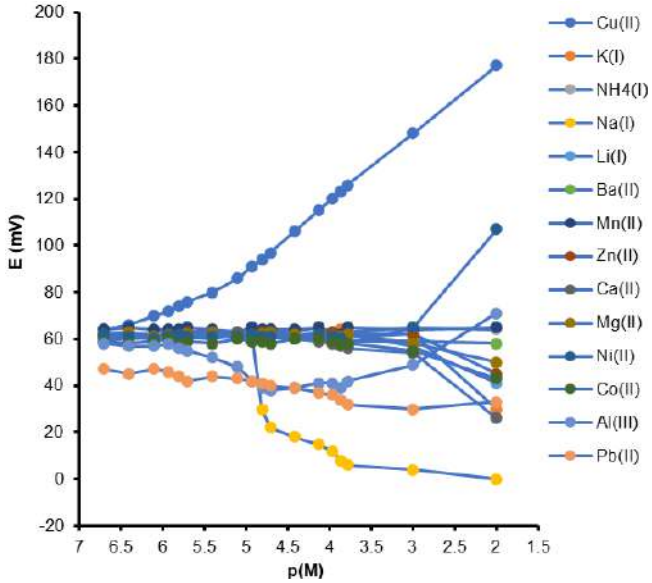

Fig 4. Potential response of various metal ions for sensor B

First, we evaluated the net effect, which is the slightly better sensor characteristics fabricated using L1. The influence of the ligands L1 and L2 in the membrane composition as the ionophore for Cu(II) on the constructed electrodes' potential response was studied. The corresponding results are summarized in Table 1.

Electrodes comprising different percentages of each ionophore were prepared: 0.2, 0.5, 1.0, 2.0, 3.0, 4.0, 5.0, and 10% (w/w). The following electrode characteristics: slopes, concentration ranges, detection limits, and response times of the calibration curves of the above electrodes were measured and shown in Table 1. Inspection of the results showed that the electrodes comprising 0.5% of the ligands: L1 and L2 indicate the best response, closest to Nernstian behavior with remarkable selectivity for Cu(II), are electrodes #2 and #16 in Table 1. Increasing the relative percent of L1 resulted in a notable deterioration in the detection limit, the slope, and the linear range of the electrode. This behavior is most probably due to some inhomogeneities and possible saturation of the paste [36]. Therefore, electrode #2 was adopted in further applications. Similar behavior was noted on L2, where electrode #16 comprising 0.5% as the ligand attained the lowest detection limit. However, further additions of L2 from 1.0–10% displayed somewhat similar sensitivity, slope, and linear range. Electrode #16 of this ligand comprises the smallest amount of the ligand and gives the best response, so it was also adopted in further applications.

Influence of the plasticizer

When making carbon paste, one must keep in mind the mechanical stability of the paste and its active surface [37]. This function is supposed to be carried by the plasticizer, i.e., it is the main role of the plasticizer used in the preparation of the paste. In addition, it should provide high lipophilicity, a low tendency for exudation from the paste matrix, and the capacity to dissolve the substrate and other additives included in the paste. Good knowledge of the properties of a plasticizer is necessary for a suitable choice of one or more compatible with those of other components of the paste, especially the ionophore responsible for the primary function of the electrode [38]. Thus, a suitable plasticizer improves the response of the electrode. Based on the structure-function relationship, the properties of a plasticizer stem from its chemical structure. It is possible to make the anticipation of a suitable plasticizer effectively improve the function of a certain ionophore. Plasticizers normally have low polarity based on their low dielectric constants. Choosing a plasticizer is based on the empirical basis where several plasticizers are tested and the one that best improves the electrode response is selected for further work, and applications of the electrode being fabricated. In this work six plasticizers were tested and listed below with the values of dielectric constants in parentheses, namely, DOS (εr = 4.2), DOP (εr = 5.1), DBP (εr = 6.4), DOPh (εr = 4.8), DOA (εr = 3.9) and P.O. (εr = 2.2) and the results obtained are shown in Table 1. Paraffin oil P.O. was found the most effective among these plasticizers. As the present ligands, L1 and L2 used as the ionophores, have characteristically low polarity, it is expected that a plasticizer with as low polarity as possible will work best with these ligands. This expectation was experimentally proven, as mentioned above.

Effect of graphite/plasticizer (g/p) ratio

Graphite and plasticizers are vital components of an ISE as their sensitivity and selectivity depend on the graphite to plasticizer ratio g/p. Therefore, electrodes comprising the following g/p ratios: 0.75, 0.90, 1.00, 1.02, 1.05, 1.20, and 1.35 were tested to spot the one that marks the best response. Tests showed that pastes with g/p more than 1.35 are "crumbly", indicating too much graphite, and those with ratios smaller than 0.75 resemble "peanut butter", i.e., contain more than enough of the plasticizer that makes the paste not workable. The best responses were attained with electrode A comprising G/P = 1.02 and electrode B comprising G/P = 1.03, which reached the lowest detection limit and the closest Nernstian slope. This mixture contains a little more graphite necessary for efficient conductivity of the paste and enough plasticizer (paraffin oil) to provide the needed flexibility and workability and be sufficient to dissolve the constituents of the paste. The optimum physical properties of the paste were reached based on enabling high enough mobilities of all of its components.

Therefore, this ratio was adopted in further developments of the present electrodes. Inspection of the results, collected in Table 1 indicates that electrodes #2 composed of 0.5% L1, 51.0% graphite, and 48.5% P.O. and #16 with the same composition but using L2 instead of L1 gave the best results and were adopted in more experiments toward the complete characterization of these electrodes.

pH dependence

The influence of the pH of the analyte solution on the potential of the present electrodes should be determined. It was studied for 1.0×10^{-5} and 1.0×10^{-3} M $CuCl_2$ solutions. The pH of the analyte solution affects the potential of the present electrodes. Therefore, this effect should be determined. Practically, it was studied in 1.0×10^{-5} and 1.0×10^{-3} M $CuCl_2$ solutions. The solution's acidity was adjusted by adding small amounts of (1 M) HCl or NaOH, and the resulting potentials were measured. The results obtained using the two electrodes are practically linear over the pH range 1.5–5.5, as seen from the representative plot in Fig. 5 for electrode A which collectively indicates that both electrodes satisfactorily behave over this range. Testing the electrodes in a solution with a pH lower than 1.5 was not performed as it is unlikely that Cu(II) analysis is requested in such strongly acidic solutions. In solutions having pH above 5.5, copper hydroxide precipitate as it has a relatively low solubility product. More copper hydroxide precipitates in solutions with higher pH, leaving lower amounts and concentrations of copper ion and correspondingly lower measure potential.

Response time, homogeneity, surface-renewal, and reproducibility

The response time of an electrode depends on the membrane type and the interferents. Therefore, all relevant measurements must be made under the same experimental conditions when addressing this issue. It indicates how fast the unstirrable layer of sample adhering to the ISE membrane can be exchanged for a new layer noting that routine potentiometric measurements are associated with responses involving ion movements over nanometers at the phase boundary of the sample and the ion-selective membrane [39].

In the present work, the response time was measured by varying Cu(II) concentration over the range 4.0×10^{-7}–4.0×10^{-3} M for electrode A and from 4.0×10^{-6}–4.0×10^{-3} M for electrode B. It was found that electrode A reached equilibrium in about 3 s, as shown in Fig. 6 for electrode A and was slightly longer (about 5 sec) for electrode B. The modified carbon paste electrodes are famous for their attractive possibility of renewal of the electrode surface whenever needed. The renewal is achieved by squeezing a little carbon paste out of the tube to expose a new amount which can be smoothed on a piece of weighing paper to a shiny surface [40]. The procedure requires making about 1.0 g of a paste with optimum

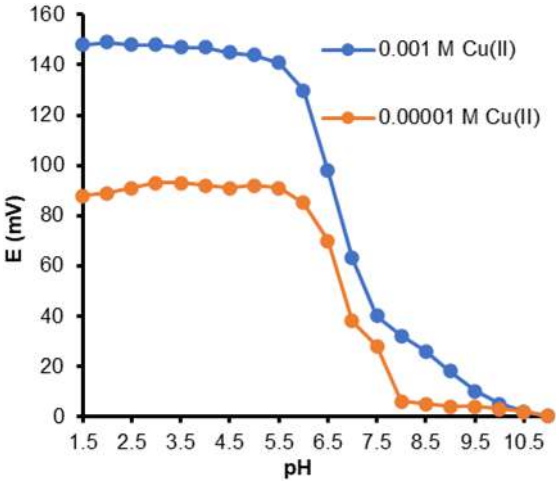

Fig 5. Effect of pH on potential response of electrode A using 1.0×10^{-5} and 1.0×10^{-3} M Cu(II) solutions

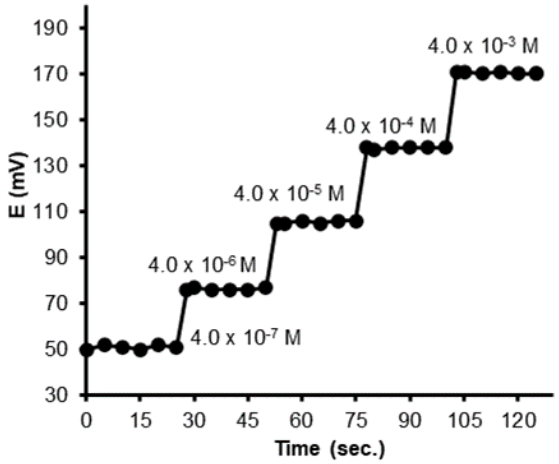

Fig 6. Dynamic responses of electrode A obtained by a successive increase of Cu(II) ion

composition by intimately mixing its ingredients. This amount was suitable for use for over a month to get a stable response without any deterioration. However, more prolonged periods cause slight deterioration in the measured potentials, likely due to the evaporation of some of the incorporated plasticizers.

Homogeneity of the present electrodes was tested by applying the electrodes for measurement in a 1.0×10^{-4} M Cu(II) solution which was repeated seven times on a freshly exposed paste for each measurement as explained above. The average relative standard deviation (R.S.D.) for the proposed electrodes was ~0.91, which are reasonable values. However, after five times of use, it was noticed that the slope of the calibration graphs measured using electrode 1 decreased slightly from 29.13–26.95 mV/decade, and the slopes measured using electrode 2 decreased from 30.85–26.73 mV/decade.

However, it was noticed that the slope of the calibration graphs measured using electrode 1 decreased slightly from 29.13–26.95 mV/decade after five times of use. Similarly, the slopes measured using electrode 2 decreased from 30.85–26.73 mV/decade. This decrease is likely due to surface contamination and memory effects and makes polishing the electrode necessary to expose a new fresh layer ready for use after each calibration. The standard deviation of five replicate measurements of the electromotive force (emf) is 1.23, 1.13 for electrodes A and B in 1.0×10^{-6} M solution, and 0.98, 1.08 in 1.0×10^{-5} M solution, respectively. These results indicate excellent repeatability of the potential response of the electrodes.

Effect of temperature

The thermal stability of an electrode must be checked and determined being one of its characteristics. Practically, this is done by constructing the calibration graphs of the electrodes in test solutions at different temperatures covering the range of 20–50 °C. No appreciable change was found in the calibration characteristics of both electrodes over the temperature range covered. These observations indicate the high thermal stability of these electrodes.

Effect of other ions

Selectivity is a salient feature of an ion-selective electrode (ISE) and is considered its primary characteristic as it is constructed to do [41]. The selectivity of an ISE is quantitatively related to equilibria at the interface between the sample and the electrode. The response of an electrode is generally affected by the presence of other ions in solution, and the Nernst equation should be modified to the simplified Nicolsky-Eisenman equation [42].

Selectivity coefficients depend upon the composition of the paste and may take values ranging from zero (indicating no interference) to greater than unity (where the electrode responds to the interferent more strongly than to the primary species). The selectivities determined by the Eisenman equation are incorrect when two ions of different charges significantly contribute to the emf. Besides, K_{IJ} has different dimensions for different charges of the interfering ion J^{z+}. If the charges are different, an alternative approach, modified separate solution method, is used to determine the selectivity [42]. The electrodes' response towards different cations was tested and measured as described in the experimental section. For example, K_{IJ} = 1.0 for two ions with equivalent responses. Ions with low K_{IJ} values have less impact and a lower interfering effect on the measured potential. When K_{IJ} values are greater than 1, the ISE is more responsive to the interfering ion. The resulting values, presented in Table 2, show that these sensors display significantly high selectivity for Cu(II) over many common inorganic ions. It is noteworthy that the results obtained from the two methods are different. The MSSM produced much better values than those obtained by the SSM, following expectations that the MSSM produces unbiased, thermodynamic selectivity coefficients.

Recovery and Determination of Copper Ions in Urine and Serum Samples

Physiological concentrations of copper in human blood serum range from $1.1–2.4 \times 10^{-3}$ M. Ceruloplasmin is an enzyme synthesized in the liver and is the main carrier of copper ions in the human blood. Wilson's disease (WD) results from serum deficiency of ceruloplasmin. The progression of this disease leads to a significant increase of free copper ions circulating in the bloodstream and accumulation of copper ions in organs

Table 2. Selectivity coefficient for electrode A and electrode B

Interfering species	Electrode A		Electrode B	
	SSM	MSSM	SSM	MSSM
K(I)	4.14×10^{-6}	1.12×10^{-6}	5.46×10^{-6}	2.15×10^{-6}
NH_4(I)	3.51×10^{-6}	1.28×10^{-6}	7.33×10^{-6}	1.48×10^{-6}
Na(I)	4.72×10^{-6}	1.41×10^{-6}	6.78×10^{-6}	2.74×10^{-6}
Li(I)	3.25×10^{-6}	1.77×10^{-6}	3.96×10^{-6}	3.46×10^{-6}
Ca(II)	5.41×10^{-6}	1.98×10^{-6}	7.55×10^{-6}	3.42×10^{-6}
Ba(II)	4.78×10^{-6}	2.13×10^{-6}	8.89×10^{-6}	4.26×10^{-6}
Zn(II)	6.33×10^{-6}	4.15×10^{-6}	9.11×10^{-6}	6.32×10^{-6}
Ni(II)	3.78×10^{-6}	2.42×10^{-6}	8.63×10^{-6}	5.93×10^{-6}
Co(II)	5.19×10^{-6}	2.38×10^{-6}	7.76×10^{-6}	4.11×10^{-6}
Pb(II)	4.73×10^{-6}	3.22×10^{-6}	6.19×10^{-6}	4.27×10^{-6}
Mg(II)	5.22×10^{-6}	3.17×10^{-6}	6.13×10^{-6}	4.66×10^{-6}
Mn(II)	5.31×10^{-6}	3.77×10^{-6}	7.36×10^{-6}	5.47×10^{-6}
Al(III)	3.31×10^{-6}	1.88×10^{-6}	5.41×10^{-6}	2.93×10^{-6}

Table 3. Analysis of Cu(II) in tap water and biological fluids samples using calibration curve method

Sample	Taken (M)	Found (M)	X%	R.S.D.%
Electrode A				
Serum	1.96×10^{-5}	1.91×10^{-5}	97.44	1.98
	7.14×10^{-5}	6.93×10^{-5}	97.06	2.31
	1.66×10^{-4}	1.61×10^{-4}	97.00	2.67
Urine	1.96×10^{-5}	1.92×10^{-5}	97.96	2.39
	7.14×10^{-5}	7.01×10^{-5}	98.18	2.14
	1.66×10^{-4}	1.62×10^{-4}	97.59	2.54
Drinking water	5.00×10^{-7}	4.97×10^{-7}	99.40	1.13
	5.00×10^{-6}	4.98×10^{-6}	99.60	1.04
	5.00×10^{-4}	5.00×10^{-4}	100.0	0.89
	5.00×10^{-3}	4.99×10^{-3}	99.80	0.78
Electrode B				
Serum	1.96×10^{-5}	1.89×10^{-5}	96.43	2.15
	7.14×10^{-5}	6.94×10^{-5}	97.20	2.33
	1.66×10^{-4}	1.60×10^{-4}	96.39	2.58
Urine	1.96×10^{-5}	1.90×10^{-5}	96.94	2.11
	7.14×10^{-5}	6.98×10^{-5}	97.76	2.32
	1.66×10^{-4}	1.62×10^{-4}	97.59	2.36
Drinking water	5.00×10^{-7}	4.93×10^{-7}	98.60	1.45
	5.00×10^{-6}	4.96×10^{-6}	99.40	1.21
	5.00×10^{-4}	5.00×10^{-4}	100.0	1.18
	5.00×10^{-3}	4.98×10^{-3}	99.60	0.93

R.S.D.: relative standard deviation, the number of replicate measurements = 5; X: recovery

such as the brain, liver, and cornea (Kayser–Fleischer rings) [43]. Basal 24-h urinary excretion of copper in WD is typically greater than 100 g (1.6 mol) in symptomatic patients [44]. Therefore, the 24-h urinary excretion of Cu(II) is measured to aid in diagnosing WD that needs proper chelation therapy. The present electrodes were

used to determine Cu(II) in spiked urine and blood serum samples as recovery experiments. Tests showed that the addition of 0.1 mL urine or blood serum did not affect the further measurement of Cu(II) in the samples. However, adding 1.0 mL of the body fluids significantly lowered potential values measured by the electrodes. These observations are in line with expectations based on blood serum and urine properties as fluid extracts from the body that generally contain amino acids and other ligands capable of sequestering Cu(II). After reaction and consumption of the low added amounts of serum or urine with an equivalent amount of Cu(II), the rest of the samples show linear response as anticipated. These test results collectively indicate that the present electrodes may be successfully used to determine Cu(II) in urine and blood serum. The results collected using the calibration curve method are presented in Table 3. Recoveries and R.S.D. values range between 98.18–96.39% of Cu(II), and 2.67–1.98, respectively. Therefore, the present sensors are applicable for the quantification of Cu(II) in urine samples.

Determination of copper ions in drinking water samples

Similarly, Cu(II) in drinking water samples was potentiometrically determined using these electrodes as indicators, and the results are presented in Table 3. They have reasonable recovery ranges of 100.0–98.60% and R.S.D. ranges of 0.78–1.45, which indicates the electrodes are satisfactory for analysis.

Titration of a copper solution with a standard EDTA solution

Each of the present electrodes was applied as an indicator in titration of 20.0-mL samples of 1.0×10^{-3} M Cu^{2+} with a standard 0.01 M EDTA solution. The resulting titration curve is shown in Fig. 7. These electrodes provide accurate means for determination.

Comparison with Other Electrodes

The performance characteristics of the proposed electrode A and those of some reported carbon paste electrodes are compiled in Table 4 for comparison. The detection limit of electrode A is lower than those of the other electrodes. In addition, its working range is wider than those of the others [18,26-28]. In brief, electrode A excels the relevant electrodes and is more useful for the intended applications with the aforementioned properties.

■ CONCLUSION

Two competitive newly fabricated Cu(II)-selective carbon paste electrodes have been built, characterized,

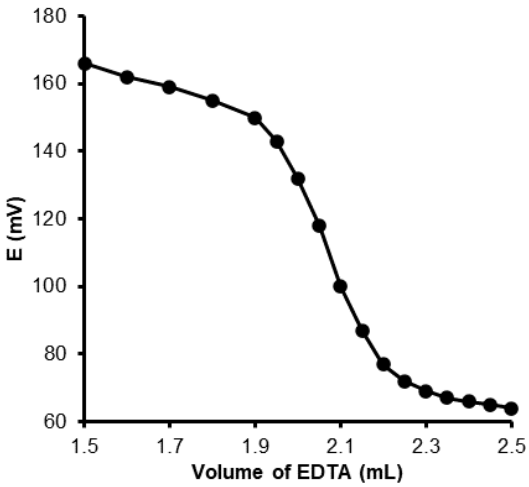

Fig 7. Potential titration curves of 20.0 mL 1.0×10^{-3} M Cu(II) solution with 1.0×10^{-2} M of EDTA of the electrode A

Table 4. Comparison of the proposed Cu-CMCPE with reported electrodes

Modifier	Slope	C.R. (M)	LOD (M)	R(s)	Ref.
2-N, N-dimethylcarbamimidoyl (met-formin)	30.2	1.0×10^{-6}–5.0×10^{-2}	3.3×10^{-6}	10	[17]
2-((3silylpropylaminoethylimino) methyl) phenol in presence of Ag-NP-AC	29.1	5.0×10^{-7}–1.0×10^{-1}	2.5×10^{-7}	15	[28]
CuNiO/Gt nanocomposite	30.2	1.0×10^{-6}–5.0×10^{-2}	1.0×10^{-6}	5	[29]
(3,4-dihydro-4,4,6-trimethyl-2(1H)-pyrimidine thione	30.0	9.77×10^{-7}–7.6×10^{-2}	7.0×10^{-7}	45	[30]
etioporphyrin I dihydrobromide	30.3	1.28×10^{-6}–1.28×10^{-2}	8.99×10^{-7}	5	[31]
2-(furan-2-ylmethyleneamino) phenol	29.1	3.98×10^{-7}–1.00×10^{-2}	2.32×10^{-7}	3	Present work

and tested for applicability. Two Schiff base ligands, 2-((2-hydroxybenzylidene)amino) benzoic acid and 2-(furan-2-ylmethyleneamino) phenol, were utilized as the ionophores of Cu(II) based on the distinct stability of these chelating ligands and the flexibility of bonding provided by Cu(II) over other cations. These sensors have notably good characteristics: low detection limits: 2.32×10^{-7} and 1.14×10^{-6} M Cu(II), Nernstian slope of 29.13 and 30.85 mV/decade Cu(II), wide concentration ranges from 3.98×10^{-7}–1.00×10^{-2} and 1.52×10^{-6}–1.00×10^{-2} M for the two sensors, respectively. Also, they have a short response time (ca. 3–5 sec), distinct Cu(II) selectivity over other cations, thermal stability up to 50 °C, and applicability over the pH range 1.5–5.5 for miscellaneous samples. They were proven successful in determining Cu(II) in aqueous solutions, urine, and blood serum.

■ ACKNOWLEDGMENTS

The authors extend their appreciation to the Deanship of Scientific Research at King Saud University for funding this work through the research group project No. RG-1436-024.

■ REFERENCES

[1] Housecroft, C.E., and Sharpe, A.G., 2012, *Inorganic Chemistry*, 4th Ed., Pearson Education Limited, Harlow, UK.

[2] Herman, M., Przybylowicz, A., Florek, E., and Piekoszewski, W., 2013, Method of determination of low copper concentration in human hair and nails, *J. Anal. Chem.*, 68 (4), 360–367.

[3] WHO, 2019, *Water, Sanitation, Hygiene and Health: A Primer for Health Professionals*, World Health Organization, Geneva (WHO/CED/PHE/WSH/19.149).

[4] Mehrani, Z., Ebrahimzadeh, H., Asgharinezhad, A.A., and Moradi, E., 2019, Determination of copper in food and water sources using poly m-phenylenediamine/CNT electrospun nanofiber, *Microchem. J.*, 149, 103975.

[5] Hassan, M., Erbas, Z., Alshana, U., and Soylak, M., 2020, Ligandless reversed-phase switchable-hydrophilicity solvent liquid–liquid microextract-ion combined with flame-atomic absorption spectrometry for the determination of copper in oil samples, *Microchem. J.*, 156, 104868.

[6] Hevia, K., Arancibia, V., and Rojas-Romo, C., 2015, Levels of copper in sweeteners, sugar, tea, coffee and mate infusions. Determination by ad-sorptive stripping voltammetry in the presence of α-lipoic acid, *Microchem. J.*, 119, 11–16.

[7] Członkowska, A., Litwin, T., Dusek, P., Ferenci, P., Lutsenko, S., Medici, V., Rybakowski, J.K., Weiss, K.H., and Schilsky, M.L., 2018, Wilson disease, *Nat. Rev. Dis. Primers*, 4 (1), 21.

[8] WHO, 2004, *Copper in Drinking-water. Background document for development of WHO Guidelines for Drinking-water Quality*, World Health Organization, Geneva (WHO/SDE/WSH/03.04/88).

[9] Ghaebi, M., and Saadati, M., 2016, Abundance determination of copper in the soil of mine sungun using Neutron activation analysis, *J. Radiat. Nucl. Technol.*, 1 (3), 29–34.

[10] Escárate, P., Hein, R., Durán, M., and Ramaciotti, P., 2015, X-ray fluorescence spectroscopy for accurate copper estimation, *Miner. Eng.*, 71, 13–15.

[11] Payehghadr, M., and Nourifard, F., 2017, Determination of ultra trace copper in water samples by differential pulse polarography after solid phase extraction, *Orbital: Electron. J. Chem.*, 9 (5), 354–359.

[12] Liu, Y., Liang, P., and Guo, L., 2005, Nanometer titanium dioxide immobilized on silica gel as sorbent for pre-concentration of metal ions prior to their determination by inductively coupled plasma atomic emission spectrometry, *Talanta*, 68 (1), 25–30.

[13] Zhong, W.S., Ren, T., and Zhao, L.J., 2016, Determination of Pb (Lead), Cd (Cadmium), Cr (Chromium), Cu (Copper), and Ni (Nickel) in Chinese tea with high-resolution continuum source graphite furnace atomic absorption spectrometry, *J. Food Drug Anal.*, 24 (1), 46–55.

[14] Behbahani, M., Bide, Y., Salarian, M., Niknezhad, M., Bagheri, S., Bagheri, A., and Nabid, M.R., 2014, The use of tetragonal star-like polyaniline

nanostructures for efficient solid phase extraction and trace detection of Pb(II) and Cu(II) in agricultural products, sea foods, and water samples, *Food Chem.*, 158, 14–19.

[15] Ebrahimzadeh, H., Behbahani, M., Yamini, Y., Adlnasab, L., and Asgharinezhad, A.A., 2013, Optimization of Cu(II)-ion imprinted nanoparticles for trace monitoring of copper in water and fish samples using a Box–Behnken design, *React. Funct. Polym.*, 73 (1), 23–29.

[16] Behbahani, M., Salarian, M., Amini, M.M., Sadeghi, O., Bagheri, A., and Bagheri, S., 2013, Application of a new functionalized nanoporous silica for simultaneous trace separation and determination of Cd(II), Cu(II), Ni(II), and Pb(II) in food and agricultural products, *Food Anal. Methods*, 6 (5), 1320–1329.

[17] Barache, U.B., Shaikh, A.B., Lokhande, T.N., Kamble, G.S., Anuse, M.A., and Gaikwad, S.H., 2018, An efficient, cost effective, sensing behaviour liquid-liquid extraction and spectrophotometric determination of copper(II) incorporated with 4-(4′-chlorobenzylideneimino)-3-methyl-5-mercap- to-1,2,4-triazole: Analysis of food samples, leafy vegetables, *Spectrochim. Acta A*, 189, 443–453.

[18] Frag, E.Y., Mohamed, M.E.B., and Fahim, E.M., 2018, Application of carbon sensors for potentiometric determination of copper(II) in water and biological fluids of Wilson disease patients. Studying the surface reaction using SEM, EDX, IR and DFT, *Biosens. Bioelectron.*, 118, 122–128.

[19] Tutulea-Anastasiu, M., Wilson, D., del Valle, M., Schreiner, C., and Cretescu, I., 2013, A Solid-contact ion selective electrode for copper(II) using a succinimide derivative as ionophore, *Sensors*, 13 (4), 4367–4377.

[20] Ansari, R., Mosayebzadeh, Z., Arvand, M., and Mohammad-khah, A., 2013, A potentiometric solid state copper electrode based on nanostructure polypyrrole conducting polymer film doped with 5-sulfosalicylic acid, *J. Nanostruct. Chem.*, 3 (1), 33.

[21] Birinci, A., Eren, H., Coldur, F., Coskun, E., and Andac, M., 2016, Rapid determination of trace level copper in tea infusion samples by solid contact ion selective electrode, *J. Food Drug Anal.*, 24 (3), 485–492.

[22] Topcu, C., Lacin, G., Yilmaz, V., Coldur, F., Caglar, B., Cubuk, O., and Isildak, I., 2018, Electro-chemical determination of copper(II) in water samples using a novel ion-selective electrode based on a graphite oxide–imprinted polymer composite, *Anal. Lett.*, 51 (12), 1890–1910.

[23] Abu Ghalwa, N., Abed Almonem, K.I., Al-Kashef, I.D., Saadeh, S.M., and Abu Shawish, H.M., 2020, Comparative effects of surfactants on the behavior of an anticancer drug potentiometric sensor, *Anal. Methods*, 12 (5), 679–686.

[24] Abu Shawish, H.M., Abu Ghalwa, N., Al-Kashef, I.D., Saadeh, S.M., and Abed Almonem, K.I., 2020, Extraordinary enhancement of a 5-fluorouracil electrode by praepagen HY micellar solutions, *Microchem. J.*, 152, 104316.

[25] Rouhani, M., and Soleymanpour, A., 2019, A new selective carbon paste electrode for potentiometric analysis of olanzapine, *Measurement*, 140, 472–478.

[26] Ghaedi, M., Naderi, S., Montazerozohori, M., Taghizadeh, F., and Asghari, A., 2017, Chemically modified multiwalled carbon nanotube carbon paste electrode for copper determination, *Arabian J. Chem.*, 10, S2934–S2943.

[27] Frag, E.Y., and Abdel Hameed, R.M., 2019, Preparation, characterization and electro-chemical application of CuNiO nanoparticles supported on graphite for potentiometric determination of copper ions in spiked water samples, *Microchem. J.*, 144, 110–116.

[28] Issa, Y.M., Ibrahim, H., and Shehab, O.R., 2012, New copper(II)-selective chemically modified carbon paste electrode based on etioporphyrin I dihydrobromide, *J. Electroanal. Chem.*, 666, 11–18.

[29] Mazzoni, R., Roncaglia, F., and Rigamonti, L., 2021, When the metal makes the difference: Template syntheses of tridentate and tetradentate salen-type schiff base ligands and related complexes, *Crystals*, 11 (5), 483.

[30] Yuan, X., Chai, Y., Yuan, R., Zhao, Q., and Yang, C., 2012, Functionalized graphene oxide-based carbon

paste electrode for potentiometric detection of copper ion(II), *Anal. Methods*, 4 (10), 3332–3337.

[31] Govindaraj, V., Ramanathan, S., and Murgasen, S., 2018, Synthesis, characterization, antibacterial, antifungal screening and cytotoxic activity of Schiff base nickel(II) complexes with substituted benzylidine aminobenzoic acid, *Chem. Sin.*, 9 (3), 736–745.

[32] Chaudhary, N., 2013, *In vitro* antibacterial studies of some transition metal complexes of Schiff base derived from 2-aminophenol and furan-2-carbaldehyde, *Arch. Appl. Sci. Res.*, 5 (6), 227–231.

[33] Egorov, V.V., Zdrachek, E.A., and Nazarov, V.A., 2014, Improved separate solution method for determination of low selectivity coefficients, *Anal. Chem*., 86 (8), 3693–3696.

[34] Radu, A., Peper, S., Bakker, E., and Diamond, D., 2007, Guidelines for improving the lower detection limit of ion-selective electrodes: A systematic approach, *Electroanalysis*, 19 (2-3), 144–154.

[35] Bhat, V.S., Ijeri, V.S., and Srivastava, A.K., 2004, Coated wire lead(II) selective potentiometric sensor based on 4-*tert*-butylcalix[6]arene, *Sens. Actuators, B*, 99 (1), 98–105.

[36] Ramezani, S., Mashhadizadeh, M.H., Ghobadi, M., and Jalilian, S., 2016, Silica gel/gold nanoparticles/(NS)2 ligand nanoporous platform-modified ionic liquid carbon paste electrode for potentiometric ultratrace assessment of Ag(I), *Int. J. Environ. Sci. Technol.*, 13 (9), 2175–2188.

[37] Zayed, M.A., Mahmoud, W.H., Abbas, A.A., Ali, A.E., and Mohamed, G.G., 2020, A highly sensitive, selective and renewable carbon paste electrode based on a unique acyclic diamide ionophore for the potentiometric determination of lead ions in polluted water samples, *RSC Adv*., 10 (30), 17552–17560.

[38] Pechenkina, I.A., and Mikhelson, K.N., 2015, Materials for the ionophore-based membranes for ion-selective electrodes: Problems and achievements (review paper), *Russ. J. Electrochem.*, 51 (2), 93–102.

[39] García-España, E., Belda, R., González, J., Pitarch, J., and Bianchi, A., 2012, "Receptors for Nucleotides" in *Supramolecular Chemistry: From Molecules to Nanomaterials*, John Wiley & Sons, Ltd, Chichester, UK.

[40] Švancara, I., Vytřas, K., Kalcher, K., Walcarius, A., and Wang, J., 2009, Carbon paste electrodes in facts, numbers, and notes: A review on the occasion of the 50-years jubilee of carbon paste in electrochemistry and electroanalysis, *Electroanalysis*, 21 (1), 7–28.

[41] Ibupoto, Z.H., Khun, K., and Willander, M., 2013, A selective iodide ion sensor electrode based on functionalized ZnO nanotubes, *Sensors*, 13 (2), 1984–1997.

[42] Bakker, E., Pretsch, E., and Bühlmann, P., 2000, Selectivity of potentiometric ion sensors, *Anal. Chem.*, 72 (6), 1127–1133.

[43] Blicharska, B., Witek, M., Fornal, M., and MacKay, A.L., 2008, Estimation of free copper ion concentrations in blood serum using T1 relaxation rates, *J. Magn. Reson.*, 194 (1), 41–45.

[44] Brewer, G.J., Gow, P.J., Smallwood, R.A., Angus, P.W., Sewell, R.B., Smith, A.L., and Wall, A.J., 2002, Diagnosis of Wilson's disease: An experience over three decades, *Gut,* 50 (1), 136–136.

Molecular Imprinted of Nylon 6 for Selective Separation of Procaine by Solid-Phase Extraction

Muhammed Emad Abood and Sumayha Muhammed Abbas*

Department of Chemistry, College of Education for Pure Science Ibn Al-Haitham, University of Baghdad, Baghdad, Iraq

* ***Corresponding author:***

tel: +9641-7700876525
email:
sumayha.m.a@ihcoedu.uobaghdad.edu.iq

Received: June 24, 2021
Accepted: August 16, 2021

DOI: 10.22146/ijc.66997

Abstract: *The study is based on the selective binding ability of the drug compound procaine (PRO) on a surface imprinted with nylon 6 (N6) polymer. Physical characterization of the polymer template was performed by X-ray diffraction and DSC thermal analysis. The imprinted polymer showed a high adsorption capacity to trap procaine (237 µg/g) and excellent recognition ability with an imprinted factor equal to 3.2. The method was applied to an extraction column simulating a solid-phase extraction to separate the drug compound in the presence of tinoxicam and nucleosimide separately and in a mixture of them with a recovery rate more than the presence of tinoxicam and nucleosimide separately and in a mixture of them with a recovery rate of more than 82%. Separation efficiency and excellent selectivity for procaine were ensured using a mixed solution injected into an HPLC technique consisting of a C18 column with a mobile phase mixture of water-acetonitrile (75:25) at pH 3.3. The study of drug control using an imprinted polymer with procaine compound showed that the complete drug release process is faster at pH1 in a maximum period of 80 min. The proposed method was successfully applied on some of the available pharmaceuticals, and it showed high selectivity for the separation of PRO, RE % was < 1.18, and RSD was less than 0.447.*

Keywords: *imprinting polymer; nylon 6; phase inversion method; solid-phase extraction; procaine*

■ INTRODUCTION

Procaine [2-(diethylamino) ethyl4-aminobenzoate) (Fig. 1) is considered a powerful aesthetic with anti-inflammatory properties [1]. The main purpose of the drug is to minimize intramuscular injection pain of penicillin and dentistry. As the trade name in several countries, novocaine is the generic name referring to procaine. Its main performance is to block the sodium channels. Because of its anti-inflammatory, mood-improving, sympatholytic, and perfusion-enhancing effects, it was used for therapeutic reasons in some regions. PRO was prepared in 1905 for the first time afterward, amylocaine. PRO is used for spinal anesthesia, therapeutic, and local infiltration blockade [2].

Imprinted polymer technique is used to create cavities or molecular fingerprints with high selectivity for the analyte and using polymers for this purpose called molecularly imprinted polymers. These cavities can be specially designed according to different requirements, thus demonstrating a high selectivity towards imprinted particles. Moreover, the advantages of the MIP technique are low cost, easy to synthesize, chemical and physical stability, and re-use ability. Identification cavities defined in an artificial polymer are referred to as molecularly imprinted polymer (MIP). Recognition of MIP mostly mimics biological routes that have been employed in many fields [3], such as biological [4-6] and chemical detecting [7-10], quantitative detection [11-13], extraction, and purification [14-16]. Nylon 6 is biocompatible, mechanically, and thermally stable. It has been used in various sensors, the most important of which is in DNA sensor chips. The preparation method of molecularly imprinted nylon 6 is achieved by a phase inversion method from the liquid phase to the solid phase.

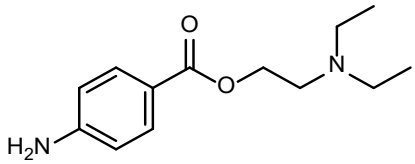

Fig 1. Chemical structure of procaine

There are many suitable solvents for polyamide, including formic acid, hydrochloric acid, and acetic acid. The polymer structure is characterized by being porous and having very great importance [17]. The procaine component is an amino ester local anesthetic acting on the fast sodium channel to produce local anesthesia. This anesthetic addition intends primarily to ease the pain of IM injection in large enough doses to reach therapeutic concentrations. Therefore it will be combined with other drugs that the patient takes it. We choose tinoxicam and nucleosimide as a matrix with procaine. This study includes using nylon 6 as a suitable polymer for establishing the molecular imprinting of procaine based on its phase inversion to the purpose of the selective separation and extraction of procaine in its pure form and its pharmaceuticals.

■ EXPERIMENTAL SECTION

Materials

Pure form (99.99%) pharmaceutical grade procaine powder was obtained as a gift from State Corporation for Drug Industries and Medical Appliances Samara/Iraq (SDI). The chemicals and reagents used are of analytical grade. The solutions used in this study were prepared as the following: the stock solution of each procaine (100 μg mL^{-1}), tinoxicam (SDI), and niclosemide (SEGMA) drugs were prepared by weighing 0.01 g of the drug and dissolving it in a 100 mL volumetric flack filled with distilled water. K_2HPO_4 (0.5 M) solution prepared by dissolving 43.60 g in a 500 mL volumetric flask. Na_2HPO_4 (0.5 M) solution was set by dissolving 35.80 g in a 500 mL volumetric flask. KH_2PO_4 (0.2 M) solution was prepared by dissolving 13. 60 g in a 500 mL volumetric flask. NaOH (0.1 M) solution was acquired by dissolving 0.40 g in a 100 mL volumetric flask of distilled water. Buffer solution (pH 1) to simulate gastric fluids was prepared by adding 0.83 mL of HCl to a 50 mL volumetric flask and then completing the volume was completed to the mark with distilled water while monitoring the pH. Buffer solution of pH 6.8 was prepared to simulate intestinal fluids by mixing 25.5 mL of K_2HPO_4 (0.5 M) with 25.5 mL of Na_2HPO_4 (0.5 M) solution with continuous stirring by a magnetic stirrer, while monitoring the pH with a pH meter [18]. Buffer solution (pH 7.4) simulated blood plasma was prepared by mixing 250 mL of KH_2PO_4 at a concentration of 0.2 M with 393.4 mL of 0.1 M NaOH, with continuous stirring by a magnetic stirrer, while monitoring the pH with a pH meter [18].

Instrumentation

All spectroscopic measurements were performed, and absorption spectra were recorded on a Shimadzu UV-Vis dual-beam spectrophotometer with an identical 1 cm quartz cell. HPLC KNAUER Wissenschaftliche Geräte GmbH, Germany, Ultra-Sonic devise, Germany – SONOREX and XRD spectroscopy Shimadzu 6000, Japan, Differential scanning calorimetry (DSC) of samples were performed by DSC-60 system Shimadzu company-Japan.

Procedure

Determine the maximum wavelength and calibration curve for procaine

The maximal absorption of PRO was determined using the UV-Vis spectrophotometric method, which involved pouring 1 mL of PRO from a 100 μg mL^{-1} stock solution into a 10 mL volumetric flask and filling the flask with distilled water. Against the blank, the final solution shows a maximum absorption at 290 nm. Solutions of different drug concentrations were prepared to study the calibration curve by taking different volumes of the drug ranging from 0.1–1.4 mL and placing them in 10 mL volumetric flask, then completing the volume with distilled water to the mark.

Preparation of molecularly imprinted polymer (MIP)

Two chemicals, 1.6 g of N6 and 0.02 g for PRO, were weighed separately and mixed well, dissolved in 20 mL of formic acid to prepare MIP (molecularly imprinted polymer) against NIP (non-imprinted polymer) that was prepared with the same procedure but without PRO. After that, the mixture was agitated at

room temperature for 5 min to achieve complete dissolution. The mixture was then placed into 200 mL of cold distilled water to solidify the polymer. After phase inversion, the imprinted polymer was washed with distilled water to eliminate the drug compound and leave its imprint on the polymer surface. The washing was done in an ultrasonic bath with 250 mL of distilled water for 15 min. Next, the polymer was filtered and rinsed with 50 mL of distilled water several times. Then, the MIP polymer was allowed to dry at room temperature, after which it was ground and stored. 1.53 g of PRO/N6-MIP was obtained. Finally, for non-imprinted polymer (NIP), all of the previous steps was repeated, but without the PRO drug.

Pharmaceutical preparation

Devapen Injection, DEVA, Turkey (800 mg/2 mL). The extraction sample was prepared by mixing the contents of 10 vials of powder of the injection, then weighing 0.01 g from the mixture and dissolving it in a 100 mL volumetric flask with distilled water to obtain 100 μg mL^{-1} stock solution. Then 0.7, 1.0, and 1.3 mL was drawn from the stock solution and placed in 10 mL volumetric flask. The volume was completed with distilled water. The extraction process was duplicated three times under the same conditions.

Separation column design

A 20 mL glass syringe (150 mm × 20 mm) with a mechanical press was used as a column. First, a double layer of filter paper (WIN LAB, Germany, and 150 mm) was placed inside the syringe, and then 0.5 g of MIP and NIP were separately inserted into the column for the initial study. After that, the mechanical press was assembled as well.

The initial approach of solid-phase extraction by MIP

A 0.5 g for each PRO/N6 MIP and NIP were weighed and placed in separation columns activated with 10 mL of distilled water in five batches. First, 10 mL of a 10 g mL^{-1} drug solution was put into the column and permitted to equilibrate for 5 min before being mechanically pressed. Next, the solution extracted from the column was collected in a 10 mL volumetric flask, and the absorption was measured for those solutions with a UV-Vis spectrophotometer at 290 nm and room temperature for PRO. The binding capacity was estimated by the following equation [19]:

$$Q = \frac{(C_0 - C_e) \times V}{W} \quad (1)$$

Q (μg/g) is referred to the holding capacity for the MIP, C_0 (μg/mL) was the primary concentration, V referred to the primary sample solution volume, C_e (μg/mL) referred to the sample solution equilibrium concentration, W (g) referred to the MIP quantity in gram.

The dissociation constant K_d was estimated by the following equation [19]:

$$\frac{Q}{C_e} = \frac{Q_{max-Q}}{K_d} \quad (2)$$

Q is the holding capacity, C_e refers to the sample solution equilibrium concentration, Q_{max} refers to the extreme holding capacity, and K_d is the division constant correlated with adsorption site attraction.

The calculation of the Imprinting factor IF was done by the fraction of Q_{max}-MIP to the Q_{max}-NIP and then utilized to evaluate non-specific and specific interactions [19]:

$$IF = \frac{Q_{max}(MIP)}{Q_{max}(NIP)} \quad (3)$$

Finally, the calculation of an accumulative rate of release (%) was done by the following relation [20]:

$$\text{Accumulation release rate } (\%) = \frac{M_t}{M_\infty} \times 100\% \quad (4)$$

M_t is the increasing quantity of the drug at a specific time. M_∞ referred to the increasing quantity of the drug at an endless time.

Binding performance assessment

In this study, the optimal circumstances for the separation process were evaluated. Furthermore, the factors affecting the efficiency of the binding capacity, such as the quantity of MIP, the optimum temperature, and the equilibrium duration, were also studied.

Scatter plot study of PRO

Different drug solutions were separately prepared with concentrations ranging from 2–13 μg mL^{-1} by transferring 0.2–1.3 mL from a 100 μg mL^{-1} stock

solution by placing them in a 10 mL volumetric flask and completing the volume with distilled water. After that, the extraction process was performed with MIP and NIP at optimum temperature and equilibrium time, and then the absorption of the extracted solution was measured at 290 nm for PRO.

■ RESULTS AND DISCUSSION

The Absorption Spectra and Calibration Curve

The maximum wavelength of 10 μg mL^{-1} PRO was determined by a UV-Vis spectrophotometric. Fig. (2-3) shows different concentrations of the drug with the absorption spectrum and linear range that obey beers law.

Characterization of Imprinting Polymer

XRD identification

Fig. 4 presents the X-ray diffraction (XRD) structure of NIP and MIP with procaine. The X-ray spectrum reveals the three strongest crystalline peaks at 2-theta of 24.38°, 20.41°, and 12.13°. The intensity of each peak increased, indicating that the crystalline increased because the pharmaceutical particle became a source of nucleation, resulting in greater crystal growth [21].

DSC analysis

The sample was examined by weighing 25 mg of the sample and increasing the temperature at a 10 °C/min rate. As illustrated in Fig. 5, DSC analysis for NIP shows the endothermic point at 199 °C which is related to the melting point. The peak at 178.71 °C shows the process of thermal recrystallization. On the other hand, the figure shows that the melting point value of MIP did not change much from NIP, appeared at 199.35 °C, while the peak of recrystallization showed a clear difference and appeared close to 163.21 °C.

Elementary Study of Solid-Phase Extraction by PRO/N6-MIP

The first solid phase extraction attempt by each of the MIP and NIP was done using the separation column to 10 mL solution of the drug of 10 μg mL^{-1} concentration with an equilibrium time of 5 min. Following results illustrated in Table 1 indicated a large variance in Q value amongst imprinted MIP and non-imprinted polymer NIP, which confirms the effectiveness of templet formation.

The Effect of PRO/N6-MIP Weight Study

Different weights were taken from the MIP, ranging from (0.1–0.7) g, and the extraction process was

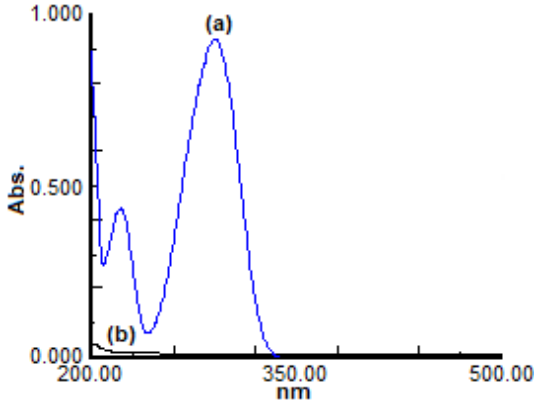

Fig 2. (a) Absorption spectrum of 10 μg mL^{-1} of PRO with maximum absorption band at 290 nm, (b) Blank solution

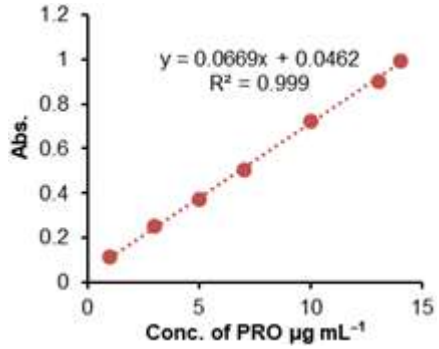

Fig 3. Calibration curve of procaine

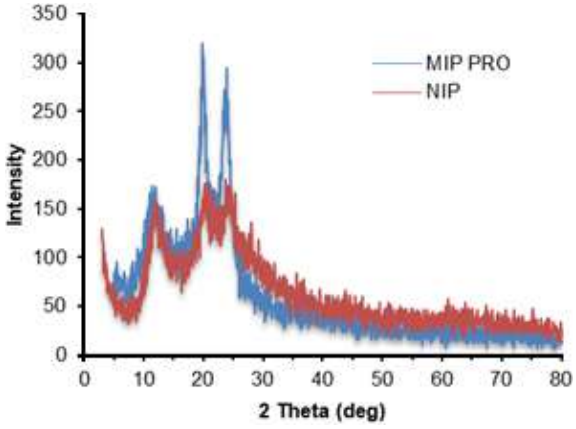

Fig 4. X-ray (Cu Kα λ =1.54060 A) diffraction of NIP and PRO/N6-MIP

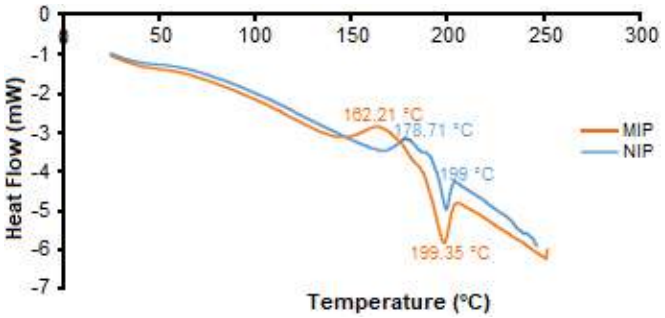

Fig 5. DSC analysis for NIP and PRO/N6-MIP

Table 1. Adsorption capacity related to NIP, MIP, for a 10 μg mL^{-1} PRO

Sample	Abs	Ce (μg mL^{-1})	Q (μg g^{-1})
MIP	0.510	6.9	62.0
NIP	0.700	9.77	4.6
STOCK	0.725	10.00	-

executed under the same circumstances. Table 2 showed that the weight of 0.5g of MIP gives the best binding capacity at 67.20 μg g^{-1}. Q remains constant in the higher weights, and the reason was the selective holes in PRO/N6-MIP being saturated with PRO [22]. So it has been established in the next study.

The Effect of Solution Temperature

Different drug samples were prepared with the same concentration and applied with MIP and NIP to evaluate the effect of temperature on the separation process. Fig. 6 showed that the temperature of 70 °C gives the best binding capacity value equal to 136.80 μg g^{-1} compared to 69 mg g^{-1} for the NIP. The changes of Q with temperature are due to many reasons, such as modification of hole size, hydrophobic interaction, hydrogen bonding interaction [23-25]. There is a strong inclination that the pore size in the polymer is amplified with the increase in temperature. Thus, pore size is an essential reason for the rise in binding capacity with increased temperature, which enables the approximation of PRO molecules to the specific holes. [26].

The Effect of Equilibrium Time Study

The extraction process was performed with different equilibrium times for the drug solution under the optimum conditions. Results showed in Fig. 7 illustrated that the best holding capacity, 199.10 μg g^{-1}, was obtained at 40 min, which was applied in subsequent studies.

The dynamic adsorption curves of the NIP, MIP were recognized through observing procaine concentration over 1–60 min. As shown in Fig. 8, the Q value of MIP improved rapidly after 5 min and reached

Table 2. The effect of PRO/N6-MIP weight on the binding capacity

Sample(g)	Abs	Ce(μg mL^{-1})	Q(μg g^{-1})
0.10	0.650	9.02	19.60
0.20	0.631	8.74	25.20
0.30	0.617	8.53	29.40
0.50	0.491	6.64	67.20
0.60	0.491	6.64	67.20
0.70	0.491	6.64	67.20

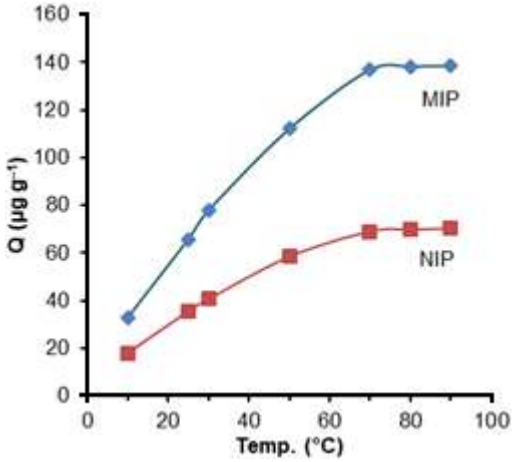

Fig 6. Isotherm curves of PRO/N6-MIP, NIP

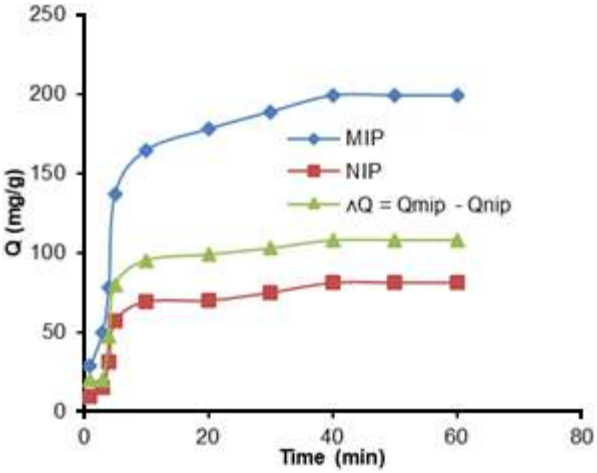

Fig 7. Dynamic curves of adsorption for the PRO/N6-MIP, NIP toward PRO

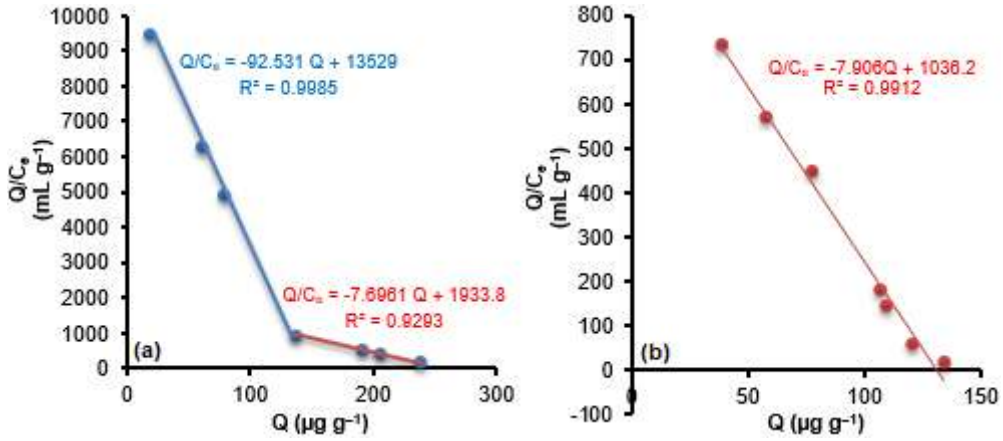

Fig 8. Scatter plot study of the (a) PRO/N6-MIP, (b) NIP

its optimum equilibrium time at 40 min. After 40 min, the Q value was nearly unaffected, suggesting that MIP selective holes were saturated by procaine adsorption and stabilized. The specific adsorption Q amplified through time, signifying the procaine imprinting efficiency. Results exposed that MIP could be utilized as a transporter for the separation and adsorption of procaine [20], and this was acceptable when compared with that obtained by Surikumaran et al. [27].

PRO/N6-MIP Scatter Plot Study

Different drug solutions were prepared as mentioned in the experimental part, and the extraction process was performed with MIP and NIP at the temperature of 70 °C, and an equilibrium time of 40 minutes. The results showed in Fig. 8(a, b) for MIP and NIP, respectively.

Scatter plots were an additional examination of the adsorption capacity, which was useful for assessing adsorption positions. The Scatter plot (Fig. 8(a)) for MIP exhibited two lines, the first positions with low affinity and the other representing high-affinity positions, suggesting that there were two different kinds of adsorption spots (superficial positions besides cavities) in the MIP. While the plot for NIP (Fig. 8(b)) showed the same line of surface site in MIP (have the same slop), this result is consistent with Ma et al. [19]. The positions of low affinity showed a dissociation constant that was similar to that of the non-imprinted polymer but greater than that of the positions of high-affinity Table 3. The positions of low affinity showed an IF, Q_{max} that was superior to that of the positions of high affinity. The least Q_{max} was to that of the NIP. Thus, the results proposed that positions of low affinity existed on the surface of the MIP and the positions of high affinity situated in the cavities of the imprinted polymer. The non-imprinted N6 had only positions that were non-selective and on the surface only [19].

The Selectivity of PRO/N6-MIP

Two different solutions were prepared by mixing 10 µg mL^{-1} of procaine with 10 µg mL^{-1} for each niclosemide and tinoxicam separately in a 10 mL volume flask. Then the extraction process was performed to separate procaine in the presence of the two different matrices (niclosemide and tinoxicam). PRO/N6-MIP showed very good selectivity for PRO with 85% recovery compared with the NIP as shown in Table 4.

Extraction Efficiency Estimation of PRO/N6-MIP

The selectivity of PRO-MIP by HPLC technique was studied, using a C18 column, the mobile phase was

Table 3. Maximum binding capacity (Q_{max}) and imprinting factor (IF) acquired by the Scatter plot for procaine

Polymer	K_d	Q_{max}	IF
MIP-high	0.058	191	1.42
MIP-low	0.137	237	1.76
NIP	0.147	134	-

Table 4. Selective adsorption of the PRO/N6-MIP to PRO in the presence of niclosemide and tinoxicam

Matrix	MIP				NIP			
	Abs	C_e (μg mL^{-1})	Q (μg g^{-1})	Rec (%)*	Abs	C_e (μg mL^{-1})	Q (μg g^{-1})	Rec (%)*
Niclosemide	0.078	0.47	190.6	85.0	0.350	4.5	110	44
Tinoxicam	0.086	0.59	188.2	82.6	0.374	4.8	104	45

water-acetonitrile (75:25) modified to pH 3.3 by glacial acetic acid at 40 °C, the sample was prepared by mixing equal quantities of PRO with both tenoxicam and Niclosemide. Fig. 9 showed a significant decrease in the peak height of PRO extracted from PRO-MIP compared to NIP and the mixture (PRO, CLP, and TNX) without the extraction process.

Drug Release Study of PRO/N (6)-MIP

Three solutions were prepared with different pH values: 1, 6.8, and 7.4 simulating to gastric, intestinal, and blood plasma fluids, respectively. After that, MIP performed the extraction process of a 10 μg mL^{-1} solution of the drug. In this process, the MIP polymer was transferred from the extraction column and placing in 100 mL buffer solutions, and the absorption at different periods was measured and plotted in Fig. 10.

The measured release of PRO/N6-MIP was conceded under stirring at 25 °C. The results specified that the accumulative release rate of PRO was pH dependant. The release rate in the acidic buffer was remarkably faster than that of pH 6.8 and pH 7.4 because procaine is a weak organic base. Thus it dissolved in the stomach fluid effortlessly, leading to a breakdown of imprinted N6. On the other hand, the imprinted N6 presented an excellent capability of PRO release control at pH 7.4 and 6.8. This result is attributed to the selective binding positions present in the polymer matrix that gradually releases PRO. Therefore, imprinted N6 could be exploited by way of possible unique substance to the purpose of organized discharge, allowing the delivery of procaine to a fixed position in the clinical uses [28].

Application of the Proposed Method on Pharmaceuticals

Pharmaceuticals in the form of Devapen injections had been used, and the proposed method was applied to these injections. Different volumes of pharmaceutical solutions were taken with a final volume of 10 mL. The extraction process was performed with MIP and NIP under the same conditions. Table 5 showed that PRO/N6–MIP gives a high selectivity for PRO extraction from pharmaceuticals compared with NIP.

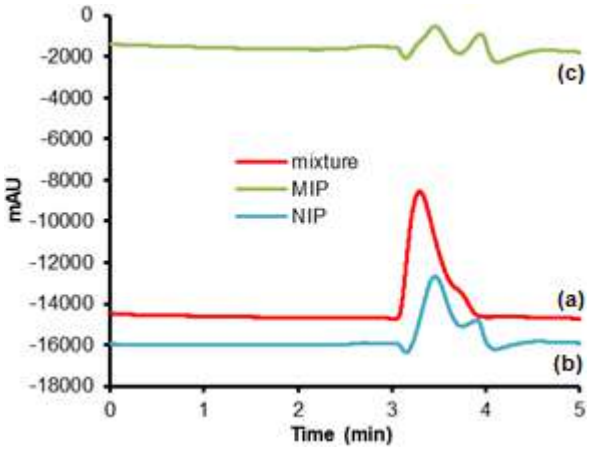

Fig 9. HPLC chromatogram of (a) Mixture of 10 μg mL^{-1} of each PRO, tenoxicam, and niclosemide, (b) The mixture after extraction with NIP, and (c) The mixture after extraction with PRO/N6-MIP

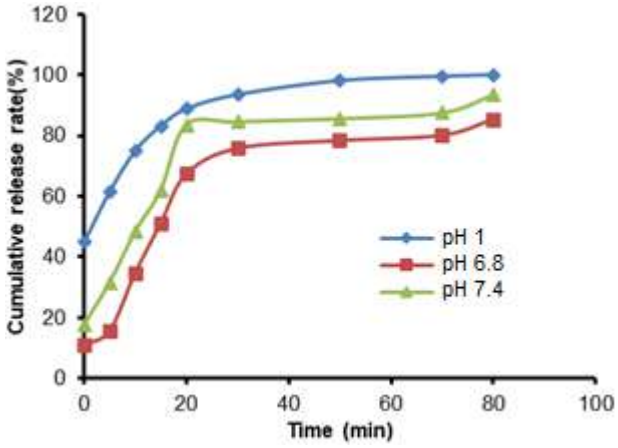

Fig 10. Control curves of PRO/N6–MIP in the various pH solutions

Table 5. Application of the proposed method to the separation of PRO in dosage form

Pharma. Preparation	Labeled amount (mg)	Conc. taken (μg mL^{-1})	MIP				NIP			
			C_e (μg mL^{-1})*	Q (μg g^{-1})	RE (%)	RSD %	Ce (μg mL^{-1})*	Q (μg g^{-1})	RE (%)	RSD (%)
Devapen injection/Turkey	800	7	0.148	137.38	0.218	0.026	3.433	71.34	-47.957	0.991
		10	0.475	190.78	-0.313	0.747	4.556	108.88	-43.181	0.846
		13	1.010	239.80	1.180	0.004	5.452	150.96	-36.303	0.951

*Each measurement is repeated three times

■ CONCLUSION

In this study, the polymer nylon 6 was molecularly imprinted with procaine by a phase inversion method. The molecular imprinting polymer was applied to separate the drug compound successfully by using the SPE technique. The study showed the importance of experimental conditions for efficient separation, extraction, and obtaining the highest binding capacity value. The separation efficiency was monitored using the HPLC technique, were showed good selectivity for the drug compound in the presence of tinoxicam and nucleosemide. The study showed the possibility of efficiently using the imprinted polymer to study the controlled release of procaine in different acidic media. The proposed method was successful in separating PRO in its pure form and in pharmaceuticals.

■ REFERENCES

[1] Fleckenstein, J., König, M., and Banzer, W., 2018, Neural therapy of an athlete's chronic plantar fasciitis: A case report and review of the literature, *J. Med. Case Rep.*, 12 (1), 233.

[2] Plotycya, S., Strontsitska, O., Pysarevska, S., Blazheyevskiy, M., and Dubenska, L., 2018, A new approach for the determination of benzocaine and procaine in pharmaceuticals by single-sweep polarography, *Int. J. Electrochem.*, 2018, 1376231.

[3] Lu, L., Yue, X., Lin, F., Huang, F., Zhang, B., and Lin, Z., 2015, Template-synthesized ultra-thin molecularly imprinted polymers membrane for the selective preconcentration of dyes, *J. Mater. Chem. A*, 3 (20), 10959–10968.

[4] Xu, X., Chen, X., Yang, L., Zhao, Y., Zhang, X., Shen, R., Sun, D., and Qian, J., 2020, Film-like bacterial cellulose-based molecularly imprinted materials for highly efficient recognition and adsorption of cresol isomers, *Chem. Eng. J.*, 382, 123007.

[5] Bereli, N., Akgönüllü, S., Asliyüce, S., Çimen, D., Göktürk, İ., Türkmen, D., Yavuz, H., and Denizli, A., 2020, Molecular imprinting technology for biomimetic assemblies, *Hacettepe J. Biol. Chem.*, 48 (5), 575–601.

[6] Li, D.W., Zhai, W.L., Li, Y.T., and Long, Y.T., 2014, Recent progress in surface-enhanced Raman spectroscopy for the detection of environmental pollutants, *Microchim. Acta*, 181 (1), 23–43.

[7] Chen, L., Wang, X., Lu, W., Wu, X., and Li, J., 2016, Molecular imprinting: Perspectives and applications, *Chem. Soc. Rev.*, 45 (8), 2137–2211.

[8] Herrera-Chacón, A., Cetó, X., and del Valle, M., 2021, Molecularly imprinted polymers-towards electrochemical sensors and electronic tongues, *Anal. Bioanal. Chem.*, 413 (24), 6117–6140.

[9] Saylan, Y., Yilmaz, F., Özgür, E., Derazshamshir, A., Yavuz, H., and Denizli, A., 2017, Molecular imprinting of macromolecules for sensor applications, *Sensors*, 17 (4), 898.

[10] Yang, Q., Li, J., Wang, X., Peng, H., Xiong, H., and Chen, L., 2018, Strategies of molecular imprinting-based fluorescence sensors for chemical and biological analysis, *Biosens. Bioelectron.*, 112, 54–71.

[11] Zhang, Y., Wang, H.Y., He, X.W., Li, W.Y., and Zhang, Y.K., 2021, Homochiral fluorescence responsive molecularly imprinted polymer: Highly chiral enantiomer resolution and quantitative detection of L-penicillamine, *J. Hazard. Mater.*, 412, 125249.

[12] Ashley, J., Wu, K., Hansen, M.F., Schmidt, M.S., Boisen, A., and Sun, Y., 2017, Quantitative detection of trace-level cloxacillin in food samples using

magnetic molecularly imprinted polymer extraction and surface-enhanced Raman spectroscopy nanopillars, *Anal. Chem.*, 89 (21), 11484–11490.

[13] Zhao, X., Cui, Y., He, Y., Wang, S., and Wang, J., 2020, Synthesis of multi-mode quantum dots encoded molecularly imprinted polymers microspheres and application in quantitative detection for dopamine, *Sens. Actuators, B*, 304, 127265.

[14] Wang, C., Hu, X., Guan, P., Wu, D., Qian, L., Li, J., and Song, R., 2015, Separation and purification of thymopentin with molecular imprinting membrane by solid-phase extraction disks, *J. Pharm. Biomed. Anal.*, 102, 137–143.

[15] Yang, Z., Wang, J., Shah, T., Liu, P., Ahmad, M., Zhang, Q., and Zhang, B., 2021, Development of surface imprinted heterogeneous nitrogen-doped magnetic carbon nanotubes as promising materials for protein separation and purification, *Talanta*, 224, 121760.

[16] Shi, W., Zhang, S.Q., Li, K.B., Jia, W.P., and Han, D.M., 2018, Integration of mixed-mode chromatography and molecular imprinting technology for double recognition and selective separation of proteins, *Sep. Purif. Technol.*, 202, 165–173.

[17] Dmitrienko, E.V., Bulushev, R.D., Haupt, K., Kosolobov, S.S., Latyshev, A.V., Pyshnaya, I.A., and Pyshnyi, D.V., 2013, A simple approach to prepare molecularly imprinted polymers from nylon-6, *J. Mol. Recognit.*, 26 (8), 368–375.

[18] Vogel, A.I., Mendham, J., Denney, R.C., Barnes, J.D., and Thomas, M.J.K., 2000, *Vogel's Textbook of Quantitative Chemical Analysis*, 6th Ed., Prentice Hall, Harlow, UK.

[19] Ma, X., Lin, H., Zhang, J., Zhou, X., Han, J., She, Y., Qiu, C., He, Q., Wang, J., and Rabah, T., 2018, Preparation and characterization of dummy molecularly imprinted polymers for separation and determination of farrerol from *Rhododendron aganniphum* using HPLC, *Green Chem. Lett. Rev.*, 11 (4), 513–522.

[20] Zhang, W., She, X., Wang, L., Fan, H., Zhou, Q., Huang, X., and Tang, J.Z., 2017, Preparation, characterization and application of a molecularly imprinted polymer for selective recognition of sulpiride, *Materials*, 10 (5), 475.

[21] Meenan, P.A., Anderson, S.R., and Klug, D.L., 2002, "The Influence of Impurities and Solvents on Crystallization" in *Handbook of Industrial Crystallization*, 2nd Ed., Eds. Myerson, A.S., Butterworth–Heinemann, Oxford, UK, 67–100.

[22] Olcer, Y.A., Demirkurt, M., Demir, M.M., and Eroglu, A.E., 2017, Development of molecularly imprinted polymers (MIPs) as solid-phase extraction (SPE) sorbent for the determination of ibuprofen in water, *RSC Adv.*, 7 (50), 31441–31447.

[23] Saeed, A., Sharif, M., and Iqbal, M., 2010 Application potential of grapefruit peel as dye sorbent: Kinetics, equilibrium, and mechanism of crystal violet adsorption, *J. Hazard. Mater.*, 179 (1-3), 564–572.

[24] Zabihi, M., Asl, A.H., and Ahmadpour, A., 2010, Studies on adsorption of mercury from aqueous solution on activated carbons prepared from walnut shell, *J. Hazard. Mater.*, 174 (1-3), 251–256.

[25] Komiyama, M., Takeuchi, T., Mukawa, T., and Asanuma, H., 2003, *Molecular Imprinting: From Fundamentals to Applications*, Wiley-VCH Verlag GmbH & Co. KGaA, Weinheim.

[26] Tao, Y., Dai, J., Kong, Y., and Sha, Y., 2014, Temperature-sensitive electrochemical recognition of tryptophan enantiomers based on β-cyclodextrin self-assembled on poly (L-glutamic acid), *Anal. Chem.*, 86 (5), 2633–2639.

[27] Surikumaran, H., Mohamad, S., and Sarih, N.M., 2014, Molecularly imprinted polymer of methacrylic acid functionalised β-cyclodextrin for selective removal of 2,4-dichlorophenol, *Int. J. Mol. Sci.*, 15 (4), 6111–6136.

[28] Ruela, A.L.M., Figueiredo, E.C., and Pereira, G.R., 2014, Molecularly imprinted polymers as nicotine transdermal delivery systems, *Chem. Eng. J.*, 248, 1–8.

Supplementary Data

This supplementary data is a part of paper entitled "Synthesis, Characterization and Antibacterial Activity Study of Cobalt(II), Nickel(II), Copper(II), Palladium(II), Cadmium(II) and Platinum(IV) Complexes with 4-Amino-5-(3,4,5-trimethoxyphenyl)-4*H*-1,2,4-triazole-3-thione".

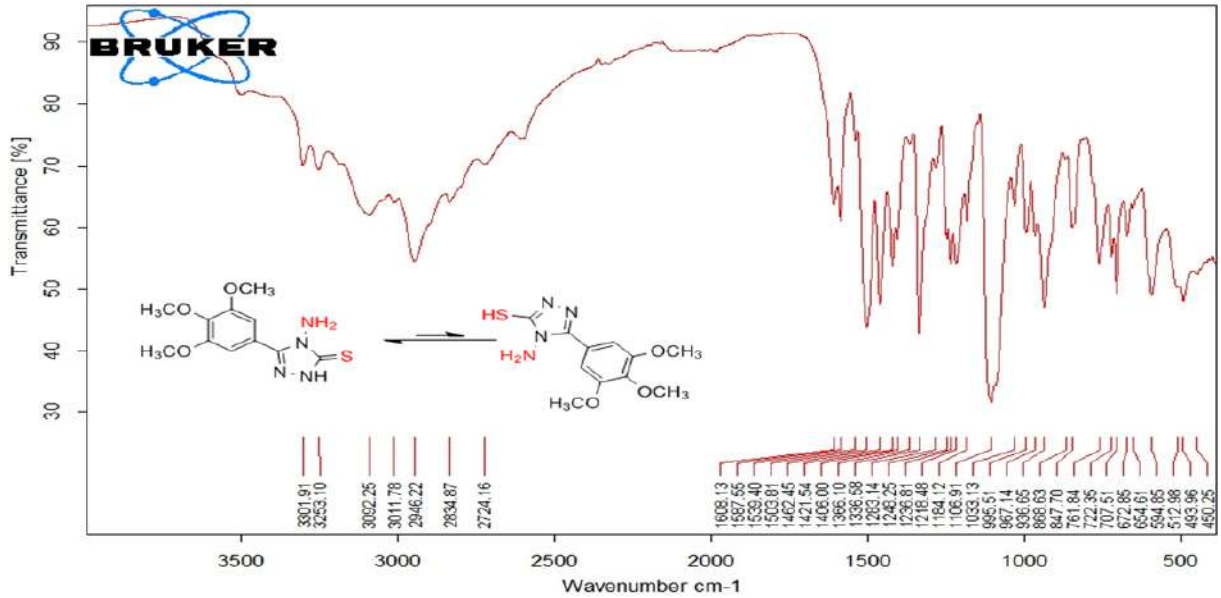

Fig S1. FT-IR spectrum of 4-amino-5-(3,4,5-trimethoxiyphenyl)-4*H*-1,2,4-triazole-3-thione, L

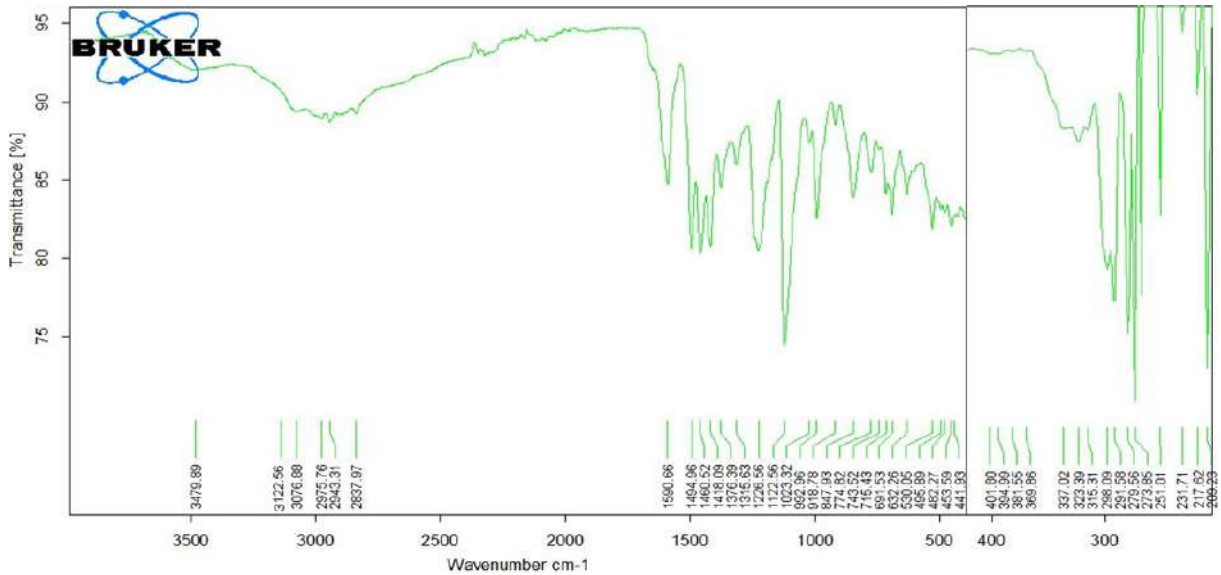

Fig S2. FT-IR spectrum of metal complex C6

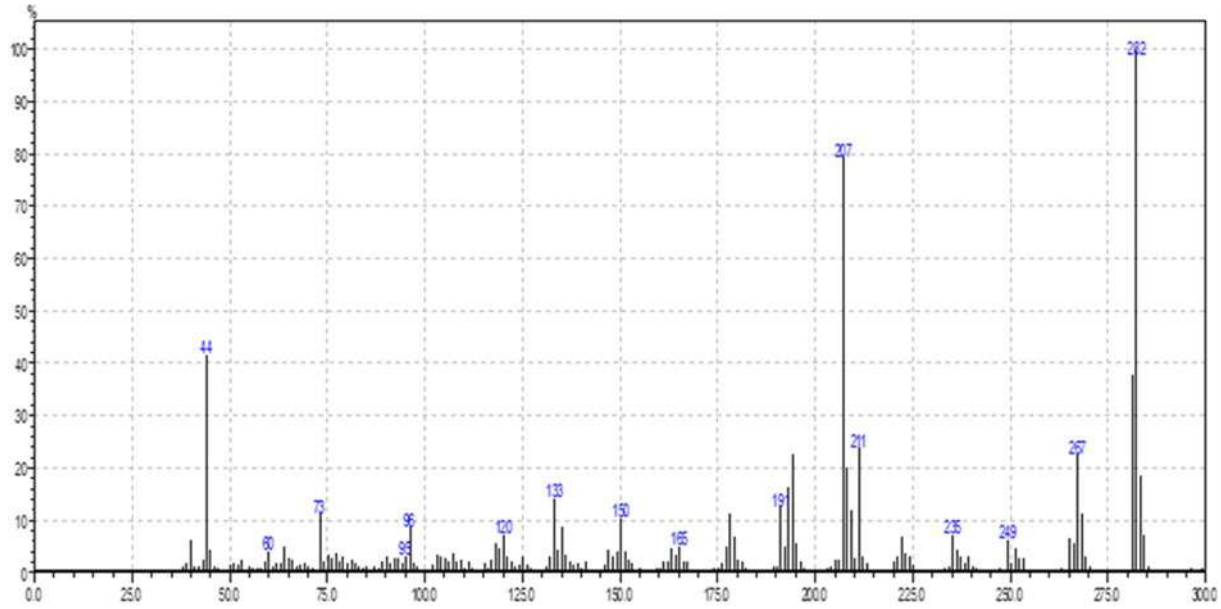

Fig S3. Mass spectrum of L

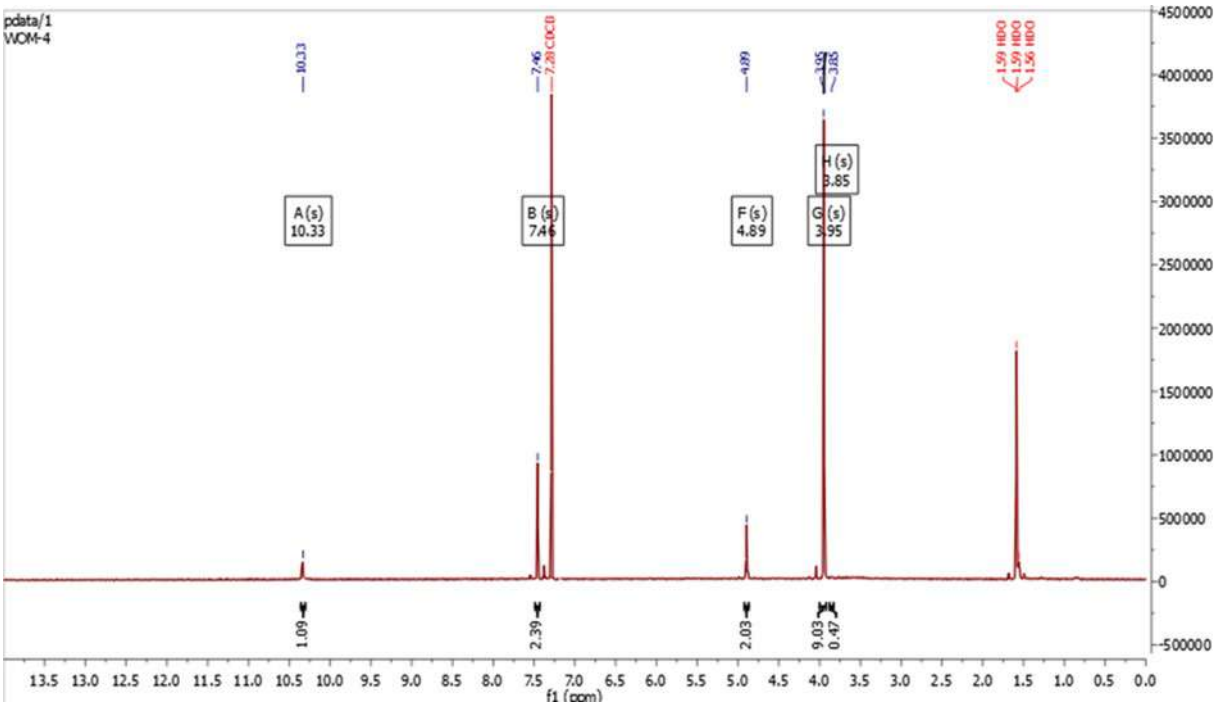

Fig S4. ^{1}H-NMR spectrum of ligand, L

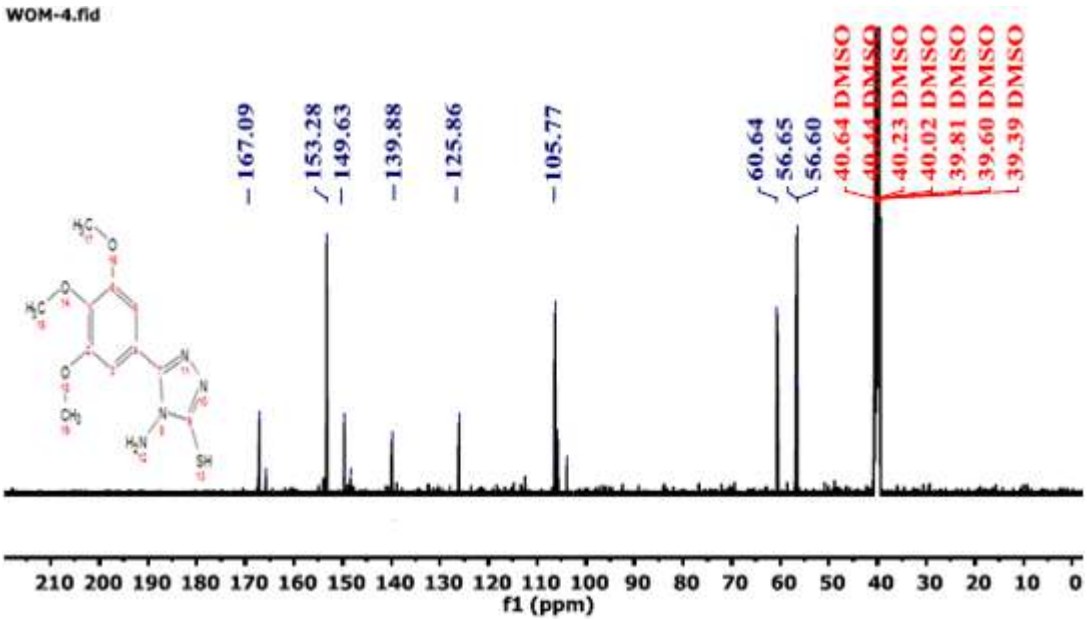

Fig S5. ^{13}C-NMR spectrum of Ligand, L

Synthesis, Characterization and Antibacterial Activity Study of Cobalt(II), Nickel(II), Copper(II), Palladium(II), Cadmium(II) and Platinum(IV) Complexes with 4-Amino-5-(3,4,5-trimethoxyphenyl)-4*H*-1,2,4-triazole-3-thione

Waleed Abbas Jawad[1], Asim Alaa Abd Al-Hussein Balakit[2], and Mahmoud Najim Abid Al-Jibouri[3*]

[1]*Ministry of Education, Babylon Education Directorate, Hilla-Iraq*

[2]*College of Pharmacy, University of Babylon, Hilla-Iraq*

[3]*Department of Chemistry, College of Science, Mustansiriyah University, Baghdad-Iraq*

Corresponding author:

email: mahmoudaljibouri@gmail.com

Received: June 25, 2021
Accepted: August 8, 2021

DOI: 10.22146/ijc.67021

Abstract: *New transition metal complexes of cobalt(II), nickel(II), copper(II), palladium(II), cadmium(II), and platinum(IV) with bidentate ligand 4-amino-5-(3,4,5-trimethoxyphenyl)-4*H*-1,2,4-triazole-3-thiol were synthesized and characterized by microelemental analyses (CHNS), Fourier-transform infrared (FT-IR), UV-Visible spectra, molar conductance, magnetic susceptibility and thermal analyses (TG-DSC). The ligand was synthesized by ring closure of potassium-2-(3,4,5-trimethoxybenzoyl) hydrazine carbodithioate with an excess amount of hydrazine, and then was acidified using hydrochloric acid. The ligand was used as Lewis bases to prepare metal complexes through the reaction of ratio (1:2) metal:ligand. The ligand was characterized by ^{1}H-NMR and ^{13}C-NMR and the previously described methods to identify the complexes. The results obtained from spectra and elemental analyses indicated the tetrahedral geometry around Cd(II) ion, square-planar for Cu(II) and Pd(II), and octahedral geometry around Co(II), Ni(II), and Pt(IV). All the metal complexes showed significant antibacterial activity in comparison with the free ligand. The antibacterial test of the platinum(IV) complex showed higher activity than other metal complexes against bacteria* Staphylococcus aureus *(G-positive) and* Escherichia coli *(G-negative).*

Keywords: *1,2,4-triazole-3-thione derivatives; new metal complexes; antibacterial activity*

■ INTRODUCTION

The 1,2,4-triazole parent consists of a five-membered aromatic ring containing three atoms of nitrogen, two of which are adjacent to a stable, water-soluble solid. It is possible to envisage two tautomeric forms, 1*H*-tautomer and 4*H*-tautomer. Theoretical and empirical approaches suggest that the preferred structure is the 1*H*-tautomer. Two nitrogen atoms are connected to any carbon atom in 1,2,4-triazole, and thus, the ring structure is deficient in electrons. For electrophilic attack, the ring is deactivated so that nitration and other typical carbon reactions of aromatic chemistry do not occur to the parent compound. However, in the literature, electrophilic attacks on nitrogen are found in abundance [1-2].

3-Mercapto-1*H*-1,2,4-triazol-5-yl derivatives have been reported in numerous studies, a thiol-thione group leading to an increase in biological activity linked to the triazole moiety [3]. In addition, the triazolethione system is known as a cyclic analog of very significant components such as thiosemicarbazides and thiocarbohydrazides, which are widely distributed in many organic reactions as a reactive building block leading to deferential heterocyclic rings and successful biological applications. The nucleus of mercapto-1,2,4-triazole is also present in many natural products and pharmaceuticals [4]. Those having 1,2,4-riazole thione-

thiol derivatives have gained considerable importance in medicinal chemistry due to their anticancer [5], antimicrobial [6], antioxidant, antitumor, anti-tuberculosis, anticonvulsant [7], fungicidal [8], antiepileptic, and anti-inflammatory activities [9]. The interaction of these donor ligands and metal ions gives complexes of different geometries, and a literature survey reveals that these complexes are potentially more biologically active [5]. Dallavalle et al. [10] synthesized copper(II) and palladium(II) complexes of 4-amino-5-methylthio-3-(2-pyridyl)-1,2,4-triazole. These complexes' antiproliferative activity and ligands were assessed on regular human fibroblasts (HF) and human fibrosarcoma tumor (HT1080) cells. The copper(II) complex displayed potent antiproliferative activity for both normal and neoplastic cells. Al-Masoudi et al. [11], identified mixed ligand complexes of 4,5-diphenyl-1,2,4-triazole-3-thione (LH) and diphosphines $Ph_2P(CH_2)nPPh_2$ with platinum(II) and palladium(II). The antiproliferative activity of these complexes was evaluated against a panel of human cancer cell lines derived from hematological CD4+ human T-cells with an integrated HTLV-1 genome (MT-4). The platinum-based complex was the most active in the series, with antiproliferative activity against various cancer cell lines. The present work described the synthesis of some transition metal complexes with bidentate ligand 4-amino-5-(3,4,5-trimethoxyphenyl)-4*H*-1,2,4-triazole-3-thiol, and then antibacterial activity study of the ligand and their metal complexes.

■ EXPERIMENTAL SECTION

Materials

All starting materials, namely gallic acid and hydrazine hydrate, were used in this study without further purification. All chemicals including $CoCl_2{\cdot}6H_2O$, $CuCl_2{\cdot}2H_2O$, $NiCl_2{\cdot}4H_2O$, $CdCl_2{\cdot}2H_2O$, $H_2PtCl_6{\cdot}2H_2O$ and $PdCl_2$ were procured from Sigma-Aldrich and CDH.

Instrumentation

Electrical conductivity measurements of the complexes were made with 10^{-3} M of DMF solvent at 25 °C using WTW Cond 7300 digital conductivity meter. Melting points of the ligands and their metal ion complexes were measured using Stuart SMP 10 UK at the College of Pharmacy, the University of Babylon. The electronic spectra of the ligands and their ion metal complexes were recorded on an 1800-UV Shimadzu spectrophotometer in the range of 200–1100 nm using quartz cell of length 1 cm and concentration 10^{-3} M by using DMSO as a solvent at the College of Pharmacy, University of Babylon. Infra-red spectra are recorded in the range 4000–500 cm^{-1} using KBr disk for the ligands and CsI disk in the range 4000–200 cm^{-1} for their complexes (Bruker Optics, Japan) College of Pharmacy, the University of Babylon. Magnetic susceptibility measurements for the synthesized complexes have been measured at room temperature using Auto Magnetic Susceptibility Balance Model Sherwood Scientific at Department of Chemistry, College of Sciences, Al-Mustansiriyah University. The spectra of ^{1}H-NMR and ^{13}C-NMR have been measured using Bruker Bio-Spin GmbH 400 MHz and 100 MHz instruments with tetramethylsilane as the internal standard. The mass spectra for the intermediate and ligand were recorded with Shimadzu QP-1000EX GC/MS instrument, Japan, at the Department of Chemistry, College of Sciences, Mustansiriyah University. The metal contents of the synthesized complexes were determined by using FL Aspect LS 131 RC1 at Ibn-Sina Center, Baghdad, Iraq. Thermal analysis of the synthesized ligand and its metal complexes was measured using Shimadzu 60-H Thermal Analyzer at Vit Vellore, Perkin Elmer STA6000 thermal analyzer, the National Center for Research and Development Science and Materials Engineering, Iran. The ligands' carbon, hydrogen, nitrogen, and sulfur contents and their metal ion complexes were recorded on a Vario ELV5 CHNS Mode, S. No.: 11086109, at the National center for research and development science and materials engineering, Iran.

Synthesis

Synthesis of 3,4,5-trimethoxybenzoic acid (S1)

Gallic acid monohydrate 25 g (0.133 mol) was added to a cold solution of 40 g (1.0 mol) sodium hydroxide in 250 mL water in a 3-neck round bottom flask. The flask was closely stopped immediately, and the

mixture was periodically mixed until all of the acids were dissolved. First, dimethyl sulfate 0.36 mol (33 mL) was added, and the flask was stirred for 20 min. In order to prevent the temperature from increasing above 30–35 °C, the mixture was kept cold. The cover was occasionally lifted to release some pressure. Next, a second similar volume of dimethyl sulfate was added, and stirring continued for a greater range of 20 min. The temperature increased to 40–45 °C during this second addition. The flask was then fitted with a reflux condenser, and the contents were cooked for two hours by stirring. Sodium hydroxide (10 g) was then added to 15 mL of water, and the boiling continued for an additional two hours. The reaction mixture was then cooled and acidified with 5% hydrochloric acid. The precipitated was filtered with suction and washed well with cold water and recrystallized from ethanol to give a compound of S1 as given in Scheme 1 [12] Color (brown crystal), yield (85%), M.p (170–172) °C, M.wt (212 g/mol), FT-IR (KBr, cm^{-1}): broad bend ν(O–H) (3020–2516), ν(C=O) acid (1681), νC–H aliph. (2945 and 2836).

Synthesis of 3,4,5-trimethoxymethylbenzoate (S2)

Sulfuric acid (1.5 mL) was added dropwise to the mixture of compound S1 (10.6 g, 0.05 mol) in 30 mL methanol for 8 h. The mixture was heated under reflux, and the reaction was controlled using thin-layer chromatography (TLC). After cooling, the precipitate formed and the methanol excess was evaporated. The solid product was washed with a solution of sodium bicarbonate, filtered, washed with cold water, dried, and recrystallized from ethanol to give compound of S2, as presented in Scheme 1 [13]: Color (white crystal), Yield (95%), M.p (83–85 °C), M.wt (226 g/mol), R_f = 0.87 (ethyl acetate:chloroform, 1:2). FT-IR (KBr, cm^{-1}): ν(C=O) ester (1713), νC–H. (3079), ν C–H aliph. (2951).

Synthesis of 3,4,5-trimethoxybenzohydrazide (S3)

To the solution of compound S2 prepared by dissolving 9 g (0.04 mol) in 40 mL of absolute ethanol, 15 mL of hydrazine hydrate (80%) was added. The mixture was refluxed for 14 h, the reaction was controlled using thin-layer chromatography (TLC), and then the mixture was allowed to cool down. Finally, a

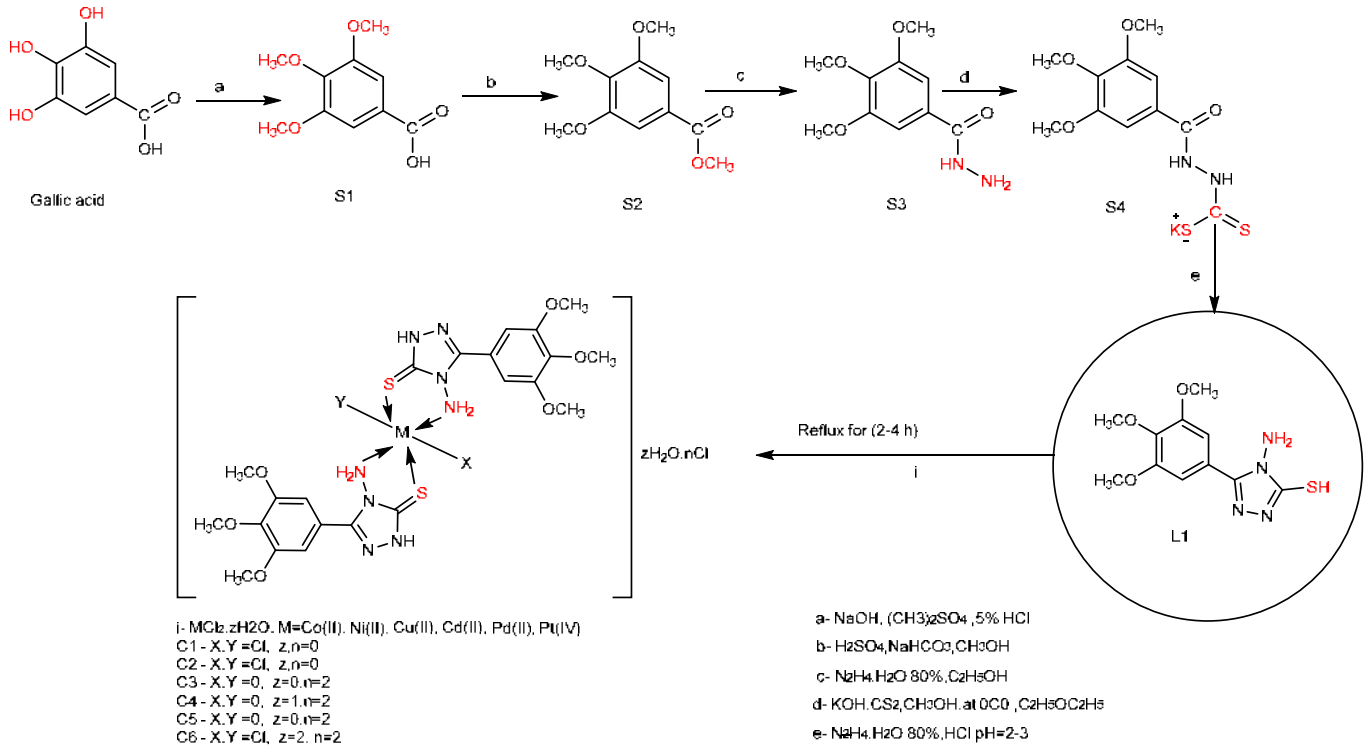

Scheme 1. Synthesis of L and their complexes C1–C6

solid product was filtered, washed with cold water, dried, and recrystallized from ethanol to give compound S3, Scheme 1 [14]: Color (white), Yield (90%), M.p (160–163 °C), M.wt (226 g/mol), R_f = 0.25 (ethyl acetate: chloroform, 1:2). FT-IR (KBr, cm^{-1}): ν(NH_2) asym. and sym. (3366 and 3334), ν(NH) (3292), ν(C=O) amide (1651), νC–H arom. (3010), νC–H aliph. (2938).

Synthesis of potassium-2-(3,4,5-trimethoxybenzoyl) hydrazine carbodithioate (S4)

Compound S3 (4.5 g, 0.0195 mol) was treated with a solution of 1.8 g (0.0321 mol) of potassium hydroxide in 35 mL methanol at 0 °C with stirring. Carbon disulfide (0.2 mol, 7 mL) was added dropwise, and the reaction mixture was stirred overnight at room temperature. And then, 100 mL diethyl ether was added to cool the reaction with stirred for 10 min. Finally, the solid product was filtered, washed with cold methanol, and dried to give compound S4, Scheme 1 [15]: Color (pale yellow powder), Yield (95%), M.p (225–227 °C), M.wt (340 g/mol), FT-IR (KBr, cm^{-1}): ν(NH) (3275–3223), ν(C=O)amide (1649), ν(C=S) (1262), νC–H arom. (2998), νC–H aliph. (2939).

Synthesis of 4-amino-5-(3,4,5-trimethoxiyphenyl)-4H-1,2,4-triazole-3-thione, L

A compound S4 (4.5 g, 0.0132 mol) in an excess amount of hydrazine hydrate (about 25 mL) was heated under reflux for 6 h. A color change of mixture from black-green into light yellow is to release hydrogen sulfide gas by changing the lead acetate sheet from black to white. The reaction was controlled using thin-layer chromatography (TLC). The cooled mixture was poured into ice water (30 mL) and acidified with conc. hydrochloric acid (pH = 2–3). The precipitate was filtered, washed with cold water, dried and recrystallized from ethanol to give ligand (L1), Scheme 1 [16]: Color (grey powder), Yield (55%), M.p (214–216 °C), M.wt (282 g/mol), R_f = 0.5 (ethyl acetate:chloroform, 1:2). FT-IR (KBr, cm^{-1}): ν(NH_2) asym. and sym.(3300 and 3247), ν(NH) (3189), ν(S–H) (2728), ν(C=S) (1237).^{1}H-NMR (400 MHz, CDCl3, δ ppm): 10.33 (s, weak, SH), 7.46 (s, 2H, aromatic), 4.89 (S, broad, NH_2) 3.9 (s, 6H, 2OCH_3), 3.8 (s, 3H, OCH_3), ^{13}C-NMR (100-MHz, DMSO) 56.60, 56.65, 60.64, 105.77, 125.86, 139,88, 149.63, 153.28, 167.09. MS (*m/z*%): 282 [M^+].

Synthesis of the metal complexes from (C1-C6)

Complexes were synthesized by dissolving 2 mmol (0.564 g) of ligand L1 in 15 mL ethanol absolute and mixing with 15 mL (1 mmol) of the metal ion ($CoCl_2{\cdot}6H_2O$, $CuCl_2{\cdot}2H_2O$, $NiCl_2{\cdot}4H_2O$, $CdCl_2{\cdot}2H_2O$, $H_2PtCl_6 2H_2O$ and $PdCl_2$ in 1:2 as a mol ratio of metal to the ligand following Scheme 1. The mixture was left under reflux for 2–4 h and then allowed the solid complexes to be cooled and added 10 mL of diethyl ether to precipitate. Next, the crystals were filtered and washed with cold water and ethanol. It was followed with drying and then recrystallized with ethanol. Table 1 shows the percentage yield and physical characteristics of the ligand and its complexes.

■ RESULTS AND DISCUSSION

The metal complexes prepared in the recent study were non-hygroscopic (stable at room temperature) and amorphous solids. The solubility of the metal complexes in common organic solvents was investigated. It was discovered that all complexes were sparingly soluble in methanol, ethanol, and chloromethane but were highly soluble in DMSO, DMF, and chloroform. When the results of (CHNS) tests agree with their calculated values, the expected structures and molecular formulas are verified. Except for the cobalt(II) and nickel(II) complexes, the molar conductance data of complexes solutions in DMF revealed electrolytic properties, conductive between 135–168 ohm^{-1} cm^2 mol^{-1} shown in Table 1.

FT-IR Spectral Study

The FT-IR spectrum of ligand L1 showed some characteristic stretching bands at 3301 3253, 2724, 1608, and 1236 $cm^{-1,}$ which are assigned to ν(NH_2), ν(S–H), ν(C=N) of triazole ring and the stretching of C=S bond, respectively. These bands in all-metal complexes C1–C6 demonstrated significant changes in the positions and intensities as the complexation results [17-18] as given in Fig. S1-S2 (see Supplementary Data). Thus, the tautomerism form could occur in the triazole ring, and

Table 1. Physical properties and analytical data of the Schiff base ligand (L1) and its metal complexes

Symbol	Compound	Color	M.wt	Yield %	M.p c°	Micro Elemental Analysis Found (calc.)				Metal content Found (calc.)
						C%	N%	H%	S%	
L.	$C_{11}H_{14}N_4O_3S$	White	282	55	214–216	(46.80)	(19.85)	(5.00)	(11.36)	-
						45.55	19.23	4.56	11.89	
C1	$[CoL)_2Cl_2]$	Brown	694.7	67	225–227	(38.05)	(16.14)	(4.06)	(9.23)	(8.49)
						37.98	16.78	3.84	9.08	7.91
C2	$[Ni(L)_2Cl_2]$	Pale blue	694.2	64	219–221	(38.06)	(16.14)	(4.07)	(9.24)	(8.45)
						37.78	16.33	3.19	9.29	8.11
C3	$[Cu(L)_2]Cl_2$	Dark gray	699.1	72	290–292	(37.80)	(16.03)	(4.04)	(9.17)	(9.09)
						36.89	15.43	4.21	9.65	8.67
C4	$[Pd(L)_2]Cl_2.H_2O$	Dark brown	741.9	69	296 dec	(35.96)	(15.10)	(3.80)	(8.64)	(14.34)
						35.65	15.78	3.36	8.45	14.89
C5	$[Cd(L)_2]Cl_2$	Off white	747.9	71	241-243	(35.33)	(14.98)	(3.77)	(8.57)	(15.03)
						34.92	14.49	3.21	8.04	14.67
C6	$[Pt(L)_2Cl_2]Cl_2.2H_2O$	Pale brown	937.5	59	272 dec	(28.18)	(11.95)	(3.44)	(6.84)	(20.81)
						28.76	11.40	3.76	6.59	21.21

it is responsible for the disappearance of the thiol functional group in the ligand molecule after complexation. After tautomerism forms, the ligand can link with the metal ion either by N or the thioamide group's S. Bonding at S is favorable because it would result in a stable five-membered chelate [19]. The exceptional case is that the ν(C=N) of complexes C1–C6 were found to be shifted to a lower wavelength number compared to the ligand L1, signifying that the coordination took place via the nitrogen atom of the ligand L1 [20]. The frequencies of $ν(NH_2)$ sym. and asymmetric bands were shift due to complexation. The band of ν(S–H) in the ligand was disappeared when complexation occurred, and the bands of ν(C=S) also shifted to the higher or lower frequency due to an increase of the bond order of carbon–sulfate bond result from complexation of the metal ion to the ligand through sulfate. Another new band was appeared, which was supported by the appearance frequencies of (M–S), (M–N), and (M–Cl) [21-22]. The major FT-IR bands and their probable assignment are given in Table 2.

Mass Spectral Studies

The mass spectrum of ligand L1 in Fig. S3 showed several peaks attributed to the presence of 1,2,4-triazole rings. This spectrum showed the mother ion peak at *m/z*: 282 as a base peak for L1 and peaks at *m/z* 249, 235, 165, 193, and 134 for the triazole ring. The most characteristic fragments of this compound were illustrated in Scheme 2.

Table 2. FT-IR data of ligand L1 and their complexes

No	$ν_{as,s}(NH_2)$ $ν_{as,s}(O–H)$	ν(S–H)	ν(C=N)	ν(C=S)	ν(M–N)	ν(M–S)	ν(M–Cl)
L	3301, 3253	2724	1608	1236	-	-	-
C1	3293, 3214	-	1600	1236	486	358	314
C2	3284, 3214	-	1600	1236	485	350	304
C3	3298, 3223	-	1604	1216	484	361	315
C4	3218, 3400	-	1587	1218	460	380	302
C5	3293, 3241	-	1601	1239	485	350	315
C6	3479, 3122	-	1590	1226	482	369	315

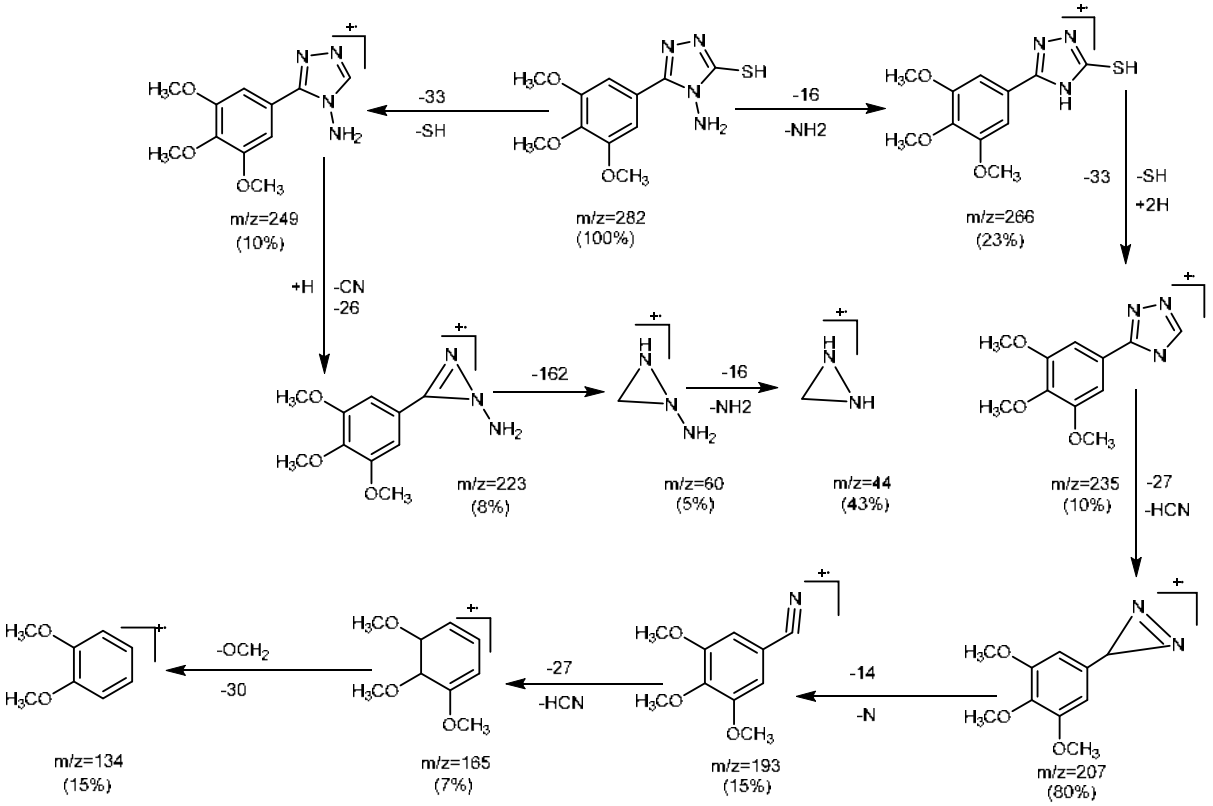

Scheme 2. Proposed Mass fragmentation of L

^{1}H and ^{13}C-NMR Studies

The ^{1}H-NMR spectrum of the free ligand in Fig. S4 showed four singlet signals at δ = 3.8, 3.9, 4.89 and 7.46 ppm corresponding to the protons of $pOCH_3$, $2mOCH_3$, NH_2, and aromatic group, respectively. The singlet peak at δ = 10.35 ppm corresponds to the state of SH–NH tautomeric. In addition, the ^{13}C-NMR spectra in Fig. S5 show eight signals, six in the aromatic region of the spectrum corresponding to the carbon atoms of the trimethoxyphenyl and triazole ring, and two signals for the two different types of $–OCH_3$ groups present in the structure. The high-intensity signal at 56.60 ppm was recorded for the 2C symmetrical $–OCH_3$ group at positions two and six, and the other with low intensity at 60.64 ppm due to the $–O\boldsymbol{C}H_3$ group at position one. While the high-intensity signal at 105.77 ppm due to 2C is symmetrical at position ortho of the trimethoxyphenyl ring. The signal at 125.86 ppm is due to carbon atom attachment in the triazole ring, and the signal at 139.88 ppm is due to $–\boldsymbol{C}OCH_3$ at position one. The signal at 149.63 ppm is due to the N***C***N of the triazole ring. The high-intensity signal at 153.28 ppm is due to 2C symmetrical $–\boldsymbol{C}OCH_3$ groups at positions 2 and 6 of the trimethoxyphenyl ring. Moreover, a signal at 167.09 ppm is from the ***C***S of the thione group.

Electronic Spectra and Magnetic Properties

The UV-Visible absorption spectrum of ligand L in an ethanol solution is presented in Fig. 1 and summarized in Table 3. It can be observed that two bands at 216 nm and 259 nm were allocated to π-π* transition and a band 305 nm is assigned to n-π* transition [23].

The electronic spectrum of C1 complex in DMSO solvent shown in Fig. 2, reveals two spin-allowed bands in the visible region at 656 nm and 557 nm, which might be related to the transition of $^{4}T_1g \rightarrow {}^{4}A_2g$ (F) (ν2) and $^{4}T_1g \rightarrow {}^{4}T_1g$ (P) (ν3) respectively. The bands' positions agree with the reported values for an octahedral geometry. Refer to the Tanabe-Sugano diagram, the numerous parameters of ligand field, namely ν_1, B', β, and 10Dq have

Table 3. Conductivity, magnetic and electronic spectra of metal complexes C1–C6

No	λ_{max} nm (υ cm^{-1})	Assignment	ohm^{-1} cm^2 mol^{-1}	μ BM found (calc)	Suggested Structure
L	305 (32786)	$n \rightarrow \pi^*$	-	-	-
	259 (38610)	$\pi \rightarrow \pi^*$			
	216 (46296)	$\pi \rightarrow \pi^*$			
C1	1243 (8042)	$^4T_1g \rightarrow {}^4T_2g$ (F)	13.4	4.21	Octahedral
	656 (15243)	$^4T_1g \rightarrow {}^4A_2g$ (F)		(3.87)	
	557 (17953)	$^4T_1g \rightarrow {}^4T_1g$ (P)			
C2	863 (11583)	$^3A_2g \rightarrow {}^3T_2g$ (F)	15.6	3.11	Octahedral
	508 (19685)	$^3A_2g \rightarrow {}^3T_1g$ (F)		(2.82)	
	414 (24154)	$^3A_2g \rightarrow {}^3T_1g$ (P)			
C3	507 (19723)	$^2B_1g \rightarrow {}^2B_2g + {}^2Eg$	169.4	1.85	Square planer
	419 (23866)	$^2B_1g \rightarrow {}^2A_1g$		(1.73)	
C4	495 (20202)	$^1A_1g \rightarrow {}^1Eg$	171.3	Dia	Square planer
	475 (20876)	$^1A_1g \rightarrow {}^1T_1g$ (G)			
C5	325 (30796)	MLCT	163.7	Dia	Tetrahedral
	257 (38910)	$n \rightarrow \pi^*$			
	25 1(39840)	$\pi \rightarrow \pi^*$			
C6	550 (18181)	$^1A_1g \rightarrow {}^3T_1g$	172.3	1.18	Octahedral
	519 (19267)	$^1A_1g \rightarrow {}^3T_2g$			
	361 (27700)	LMCT			

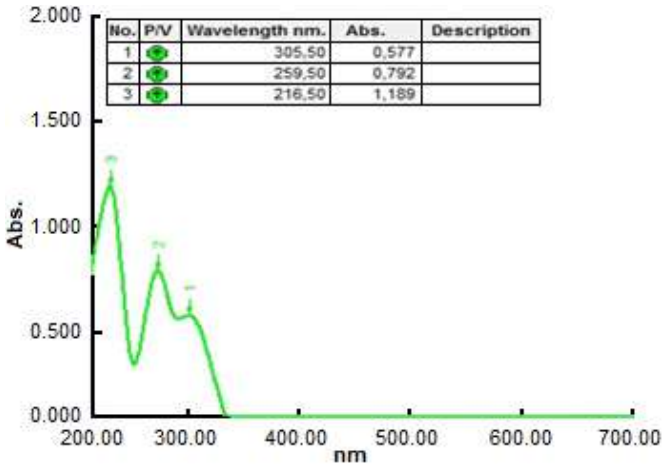

Fig 1. The UV-Vis spectrum of ligand (L)

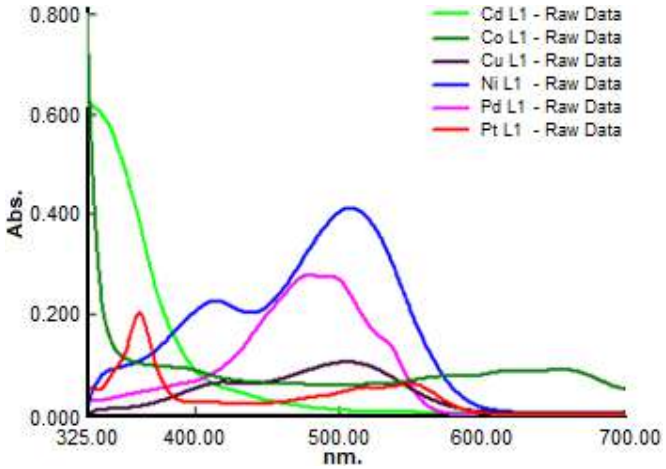

Fig 2. The UV-Vis spectrum of metal complexes

been calculated for (d^7) configuration, to be 1243 nm, 608 cm^{-1}, 0.66, and 10052 cm^{-1}, respectively. The factor of the nephelauxetic (β) was calculated and found to be 0.66. Representative bonding was a high degree of ionic from atoms in ligand donor with cobalt(II) ion, hence inter electronic repulsion has been decreased during the process of complexation, as well as the calculated value of ν1 to be 8042 cm^{-1} due to the transition $^4T_1g \rightarrow {}^4T_2g$ (F). The transition ratio ν2/ν1 gave a value of 1.89 provided further indications for octahedral geometry for the Co(II) complex. The magnetic susceptibility of 4.21 BM indicates that the cobalt(II) complex is paramagnetic. The molar conductivity of 13.42 means that the complex is nonconductive, as shown in Table 3. In addition to this data, the results of elemental (CHNS) analysis, flame atomic absorption, and FT-IR spectrum united in

opinion with this condition and can be suggested octahedral structure for the CoL1 complex, as expressed in Fig. 4(a) [24].

The electronic spectrum of the C2 complex in DMSO solution shows two spin-allowed bands 508 nm and 414 nm allocated to $^3A_2g \rightarrow {}^3T_1g$ (F) (ν2) and $^3A_2g \rightarrow {}^3T_1g$ (P) (ν3) transitions, respectively. These bands indicate an octahedral geometry around Ni(II) ion. At the same time, the value of the third transition (ν1) was calculated by fitting the ratio ν3/ν2 for the octahedral d^8 system of Tanabe-Sugano diagram. The calculated value of ν1 was 863 nm due to the transition $^3A_2g \rightarrow {}^3T_2g$ (F). As well as the ligand field parameters (B', β, and 10Dq) have been calculated using the Tanabe-Sugano diagram for the d^8 system and found to be 726 cm^{-1}, 0.673, and 15254 cm^{-1}, respectively. The constant field splitting (10Dq) value will be 11583 cm^{-1}, approximately close to the first transition (ν1). The (ν2/ν1) ratio is 1.96, indicating octahedral geometry less than tetrahedral stereochemistry of Ni(II). The magnetic value for Ni(II) in Table 3 gave a magnetic moment value of 3.11 BM, and it is about the range of 2.8–3.5 BM with octahedral geometry for Ni(II) ion. The conductivity refers to the non-ionic performance of this complex. Thus from the data above and those obtained from FT-IR spectra and flame atomic absorption, an octahedral geometry around Ni(II) ion can be suggested as given in Fig. 4(a) [25-26].

The d^9 ion is characterized by a large distortion from the octahedral symmetry, and the band is asymmetrical. Several transformations have occurred, and these transitions have emerged, which cannot be easily set without ambiguity. The free ion ^2D term is expected to split in a crystal field in the same way as the ^5D term of the d^4 ion, and a similar interpretation of the spectra is likewise expected. The spectrum of copper(II) complex in DMSO solution shows one broadband at 507 nm which agrees to $^2B_1g \rightarrow {}^2B_2g + {}^2Eg$ (ν2 + ν3) transition, and shoulder band at 419 nm allocated to $^2B_1g \rightarrow {}^2A_1g$ (ν1) transitions. The position of these bands is to approve with configuration highly distorted octahedral geometry. The magnetic moment value was 1.85 BM at room temperature, approved with square planar geometry for the Cu(II) complex. The conductivity in DMF showed that the complex has electrolytic nature. From the electronic spectra data, FT-IR spectroscopy data and flame atomic absorption can be suggested as a square planar geometry around the Cu(II) ion, as can be seen in Fig.(4(b) [27].

The Pd(II) ion has a (d^8) configuration that favors square planar geometry formation. The electronic spectrum of C4 complex in (DMSO) displays two spin-allowed at 495 nm and 475 nm and are assigned to $1A_{1g} \rightarrow 1B_{1g}$ and $1A_1g \rightarrow 1Eg$ transitions in a square planar geometry, respectively. The magnetic moment of the solid complex showed diamagnetic behavior (Table 3) approved with square-planar geometry of Pd(II) ion. The conductivity measurement in DMF showed that the complex has a higher conducting property (Table (3)), and therefore the two Cl^- ions are located outside the coordination. From these results and that of the elemental analysis, FT-IR, and flame atomic absorption studies, it can be suggested as square planar geometry around the Pd(II) ion as shown in Fig. 4(b) [28].

The electronic spectrum of the C6 complex showed bands at 550 nm, 519 nm, and 361 nm assigned to $^1A_1g \rightarrow {}^3T_1g$, $^1A_1g \rightarrow {}^3T_2g$, and (LMCT), respectively. The complex may have octahedral coordination of the central metal ion by the surrounding ligands. The magnetic moment value of solid complex (1.18 BM) for Pt(IV) is observed. It agrees with the octahedral geometry. The increase in the magnetic moment is expected due to the presence of the contribution of spin-orbital coupling. The conductance measurements indicate the ionic behavior of this complex according to these results and that of the elemental analysis, FT-IR, and flame atomic absorption studies. Therefore, Pt(IV) ion has an octahedral geometry, as shown in Fig. 4(a) [29].

The electronic spectrum of the C5 complex has no (d-d) transition and belongs to d^{10}. The prepared complexes are off-white in color, with the diamagnetic being expected. Therefore, the UV-Vis spectrum of this complex shows a relative change in the bands' position compared to that of the free ligand (L). The UV-Vis spectrum of C5 in DMSO displayed three bands at 325, 257, and 251 nm, respectively, assigned to (MLCT), ($n \rightarrow \pi^*$) and ($\pi \rightarrow \pi^*$) transition, respectively. The

conductivity measurements indicate the ionic conducting behavior of the complex. According to these results, in addition to the results of elemental analysis, we can suggest a tetrahedral geometry around Cd(II) ion as illustrated in Fig. 4(c) [30].

Thermal Analyses (TGA-DSC)

The thermogravimetric curve of ligand L is shown in Fig. 3(a) at the temperature range of 10–696 °C to reveal two decomposition steps. The TGA peak observed at temperature range of 100–355 °C indicated the loss of $2OCH_3$, NH_2 fragment (det. = 2.846 mg, 27.77%, calc.= 27.65%). The second step recorded at temperature range of 355–696 °C (det. = 3.246 mg, 31.68%, calc. = 32.62%) indicated the loss of C_7H_8. The final residue of the complex recorded above 696 °C attributed to C_2S, N_3O, (det. = 4.001 mg, 39.04%, calc. = 40.42%). The DSC curve indicates exothermic decomposition processes at 246.5 °C (56.3 mW) and 500.4 °C (86.2 mW). The TGA curves of complex PdL1 displayed thermal decomposition with loss weight percent (det. = 1.165 mg, 11.3%, calc. = 11.9%) in the temperature range 25–100 °C indicating the cleavage of chloride ions present in the outside of the coordination sphere and one molecule of water in Pd(II) complex. As well as the degradation of the organic molecule started before the temperature of 200 °C. The second step of TGA curve exhibited (det. = 2.407 mg, 23.0%, calc.= 22.64%) due to decomposition of $C_6H_3{\cdot}3OCH_3$ at 100–345 °C, and the third step is assigned to the loss of PdO, $C_{13}H_{16}N_8O_2S$ at 345–699 °C (det. = 6.46 mg, 61.77%, calc. = 61.19%) (Fig. 3(b)). The final residue of the complex recorded above 699 °C attributed to CS (det. = 0.428 mg, 4.08%, calc. = 5.01%). The DSC curve indicated exothermic decomposition processes at 115.7 °C (43.2 mW) and 490.3 °C (95.9)

Biological Activity

The antibacterial potency of ligand L1 and their Ni(II), Cu(II), Co(II), Pd(II), Cd(II), and Pt(IV) metal complexes was evaluated in vitro against bacteria *Staphylococcus aureus* (G-positive) and *Escherichia coli* (G-negative). At a 50 µg/mL concentration, a freshly prepared liquid agar medium (20 mL/Petri dish) was poured into each Petri dish, and the plates were dried by placing in an incubator at 37 °C for 1 h. Then standardized culture of microorganisms was spread on each Petri dish by an L-shaped spreader. Wells (6 mm) were made using an agar punch and, each well was labeled accordingly. A control solvent DMSO was also included in the test. The test compound and standard drug solutions (Erythromycin, 50 µg/mL) were made in DMSO and added to each well separately, and the Petri dish was kept aseptically for 1-h diffusion of the sample. After the diffusion was complete, all the Petri dishes were kept for incubation at 37 °C for 24 h. Then the diameter of the zone of inhibition was measured in (mm). The tested ligand (L) and metal ion complexes have shown less activity than a standard Erythromycin. Metal ion complexes have been exhibited much better activity than the free ligand, L. The inhibition zone data for the entire complexes at 50 µg/mL as compared to free ligand (L1) should be discussed among the platinum(IV) complex,

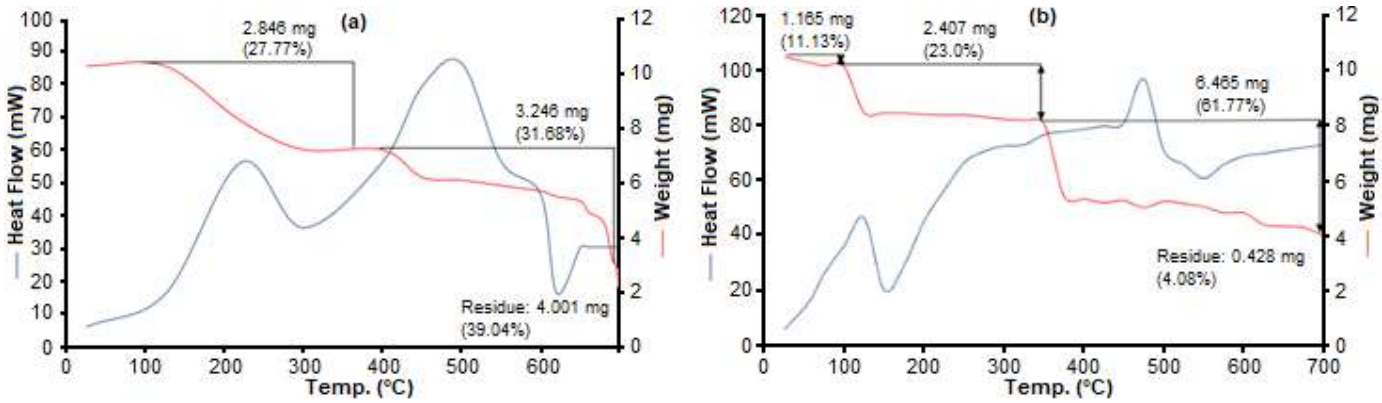

Fig 3. TG-DSC thermogram of (a) L and (b) PdL

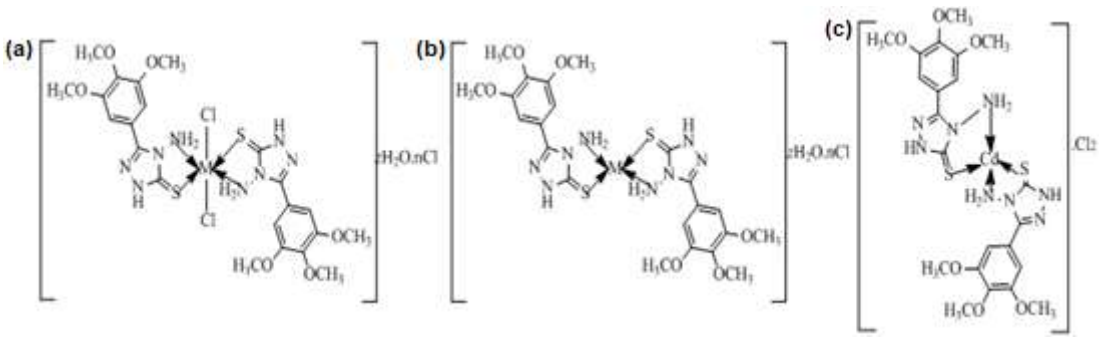

Fig 4. (a) Octahedral for Co^{2+}, Ni^{2+} and Pt^{+4} complexes, (b) square planar for Cu^{2+} and Pd^{+2} complex, and (c) tetrahedral for Cd^{2+} complex

Table 4. The inhibition zones (mm) of (L) and their metal complexes against *S. aureus* and *E. coli*

No	Compound	(G+) *S. aureus*	(G-) *E. coli*
1	$C_{11}H_{14}N_4O_3S$	7	8
2	$[Co(L)_2Cl_2]$	19	16
3	$[Ni(L)_2Cl_2]$	9	13
4	$[Cu(L)_2]Cl_2$	9	10
5	$[Pd(L)_2]Cl_2{\cdot}H_2O$	23	25
6	$[Cd(L)_2]Cl_2$	21	24
7	$[Pt(L)_2Cl_2]Cl_2{\cdot}2H_2O$	28	29
8	DMSO	0	0
9	Erythromycin	35	35

which has the highest inhibitory effect against the bacteria. The antibacterial activity of the free ligand and its complexes showed the order: PtL1 > PdL1 > CdL1 > CoL1 > NiL1 > CuL1 > L1 and PtL1 was found to have the best effect [31]. In general, the metal complexes show antibacterial activity, and the following five principal factors should be considered. The ligands' chelate effect that is bound to metal ions in a bidentate fashion through NS and NO moiety of the ligands show higher antimicrobial efficiency than the complexes uni dentate, respectively, like pyridine. However, the total charge of the complexes in general, the antimicrobial activity decreases with the order of cationic > neutral > anionic complex. Table 4 represents the inhibition zones (mm) for the L1 and its complexes against the bacteria in DMSO solvent as control. The free ligand exhibited low activity against all bacteria at around 7–8 mm, and the PtL1, PdL1, and CdL1 showed the greatest activity against *Staphylococcus aureus* and *Escherichia coli* at 28-29, 23–25, and 21–24 mm, respectively.

■ CONCLUSION

In this research work, new transition metal complexes of cobalt(II), nickel(II), copper(II), palladium(II), cadmium(II) and platinum(IV) with bidentate ligand of 4-amino-5-(3,4,5-trimethoxyphenyl) -4I-1,2,4-triazole-3-thiol were synthesized and characterized. The results obtained from spectra and elemental analyses indicated the tetrahedral geometry around Cd(II) ion, square-planner for Cu and Pd(II), and octahedral geometry around Co(II), Ni(II), and Pt(IV). The Inhibition zones of ligand (L) and their metal complexes with concentrations (50 µg/mL) against *Staphylococcus aureus* and *Escherichia coli* showed the order of PtL > PdL > CdL > CoL > NiL > CuL > L. Thus, further study on this approach could pave the way for developing 1,2,4-triazole-metal complex-based antibacterial agents.

■ ACKNOWLEDGMENTS

The authors are so thankful to the pharmacy faculty members, Babylon University for facilitating the measurements of IR and UV spectra. We are so grateful to Mustansiriyah University, College of Science, Chemistry Department for supporting the work by providing chemicals and measuring the complexes' molar conductance and magnetic susceptibility.

■ REFERENCES

[1] Sugiyarto, K.H., Louise, I.S.Y., and Wilujeng, S.S., 2020, Preparation and powder XRD analysis of tris(2,2'-bipyridine)nickel(II) trifluoroacetate, *Indones. J. Chem.*, 20 (4), 833–841.

[2] Timur, İ., Kocyigit, Ü.M., Dastan, T., Sandal, S., Ceribası, A.O., Taslimi P., Gulcin, İ., Koparir, M., Karatepe, M., and Çiftçi, M., 2019, In vitro cytotoxic and in vivo antitumoral activities of some aminomethyl derivatives of 2,4-dihydro-3H-1,2,4-triazole-3-thiones–Evaluation of their acetylcholines terase and carbonic anhydrase enzymes inhibition profiles, *J. Biochem. Mol. Toxicol.*, 33 (1), e22239.

[3] Kaproń, B., Łuszczki, J.J., Płazińska, A., Siwek, A., Karcz, T., Gryboś, A., Nowak, G., Makuch-Kocka, A., Walczak, K., Langner, E., Szalast, K., Marciniak, S., Paczkowska, M., Cielecka-Piontek, J., Ciesla, L.M., and Plech, T., 2019, Development of the 1,2,4-triazole-based anticonvulsant drug candidates acting on the voltage-gated sodium channels. Insights from in-vivo, in-vitro, and in-silico studies, *Eur. J. Pharm. Sci.*, 129, 42–57.

[4] Sugiyarto, K.H., Yunita, I., and Goodwin, H.A., 2020, Preparation, electronic properties, and powder-XRD structure analysis of 3,5-Bis(pyridin-2-yl)-H-1,2,4-triazoledichloridocopper(II), *Indones. J. Chem.*, 20 (6), 1422–1429.

[5] Obaid, S.M.H., Sultan, J.S., and Al-Hamdani, A.A.S., 2020, Synthesis, characterization and biological efficacies from some new dinuclear metal complexes for base 3-(3,4-dihydroxy-phenyl)-2-[(2-hydroxy-3-methylperoxybenzylidene)-amino]-2-methyl propio nic acid, *Indones. J. Chem.*, 20 (6), 1311–1322.

[6] Rasyda, Y.A., Widowati, M.K., Marliyana, S.D., and Rahardjo, S.B., 2021, Synthesis, characterization and antibacterial properties of nickel(II) complex with 4-aminoantipyrine ligand, *Indones. J. Chem.*, 21 (2), 391–399.

[7] Idrees, M., Nasare, R.D., and Siddiqui, N.J., 2016, Synthesis of S-phenacylated trisubstituted 1,2,4-triazole incorporated with 5-(benzofuran-2-yl)-1-phenyl-1H-pyrazol-3-yl moiety and their antibacterial screening, *Chem. Sin.*, 7 (4), 28–35.

[8] Özadalı, K., Özkanlı, F., Jain, S., Rao, P.P.N., and Velázquez-Martínez, C.A., 2012, Synthesis and biological evaluation of isoxazolo[4,5-*d*]pyridazin-4-(5*H*)-one analogues as potent anti-inflammatory agents, *Bioorg. Med. Chem.*, 20 (9), 2912–2922.

[9] Kanagarajan, V., Thanusu, J., and Gopalakrishnan, M., 2011, Synthesis and in vitro microbiological evaluation of novel 2,4-diaryl-3-azabicyclo[3.3.1] nonan-9,5′-spiro-1′,2′,4′-triazolidine-3′-thiones, *Med. Chem. Res.*, 21 (12), 3965–3972.

[10] Dallavalle, F., Gaccioli, F., Franchi-Gazzola, R., Lanfranchi, M., Marchiò, L., Pellinghelli, M.A., and Tegoni, M., 2002, Synthesis, molecular structure, solution equilibrium, and antiproliferative activity of thioxotriazoline and thioxotriazole complexes of copper(II) and palladium(II), *J. Inorg. Biochem.*, 92 (2), 95–104.

[11] Al-Masoudi, N.A., Abdullah, B.H., Essa, A.H., Loddo, R., and LaColla, P., 2010, Platinum and palladium-triazole complexes as highly potential antitumor agents, *Arch. Pharm.*, 343 (4), 222–227.

[12] Kapri, K.P., Singar, S.B., Khanal, S., and Shakya, B., 2020, Synthesis of Schiff bases of 4-amino-5-(2-hydroxyphenyl)-4H-1,2,4-triazole-3-thiol as potent antimicrobial agents, *Amrit Res. J.*, 1 (1), 29–36.

[13] Devkota, K., Pathak, G., and Shakya, B., 2020, Synthesis and evaluation of Schiff bases of 4-amino-5-(chlorine substituted phenyl)-4H-1,2,4-triazole-3-thione as antimicrobial agents, *J. Nepal Chem. Soc.*, 41 (1), 26–35.

[14] Namratha, B., and Gaonkar, S.L., 2014, 1,2,4-Triazoles: Synthetic strategies and pharmacological profiles, *Int. J. Pharm. Pharm. Sci.*, 6 (8), 73–80.

[15] Bharty, M.K., Bharti, A., Chaurasia, R., Chaudhari, U.K., Kushawaha, S.K., Sonkar, P.K., and Butcher, R.J., 2019, Synthesis and characterization of Mn(II) complexes of 4-phenyl(phenyl-acetyl)-3-thiosemicarbazide, 4-amino-5-phenyl-1,2,4-triazole-3-thiolate, and their application towards electrochemical oxygen reduction reaction, *Polyhedron*, 173, 114125.

[16] Murti, Y., Agnihotri, R., and Pathak, D., 2011, Synthesis, characterization and pharmacological screening of some substituted 1,2,3- & 1,2,4-triazoles, *Am. J. Chem.*, 1 (2), 42–46.

[17] Majeed A.S., 2010, Synthesis, structure and

antibacterial activity of some 2-amino-5-(2-acetyloxyphenyl)-1,3,4-thiadiazole complexes, *Al Mustansiriya J. Sci.*, 21 (5), 195–204.

[18] Yousif, E., Hameed, A., and Ameer, A., 2005, Synthesis and characterization of complexes of some transition metals with 2-amino-5-(4-hexyloxyphenyl) -1,3,4-thiadiazole, *J. Al-Nahrain Univ.*, 8 (1), 9–11.

[19] Narayana, B, and Gajendragad, M., 1997, Complexes of Zn(II), Pd(II), Hg(II), Pb(II), Cu(I),Ag(I), and Ti(I) with 4-amino-5-merccapto-3-(o-tolyloxymethyl)-1,2,4-troazol, *Turk. J. Chem.*, 21 (1), 71–76.

[20] Sliverstein, R., Webster, F.X., and Kiemle, D.J., 2005, *Spectrometric Identification of Organic Compounds*, 7th Ed., John Wiley & Sons, Hoboken, New York.

[21] Flifel, I., and Kadhim, S., 2012, Synthesis and characterization of 1,3,4-oxadiazole derivatives with some new transition metal complexes, *J. Kerbala Univ.*, 10 (3), 197–209.

[22] Abd El-Razek, S.E., El-Gamasy, S.M., Hassan, M., Abdel-Aziz, M.S., and Nasr, S.M., 2020, Transition metal complexes of a multidentate Schiff base ligand containing guanidine moiety: Synthesis, characterization, anticancer effect, and antimicrobial activity, *J. Mol. Struct.*, 1203, 127381.

[23] Anacona, J.R., Ruiz, K., Loroño, M., and Celis, F., 2019, Antibacterial activity of transition metal complexes containing a tridentate NNO phenoxymethylpenicillin-based Schiff base. An anti-MRSA iron(II) complex, *Appl. Organomet. Chem.*, 33 (4), e4744.

[24] Rapheal, P.F., Manoj, E., Kurup, M.R.P., and Fun, HK, 2021, Nickel(II) complexes of N(4)-substituted thiosemicarbazones derived from pyridine-2-carbaldehyde: Crystal structures, spectral aspects and Hirshfeld surface analysis, *J. Mol. Struct.*, 1237, 130362.

[25] Hamil, A., Khalifa, K.M., Almutaleb, A.A., and Nouradean, M.Q., 2020, Synthesis, characterization and antibacterial activity studies of some transition metal chelates of Mn(II), Ni(II) and Cu(II) with Schiff base derived from diacetylmonoxime with O-phenylenediamine, *Adv. J. Chem. A*, 3 (4), 524–533.

[26] Kargar, H., Torabi, V., Akbari, A., Behjatmanesh-Ardakani, R., Sahraei, A., and Tahir, M.N., 2020, Pd(II) and Ni(II) complexes containing an asymmetric Schiff base ligand: Synthesis, X-ray crystal structure, spectroscopic investigations and computational studies, *J. Mol. Struct.*, 1205, 127642.

[27] Adachi, J., Mori, T., Inoue, R., Naito, M., Le, N.H.T., Kawamorita, S., and Ariga, K., 2020, Emission control by molecular manipulation of double-paddled binuclear Pt^{II} complexes at the air-water interface, *Chem. Asian J.*, 15 (3), 406–414.

[28] Yang, Y.J., Li, Y.H., Liu, D., and Cui, G.H., 2020, A dual-responsive luminescent sensor based on a water-stable Cd(II)-MOF for the highly selective and sensitive detection of acetylacetone and $Cr_2O_7^{2-}$ in aqueous solutions, *CrystEngComm*, 22 (7), 1166–1175.

[29] Tenorio, K.V., Fortunato, A.B., Moreira, J.M., Roman, D., D'Oliveira, K.A., Cuin, A., Brasil, D.M., Pinto, L.M.C., Colman, T.A.D., and Carvalho, C.T., 2020, Thermal analysis combined with X-ray diffraction/Rietveld method, FT-IR and UV-vis spectroscopy: Structural characterization of the lanthanum and cerium(III) polycrystalline complexes, *Thermochim. Acta*, 178662.

[30] Djunaidi, M.C., Setiyo, P.D., Lusiana, R.A., and Anggun Y., 2020, In-situ ionic imprinted membrane (IIM) synthesis based on acetic polyeugenoxy acetyl tiophen methanolate for gold(III) metal ion transports, *Indones. J. Chem.*, 20 (6), 1323–1331.

[31] Bisceglie, F., Bacci, C., Vismarra, A., Barilli, E., Pioli, M., Orsoni, N., and Pelosi, G., 2020, Antibacterial activity of metal complexes based on cinnamaldehyde thiosemicarbazone analogues, *J. Inorg. Biochem.*, 203, 110888.

Supplementary Data

This supplementary data is a part of a paper entitled "An Electrochemical Aptasensor for the Detection of HER2 as a Breast Cancer Biomarker Based on Gold Nanoparticles-Aptamer Bioconjugates".

Table S1. Box-Behnken design experiment

Exp.	X_1	X_2	X_3	SD/ µA
1	25	90	25	37.535
2	25	30	5	43.970
3	10	60	5	125.568
4	40	60	5	72.925
5	40	30	15	52.675
6	25	60	15	74.660
7	25	60	15	49.775
8	10	60	25	40.115
9	25	90	5	121.240
10	40	90	15	127.172
11	25	30	25	25.290
12	10	90	15	51.715
13	40	60	25	67.205
14	25	60	15	79.200
15	10	30	15	44.870

X_1: MPA incubation time, X_2: bioconjugates incubation time, X_3: aptamer concentration

Using Minitab 18:

$$Y = 95.2 - 6.06\ X_1 + 1.80\ X_2 - 1.96\ X_3 + 0.0459\ X_1^2 - 0.0101\ X_2^2 - 0.018\ X_3^2 + 0.0376\ X_1X_2 + 0.1329\ X_1X_3 - 0.0542\ X_2X_3$$

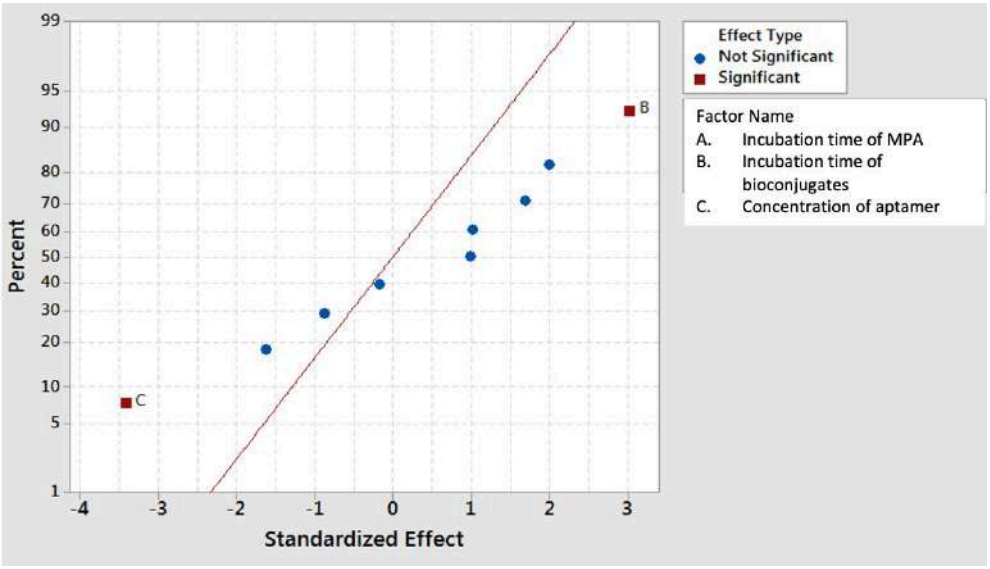

Fig S1. Normal plot (α = 0.05)

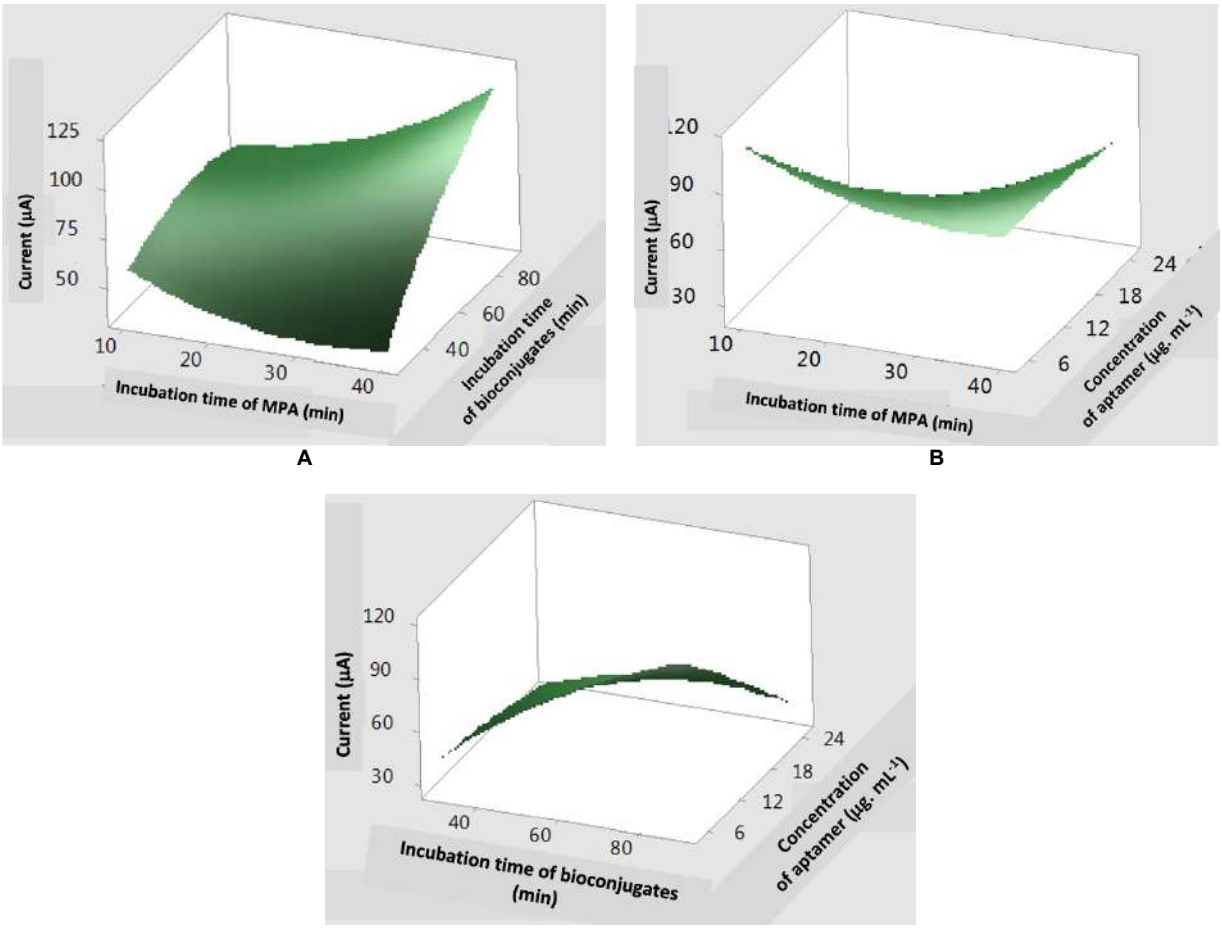

Fig S2. Surface plot 3D

An Electrochemical Aptasensor for the Detection of HER2 as a Breast Cancer Biomarker Based on Gold Nanoparticles-Aptamer Bioconjugates

Yeni Wahyuni Hartati[1,2*], Sari Syahruni[1], Shabarni Gaffar[1,2], Santhy Wyantuti[1], Muhammad Yusuf[1,2], and Toto Subroto[1,2]

[1]*Department of Chemistry, Faculty of Mathematics and Natural Sciences, Universitas Padjadjaran, Jl. Raya Bandung-Sumedang Km. 21, Jatinangor, Sumedang 45363, Indonesia*

[2]*Research Center of Molecular Biotechnology and Bioinformatics, Universitas Padjadjaran, Jl. Singaperbangsa No. 2, Bandung 40132, Indonesia*

* ***Corresponding author:***

email: yeni.w.hartati@unpad.ac.id

Received: June 28, 2021
Accepted: September 5, 2021

DOI: 10.22146/ijc.67124

Abstract: *Inaccurate diagnoses contributes to the high mortality rate of breast cancer. Human epidermal growth factor receptor 2 (HER2) is overexpressed in breast cancer tumors at around 20–30%. This study aims to develop an electrochemical biosensor for HER2 based on a gold nanoparticle-aptamer bioconjugate (AuNP@HER2 aptamer) and investigate the interaction between DNA aptamer and HER2 using computational methods. The bioconjugate was synthesized using maleimide and polyethylene glycol as a linker. The $-NH_2$ group of cysteamine that modified the gold electrode can form a covalent bond with the bioconjugate maleimide. The interaction of the bioconjugated aptamer with HER2 was measured electrochemically based on the $[Fe(CN)_6]^{3-/4-}$ redox system. The limit of detection, the linear range of HER2, precision, and accuracy in this study were 1.52 ng mL^{-1}, 0.01 to 15.0 ng mL^{-1}, 0.1298, and 94.06%, respectively. The structure of the DNA aptamer was modeled using mFold, Assemble2, and Chimera, with the interaction between the DNA aptamer and HER2 explored by NPDock. The modeling of the aptamer with HER2 showed that electrostatic interactions dominated the attractive forces. The resulting interaction pattern can be used as a template to improve the binding energy of the aptamer, thus providing insight into the development of aptamer-based biosensors.*

Keywords: *electrochemical aptasensor; HER2; aptamer; voltammetry; molecular modeling; breast cancer*

■ INTRODUCTION

Breast cancer has a high mortality rate, accounting for approximately 15% of cancer deaths among women [1]. Moreover, almost 70% of the cases were detected late. Hence treatment outcomes are poor. Earlier diagnosis would improve the chance of successful therapy by 80–90% [2]. Therefore, efforts are ongoing to develop early detection methods for breast cancer.

Human epidermal growth factor receptor 2 (HER2) protein is a breast cancer biomarker in the form of three domains; a transmembrane region, an intracellular tyrosine kinase domain, and an extracellular domain that can be released into the bloodstream [3-5]. The HER2 protein concentration in serum is less than 15 ng mL^{-1} (4–14 ng mL^{-1}) in healthy women and overexpressed in active surveillance of patients at risk or in treatment at about > 15 ng mL^{-1} [6-7].

The determination of HER2 protein based on electrochemical techniques has been widely developed and reported in the last decade. Electrochemical methods are preferable because of their rapid detection, high sensitivity, and selectivity, as well as the low limit of detection [8-11]. The use of aptamer as the biorecognition molecule that can specifically recognize the protein target in the sample has attracted much attention because of its stability, synthetic portability, and various functional design [12-14]. The methods for obtaining an aptamer such as the systematic evolution of

ligands by enrichment exponential (SELEX) [15-16], kinetics capillary electrophoresis as the equilibrium and nonequilibrium capillary electrophoresis of equilibrium mixtures (ECEEM and NECEEM) [17-19], and rational design in-silico [20-21] have been developed and applied in electrochemical aptasensors.

Modification of electrodes with aptamers is a crucial process in electrochemical aptasensor research. Various electrodes have been modified using various materials to obtain high sensitivity of the aptasensors in order to detect HER2 as a breast cancer biomarker [22]. A homemade screen-printed electrode modified with poly-L-lysine has been used for immobilizing HER2 aptamer by electrostatic adsorption. The biosensor exhibited an excellent interaction between the aptamer and the target protein [3]. HER2 aptamer was immobilized by a self-assembled monolayer (SAM) on the surface of the gold electrode (GE), which was pretreated with 3-mercaptopropionic acid (MPA), and the sensor was able to detect HER2 concentrations ranging from 10^{-5}–10^{2} ng mL^{-1} by using electrochemical impedance spectroscopy technique [19]. The sensing platforms were also developed on gold screen-printed electrodes via SAM between the thiolated DNA aptamer of HER2 and 1-mercapto-hexanol, and also a ternary SAM between the same aptamer and 1,6-hexanediol [23]. A new bimetallic ZrHf metal-organic framework (ZrHf-MOF) embedded with abundant carbon dots (CDs) (denoted as CDs@ZrHf-MOF) could be applied as the scaffold for anchoring aptamer strands to determine HER2 and living HER2-overexpressed MCF-7 cells [24].

A labeled electrochemical aptasensor using exonuclease recycling amplification and host-guest recognition system was reported to detect HER2. The HER2 aptamer was firstly hybridized with ferrocene-labeled DNA/Au nanospheres (FcNS) and then bound with the HER2 target. The released FcNS homogeneously hybridized with horseradish peroxidase-labeled DNA/Au nanospheres [25]. A label-free capacitive aptasensor was developed to capture HER2 protein by anti-HER2 ssDNA aptamers functionalized on interdigitated microelectrodes of a capacitor. The aptasensor response was measured by the non-Faradaic impedance spectroscopy (nFIS) method based on changes that occurred due to charge distribution upon the interaction of aptamer–protein molecules against the applied AC frequency (50–350 MHz) [26].

A sandwich-type electrochemical aptasensor to detect HER2 was constructed using a combination of tetrahedral DNA nanostructures (TDNs) - adapter as recognition probes and Mn_3O_4/Pd@Pt nanozymes/ horseradish peroxidase (HRP) as signal nanoprobes on the GE. The designed Mn_3O_4/Pd@Pt/HRP nanoprobe was used to amplify the biosensor signal via catalyzing the oxidation of hydroquinone (HQ) with hydrogen peroxide (H_2O_2) [27]. The biotinylated specific aptamers to HER2 positive receptor were immobilized at the neutravidin layer chemisorbed at the gold surface of the thickness-shear mode acoustics method (TSM) transducer. The LOD of the proposed aptasensor reached 550 cells mL^{-1} [28].

A bioconjugate-based aptamer for detecting HER2 was reported using gold nanorod@Pd superstructures-aptamer HER2-horseradish peroxidase (GNR@Pd SSs-Apt-HRP) as a signal probe to enable signal amplification. The aptasensor was constructed by immobilizing DNA tetrahedron with expanded aptamer on the GE [29]. Nanomaterial-based bioconjugate can provide benefits such as improving the ability of sensing by increasing sensitivity, lowering LOD, and being fast and simple. Furthermore, polyethylene glycol (PEG) can increase the solubility of reagents and bioconjugates [30-33].

The current study aims to develop an aptasensor based on a gold nanoparticle (AuNP@HER2 aptamer) bioconjugate using the PEG as a linker via maleimide binding. The response of HER2 was measured using differential pulse voltammetry techniques from the $[[Fe(CN)_6]^{4-/3-}$ redox system. Furthermore, the molecular interaction between the aptamer and HER2 was investigated using a molecular docking method, providing valuable insight into developing aptamer-based biosensors for cancer diagnosis.

■ EXPERIMENTAL SECTION

Materials

HER2 antigen, 1-ethyl-3-(3-dimethyl aminopropyl) carbodiimide (EDC), 3-aminopropyltrimethoxysilane (APTMS), 3-mercaptopropionic acid (MPA), poly(ethylene glycol)-α-maleimide-ω-NHS ester (PEG-NHS-Mal), cysteamine, N-hydroxy succinimide (NHS), 2-iminothiolane (Traut's reagent), potassium ferricyanide ($K_3[Fe(CN)_6]$), bovine serum albumin (BSA), ethanol (C_2H_6O), sodium borohydride ($NaBH_4$), citric acid ($NaC_6H_7O_7$), and sodium ethylenediaminetetraacetate (Na_2EDTA) were purchased from Sigma-Aldrich. A 99% gold bar was obtained from PT, Antam, Indonesia. The thiol-terminated ssDNA aptamer (5'–/HSC6/CTT CTG CCC GCC TCC TTC CTG GGG CCT GGA TAC GGA TTG GTA AGG ATT AGT AGG GGG CAT AGC TGG AGA CGA GAT AGG CGG ACA CT–3') was synthesized by Integrated DNA Technologies (USA). Phosphate-buffered saline (PBS) solutions were prepared by dissolving hydrogen phosphate ($Na_2HPO_4{\cdot}12H_2O$), sodium hydroxide (NaOH), sodium chloride (NaCl), and potassium chloride (KCl) (Merck).

Instrumentation

Electrochemical measurements were performed by differential pulse voltammetry (DPV) using a Metrohm μAutolab potentiostat. All experiments were conducted using a three-electrode system, with the GE as a working electrode fabricated from a 0.5 cm gold wire (diameter 0.5 mm) and copper wires. In addition, a platinum wire and Ag/AgCl electrode (Metrohm) were used as a counter and reference electrode, respectively.

Procedure

Synthesis of gold nanoparticles (AuNP)

Briefly, 0.5 mL of 0.1 M sodium citrate ($Na_3C_6H_5O_7$) was added to 1 mM of $HAuCl_4$ under constant stirring. Then, 80 μL of $NaBH_4$ 0.1 M was added dropwise, and the color of the solution turned red/purple. AuNPs were characterized using UV-Vis spectrophotometry and showed the maximum absorption at 520–530 nm.

Preparation of the bioconjugate

The AuNP-aptamer bioconjugate was synthesized adopting the metal oxide-antibody bioconjugate preparation procedure as previously described [32-33]. First, the amino modification of the AuNP surface was performed to form a stable AuNP. Briefly, 10 mL of AuNP solution was modified with 25 μL of 3-aminopropyltrimethoxysilane (APTMS) before the APTMS-coated AuNP was sonicated to prevent aggregation. The aptamer was then conjugated to AuNP using NHS-PEG-Mal as a spacer. First, 31 mg of NHS-PEG-Mal was added to the amino-AuNP solution to obtain the sulfhydryl-reactive group of pegylated AuNP, then 200 μL of the pegylated AuNP was incubated with the thiolated aptamer (5 μg mL^{-1}) overnight.

Optimization of parameters using the Box-Behnken design

The MPA incubation time (X_1), bioconjugate incubation time (X_2), and the concentration of aptamer (X_3) were optimized via different levels; the lowest level (–1), intermediate (0), and highest level (+1), as shown in Table 1. Each measurement was processed, and the optimal value for each factor was determined using the Box-Behnken experimental design with the Minitab 18 program. All measurement was carried out using the differential pulse voltammetry technique.

Fabrication of the aptasensor

Before immobilizing the bioconjugate onto the GE surface, the GE was polished with Al_2O_3 and ultrasonically cleaned with ethanol and double-distilled water (ddH_2O) for 3 min. Then, the GE was immersed in piranha solution for 5 min to remove residues from the

Table 1. Optimization of experimental conditions using the Box-Behnken design

Factors	Unit	Level		
		–1	0	+1
MPA incubation time	min	10	25	4
Time of bioconjugate immobilization	min	30	60	90
Level of aptamer	μg mL^{-1}	5	15	25

surface and washed several times with ddH_2O.

The GE was incubated in 0.1 M MPA solution for 40 min at room temperature, then rinsed with ddH_2O before incubation in 40 µL of 0.1 M EDC:NHS solution for 60 min and washed with ddH_2O. EDC:NHS coupling was carried out to activate the carboxyl group of MPA-modified GE. After rinsing with ddH_2O, the GE was incubated in 0.1 M cysteamine solution for 60 min at room temperature to form the thiol end group, a maleimide-reactive group on the GE surface. Finally, the GE was rinsed with ddH_2O, and the modified GE was incubated in 40 µL of bioconjugate for 90 min at room temperature. The double bond of the free maleimide group of the bioconjugate reacted with the thiol group of cysteamine to form a covalent bond. The unbonded bioconjugate was washed with PBS (pH 7.4).

The sensor was incubated in 1% BSA solution for 60 min at 37 °C to block unspecific binding on the GE surface, then rinsed with ddH_2O several times. Next, the GE was incubated in different concentrations of HER2 solution for 60 min at room temperature and washed with PBS. Finally, the biosensors were characterized in 10 mM of Fe $(CN)_6^{3-/4-}$ by DPV, a redox probe solution from -0.6 to +0.5 V with a scan rate of 50 mV s^{-1}.

Prediction of the secondary structure of the aptamer

The secondary structure of the DNA aptamer was predicted using the mfold web server (http://unafold.rna.albany.edu/?q=mfold/DNA-Folding-Form) [34]. The folding temperature was measured at 37 °C, and the physiological ionic conditions were fixed at $[Na^+]$ = 1 M and $[Mg^{2+}]$ = 0 M. The number of computed folds was 50, and the distance between the paired base was unlimited [35]. The most stable secondary structure of DNA aptamer was selected based on the minimum ΔG.

Construction of the aptamer 3D structure

The aptamer 3D structure was modeled using Assemble2 [36] and visualized using Chimera [37]. The structure was constructed based on the RNA model and refined using 100 times iterations. First, a hydrogen atom was added to the RNA model. Then, the RNA model was manually changed into a DNA model by modifying uracil to thymine via replacing the H5 atom with a methyl group and ribose sugar into deoxyribose using BIOVIA Discovery Studio Visualizer 4.5 [38].

Prediction of the interaction between the aptamer and HER2

The electrostatic potential on the surface of HER2 was computed through the PDB2PQR server [37] using the APBS program (http://nbcr-222.ucsd.edu/pdb2pqr_2.0.0/) [39]. The interaction between the aptamer and HER2 was predicted using NPDock (http://genesilico.pl/NPDock) [40], a molecular docking program specially built for a protein-nucleotide system. The HER2 binding site was determined at the protein electropositive region, and the decoys number was set to 20,000 with a minimum interface contact of one residue. Monte Carlo refinement was performed using 1,000 steps of simulation, with the temperature in the last step set to 295 K.

■ RESULTS AND DISCUSSION

Aptasensor Based on Bioconjugate

Fig. 1 depicts a scheme of the aptasensor based on a bioconjugate aptamer as a sensing element. Previous research showed that PEG is a compatible linker for bioconjugation of AuNP and biorecognition molecules [32-33] and is required to provide space to bind more aptamers to AuNP, as can be seen in Fig. 1. The thiol groups of aptamers were covalently attached to the unsaturated bond of maleimides linked to the nanoparticles to form the bioconjugates. The double bond in the free maleimides of the bioconjugate readily reacts with the thiol groups from cysteamine on the electrode to form a stable carbon-sulfur bond. Then the aptamer is ready to catch the HER2 biomarker.

Characterization of the Aptasensor

Fig. 2 shows the differential pulse voltammogram of each modification step of the GE surface. The maximum reduction current peak was observed in the bare GE (241 µA) at the potential of about 150 mV vs. Ag/AgCl (2a). The modification of the GE surface with MPA and cysteamine slightly reduced the peak current to 234 µA (2b) and drifted the potential to 146 mV due to the formation of carboxyl groups which facilitate electron

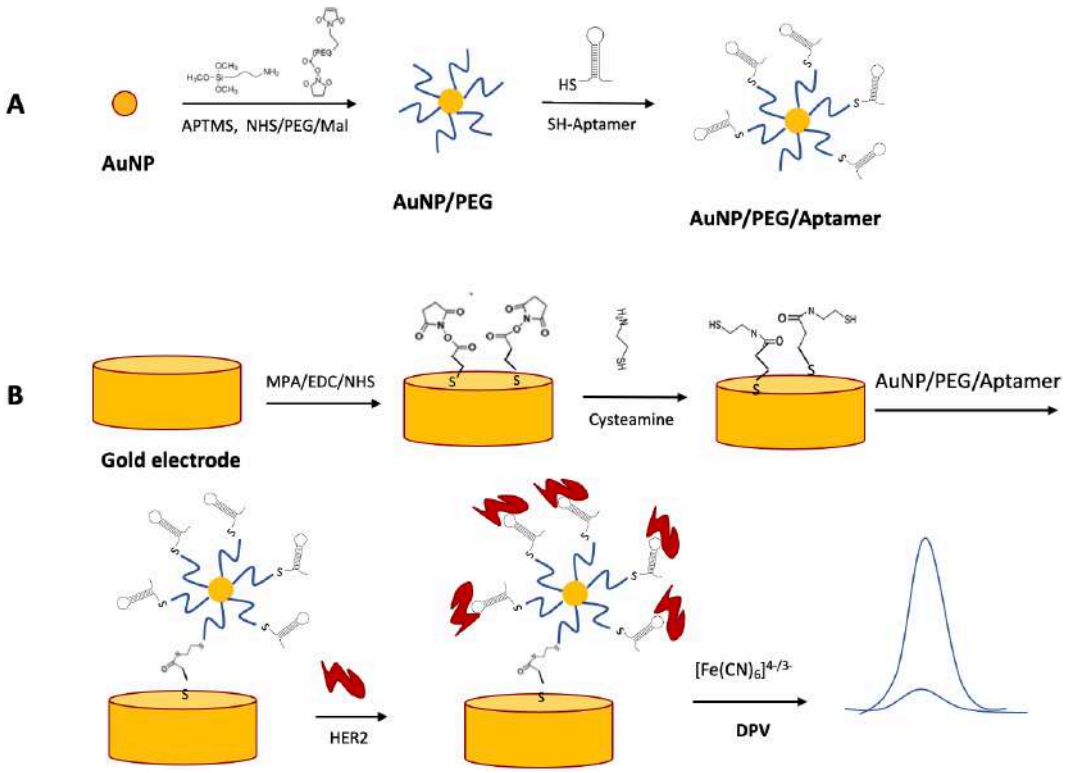

Fig 1. Scheme of the aptasensor for detection of HER2 biomarker

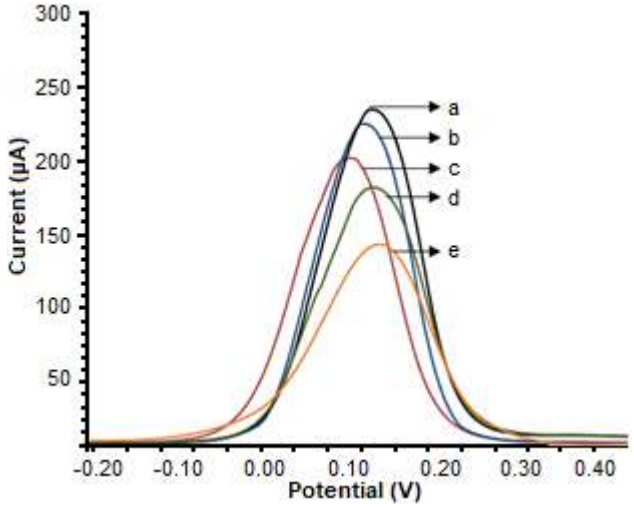

Fig 2. Voltammogram of each modification step of the GE bare (a), GE/MPA/Cys (b), GE/MPA/Cys/ bioconjugate (c), GE/MPA/Cys/bioconjugate/BSA (d), and GE/MPA/Cys/bioconjugate/BSA/HER-2 (e). The response was observed using 10 mM $[Fe(CN)_6]^{3-/4}$, recorded at -0.2 to +0.4 V, and a scan rate of 50 mV s^{-1}

transfer between the $[Fe(CN)_6]^{4-/3-}$ and the electrode. In addition, the dangling thiol group of GE/MPA/cysteamine can react with the double bond of the free maleimide group of the bioconjugate. Immobilization of the bioconjugate at the electrode surface shifts the potential to the left due to the bioconjugate containing AuNP, which can easily facilitate the electron transfer of the $[Fe(CN)_6]^{4-/3-}$ redox system. However, the non-electroactive biomolecules in the bioconjugate caused the $[Fe(CN)_6]^{4-/3-}$ peak current to decrease to 201 µA (2c). The blocking step with BSA also reduced the current to 176 µA and shifted the potential to 151 mV (2d). Finally, incubation of 5 ng mL^{-1} HER2 protein was monitored and observed in a reduction current of 147 µA at 151 mV (2e), indicating successful immobilization of each molecule on the GE surface.

Experimental Optimization

Three factors, namely MPA incubation time (X_1), bioconjugate incubation time (X_2), and the concentration of aptamer (X_3), were optimized using the Box-Behnken experimental design with the Minitab program 18. The experiments were performed 15 times in duplicate resulting in 30 experiments, and the

measurements were recorded in Minitab 18 to obtain the maximum current value. From the experimental data, the regression equation was as follows:

$Y = 95.2 - 6.06\ X_1 + 1.80\ X_2 - 1{,}96\ X_3 + 0.0459\ X_1X_2 - 0.0101\ X_2X_2 - 0.018\ X_3X_2 + 0.0376\ X_1X_2 + 0.1329\ X_1X_3 - 0.0542\ X_2X_3$

The above equation shows that the MPA incubation time and the concentration of aptamers have negative coefficients and decreased the response, while the bioconjugate incubation time has a positive value and increased the response. The ANOVA analysis of the Box-Behnken experiments revealed the P-value of each factor as $X_1 = 0.355$; $X_2 = 0.030$; and $X_3 = 0.019$. The P-value of X_2 and X_3 is ≤ 0.05, indicating that the factors are significant. The optimum experimental conditions determined from the Box-Behnken data were: MPA incubation for 40 min, the bioconjugate incubation time for 90 min, and aptamer concentration of 5 µg mL^{-1}. The optimization data is available in the Supplementary Information.

Analytical Performance of the Aptasensor

The responses of the aptamer-based biosensor to the various HER2 concentrations were investigated at optimal experimental conditions. The voltammogram at the potential range of -0.2 to +0.4 V in Fig. 3A and 3B shows that the current peak reduced with increasing HER2 level. This was due to the inhibition of the electron transfer between the redox system and the electrode by binding non-electroactive HER2 to the aptasensor surface.

The calibration curve is linear over two concentration ranges, from 0.01 to 15.0 ng mL^{-1} and 15.0 to 100.0 ng mL^{-1}, as shown in Fig. 3C. The corresponding calibration regression equations for lower and higher concentration ranges were $\Delta I = 4.1998$ [HER2] – 0.2876 with a coefficient correlation (R^2) of 0.995, and $\Delta I = 0.6782$ [HER2] + 52.217 with a coefficient correlation (R^2) of 0.995, respectively

The limit of detection (LOD) was evaluated using the blank signal, y_B, plus three standard deviations of the blank, s_B. The blank signal y_B is the intercept of a calibration curve, and s_B is obtained as random errors in the *y*-direction (41). The LOD was found at HER2 concentration level of 1.52 ng mL^{-1}, in the linear range of 0.01 to 15.0 ng mL^{-1}. This LOD was higher than several previous aptamer-based biosensors, as can be seen in Table 2. The complexity of the spacer may cause this difference. However, the LOD in this study was lower compared to our previous

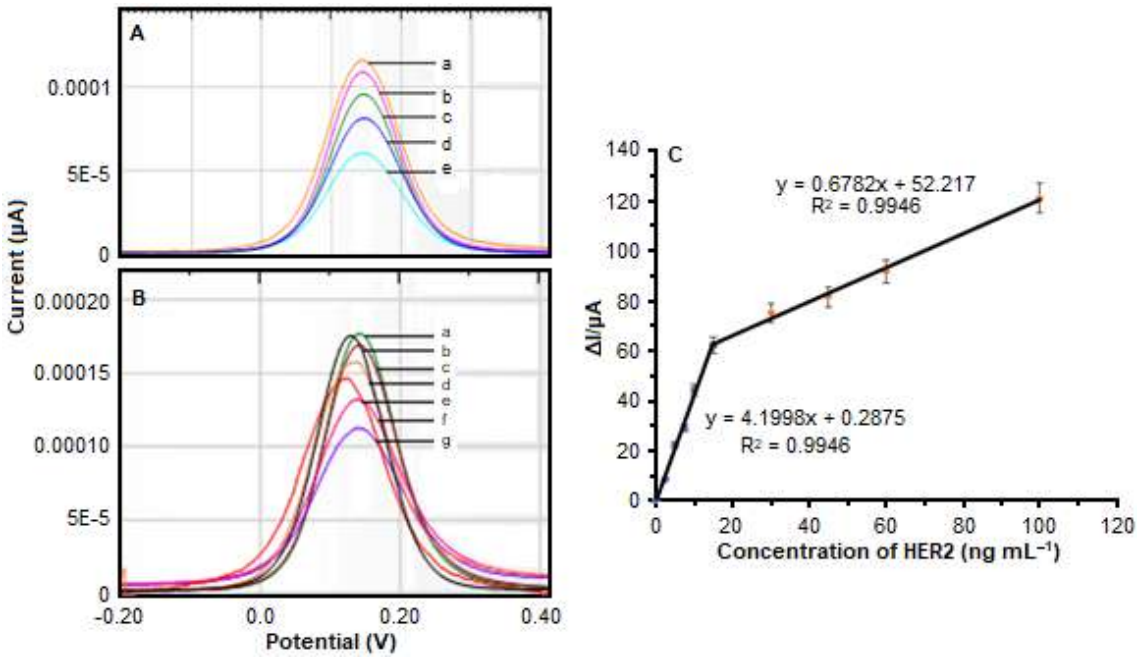

Fig 3. A and B: Voltammogram of various concentrations of HER2 0.01 to 15.0 ng mL^{-1}, and 15.0 to 100.0 ng mL^{-1}. C: Calibration curve of HER2 from 0.0 to 100 ng mL^{-1}

Table 2. The comparison of HER2 detection by using aptasensors

Technique	LOD	Reference
SPCE@L-lysine	3.0 ng mL^{-1}	[3]
GE-MPA	5.0 ng mL^{-1}	[19]
GE-MCH and GE-	172 and 179 pg mL^{-1}	[20]
Bimetallic ZrHf-MOF - CDs@ZrHf-MOF	19 fg mL^{-1}	[24]
Exonuclease recycling amplification and host-guest recognition	4.9 ng mL^{-1}	[25]
Non-Faradaic impedance spectroscopy (nFIS) of a microelectrode capacitive aptasensor	0.2-2.0 ng mL^{-1} (Dynamic range)	[26]
A tetrahedral DNA nanostructure (TDNs) - adapter as recognition probes and Mn3O4/Pd @ Pt nanozymes/HRP	0.08 ng mL^{-1}	[27]
Thickness shear mode acoustics method (TSM)	550 cells mL^{-1}	[28]
Gold nanorod@Pd superstructures-aptamer HER2-horseradish peroxidase (GNR@Pd SSs-Apt-HRP)	0.15 ng mL^{-1}	[29]
GE- Gold-aptamer bioconjugate	1.52 ng mL^{-1}	This work

study based on the antibody biosensor (an immunosensor) for HER2 detection (31-42) because of the conjugation of the aptamer with gold nanoparticles which increased electron transfer and signal amplification. The advantage of the use of aptamer as a sensing element is that it is much cheaper than antibodies. In addition, this aptasensor was able to still distinguish the concentration of HER2 in cancer and normal cells, which were 17.7 and 12.2 ng mL^{-1}, respectively (43). The precision of 5.0 ng mL^{-1} HER2 represented by the coefficient of variance was 0.1298, and the accuracy was 94.06% representing the percentage of the measured concentration value to the true concentration value ratio.

Modeling Interaction

The anti-HER2 ssDNA aptamer used in this study was retrieved as previously reported [44], and the model structure with the lowest DG of -6.15 kcal mol^{-1} was selected for this study (Fig. 4). The aptamer is composed of a negatively charged phosphate backbone. Therefore, the binding site of the aptamer in the HER2 structure is expected to be electropositive. For this reason, the crystal structure of HER2 (PDB ID 1N8Z) was submitted to the PDB2PQR server to calculate the electrostatic potential on the protein surface using the APBS method, revealing that the electropositive part of HER2 was located in the upper region of HER2 (Fig. 5A) composed of a striking

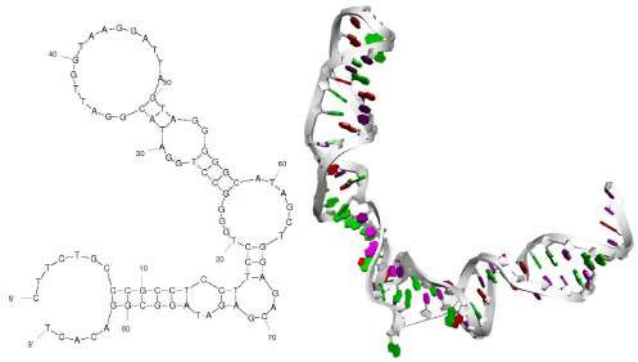

Fig 4. The secondary structure (left) and 3D structure (right) of the anti-HER2 aptamer

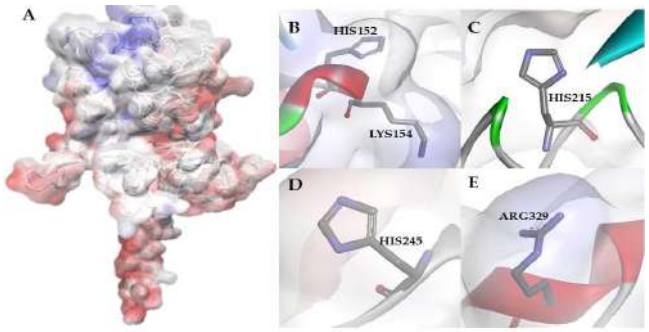

Fig 5. The electrostatic potential of HER2 from the APBS program. The electronegative and electropositive surfaces are represented by red and blue colors, respectively, with the electropositive part of HER2 located in the upper region of HER2. (A) His152, Lys153 (B), His215 (C), His245 (D) and Arg329 (E)

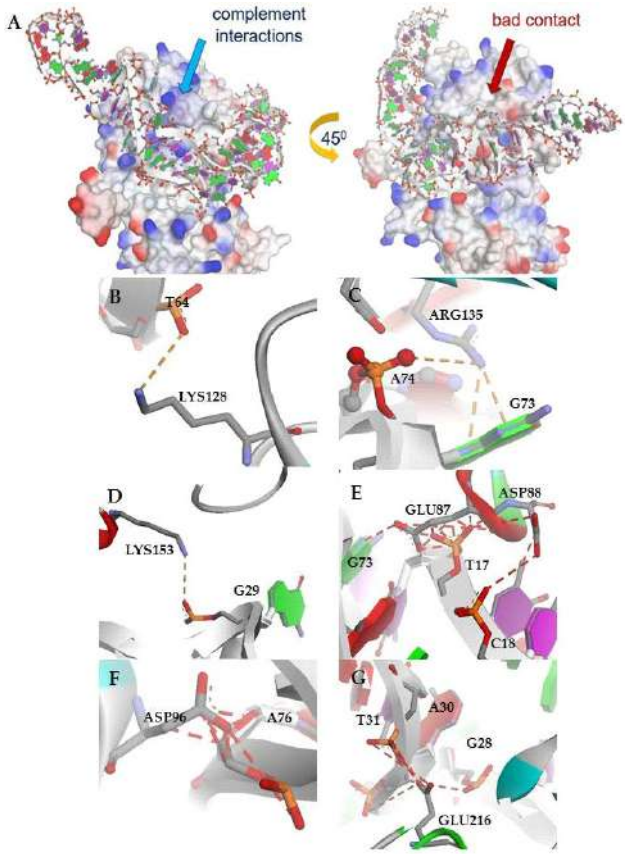

Fig 6. Complement interactions between the aptamer and HER2 (left) and the bad contacts in the other part of HER2 (right) (Fig. A). Acidic and basic residues are visualized in the red and blue colored surfaces, respectively. The orange dashed line shows the electrostatic interaction, the residues are Lys128 (Fig. B), Arg135 (Fig. C), and Lys135 (Fig. D). The red shows the unfavorable interactions dashed line with negatively charged residues, such as Glu87, Asp88 (Fig. B), Asp96 (Fig. F), and Glu216 (Fig. G)

lysine, arginine, and histidine, that was His152 (Fig. 5B), Lys153 (Fig. 5B), His215 (Fig. 5C), His245 (Fig. 5D), and Arg329 (Fig. 5E).

NPDock predicted the interaction between the aptamer and HER2, showing that the aptamer binds to the positively charged residues of HER2 (Fig. 6A), and the electrostatic interaction dominated the attractive forces, such as Lys128 (Fig. 6B), Arg135 (Fig. 6C), and Lys153 (Fig. 6D). The computed binding energy was -8.0 kcal/mol. Interestingly, not all aptamers interacted with the complement region. A few terminal nucleotides were in bad contacts, interacting with an electronegative patch on the surface of HER2. Therefore, it is predicted that the moderate binding of this aptamer is due to the unfavorable interactions with negatively charged residues, such as Glu87, Asp88 (Fig. 6E), Asp96 (Fig. 6F), and Glu216 (Fig. 6G).

Further optimization of this aptamer by removing the terminal part that interacts with those acidic residues is expected to improve its binding affinity to HER2. It is worth noting that the affinity of this aptamer to HER2 by the NECEEM method was 48% of binding affinity. However, the results of *in vitro* selectivity tests for representative molecules that might interfere with their interaction with HER2, including IgG, plasmid DNA, RNA, and glucose, indicated less than 10% interaction [31].

■ CONCLUSION

An aptasensor to detect HER2, a validated breast cancer biomarker, was developed using a bioconjugate to improve the surface area for better immobilization of the aptamer onto a gold electrode. The detection limit was 1.52 ng mL^{-1}, and the system was able to distinguish between different concentrations of HER2 in normal and cancer cells. Modeling the interaction between the aptamer and HER2 showed that electrostatic interactions dominated the attractive forces, and any unfavorable interactions could be further optimized to improve the binding affinity of this aptamer to HER2. The resulting interaction pattern can be used as a template to improve the binding energy of the aptamer, providing an insight into the development of aptamer-based biosensors for other diseases. The results revealed a promising and sensitive tool capable of detecting HER2 protein in human serum with albumin depletion, aiding in the molecular diagnosis of breast cancer. Furthermore, this proposed strategy presented good reliability and applicability in analyzing human serum samples, showing great potential for applications in the early diagnosis of breast cancer.

■ ACKNOWLEDGMENTS

This research was supported by the Ministry of Research, Technology and Higher Education, Republic

of Indonesia, through the Research Grant of *Skema Penelitian Terapan Unggulan Perguruan Tinggi*, No. 1129/UN6.D/LT/2018, and Academic Leadership Grant Universitas Padjadjaran No. 2295/UN.6.D/KS/2018.

■ AUTHOR CONTRIBUTIONS

YWH designed the experiment, SS conducted the experiment, MY conducted the DFT calculations, YW H, SG, and SW supervised, wrote, and revised the manuscript. TS was the funding leader of ALG. All authors agreed to the final version of this manuscript.

■ REFERENCES

[1] WHO, 2014, *Cancer Country Profile*, World Health Organization, Geneva, Switzerland.

[2] American Cancer Society, 2020, *Understanding a Breast Cancer Diagnosis: Survival Rates for Breast Cancer*, https://www.cancer.org/cancer/breast-cancer/understanding-a-breast-cancer-diagnosis/breast-cancer-survival-rates.html, accessed on October 8, 2020.

[3] Bezerra, G., Córdula, C., Campos, D., Nascimento, G., Oliveira, N., Seabra, M.A., Visani, V., Lucas, S., Lopes, I., Santos, J., Xavier, F., Borba, M.A., Martins, D., and Lima-Filho, J., 2019, Electrochemical aptasensor for the detection of HER2 in human serum to assist in the diagnosis of early stage breast cancer, *Anal. Bioanal. Chem.*, 411 (25), 6667–6676.

[4] Zhang, X.H., and Xiao, C., 2018, Diagnostic value of nineteen different imaging methods for patients with breast cancer: A network meta-analysis, *Cell. Physiol. Biochem.*, 46 (5), 2041–2055.

[5] Khanjani, F., Sajedi, R.H., and Hasannia, S., 2018, Rapid screening of drug candidates against EGFR/HER2 signaling pathway using fluorescence assay, *Anal. Bioanal. Chem.*, 410 (30), 7827–7835.

[6] Arya, S.K., Zhurauski, P., Jolly, P., Batistuti, M.R., Mulato, M., and Estrela, P., 2018, Capacitive aptasensor based on interdigitated electrode for breast cancer detection in undiluted human serum, *Biosens. Bioelectron.*, 102, 106–112.

[7] Vondeling, G.T., Menezes, G.L., Dvortsin, E.P., Jansman, F.G.A., Konings, I.R., Postma, M.J., and Rozenbaum, M.H., 2018, Burden of early, advanced and metastatic breast cancer in The Netherlands, *BMC Cancer*, 18 (1), 262.

[8] Huang, Y., Xu, J., Liu, J., Wang, X., and Chen, B., 2017, Disease-related detection with electrochemical biosensors: A review, *Sensors*, 17 (10), 2375.

[9] Lai, C., Liu, S., Zhang, C., Zeng, G., Huang, D., Qin, L., Liu, X., Yi, H., Wang, R., Huang, F., Li, B., and Hu, T., 2018, Electrochemical aptasensor based on sulfur–nitrogen codoped ordered mesoporous carbon and thymine–Hg^{2+}–thymine mismatch structure for Hg^{2+} detection, *ACS Sens.*, 3 (12), 2566–2573.

[10] Liu, S., Lai, C., Liu, X., Li, B., Zhang, C., Qin, L., Huang, D., Yi, H., Zhang, M., Li, L., Wang, W., Zhou, X., and Chen, L., 2020, Metal-organic frameworks and their derivatives as signal amplification elements for electrochemical sensing, *Coord. Chem. Rev.*, 424, 213520.

[11] Hartati, Y.W., Gaffar, S., Alfiani, D., Pratomo, U., Sofiatin, Y., and Subroto, T., 2020, A voltammetric immunosensor based on gold nanoparticle - Anti-ENaC bioconjugate for the detection of epithelial sodium channel (ENaC) protein as a biomarker of hypertension, *Sens. Bio-Sens. Res.*, 29, 100343.

[12] Cai, G., Yu, Z., Ren, R., and Tang, D., 2018, Exciton–plasmon interaction between AuNPs/graphene nanohybrids and CdS quantum dots/TiO_2 for photoelectrochemical aptasensing of prostate-specific antigen, *ACS Sens.*, 3 (3), 632–639.

[13] Hartati, Y.W., Komala, D.R., Hendrati, D., Gaffar, S., Hardianto, A., Sofiatin, Y., and Bahti, H.H., 2021, An aptasensor using ceria electrodeposited-screen-printed carbon electrode for detection of epithelial sodium channel protein as a hypertension biomarker, *R. Soc. Open Sci.*, 8 (2), 202040.

[14] Parashar A., 2016, Aptamers in therapeutics, *J. Clin. Diagn. Res.*,10 (6), BE01–BE06.

[15] Kinghorn, A.B., and Tanner, J.A., 2017, Selective phenome growth adapted model: A novel landscape to represent aptamer ligand binding, *Complexity*, 2017, 6760852.

[16] Trausch, J.J., Shank-Retzlaff, M., and Verch, T., 2017, Replacing antibodies with modified DNA aptamers in vaccine potency assays, *Vaccine*, 35 (41), 5495–5502.

[17] Drabovich, A.P., Berezovski, M., Okhonin, V., and Krylov, S.N., 2006, Selection of smart aptamers by methods of kinetic capillary electrophoresis, *Anal. Chem.*, 78 (9), 3171–3178.

[18] Yufa, R., Krylova, S.M., Bruce, C., Bagg, E.A., Schofield, C.J., and Krylov, S.N., 2015, Emulsion PCR significantly improves nonequilibrium capillary electrophoresis of equilibrium mixtures-based aptamer selection: Allowing for efficient and rapid selection of aptamer to unmodified ABH2 protein, *Anal. Chem.*, 87 (2), 1411–1419.

[19] Chun, L., Kim, S.E., Cho, M., Choe, W.S., Nam, J., Lee, D.W., and Lee, Y., 2013, Electrochemical detection of HER2 using single stranded DNA aptamer modified gold nanoparticles electrode, *Sens. Actuators, B*, 186, 446–450.

[20] Bang, G.S., Cho, S., Lee, N., Lee, B.R., Kim, J.H., and Kim, B.G., 2013, Rational design of modular allosteric aptamer sensor for label-free protein detection, *Biosens. Bioelectron.*, 39 (1), 44–50.

[21] Komala, D.R., Hardianto, A., Gaffar, S., and Hartati, Y.W., 2021, An epithelial sodium channel (ENaC)-specific aptamer determined through structure-based virtual screening for the development of hypertension early detection system, *Pharm. Sci.*, 27 (1), 67–75.

[22] Şahin, S., Caglayan, M.O., and Üstündağ, Z., 2020, Recent advances in aptamer-based sensors for breast cancer diagnosis: Special cases for nanomaterial-based VEGF, HER2, and MUC1 aptasensors, *Microchim. Acta*, 187 (10), 549.

[23] Ferreira, D.C., Batistuti, M.R., Junior, B.B., and Mulato, M., 2021, Aptasensor based on screen-printed electrode for breast cancer detection in undiluted human serum, *Bioelectrochemistry*, 137, 107586.

[24] Gu, C., Guo, C., Li, Z., Wang, M., Zhou, N., He, L., Zhang, Z., and Du, M., 2019, Bimetallic ZrHf-based metal-organic framework embedded with carbon dots: Ultra-sensitive platform for early diagnosis of HER2 and HER2-overexpressed living cancer cells, *Biosens. Bioelectron.*, 134, 8–15.

[25] Yang, S., You, M., Zhang, F., Wang, Q., and He, P., 2018, A sensitive electrochemical aptasensing platform based on exonuclease recycling amplification and host-guest recognition for detection of breast cancer biomarker HER2, *Sens. Actuators, B*, 258, 796–802.

[26] Qureshi, A., Gurbuz, Y., and Niazi, J.H., 2015, Label-free capacitance based aptasensor platform for the detection of HER2/ErbB2 cancer biomarker in serum, *Sens. Actuators, B*, 220, 1145–1151.

[27] Ou, D., Sun, D., Lin, X., Liang, Z., Zhong, Y., and Chen, Z., 2019, A dual-aptamer-based biosensor for specific detection of breast cancer biomarker HER2 *via* flower-like nanozymes and DNA nanostructures, *J. Mater. Chem. B*, 7 (23), 3661–3669.

[28] Poturnayová, A., Dzubinová, Ľ., Buríková, M., Bízik, J., and Hianik, T., 2019, Detection of breast cancer cells using acoustics aptasensor specific to HER2 receptors, *Biosensors*, 9 (2), 72.

[29] Chen, D., Wang, D., Hu, X., Long, G., Zhang, Y., and Zhou, L., 2019, A DNA nanostructured biosensor for electrochemical analysis of HER2 using bioconjugate of GNR@ Pd SSs—Apt—HRP, *Sens. Actuators, B*, 296, 126650.

[30] Hermanson, G.T., 2013, *Bioconjugate Techniques*, 3rd Ed., Academic Press, Cambridge, US.

[31] Hartati, Y.W., Nurdjanah, D., Wyantuti, S., Anggraeni, A., and Gaffar, S., 2018, Gold nanoparticles modified screen-printed immunosensor for cancer biomarker HER2 determination based on anti HER2 bioconjugates, *AIP Conf. Proc.*, 2049, 020051.

[32] Emami, M., Shamsipur, M., Saber, R., and Irajirad, R., 2014, An electrochemical immunosensor for detection of a breast cancer biomarker based on antiHER2–iron oxide nanoparticle bioconjugates, *Analyst*, 139 (11), 2858–2866.

[33] Hartati, Y.W., Letelay, L.K., Gaffar, S., Wyantuti, S., and Bahti, H.H., 2020, Cerium oxide-monoclonal antibody bioconjugate for electrochemical

immunosensing of HER2 as a breast cancer biomarker, *Sens. Bio-Sens. Res.*, 27, 100316.

[34] Zuker, M., 2003, Mfold web server for nucleic acid folding and hybridization prediction, *Nucleic Acids Res.*, 31 (13), 3406–3415.

[35] Jeddi, I., and Saiz, L., 2017, Three-dimensional modeling single stranded DNA hairpins for aptamer-based biosensor, *Sci Rep.*, 7 (1), 1178.

[36] Jossinet, F., Ludwig, T.E., and Westhof, E., 2010, Assemble: An interactive graphical tool to analyze and build RNA architectures at the 2D and 3D levels, *Bioinformatics*, 26 (16), 2057–2059.

[37] Pettersen, E.F., Goddard, T.D., Huang, C.C., Couch, G.S., Greenblatt, D.M., Meng, E.C., and Ferrin, T.E., 2004, UCSF Chimera–A visualization system for exploratory research and analysis, *J. Comput. Chem.*, 25 (13), 1605–1612.

[38] BIOVIA, Dassault Systèmes 2016, *BIOVIA Discovery Studio Visualizer 4.5, v.16.1.0.15350*, Dassault Systèmes, San Diego.

[39] Dolinsky, T.J., Nielsen, J.E., McCammon, J.A., and Baker, N.A., 2004, PDB2PQR: An automated pipeline for the setup of Poisson-Boltzmann electrostatics calculations, *Nucleic Acids Res.*, 32 (Suppl. 2), W665–W667.

[40] Tuszynska, I., Magnus, M., Jonak, K., Dawson, W., and Bujnicki, J.M., 2015, NPDock: A web server for protein-nucleic acid docking, *Nucleic Acids Res.*, 43 (W1), W425–W430.

[41] Miller, J.N., and Miller, J.C., 2005, *Statistics and Chemometrics for Analytical Chemistry*, 5th Ed., Pearson Prentice Hall, England.

[42] Hartati, Y.W., Beladona, S.U.M., Wyantuti, S., and Gaffar, S., 2018, A voltammetric immunosensor for detection of HER2 using gold modified-screen printed carbon electrode, *Res. J. Chem. Environ.*, 22, 294–301.

[43] Al-Khafaji, Q.A.M., Harris, M., Tombelli, S., Laschi, S., Turner, A.P.F., Mascini, M., and Marazza, G., 2012, An Electrochemical immunoassay for HER2 detection, *Electroanalysis*, 24 (4), 735–742.

[44] Kim, S.E., and Choe, W.S., 2011, Screening of ssDNA aptamers for HER2 ECD protein, *Proc. Korean Soc. Biotechnol. Bioeng.*, 291.

Supplementary Data

This supplementary data is a part of paper entitled "Computational Evaluation of Intermolecular Interaction in Poly(Styrene-Maleic Acid)-Water Complexes Using Density Functional Theory".

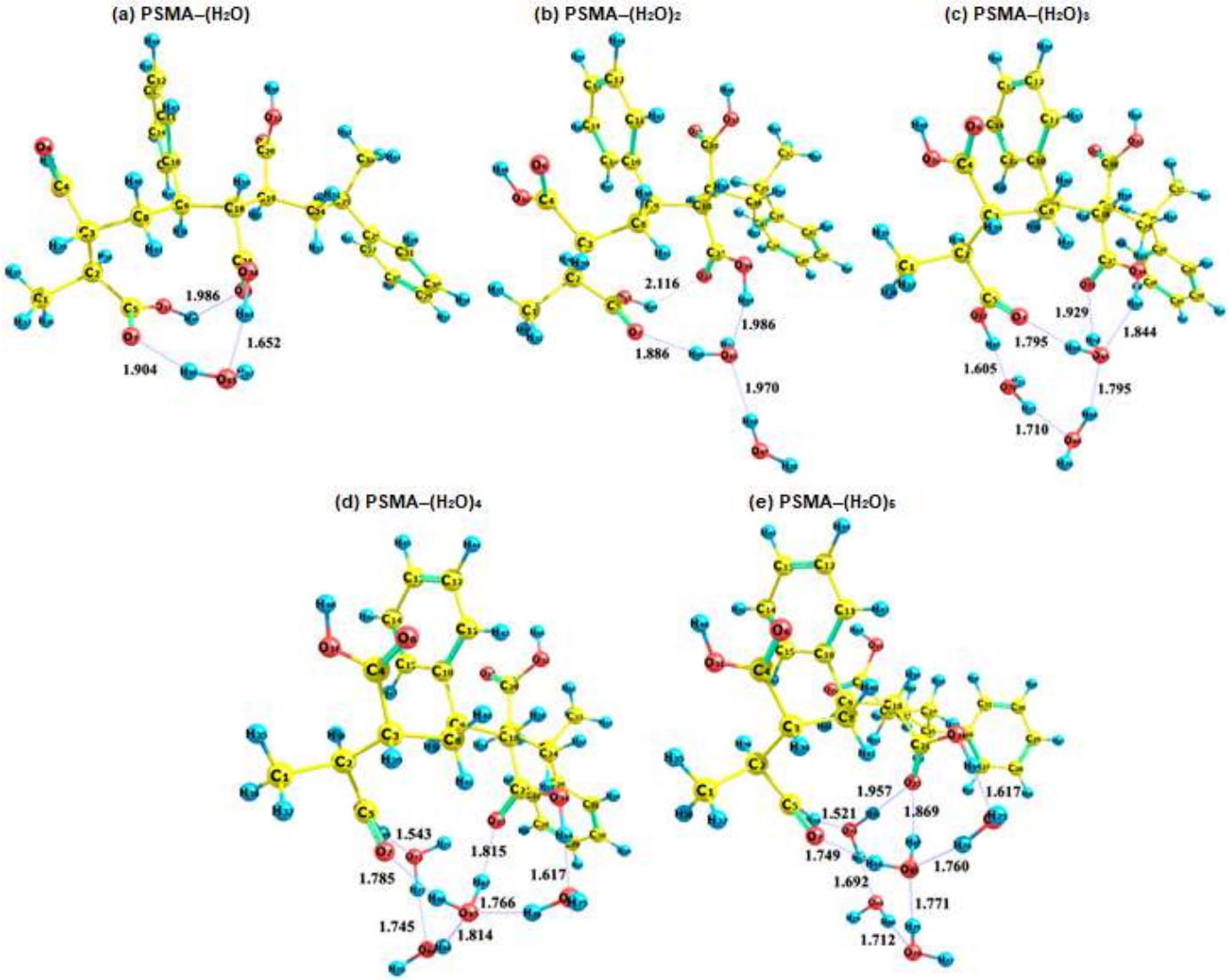

Fig S1. Optimized structures of PSMA–$(H_2O)_n$ complexes; n = 1–5

Table S1. Comparison of $E_{opt_{PSMA\cdots(H_2O)_1}}$ with DFT, HF, and MP2 methods

Method	Energy (kcal/mol)
DFT	–1058789.36
HF	–1052424.16
MP2	–1055764.52

Table S2. NBO analysis of PSMA–$(H_2O)_n$ complexes

Donor (i)	Acceptor (j)	$E^{(2)}$ (kcal/mol)	$E_{(i)} - E_{(j)}$ (a.u)	$F_{(i,j)}$ (a.u.)
PSMA–H_2O				
LP (1) O7	BD*(1) O65-H66	6.90	1.04	0.076
LP (2) O7	BD*(1) O65-H66	5.16	0.75	0.056
LP (2) O65	BD*(1) O34-H64	34.00	0.79	0.146
PSMA–$(H_2O)_2$				
LP (1) O7	BD*(1) O65-H66	7.87	1.03	0.080
LP (2) O7	BD*(1) O65-H66	6.43	0.75	0.062
LP (2) O65	BD*(1) O34-H64	24.38	0.76	0.122
LP (1) O65	BD*(1) H68-O69	7.77	1.05	0.081
PSMA–$(H_2O)_3$				
LP (1) O7	BD*(1) O65-H66	9.28	1.01	0.086
LP (2) O7	BD*(1) O65-H66	9.41	0.73	0.074
LP (1) O65	BD*(1) O34-H64	4.97	0.95	0.061
LP (2) O65	BD*(1) O34-H64	12.17	0.73	0.084
LP (2) O16	BD*(1) H47-O48	6.43	0.79	0.063
LP (1) O65	BD*(1) H68-O69	6.50	1.00	0.072
LP (2) O65	BD*(1) H68-O69	14.15	0.79	0.094
LP (1) O23	BD*(1) O65-H67	3.66	1.01	0.054
LP (2) O23	BD*(1) O65-H67	8.52	0.72	0.070
LP (2) O69	BD*(1) O72-H73	27.52	0.87	0.138
LP (2) O72	BD*(1) O17-H49	39.50	0.89	0.168
PSMA–$(H_2O)_4$				
LP (1) O7	BD*(1) O65-H66	10.77	1.02	0.094
LP (2) O7	BD*(1) O65-H66	8.75	0.74	0.072
LP (1) O23	BD*(1) O65-H67	8.22	1.03	0.082
LP (2) O23	BD*(1) O65-H67	9.12	0.75	0.074
LP (1) O23	BD*(1) H71-O72	4.38	1.06	0.061
PSMA–$(H_2O)_5$				
LP (1) O7	BD*(1) O65-H66	11.74	1.02	0.098
LP (2) O7	BD*(1) O65-H66	9.95	0.75	0.077
LP (1) O23	BD*(1) O65-H67	8.05	1.04	0.082
LP (2) O23	BD*(1) O65-H67	4.79	0.75	0.054
LP (1) O23	BD*(1) H71-O72	6.86	1.08	0.077
LP (2) O23	BD*(1) H71-O72	2.80	0.79	0.042
LP (1) O65	BD*(1) O74-H76	8.15	0.99	0.080
LP (2) O65	BD*(1) O74-H76	14.21	0.78	0.094
LP (1) O65	BD*(1) O78-H79	12.64	1.01	0.101
LP (2) O65	BD*(1) O78-H79	9.36	0.80	0.077
LP (2) O69	BD*(1) O72-H73	29.89	0.89	0.146
LP (2) O72	BD*(1) O17-H49	50.32	0.86	0.186
LP (2) O74	BD*(1) O34-H64	39.06	0.83	0.161

Table S3. QTAIM analysis of PSMA-water complexes

CP	BCP	$\rho_{(BCP)}$	$\nabla^2_{(BCP)}$	$G_{(BCP)}$	$H_{(BCP)}$	$V_{(BCP)}$	$\lvert V/G \rvert$	λ_1	λ_2	λ_3	$\varepsilon_{(BCP)}$	E_{HB}
PSMA–$(H_2O)_1$												
101	O7···H66	0.0252	0.0738	0.0187	-0.0002	-0.0189	1.0126	-0.0102	0.0708	0.0131	0.006252	-4.8890
120	O65···H64	0.0523	0.1366	0.0375	-0.0033	-0.0408	1.0884	0.2718	-0.0897	-0.0455	0.0319	-10.9296
PSMA–$(H_2O)_2$												
101	O23···H67	0.0138	0.0509	0.0118	0.0009	-0.0109	0.9223	0.0657	-0.0121	-0.0026	0.6129	-2.3407
110	O65···H68	0.0255	0.0674	0.0183	-0.0014	-0.0197	1.0770	0.1219	-0.0218	-0.0327	0.0156	-4.9535
114	O65···H64	0.0425	0.1146	0.0302	-0.0015	-0.0317	1.0497	0.1877	-0.0667	-0.0063	0.0312	-8.7310
130	O7···H66	0.0277	0.0815	0.0204	0.0000	-0.0205	1.0023	-0.0095	0.0890	0.0019	0.0099	-5.4324
PSMA–$(H_2O)_3$												
107	O23···H67	0.0293	0.0833	0.0221	-0.0013	-0.0233	1.0569	0.1305	-0.0333	-0.0139	0.0553	-5.7857
117	O65···H64	0.0343	0.0921	0.0244	-0.0014	-0.0257	1.0558	0.1368	-0.0388	-0.0059	0.0491	-6.9053
121	O7···H66	0.0377	0.1052	0.0275	-0.0012	-0.0287	1.0431	0.1927	-0.0545	-0.0331	0.0492	-7.6689
122	O69···H73	0.0455	0.1269	0.0332	-0.0015	-0.0347	1.0442	0.0136	-0.0395	0.1529	0.0307	-9.4090
130	O72···H49	0.0563	0.1543	0.0422	-0.0036	-0.0459	1.0862	0.2069	0.0471	-0.0997	0.0592	-11.8146
143	O7···H66	0.0348	0.1031	0.0258	0.0000	-0.0258	0.9998	-0.0134	0.1353	-0.0187	0.0261	-7.0111
PSMA–$(H_2O)_4$												
116	O7···H66	0.0348	0.1065	0.0262	0.0004	-0.0258	0.9846	-0.0076	0.1210	-0.0069	0.0226	-7.0289
126	O74···H64	0.0567	0.1458	0.0410	-0.0046	-0.0456	1.1110	0.3177	-0.1024	-0.0695	0.0447	-11.9100
129	O65···H76	0.0398	0.1129	0.0293	-0.0011	-0.0304	1.0371	-0.0486	-0.0544	0.2159	0.0435	-8.1279
136	O72···H49	0.0679	0.1615	0.0504	-0.0100	-0.0604	1.1988	-0.1114	0.4075	-0.1345	0.0340	-14.3956
139	O23···H67	0.0340	0.1001	0.0253	-0.0003	-0.0256	1.0119	0.1891	-0.0417	-0.0473	0.0090	-6.8437
142	O65···H68	0.0366	0.1008	0.0266	-0.0014	-0.0280	1.0522	0.0101	0.0031	0.0876	0.0493	-7.4139
143	O23···H71	0.0166	0.0540	0.0134	0.0001	-0.0132	0.9897	-0.0017	-0.0178	0.0735	0.0515	-2.9510
152	O69···H73	0.0423	0.1166	0.0305	-0.0014	-0.0319	1.0446	0.2035	-0.0516	-0.0353	0.0453	-8.6862
PSMA–$(H_2O)_5$												
118	O7···H66	0.0375	0.1161	0.0284	0.0006	-0.0278	0.9789	-0.0107	0.1341	-0.0073	-0.0107	-7.6309
130	O74···H64	0.0566	0.1464	0.0411	-0.0045	-0.0456	1.1090	0.2921	-0.0942	-0.0515	0.2921	-11.8894
131	O65···H76	0.0404	0.1138	0.0296	-0.0011	-0.0307	1.0378	-0.0310	-0.0586	0.2035	-0.0310	-8.2763
138	O72···H49	0.0703	0.1663	0.0531	-0.0116	-0.0647	1.2174	-0.1214	0.4307	-0.1429	-0.1214	-14.9458
144	O23···H67	0.0297	0.0885	0.0225	-0.0003	-0.0228	1.0150	0.1541	-0.0275	-0.0382	0.1541	-5.8784
145	O65···H79	0.0391	0.1105	0.0285	-0.0009	-0.0293	1.0301	0.1476	-0.0158	-0.0213	0.1476	-7.9731
148	O23···H71	0.0237	0.0738	0.0186	-0.0001	-0.0187	1.0077	-0.0038	-0.0297	0.1073	-0.0038	-4.5467
159	O69···H73	0.0471	0.1324	0.0345	-0.0014	-0.0359	1.0405	0.2032	0.0043	-0.0751	0.2032	-9.7638
160	O78···H68	0.0454	0.1278	0.0334	-0.0014	-0.0348	1.0432	0.0041	-0.0434	0.1672	0.0041	-9.3957

CP: critical point; BCP: Bond critical point); ρ : Electron density (a.u.); $\nabla^2\rho$: Laplacian of electron density (a.u); G: Lagrangian kinetic energy (a.u); H: Hamiltonian kinetic energy or electronic energy density (a.u); V: Potential energy density (a.u.); ε: Ellipticity of electron density (a.u); λ_1, λ_2, λ_3 : Components of Laplacian in x/y/z (a.u.); E_{HB}: Hydrogen bond energy (kcal/mol)

Table S4. Comparison of reported hydrogen bond energy

Siahaan [1]				Safia [2]				Bo Wang [3]		
Method	Functional	BCP	E_{HB}	Method	Functional	Interaction	E_{HB}	Method	Molecules	E_{HB}
		Chi-Cre				Orientation 1		DFT	Dimer H_2O	–4.76
		16	–8.3565			O151···H136	–0.998	HF		–3.60
		19	–0.8238			O150···H130	–2.225			
		27	–5.2382	DFT	WB97XD	O149···H137	–1.533			
		51	–8.0788							
DFT-D3	B3LYP					Orientation 2				
		Chi-Urea				O151···H118	–0.217			
		86	–0.7816			O149···H125	–0.373			
		91	–4.2357							
		110	–1.5222							
		119	–0.8928							

Chi: Chitosan, Cre: Creatinine, BCP: Bond critical point, and E_{HB}: Hydrogen bond energy (kcal/mol)

References of supporting information

[1] Siahaan, P., Sasongko, N.A., Lusiana, R.A., Prasasty, V.D., and Martoprawiro, M.A., 2021, The validation of molecular interaction among dimer chitosan with urea and creatinine using density functional theory: In application for hemodyalisis membrane, *Int. J. Biol. Macromol.*, 168, 339–349.

[2] Safia, H., Ismahan, L., Abdelkrim, G., Mouna, C., Leila, N., and Fatiha, M., 2019, Density functional theories study of the interactions between host β-cyclodextrin and guest 8-anilinonaphthalene-1-sulfonate: Molecular structure, HOMO, LUMO, NBO, QTAIM and NMR analyses, *J. Mol. Liq.*, 280, 218–229.

[3] Wang, B., Jiang, W., Dai, X., Gao, Y., Wang, Z., and Zhang, R.Q., 2016, Molecular orbital analysis of the hydrogen bonded water dimer, *Sci. Rep.*, 6 (1), 22099.

Computational Evaluation of Intermolecular Interaction in Poly(Styrene-Maleic Acid)-Water Complexes Using Density Functional Theory

Daru Seto Bagus Anugrah[1*], Laura Virdy Darmalim[1], Permono Adi Putro[2], Liana Dewi Nuratikah[3], Nurwarrohman Andre Sasongko[3], Parsaoran Siahaan[3], and Adi Yulandi[1]

[1]*Department of Biotechnology, Faculty of Biotechnology, Atma Jaya Catholic University of Indonesia, BSD Campus, Tangerang 15345, Indonesia*

[2]*Department of Physics, Faculty of Mathematics and Natural Sciences, IPB University, Jl. Meranti, Kampus IPB Dramaga, Bogor 16680, Indonesia*

[3]*Department of Chemistry, Faculty of Sciences and Mathematics, Diponegoro University, Jl. Prof. H. Soedarto, S.H., Tembalang, Semarang 50275, Indonesia*

**** Corresponding author:***

email: daru.seto@atmajaya.ac.id

Received: July 26, 2021
Accepted: September 13, 2021

DOI: 10.22146/ijc.67961

Abstract: *The high application of Poly(styrene-maleic acid) (PSMA) in an aqueous environment, such as biomedical purposes, makes the interaction between PSMA and water molecules interesting to be investigated. This study evaluated the conformation, the hydrogen bond network, and the stabilities of all the possible intermolecular interactions between PSMA with water (PSMA–$(H_2O)_n$, n = 1–5). All calculations were executed using the density functional theory (DFT) method at B3LYP functional and the 6–311G** basis set. The energy interaction of PSMA–$(H_2O)_5$ complex was –56.66 kcal/mol, which is classified as high hydrogen bond interaction. The Highest Occupied Molecular Orbital (HOMO) – Lowest Unoccupied Molecular Orbital (LUMO) energy gap decreased with the rise in the number of H_2O molecules, representing a more reactive complex. The strongest hydrogen bonding in PSMA–$(H_2O)_5$ was formed through the interaction on O72···O17–H49 with stabilizing energy of 50.32 kcal/mol, that analyzed by natural bond orbital (NBO) theory. The quantum theory atoms in molecules (QTAIM) analysis showed that the hydrogen bonding (E_{HB}) value on O72···O17–H49 was –14.95 kcal/mol. All computational data revealed that PSMA had moderate to high interaction with water molecules that indicated the water molecules were easily transported and kept in the PSMA matrix.*

Keywords: *Density Functional Theory; hydrogen bonding; poly(styrene-maleic acid); water*

■ INTRODUCTION

The increasing interest in synthetic polymers in various area is very high because it has uniform properties [1-3]. The polydispersity index of synthetic polymers can be close to 1, which is difficult to obtain from natural polymers. Therefore, synthetic polymers are more uniform than natural polymers. However, not all synthetic polymers are compatible with biological materials. One of the remarkable synthetic polymers is poly(styrene-maleic acid) (PSMA) due to its biological properties. The structure of PSMA can be controlled and manipulated, which makes PSMA is used for wide-ranging purposes. Research showed that PSMA was engineered as drug carriers, such as nano-micelle and hydrogel [4-7]. In its structure, PSMA has many carboxyl groups that can play a role in hydrogen bonding interactions to bind water molecules, proteins, and even drugs [8]. Recently, intermolecular interactions have been studied intensively experimentally and theoretically.

Theoretical investigations using computational can fully understand the nature and site of interaction between molecules at the level of molecules or atoms. The investigation with quantum mechanical

calculations allows the study to provide complete ideas about the mechanism at the molecular level. The density functional theory (DFT) offers an achievable computational method to include the role of electrons in quantum computations. The DFT computation can be used in various fields, such as medicine, environment, and energy. The computation can be carried out using small to large molecules such as β-Cyclodextrin and polymers [9-13]. Ferid's research team modeled the interactions that occur in the urea-water complex [10].

Computational studies of polymers usually use dimer structures due to the limitations of the computational approach [14-15]. In addition, the investigation of the dimer structure did not differ significantly from that of the trimer and oligomers [16]. Computational studies were carried out to illustrate chitosan derivatives as gene carriers [17]. Researchers also succeeded in explaining the interaction of the polyelectrolyte complex between alginate and chitosan dimers [15]. Interactions between dimer chitosan and essential amino acids were calculated to understand and predict drug delivery mechanisms by Deka and Bhattacharyya [12].

PSMA is a versatile synthetic polymer that has extensive application in aqueous solutions. Therefore, the interactions of PSMA with water molecules are fascinating to be investigated computationally. In the present study, the stabilized interactions between the PSMA and water molecules were studied by DFT. PSMA dimer structure was chosen to represent the PSMA polymer. A water microsolvation approach was used by adding one to five water molecules. This study aims to investigate the intermolecular hydrogen bond interaction in PSMA–$(H_2O)_n$ complexes by DFT/B3LYP 6–311G** with NBO, AIM, and NCI analyses. This research can be used for the development of PSMA polymer in the future.

■ COMPUTATIONAL DETAILS

Density Functional Theory Calculation

In the current study, the computational calculations of all proposed PSMA dimers and water molecules (n = 1–5) were completed with the density functional theory (DFT) by NWChem 6.8 program [16,18]. A microsolvation approach was conducted by adding one to five water molecules [15]. The lowest energy of PSMA dimer and water was obtained by individually structure optimization. The optimized molecular structure of PSMA dimer was then interacted with $(H_2O)_n$ molecules to reach the lowest energy of PSMA–$(H_2O)_n$ complexes. The stability of the molecule was evaluated by frequencies calculation. A positive value of frequency indicates that the molecule is already stable. Furthermore, Basis Set Superposition Error (BSSE) and zero-point correction to energy (ZPE) were also calculated to determine the interaction energy with the full counterpoise method [19-20]. The interaction energy was received by Eq. (1).

$$E_{int} = E_{PSMA-(H_2O)_n} - (E_{PSMA} + E_{(H_2O)_n}) + E_{BSSE\_PSMA-(H_2O)_n} \quad (1)$$

E_{PSMA/H_2O} was the lowest energy of PSMA–$(H_2O)_n$ complexes while E_{PSMA} and E_{H_2O} were the lowest energy of PSMA dimer and H_2O, respectively. $E_{BSSE\_PSMA-(H_2O)_n}$ was BSSE energy of PSMA–$(H_2O)_n$ complexes. All calculations were conducted by the DFT method with the hybrid quality of Becke's three-parameter functional (B3LYP) and the 6–311G (d,p) basis set. The PSMA–$(H_2O)_n$ complex interactions are non-covalent bonds, including hydrogen bonds [21]. Therefore, the calculation of the interaction energy helped assign the type of hydrogen bond strength.

Reactivity of the Complexes

In this study, Highest Occupied Molecular Orbital (HOMO) – Lowest Unoccupied Molecular Orbital (LUMO) energy was calculated to determine the reactivity of a molecule in the process of electron transfer in PSMA hydrogel [12,22]. HOMO energy is related to the process of releasing or donating electrons (ionization energy, I), while LUMO energy is related to the electrons' receiving process (affinity energy, A) (Eq. (2) and (3)) [23-24]. The energy gap of HOMO-LUMO energy was determined by Eq. (4). The electronegativity (χ) of the molecule was calculated by HOMO and LUMO energy values (Eq. (5)).

$$I = -E_{HOMO} \quad (2)$$

$$A = -E_{LUMO} \quad (3)$$

$$\Delta E = E_{LUMO} - E_{HOMO} \quad (4)$$

$$\chi = \frac{1}{2}(I + A) \quad (5)$$

Natural Bond Orbital (NBO) Analysis

NBO measurements were conducted to evaluate the charge distribution, interaction of electron delocalization, and type of interaction binding energy in PSMA and $(H_2O)_n$ by second-order perturbation theory [12-13,15]. The calculation was conducted by NBO 7.0 software for PSMA–$(H_2O)_n$ complexes. The orbital stabilizing energy ($E^{(2)}$) associated with the delocalization donor (i) → acceptor (j) was calculated according to Eq. (6).

$$E^{(2)} = \Delta E_{ij} = q_i \frac{F_{i,j}^2}{E_i - E_j} \quad (6)$$

where q_i is the occupancy of orbital, $F_{i,j}^2$ is NBO Fock matrix element, E_i is the energy of the NBO donor, and E_j is the energy of the NBO acceptor.

Quantum Theory Atom in Molecule (QTAIM) Analysis

The QTAIM analysis was conducted to support NBO analysis by calculating hydrogen bonding energy at Bond Critical Point (BCP) [25]. The analysis was obtained by Multiwfn 3.8 program. Parameters at the BCP that could be collected by QTAIM calculation were electron density ($\rho_{(BCP)}$), Laplacian of the charge density ($\nabla^2\rho$), ellipticity index (ε), components of Laplacian in x,y,z (λ_1,λ_2,λ_3), electronic energy density ($H_{(BCP)}$), kinetic energy density ($G_{(BCP)}$), potential energy density ($V_{(BCP)}$), and H–bond binding energy (E_{HB}) [26]. The equation of each parameter was presented in Eq. (7–9).

$$\nabla^2\rho = \lambda_1 + \lambda_2 + \lambda_3 \quad (7)$$

$$H_{(BCP)} = G_{(BCP)} + V_{(BCP)} \quad (8)$$

$$E_{HB} = (-223.8 \times \rho_{(BCP)}) + 0.7423 \text{ (for neutral H-bond)} \quad (9)$$

The relation between the values of $\nabla^2\rho$ and $H_{(BCP)}$ could identify the type of interaction that occurs in BCP. A weak covalent interaction (strong electrostatic bond) is indicated by $\nabla^2\rho$ (+) and $H_{(BCP)}$ (+). A strong interaction (strong covalent bond) is indicated by $\nabla^2\rho$ (–) and $H_{(BCP)}$ (–). A medium strength (partially covalent bond) is indicated by $\nabla^2\rho$ (+) and $H_{(BCP)}$ (–) [16]. An absolute ratio value of kinetic and potential energy density (|V/G|) is also a parameter that could categorize interactions. The value of |V/G| < 1 interprets a weak interaction, the value of 1 < |V/G| < 2 interprets a medium, and the value of |V/G| > 2 interprets a strong interaction [9,16].

Reduced Density Gradient (RDG) and Non-covalent Interaction (NCI)

RDG and NCI analyses are used to describe the non-covalent interactions in PSMA and PSMA–$(H_2O)_n$ complexes, such as steric repulsion, Van der Waals (VdW) interactions, and hydrogen bonding [27]. RDG is obtained with Eq. (10).

$$RDG = \frac{1}{2(3\pi^2)^{1/3}} \frac{|\nabla\rho_{(r)}|}{\rho_{(r)}^{4/3}} \quad (10)$$

where $|\nabla\rho_{(r)}|$ is the gradient norm of the electron density and $\rho_{(r)}$ is electron density. RDG graph and color-filled isosurface of the complexes are produced by Multiwfn 3.8 and VMD software [28]. Values of RDG and $\rho_{(r)}$ provide an analysis of non-covalent interactions in each complex through a 2D scatter graph. Additionally, the second largest eigenvalue of the electron density Hessian matrix (λ_2) at position r is an essential parameter in NCI analysis [29]. Based on the equation $\rho_{(r)}$, the sign of λ_2 changes. Thus, sign $(\lambda_2)\rho_{(r)}$ versus RDG value are plotted on the scatter graph. Strong repulsions are indicated by $(\lambda_2)\rho_{(r)} > 0$ and $\rho_{(r)} > 0$, while strong attractions are based on $(\lambda_2)\rho_{(r)} < 0$ and $\rho_{(r)} > 0$. Meanwhile, VdW interactions (the weak interaction) are presented in the value of $(\lambda_2)\rho_{(r)}$ and $\rho_{(r)} \approx 0$ [29-31].

■ RESULTS AND DISCUSSION

Optimized Structure of PSMA and Water Molecules

The geometry of molecules was measured at the level theory B3LYP/6–311G** to obtain an optimized structure with minimum energy. In this study, the dimer of PSMA was chosen to represent the PSMA polymer chain. Computational-based researchers also conducted the dimer calculation method due to the enthalpy and interaction energy between dimers, trimers, and oligomers to water were similar [15-16,32-34]. A microsolvation approach investigated the PSMA–solvent interactions. One to five water molecules interacted with PSMA. NWChem software was used to

obtain the optimized structure of PSMA and water (Fig. 1(a) and 1(c), respectively).

The optimized structure of PSMA showed linear structure due to single bonding (C–C) in the backbone. The optimized structure displayed one intramolecular hydrogen bonding (O23···H49, α = 2.389 Å), while the distance of C2–C5, C3–C4, C5–O17, and C4–O16 were 1.521, 1.525, 1.351, and 1.353 Å, respectively. The theoretical data were in good agreement with experimental data of the monomer crystal structure [35]. The experimental research showed that the C–atoms' distances were 1.52 and 1.51 Å, and the C–O distances were 1.28 and 1.31 Å. The molecular electrostatic potential (MEP) of the PSMA structure was shown as the active site to conduct interactions with water molecules (Fig. 1(b)). The red and blue colors in the MEP figure indicate the highest and lowest total density electron in structure, which reflect the negative and positive sides, respectively. O17 and O23 in the PSMA structure showed a negative side (nucleophile), whereas H49 and H64 presented a positive side (electrophile). The interaction probabilities between PSMA and $(H_2O)_n$ around O17, O23, H49, and H64 were higher than others due to a difference in charge and no obstacles. O1 presented the negative side in the water molecule, while H2 and H3 were the opposite (Fig. 1(d)).

PSMA–$(H_2O)_n$ Complexes Interaction

The optimized geometry of PSMA–$(H_2O)_n$ complexes were investigated for knowing how strong the interaction between PSMA structure and water molecules is. The most stable geometry of PSMA–$(H_2O)_n$ complexes were given in Fig. S1. The complex structure showed that PSMA–$(H_2O)_n$ complexes were linked by the hydrogen bonding O–H···H and C=O···H through carboxylate groups. In addition to the bonds between molecules PSMA and water, there were also bonds between water–water.

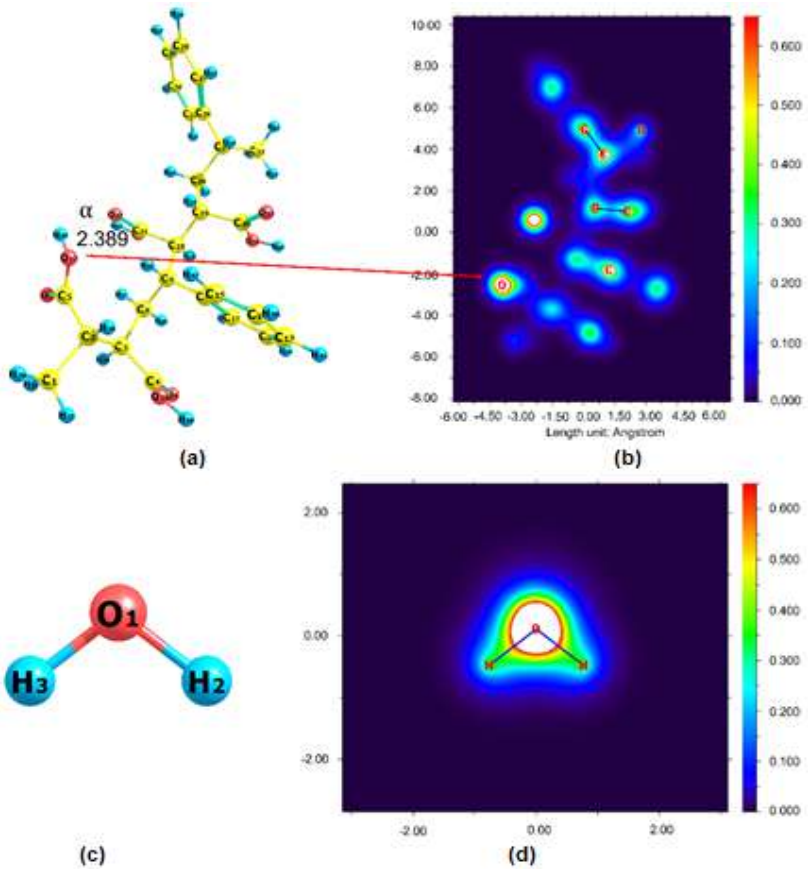

Fig 1. Optimized geometry and MEP of PSMA (a, b) and H_2O (c, d)

The hydrogen bond lengths and interaction energy of PSMA–$(H_2O)_n$ complexes were presented in Table 1. One hydrogen bond in the water molecule interacted with the carbonyl group (C=O) via a hydrogen bond (O7···H66, r_{OH} = 1.904 Å). Meanwhile, the other hydrogen bond (O65···H64) was a bit shorter (r_{OH} = 1.652 Å). The intramolecular hydrogen bond in PSMA geometry appeared between O23···H49 (r_{OH} = 1.986 Å). Three hydrogen bonds stabilized the PSMA–$(H_2O)_2$ complex. The length of the intermolecular hydrogen bond varies from 1.886–1.986 Å, and a bond was the interaction between water molecules (r_{OH} = 1.970 Å). The intramolecular hydrogen force in the PSMA–$(H_2O)_n$ complex decreased when water molecules appeared. The distance of O23···H49 in PSMA–$(H_2O)_2$ complex was more extended (r_{OH} = 2.116 Å) than PSMA–$(H_2O)_1$ complex, which was due to the interaction of O23 and H49 with water molecules. Furthermore, the addition of water molecules in the PSMA–$(H_2O)_3$, PSMA–$(H_2O)_4$, and PSMA–$(H_2O)_5$ complexes caused a cyclic formation involving several water molecules and PSMA molecules. An increase in the number of water molecules raised the number of hydrogen bonds and shortened the distance. Moreover, the data displayed all hydrogen bond lengths in PSMA–$(H_2O)_n$ complexes ranged from 1.517 Å to 1.96 Å, categorized as strong to medium hydrogen bonds [13,16]. As a comparison, the calculation with the ab initio methods, such as Hartree–Fock (HF) and Second-order Møller–Plesset perturbation theory (MP2), were conducted to determine the optimization energy of PSMA–$(H_2O)_1$ ($E_{opt_{PSMA\cdots(H_2O)_1}}$) (Table S1). The energy from DFT was lower than HF and MP2, indicating that the calculation with the DFT method was more stable and reliable for this study.

Hydrogen bond interaction is classified based on the energy value. The energy above 20 kcal/mol is classified as a strong bond, while the energy of 4–20 kcal/mol is classified as a moderate bond. A weak bond is indicated by the energy below 4 kcal/mol. PSMA–$(H_2O)_5$ and PSMA–$(H_2O)_4$ were categorized as a strong hydrogen bond, whereas the rest of PSMA–(H_2O) complexes were classified as a moderate hydrogen bond interaction. The interaction energy of the PSMA–$(H_2O)_n$ complexes escalated as the number of water molecules increased. The high water uptake is essential for a material to be used as a water-based material [1,36-38]. Besides, this particular examination revealed that the increase in water molecules further augmented the hydrogen bonds formed, shortened the hydrogen bonds, and enhanced the interaction energy in PSMA–$(H_2O)_n$ complexes. These data showed that water molecules are maintained in the PSMA matrix through strong bonds.

The results of modeling the interaction energy of PSMA–$(H_2O)_n$ complexes are restricted to a minimum of five water molecules. It was selected to represent a microsolvation model in the gas phase calculations [15]. The result may change if H_2O molecules are increased

Table 1. The interaction energy of PSMA–$(H_2O)_n$ complexes

Complexes	Hydrogen bond (Å)	Interaction energy (kcal/mol)
PSMA–$(H_2O)_1$	r(O7···H66) = 1.904 r(O65···H64) = 1.652	–12.517
PSMA–$(H_2O)_2$	r(O7···H66) = 1.886 r(O65···H64) = 1.986 r(O65···H68) = 1.970	–21.725
PSMA–$(H_2O)_3$	r(O7···H66) = 1.795 r(O65···H64) = 1.844 r(O23···H67) = 1.929 r(O65···H68) = 1.795 r(O69···H73) = 1.710 r(O72···H49) = 1.605	–32.655
PSMA–$(H_2O)_4$	r(O7···H66) = 1.785 r(O65···H76) = 1.766 r(O23···H67) = 1.815 r(O65···H68) = 1.814 r(O69···H73) = 1.745 r(O72···H49) = 1.543 r(O74···H64) = 1.617	–47.474
PSMA–$(H_2O)_5$	r(O7···H66) = 1.749 r(O65···H76) = 1.760 r(O23···H67) = 1.869 r(O65···H79) = 1.771 r(O69···H73) = 1.692 r(O72···H49) = 1.521 r(O23···H71) = 1.957 r(O74···H64) = 1.617 r(O78···H68) = 1.712	–56.660

(e.g., 50 to 100 molecules). The changes are due to increased intermolecular forces, dispersion, many-body effect, etc. [15,39-40]. Moreover, increasing the number of molecules is modeled by DFT can elevate the computational cost. Nevertheless, this simple approach allowed observing the PSMA–$(H_2O)_n$ complexes properties. The calculations using dimer structure and small molecules (1 to 5 molecules) had been carried out by researchers to study optimized structures, properties, and interactions mechanisms [10,13,15-16]. Therefore, the data in this study could still be relied upon by future comprehension computational investigations carried out with elaboration of solvation models.

The construction of intermolecular hydrogen bonds in the complex structures influenced the intramolecular structure of PSMA. The hydration process tended to weaken the C=O and O–H bonds of PSMA. The increase in bond length indicated this. Table 2 presented C=O and O–H bond lengths in the PSMA structure before and after hydration. These results also showed that PSMA could dissociate in the presence of one water molecule, which could be seen at the O34–H64 bond length of more than 1 Å. In addition, H64 was more easily dissociated than H49.

Parameters Reactivity of the Complexes

Molecular reactivity can be predicted by means of molecular orbital theory. Quantum chemical parameters that describe the reactivity of molecules are electron affinity (A), ionization energy (I), and electronegativity (χ). The parameters were used to determine the HOMO and LUMO energies. HOMO and LUMO energy describe the molecular ability to donate and receive electrons, respectively [23]. The energy gap between HOMO and LUMO defines the chemical activities of molecules. All molecular parameters are presented in Table 3.

The HOMO–LUMO energy gap on the PSMA complex decreased due to the presence of one water molecule (6.04 → 5.8 eV). Then, the value slightly increased to 6.47 eV on PSMA–$(H_2O)_2$. The addition of two water molecules on PSMA presented the greatest ΔE. The energy gap gradually declines as the water molecules increase. The energy gap value of PSMA–$(H_2O)_3$, PSMA–$(H_2O)_4$, and the PSMA–$(H_2O)_5$ were 6.44, 5.84, and 5.87 eV, respectively. A higher ΔE indicated that the complex was harder to transfer electrons. On the other hand, a lower ΔE showed the complex was easier to transfer electrons [41]. Compared

Table 2. Bond length detail of PSMA and PSMA–$(H_2O)_n$ complexes

Complexes	Bond length (Å)			
	C5=O7	C21=O23	O17–H49	O34–H64
PSMA	1.2133	1.2156	0.9738	0.9736
PSMA–$(H_2O)_1$	1.2219	1.2320	0.9777	1.0104
PSMA–$(H_2O)_2$	1.2225	1.2289	0.9755	0.9984
PSMA–$(H_2O)_3$	1.2320	1.2267	0.9914	1.0114
PSMA–$(H_2O)_4$	1.2323	1.2358	1.0256	1.0148
PSMA–$(H_2O)_5$	1.2332	1.2350	1.0288	1.0147

Table 3. The chemical parameters of the complexes

Complexes	E_{HOMO} (eV)	E_{LUMO} (eV)	ΔE (eV)	A (eV)	I (eV)	χ (eV)
0	–6.508290	–0.463756	6.044534	0.463756	6.50829	-3.48602
1	–6.455376	–0.574396	5.880980	0.574396	6.455376	-3.51489
2	–6.497964	–0.025598	6.472366	0.025598	6.497964	-3.26178
3	–6.462384	–0.018804	6.443580	0.018804	6.462384	-3.24059
4	–6.423786	–0.575764	5.848022	0.575764	6.423786	-3.49978
5	–6.465953	–0.595711	5.870242	0.595711	6.465953	-3.53083

to the individual PSMA structure, the reduced energy gap allowed the electron to be easily transferred in the complex structures.

The HOMO–LUMO results were also supported by the affinity energy, ionization energy, and electronegativity (A, I, and χ, respectively). The affinity energy for the complex was enhanced with the increase in water molecules, which indicated the stronger the PSMA and water molecules were attracted and bound to each other [42-43]. The decrease in ionization energy represented that the complex was easier to transfer electrons [44-45]. Moreover, the electronegativity value became more negative with the increase in water molecules, demonstrating that the PSMA and the water molecules attracted each other [45]. Thus, the promising hydrogel is formed from a different electronegativity material with the target molecule to attract it into the matrix [16,46-47].

NBO Analysis

In this study, the natural orbitals involved in H–bonding interactions were investigated by the NBO approach with the DFT method to support interaction energy data. The analysis was done because the interaction energy result is insufficient to identify the hydrogen bond strength [10,48]. The type of hydrogen bonding interaction was characterized by the stabilizing energy value ($E^{(2)}$) that represented the delocalization of electron from a donor (i) (a lone pair orbital (LP) or an occupied bond (BD)) to acceptor (j) (an unoccupied anti-bond orbital (BD*)) (Table S2) [9,13]. From the NBO data, it has become clear that hydrogen bonds were formed between the PSMA and the water molecules and between the water molecules themselves. Moreover, the result supported the previous statement on the increase in intermolecular hydrogen bonds as donors and acceptors enhance.

The PSMA–$(H_2O)_1$ complex was stabilized by the carboxyl group (C=O, O–H) of PSMA and the O–H groups in the water molecule. NBO data proved that interaction between O7 lone pair donating orbital and O65–H66 antibonding orbital was given a weaker stabilizing energy compared to O65···H64 (LP(2) O65 → BD*(O34–H64), 34 kcal/mol). A similar report was also stated for the PSMA–$(H_2O)_2$. In addition, there was an H_2O···H_2O interaction in PSMA–$(H_2O)_2$ complex that LP(1) O65 contributed as the donor and BD*(H68–O69) as the acceptor with an $E^{(2)}$ of 7.7 kcal/mol.

In PSMA–$(H_2O)_3$ complex, LP(1) O65, LP(2) O65, LP(2) O69 contributed as the donors and BD*(H68–O69) and BD*(O72–H73) as the acceptors in the interaction between water molecules and participated to the stabilization by 6.50, 14.15, and 27.52 kcal/mol, respectively. The carbonyl group of the PSMA structure contributed to intermolecular hydrogen bond interactions through LP(1) O7 → BD*(O65–H66), LP(2) O7 → BD*(O65–H66), LP(1) O23 → BD*(O65–H67), and LP(2) O23 → BD*(O65–H67) which the calculated secondary perturbation energies were 9.28, 9.41, 3.66, and 8.52 kcal/mol, respectively. The carboxyl group via O–H also participated in the hydrogen bonding as acceptors, while oxygen in water molecules had a role as donors. The energies of LP(1) O65 → BD*(O34–H64) and LP(2) O65 → BD*(O34–H64) were about 4.97 and 12.17 kcal/mol, respectively. In addition, LP(2) O72 → BD*(O17–H49) provided a stronger stabilization of 39.50 kcal/mol, which is classified as a strong hydrogen bond.

The PSMA–$(H_2O)_4$ and the PSMA–$(H_2O)_5$ complex showed hydrogen bond interactions that resemble the PSMA–$(H_2O)_3$ because the two carboxylate groups in PSMA interacted with water molecules. The most considerable hydrogen bonding occurred on LP(2) O72 → BD*(O17–H49) in the PSMA–$(H_2O)_4$ and the PSMA–$(H_2O)_5$ complex with energy stability of 48.33 and 50.32 kcal/mol, respectively. The increase in energy stability of O72···H49–O17 in the PSMA–$(H_2O)_3$, the PSMA–$(H_2O)_4$, and the PSMA–$(H_2O)_5$ complexes caused an increase in the length of the H49–O17 bond and a shorter interaction distance (Table 1 and 2, respectively). The bond length in the range of 1.5–1.6 Å and energy stability of >20 kcal/mol made the interaction in O72···H49 was categorized as a strong hydrogen bonding system [13]. High stabilization energy means that the stronger the hydrogen bonding interaction, the easier the proton transfer [10,49-51].

The NBO data could also explain the increase in length of C5=O7 in the PSMA–$(H_2O)_1$ to PSMA–$(H_2O)_5$ complexes by an increase in the stability energy on LP(1) O7 → BD*(O65–H66). Furthermore, the energy was in line with the increase in water molecules (n). Fig. 2 displayed the good correlation between $E^{(2)}$ of O7···H66 and $(H_2O)_n$ with an R^2 = 0.994. Therefore, it can be inferred that the hydrogen bond interaction of the PSMA···H_2O complex was strong, which was great for maintaining water inside its three-dimensional matrix [38,52].

QTAIM Analysis

The QTAIM analysis was conducted due to the study of hydrogen bonding interaction type at BCP. Therefore, essential topological parameters, such as $\nabla^2\rho$, ρ, G, H, V, and ratio |V/G|, were crucial to identify the H–bond critical points (3,–1) achieved from QTAIM computation [9]. The Multiwfn program calculated the QTAIM calculation. The BCP of PSMA–$(H_2O)_n$ complexes were presented in Fig. 3, whereas the parameters were displayed in Table S3.

According to BCP visualization, new hydrogen bonding was formed in PSMA–$(H_2O)_n$ complexes when water molecules were added. All BCP presented positive value from $\nabla^2\rho$, and major BCP showed negative value from $H_{(BCP)}$. There were small portions of BCP that showed positive values from $H_{(BCP)}$. Therefore, the PSMA–$(H_2O)_n$ complexes were considered weak to medium interactions. It was also supported by the value of the |V/G| ratio at most BCPs in the range of 1–2, while the minority presented |V/G| < 1. The QTAIM calculation supported the claim that the hydrogen bond of O7···H66 enhanced with the increase in the number of water molecules. The same thing was found in the O72···H49 bond in PSMA–$(H_2O)_3$, PSMA–$(H_2O)_4$, and PSMA–$(H_2O)_5$. The results showed that the hydrogen bond energy in the complex was in the range of –2.3407 to –14.946 kcal/mol. The results showed similar hydrogen

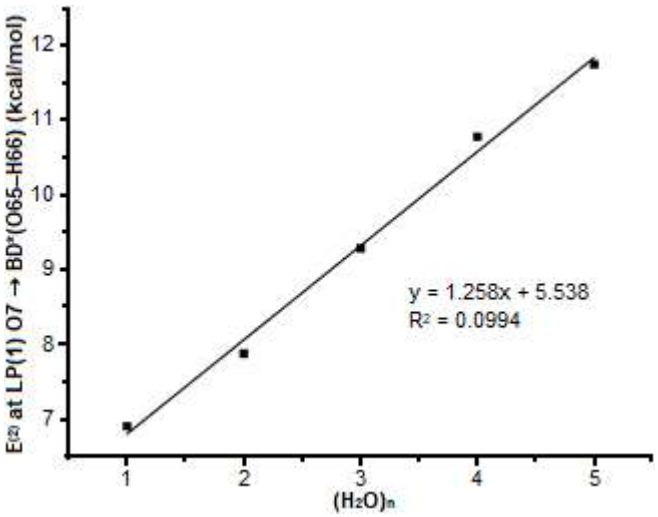

Fig 2. Correlation of the $E^{(2)}$ of O7···H66 versus the number of H_2O molecules within PSMA–$(H_2O)_n$ complexes

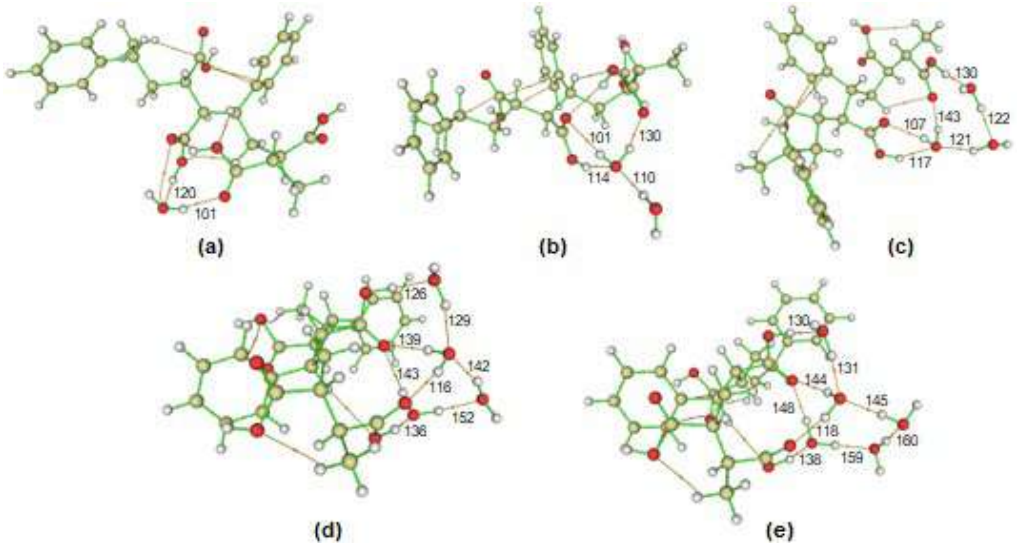

Fig 3. BCP for (a) PSMA–$(H_2O)_1$, (b) PSMA–$(H_2O)_2$, (c) PSMA–$(H_2O)_3$, (d) PSMA–$(H_2O)_4$, and (e) PSMA–$(H_2O)_5$

bonding values in previous computational studies [9,16,53] (Table S4). In addition, both NBO and QTAIM analyses showed the strongest intermolecular hydrogen bond at $O_{72}\cdots H_{49}$ in PSMA–$(H_2O)_5$ complex. The QTAIM results successfully demonstrated that PSMA was a potential polymeric material as a hydrogel due to its ability to make medium hydrogen bonds with water molecules.

RDG and NCI Analyses

The NCI study described intra-intermolecular interactions and assessed the nature of weak interactions in PSMA–$(H_2O)_n$ complexes. The NCI index gave additional information regarding non-covalent interaction based on RDG [54]. The 2D RDG graph of sign $(\lambda_2)\rho_{(r)}$ versus RDG value was plotted in Fig. 4. Blue, green, and red colors in the RDG graph represented the

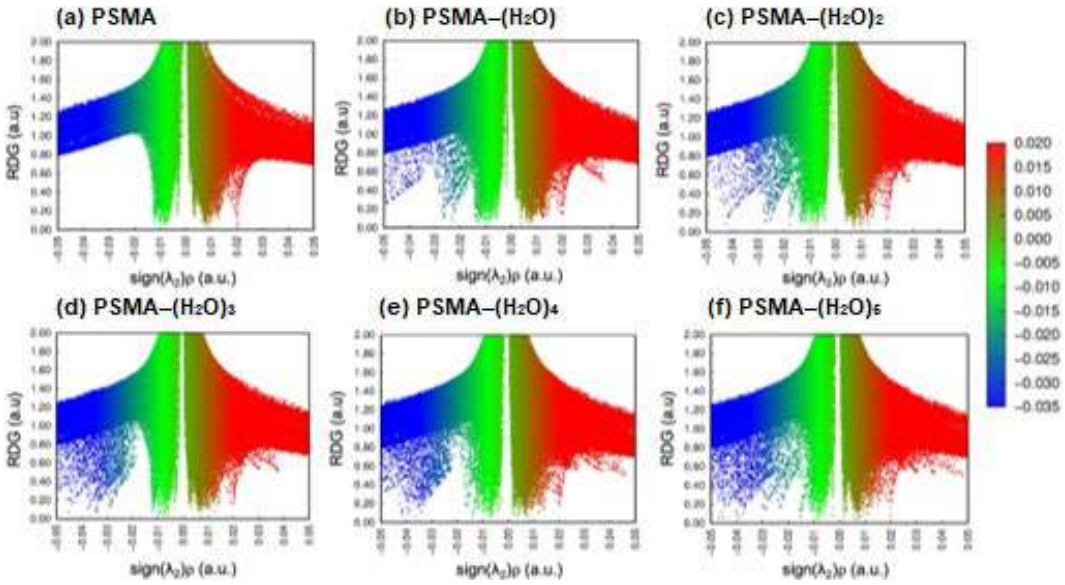

Fig 4. RDG's scatter graphs of PSMA and PSMA–$(H_2O)_n$ complexes; n = 1–5

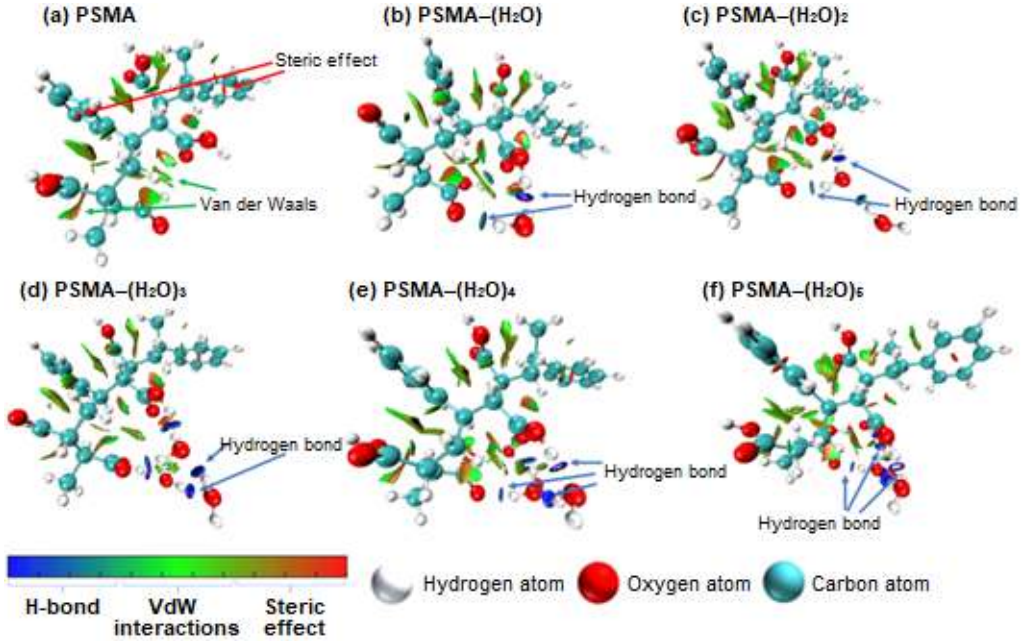

Fig 5. Three-dimensional RDG isosurfaces of PSMA and PSMA–$(H_2O)_n$ complexes; n = 1–5

hydrogen bond, the VdW interaction, and the steric effect, respectively. Visualization of non-covalent interaction was performed with a three-dimensional (3D) RDG isosurface (Fig. 5) to provide a deeper understanding. In the 3D RDG graph, green, blue, and red represented the VdW interaction, H-bond, and steric effect.

The PSMA graph emphasized that VdW interaction and steric effect were dominant in the structure (Fig. 4(a)). The intramolecular bond of O23···H49 was shown as VdW interaction (green color) (Fig. 5(a)). The steric effect occurred due to the presence of phenyl rings of the PSMA structure. On the other hand, the PSMA–$(H_2O)_n$ complexes became denser in the blue and green areas (Fig. 4(b–e)). The trends indicated an increase in the number of hydrogen bonds and VdW interaction. Fig. 5(b–e) supported the explanation by showing more blue and green colors. The computational investigation revealed that PSMA was able to interact strongly with water molecules. These results also reinforced the previous experimental research that stated the PSMA hydrogel with polyethylene glycol as a crosslinker could swell up to 14.58% [8]. The other research of PSMA hydrogel presented the total water absorption ratio in the range of 13.6–71 g/g [55].

■ CONCLUSION

The *in silico* study of PSMA–$(H_2O)_n$ complexes were carried out to evaluate the interaction between PSMA and $(H_2O)_n$ (n = 1–5). The calculation was conducted by the DFT method and 6–311G** basis set. By the structure optimization of PSMA dimer, water, and PSMA–$(H_2O)_n$ complexes, serial properties of those complexes were attained. The hydration affects the intramolecular structure of PSMA. The interaction between PSMA and water molecules was conducted at carboxyl groups. The increase in the number of water molecules enhanced the interaction energy and reactivity of PSMA–$(H_2O)_n$ complexes. The intermolecular hydrogen bonds in the complexes were evaluated by NBO, AIM, and RDG–NCI analyses. The easiest electron lone-pairs donating was found on PSMA–$(H_2O)_5$ complex through LP(2) O72 → BD*(O17–H49) with the stabilizing energy of 50.32 kcal/mol. The AIM results also approved the statement. Moreover, the RDG and NCI analyses supported the results by improving hydrogen bond interactions as the water molecule increased. The examination categorized the hydrogen bond between PSMA and water as the medium to the strong bond interaction. All data presented indicate PSMA is a potential polymer to be developed in an aqueous solution

■ ACKNOWLEDGMENTS

The research was funded by Atma Jaya Catholic University of Indonesia (Number: 0659/III/LPPM-PM.10.01/05/2021).

■ REFERENCES

[1] Anugrah, D.S.B., Ramesh, K., Kim, M., Hyun, K., and Lim, K.T., 2019, Near-infrared light-responsive alginate hydrogels based on diselenide-containing cross-linkage for on demand degradation and drug release, *Carbohydr. Polym.*, 223, 115070.

[2] Sung, Y.K., and Kim, S.W., 2020, Recent advances in polymeric drug delivery systems, *Biomater. Res.*, 24 (1), 12.

[3] Jia, Y.G., Jin, J., Liu, S., Ren, L., Luo, J., and Zhu, X.X., 2018, Self-healing hydrogels of low molecular weight poly(vinyl alcohol) assembled by host-guest recognition, *Biomacromolecules*, 19 (2), 626–632.

[4] Deák, Á., Sebők, D., Csapó, E., Bérczi, A., Dékány, I., Zimányi, L., and Janovák, L., 2019, Evaluation of pH-responsive poly(styrene-co-maleic acid) copolymer nanoparticles for the encapsulation and pH-dependent release of ketoprofen and tocopherol model drugs, *Eur. Polym. J.*, 114, 361–368.

[5] Larson, N., Greish, K., Bauer, H., Maeda, H., and Ghandehari, H., 2011, Synthesis and evaluation of poly(styrene-co-maleic acid) micellar nanocarriers for the delivery of tanespimycin, *Int. J. Pharm.*, 420 (1), 111–117.

[6] Fang, J., Gao, S., Islam, R., Nema, H., Yanagibashi, R., Yoneda, N., Watanabe, N., Yasuda, Y., Nuita, N., Zhou, J.R., and Yokomizo, K., 2021, Styrene maleic acid copolymer-based micellar formation of temoporfin (SMA@mTHPC) behaves as a nanoprobe for tumor-targeted photodynamic

therapy with a superior safety, *Biomedicines*, 9 (10), 1493.

[7] Moghadam, P.N., Azaryan, E., and Zeynizade, B., 2010, Investigation of poly(styrene-alt-maleic anhydride) copolymer for controlled drug delivery of ceftriaxone antibiotic, *J. Macromol. Sci., Part A: Pure Appl. Chem.*, 47 (8), 839–848.

[8] Anugrah, D.S.B., Patil, M.P., Li, X., Le, C.M.Q., Ramesh, K., Kim, G.D., Hyun, K., and Lim, K.T., 2020, Click-cross-linked, doxorubicin-loaded hydrogels based on poly(styrene-alt-maleic anhydride), *eXPRESS Polym. Lett.*, 14 (3), 248–260.

[9] Safia, H., Ismahan, L., Abdelkrim, G., Mouna, C., Leila, N., and Fatiha, M., 2019, Density functional theories study of the interactions between host β-cyclodextrin and guest 8-anilinonaphthalene-1-sulfonate: Molecular structure, HOMO, LUMO, NBO, QTAIM and NMR analyses, *J. Mol. Liq.*, 280, 218–229.

[10] Hammami, F., Ghalla, H., and Nasr, S., 2015, Intermolecular hydrogen bonds in urea-water complexes: DFT, NBO, and AIM analysis, *Comput. Theor. Chem.*, 1070, 40–47.

[11] Venkataramanan, N.S., Suvitha, A., and Kawazoe, Y., 2017, Intermolecular interaction in nucleobases and dimethyl sulfoxide/water molecules: A DFT, NBO, AIM and NCI analysis, *J. Mol. Graphics Modell.*, 78, 48–60.

[12] Deka, B.C., and Bhattacharyya, P.K., 2017, DFT study on host-guest interaction in chitosan–amino acid complexes, *Comput. Theor. Chem.*, 1110, 40–49.

[13] Rahmawati, S., Radiman, C.L., and Martoprawiro, M.A., 2018, Density functional theory (DFT) and natural bond orbital (NBO) analysis of intermolecular hydrogen bond interaction in "Phosphorylated nata de coco - water", *Indones. J. Chem.*, 18 (1), 173–178.

[14] Cortes, E., Márquez, E., Mora, J.R., Puello, E., Rangel, N., De Moya, A., and Trilleras, J., 2019, Theoretical study of the adsorption process of antimalarial drugs into acrylamide-base hydrogel model using DFT methods: The first approach to the rational design of a controlled drug delivery system, *Processes*, 7 (7), 396.

[15] Costa, M.P.M., Prates, L.M., Baptista, L., Cruz, M.T.M., and Ferreira, I.L.M., 2018, Interaction of polyelectrolyte complex between sodium alginate and chitosan dimers with a single glyphosate molecule: A DFT and NBO study, *Carbohydr. Polym.*, 198, 51–60.

[16] Siahaan, P., Sasongko, N.A., Lusiana, R.A., Prasasty, V.D., and Martoprawiro, M.A., 2021, The validation of molecular interaction among dimer chitosan with urea and creatinine using density functional theory: In application for hemodyalisis membrane, *Int. J. Biol. Macromol.*, 168, 339–349.

[17] Deka, B.C., and Bhattacharyya, P.K., 2015, Understanding chitosan as a gene carrier: A DFT study, *Comput. Theor. Chem.*, 1051, 35–41.

[18] Martins, J.B.L., Quintino, R.P., Politi, J.R.S., Sethio, D., Gargano, R., and Kraka, E., 2020, Computational analysis of vibrational frequencies and rovibrational spectroscopic constants of hydrogen sulfide dimer using MP2 and CCSD(T), *Spectrochim. Acta, Part A*, 239, 118540.

[19] Nikoo, S., and Rawson, J.M., 2021, Assessment of computational methods for calculating accurate non-covalent interaction energies in 1,2,3,5-dithiadiazolyl radicals, *Cryst. Growth Des.*, 21 (9), 4878–4891.

[20] Lei, J., Zhang, J., Feng, G., Grabow, J.U., and Gou, Q., 2019, Conformational preference determined by inequivalent n-pairs: Rotational studies on acetophenone and its monohydrate, *Phys. Chem. Chem. Phys.*, 21 (41), 22888–22894.

[21] Řezáč, J., and Hobza, P., 2016, Benchmark calculations of interaction energies in noncovalent complexes and their applications, *Chem. Rev.*, 116 (9), 5038–5071.

[22] Li, L., Wu, C., Wang, Z., Zhao, L., Li, Z., Sun, C., and Sun, T., 2015, Density functional theory (DFT) and natural bond orbital (NBO) study of vibrational spectra and intramolecular hydrogen bond interaction of l-ornithine–l-aspartate, *Spectrochim. Acta, Part A*, 136, 338–346.

[23] Abou-Yousef, H., Dacrory, S., Hasanin, M., Saber, E., and Kamel, S., 2021, Biocompatible hydrogel based on aldehyde-functionalized cellulose and

chitosan for potential control drug release, *Sustainable Chem. Pharm.*, 21, 100419.

[24] Awasthi, S., Gaur, J.K., Pandey, S.K., Bobji, M.S., and Srivastava, C., 2021, High-strength, strongly bonded nanocomposite hydrogels for cartilage repair, *ACS Appl. Mater. Interfaces*, 13 (21), 24505–24523.

[25] Rincón, D.A., Doerr, M., and Daza, M.C., 2021, Hydrogen bonds and n → π* interactions in the acetylation of propranolol catalyzed by *Candida antarctica* lipase B: A QTAIM study, *ACS Omega*, 6 (32), 20992–21004.

[26] Emamian, S., Lu, T., Kruse, H., and Emamian, H., 2019, Exploring nature and predicting strength of hydrogen bonds: A correlation analysis between atoms-in-molecules descriptors, binding energies, and energy components of symmetry-adapted perturbation theory, *J. Comput. Chem.*, 40 (32), 2868–2881.

[27] Shen, J., Wu, X., Yu, J., Yin, F., Hao, L., Lin, C., Zhu, L., Luo, C., Zhang, C., and Xu, F., 2021, Hydrogen bonding interactions between arsenious acid and dithiothreitol/dithioerythritol at different pH values: A computational study with an explicit solvent model, *New J. Chem.*, 45 (43), 20181–20192.

[28] An, X., Kang, Y., and Li, G., 2019, The interaction between chitosan and tannic acid calculated based on the density functional theory, *Chem. Phys.*, 520, 100–107.

[29] Cao, S., Wang, J., Ding, Y., Sun, M., and Ma, F., 2017, Visualization of weak interactions between quantum dot and graphene in hybrid materials, *Sci. Rep.*, 7 (1), 417.

[30] Wang, J., Wang, C., Zhang, H., Liu, Y., and Shi, T., 2021, Mass spectral and theoretical investigations of the transient proton-bound dimers on the cleavage processes of the peptide GHK and its analogues, *RSC Adv.*, 11 (7), 4077–4086.

[31] Thakur, T.S., and Singh, S.S., 2015, Studying the role of C=O···C=O, C=O···N–O, and N–O···N–O dipole–dipole interactions in the crystal packing of 4-nitrobenzoic acid and 3,3′-dinitrobenzophenone polymorphs: An experimental charge density study, *Cryst. Growth Des.*, 15 (7) 3280–3292.

[32] Cisneros, G.A., Wikfeldt, K.T., Ojamäe, L., Lu, J., Xu, Y., Torabifard, H., Bartók, A.P., Csányi, G., Molinero, V., and Paesani, F., 2016, Modeling molecular interactions in water: From pairwise to many-body potential energy functions, *Chem. Rev.*, 116 (13), 7501–7528.

[33] Lusiana, R.A., Sasongko, N.A., Sangkota, V.D.A., Prasetya, N.B.A., Siahaan, P., Kiswandono, A.A., and Othman, M.H.D., 2020, In-vitro study of polysulfone-polyethylene glycol/chitosan (PEG-PSf/CS) membranes for urea and creatinine permeation, *J. Kim. Sains Apl.*, 23 (8), 283–289.

[34] Lima, F.C.D.A., Alvim, R.S., and Miranda, C.R., 2017, From single asphaltenes and resins to nanoaggregates: A computational study, *Energy Fuels*, 31 (11), 11743–11754.

[35] Verweel, H.J., and Macgillavry, C.H., 1938, Crystal structure of succinic acid, *Nature*, 142 (3586), 161–162.

[36] Siboro, S.A.P., Anugrah, D.S.B., Ramesh, K., Park, S.H., Kim, H.R., and Lim, K.T., 2021, Tunable porosity of covalently crosslinked alginate-based hydrogels and its significance in drug release behavior, *Carbohydr. Polym.*, 260, 117779.

[37] Eivazzadeh-Keihan, R., Khalili, F., Khosropour, N., Aliabadi, H.A.M., Radinekiyan, F., Sukhtezari, S., Maleki, A., Madanchi, H., Hamblin, M.R., Mahdavi, M., Haramshahi, S.M.A., Shalan, A.E., and Lanceros-Méndez, S., 2021, Hybrid bionanocomposite containing magnesium hydroxide nanoparticles embedded in a carboxymethyl cellulose hydrogel plus silk fibroin as a scaffold for wound dressing applications, *ACS Appl. Mater. Interfaces*, 13 (29), 33840–33849.

[38] Zhang, Y.S., and Khademhosseini, A., 2017, Advances in engineering hydrogels, *Science*, 356 (6337), eaaf3627.

[39] Liu, C., Min, F., Liu, L., and Chen, J., 2019, Density functional theory study of water molecule adsorption on the α-quartz (001) surface with and without the presence of Na^+, Mg^{2+}, and Ca^{2+}, *ACS Omega*, 4 (7), 12711–12718.

[40] Chen, M., Ko, H.Y., Remsing, R.C., Calegari Andrade, M.F., Santra, B., Sun, Z., Selloni, A., Car, R., Klein, M.L., Perdew, J.P., and Wu, X., 2017, Ab initio theory and modeling of water, *Proc. Natl. Acad. Sci. U.S.A.*, 114 (41), 10846–10851.

[41] Rieloff, E., Tully, M.D., and Skepö, M., 2019, Assessing the intricate balance of intermolecular interactions upon self-association of intrinsically disordered proteins, *J. Mol. Biol.*, 431 (3), 511–523.

[42] Uto, T., and Yui, T., 2018, DFT optimization of isolated molecular chain sheet models constituting native cellulose crystal structures, *ACS Omega*, 3 (7), 8050–8058.

[43] You, W., Liu, Y., Howe, J.D., and Sholl, D.S., 2018, Competitive binding of ethylene, water, and carbon monoxide in metal-organic framework materials with open Cu sites, *J. Phys. Chem. C*, 122 (16), 8960–8966.

[44] Gershoni-Poranne, R., Rahalkar, A.P., and Stanger, A., 2018, The predictive power of aromaticity: quantitative correlation between aromaticity and ionization potentials and HOMO–LUMO gaps in oligomers of benzene, pyrrole, furan, and thiophene, *Phys. Chem. Chem. Phys.*, 20 (21), 14808–14817.

[45] Li, H., Zhu, W., Zhu, S., Xia, J., Chang, Y., Jiang, W., Zhang, M., Zhou, Y., and Li, H., 2016, The selectivity for sulfur removal from oils: An insight from conceptual density functional theory, *AIChE J.*, 62 (6), 2087–2100.

[46] Subramanian, B., Rameshbabu, A.P., Ghosh, K., Jha, P.K., Jha, R., Murugesan, S., Chattopadhyay, S., Dhara, S., Mondal, K.C., Basak, P., and Guha, S.K., 2019, Impact of styrene maleic anhydride (SMA) based hydrogel on rat fallopian tube as contraceptive implant with selective antimicrobial property, *Mater. Sci. Eng., C*, 94, 94–107.

[47] Ngo, T.M.P., Dang, T.M.Q., Tran, T.X., and Rachtanapun, P., 2018, Effects of zinc oxide nanoparticles on the properties of pectin/alginate edible films, *Int. J. Polym. Sci.*, 2018, 5645797.

[48] Ghosh, S., Chopra, P., and Wategaonkar, S., 2020, C–H···S Interaction exhibits all the characteristics of conventional hydrogen bonds, *Phys. Chem. Chem. Phys.*, 22 (31), 17482–17493.

[49] Yamada, Y., Goto, Y., Fukuda, Y., Ohba, H., and Nibu, Y., 2020, Excited-state dynamics affected by switching of a hydrogen-bond network in hydrated aminopyrazine clusters, *J. Phys. Chem. A*, 124 (48), 9963–9972.

[50] Lütteke, T., and Martin, F., 2015, *Glycoinformatics*, Humana Press, New Jersey, US.

[51] Li, Z.J., Srebnik, S., and Rojas, O.J., 2021, Revisiting cation complexation and hydrogen bonding of single-chain polyguluronate alginate, *Biomacromolecules*, 22 (9), 4027–4036.

[52] Li, J., and Mooney, D.J., 2016, Designing hydrogels for controlled drug delivery, *Nat. Rev. Mater.*, 1 (12), 16071.

[53] Wang, B., Jiang, W., Dai, X., Gao, Y., Wang, Z., and Zhang, R.Q., 2016, Molecular orbital analysis of the hydrogen bonded water dimer, *Sci. Rep.*, 6 (1), 22099.

[54] Akman, F., Issaoui, N., and Kazachenko, A.S., 2020, Intermolecular hydrogen bond interactions in the thiourea/water complexes (Thio-$(H_2O)_n$) (n = 1, ···, 5): X-ray, DFT, NBO, AIM, and RDG analyses, *J. Mol. Model.*, 26 (6), 161.

[55] Tang, C., Ye, S., and Liu, H., 2007, Electrospinning of poly(styrene-co-maleic anhydride) (SMA) and water-swelling behavior of crosslinked/hydrolyzed SMA hydrogel nanofibers, *Polymer*, 48 (15) 4482–4491.

Preliminary Evaluation of Gunshot Residue (GSR) Using 3-Aminophenol as a Substitute in Modified Griess Test

Siti Nurhazlin Jaluddin[1*], Zainiharyati Mohd Zain[1], Mohamed Izzharif Abdul Halim[1], Muhd Fauzi Safian[1], Mohd Azri Abdul Rani[1], and Mohamed Sazif Mohamed Subri[2]

[1]*Faculty of Applied Sciences, Universiti Teknologi MARA, 40450 Shah Alam, Selangor, Malaysia*

[2]*Forensic Laboratory Royal Malaysia Police, 43200, Cheras, Selangor, Malaysia*

* ***Corresponding author:***

email: hazlinjaluddin@gmail.com

Received: August 6, 2021
Accepted: October 26, 2021

DOI: 10.22146/ijc.68265

Abstract: *In forensic ballistics, gunshot residue (GSR) particles can be detected using screening or presumptive tests which are mainly focused on the chromophoric reaction. Most tests serve as an initial indication for a forensic investigator at the crime scene before instrumental analysis for definitive identification. The screening methods are known to be convenient, have fast analysis, and minimal preparation. In GSR analysis, the well-known method of detecting GSR known as the Modified Griess Test (MGT) requires acid and heat for the reaction. Therefore, this study demonstrated a new and rapid screening test named the Rapid Griess Test (RGT) for the detection of GSR. This study intends to improve the functionality of previous screening reagents in determining nitrite (NO_2^-), the composition present after shooting activity. To do this, chemical reagents with an amino group, 3-aminophenol, were substituted with alpha-naphthol. The experiment showed that the reactions were positive color changes using standard NO_2^- and real GSR samples. The diazotization reactions involving sulfanilic acid and 3-aminophenol produced azo dyes that changed the solution from colorless to orange in the presence of NO_2^-. The RGT reagent will make it possible to avoid using heat and the addition of acetic acids in a sample to form chromophoric reactions. Moreover, the colorimetric method using Video Spectral Comparator (VSC) showed that RGT had higher intensity of the orange color when compared to MGT.*

Keywords: *gunshot residue (GSR); colorimetric method; screening test; nitrite (NO_2^-) detection; Modified Griess Test*

■ INTRODUCTION

GSR evidence has become a substantial help in certain investigations by providing clues of the individuals who fired a gun. It has been used to estimate firing distances, identify bullet holes, differentiate entry and exit wounds, establish the kind of ammunition used, trace the trajectory of a projectile, and determine whether or not a person has discharged a firearm [1-4]. Generally, only trace amounts of GSR are deposited on the back of the hand, face, hair, and clothing of the shooter, and this material can be used to determine if the person has discharged a weapon. The analysis of GSR is essential evidence in forensics, and there is a need to develop a more sensitive and selective technique that performs more conclusive results for a more significant number of cases [5].

In recent years, the focus in forensic investigation has shifted towards portable and fast methods that can be performed *in-situ* rather than in an analytical laboratory [6-7]. Unfortunately, the current technique for detecting GSR cannot provide fast detection at a crime scene [8]. The screening method is an essential technique in forensic analysis that can minimize the time taken to analyze data. This technique can be achieved if the screening and confirmatory methods can be done at the crime scene. Most forensic analysts apply the use of color changes in order to determine the presence of nitro groups or heavy metals in GSR

particles [9-10]. Griess [11] invented a novel screening method for detecting NO_2^- in gunshot residues in 1858. This method, also known as The Griess test, is used to detect the presence of NO_2^- by the combustion product of smokeless gun powder.

Nowadays, the Modified Griess Test (MGT) has been used to replace the original Griess test. The MGT has avoided the use of the toxic chemical 1-naphthylethylenediamine dihydrochloride that was used in the original Griess test. The modified method is safer and uses a less expensive reagent than the original Griess test. However, the Griess test and MGT give several disadvantages to forensic analysis, namely requiring heat for the reaction to occur. Besides that, color tests show drawbacks like non-specificity to GSR and the requirement of proper storage and disposal of hazardous chemicals [12-14]. The significance of this study is to improve the functionality of previous screening reagents in the determination of NO_2^- composition that is present after shooting activity. For this reason, a slight modification of MGT has been made.

The new Rapid Griess Test (RGT) reagent was used to detect the presence of NO_2^- ions. This compound is mainly found after shooting due to the oxidation of nitrate (detected compound before shooting). In this study, a slight modification on the established Griess Test was done. RGT reagent was prepared with the substitution of alpha-naphthol, the main reagent in MGT, to 3-aminophenol. This reagent substitution is necessary to avoid the use of heat and the addition of nitric acid in conventional methods. Besides that, the selected chemical reagent is less toxic and less expensive compared to alpha-naphthol.

This study also reported the usage of Video Spectral Comparator (VSC) as a colorimetric analysis in the determination of NO_2^- in the GSR sample. Previous research proved that this rapid and non-destructive method had successfully revealed the GSR pattern on clothing, including dark and bloodstained clothing [15-16].

This spectrum intensity can be accurately measured by the value of CIELAB or L* a* b*. In 1931, Commission Internationale de I'Eclairage (CIE) established a colorimetric method to quantify and physically describe human color perception [17]. The colorimetric method is widely used in industries to define a standard for the quality control of products [18]. The colorimetric method has a function as color coordination in the color space. Brightness and chromaticity are two important factors in determining the colorimetric spectrum. Brightness is symbolized as L* (Lightness, luminosity, or luminance) and has a range from '0' (dark/black) to '100' (light/white) [19]. The intensity is measured as follows; high concentrated solutions have low numbers (0–50) and low concentrated solutions have high numbers (51–100). The chromaticity spectrum is based on three primary colors of blue, green, and red [20]. The a* scale value indicates the degree of redness with a positive (+) number and greenness with a negative (–) number.

Meanwhile, the b* scale measures the yellow and blue colors, where positive numbers represent yellowness, and negative numbers represent blueness. Indeed, all visible colors are present by mixing these colors in different quantities. Meanwhile, the central point on the colorimetric spectrum shows the white color spot. This central area represents an equal mixture of the primary colors [21].

■ EXPERIMENTAL SECTION

Materials

All reagents and chemicals used in these experiments were of analytical grade. Alpha naphthol and the chemicals used for the preparation of the RGT reagent that include 3-Aminophenol ($C_6H_4(NH_2)OH$, ≥ 99%) and Sulfanilic Acid ($C_6H_7NO_3S$, ≥ 99%), were purchased from Sigma Aldrich. Methanol (MeOH, ≥ 99%) purchased from Merck was used without further purification.

Procedure

Preparation of the Rapid Griess Test (RGT) reagent

The method for the MGT reagent preparation in this study followed the steps of a previous study [16]. Furthermore, the RGT reagent was prepared by substitution of alpha naphthol in MGT with 3-aminophenol. Then, 28 g of 3-aminophenol in 100 mL of methanol was added into 5 g of sulfanilic acid solution. The solution was stored in a sealed amber bottle.

Preparation of the standard nitrite (NO_2^-) solution

The screening test method was performed using standard NO_2^- solutions with different concentrations: 250, 200, 150, 100, and 50 ppm. This step was conducted to identify the concentration of NO_2^- that can react with the RGT reagent. Meanwhile, the samples of GSR collected on the target materials were tested directly at the shooting location.

Collection of GSR samples

In order to investigate the effectiveness of the RGT reagent on GSR samples, a shooting test was performed using a Colt (F1) revolver and Smith & Wesson Special +P (F2) revolver, Sig Sauer P226 (F3) pistol, and Walther P99 (F4) pistol. The ammunition used was from Syarikat Malaysia Explosive (SME), 0.38 inch and 9 mm. GSR was directly collected from the target materials before it was tested using the RGT reagent. A shooter conducted the shooting test on duty from the Royal Malaysian Police. This shooting and screening test for detecting NO_2^- in GSR was done in the Forensic Laboratory of the Royal Malaysia Police (RMP) Cheras, Kuala Lumpur. Next, to confirm the presence of NO_2^- in GSR, the sample was analyzed using Video Spectral Comparator (VSC).

■ RESULTS AND DISCUSSION

Color Changes of Standard Nitrite (NO_2^-)

According to Dalby and co-workers [12], the inexpensive, simple, and rapid color test has become an attractive method even though the results are only for screening purposes. However, very few studies on chemical color tests can be used for screening purposes during forensic investigation [22]. Furthermore, conventional chemical color tests are troublesome as some require heat and bulk analysis techniques with a lack of specificity. For instance, the established Griess test method for the detection of NO_2^- in GSR is contributing contamination as the result of heat from the iron [23]. Therefore, this research would address these difficulties by providing an *in-situ,* reliable and valid method for analyzing GSR samples. Furthermore, the effectiveness of the reagent can be achieved by modifying the substance used in a chemical color test so that it can provide a color change *in situ* for screening purposes.

The presence of NO_2^- residue will cause the formation of an orange color as a result of the chromophoric reaction. This reaction occurs due to the formation of Azo-dyes. The reaction known as the diazotization reaction occurs when nitrosating agent reacts with sulfanilic acid to produce a diazonium ion [24-25]. The nitrosating agents are derived from the acid-catalyzed formation of nitrous acid from NO_2^-. In this case, NO_2^- was obtained from the GSR. Next, the diazonium ion will react with aminophenol to form an azo dye (orange color solution). Fig. 1 shows the schematic reactions of NO_2^- and aminophenol to form an azo dye.

Ideally, NO_2^- reacts with 3-aminophenol to form an orange-yellow color solution. The concentrations of an element in a solution can be determined using colorimetric analysis. Colorimetric analysis can be defined as a technique in determining the concentration of chemical compounds such as organic or inorganic compounds in a solution with a color reagent. In this study, a video spectral comparator was used to measure the colorimetrics of the reagent solution that was used to react with the samples. Fig. 2 shows the color changes with the different concentrations of NO_2^- solution that are visible to the human eye.

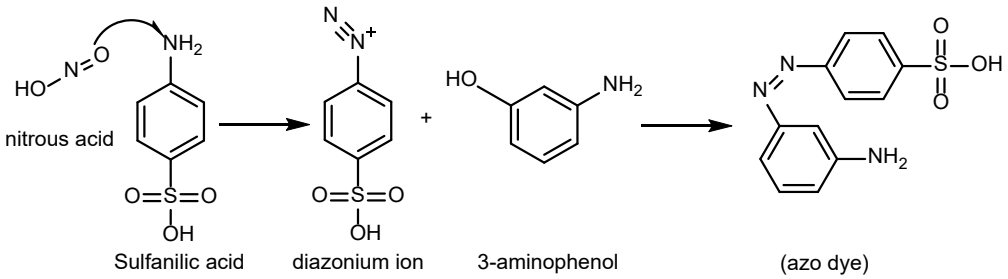

Fig 1. Schematic reactions of nitrite (NO_2^-) and 3-aminophenol.

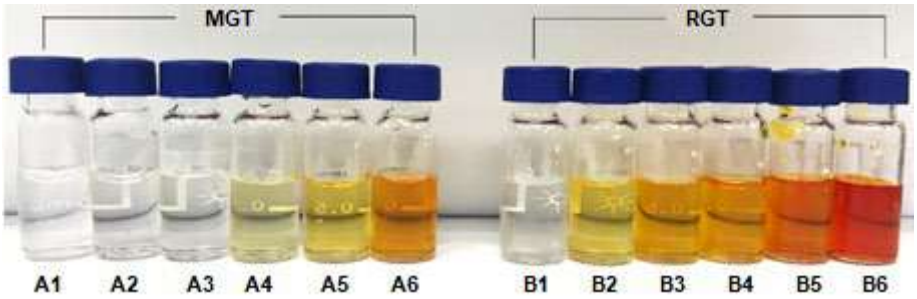

Fig 2. Vials contain (A1) MGT blank, with (A2) 50 ppm, (A3) 100 ppm, (A4) 150 ppm, (A5) 200 ppm, and (A6) 250 ppm of NO_2^- solution, while vial (B1) contain RGT blank, with (B2) 50 ppm, (B3) 100 ppm, (B4) 150 ppm, (B5) 200 ppm, and (B6) 250 ppm of NO_2^- solution

Fig. 2 shows the color changes of the solution from colorless (blank) to different tones of yellow and orange. No color formation occurred in vials A2 and A3 because the concentration of the NO_2^- solutions were too low to react to the MGT. Thus, the earliest change due to the reaction of the MGT reagent and the NO_2^- solution occurred in vial A4. The reaction between MGT and 150 ppm of standard NO_2^- resulted in a yellowish color solution. Meanwhile, vials A5 and A6 show the formation of a yellow and orange color solution, respectively. Unlike the RGT reagent, acetic acid needs to be added to the MGT solution. This solution also required heating for the reaction to occur. In the meantime, the reaction of the standard NO_2^- solution and RGT had occurred in all vials. Vial B5 and B6 showed the darkest color solutions. This detection will help in the determination of particle compounds in crime scenes. Furthermore, the reactions between the RGT reagent and the standard NO_2^- solution showed color changes without adding acetic acid or heating process. Fig. 3 shows the colorimetric spectrum of the blank and test reagent with NO_2^- solution. Both the blank solution in vial A1 and B1 marked the white color spectrum with the values (L^* = 82.6, a^* = 1.7, b^* = 2.8) and (L^* = 87.5, a^* = 1.2, b^* = 3.4) respectively.

MGT with 50 ppm and 100 ppm of NO_2^- solution in vial A2 (L^* = 82.5, a^* = 0.7, b^* = 11.4), and A3 (L^* = 82.5, a^* = 0.9, b^* = 14.4) respectively showed unchanged color solutions. The reaction of the MGT reagent towards the NO_2^- solution in vial A4 (L^* = 78.9, a^* = 3.6, b^* = 14.8) showed a yellowish color solution. Meanwhile, the spectrum shows that A5 (L^* = 73.3, a^* = –1.7, b^* = 17.1) was plotted near B2 (L^* = 77.5, a^* = 1.3, b^* = 17.6). Similar to

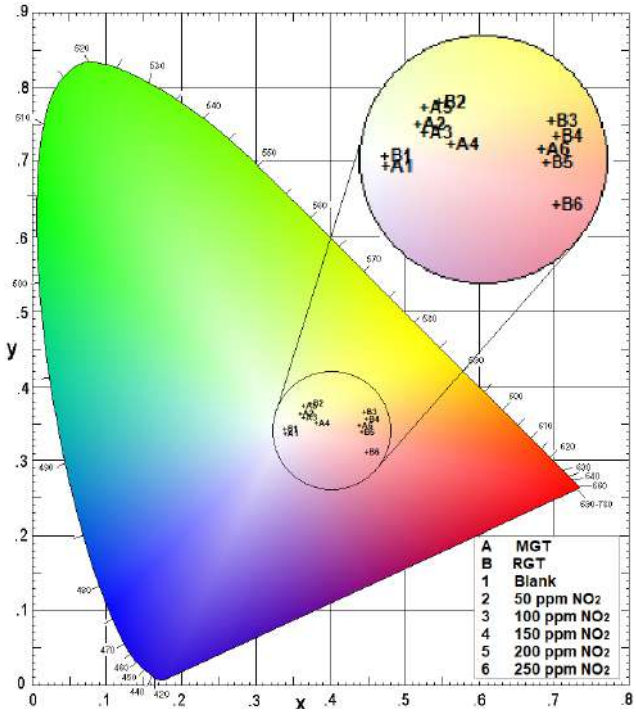

Fig 3. The colorimetric spectrum of (A) MGT and (B) RGT reagent with different concentrations of NO_2^- solution

colorimetric spectrum detection, both A5 and B2 vials showed almost the same yellow color solutions. However, the negative value of a^* for A5 indicates that the solution is near to the green color spectrum. While, vial A6 (L^* = 67.3, a^* = 29.9, b^* = 22.1) showed an orange solution.

Meanwhile, the reactions of the RGT reagent and the standard NO_2^- solution in vial B3 (L^* = 73.3, a^* = 29.9, b^* = 30.0), and B4 (L^* = 71.7, a^* = 32.5, b^* = 27.4) showed bright orange solutions. The orange solution in vial B5 (L^* = 64.3, a^* = 30.9, b^* = 20.6) was formed when

200 ppm of NO_2^- standard solution reacted with the RGT reagent. Vial B6 (L^* = 62.2, a^* = 44.6, b^* = 12.7) which contained the RGT reagent and 250 ppm of NO_2^- solution showed the formation of a dark orange solution after the reaction occurred.

Indeed, the reaction between the RGT reagent and the standard NO_2^- solutions showed the different values of colorimetric data. The RGT reagent containing 250 ppm of NO_2^- (vial B6) showed a low number of L^*, which indicated the dark color of the solution or the highest solution concentration. The color of the solution in vial B6 was significantly darker compared to MGT that reacted with 250 ppm of NO_2^- solution in vial A6. Moreover, the colorimetric measurements showed an increasing redness value, a^*, when the concentration of the standard NO_2^- solutions that reacted with the RGT reagent increased. Therefore, it can be stated that the color tone of the solution becomes darker as the concentration increases. The color changes of the solution proved that RGT is more efficient compared to conventional MGT.

However, to determine the parameter and performance of the RGT reagent, the sensitivity tests were done in this study. Table 1 represents the absorbance versus concentration of NO_2^- (ppm) in MGT and RGT that were measured by UV-VIS spectrometry at 354 nm. Based on the signals obtained from the UV-VIS spectrometer, the calibration curves for MGT and RGT reagents were plotted for five different concentrations of NO_2^- and are presented in Fig. 4.

The linear regression data for the calibration curves showed a good linear relationship over the concentration range of 50 ppm to 250 ppm for nitrite. The linear regression equation for RGT was Y = 0.0035x + 0.0136, where R^2 = 1. Meanwhile, linear regression for MGT was Y = 0.0019x + 0.032, where R^2 = 0.9864. The sensitivity of the analyte towards the reagents can be verified using the limit of detection (LOD) and limit of quantification (LOQ). According to Shrivastava [26], LOD is the lowest analyte concentration that can be measured or detected by a given analytical procedure. Meanwhile, LOQ is the lowest concentration that can be quantitated reliably [27-28].

The LOD was determined as $3.3*S_{y/x}/b$, where $S_{y/x}$ is the residual standard deviation while b is equal to the slope or sensitivity corresponding to the calibration curve [29]. Meanwhile, LOQ can be calculated using the formula $10*S_{y/x}/b$. In this study, the LOD and LOQ for the RGT reagent were found at 1.5 ppm and 4.6 ppm, respectively. Meanwhile, the MGT reagent had a LOD value of 35.8 and a LOQ value of 108.6. Even though MGT reagents are the most frequently used method to determine nitrite, the method is not suitable for GSR determination. It is because MGT requires the addition of acid and heat for the reaction to occur. In conclusion,

Table 1. The data of absorbance and concentration from UV-VIS spectrometry.

MGT			RGT		
vials	Conc. of NO_2^- (ppm)	Abs.	vials	Conc. of NO_2^- (ppm)	Abs.
A2	50	0.084	B2	50	0.186
A3	100	0.137	B3	100	0.359
A4	150	0.258	B4	150	0.534
A5	200	0.341	B5	200	0.703
A6	250	0.463	B6	250	0.878

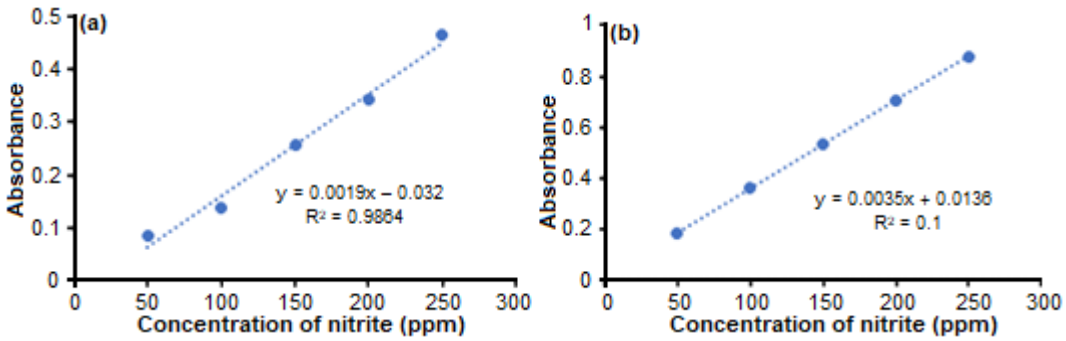

Fig 4. Calibration curve of (a) MGT and (b) RGT reagent using UV-VIS spectrometry

the LOD and LOQ values confirmed the effectiveness of the RGT reagent compared to the MGT reagent in determining GSR. Therefore, this reagent has the potential to become a simple and fast screening test at the crime scene.

Color Changes of the RGT Reagent on GSR Samples

The effectiveness of the RGT reagent at a crime scene can be determined using the GSR samples. For this purpose, the shooting test was done at a closed, unventilated area using SME ammunition fired from four types of firearms, namely Colt revolver (F1), Smith & Wesson special P revolver (F2), Sig Sauer P226 pistol (F3), and Walther P99 pistol (F4).

Fig. 5 shows the color changes of the RGT reagent when reacting with different amounts (mg) of GSR samples from the F1 and F2 revolver. The reaction between the RGT reagents and the GSR samples took place within 30 min, forming color changes, as shown in Fig. 5. The observations showed different color ranges that is visible to the human eye. There are different colors of the solutions, which include the yellowish color, yellow, orange and dark orange. However, the color changes that are measured by human eyes might cause biased results. Therefore, the intensity of the color of the solutions was measured using a colorimetric test for more accurate results, as shown in Fig. 6.

Fig. 6 represents the colorimetric spectrum of the RGT reagent with the GSR samples, from the F1 and F2 revolver. Vial 1 that contained the blank reagent marked the white color spectrum with the value of (L^* = 87.5, a^* = 1.2, b^* = 3.4). Referring to the observation on Fig. 5 and the spectrum from Fig. 6, vial 2a that consisted of 5 mg GSR from F1 showed a yellowish color (L^* = 77.1, a^* = 1.3, b^* = 13.0), while 10 mg of GSR in vial 2b (L^* = 73.1, a^* = 2.5, b^* = 32.4) formed a yellow solution when it reacted with the RGT reagent. Furthermore, both vial 2c and 2d showed yellow colored solutions with the value of (L^* = 73.1, a^* = 14, b^* = 35.2), and (L^* = 67.1, a^* = 19.6, b^* = 26.6), respectively. Vial 2e that consisted of 25 mg GSR from F1 showed a dark orange solution that remarked the color intensity at (L^* = 60.5, a^* = 35.5, b^* = 7.0).

Meanwhile, the GSR from F2 in vial 3a and 3b

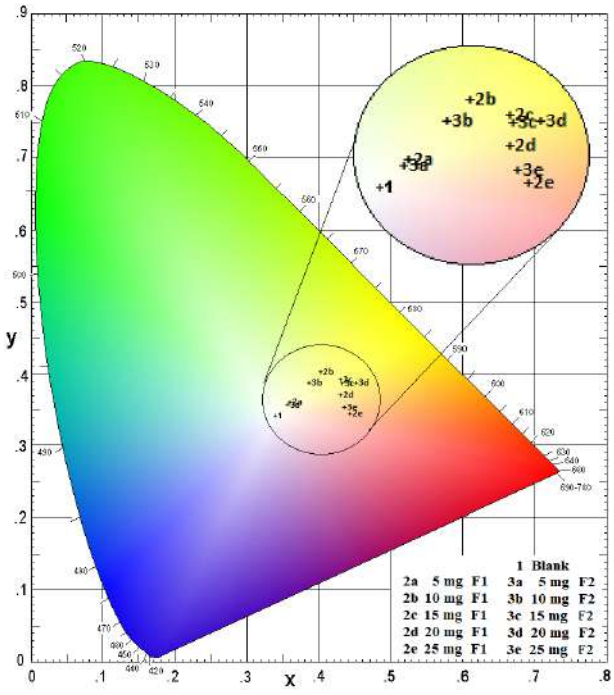

Fig 6. The colorimetric spectrum of the RGT reagent with different weights of GSR samples from the F1 and F2 revolver

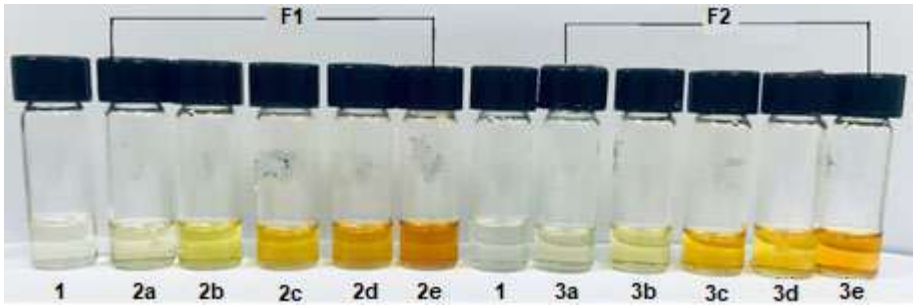

Fig 5. Color changes of the RGT reagent (1) Blank with GSR samples of (a) 5 mg, (b) 10 mg, (c) 15 mg, (d) 20 mg and (e) 25 mg from (2) F1 and (3) F2 revolver

showed a yellowish solution with the value of intensity (L^* = 80.6, a^* = 0.2, b^* = 11.7) and (L^* = 75.2, a^* = 1.6, b^* = 26.1) respectively. The minimum value of a^* (0.2) for 3a indicates that the solution was near to the white color spectrum. The orange solution in vial 3c and 3d had intensity value of (L^* = 74.0, a^* = 16.6, b^* = 34.5) and (L^* = 74.9, a^* = 17.6, b^* = 37.3) respectively. The solution in vial 3e with the intensity value of (L^* = 62.2, a^* = 44.6, b^* = 12.7) showed a dark orange solution that is visible to the human eye. The 25 mg GSR from F1 in vial 2e showed the highest redness value, a^*, followed by 25 mg of GSR from F2 in vial 3e. The high value of redness is caused by the dark colored solution from both samples. Moreover, the lowest L^* value in vials 2e and 3e also indicated a darker colored solution compared to the other samples. The different colors of the solutions indicates that the amount of GSR affected the formation of the color of the solutions.

Fig. 7 shows the color changes of the RGT reagent when reacting with different amounts (mg) of GSR samples from the F3 and F4 pistols, while Fig. 8 represents the colorimetric spectrum of the RGT reagent with different weights of GSR from the F3 and F4 pistols. Fig. 7 shows that the vials that consisted of GSR from F3 showed different color changes: a yellowish solution in vial 4a, yellow solutions in vial 4b and 4c, an orange solution in vial 4d, and a dark orange solution in vial 4e. Meanwhile, vials that consisted of GSR from F4 showed a yellowish solution in vial 5a, a yellow solution in vial 5b, and a dark orange solution in vial 5e, leaving the rest of the vials with orange colored solutions.

Fig. 8 shows that the blank solution, located on the white color spectrum, has the intensity value of (L^* = 87.5, a^* = 1.2, b^* = 3.4). The colorimetric spectrum shows that 4a (L^* = 81.6, a^* = -0.4, b^* = 16.1) and 5a (L^* = 77.8, a^* = 1.9, b^* = 12.9) were located near the white spectrum. The negative redness value, a^* = −0.4 for 4a indicates that the solution is leaning toward the green spectrum. Similarly, when observed through the human eyes, the color of the solution of vials 4a and 5a was very close to white. However, the minimum changes from colorless to yellowish solution prove the effectiveness of the RGT reagent as a screening test reagent in determining GSR.

The yellow solution in vial 4b (L^* =81.7, a^* = 0.2, b^* = 35.1) and 4c (L^* = 72.6, a^* = 9.5, b^* = 35.1) showed the highest value of yellowness, b^* in the colorimetric spectrum followed by 5b (L^* = 69.1, a^* = 10.1, b^* = 29.0)

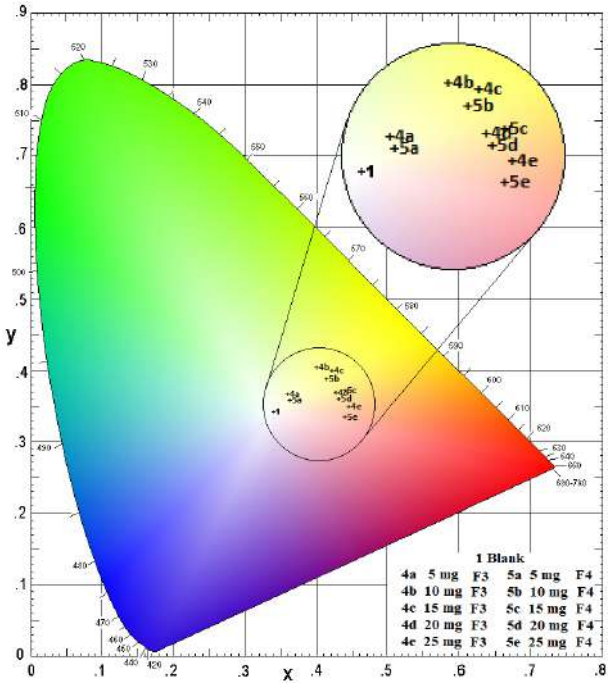

Fig 8. The colorimetric spectrum of RGT reagent with different weights of GSR samples from F3 and F4 pistols

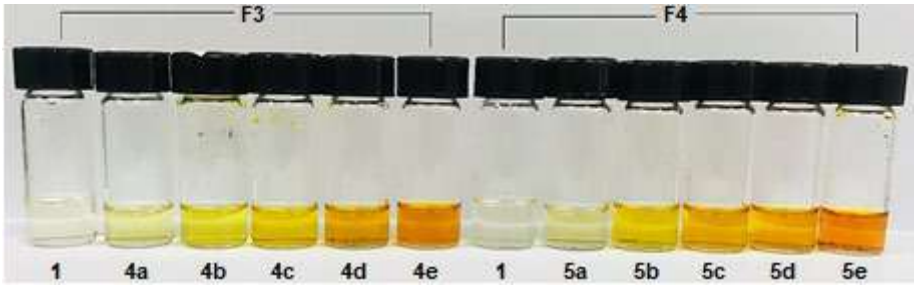

Fig 7. Color changes of RGT reagent (1) Blank with GSR samples of (a) 5 mg, (b) 10 mg, (c) 15 mg, (d) 20 mg and (e) 25 mg from (4) F3 and (5) F4 pistol

which also formed a yellow solution. Meanwhile, the grouping of vial 4d (L* = 68.1, a* = 20.5, b* = 26.1), 5c (L* = 69.2, a* = 23.3, b* = 29.7) and 5d (L* = 66.2, a* = 23.4, b* = 23.4) are due to the similar values of L*, a*, and b*. The grouping of the samples showed the intensity of the color of the solution that were slightly similar to each other. In addition, both 25 mg of GSR from F3 in vial 4e (L* = 63.7, a* = 30.6, b* = 21.8) and F4 in vial 5e (L* = 60.2, a* = 33.1, b* = 15.3) showed dark orange solutions.

The data of the colorimetric measurement shows that increasing the amounts of the GSR samples will increase the redness value, a*. For instance, 4e and 5e had the highest redness value a*, while 4a and 5a had the lowest redness value, a*. The GSR samples of F3 and F4 showed diffuse white or light colored solution due to the high value of luminosity, L*.

Even though the analysis used the same amount (mg) of GSR to react with the RGT reagent, the observation through the human eyes showed that the color changes of RGT towards NO_2^- were different between firearms. The difference is because the GSR particles consist of partially burnt and unburnt chemical composition, in which the main composition is nitrocellulose. During the shooting process, the nitrocellulose had undergone degradation to form NO_2^-. In other words, the GSR from F4 contained higher amounts of NO_2^- in compared to the GSR from F3.

In addition, 10 mg of GSR sample is the minimum amount that can differentiate the color of the reaction solution from the blank solution. Therefore, this amount should be the benchmark value in observing the effectiveness of the RGT reagent. Consequently, the RGT reagent successfully determined the nitrite compound in the GSR particles. The substitution of alpha-naphthol in the previous MGT reagent with 3-aminophenol will eliminate the need to use heat and the addition of acetic acid. Therefore, the invention of the RGT reagent can increase the efficiency of GSR screening tests at crime scenes by providing a portable and easy to use reagent.

■ CONCLUSION

Using the RGT reagent to detect GSR on a shooter's hand and clothes will lead the investigators towards a better option to perform screening tests at crime scenes. The RGT analysis gave a slightly similar result to MGT. Although color intensity is not the main point for NO_2^- determination, there is an observable difference in color intensity between MGT and RGT. The effectiveness of the RGT chemical reagents will avoid the use of heat and acetic acid to facilitate the chromophoric reaction. Therefore, substituting the MGT with the RGT reagent as a screening method in detecting NO_2^- as the main component in GSR will become a new alternative in forensic chemistry analysis. However, this method depends on the availability of the samples collected at the time an incident occurs.

■ ACKNOWLEDGMENTS

The authors gratefully acknowledge and express gratitude to the Royal Malaysian Police for permitting the use of their facilities in the Ballistic Department, Forensic Laboratory Cheras, Malaysia. The authors also wish to thank CP Dato' Narenasegaran AL Thangaveloo, Supt Tan Yan Thian, and ASP Nik Norhisham Nik Ismail for a fruitful discussion and precious advice. Furthermore, the authors thank UiTM for the financial support through the Journal Support Fund. Lastly, the authors would also like to thank the Institute of Research Management and Innovation (IRMI), UiTM, for funding the study under BESTARI PERDANA Grant No: 600-IRMI/PERDANA 5/3 BESTARI (057/2018).

■ AUTHOR CONTRIBUTIONS

SNJ analyzed and interpreted the shooting data and wrote the manuscript. ZNZ supervised SNJ's research work. MSMS prepared the shooting materials and performed the shooting test. MFS, MAAR, and MIAH mooted the idea, designed, and co-supervised SNJ's work. All authors read and approved the final manuscript.

■ REFERENCES

[1] Vanini, G., Souza, M.O., Carneiro, M.T.W.D., Filgueiras, P.R., Bruns, R.E., and Romão, W., 2015, Multivariate optimisation of ICPOES instrumental parameters for Pb/Ba/Sb measurement in gunshot residues, *Microchem. J.*, 120, 58–63.

[2] Gassner, A.L., Ribeiro, C., Kobylinska, J., Zeichner, A., and Weyermann, C., 2016, Organic gunshot residues: Observations about sampling and transfer mechanisms, *Forensic Sci. Int.*, 266, 369–378.

[3] Maitre, M., Kirkbride, K.P., Horder, M., Roux, C., and Beavis, A., 2017, Current perspectives in the interpretation of gunshot residues in forensic science: A review, *Forensic Sci. Int.*, 270, 1–11.

[4] Vander Pyl, C., Ovide, O., Ho, M., Yuksel, B., and Trejos, T., 2019, Spectrochemical mapping using laser-induced breakdown spectroscopy as a more objective approach to shooting distance determination, *Spectrochim. Acta, Part B*, 152, 93–101.

[5] Tarifa, A., and Almirall, J.R., 2015, Fast detection and characterization of organic and inorganic gunshot residues on the hands of suspects by CMV-GC–MS and LIBS, *Sci. Justice*, 55 (3), 168–175.

[6] Bueno, J., and Lednev, I.K., 2014, Attenuated total reflectance-FTIR imaging for rapid automated detection of gunshot residue, *Anal. Chem.*, 86 (7), 3389–3396.

[7] Doty, K.C., Muro, C.K., Bueno, J., Halámková, L., and Lednev, I.K., 2016, What can Raman spectroscopy do for criminalistics?, *J. Raman Spectrosc.*, 47 (1), 39–50.

[8] Bueno, J., Sikirzhytski, V., and Lednev, I.K., 2013, Attenuated total reflectance-FT-IR spectroscopy for gunshot residue analysis: potential for ammunition determination, *Anal. Chem.*, 85 (15), 7287–7294.

[9] López-López, M., Alvarez-Llamas, C., Pisonero, J., García-Ruiz, C., and Bordel, N., 2017, An exploratory study of the potential of LIBS for visualizing gunshot residue patterns, *Forensic Sci. Int.*, 273, 124–131.

[10] Berger, J., Upton, C., and Springer, E., 2019, Evaluation of total nitrite pattern visualization as an improved method for gunshot residue detection and its application to casework samples, *J. Forensic Sci.*, 64 (1), 218–222.

[11] Heines, S.V., 1958, Peter Griess—Discoverer of diazo compounds, *J. Chem. Educ.*, 35 (4), 187.

[12] Dalby, O., Butler, D., and Birkett, J.W., 2010, Analysis of gunshot residue and associated materials – A review, *J. Forensic Sci.*, 55 (4), 924–943.

[13] Costa, R.A., Motta, L.C., Destefani, C.A., Rodrigues, R.R.T., do Espirito Santo, K.S., Aquije, G.M.F.V., Boldrini, R., Athayde, G.P.B., Carneiro, M.T.W.D., and Romão, W., 2016, Gunshot residues (GSR) analysis of clean range ammunition using SEM/EDX, colorimetric test and ICP-MS: A comparative approach between the analytical techniques, *Microchem. J.*, 129, 339–347.

[14] Chabaud, K.R., Thomas, J.L., Torres, M.N., Oliveira, S., and McCord, B.R., 2018, Simultaneous colorimetric detection of metallic salts contained in low explosives residue using a microfluidic paper-based analytical device (μPAD), *Forensic Chem.*, 9, 35–41.

[15] Bailey, J.A., Casanova, R.S., and Bufkin, K., 2006, A method for enhancing gunshot residue patterns on dark and multicolored fabrics compared with the modified Griess test, *J. Forensic Sci.*, 51 (4), 812–814.

[16] Kersh, K.L., Childers, J.M., Justice, D., and Karim, G., 2014, Detection of gunshot residue on dark-colored clothing prior to chemical analysis, *J. Forensic Sci.*, 59 (3), 754–762.

[17] Rosli, N.A., Osman, R., Saim, N., and Jaafar, M.Z., 2015, Application of chemometric techniques to colorimetric data in classifying automobile paint, *Malays. J. Anal. Sci.*, 19 (4), 790–798.

[18] Neuhauser, S., and Handler, J., 2013, Color analysis of the equine endometrium: Comparison of spectrophotometry and computer-assisted analysis of photographs within the $L^*a^*b^*$ color space system, *Vet. J.*, 197 (3), 753–760.

[19] Was-Gubala, J., and Starczak, R., 2015, UV-Vis microspectrophotometry as a method of differentiation between cotton fibre evidence colored with reactive dyes, *Spectrochim. Acta, Part A*, 142, 118–125.

[20] Caswell, L.R., 2013, "Reflectance Spectroscopy of Colored Overprints" in *Proceedings of the First International Symposium on Analytical Methods in Philately*, Eds. Lera, T.M., Barwis, J.H., and Herendeen, D.L., 101–107.

[21] Aambø, M., 2011, Use of the "Video Spectral Comparator 6000" as a non-destructive method for pigment identification-An experiment, *Undergraduate Thesis*, Gothenburg Uni., Sweeden.

[22] Goudsmits, E., Sharples, G.P., and Birkett, J.W., 2015, Recent trends in organic gunshot residue analysis, *TrAC, Trends Anal. Chem.*, 74, 46–57.

[23] Haag, L.C., 2006, *Shooting Incident Reconstruction*, 3rd Ed., Academic Press, London, UK.

[24] Haiyan, Y., Romain, S., Anne, S., Patrick, C., and Pierre, L., 2018, Comparison between two derivatization methods of nitrite ion labeled with 15 N applied to liquid chromatography-tandem mass spectrometry, *Anal. Methods*, 10 (31), 3830–3836.

[25] Waring, R.H., Hunter, J.O., Turner, C., Batty, C., and Ramzan, P.H.L, 2019, Nitrate supplementation in thoroughbred racehorses: Addition of beetroot juice to the equine diet and effects on the gut metabolome, *Integr. Food Nutr. Metab.*, 6 (2), 1000246.

[26] Shrivastava, A., and Gupta, V.B., 2011, Methods for determination of limit of detection and limit of quantification of the analytical methods, *Chron. Young Sci.*, 2 (1), 21–25.

[27] Samal, L., and Prusty, A., 2019, Development and validation of UV-Visible spectrometric method for determination of duloxetine, *Int. J. Pharm. Pharm. Sci.*, 11 (3), 27–31.

[28] Lappas, N.T., and Lappas, C.M., 2016, *Forensic Toxicology: Principles and Concepts*, 1st Ed., Academic Press, London, UK.

[29] Guimarães, V., Durão, H., and Azenha, M., 2014, Detailed validation of a method for the determination of nitrate in water by UV/Vis spectroscopy, *J. AOAC Int.*, 2014, 12-007.

Supplementary Data

This supplementary data is a part of paper entitled "Sesquiterpenoids from the Stem Bark of *Aglaia simplicifolia* and Their Cytotoxic Activity against B16-F10 Melanoma Skin Cancer Cell".

Table of Contents

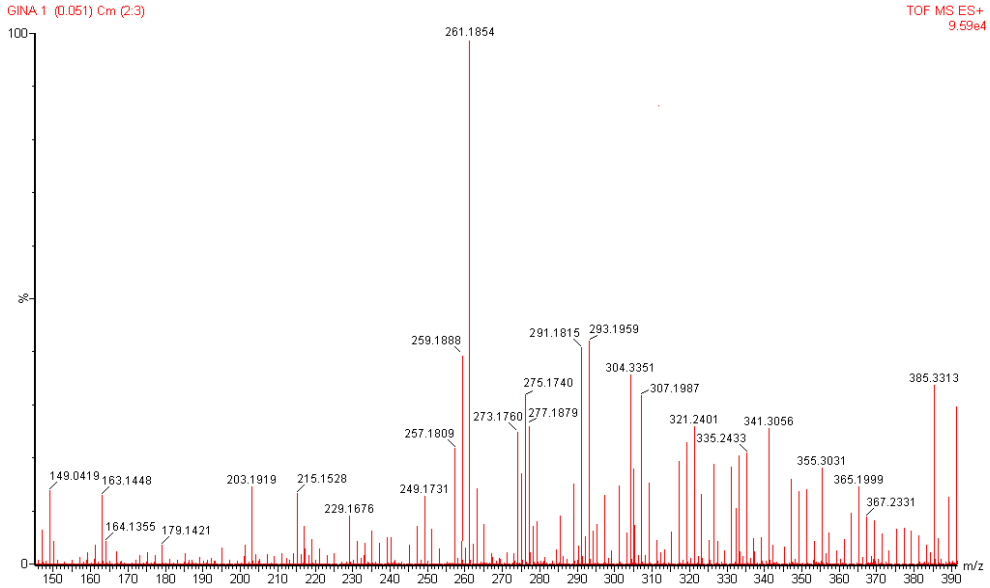

Fig S1. HRTOF-MS spectrum of (**1**)

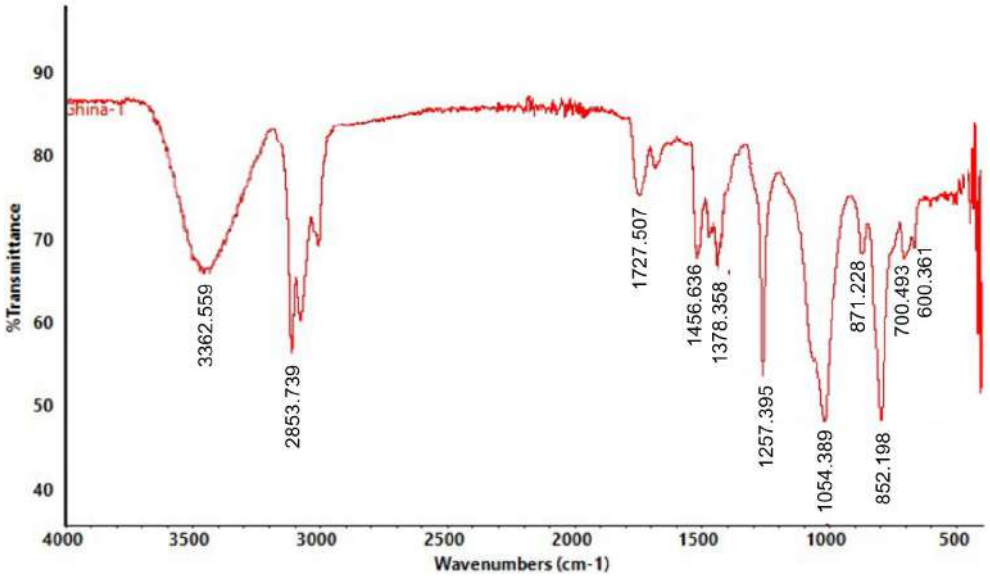

Fig S2. FT-IR spectrum of (**1**)

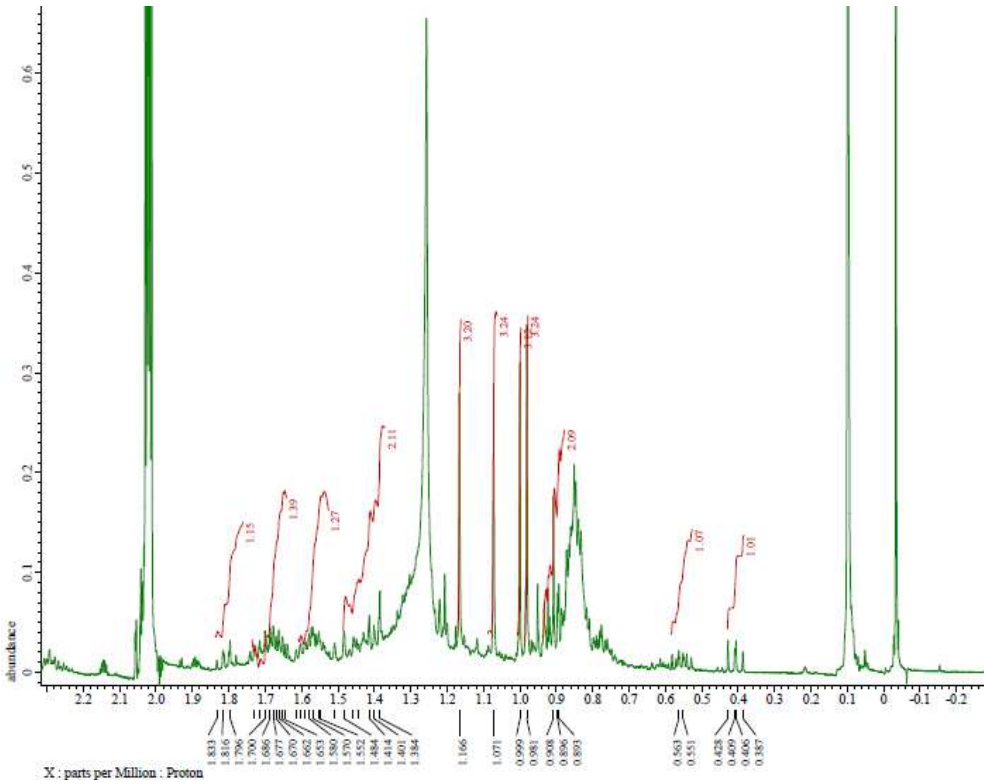

Fig S3. ^{1}H-NMR spectra of (**1**) (500 MHz in Acetone-d6)

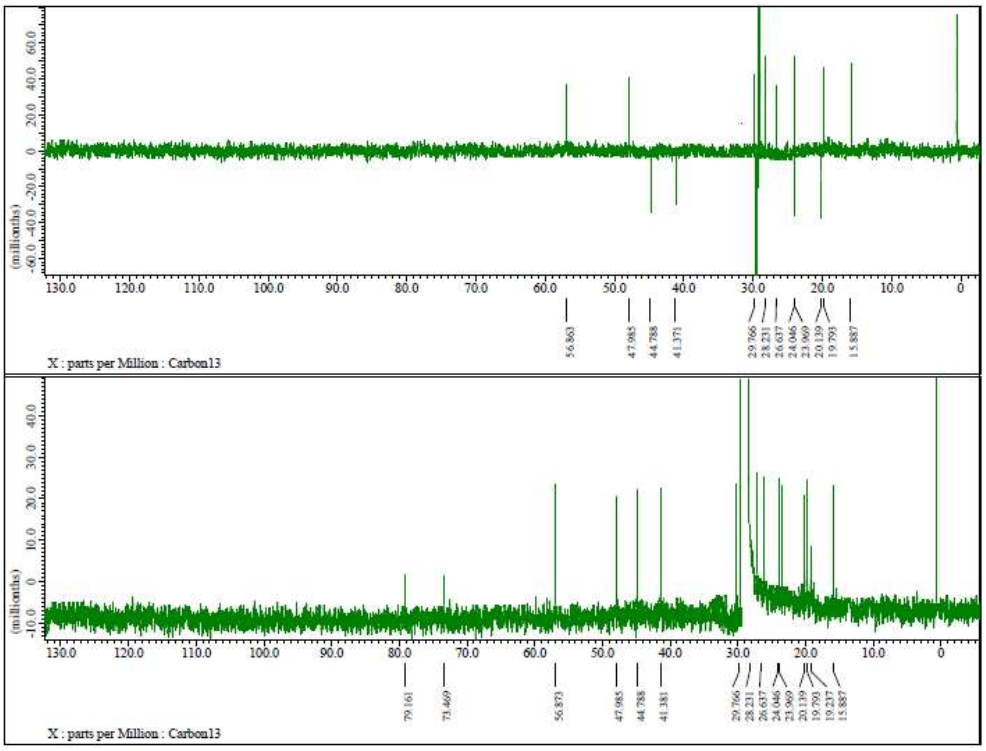

Fig S4. ^{13}C-NMR and DEPT- 135° spectrum of (**1**) (125 MHz in CDCl3)

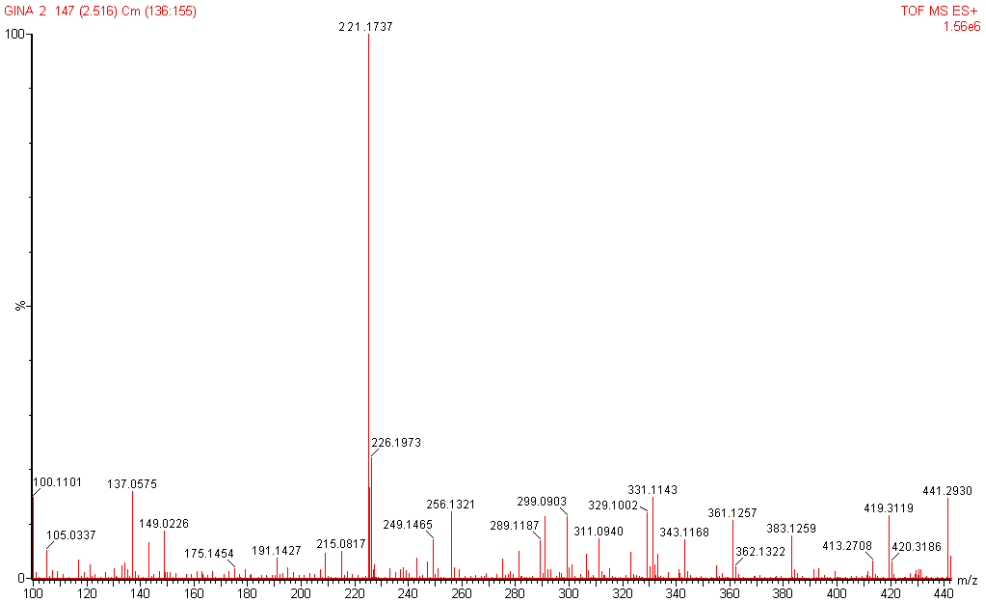

Fig S5. HRTOF-MS spectrum of (**2**)

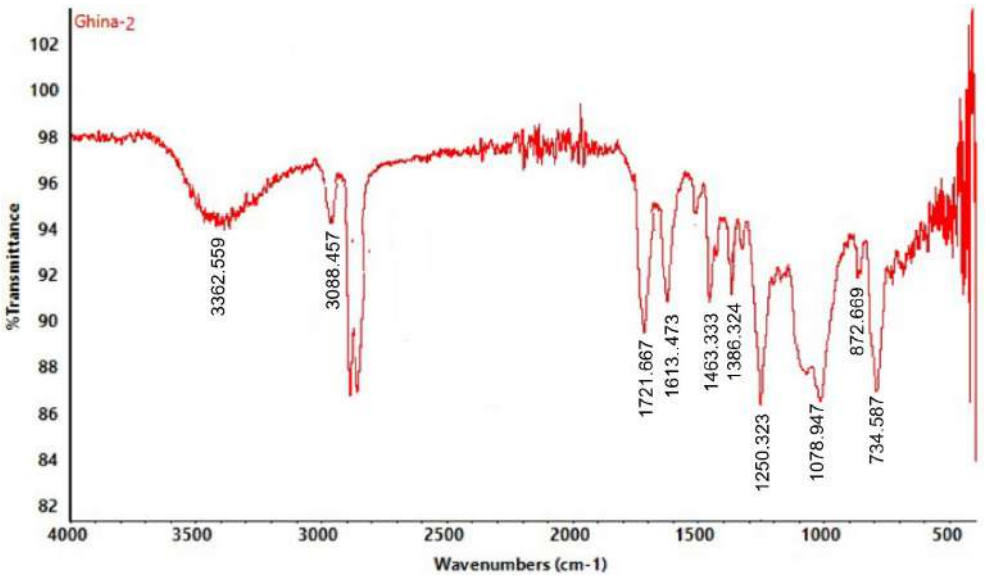

Fig S6. FT-IR spectrum of (**2**)

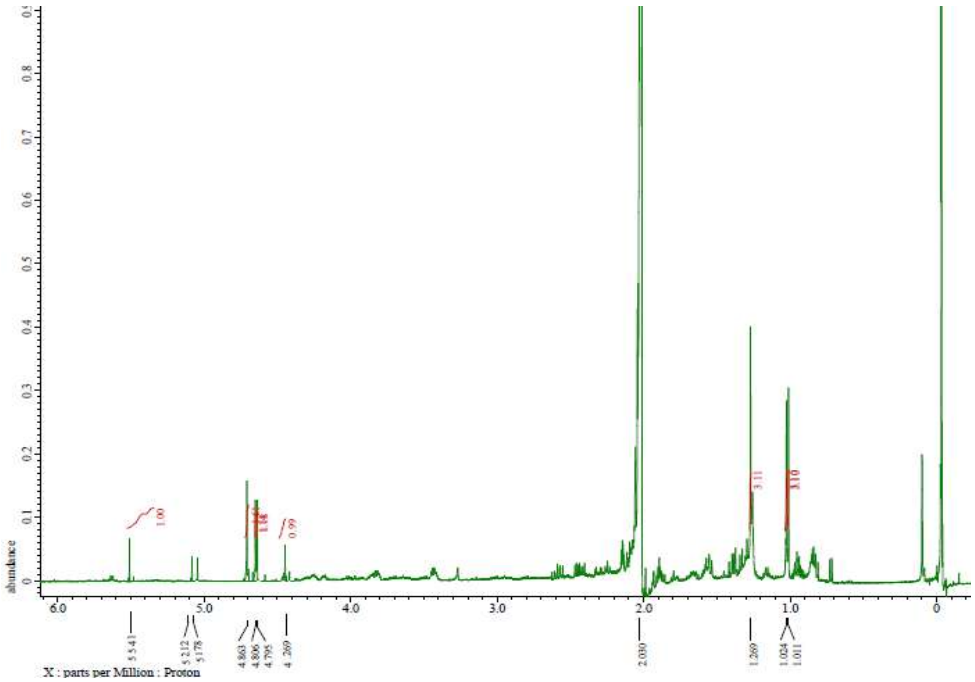

Fig S7. [1]H-NMR spectra of (**2**) (500 MHz in Acetone-d6)

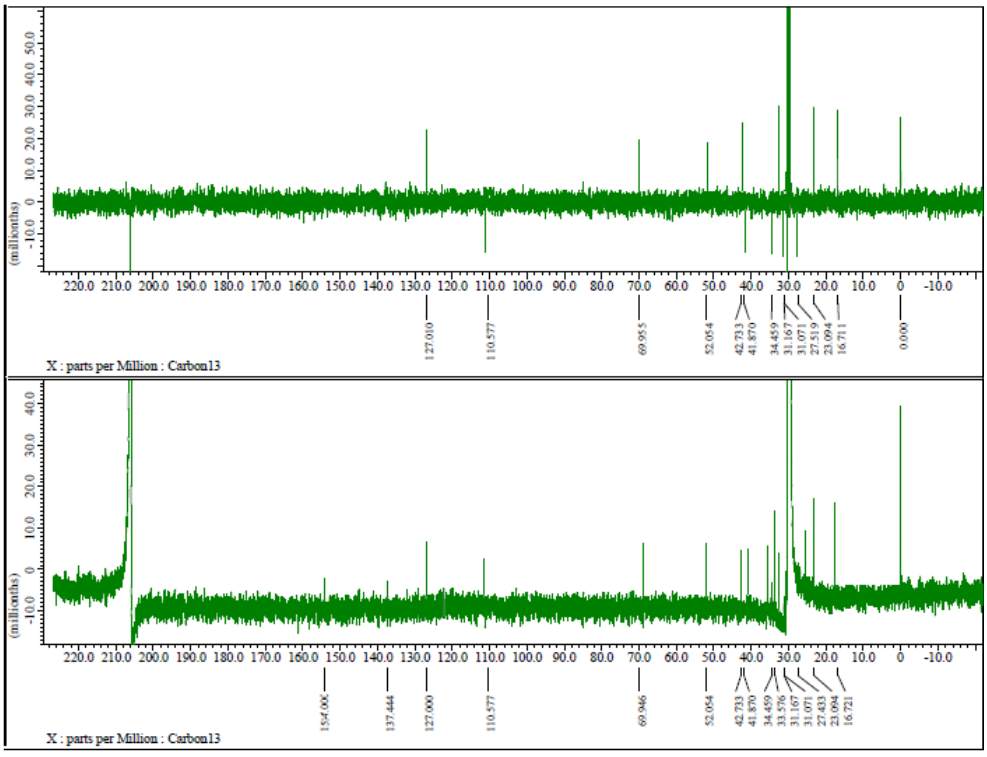

Fig S8. [13]C-NMR and DEPT- 135° spectrum of (**2**) (125 MHz in CDCl3)

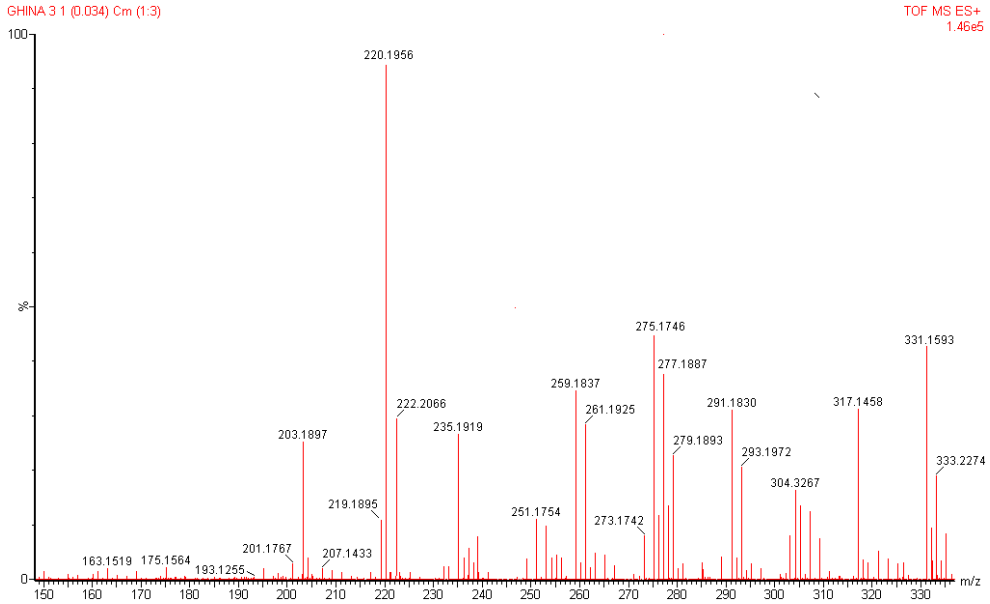

Fig S9. HRTOF-MS spectrum of (**3**)

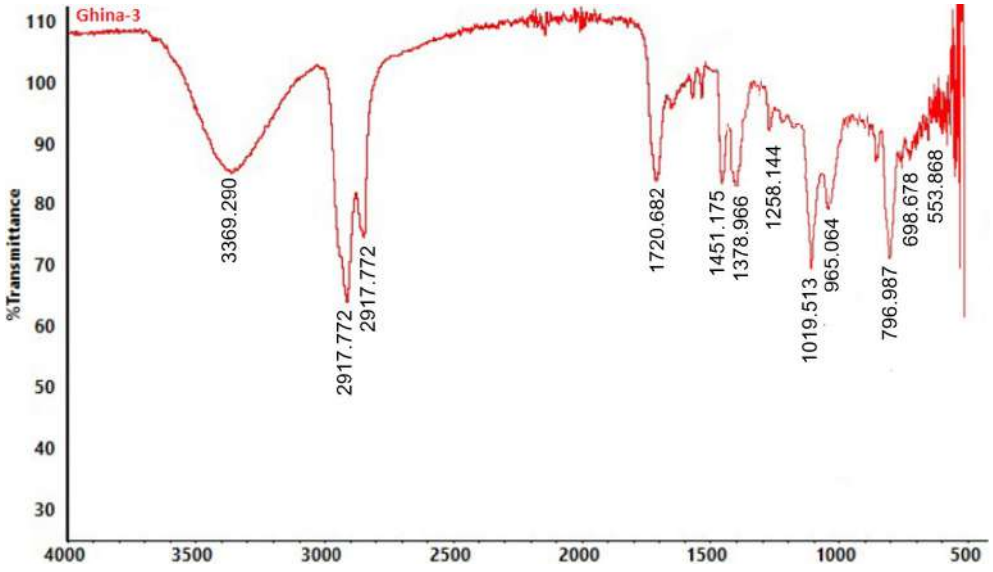

Fig S10. FT-IR spectrum of (**3**)

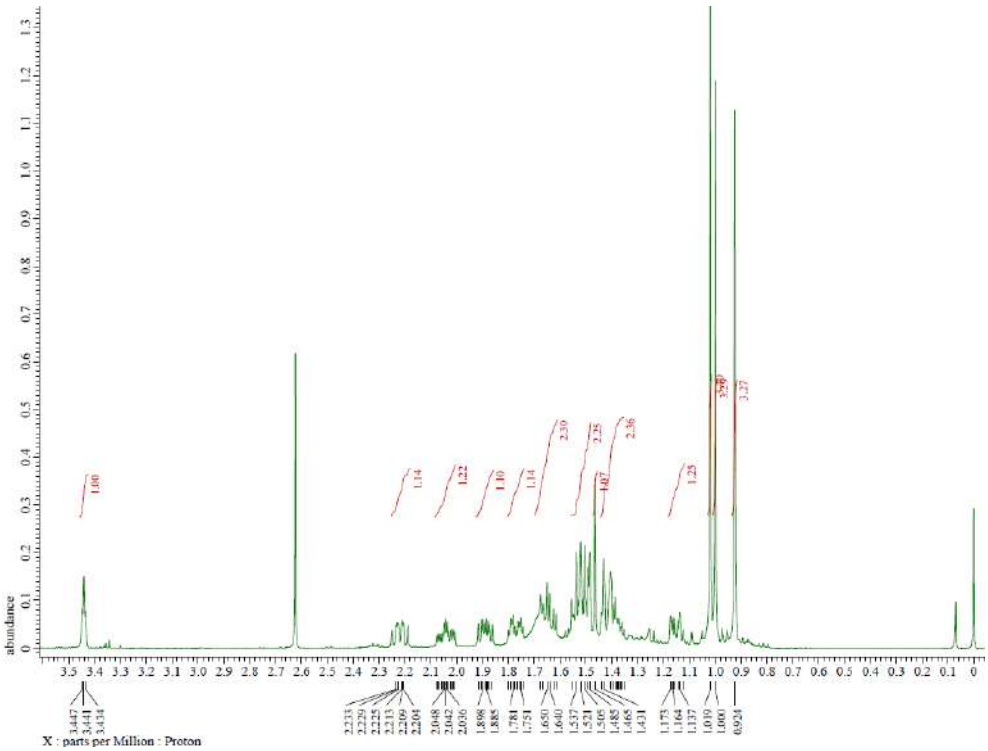

Fig S11. ^{1}H-NMR spectra of (**3**) (500 MHz in $CDCl_3$)

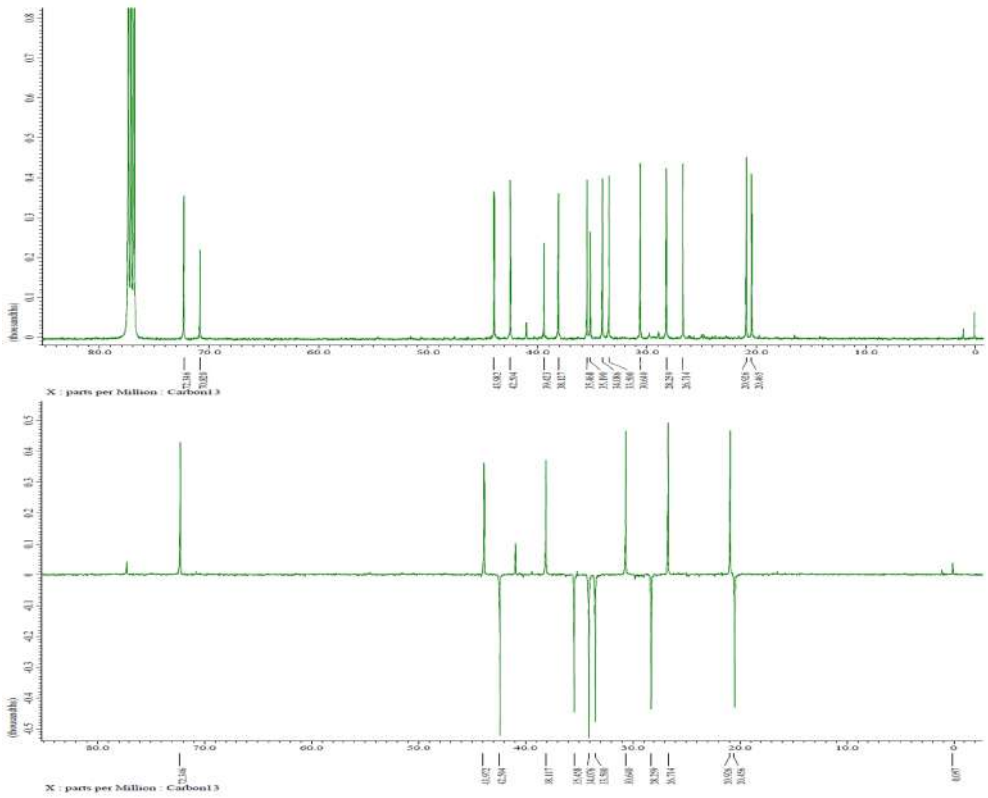

Fig S12. ^{13}C-NMR and DEPT 135° spectrum of (**3**) (125 MHz in $CDCl_3$)

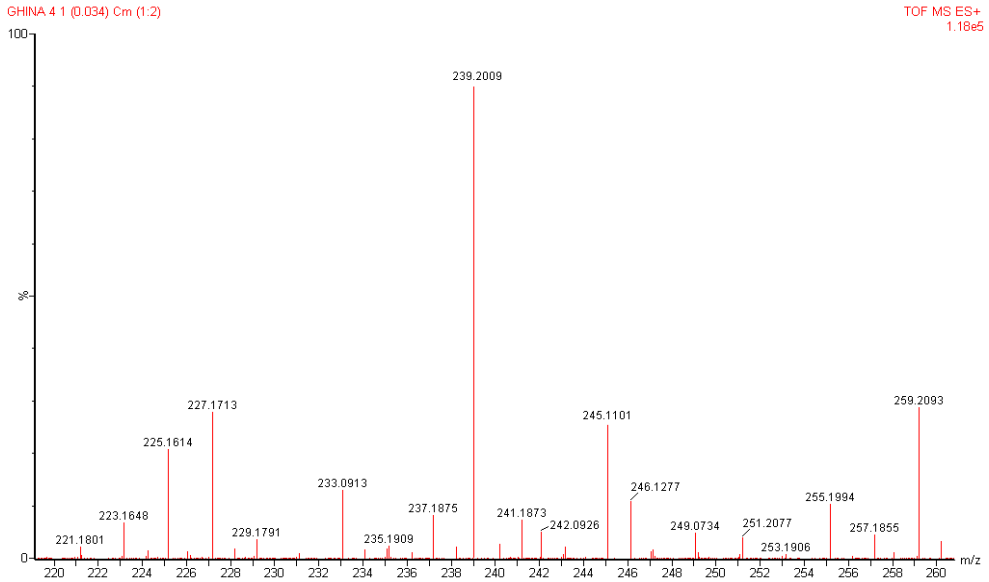

Fig S13. HRTOF-MS spectrum of (**4**)

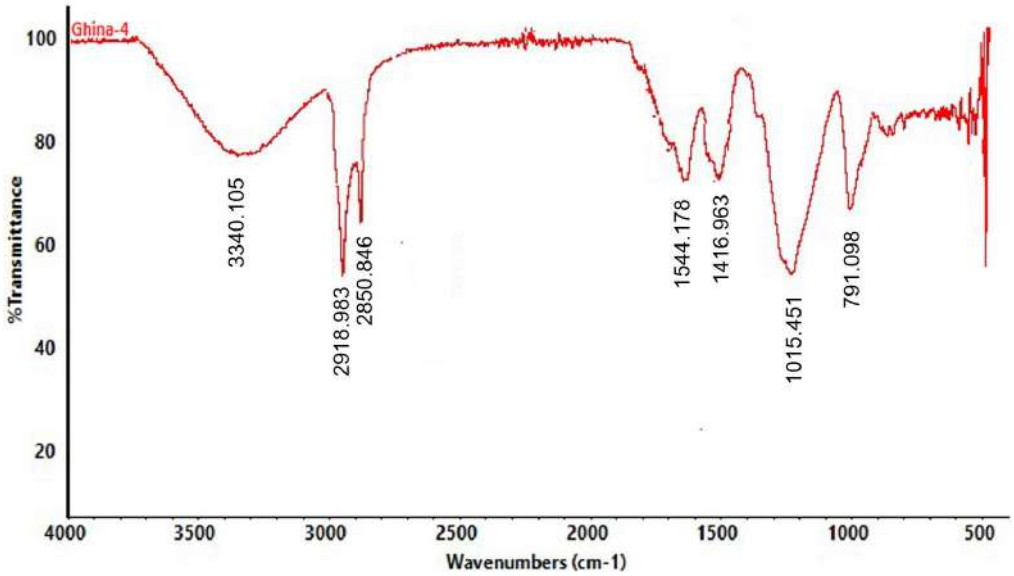

Fig S14. FT-IR spectrum of (**4**)

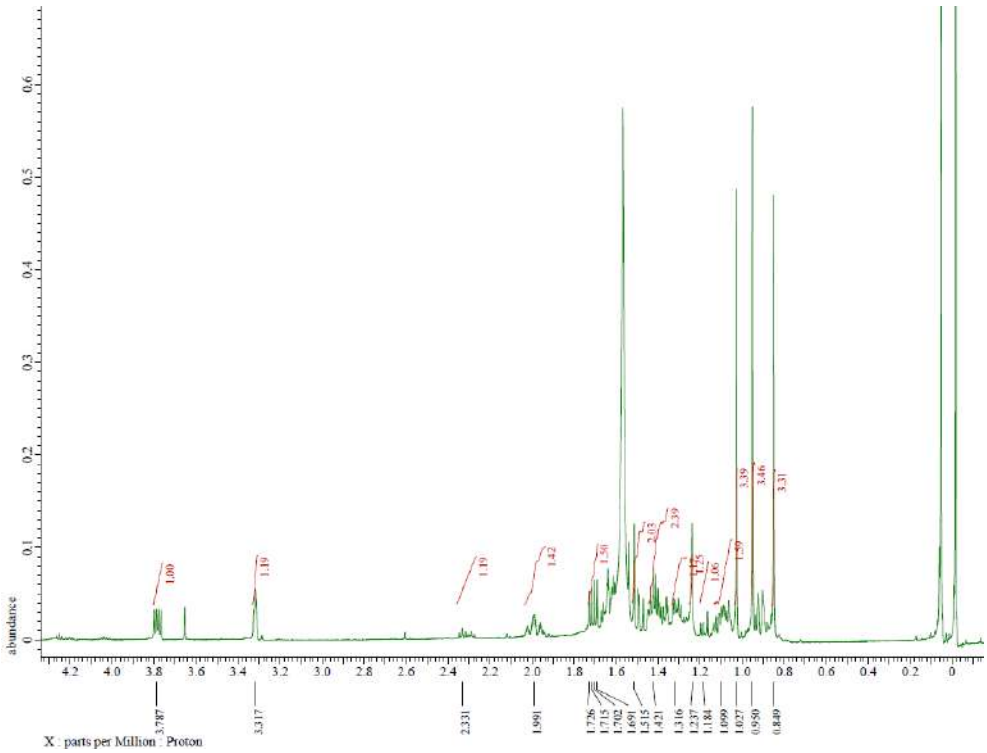

Fig S15. ^{1}H-NMR spectra of (**4**) (500 MHz in $CDCl_3$)

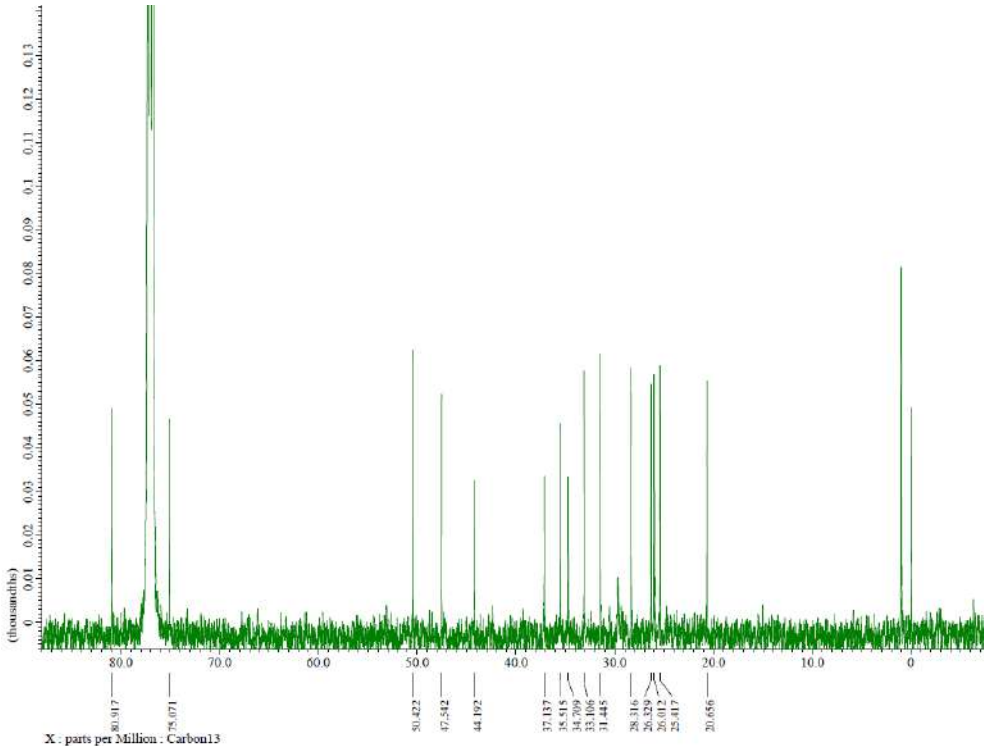

Fig S16. ^{13}C-NMR spectrum of (**4**) (125 MHz in CDCl3)

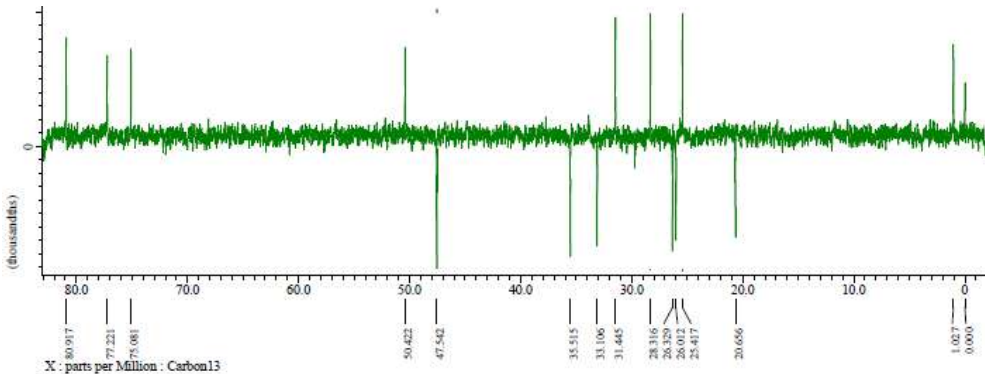

Fig S17. DEPT-135° Spectrum of (**4**) (125 MHz in CDCl3)

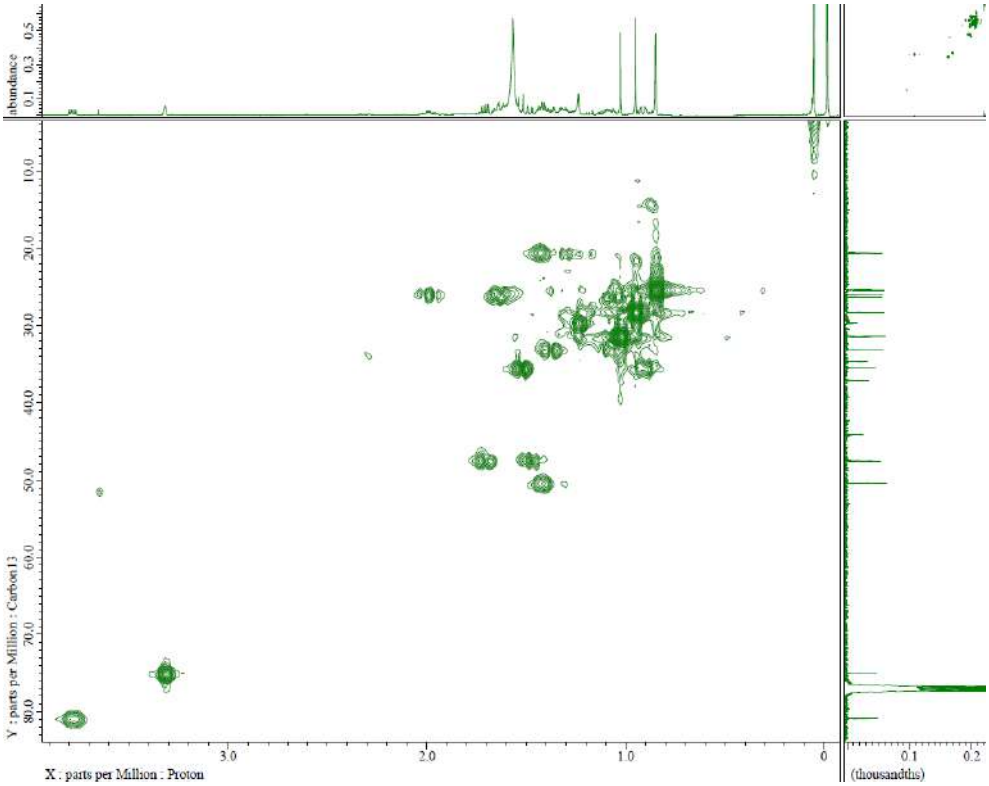

Fig S18. HMQC spectrum of (**4**)

Sesquiterpenoids from the Stem Bark of *Aglaia simplicifolia* and Their Cytotoxic Activity against B16-F10 Melanoma Skin Cancer Cell

Ghina Izdihar[1], Al Arofatus Naini[1], Desi Harneti[1], Rani Maharani[1,2], Nurlelasari Nurlelasari[1], Tri Mayanti[1], Agus Safari[1], Kindi Farabi[1], Unang Supratman[1,2*], Mohamad Nurul Azmi[3], and Yoshihito Shiono[4]

[1]*Department of Chemistry, Faculty of Mathematics and Natural Sciences, Universitas Padjadjaran, Jl. Raya Bandung-Sumedang Km. 21, Jatinangor, Sumedang 45363, Indonesia*

[2]*Central Laboratory of Universitas Padjadjaran, Jl. Raya Bandung-Sumedang Km. 21, Jatinangor, Sumedang 45363, Indonesia*

[3]*School of Chemical Sciences, Universiti Sains Malaysia, 11800 Minden, Penang, Malaysia*

[4]*Department of Bioresources Engineering, Faculty of Agriculture, Yamagata University, Tsuruoka-shi, Yamagata 997-8555, Japan*

* ***Corresponding author:***

email: unang.supratman@unpad.ac.id

Received: August 13, 2021
Accepted: October 25, 2021

DOI: 10.22146/ijc.68383

Abstract: *Four sesquiterpenoid derivatives, i.e., 4β,10α-dihydroxyaromadendrane (**1**), caryophyllenol-II (**2**), senecrassidiol (**3**), and clovane-2β,9α-diol (**4**) have been isolated from the stem bark of* Aglaia simplicifolia. *The chemical structures of compounds **1**-**4** were determined based on spectroscopic data, including one and two-dimensional NMR and mass spectroscopy. In addition, these sesquiterpenoids **1**-**4**, were also tested for their cytotoxic activity against B16-F10 melanoma skin cancer cell lines through* in vitro *assay. Among the isolated compounds **1**-**4**, compound **1** showed the highest activity with an IC_{50} value of 44.8 µg/mL, suggesting the presence of a cyclopropane ring that plays an essential role in cytotoxic activity against B16-F10 melanoma skin cancer cell lines.*

Keywords: Aglaia simplicifolia*; cytotoxic activity; B16-F10 cell lines; sesquiterpenoid; Meliaceae*

■ INTRODUCTION

Sesquiterpenoids are secondary metabolites derived from three isoprene units 2-methyl-1,3-diene with 15 carbon atoms and 24 hydrogens per molecule ($C_{15}H_{24}$) [1]. Sesquiterpenoids were classified using the number of cyclic formed by modification of the cyclization reaction and rearrangement of the carbon skeleton. For example, acyclic, monocyclic, bicyclic, and tricyclic sesquiterpenoids, with several types of cyclic, cyclopropane, cyclobutane, cyclopentane, cyclohexane, and cycloheptane [2-3]. The characteristic of sesquiterpenoids are oils with volatile properties but less volatile than monoterpenoids, the main components of essential oil with more pungent odors, and can be found in plants, mainly in higher plants [3].

Currently, there are more than 10,000 known types of sesquiterpenoids in nature [1]. The diversity of sesquiterpenoids comes from farnesyl pyrophosphate (FPP) as a precursor, which has three double bonds, so the carbon chain is more flexible, so makes the structural diversity in the carbon skeleton (C_{15}) sesquiterpenoid [4]. In addition, the presence of functional groups and substituents arranged regionally and stereospecifically made sesquiterpenoids diverse skeletons [5]. Sesquiterpenoids are very useful because these compounds have many biological activities such as anti-inflammatory [6], antibacterial [7], antioxidant [8], antitumor [9-10], and antimalarial [11] agents. For example, artemisinin is a sesquiterpenoid lactone isolated from *Artemisia annua* and has been used as a malarial drug [12].

Aglaia is a kind of higher plant in the tropical rainforest. *Aglaia* is the largest genus that belongs to the Meliaceae family, which contains more than 150 species

and about 65 species grown only in Indonesia. The *Aglaia* genus has been identified in Southern Asia's tropical and subtropical rainforest, Northern Australia, and the pacific region. The distributions of the *Aglaia* genus can be found in many countries, such as India, Thailand, Vietnam, Malaysia, and Indonesia [13-14]. Traditionally, the bark of *Aglaia* has been used as traditional Indonesian herbal medicine for healing fever, influenza, cough, and other skin diseases [3,13-14].

A. simplicifolia is one of *Aglaia* plants that has been phytochemically investigated before, and it has been proven to contain ergosterol peroxide, stigmasterol, and senecrassidiol with cytotoxic activity against HeLa cervical cancer [15-16]. So far, about twenty-three sesquiterpenoids have been investigated separately from the *Aglaia* species [13]. Therefore, to observe the cytotoxic constituents of Indonesian *Aglaia* plants against B16-F10 melanoma skin cancer cell lines, we report herein the isolation, structure elucidation, and cytotoxic evaluation of four types of aromadendrane, caryolan, clovane, and caryophyllene sesquiterpenoids **1**-**4** from *A. simplicifolia.*

■ EXPERIMENTAL SECTION

Materials

The stem bark of *A. simplicifolia* was collected in January 2016 at Bogor Botanical Garden, Bogor, West Java Province, Indonesia. The voucher specimen was authenticated by the staff of the Bogoriense Herbarium, Research Centre for Biology, Indonesian Institute of Science, Bogor, Indonesia, and deposited at that herbarium (No. BO-1295311).

Organic solvents such as *n*-hexane, ethyl acetate, methanol, *n*-butanol, methylene chloride, and acetone were purchased from the Kristata Gemilang Company, Bandung in technical quality and distilled. The B16-F10 cell was acquired from American Type Culture Collection (ATCC® CRL-6475™, Manassas, Virginia, USA). The medium used was Dulbecco's Modified Eagle's Medium (DMEM high glucose) (Cat. No. 11965118, Gibco, New York, USA) added with 10% Fetal Bovine Serum (FBS) (Cat. No. 10082147, Gibco) and 1% Penicillin-streptomycin (Cat. No. 15140112, Gibco). Cell incubation was conducted at 37 °C in a 5% CO_2 incubator (Cat. No. 8000DH, Thermo Fisher Scientific, Waltham, Massachusetts, USA).

Instrumentation

The IR spectra were obtained on Perkin Elmer Spectrum 100 FT-IR spectrometer using NaCl plate. The mass spectra were obtained with Waters Q-TOF Xevo mass spectrometer instrument. The NMR spectra were recorded on the JEOL JNM-ECX500R/S1 spectrometer at 500 MHz for ^{1}H and 125 MHz for ^{13}C with TMS as an internal standard. The column chromatography was performed on silica gel 60 (Merck, 70–230 and 230–400 mesh) and octadecyl silane (Fuji Sylisia, 200-400 mesh). The TLC analyses were conducted with TLC silica gel 60 GF_{254} (Merck, 0.25 mm) using various solvent systems, and spot detection was obtained by spraying with 10% H_2SO_4 in EtOH, followed by heating and irradiating under ultraviolet-visible light at wavelength 254 and 365 nm, respectively.

Procedure

Extraction and isolation

A 1.01 kg of dried bark *A. simplicifolia* was extracted with methanol (12 L) at room temperature for 3 d. The methanol extract was evaporated with a rotary evaporator at 40 °C under reduced pressure to yield a residue of the concentrated methanol extract (194.9 g). Then, this residue was dissolved in water and portioned successively with *n*-hexane (10 L), ethyl acetate (10 L), and *n*-butanol (10 L). The evaporated these extracts resulted in *n*-hexane (14.5 g), ethyl acetate (28.0 g), and *n*-butanol (14.5 g), respectively. The ethyl acetate extract (28.0 g) was separated by vacuum liquid chromatography (VLC) on silica gel G60 using a gradient solvent of *n*-hexane-ethyl acetate, 20% gradient, then ethyl acetate-methanol, 10% gradient to give eight fractions (A-H). The E fraction (1.54 g) was column chromatographed on silica gel (70–230 mesh) using an isocratic solvent of *n*-hexane:ethyl acetate (8:2) to yield eleven fractions (E1-E11). Furthermore, the E7 fraction (58.6 mg) was column chromatographed on silica gel (230–400 mesh), eluted with methylene chloride:ethyl acetate (9:1) to give five fractions (E7.A-E7.E). The E7.B fraction (32.7 mg) was column chromatographed on silica gel (230–400 mesh)

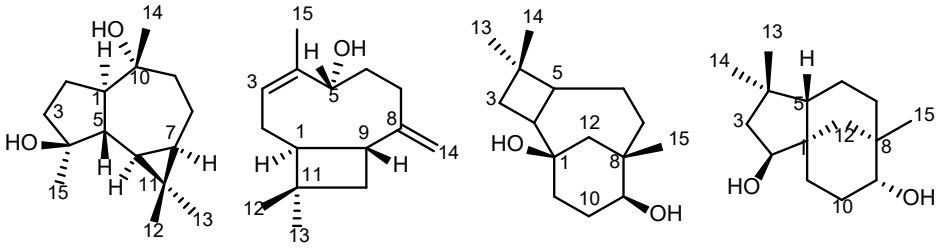

Fig 1. Chemical structures of compounds **1**-**4**

eluted with *n*-hexane:methylene chloride:acetone (2:7.5.0:0.5) to give four fractions (E7.B1-E7.B4). Furthermore, the E7.B3 fraction was column chromatographed on silica gel (230–400 mesh) eluted with *n*-hexane:methylene chloride: acetone (3.0:6.5:0.5) to yield compound **1** (7.8 mg).

The E8 fraction (115.3 mg) was column chromatographed on silica gel (230–400 mesh) using a isocratic elution of *n*-hexane:methylene chloride:acetone (2.0:7.5:0.5) to give three fractions (E8.A-E8.C). The E8.A fraction (30.3 mg) was column chromatographed on silica gel (230–400 mesh) eluted with *n*-hexane:methylene chloride:acetone (2.0:7.5:0.5) to yield compound **2** (5.5 mg). The E8.C fraction (70.3 mg) was column chromatographed on silica gel (230–400 mesh) eluted with *n*-hexane: methylene chloride:ethyl acetate (0.5:9.0:0.5) to give three fractions (E8.C1-E8.C3). Finally, the E8.C1 fraction (50.8 mg) was further column chromatographed on octadecyl silane (ODS) eluted with methanol:water (5:5) to obtained compound **3** (7.4 mg) and compound **4** (4.2 mg).

4β,10α-Dihydroxyaromadendrane (1). Pale yellow oil; $[\alpha]_D^{26.1^\circ}$ -25.0 (c 0.2, $CHCl_3$); IR (NaCl) ν_{max} 3362, 2853, 1456, 1378, and 1054 cm^{-1}; ^{1}H-NMR (acetone-d_6, 500 MHz): δ_H 1.82 (1H, dd, *J* = 10.0, 18.5 Hz, H-1), 1.57 (2H, m, H-2), 1.67 (2H, m, H-3), 1.12 (1H, m, H-5), 0.41 (1H, dd, *J* = 9.5, 11.0 Hz, H-6), 0.56 (1H, dd, *J* = 9.5, 11.0 Hz, H-7), 0.9 (1H, m, H-8a), 2.05 (1H, m, H-8b), 1.57 (1H, m, H-9a), 1.67 (1H, m, H-9b), 0.98 (3H, s, H-12), 0.99 (3H, s, H-13), 1.1 (3H, s, H-14), 1.16 (3H, s, H-15); ^{13}C-NMR (acetone-d_6, 125 MHz) see Table 1. HR-TOFMS *m/z* found 261.1854 $[M+Na]^+$, (calculated for $C_{15}H_{26}O_2Na$, *m/z* 261.1831).

Caryophyllenol-II (2). Pale yellow oil; $[\alpha]_D^{26.1^\circ}$ -54.2 (c 0.2, $CHCl_3$); IR (NaCl) ν_{max} 3362, 3088, 1721, 1613, 1386, 1463, and 1078 cm^{-1}; ^{1}H-NMR (acetone-d_6, 500 MHz) δ_H 2.07 (1H, m, H-1), 1.94 (1H, m, H-2a), 2.17 (1H, m, H-2b), 5.54 (1H, td, *J* = 1.2, 10.2 Hz, H-3), 4.86 (1H, dd, *J* = 4.2, 10.2 Hz, H-5a), 2.67 (1H, q, *J* = 12.6, 10.2 Hz, H-5b), 1.71 (1H, m, H-6), 1.82 (1H, m, H-7a), 1.6 (1H, m, H-7b), 2.33 (1H, m, H-9), 1.68 (1H, m, H-10a), 1.51 (1H, m, H-10b), 1.26 (3H, s, H-12), 1.01 (3H, s, H-13), 4.8 (1H, q, *J* = 2.4 Hz, H-14a), 4.27 (1H, t, *J* = 2.4 Hz, H-14b), 1.02 (3H, s, H-15); ^{13}C-NMR (acetone-d_6, 125 MHz) see Table 1; HR-TOFMS *m/z* found 221.1737 $[M+H]^+$, (calculated for $C_{15}H_{25}O$, *m/z* 221.1702).

Senecrassidiol (3). Pale yellow oil; IR (NaCl) ν_{max} 3369, 2917, 1451, 1378, 1019 cm^{-1}; ^{1}H-NMR ($CDCl_3$, 500 MHz) δ_H 2.18 (1H, t, *J* = 12.0 Hz, H-2), 1.15 (1H, d, *J* = 3.5 Hz, H-2a), 1.13 (1H, d, *J* = 4.0 Hz, H-2b), 1.8 (1H, m, H-5), 1.46 (1H, m, H-6a), 1.33 (1H, m, H-6b), 1.38 (1H, m, H-7a), 1.35 (1H, m, H-7b), 3.44 (1H, t, *J* = 3.0 Hz, H-9), 2.01 (1H, m, H-10a), 1.74 (1H, m, H-10b), 1.61 (1H, d, *J* = 5.0 Hz, H-11a), 1.48 (1H, d, *J* = 3.0 Hz, H-11b), 1.4 (1H, d, *J* = 13.5 Hz, H-12a), 1.13 (1H, d, *J* = 13.5 Hz, H-12b), 1.01 (3H, s, H-13), 1.0 (3H, s, H-14), 0.92 (3H, s, H-15); ^{13}C-NMR ($CDCl_3$, 125 MHz) see Table 1; HR-TOFMS *m/z* found 256.1956 $[M+H_2O]^+$, (calculated for $C_{15}H_{26}O_2$, *m/z* 238.1905).

Clovane-2β,9α-diol (4). Amorphous powder; IR (NaCl) ν_{max} 3340, 2918, 1544, 1416, and 1019 cm^{-1}; ^{1}H-NMR ($CDCl_3$, 500 MHz) δ_H 3.78 (dd, *J* = 10.5, 5.5 Hz, H-2), 1.5 (dd, *J* = 12.0, 10.0 Hz, H-3a), 1.72 (dd, *J* = 12, 5.5 Hz, H-3b), 1.41 (1H, m, H-5), 1.43 (1H, m, H-6a), 1.31 (1H, m, H-6b), 1.35 (1H, m, H-7a), 1.09 (1H, m, H-7b), 3.31 (br s, H-9), 1.99 (1H, m, H-10a), 1.61 (1H, m, H-10b), 1.66 (1H, m, H-11a), 1.08 (1H, m, H-11b), 0.9 (br d, *J* = 12.5 Hz, H-12a), 1.54 (d, *J* = 12.5 Hz, H-12b), 0.85 (3H, s, H-13), 1.03 (3H, s, H-14), 0.95 (3H, s, H-15); ^{13}C-NMR

Table 1. ^{13}C-NMR data of compound **1**-**4**

Position carbon	Compounds			
	1*	2*	3**	4**
	δ_C (mult.)	δ_C (mult.)	δ_C (mult.)	δ_C (mult.)
1	56.8 (d)	50.2 (d)	70.8 (s)	44.2 (s)
2	23.9 (t)	27.5 (t)	38.1 (d)	80.9 (d)
3	41.3 (t)	127.0 (d)	33.5 (t)	47.5 (t)
4	79.2 (s)	137.4 (s)	35.2 (s)	37.1 (s)
5	48.0 (d)	69.9 (d)	43.9 (d)	50.4 (d)
6	28.2 (d)	34.4 (t)	20.4 (t)	20.6 (t)
7	26.6 (d)	31.0 (t)	42.5 (t)	33.1 (t)
8	20.1 (t)	154.5 (s)	39.4 (s)	34.7 (s)
9	44.7 (t)	42.7 (d)	72.3 (d)	75.0 (d)
10	73.5 (s)	41.8 (t)	28.2 (t)	26.0 (t)
11	19.2 (s)	33.6 (s)	35.4 (t)	26.3 (t)
12	15.9 (q)	23.1 (q)	34.1 (t)	35.5 (t)
13	29.7 (q)	31.2 (q)	20.9 (q)	25.4 (q)
14	19.8 (q)	110.57 (t)	30.6 (q)	31.4 (q)
15	24.0 (q)	16.7 (q)	26.7 (q)	28.3 (q)

(* Measured in acetone-d_6)
(** Measured in $CDCl_3$)

($CDCl_3$, 125 MHz) see Table 2; HR-TOFMS *m/z* found 221.2009 $[M+H]^+$, (calculated for $C_{15}H_{26}O_2$, *m/z* 220.2011).

Cytotoxic activity assay

Cell viability was assessed with Presto Blue reagent (Thermo Fisher Scientific, Uppsala, Sweden) to evaluate various resazurin-based cell types' viability rapidly and quantitatively proliferation using live-cell reduction capabilities. When cells are alive and healthy, they maintain a reduced environment in their cytosol. Reducing resazurin (blue) works as a cell viability indicator by using absorbance or fluorescent outputs to reduce resorufin (purple). The conversion is proportional to the number of metabolically active cells. Briefly, B16-F10 cell lines were grown in 70% confluent were harvested and counted, then diluted with complete culture RPMI medium. The cells then were transferred into 96 well-plates with a total of 170,000 cells/well. After overnight growth, the cells were treated with increasing concentrations of compounds **1**-**4** (3.91, 7.81, 15.63, 31.25, 62.50, 125, 250, 5,000 ppm) with co-solvent 2% (v/v) DMSO in PBS. Cisplatin was used as the positive control. All samples were incubated at 37 °C in a 5% CO_2 incubator for 24 h. After incubation, the medium was immediately replaced by 10 µL PrestoBlue reagent in a 90 µL RPMI medium. The plates were incubated for 1–2 h until resorufin was formed (color changes from blue to purple). The absorbance was measured at 570 nm using a microplate reader. The IC_{50} value is the concentration for 50% growth inhibition. The percentage of cytotoxicity compared to untreated cells was determined with the equation given below. A plot of % cytotoxicity versus sample concentrations was used to calculate the concentration, which showed 50% cytotoxicity (IC_{50}) [17-18]. All assay and analyses were each run in duplicate, and all were averaged.

■ RESULTS AND DISCUSSION

The ethyl acetate extract of the stem bark of *A. simplicifolia* was subjected to repeated column chromatography to afford four sesquiterpenoids, **1**-**4** (Fig. 1). Compound **1** was obtained as a pale yellow oil. The molecular formula was established with HR-TOF-MS as $C_{15}H_{26}O_2$ from the molecular ion peak of 261.1854 ($[M+Na]^+$ calculated for $C_{15}H_{26}O_2Na$ *m/z* 261.1831 in the HR-TOF-MS (Fig. S1), indicating three degrees of

unsaturation. The IR spectrum (Fig. S2) showed the absorption band of the hydroxyl group (3362 cm^{-1}), C–H stretching of aliphatics (2959 and 2853 cm^{-1}), *gem*-dimethyl (1456 and 1378 cm^{-1}), and C–O stretching (1054 cm^{-1}). The ^{1}H-NMR spectrum (Fig. S3) showed the presence of four tertiary methyls at δ_H 0.98 (CH_3-12), 0.99 (CH_3-13), 1.07 (CH_3-14), and 1.16 ppm (CH_3-15). The ^{13}C-NMR spectrum (Fig. S4) showed fifteen carbon signals classified by their chemical shifts and DEPT spectra as four methyls, four methylenes, four methines, and three quaternary carbons (including two oxygenated quaternary carbon). Two oxygenated quaternary carbons were bound with the hydroxyl group, marked with a more deshielded chemical shift value [19]. Based on the type of carbon in compound **1**, there are no double bonds, so three degrees of unsaturation originated from the tricyclic sesquiterpenoid framework, namely aromadendrane-type sesquiterpenoid. The specific characteristic of aromadendrane-type sesquiterpenoid is the presence of a *gem*-dimethyl cyclopropane ring marked with one quaternary carbon at δ_C 19.2 ppm. Based on the data spectrum ^{1}H-NMR, ^{13}C-NMR, DEPT 135°, optical rotation, and agreed with the literature, compound **1** was determined as the known compound 4β,10α-dihydroxyaromadendrane, that was reported for the first time from *A. Simplicifolia*.

Compound **2** was obtained in a pale yellow oil. The molecular formula was established with HR-TOF-MS as $C_{15}H_{24}O$ from the molecular ion peak of 221.1737 ($[M+H]^+$ calculated for $C_{15}H_{25}O$, *m/z* 221.1702 in the HR-TOF-MS (Fig. S5), indicating four degrees of unsaturation. IR spectrum (Fig. S6) showed the absorption band of the hydroxyl group (3362 cm^{-1}), C–H sp^2 (3088 cm^{-1}), *gem*-dimethyl (1386 and 1463 cm^{-1}), C=C double bonds (1721 and 1613 cm^{-1}), and C–O stretching (1078 cm^{-1}). The ^{1}H-NMR spectrum (Fig. S7) showed the presence of three tertiary methyls at δ_H 1.01 (CH_3-13), 1.02 (CH_3-15), and 1.26 (CH_3-12). The ^{13}C-NMR spectrum (Fig. S8) showed fifteen carbon signals classified based on their chemical shifts and DEPT spectra as three methyls, four methylenes, two methines, one quaternary carbon, four olefinic carbons (including two quaternary carbon, one methylene, and one oxygenated methine. Based on the type of carbon in compound **2**, there are four degrees of unsaturation originating from two double bonds and bicyclic sesquiterpenoid framework, namely caryophyllene-type sesquiterpenoid. Based on the data spectrum ^{1}H-NMR, ^{13}C-NMR, DEPT 135°, optical rotation, and agreed with the literature, compound **2** was determined as the known compound caryophyllenol-II.

Compound **3** was obtained as pale yellow oil. The molecular formula was established with HR-TOF-MS as $C_{15}H_{26}O_2$ from the molecular ion peak of 256.1956 ($[M-H_2O]^+$ calculated for $C_{15}H_{26}O_2$, *m/z* 238.1905) in the HR-TOF-MS (Fig. S9), indicating three degrees of unsaturation. The IR spectrum (Fig. S10) showed the absorption band of the hydroxyl group (3369 cm^{-1}), C–H sp^3 (2917 cm^{-1}), *gem*-dimethyl (1451 and 1378 cm^{-1}), and C–O stretching (1019 cm^{-1}). The ^{1}H-NMR spectrum (Fig. S11) showed the presence of three tertiary methyls at δ_H 0.92 (CH_3-15), 1.0 (CH_3-14), and 1.01 (CH_3-13). An oxygenated methine proton signal at δ_H 3.44 ppm (1H, t, J = 3.0 Hz) was also observed in the ^{1}H-NMR spectrum. The ^{13}C-NMR (Fig. S12) spectrum showed fifteen carbon signals classified by their chemical shifts and DEPT spectra as three methyls, six methylenes, four methines (including one oxygenated methine), and two quaternary carbons. Based on the type of carbon in compound **3**, there are three degrees of unsaturation originating from the tricyclic sesquiterpenoid framework, namely caryolane-type sesquiterpenoid with specific characteristic is β-methano bridge between two quaternary carbons C-1 and C-8. Based on the data spectrum ^{1}H-NMR, ^{13}C-NMR, DEPT 135°, optical rotation, and agreed with the literature, compound **3** was determined as the known compound caryolan-1,9-diol known as a senecrassidiol.

Compound **4** was obtained as an amorphous powder. The molecular formula was established with HR-TOF-MS as $C_{15}H_{26}O_2$ from the molecular ion peak of 221.2009 ($[M+H]^+$ calculated for $C_{15}H_{26}O_2$ *m/z* 220.2011 in the HR-TOF-MS (Fig. S13), indicating three degrees of unsaturation. The IR spectrum (Fig. S14), showed the absorption band of the hydroxyl group (3340 cm^{-1}), C–H stretching of aliphatics (2918 and 2850 cm^{-1}), *gem*-

dimethyl (1544 and 1416 cm^{-1}), and C–O stretching (1015 cm^{-1}). The ^{1}H-NMR spectrum (Fig. S15), showed the presence of three tertiary methyls at δ_H 0.85 (CH_3-13), 1.02 (CH_3-14), and 0.95 (CH_3-15). In addition, two oxygenated methine proton signals were observed at δ_H 3.31 (1H, m) and δ_H 3.77 (1H, m). The DEPT and HMQC experiments (Fig. S17-S18), could differentiate the 15 atoms of carbon in the ^{13}C-NMR (Fig. S16) into three methyls, six methylenes, three methines (including two oxygenated methine carbons), and three quaternary carbons. The type of carbon in compound **4** shows no double bonds, so it has three degrees of unsaturation originating from the tricyclic sesquiterpenoid framework. The remaining three degrees of unsaturation were consistent with clovane-type sesquiterpenoid skeleton [20].

The position of functional groups in compound **4** was clarified from the ^{1}H-^{1}H COSY and HMBC experiments, and the results are shown in Fig. 2. The ^{1}H-^{1}H COSY spectrum of **4** (Fig. S19) showed correlations in H_2-H_3, H_5-H_6-H_7, and H_9-H_{10}-H_{11}, supporting the presence of rings A, B, and C in the clovane-type sesquiterpenoid skeleton. The skeleton of clovane-type sesquiterpenoid was determined by HMBC correlation (Fig. S20) of tertiary methyls. The correlations of CH_3-13 (δ_H 0.85) to C-14 (δ_C 31.44), C-4 (δ_C 37.14), C-5 (δ_C 50.42), and C-3 (δ_C 47.54) and correlation of CH_3-14 (δ_H 1.02) to C-13 (δ_C 25.42), C-4 (δ_C 37.14), C-5 (δ_C 50.42), and C-3 (δ_C 47.54), showed that C-13 and C-14 are *gem*-dimethyl groups attached to C-4 quaternary carbon. The correlations of methylene protons at δ_H 1.50 and 1.72 (H-3) to C-2 (δ_C 80.91), C-1 (δ_C 44.19), C-4 (δ_C 37.14), and C-5 (δ_C 50.42), whereas an oxygenated proton at δ_H 3.78 (H-2) was correlated to C-12 (δ_C 35.51), indicated that the partial structure of **4** contains cyclopentane ring at C-1, C-2, C-3, C-4, and C-5 with the presence of hydroxyl group located in C-2. The other methyl group was determined by the strong correlation between CH_3-15 (δ_H 0.95) to C-7 (δ_C 33.11), C-9 (δ_C 75.07), and C-12 (δ_C 35.51) showed that C-15 attached to C-8 of quaternary carbon. In addition, the correlation of another oxygenated proton at δ_H 3.31 (H-9) to C-11 and C-12 and supported by the correlation of δ_H 1.35 (H-7) to C-9 (δ_C 75.07) and δ_H 1.61 (H-10) to C-9 (δ_C 75.07). This correlation indicated that the hydroxyl group was located in C-9. Furthermore, a correlation between protons at δ_H 1.54 (H-12) to C-5, C-1, C-7, C-8, and C-11 indicated the location of C-12 between two quaternary carbons C-1 and C-8, which connected the ring B and C to form the skeleton of the bicyclononane bridge. The relative stereochemistry of compound **4** was supported by NOESY correlations (Fig. S21). The results displayed that correlation of H-5 (β-oriented) with CH_3-13, and methylene proton oxygenated H-2 (α-oriented) with CH_3-14 suggested CH_3-13 was β-oriented while CH_3-14 was α-oriented, whereas hydroxyl group at C-2 was β-oriented. The correlations of H-5 (β-oriented) with H-10, and H-10 (β-oriented) with oxygenated methylene proton (H-9), proposed that H-9 was β-oriented and the other hydroxyl group at C-9 was α–oriented (Fig. 2). The detailed examination of the NMR spectral data and comparison with those reported for c lovane-2β,9α-diol [21] showed that the structures of these two compounds are very similar. Compound **2** was isolated for the first time in genus *Aglaia*. Therefore, the structure of compound **4** was identified as a clovane-2β,9α-diol.

The cytotoxic activities of the isolated compounds **1**-**4** were evaluated against the B16-F10 melanoma skin cancer cell lines according to a method described [22]. Cisplatin (12.9 μg/mL) was used as a positive control.

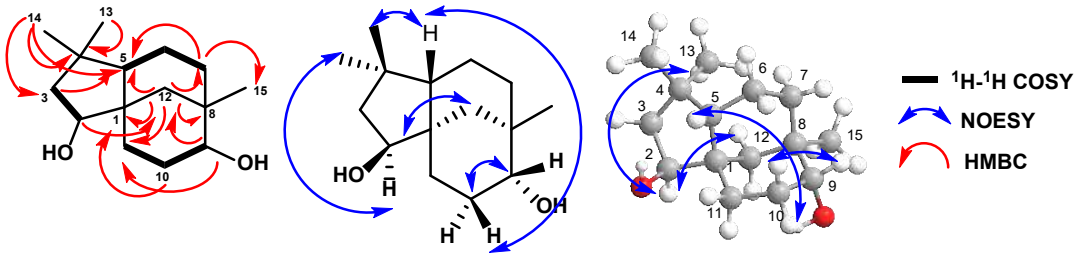

Fig 2. Selected HMBC, ^{1}H-^{1}H-COSY, and NOESY correlations of compound **4**

Table 2. Cytotoxic activity of compound **1**-**3** against B16-F10 melanoma skin cancer cell lines

Compounds	IC_{50} (μg/mL)
4β,10α-dihydroxyaromadendrane (**1**)	44.8
Caryophyllenol-ii (**2**)	483.2
Senecrassidiol (**3**)	327.6
Clovane-2β,9α-diol (**4**)	176.6
Cisplatin (+)	12.9

The results are shown in Table 2. Among all sesquiterpenoid compounds, 4β,10α-dihydroxyaroma dendrane (**1**) showed the strongest cytotoxic activity with IC_{50} values of 44.8 μg/mL, while compound (**2**) showed the lowest activity with an IC_{50} value of 483.2 μg/mL. This result shows that the value of cytotoxic activity against B16-F10 melanoma skin cancer cells is influenced by the presence of a cyclopropane ring and α-oriented hydroxyl group. The cyclopropane ring and hydroxyl group can increase cytotoxic activity. The 4β,10α-dihydroxy aromadendrene compound from the stem bark of *Aglaia harmsiana* can inhibit the growth of MCF-7 breast cancer cells with an IC_{50} value of 8.4 μM [3]. At the same time, the presence of an olefinic group in compound (**2**) decreases the cytotoxic activity. These results indicated that the cytotoxic activity of sesquiterpenoids is affected by the presence of a cyclopropane ring and α-oriented hydroxyl group that plays an important role in cytotoxic activity.

■ CONCLUSION

Four type sesquiterpenoid compounds, 4β,10α-dihydroxyaromadendrane (**1**), caryophylenol-II (**2**), senecrassidiol (**3**), and clovane-2β,9α-diol (**4**) were isolated from ethyl acetate extract of the stem bark of *A. simplicifolia*. Compound (**1**) was reported from *A. simplicifolia* for the first time, while compound (**4**) itself was isolated from genus *Aglaia* for the first time. Compounds **1**-**4** were evaluated for their cytotoxic activity against B16-F10 melanoma skin cancer cell lines. Among the sesquiterpenoids, compound (**1**) showed the strongest cytotoxic activity with IC_{50} values 44.8 μg/mL, while compound (**2**) showed the lowest activity. These results indicated that the cytotoxic activity of sesquiterpenoids is affected by the presence of a cyclopropane ring and α-oriented hydroxyl group that plays an important role in cytotoxic activity.

■ ACKNOWLEDGMENTS

This research was financially supported by the Ministry of Education and Culture, Innovative and Research Council, Indonesia, Higher Education Basic Research Grant, No. 1207/UN6.3.1/PT.00/2021 by Desi Harneti and Academic Leadership Grant from Universitas Padjadjaran, Indonesia (No: 1959/UN6.3.1/PT.00/2021) by Unang Supratman.

■ REFERENCES

[1] Çelik, K., Toğar, B., Türkez, H., and Taşpinar, N., 2014, *In vitro* cytotoxic, genotoxic, and oxidative effect of acyclic sesquiterpene farnesene, *Turk. J. Biol.*, 38, 253–259.

[2] Jaeger, R., and Cuny, E., 2016, Terpenoids with special pharmacological significance: A review, *Nat. Prod. Commun.*, 11 (9), 1373–1390.

[3] Milawati, H., Sukmawati, W., Harneti, D., Maharani, R., Nurlelasari, N., Hidayat, A.T., Darwati, D., Supratman, U., and Shiono, Y., 2020, Cytotoxic sesquiterpenoids from the stem bark of *Aglaia harmsiana* (Meliaceae), *Indones. J. Chem.*, 20 (6), 1448–1454.

[4] Degenhardt, J., Köllner, T.G., and Gershenzon, J., 2009, Monoterpene and sesquiterpene synthases and the origin of terpene skeletal diversity in plants, *Phytochemistry*, 70 (15-16), 1621–1637.

[5] Gong, D.Y., Chen, X.Y., Guo, S.X., Wang, B.C., and Li, B., 2021, Recent advances and new insights in biosynthesis of dendrobine and sesquiterpenes, *Appl. Microbiol. Biotechnol.*, 105 (18), 6597–6606.

[6] Jeena, K., Liju, V., and Kuttan, R., 2013, Antioxidant, anti-inflammatory and antinociceptive activities of essential oil from ginger, *Indian J. Physiol. Pharmacol.*, 57 (1), 51–62.

[7] Ishnava, K.B., Chauhan, J.B., and Barad, M.B., 2013, Anticariogenic and phytochemical evaluation of *Eucalyptus globulus* Labill., *Saudi J. Biol. Sci.*, 20 (1), 69–74.

[8] Ornano, L., Venditti, A., Ballero, M., Sanna, C., Quassinti, L., Bramucci, M., Lupidi, G., Papa, F.,

Vittori, S., Maggi, F., and Bianco, A., 2013, Chemopreventive and antioxidant activity of the chamazulene-rich essential oil obtained from *Artemisia arborescens* L. growing on the Isle of La Maddalena, Sardinia, Italy, *Chem. Biodivers.*, 10 (8), 1464–1474.

[9] Feraz, R.P.C., Cardozo, G.M.B., da Silva T.B., Fontes, J.E.N., Prata, A.P.N., Carvalho, A.A., Moraes, M.O., Pessoa, C., Costa, E.V., and Bezerra, D.P., 2013, Antitumour properties of the leaf essential oil of *Xylopia frutescens* Aubl. (Annonaceae), *Food Chem.*, 141 (1), 196–200.

[10] Park, K.R., Nam, D., Hun, H.M., Le, S.G., Jang, H.J., Sethi, G., Cho, S.K., and Ahn, K.S., 2011, β-Caryophyllene oxide inhibits growth and induces apoptosis through the suppression of PI3K/AKT/mTOR/S6K1 pathways and ROS-mediated MAPKs activation, *Cancer Lett.*, 312 (2), 178–88

[11] Awouafack, M.D., Tane, P., Kuete, V., and Eloff, J.N., 2013, "Sesquiterpenes from the medicinal plants of Africa" in *Medicinal Plant Research in Africa*, Eds. Kuete, V., Elsevier, Oxford, 33–103.

[12] Milawati, H., Harneti, D., Maharani, R., Nurlelasari, N., Hidayat, A.T., Azmi, M.N., Shiono, Y., and Supratman, U., 2019, Caryophyllene-type sesquiterpenoids from the stembark of *Aglaia harmsiana* and their cytotoxic activity against MCF-7 breast cancer cells, *Molekul*, 14 (2), 126–132.

[13] Harneti, D., and Supratman, U., 2021, Phytochemistry and biological activities of *Aglaia* species, *Phytochemistry*, 181, 112540.

[14] Sianturi, J., Purnamasari, M., Darwati, Harneti, D., Mayanti, D., Supratman, U., Awang, K., and Hayashi, H., 2015, New bisamide compounds from the bark of *Aglaia eximia* (Meliaceae), *Phytochem. Lett.*, 13, 297–301.

[15] Kurniasih, N., Supriadin, A., Harneti, D., Abdulah, R., Mohamad Taib, M.N.A., and Supratman, U., 2021, Ergosterol peroxide and stigmasterol from the stembark of *Aglaia simplicifolia* (Meliaceae) and their cytotoxic against HeLa cervical cancer cell lines, *J. Kim. Valensi*, 7 (1), 46–51.

[16] Kurniasih, N., Supriadin, A., Fajar, M., Abdulah, R., Harneti, D., Supratman, U., and Mohamad Taib, M.N.A., 2019, Cytotoxic sesquiterpenoid compound from the stembark of *Aglaia simplicifolia* (Meliaceae), *J. Phys.: Conf. Ser.*, 1402 (5), 055037.

[17] Camarillo, I.G., Xiao, F., Madhivanan, S., Salameh, T., Nichols, M., Reece, L.M., Leary, J.F., Otto, K.J., Natarajan, A., Ramesh, A., and Sundararajan, R., 2014, "Low and High Voltage Electrochemotherapy for Breast Cancer: An *in vitro* Model Study" in *Electroporation-Based Therapies for Cancer*, Eds. Sundararajan, R., Woodhead Publishing, Cambridge, UK, 55–102.

[18] Machana, S., Weerapreeyakul, N., Barusrux, S., Nonpunya, A., Sripanidkulchai, B., and Thitimetharoch, T., 2011, Cytotoxic and apoptotic effect of six herbal plants against the human hepatocarcinoma (HepG2) cell line, *Chin. Med.*, 6 (1), 39.

[19] Moreira, I.C., Lago, J.H., Young, M.C.M., and Roque, N.F., 2003, Antifungal aromadendrane sesquiterpenoids from the leaves of *Xylopia brasiliensis*, *J. Braz. Chem. Soc.*, 14, 828–831.

[20] Le Bideau, F., Kousara, M., Chen, L., Wei, L., and Dumas, F., 2017, Tricyclic sesquiterpenes from marine origin, *Chem. Rev.*, 117 (9), 6110–6159.

[21] Chang, Y.C., Chiang, C.C., Chang, Y.S., Chen, J.J., Wang, W.H., Fang, L.S., Chung, H.M., Hwang, T.L., and Sung, P.J., 2020, Novel caryophyllane-related sesquiterpenoids with anti-inflammatory activity from *Rumphella antipathes* (Linnaeus, 1758), *Mar. Drugs*, 18 (11), 554.

[22] Xu, M., McCanna, D.J., and Sivak, J.G., 2015, Use the viability reagent PrestoBlue in comparison with alamarBlue and MTT to assess the viability of human corneal epithelial cells, *J. Pharmacol. Toxicol. Methods*, 71, 1–7.